frontiers | Research Topics

From preparation to faulting: Multidisciplinary investigations on earthquake processes

Edited by
Fuqiong Huang, Huajian Yao, Jie Liu, Hongfeng Yang and Giovanni Martinelli

Published in
Frontiers in Earth Science

ISSN 1664-8714
ISBN 978-2-8325-2751-1
DOI 10.3389/978-2-8325-2751-1

About Frontiers

Frontiers is more than just an open access publisher of scholarly articles: it is a pioneering approach to the world of academia, radically improving the way scholarly research is managed. The grand vision of Frontiers is a world where all people have an equal opportunity to seek, share and generate knowledge. Frontiers provides immediate and permanent online open access to all its publications, but this alone is not enough to realize our grand goals.

Frontiers journal series

The Frontiers journal series is a multi-tier and interdisciplinary set of open-access, online journals, promising a paradigm shift from the current review, selection and dissemination processes in academic publishing. All Frontiers journals are driven by researchers for researchers; therefore, they constitute a service to the scholarly community. At the same time, the *Frontiers journal series* operates on a revolutionary invention, the tiered publishing system, initially addressing specific communities of scholars, and gradually climbing up to broader public understanding, thus serving the interests of the lay society, too.

Dedication to quality

Each Frontiers article is a landmark of the highest quality, thanks to genuinely collaborative interactions between authors and review editors, who include some of the world's best academicians. Research must be certified by peers before entering a stream of knowledge that may eventually reach the public - and shape society; therefore, Frontiers only applies the most rigorous and unbiased reviews. Frontiers revolutionizes research publishing by freely delivering the most outstanding research, evaluated with no bias from both the academic and social point of view. By applying the most advanced information technologies, Frontiers is catapulting scholarly publishing into a new generation.

What are Frontiers Research Topics?

Frontiers Research Topics are very popular trademarks of the *Frontiers journals series*: they are collections of at least ten articles, all centered on a particular subject. With their unique mix of varied contributions from Original Research to Review Articles, Frontiers Research Topics unify the most influential researchers, the latest key findings and historical advances in a hot research area.

Find out more on how to host your own Frontiers Research Topic or contribute to one as an author by contacting the Frontiers editorial office: frontiersin.org/about/contact

From preparation to faulting: Multidisciplinary investigations on earthquake processes

Topic editors

Fuqiong Huang — China Earthquake Networks Center, China
Huajian Yao — University of Science and Technology of China, China
Jie Liu — Sun Yat-sen University, Zhuhai Campus, China
Hongfeng Yang — The Chinese University of Hong Kong, China
Giovanni Martinelli — National Institute of Geophysics and Volcanology, Italy

Citation

Huang, F., Yao, H., Liu, J., Yang, H., Martinelli, G., eds. (2023). *From preparation to faulting: Multidisciplinary investigations on earthquake processes*. Lausanne: Frontiers Media SA. doi: 10.3389/978-2-8325-2751-1

Table of contents

frontiers | Frontiers in Earth Science

TYPE Editorial
PUBLISHED 06 June 2023
DOI 10.3389/feart.2023.1220232

OPEN ACCESS

EDITED AND REVIEWED BY
Jeroen Van Hunen,
Durham University, United Kingdom

*CORRESPONDENCE
Fuqiong Huang,
hfqiong@seis.ac.cn
Giovanni Martinelli,
Giovanni.martinelli15@gmail.com

RECEIVED 10 May 2023
ACCEPTED 30 May 2023
PUBLISHED 06 June 2023

CITATION
Huang F, Yao H, Liu J, Yang H and Martinelli G (2023), Editorial: From preparation to faulting: multidisciplinary investigations on earthquake processes. *Front. Earth Sci.* 11:1220232. doi: 10.3389/feart.2023.1220232

Editorial: From preparation to faulting: multidisciplinary investigations on earthquake processes

Fuqiong Huang[1,2,3]*, Huajian Yao[4], Jie Liu[5], Hongfeng Yang[6] and Giovanni Martinelli[7,8]*

[1]China Earthquake Networks Center, Beijing, China, [2]Institute of Disaster Prevention, Beijing, China, [3]North China Institute of Science and Technology, Beijing, China, [4]Laboratory of Seismology and Physics of Earth's Interior, School of Earth and Space Science, University of Science and Technology of China, Hefei, Anhui, China, [5]School of Earth Sciences and Engineering, Sun Yat-sen University, Zhuhai, Guangdong, China, [6]Earth System Science Programme, The Chinese University of Hong Kong, Hong Kong, China, [7]INGV National Institute of Geophysics and Volcanology, Palermo, Italy, [8]Institute of Eco-Environment and Resources, Chinese Academy of Sciences, Lanzhou, China

KEYWORDS

earthquake preparation process, physics of earthquake sources, evidence for risk evaluation and forecasting, monitoring systems of networks, multidisciplinary approaches

Editorial on the Research Topic
From preparation to faulting: multidisciplinary investigations on earthquake processes

1 Aims and content of this research topic

In seismically active areas (e.g., Han et al., 2022), the best way for disaster mitigation is to enhance the skills of risk evaluation and prediction (Shao et al., 2023). What happens before an earthquake occurs? Which are the physical processes that take place in the Earth's crust before the earthquake nucleates? How can we observe, describe, and model them statistically, numerically, and physically in multi-scales from laboratory samples to tectonic earth plates? Those questions are fundamental but have not been completely solved (Geller, 1997; Pritchard, et al., 2020).

Over the last few decades multidisciplinary studies have attempted to answer these fundamental questions (e.g., King, 1978; Ma, 1987; Kanamori and Brodsky, 2001). In the early days, the Institute Physics of the Earth (IPE) model (dry) (Myachkin et al., 1975) and the Dilatance Diffusion (DD) model (wet) (Scholz et al., 1973) were proposed for earthquake processes. Like Schrödinger's cat, an earthquake is unpredictable—according to the IPE model, yet it can be predictable—according to the DD model (Ma, 1987). Recently, with advanced techniques, some scientists have discovered the meta-instable stage before failure to slip (Ma et al., 2012) and assuredly claimed that there are precursors to be used for earthquake forecasting (Ma, 2016), which envisages new opportunities to study earthquake precursors (Pritchard, et al., 2020).

An understanding of the governing laws (e.g., King, 1978; Zöller et al., 2010; Shi et al., 2020; Chen et al., 2022), from long-term tectonic loading (Zhang et al., 2022) and nucleation

to rapid rupture propagation (Yang et al., 2022), is significant to earthquake forecasting and demands a comprehension of the stress state and evolution during the time of geophysical observations around seismically active areas (Zhao et al., 2020; Zhao et al., 2022). The evidence from multiscale experiments (Ma and Guo, 2014; Huang et al., 2019; Huang et al., 2020; Martinelli et al., 2020), multidisciplinary monitoring system networks (Huang FQ. et al., 2017; Martinelli et al., 2021), numerical modeling (Barbot et al., 2012; Huang FQ. et al., 2017; Ben-Zion, 2017), and field investigations (e.g., King, 1978), are the keys to advance our understanding of earthquake mechanics.

Earthquakes do not occur everywhere. Fault geometry and the physical properties of fault zones (namely, seismogenic structure), geological and tectonic settings (Wang et al., 2014; Dascher-Cousineau et al., 2020; Gong et al., 2020), as well as crustal movement and the geodynamic environment, play pivotal roles in the seismic patterns (e.g., King, 1978; Ikeda, 2009; Luo et al., 2023). A variety of geophysical and geochemical observations, ranging from ground-related deformation patterns (GPS, SAR, *etc.*) (Bürgmann et al., 2000; Zhao et al., 2020) to pre-earthquake changes (geochemical, electromagnetic, hydro-geological, geodetic, or thermodynamic) (Huang F. Q. et al., 2017; Zhou et al., 2020; Chen et al., 2021; Martinelli et al., 2021; Zhou et al., 2021), recorded by ground-based (Li et al., 2022) or satellite-based techniques (Li et al., 2020) may be related to stress variations in the lithosphere (Luo et al., 2023) prior to an eventual large earthquake (Zhao et al., 2022). Even though much effort has been invested, the earthquake "elephant in the room" is still in the process of being understood.

This Research Topic aims to provide state-of-the-art studies on earthquake processes via multidisciplinary approaches from geophysical, geochemical, geodetical, and geological routines which are mostly exchanged at the annual conference of the China Earthquake Prediction Forum (Huang et al., 2023). Pre-earthquake observations, methods, and perspectives, can provide a current view in the knowledge of processes preceding earthquake occurrence in China, which can be possibly employed to set up earthquake forecasting experiments, aimed at their verification Test Site areas, whether large or small.

2 Overview on published contributions

There are eleven articles collected for this Research Topic, involving precursors of monitoring networks and earthquake prediction methods (four articles), stress state of the geodynamic environment inferred from recent earthquakes (two articles), seismogenic structure and fault geometry from deep to surface (four articles) and models for earthquake risk assessment of the National Test site (one article).

2.1 Precursors of monitoring networks and earthquake prediction method

Extracting anomalous changes relevant to earthquake processes from observation systems is the key step to routine earthquake prediction. Here we have collected one article based on laboratory work that involves judging rock instability by enhanced LURR (short-term to imminent before "earthquakes," by Zhang et al., *The evolution characteristics of rock fracture instability under cyclic loading on the basis of the enhanced LURR*), and three articles involving the extraction of anomalous changes before strong earthquakes on the China Mainland from seismograph observation systems from the long-term to the short-term stage. Frequency field (Luo et al., *Pre-quake frequency characteristics of Ms ≥7.0 earthquakes in mainland China*), b-value (Bi et al., *Strong aftershocks traffic light system: A case study of the 8 January 2022 MS6.9 Menyuan earthquake, Qinghai Province, China*) and anomalous quiet or enhanced processes of small to moderate earthquakes before the strong earthquakes (Gao et al., *Low-intensity anomaly involving ML≥4 events preceding strong earthquakes in Tibet*) are the main items to be discussed.

2.2 Stress state of the geodynamic environment inferred from recent earthquakes

Stress state is significant for the geodynamic environment of seismic source. The measurement of *in situ* stress state is quite difficult. Inference from existing earthquake sequences is an effective way. The article entitled *Seismogenic structures and spatiotemporal seismicity patterns of the 2022 Ms6.0 Maerkang earthquake sequence, Sichuan, China* (Feng et al.) investigates the seismogenic structures and mechanics of this sequence by relocating the earthquake sequence, inverting for the focal mechanisms, and calculating the rupture directivity of the Maerkang earthquake sequence. The paper of *Eastward expansion of the Tibetan plateau: Insights from stress drops of the 2021 Ms 6.4 Yangbi, Yunnan and Ms7.4 Maduo, Qinghai earthquake sequences in China* (He et al.) estimates the stress drops of the Yangbi and Maduo earthquake sequences for all M ≥ 3.0 events from the Lg-wave spectra. The results of the stress drops of two sequences are very likely linked with patterns of crustal motion and deformation in the eastern Tibetan Plateau.

2.3 Deep to surface seismogenic structure and fault geometry

Geometry and movement are the main objectives, which can be used in prediction models. We collected four articles investigating the deep to surface seismogenic structure and fault geometry, which deal with inference from seismic waves of natural earthquakes, active seismic sources or ambient noise (Li et al., *High resolution upper crustal velocity and seismogenic structure of the Huoshan "seismic window" in the Dabie orogenic belt*), and from electric resistivity of the mass beneath the earth surface (Yan et al., *Deep electrical structure of the hinterland of Yunkai magmatic arc in South China and the seismogenic environment of the 2019 Beiliu earthquake*), from relocations of earthquake sequences observed in a permanent station and portable dense array (Zeng et al., *Investigation of the 2015 Ms5. 8 Alxa Left Banner earthquake sequence: Aftershock evolution*

and seismogenic structure by here), as well as from field investigations of surface fault trace in detail (Ma et al., *Active faulting of the Nanhe fault and relation to the Anninghe Fault Zone in late Quaternary, eastern Tibetan plateau*).

2.4 Models for earthquake risk assessment of national test site

The straightforward dedicated models are significant for earthquake risk assessment (Zhang et al. *Statistical evaluation of earthquake forecast efficiency using earthquake-catalog and fault slip rate in the Sichuan-Yunnan region, China*). The works indicate that the model-driven and hyper-parameter controlled mode is a promising approach to implement operational earthquake forecasting at the National Test site of China.

All the above progress is based on advanced observation techniques and monitoring systems from ground to space currently operated in China.

3 Discussion and perspectives

3.1 The physical nature of the empirical operation routine for earthquake prediction

Since the 1966 Xingtai earthquake, routine prediction operations have been practiced continuously in China. The progress was named as a step-by-step strategy from long-term, medium-term, short-term to imminent relevant to ≤10 years, 1–3 years, 3 months to 1 year and days to 3 months respectively, which were summed from an operational process of empirical earthquake prediction activities (Ma et al., 1989) and tested *a posteriori* by experiments of tectonophysics (Ma, 2016). Here in this volume, the works of Luo et al., Gao et al., Bi et al. provide practical evidence to support the results from tectonophysics experiments, the works of Zhang et al. provided new kind of criteria to judge the meta-instable stage. How to transfer the empirical operation routine into a physical operation process may be a prospective road guiding to physical earthquake predictions in numerical modelling.

3.2 How to use engineering disaster events to understand the physics of natural earthquakes calls for further investigation

Stress state and focal mechanisms supply a wide view with which to understand the nature of the earthquake process. In practice, events with a depth of within 5 km are generally considered as events induced by human activities, e.g., mining exploration and reservoir pounding, and so on. Thus, the significance of shallow earthquakes, namely, "engineering disaster events," is overlooked. No matter how deep the event occurs, the stress state is the main factor to understand the physics of rock failure and fault slip in nature (Chen et al., 2022). Research into the stress state and the geodynamic environment from shallow to deep is welcome in the future, being useful to understand the unified nature of earthquakes.

3.3 What controls the precursor patterns for different earthquake relevant to earthquake modeling aimed at earthquake prediction?

From a general view, seismogenic structure and stress state control the earthquake process. Fault geometry and movement are the main objectives, which can be used in prediction models. In fact, in the short-term to imminent stage before earthquake occurrence, the correlation between precursors and the targeted earthquake is not unique (Ma et al., 1989). What controls the precursor patterns for different events relevant to earthquake modeling aimed at earthquake prediction? At the very start of this Research Topic, the difference between IPE (dry model) and DD (wet model) models is the fluid involved. Do rock fluids control the precursor pattern for different earthquakes? More articles related to this Research Topic are welcome in the future.

Author contributions

FH and GM revised the paper. All authors contributed to the article and approved the submitted version.

Acknowledgments

This Research Topic originates from expanding the influence of the annual conference on the China Earthquake Prediction Forum which was sponsored by Earthquake Prediction Committee of Seismological Society of China and co-sponsored and partly supported by Department of Earthquake Monitoring and Prediction of China Earthquake Administration. The Editors wish to thank all the authors who contributed their manuscripts, and reviewers who contributed their time, expertise and patience to reviewing the manuscripts and interacting with the authors, which has significantly improved the quality of the articles for this Research Topic.

Conflict of interest

The authors declare that the research was conducted in the absence of any commercial or financial relationships that could be construed as a potential conflict of interest.

Publisher's note

References

Barbot, S., Lapusta, N., and Avouac, J. P. (2012). Under the hood of the earthquake machine: Toward predictive modeling of the seismic cycle. *Science* 336 (6082), 707–710. doi:10.1126/science.1218796

Ben-Zion, Y. (2017). On different approaches to modeling. *J. Geophys. Res. Solid Earth* 122, 558–559. doi:10.1002/2016JB013922

Bürgmann, R., Rosen, P. A., and Fielding, E. J. (2000). Synthetic aperture radar interferometry to measure Earth's surface topography and its deformation. *Annu. Rev. Earth Planet. Sci.* 28, 169–209. doi:10.1146/annurev.earth.28.1.169

Chen, T., Li, L., Zhang, X. X., Ma, Q. M., Li, W., Ti, S., et al. (2021). Near-epicenter weather conditions several hours before strong earthquakes (Ms≥6). *Nat. Hazards* 110, 57–68. doi:10.1007/s11069-021-04907-2

Chen, Y., Wang, Y., Huang, F., Ma, L., Yang, C., and Shi, H. (2022). Mechanical mechanism of *in situ* stress ratio limit and its evolution simulation. *Front. Earth Sci.* 10, 941239. doi:10.3389/feart.2022.941239

Dascher-Cousineau, K., Brodsky, E. E., Lay, T., and Geobel, T. (2020). What controls varaitions in aftershock productivity? *Joural Geopgysical Res. Solid Earth* 125, e2019JB018111. doi:10.1029/2019JB018111

Geller, R. J. (1997). Earthquake prediction: A critical review. *Geophys. J. Int.* 131, 425–450. doi:10.1111/j.1365-246x.1997.tb06588.x

Gong, M., Xu, X. W., and Li, K. (2020). Fault Geometry responsible for the initial rupture process of Wenchuan earthquake. *Chin. J. Geophys.* 63 (3), 1224–1234. (in Chinese). doi:10.6038/cjg2020N0255

Han, Y. Y., Zang, Y., Meng, L. Y., Wang, Y., Deng, S. G., Ma, Y., et al. (2022). A summary of seismic activities in and around China in 2021. *Earthq. Res. Adv.* 2, 100157. doi:10.1016/j.eqrea.2022.100157

Huang, F. Q., Liu, J., Yao, H. J., Shao, Z. G., Wang, Q., Liu, J., et al. (2023). Introduction to the special issue of 2022 annual conference on China earthquake prediction Forum (CEPF) (in chinses). *Seismol. Geomagnetic Observation Res.* (1). doi:10.3969/j.issn.1003-3246.2022.S1.001http://www.dzdczz.com/bookmululist.aspx?qi_id=2420.Suppl. 0

Huang, F. Q., Zhang, X. D., Cao, Z. X., Li, J. P., and Li, S. H. (2017a). The roadmap of numerical earthquake prediction in China. *Recent Dev. World Seismol.* 460 (4), 4–10. (in Chinese).

Huang, F. Q., Li, M., Ma, Y. C., Han, Y. Y., Tian, L., Yan, W., et al. (2017b). Studies on earthquake precursors in China: A review for recent 50 years. *Geod. Geodyn.* 8, 1–12. doi:10.1016/j.geog.2016.12.002

Huang, L. C., Baud, P., Cordonnier, B., rançois Renard, F., Liu, L., and Wong, T. F. (2019). Synchrotron X-ray imaging in 4D: Multiscale failure and compaction localization in triaxially compressed porous limestone. *Earth Planet. Sci. Lett.* 528, 115831. doi:10.1016/j.epsl.2019.115831

Huang, W. Y., Wu, J. T., and Liu, J. (2020). Visualization of pore-structural deformation of dynamic CT images of a leitha limestone. *CT Theory Appl.* 29 (4), 424–434. (in Chinese). doi:10.15953/j.1004-4140.2020.29.04.05

Ikeda, M., Toda, S., Kobayashi, S., Oho, Y., Nishizaka, N., and Ohno, I. (2009). Tectonic model and fault segmentation of the Median Tectonic Line active fault system on Shikoku, Japan. *TECTONICS* 28, TC5006. doi:10.1029/2008TC002349

Kanamorori, H., and Brodsky, E. E. (2001). The physics of earthquakes. *Phys. Today* 54 (6), 34–40. doi:10.1063/1.1387590

King, G. C. P. (1978). Geological faults: Fracture, creep and strain. *Phil. Trans. R. Soc. Lond. A* 288, 197–212.

Li, J., Yao, H., Wang, B., Yang, Y., Hu, X., Zhang, L., et al. (2022). A real-time AI-assisted seismic monitoring system based on new nodal stations with 4G telemetry and its application in the Yangbi MS 6.4 aftershock monitoring in southwest China. *Earthq. Res. Adv.* 2, 100033. doi:10.1016/j.eqrea.2021.100033

Li, M., Shen, X., Parrot, M., Zhang, X., Zhang, Y., Yu, C., et al. (2020). Primary joint statistical seismic influence on ionospheric parameters recorded by the CSES and DEMETER satellites. *J. Geophys. Res. Space Phys.* 125, e2020JA028116. doi:10.1029/2020JA028116

Luo, S., Yao, H., Wen, J., Yang, H., Tian, B., and Yan, M. (2023). Apparent low-velocity belt in the shallow Anninghe Fault Zone in SW China and its implications for seismotectonics and earthquake hazard assessment. *J. Geophys. Res. Solid Earth* 128, e2022JB025681. doi:10.1029/2022JB025681

Ma, J., and Guo, Y. S. (2014). Accelerated synergism prior to fault instability: Evidence from laboratory experiments and an earthquake case. *Seismol. Geol.* 36 (3), 548–562. (in Chinese). doi:10.3969/j.issn.0253-4967.2014.03.00

Ma, J. (2016). On "whether earthquake precursors help for prediction do exist". *Chin. Sci. Bull.* 61, 409–414. (in Chinese). doi:10.1360/N972015-01239

Ma, J., Sherman, S. I., and Guo, Y. S. (2012). Identification of meta-instable stress state based on experimental study of evolution of the temperature field during stick-slip instability on a 5 °bending fault. *Sci. China Earth Sci.* 55, 869–881. doi:10.1007/s11430-012-4423-2

Ma, J. (1987). *Introduction to tectonophysics*. Beijing, China: Seismological Press. (in Chinese).

Ma, Z. J., Fu, Z. X., Zhang, Y. Z., Wang, C. M., Zhang, G. M., and Liu, D. F. (1989). *Earthquake prediction: Nine major earthquakes in China (1966-1976)*. Beijing, China: Seismological Press and Berlin Heidelberg: Springer-Verlag, 311–322.

Martinelli, G., Ciolini, R., Facca, G., Fizio, F., Gherardi, F., Heinicke, J., et al. (2021). Tectonic-related geochemical and hydrological anomalies in Italy during the last fifty years. *Minerals* 11, 107. doi:10.3390/min11020107

Martinelli, G., Plescia, P., and Tempesta, E. (2020). "Pre-Earthquake" micro-structural effects induced by shear stress on α-quartz in laboratory experiments. *Geosciences* 10, 155. doi:10.3390/geosciences10050155

Myachkin, V. I., Kostrov, B. V., Sobolev, G., and Shamina, O. G. (1975). Fundamentals of the physics of earthquake origin and precursors of earthquakes. *Phy. Earthquake Origin [in Russian]*, 6–29.

Pritchard, M. E., Allen, R. M., Becker, T. W., Behn, M. D., Brodsky, E. E., Bürgmann, R., et al. (2020). New opportunities to study earthquake precursors. *Seismol. Res. Lett.* 91 (5), 2444–2447. doi:10.1785/0220200089

Scholz, C. H., Syke, L. R., and Aggarwal, Y. P. (1973). Earthquake prediction: A physical basis. *Science* 181, 803–810. doi:10.1126/science.181.4102.803

Shao, Z., Wu, Y., Ji, L., Diao, F., Shi, F., Li, Y., et al. (2023). Assessment of strong earthquake risk in the Chinese mainland from 2021 to 2030. *Earthq. Res. Adv.* 3 (1), 100177. doi:10.1016/j.eqrea.2022.100177

Shi, H., Huang, F., Ma, Z., Wang, Y., Feng, J., and Gao, X. (2020). Mechanical mechanism of fault dislocation based on *in situ* stress state. *Front. Earth Sci.* 8, 52. doi:10.3389/feart.2020.00052

Wang, Y., Zhang, B., Hou, J. J., and Xu, X. W. (2014). Structure and tectonic geomorphology of the Qujiang fault at the intersection of the Ailao Shan–Red River fault and the Xianshuihe–Xiaojiang fault system, China. *Tectonophysics* 634, 156–170. doi:10.1016/j.tecto.2014.07.031

Yang, H. F., Yao, S. L., and Chen, X. (2022). Rupture propagation on heterogeneous fault: Challenges for predicting earthquake magnitude. *Chin. Sci. Bull.* 67, 1390–1403. doi:10.1360/TB-2021-1086

Zhang, Z., Yao, H., Wang, W., and Liu, C. (2022). 3-D crustal azimuthal anisotropy reveals multi-stage deformation processes of the sichuan basin and its adjacent area, SW China. *J. Geophys. Res. Solid Earth* 127, e2021JB023289. doi:10.1029/2021JB023289

Zhao, J., Ren, J., Liu, J., Jiang, Z., Liu, X., Liang, H., et al. (2020). Coupling fraction and relocking process of the Longmenshan Fault Zone following the 2008 M_W7.9 Wenchuan earthquake. *J. Geodyn.* 137, 101730. doi:10.1016/j.jog.2020.101730

Zhao, J., Yuan, Z., Ren, J., Jiang, Z., Yao, Q., Zhou, Z., et al. (2022). Acceleration of deep slip along the longmenshan fault plane before the 2008 M8.0 wenchuan earthquake. *Front. Earth Sci.* 10, 830317. doi:10.3389/feart.2022.830317(GPS related)

Zhou, Z., Tian, L., Zhao, J., Wang, H., and Liu, J. (2020). Stress-related pre-seismic water radon concentration variations in the Panjin observation well, China (1994–2020). *Front. Earth Sci.* 8, 596283. doi:10.3389/feart.2020.596283

Zhou, Z., Zhong, J., Zhao, J., Yan, R., Tian, L., and Fu, H. (2021). Two mechanisms of earthquake-induced hydrochemical variations in an observation well. *Water* 13, 2385. doi:10.3390/w13172385

Zöller, G., Hainzl, S., Holschneider, M., and Brietzke, G. B. (2010). Steady-state solutions of rupture propagation in an earthquake simulator governed by rate and state dependent friction. *Eur. Phys. J. Spec. Top.* 191, 105–115. doi:10.1140/epjst/e2010-01344-6

frontiers | Frontiers in Earth Science

TYPE Original Research
PUBLISHED 16 January 2023
DOI 10.3389/feart.2022.994850

OPEN ACCESS

EDITED BY
Hongfeng Yang,
The Chinese University of Hong Kong, China

REVIEWED BY
Andrea Llenos,
U.S. Geological Survey, United States
Rita Di Giovambattista,
Istituto Nazionale di Geofisica e Vulcanologia (INGV), Italy

*CORRESPONDENCE
Fengling Yin,
yinfengling@cea-igp.ac.cn
Changsheng Jiang,
jiangcs@cea-igp.ac.cn

SPECIALTY SECTION
This article was submitted to Solid Earth Geophysics,
a section of the journal
Frontiers in Earth Science

RECEIVED 15 July 2022
ACCEPTED 15 November 2022
PUBLISHED 16 January 2023

CITATION
Bi J, Yin F, Jiang C, Yin X, Ma Y and Song C (2023), Strong aftershocks traffic light system: A case study of the 8 January 2022 M_S6.9 Menyuan earthquake, Qinghai Province, China. *Front. Earth Sci.* 10:994850. doi: 10.3389/feart.2022.994850

Strong aftershocks traffic light system: A case study of the 8 January 2022 M_S6.9 Menyuan earthquake, Qinghai Province, China

Jinmeng Bi[1,2], Fengling Yin[1]*, Changsheng Jiang[1]*, Xinxin Yin[1,3], Yong Ma[2] and Cheng Song[2]

[1]Institute of Geophysics, China Earthquake Administration, Beijing, China, [2]Tianjin Earthquake Agency, Tianjin, China, [3]Gansu Earthquake Agency, Lanzhou, China

Strong aftershocks, especially the disaster-causing M≥5.0 kind, are a key concern for mitigation of seismic risks because they often lead to superimposed earthquake damage. However, the real-time forecasting results of the traditional probability prediction models based on statistics are usually far from accurate and therefore unsatisfactory. Borrowing an idea from the foreshock traffic light system (FTLS), which is based on observations of decreasing b-values or increasing differential stress just before a strong aftershock, we constructed a strong aftershock traffic light system (SATLS) that uses data-driven technology to improve the reliability of time sequence b-value calculations, and analyzed the b-value variations of strong aftershocks in the China continent. We applied this system to the M_S6.9 Menyuan earthquake occurred on 8 January 2022. The earthquake occurrence rates before the largest aftershock (M_S5.2) forecast by the Omi-R-J model were too low, although the model could accurately forecast aftershock rates for each magnitude interval in most time-periods. However, reliable b-values can be calculated using the time-sequence b-value data-driven (TbDD) method, and the results showed that the b-values continued declining from 1.3 days before the M_S5.2 aftershock and gradually recovered afterward. This would suggest that the stress evolution in the focal area can provide data for deciding when to post risk alerts of strong aftershocks. In the process of building the SATLS, we studied thirty-four M≥6.0 intraplate earthquake sequences in the China continent and concluded that the differences between the b-values of the aftershock sequences and of the background events, $\triangle b = b_{after} - b_{bg} = \pm 0.1$, could be used as thresholds to determine whether M≥5.0 aftershocks would occur. The $\triangle b$ value obtained using the events before the M_S5.2 aftershock of the M_S6.9 Menyuan sequence was about -0.04, which would have caused the SATLS to declare a yellow alert, but there would have been some gap expected before a red alert was triggered by the b-value difference derived from the events associated with this strong aftershock. To accurately forecast a strong aftershock of M≥5.0, a deeper understanding of the true b-value and a detailed description of the stress evolution state in the source area is necessary.

KEYWORDS

Ogata–Katsura 1993 model, Omi–Reasenberg–Jones model, time-sequence *b*-value data-driven (TbDD) method, aftershock forecasting, traffic light system

Introduction

The disastrous effects of superimposed strong aftershocks on buildings and structures have aggravated casualties and property losses, such as occurred in the *M*7.1 Luanxian strong aftershock and the *M*6.9 Ninghe strong aftershock after the 1976 *M*7.8 Tangshan earthquake (Lv et al., 2007) and the strong *M*6.3 aftershock after the 2010 *M*7.1 earthquake in New Zealand (Zhang et al., 2011). Accurate and reliable forecasting of strong aftershocks is of great importance to post-earthquake emergency evacuation, secondary disaster disposal, and decision-making for restoration and reconstruction (Woessner et al., 2011; Nanjo et al., 2012; Ogata et al., 2013). Traditional strong aftershock forecasting, which is realized mainly by short-term probability forecasting models (Jiang et al., 2018; Bi et al., 2020; Bi and Jiang, 2020) such as the Reasenberg–Jones (R-J) model (Reasenberg and Jones, 1989), the epidemic-type aftershock sequence (ETAS) model (Ogata, 1989), and the Omi-R-J model (Omi et al., 2013, 2015, 2016), still faces great challenges in real-time functionality and accuracy (Lippiello et al., 2017). For example, the Japan Meteorological Agency (JMA) announced a low-probability forecast of $M \geq 5.5$ aftershocks for the 2005 *M*7.0 earthquake off the coast of western Fukuoka Prefecture, Kyushu District, Japan; but, in fact, the earthquake was followed by the largest aftershock of *M*5.8 (Ogata, 2006). In addition, using only the ETAS model to predict the frequency of strong aftershocks in Japan and Southern California (Grimm et al., 2021) and the largest expected aftershock of the 2019 Ridgecrest earthquake sequence in the United States (Shcherbakov, 2021) revealed the model's obvious shortcomings.

In recent years, a new route for the development of strong aftershock forecasting technology has employed the concept of graded risk assessment to improve the operability of forecasting based on abnormal aftershock activity (Matsu'ura, 1986; Ogata, 2001). Gulia and Wiemer (2019) proposed the foreshock traffic light system (FTLS), which uses *b*-values that are sensitive to stress changes, and achieved good results in earthquake cases studies. The theoretical basis of FTLS posits that the *b*-value in relation to G-R can be used as an indirect description of underground differential stress (Gutenberg and Richter, 1944; Scholz, 1968; Scholz, 2015), and that the change in *b*-value is related to the state of underground stress load (Chan and Chandler, 2001; Nandan et al., 2017; Si and Jiang, 2019); some earthquake cases studies showed that the *b*-value can increase by 20% after the main shock and decrease by 10% or more before the strong aftershock (Gulia et al., 2018; Gulia and Wiemer, 2019). Nanjo *et al.* (2022) further improved FTLS by combining local aseismic slips with stress changes. In addition, the idea of a risk classification traffic light system was also widely applied in research of induced earthquake risk control (Jiang et al., 2021b), aftershock hazard analysis (Gulia et al., 2020), and risk assessment of cumulative structural damage caused by aftershocks (Trevlopoulos et al., 2020). However, there is still room for further development in the technical route of strong aftershock forecasting. This can be accomplished through improvements in the risk classification method by an empirical understanding that the *b*-value change of aftershocks compared to that before the earthquake is universal in different tectonic regions and an increased awareness of the influence of subjectivity in the calculation of time series *b*-values (Jiang et al., 2021a; Jiang et al., 2021).

On 8 January 2022, an M_S6.9 earthquake struck Menyuan County, Qinghai Province, northwestern China, and ruptured the Tuolaishan fault (TLSF) and the Lenglongling fault (LLLF) for about 415 km. It affected nearly 6,000 people, damaged more than 4,000 homes and buildings, and caused a large number of secondary disasters such as local slope collapse, rolling stones, cracking of frozen soil, and arch deformation of ice surfaces (https://m.gmw.cn/baijia/2022-01/20/35460649.html). Two strong aftershocks of M_S5.1 and M_S5.2 occurred on January 8 and January 12, respectively, and the latter caused the aftershock area to extend more than 10 km toward the southeast, which was close to the aftershock area of the 2016 M_S6.4 Menyuan earthquake. This phenomenon brought widespread concerns about the strong aftershock risk of the 2022 M_S6.9 Menyuan earthquake. To investigate this risk, we first carried out quantitative aftershock probability forecasting and analyzed the forecasting effectiveness. Second, based on cases studies of the time evolution of *b*-values of intraplate earthquake sequences in the China continent and the occurrence regularity of strong aftershocks, we constructed a strong aftershock traffic light system (SATLS), which is more universal than the FTLS, to qualitatively evaluate the risk of strong aftershocks after the 2022 M_S6.9 Menyuan earthquake. This study provides a scientific basis for improving the forecasting of strong aftershocks following similar complex earthquake sequences.

Quantitative forecasting using the Omi-R-J model

We used the Omi-R-J model (Omi et al., 2013) to conduct aftershock probability forecasting for the M_S6.9 Menyuan earthquake sequence and evaluated the performance of this forecasting method. The Omi-R-J model, which combines the traditional R-J model (Reasenberg and Jones, 1989) with the OK1993 model (Ogata and Katsura, 1993) describing the

magnitude–frequency relationship in the form of a continuous function, can make full use of a large number of small earthquakes below the completeness magnitude in the early stages of an earthquake sequence and produce relatively reliable and stable results in terms of parameter fitting to the model and forecasting of the aftershock occurrence rate. Under the conditions of a non-cumulative magnitude–frequency distribution, the OK1993 model is expressed as:

$$\lambda(M) = \lambda_0(M)q(M), \tag{1}$$

$$\lambda_0\left(M|\beta\right) = \exp\left(-\beta M\right), \tag{2}$$

where M is magnitude and $\beta = b\ln 10$. $q(M)$ is a probability function, which describes the detection-rate of earthquakes and ranges [0, 1]. It is expressed in the form of a cumulative normal distribution:

$$q\left(M|\mu,\sigma\right) = \frac{1}{\sqrt{2\pi\sigma^2}}\int_{-\infty}^{M} e^{-\frac{(x-\mu)^2}{2\sigma^2}}dx, \tag{3}$$

where the parameter μ indicates the magnitude where earthquakes are detected at a rate of 50% and $\sigma(\sigma>0)$ represents the range of magnitudes where earthquakes are more or less partially detected (Ogata and Katsura, 1993). The two parameters can generally be combined to describe the completeness of earthquake catalogs. Specifically, the minimum magnitude of completeness, M_C, can be approximately expressed using $\mu + 2\sigma$ or $\mu + 3\sigma$, which represents the complete record of magnitude at the 95.44% or 99.74% confidence level, respectively (Mignan and Woessner, 2012; Iwata, 2013).

Given a set of magnitudes $\{M_1, M_2, \ldots, M_n\}$, the seismic probability density function and the log-likelihood function can be written as:

$$\begin{aligned} P\left(M|\beta,\mu,\sigma\right) &= \frac{e^{-\beta M}q\left(M|\mu,\sigma\right)}{\int_{-\infty}^{+\infty} e^{-\beta M}q\left(M|\mu,\sigma\right)dM} \\ &= e^{-\beta M}q\left(M|\mu,\sigma\right)/e^{\left(-\beta\mu+\beta^2\sigma^2/2\right)}/\beta \\ &= \beta e^{-\beta\left(M-\mu\right)-\beta^2\sigma^2/2}q\left(M|\mu,\sigma\right), \end{aligned} \tag{4}$$

$$\begin{aligned} \ln L(\theta) = n\ln\beta - \sum_{i=1}^{n}\left[\beta M_i - \ln q\left(M_i|\mu,\sigma\right)\right] \\ + n\beta\mu - \frac{n}{2}\beta^2\sigma^2. \end{aligned} \tag{5}$$

Furthermore, we can obtain the parameters β, σ, and the dynamic $\mu(t)$ by the 'state-space' model, as well as p, c, k, and their standard deviations (Omi et al., 2013) by the Omori–Utsu formula (Omori, 1894; Utsu, 1961). Finally, we forecast the number of aftershocks with magnitudes $M>M_p$ (here M_p represents the minimum forecasting magnitude), which would take place during an arbitrary time interval $[t_2, t_e]$:

$$N = \int_{t_2}^{t_e}\int_{M_p}^{\infty}\lambda(t, M)dtdM. \tag{6}$$

In the study of the 2022 M_S6.9 Menyuan earthquake sequence, we used the catalog provided by the China Earthquake Networks Center (37.6–37.9°N, 100.9–101.6°E) between 2022/01/08 and 2022/01/13. Statistically, the aftershock sequence of the M6.9 Menyuan earthquake included two $M\geq5.0$ aftershocks, nine M4.0~4.9 earthquakes, and forty-one M3.0~3.9 earthquakes (Figure 1). Parameter fitting and aftershock forecasting were performed using the Omi-R-J model, from 0.05 days after the main shock until 5.15 days, with steps of 0.05 days, totaling 103 time periods. It can be seen from Figure 2 that the expected parameters of the early post-earthquake sequence (t_2 = 1.00 days) are β =1.927 ± 0.083, k = 0.004 ± 0.002, p = 0.900 ± 0.051, and c = 0.004 ± 0.002, where the parameter β was calculated from $\beta = \ln(10)\times b$. In order to illustrate the evaluation results, Figures 2B,D depict the forecasted occurrence rates of $M>2.95$ for two periods of 1.00~2.00 days and 1.00~4.00 days after the main shock. The observed earthquake numbers for the two time periods were both within the 95% confidence intervals of the forecasted numbers, and the score values were [0.4238, 0.7283] and [0.4009, 0.7067] by the N-test (Kagan and Jackson, 1995; Schorlemmer et al., 2007; Zechar, 2010), respectively.

The N-test was intended to measure how well the total number of forecasted earthquakes matched the number of events observed. We used a one-sided test with an effective significance value, α_{eff}, which is half of the intended significance value, α. In other words, we intended to maintain an error rate of α= 5% and to compare both δ_1 and δ_2 with a critical value of α_{eff} = 0.025. If δ_1 is less than α_{eff}, the forecast rate is too low (under-prediction) and if δ_2 is less than α_{eff}, the forecast rate is too high (over-prediction). To quantitatively investigate the accuracy of the forecasted occurrence rates of strong aftershocks for different target magnitudes, M_T = [3.0, 3.5, 4.0] of the M_S6.9 Menyuan earthquake sequence, the N-test method was used to evaluate the performance results (Figure 3). The gray vertical line denotes the connection between the δ_1 score and the δ_2 score. Black diamonds and blue squares represent the results of δ_1<0.025 and δ_2<0.025, respectively. There is no blue square (δ_2 <0.025) in Figure 3, which indicates that there was no over-prediction in the forecasting period. The Omi-R-J method shows good forecasting ability for early strong aftershocks, and the blank space indicates that the actual number of earthquakes was zero. Ignoring the influence of 'no earthquakes', there was no over-prediction forecasting. The Omi-R-J model had 9, 8, and 7 forecasting failures before and after the strong aftershocks of $M_S5.2$ with respect to M_T = [3.0, 3.5, 4.0]; thus, for complex earthquake sequences, the Omi-R-J model with good fitting performance has some limitations. Further analysis of the period of forecasting failure shows that before and after the M_S5.2 strong aftershock of January 12, there was

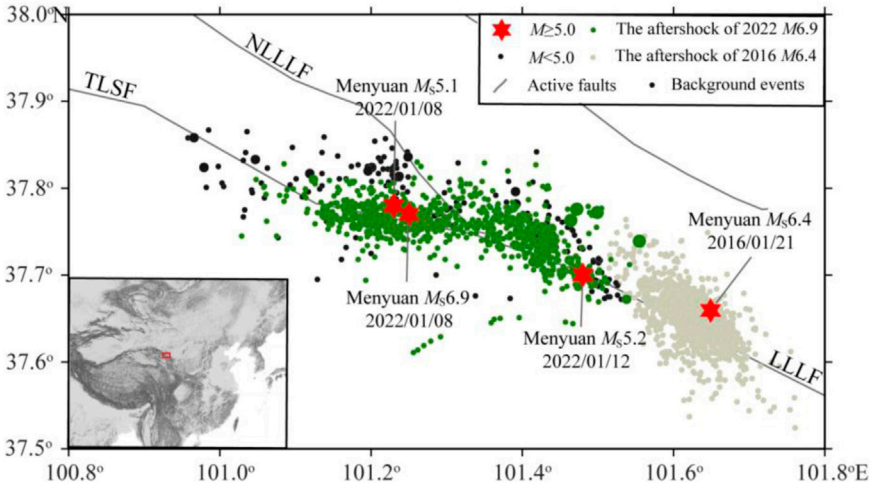

FIGURE 1
Spatial distribution of epicenters. The black dots represent background events before the Menyuan M_S6.9 since 1970. The gray dot represents the 2016 M_S6.4 Menyuan earthquake sequence, and the green dots represent the 2022 M_S6.9 Menyuan earthquake sequence. LLLF stands for Lenglongling fault, NTLSF is the north Lenglongling fault, and TLSF is the Tuolaishan fault.

obvious under-prediction forecasting, which coincides with the main period of forecasting failure.

Time-series *b*-value calculations based on a data-driven method

Data-driven technology provides a new solution to the problem of subjectivity of model selection in the calculation of seismicity parameters. In this paper, we utilized the time-sequence *b*-value data-driven (TbDD) method proposed by Jiang et al. (2021a) to analyze the M_S6.9 Menyuan earthquake sequence. The TbDD method consists of three major steps:

1) Selection of the magnitude–frequency distribution function. TbDD adopts the OK1993 model of a continuous distribution function given by Ogata and Katsura (1993) in a magnitude–frequency distribution relationship, which makes it superior by simultaneously determining the minimum magnitude of completeness and obtaining *b*-values.
2) Random partitioning in the time axis. In the model construction, it is necessary to randomly partition the given research time period $[t_0, t_1]$ between the start time, t_0, and the end time, t_1.① A random number generator was used to generate random time nodes, $T = \{T_1, T_2, \ldots, T_k\}$, where k is the number of time nodes. Correspondingly, the time period $[t_0, t_1]$ was divided into time segments $S = \{S_1, S_2, \ldots, S_{k+1}\}$, which constitute a model. ② We repeated step ① w times to obtain the w group partitioning schemes $\{P_i, i = 1, 2, \ldots, w\}$ on the time axis, that is, w models. ③ We repeated the aforementioned partitioning steps ① and ② with increasing k from 1 to n, where n is the maximum number of time nodes. For the time segments $S = \{S_1, S_2, \ldots, S_{k+1}\}$ of each model (or each partitioning scheme), the parameters of the OK1993 model $[\beta, \mu, \sigma]$ can be calculated using the events included in each time segment, and the total number of calculations was $w\times(n+1)$ times.

For any moment t_i in the time interval (t_0, t_1), the *b*-value is derived from the events both before and after t_i. For the moment t_0, the *b*-value is calculated by using only the events after t_0, and for the moment t_1, the *b*-value is obtained by using only the events before t_1. Therefore, only at the moment of t_1, the TbDD method has the characteristic of forward-forecasting. As time continues to move forward, the *b*-value at the original t_1 will be changed and updated.

3) Selection of the optimal models and calculation of ensemble median *b*-values. In order to select the optimal models most likely to reflect the final calculation results among a large number of models, the TbDD method adopted Bayesian information criteria (BIC) (Schwarz, 1978):

$$BIC = -2 \cdot \ln L(\theta) + k \cdot \ln(N), \tag{7}$$

where $\ln L(\theta)$ is the log-likelihood value of the OK1993 model given by formula (5), k is the degrees of freedom of the model, and N is the number of events for calculation. Because BIC is a penalized log-likelihood function, the smaller that BIC is, the closer to the true value the estimated parameters are. We ranked the BIC values of all the models obtained using Eq. 7 and selected the 5% models with

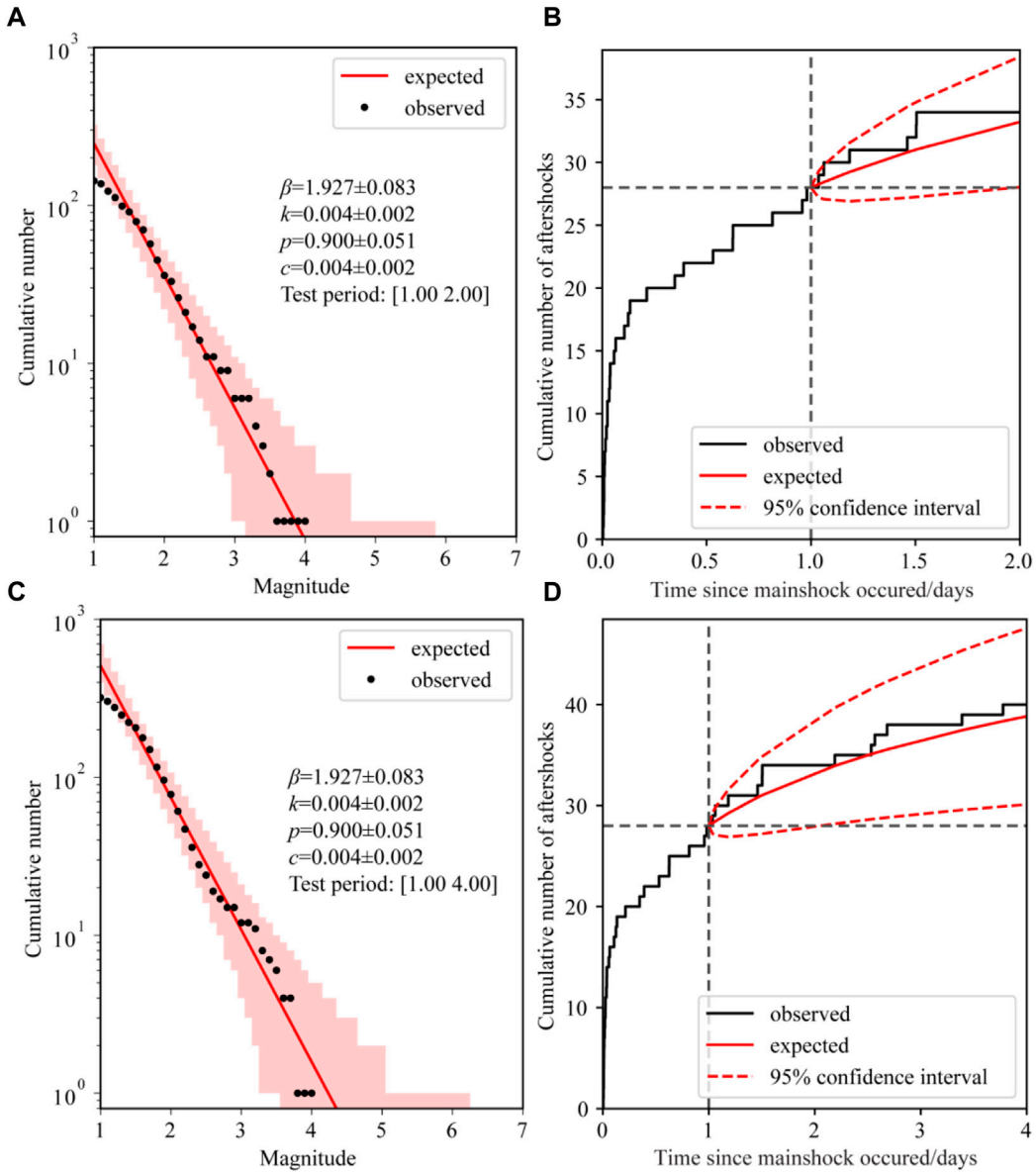

FIGURE 2
Future 1-day and 3-day aftershock forecasting for the Menyuan M_S6.9 earthquake sequence using the Omi-R-J model. **(A,B)** Time period of 1.00–2.00 days and **(C,D)** time period of 1.00–4.00 days after the main shock. **(A,C)** Comparison of magnitude–cumulative frequency between forecasting (red lines) and actual observed aftershocks (black dots) and their 95% confidence intervals (pink areas). **(B,D)** Comparison of magnitude–cumulative frequency between forecasting (red curves) and actual observed aftershocks (black curves) of M>2.95 and their 95% confidence intervals (red dashed lines), and the forecasting starting and ending times (black vertical dashed lines) are delineated.

minimum BIC values as the optimal ones. We used these optimal models to form an ensemble model and obtained the ensemble median b-value of the time-sequence as the final result. The median absolute deviation (MAD) was used as the uncertainty of the b-value.

We implemented TbDD to calculate the b-values of the M_S6.9 Menyuan earthquake sequence, attempting to use different maximum time segments (n+1) and different partitioning times (w). The models with the 5% lowest BIC values were taken as the optimal models, and the ensemble median values of the b-values were calculated as the final result. The BIC value distribution and the b-values of time sequences with the number of time segments $n + 1 = \{2,3,...11\}$ and $w = 100$ are shown in Figures 4A,B, separately. For the partitioning with $n + 1 =$

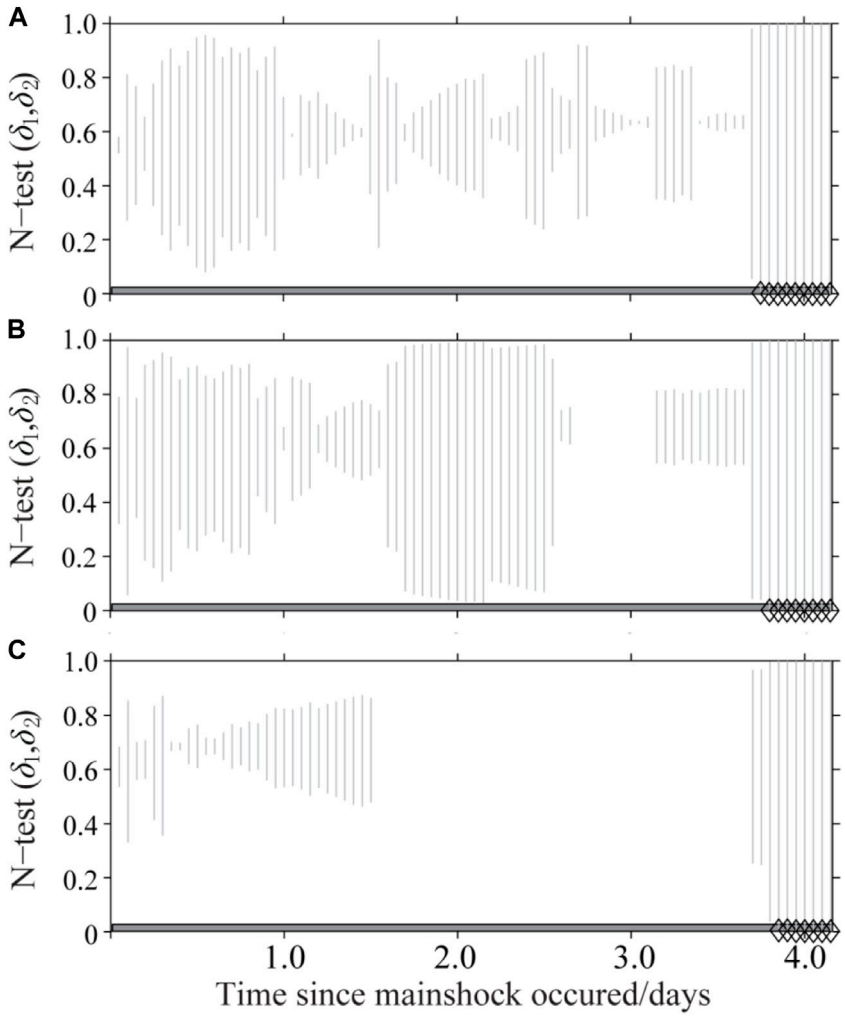

FIGURE 3
N-test results for future 1-day aftershock forecasting of the Menyuan M_S6.9 earthquake sequence. **(A–C)** Forecasting performance evaluation of the Omi-R-J model for the three target magnitudes, 3.0, 3.5, 4.0, respectively. The vertical gray dashed lines connect the δ_1 and δ_2 values, while the black diamonds and blue squares show the results with δ_1<0.025 and δ_2<0.025, respectively. The blank area indicates that no event of corresponding magnitudes have occurred in the forecasting period.

{2,3,...21} and w = 300, the results are shown in Figures 4C,D and for the partitioning with n + 1 = {2,3,...21} and w = 1000, the results are shown in Figures 4E,F. From the aforementioned calculation results, it can be seen that the b-values obtained under different combinations of maximum time segments (n + 1) and various partitioning times w are relatively close, which confirms the stability of the TbDD method. It is worth noting that, from 1.3 days before the January 12 M_S5.2 strong aftershock, the b-value dropped significantly, from b = 0.93 to b = 0.63, with a drop as high as $\triangle b$ = 0.30, which is the only time that the b-value of aftershocks dropped significantly over the study period. This phenomenon makes it possible to give an alarm before this strong aftershock.

SATLS for determining the risk level of strong aftershocks

To obtain a general threshold standard for the b-value changes of time series of strong aftershock risk alerts, which we used as a reference to conduct the strong aftershock forecasting of the M_S6.9 Menyuan earthquake sequence, we studied the b-value changes of time series before strong aftershocks of M≥5.0 based on 86 intraplate earthquake sequences in the China continent whose main shock had a magnitude of M_S≥6.0, as screened by Bi *et al.* (2022).We used the National Unified Official Catalogue produced by the China Earthquake Networks Center (CENC). Since 1 January 1970, the catalog has provided earthquake locations, occurrence

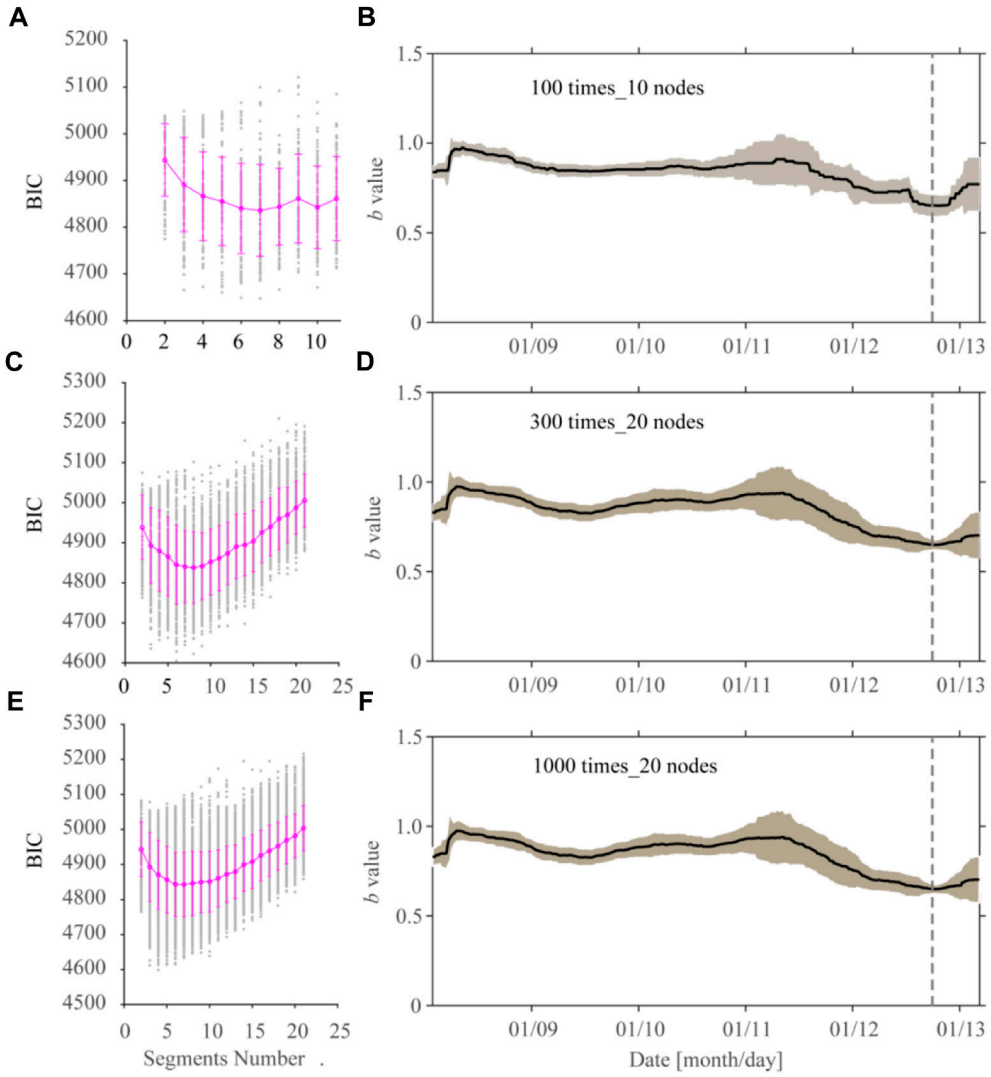

FIGURE 4
TbDD method calculation results for the 8 January 2022 Menyuan M_S6.9 earthquake sequence. **(A,C,E)** BIC value distribution under different partition periods. The gray dots denote the calculation results of BIC values, and the pink dots and vertical lines denote the corresponding means and standard deviations of the BIC values, respectively. **(B,D,F)** Time-sequence changes of *b*-values calculated by TbDD. The black curves indicate the ensemble medians of *b*-values, the gray areas indicate the MAD of corresponding *b*-values, and the gray vertical dotted lines show the time of occurrence of strong aftershocks of the Menyuan M_S5.2 aftershock on 12 January 2022.

times, and local magnitudes, M_L, obtained using the same formula (Mignan et al., 2013). Thus the homogeneity of the reported magnitude was ensured for the whole period. Since the National Unified Official Catalogue starts from 1970, earthquakes were selected from the period between 1970/01/01 and the time immediately before each of 86 main shocks, as well as spatial restrictions on the distribution of aftershocks. Then we used the Gardner–Knopoff method (Gardner and Knopoff, 1974) to decluster catalogs to obtain the background seismicity of the corresponding earthquake sequence. Because of the absence of a large number of aftershock events in the early post-earthquake period, which seriously affected the stability of model parameters, only the events from 0.50 days after the main shock to the occurrence of the strongest aftershock were used to ensure the stability and quality of parameter fitting. Additionally, both the number of background events and aftershocks of the selected earthquake sequence amounted to no fewer than 30 results in a total of 34 earthquake sequences. The parameters of 34 main shocks are shown in Table 1, and the spatial distribution of the epicenters of the main shocks is mapped in Figure 5A.

The parameters of 34 earthquake sequences were fitted using the OK1993 model, and the *b*-values of both background events

TABLE 1 Sequence parameters of intraplate earthquakes built for the SATLS in the China continent.

No.	Date	Time	Long	Lat	Mag	Mm	N_{bg}	N_{after}	b_{bg}	b_{after}
1	1976/11/07	02:04:05	101.08	27.50	6.7	4.9	0089	0730	1.01	1.02
2	1979/07/09	18:57:23	119.25	31.45	6.0	5.2	0057	0037	0.71	0.58
3	1981/01/24	05:13:47	101.17	31.00	6.9	4.3	0042	0055	0.85	0.91
4	1982/06/16	07:24:29	99.85	31.83	6.0	3.0	0299	0183	1.12	1.08
5	1985/08/23	20:41:55	75.32	39.53	7.1	6.6	0074	0048	1.00	0.93
6	1991/02/25	22:30:25	79.00	40.33	6.5	4.9	0117	0041	0.74	0.76
7	1996/07/03	14:44:44	88.60	30.25	6.0	5.4	0080	0047	0.78	0.76
8	1998/08/27	17:03:33	77.13	39.82	6.4	5.1	0759	0089	0.90	0.60
9	2001/10/27	13:35:40	100.57	26.23	6.0	4.1	0198	0069	0.65	0.96
10	2003/07/21	23:16:30	101.23	25.95	6.2	4.9	0283	0149	0.89	1.36
11	2003/10/16	20:28:03	101.30	25.92	6.1	5.1	0369	0223	1.00	1.08
12	2003/10/25	20:41:36	100.93	38.35	6.1	4.3	0047	0261	0.78	0.89
13	2005/02/15	07:38:07	79.37	41.72	6.2	5.1	0318	0036	0.86	0.78
14	2007/06/03	05:34:56	101.02	23.05	6.4	5.1	1656	0224	1.00	0.87
15	2008/05/12	14:28:04	103.40	31.00	8.0	6.4	2487	3014	0.86	1.25
16	2008/08/30	16:30:51	101.92	26.28	6.1	5.6	0247	0035	0.93	0.73
17	2008/11/10	09:21:59	95.91	37.66	6.6	5.3	0053	0116	0.70	0.68
18	2009/08/28	09:52:06	95.90	37.60	6.6	6.1	0144	0437	0.85	0.73
19	2012/06/30	05:07:31	84.74	43.42	6.6	4.6	0266	0298	0.76	0.88
20	2013/01/29	00:38:52	79.75	42.55	6.3	4.0	0074	0244	0.83	0.86
21	2013/04/20	08:02:47	102.99	30.30	7.0	5.4	0415	0188	0.99	0.87
22	2013/07/22	07:45:56	104.21	34.54	6.7	4.1	0202	0279	0.75	0.78
23	2013/08/12	05:23:42	97.96	30.04	6.1	4.1	0089	0113	0.91	0.97
24	2014/02/12	17:19:48	82.51	36.14	7.3	4.5	0060	0483	0.70	1.00
25	2014/05/30	09:20:13	97.80	25.02	6.1	4.6	3840	2974	0.88	1.02
26	2014/08/03	16:30:12	103.33	27.11	6.6	4.4	0677	1514	1.16	1.11
27	2016/01/21	01:13:12	101.65	37.66	6.4	4.1	0374	0425	0.85	0.81
28	2016/10/17	15:14:47	95.02	32.89	6.3	4.4	0063	0526	0.70	0.95
29	2016/12/08	13:15:03	86.30	43.80	6.2	4.6	0982	0879	0.72	0.83
30	2017/08/08	21:19:48	103.82	33.20	7.0	4.3	4503	4884	0.80	0.86
31	2017/11/18	06:34:18	95.00	29.75	6.9	4.3	0131	2749	0.77	1.17
32	2019/06/17	22:55:43	104.96	28.34	6.0	5.6	3194	1800	0.73	0.73
33	2020/01/19	21:27:56	77.21	39.83	6.4	4.8	0542	1077	0.72	0.86
34	2020/06/26	05:05:19	82.34	35.69	6.4	4.9	0282	0539	0.85	0.79

(b_{bg}) and aftershocks (b_{after}) are shown in Table 1. Statistical analyses indicated 13 earthquake sequences with M≥5.0 aftershocks. The average was b_{bg} = 0.87 ± 0.11 and b_{after} = 0.81 ± 0.19, and b_{bg}>b_{after} accounted for 84.62% (11/13) and b_{bg}<b_{after} accounted for 15.38% (2/13); there were 21 earthquake sequences without strong M≥5.0 aftershocks in the fitting period, with average b_{bg} = 0.83 ± 0.13 and b_{after} = 0.95 ± 0.15, of which b_{bg}>b_{after} accounted for 19.05% (4/21) and b_{bg}<b_{after} accounted for 80.95% (17/21). The statistical distribution of the differences in b-values between the background events b_{bg} and the aftershocks b_{after}, ($\triangle b$ = b_{after} - b_{bg}), and the ratio $\triangle b/b_{bg}$ are given in Figures 5B,C. The results show that the mean $\triangle b$ value and the median $\triangle b$ value of the sequences having strong aftershocks of M≥5.0 were −0.13 and −0.16, separately, and that the mean and the median of $\triangle b/b_{bg}$ were −0.06 and −0.08, separately. However, the $\triangle b$ of the sequences without strong aftershocks of M≥5.0 had a mean value of 0.27 and a median value of 0.15, and the mean value of $\triangle b/b_{bg}$ was 0.16 and the median value was 0.08.

The aforementioned analysis shows that b_{after}<b_{bg} for the sequences with M≥5.0 aftershocks and b_{after}>b_{bg} for the sequences without M≥5.0 aftershocks are statistically significant. If we conduct the risk assessment of M≥5.0 aftershocks according to the aforementioned relationship, it can be seen that when $\triangle b$>0, two earthquake

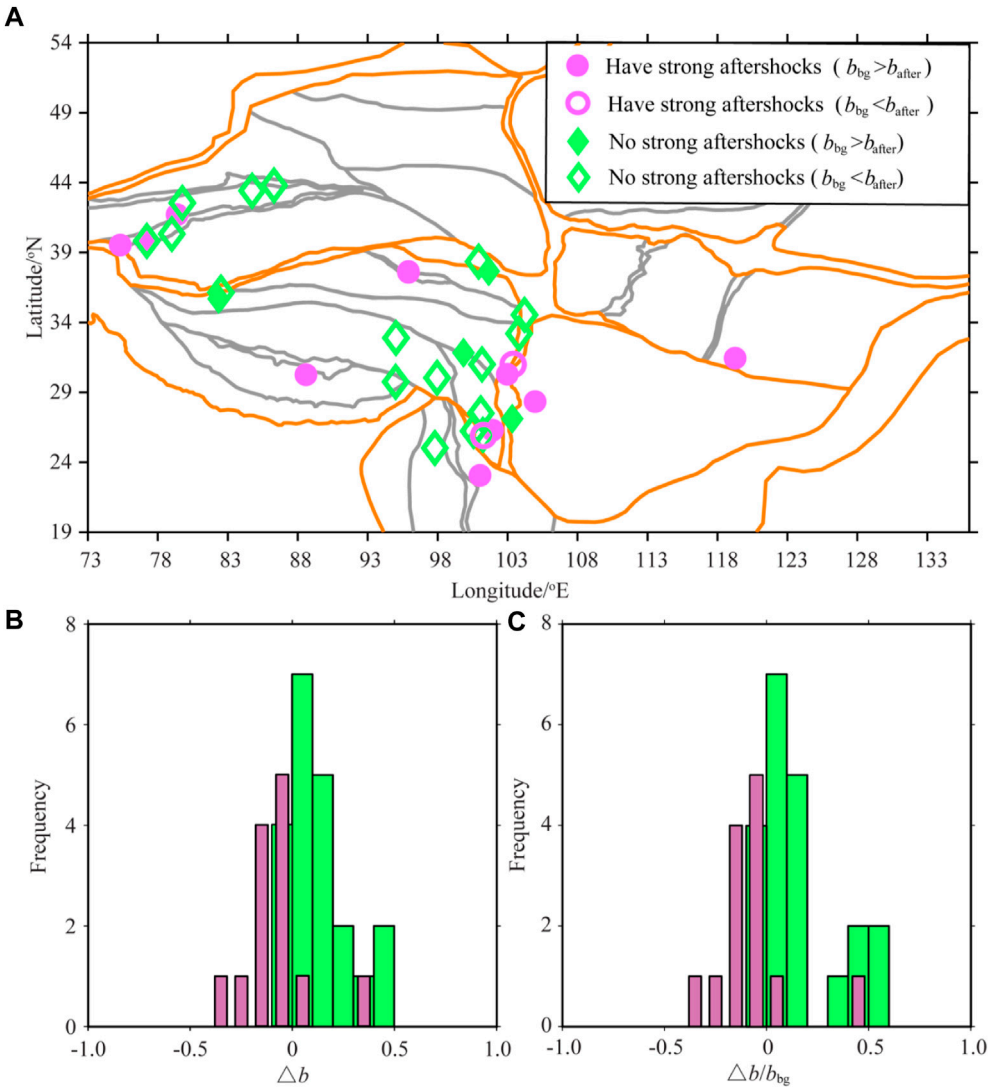

FIGURE 5
Distribution characteristics of 34 M_S≥6.0 earthquake sequences in the China continent. **(A)** Distribution of the epicenters of the main shocks. They are classified according to the presence or absence of strong aftershocks of M≥5.0 and the relative size relationship between b-values of background events (b_{bg}) and that of aftershocks (b_{after}), and indicated by different colors. The brown represents the boundary line of the primary plate, and the gray represents the boundary line of the secondary plate. **(B)** Statistical distribution of differences between background events b_{bg} and aftershock b_{after}, $\triangle b$. **(C)** Statistical relationship of $\triangle b/b_{bg}$. In **(B,C)**, light red represents the earthquake sequences having strong aftershocks of M≥5.0, and light green represents the earthquake sequences having no strong aftershocks of M≥5.0.

sequences have M≥5.0 aftershocks, and 17 earthquake sequences have no aftershocks with M≥5.0; when $\triangle b$<0, eleven earthquake sequences have M≥5.0 aftershocks, and four earthquake sequences have no aftershocks with M≥5.0. Furthermore, when $\triangle b$>0.1, only one earthquake event had aftershocks of M≥5.0, while when $\triangle b$<-0.1, all earthquake sequences had aftershocks of M≥5.0. The statistical results are illustrated in Figure 6A. This shows that the possibility of strong aftershocks with M≥5.0 can be reliably determined by defining $\triangle b$=±0.1. Moreover, from Figure 6A, when $\triangle b$<0, especially $\triangle b$<-0.1, the magnitude difference between a main shock and its largest aftershock mainly ranged from 0 to 1.5. While, when $\triangle b$>0, the magnitude difference ranged from 1.5 to 3.0.

The earthquake monitoring capability of the China Earthquake Networks Center was significantly improved after the 2008 M_S8.0 Wenchuan earthquake (Huang et al., 2017). To eliminate the influence of the change in earthquake monitoring capability, we excluded the earthquake sequences before the 2008 M_S8.0 Wenchuan earthquake and investigated the relationship between $\triangle b$ and the occurrence of strong

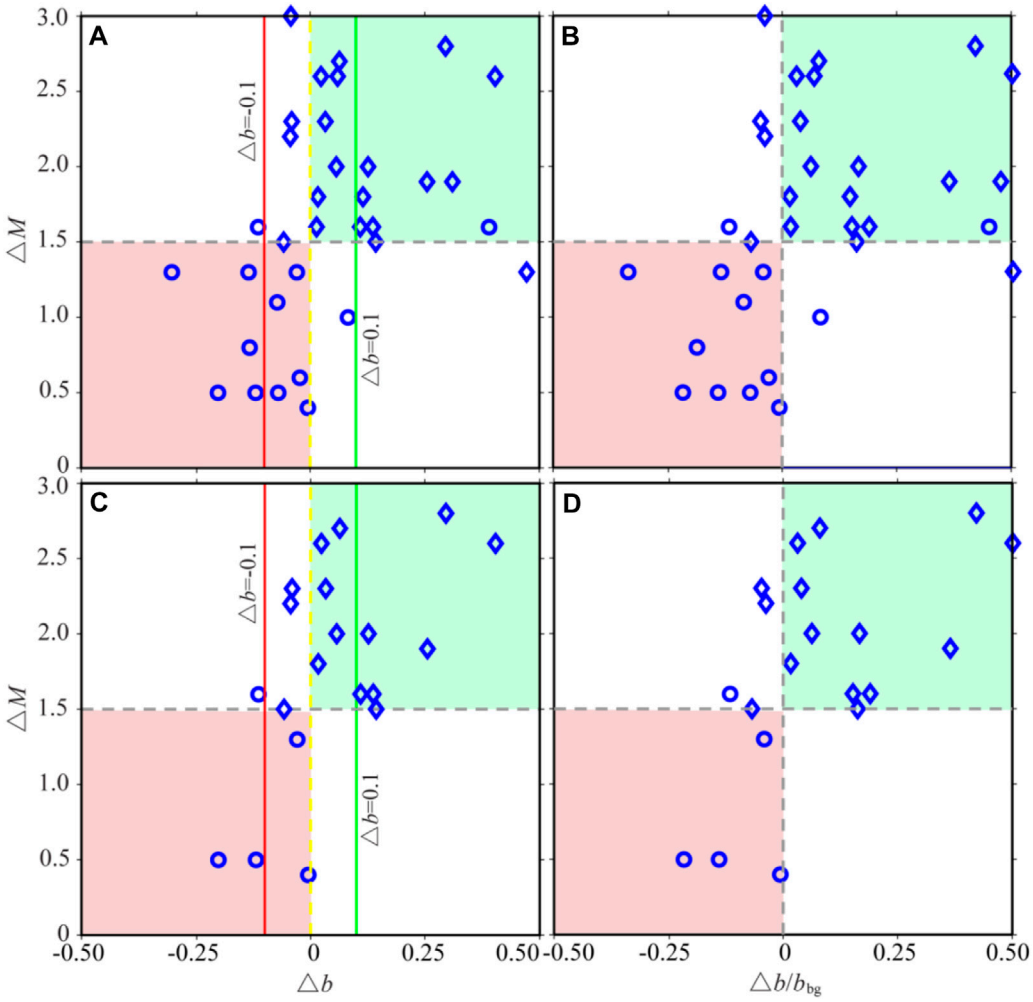

FIGURE 6
Relationship between magnitude difference and sequence parameters. **(A)** Relationship between $\triangle M$ and $\triangle b$ ($\triangle b = b_{after} - b_{bg}$) (1970.01.01–2020.07.30); **(B)** relationship between $\triangle M$ and $\triangle b/b_{bg}$ (1970.01.01–2020.07.30); **(C)** relationship between $\triangle M$ and $\triangle b$ of the sequences after 12 May 2008; **(D)** relationship between $\triangle M$ and $\triangle b/b_{bg}$ of the sequences after 12 May 2008. The circle represents the earthquake sequence having strong aftershocks with $M \geq 5.0$, and the diamond represents the earthquake sequence having no strong aftershocks with $M \geq 5.0$ in the fitting period. The red, yellow, and green lines indicate $\triangle b = 0.1$, $\triangle b = 0$ and $\triangle b = -0.1$, respectively. The green area represents $\triangle M > 1.5$ and $\triangle b > 0$, while the red area represents $\triangle M < 1.5$ and $\triangle b < 0$.

aftershocks of $M \geq 5.0$. The results demonstrate that all earthquake sequences have no strong aftershocks with $M \geq 5.0$ when $\triangle b > 0.1$, while when $\triangle b < -0.1$, all earthquake sequences have strong aftershocks with $M \geq 5.0$ (Figure 6C). In addition, we also used $\triangle b/b_{bg}$ for similar analyses, and found the same risk classification effectiveness using $\triangle b/b_{bg} = \pm 0.1$ as using $\triangle b = \pm 0.1$, as shown in Figures 6B,D.

Based on the aforementioned calculations, we defined $\triangle b = 0.1$ as the green threshold with low risk of $M \geq 5.0$ strong aftershocks, that is, when $\triangle b \geq 0.1$, the possibility of $M \geq 5.0$ strong aftershocks is low; $\triangle b = -0.1$ is a high-risk red threshold for strong aftershocks with $M \geq 5.0$. When $\triangle b$ is lower than this threshold, that is $\triangle b \leq -0.1$, the possibility of strong aftershocks with $M \geq 5.0$ is high; $\triangle b = 0$ represents a distinct yellow threshold. When $-0.1 < \triangle b < 0.1$, we should pay attention to the occurrence of strong $M \geq 5.0$ aftershocks. By combination with the TbDD method based on data-driven technology to calculate b_{bg}, b_{after}, and $\triangle b$, a strong aftershock traffic light system (SATLS) was constructed to accurately determine the risk of strong $M \geq 5.0$ aftershocks in real time, which makes it feasible to make targeted disaster mitigation decisions.

We performed SATLS classification of the occurrence of strong aftershocks with $M \geq 5.0$ for the 2022 M_S6.9 Menyuan earthquake sequence followed by only two aftershocks of $M \geq 5.0$. The M_S5.1 aftershock occurred within just a few hours after the main shock, and the poor data availability

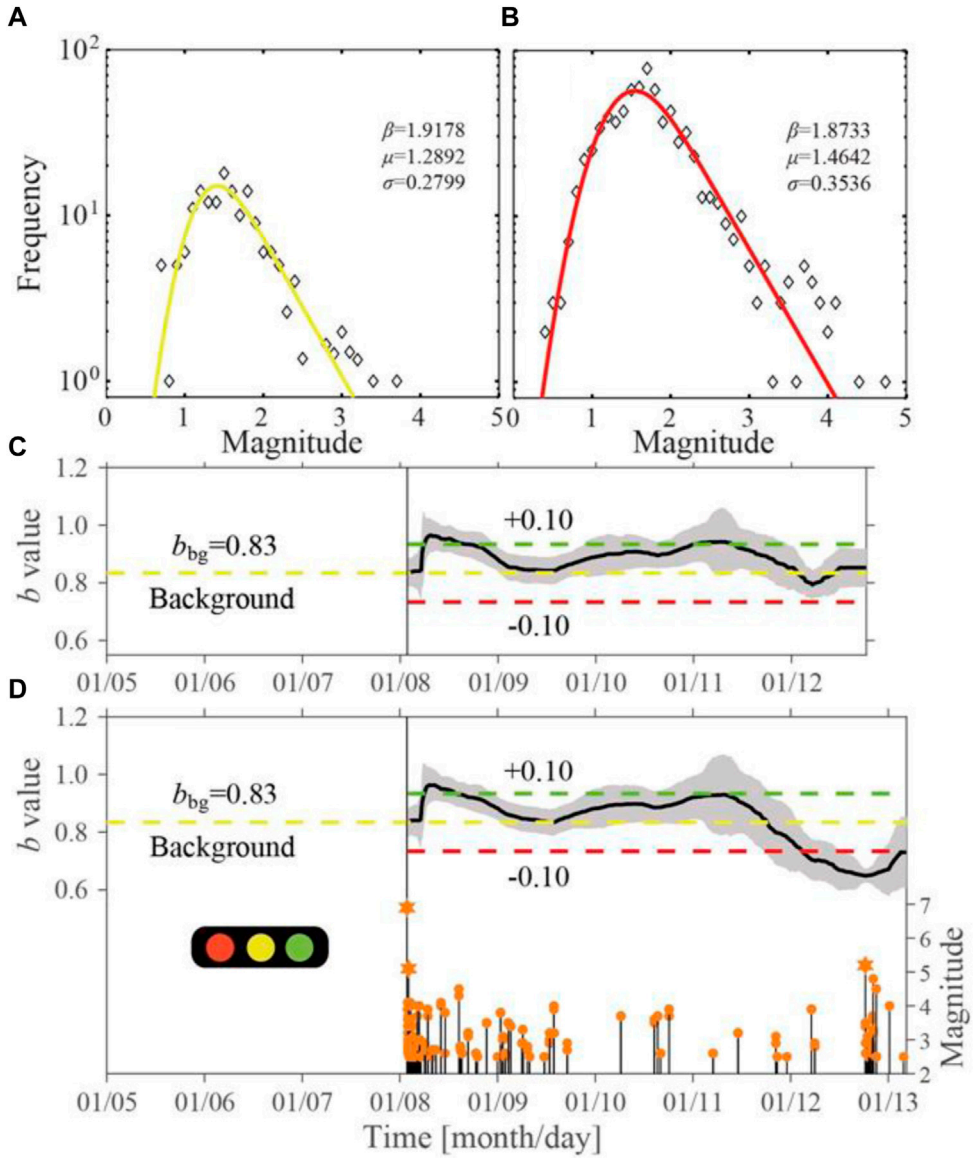

FIGURE 7
Characteristics of the *b*-value evolution for the 8 January 2022 Menyuan M_S6.9 earthquake sequence and SATLS settings. **(A,B)** Magnitude–frequency distribution (FMD) and the fitting results of the OK1993 model. They correspond to the background earthquake sequence (1970.01.01~2022.01.08) and aftershock sequence (2022.01.08~2022.01.12), respectively. The diamonds denote the FMD of the events. The solid curve indicates the fitting results of the OK1993 model, and the actual parameters are marked in each subgraph in the order of β, μ, and σ. **(C)** *b*-value of time series obtained using the events immediately before the strong aftershock (2022.01.08~2022.01.12). **(D)** *b*-value of time series calculated using the events between the main shock and the time after the strong aftershock (2022.01.08~2022.01.13). The yellow dotted line indicates background value b_{bg} (yellow threshold), the red dotted line denotes the red threshold (0.1 lower than the background value), the green dotted line represents the green threshold (0.1 higher than the background value), and the magnitude–time distribution (*M*-*t*) of the earthquake sequence is displayed.

before this event may result in large uncertainties in the *b*-values. Therefore, only the January 12 M_S5.2 aftershock was discussed here. The data for calculation were obtained from the National Unified Official Catalogue, and the spatial range covered was the same as the distribution of aftershocks. The events from 1970 to the time before the main shock were taken as background events, and those between the main shock and the M_S5.2 aftershock were taken as aftershock sequences.

The results showed that b_{bg} = 0.83 and b_{after} = 0.81, and the corresponding fitting curves of the OK1993 model are shown in Figures 7A,B. Because b_{after}<b_{bg}, it can be determined that the

yellow threshold of SATLS has been reached. The *b*-values of the time series were calculated by TbDD as shown in Figure 7C. Before the M_S5.2 aftershock, the *b*-value had dropped to about 0.79, that is, $\triangle b \approx$-0.04, according to which a yellow alert for the possibility of a strong aftershock with $M \geq 5$ would be declared.

We further investigated the *b*-values of the time-series between the main shock and the time after the M_S5.2 aftershock as shown in Figure 7D. The results indicated that before the M_S5.2 strong aftershock, the *b*-value decreased to about 0.63, $\triangle b \approx$-0.2, the magnitude of which is larger than that of $\triangle b \approx$-0.04, as obtained using events between the main shock and the M_S5.2 aftershock. After the M_S5.2 strong aftershock, the stress around the focal area changed and the *b*-value continued to decrease. Yang et al. (2022) obtained the background *b*-value of 0.84 using the maximum-likelihood method and the whole aftershock *b*-value of 0.67 using the least-squares method for the Menyuan earthquake, and our results were similar to theirs. The *h*-value is a constant in the revised Omori's law which describes the number of aftershocks after the main shock. It can be used to determine whether there might be future events with larger magnitudes during an ongoing sequence (Liu et al., 1979). If $h \gg 1$, it indicates that the largest magnitude earthquake already occurred as the main shock. If $h \ll 1$, then it was considered a foreshock sequence. The 2022 Menyuan sequence showed that the overall *h*-value was significantly larger than 1. (Yang et al., 2022).

Discussion

The SATLS proposed in this paper is, in a more general sense, an extension of the FTLS which determined whether an event was a main shock or a foreshock to an even stronger event yet to come. However, there are several limitations to the SATLS. First, the threshold settings of the SATLS are only based on a limited number of earthquake cases, and it is only suitable for the intraplate earthquake sequences of the $M \geq 6.0$ main shock in the China continent followed by $M \geq 5.0$ aftershocks. Moreover, there is a lack of systematic and comprehensive understanding of the relative relationship between the values of b_{after} and b_{bg} in different tectonic regions, which limits the general applicability of the SATLS. In addition, some researchers argue that the spatial distribution of *b*-values is highly variable. For example, the ductile shear zone has a higher *b*-value than the brittle-ductile shear zone (Villiger et al., 2020). Also, it is easy for a high *b*-value to be produced in rocks with low Young's modulus (Zorn et al., 2019) or high organic content, which causes difficulties in the application of SATLS for earthquake sequences with large-scale spatial distribution in aftershock zones, and it may be necessary to develop a set of two-dimensional time-space $\triangle b$ risk classification thresholds. There are also some shortfalls in this research. Thirty-four events may not be enough to derive exact thresholds. With respect to the whole *b*-value calculated by the OK1993 model, the uncertainty and the confidence interval of the whole *b*-value has not been resolved, which needs to be addressed in subsequent research.

During revision of this paper, there occurred in China on 5 September 2022, the M_S6.8 Luding earthquake with an M_S5.0 aftershock, which provided a new opportunity to verify the effectiveness of the SATLS. Therefore, along with the Menyuan earthquake, we also applied SATLS to the M_S6.8 2022 Luding earthquake sequence. We obtained b_{bg} = 0.9672 from the OK1993 model and *b*-values of time series by TbDD. The results showed that three days before the M_S5.0 earthquake, the *b*-value started to decrease. As of 13: 17 on October 23 when the M_S5.0 aftershock occurred, the *b*-value had decreased to about 0.86, for a $\triangle b \approx$ -0.1, which suggests that a red alert could have been declared for a strong aftershock of $M \geq 5.0$. To some extent, this event demonstrates the effectiveness of SATLS.

Although the N-test results showed that the Omi-R-J model failed in forecasting the strong M_S5.2 aftershock, the failure reason could not rule out the possibility that the Omi-R-J method is based on the Omori–Utsu formula with a relatively simple aftershock attenuation law, and it only demonstrates obvious forecasting effectiveness for aftershock sequences with underdeveloped secondary aftershocks. For more complex earthquake sequences, the analysis may need to be combined with the ETAS model. In fact, CSEP also focuses on the predictability of some huge earthquake cases (Schorlemmer et al., 2018). For example, after the 2011 *M*9.0 earthquake in East Japan, Nanjo *et al.* (2012) and Ogata *et al.* (2013) systematically tested the forecasting effectiveness of various versions of the ETAS model and confirmed that it showed good forecasting performance on complex aftershock sequences. In the future, a combination of the semi-quantitative and semi-qualitative SATLS and the quantitative statistical probability forecasting models is still a realistic and feasible choice.

Conclusion

It is difficult to accurately forecast a disaster-causing aftershock using only traditional statistical forecasting models. We first used the TbDD method based on data-driven technology to obtain reliable *b*-values of time series. Second, based on the empirical relationship, $\triangle b = b_{after} - b_{bg}$, from 34 $M \geq 6.0$ intraplate earthquake sequences in the China continent and their strongest aftershocks of $M \geq 5.0$, a strong aftershock traffic light system (SATLS) was constructed. Taking the 8 January 2022 M_S6.9 Menyuan earthquake in Qinghai Province as an example, a yellow alert attempt was made by using SATLS for the M_S5.2 strong aftershocks that occurred several days after the main shock. The main results are summarized as follows:

1) The Omi-R-J model for aftershock probability forecasting was employed to conduct 83 consecutive sliding forecasts of strong aftershocks of the M_S6.9 Menyuan earthquake sequence, and the forecasting performance was assessed by the N-test method. The results showed that the earthquake occurrence rates forecast by the Omi-R-J model before the largest aftershock (M_S5.2) were too low; however, the model can accurately forecast aftershock rates for each magnitude interval in most time-periods, which makes it difficult to accurately forecast this strong aftershock.
2) The data from our research on the 34 M≥6.0 intraplate earthquake sequences in the China continent showed that $\triangle b = b_{after} - b_{bg} = \pm 0.1$ can act as a discriminator to determine whether strong aftershocks of magnitude 5.0 or higher will occur. If the difference ($\triangle b = b_{after} - b_{bg}$) exceeded +0.1 ($\triangle b$ = 0.1) or was -0.1 ($\triangle b$ = -0.1), we assigned a traffic light color of green or red, respectively, otherwise yellow. We can further infer the possible magnitude of an aftershock based on the relationship between $\triangle M$ and $\triangle b$.
3) The b-value calculation of the M_S6.9 Menyuan earthquake sequence using TbDD showed that, for different time partitioning schemes, random partitioning times, and other technical rules, the perturbation of determined time series b-values was negligible. The b-value obtained using the events between the main shock and the M_S5.2 event decreased 0.04 ($\triangle b \approx$ -0.04) from 1.3 days before the M_S5.2 strong aftershock, while the b-value calculated using the events between the main shock and the time after the M_S5.2 earthquake decreased 0.2 and gradually recovered after this strong aftershock. From the time-series of b-values of the 2022 M_S6.9 Menyuan earthquake sequence, before the M_S5.2 event, only a yellow alert could be declared, which shows a gap from the expected determined red alert. One reason may be that it is questionable if the seismicity before an M≥5.0 strong aftershock could reveal the stress status of that moment. The fact that a strong aftershock of M≥5.0 abruptly changes the stress status in the focal area may be another factor. To improve the accuracy of forecast making, a deeper understanding of the true b-value and the detailed description of the stress evolution state in the source area is needed.(Gutenberg and Richter, 1944; Nandan et al., 2017; Si and Jiang, 2019; Jiang et al., 2021).

Data and resources

The earthquake catalog used in this paper was provided by the China Earthquake Networks Center. The Multi-Parametric Toolbox 3.0 (https://www.mpt3.org/Main/HomePage, last accessed February 2022) is used for the analysis of parametric optimization.

Data availability statement

The original contributions presented in the study are included in the article/Supplementary Material, and further inquiries can be directed to the corresponding author.

Author contributions

JB, FY, and CJ contributed to conceptualization. JB prepared the manuscript with contributions from all authors. JB, FY, and CJ wrote software for data processing. XY, YM, and CS contributed to the revised manuscript version.

Funding

This study was supported by the Joint Funds of the National Natural Science Foundation of China and the Foundation of Earthquake Science (U1839207), the Special Fund of the Institute of Geophysics, China Earthquake Administration (DQJB22Z01) and the 2022 Earthquake Regime Tracking Work of the CEA (2022010116).

Acknowledgments

The authors thank Yan Zhang and Hongyu Zhai of the Institute of Geophysics, China Earthquake Administration, for their constructive suggestions on this paper. We also thank the editor and two anonymous reviewers for their very helpful comments and suggestions. This study used the National Unified Official Catalogue provided by the China Earthquake Networks Center.

Conflict of interest

The authors declare that the research was conducted in the absence of any commercial or financial relationships that could be construed as a potential conflict of interest.

Publisher's note

References

Bi, J. M., and Jiang, C. S. (2020). Comparison of early aftershock forecasting for the 2008 Wenchuan M_S8.0 earthquake. *Pure Appl. Geophys.* 177, 9–25. doi:10.1007/s00024-019-02192-6

Bi, J. M., Jiang, C. S., Lai, G. J., and Song, C. (2022). Effectiveness evaluation and constraints of early aftershock probability forecasting for strong earthquakes in continental China. *Chin. J. Geophys.* (in Chinese) 65 (7), 2532–2545. doi:10.6038/cjg2022P0411

Bi, J. M., Jiang, C. S., and Ma, Y. (2020). The study on early sequence parameters and probability forecasting of strong aftershocks of Changning M_S6.0 earthquake on June 17, 2019, Sichuan Province. *Earthquake* (in Chinese) 40 (2), 140–154. doi:10.12196/j.issn.1000-3274.2020.02.011

Chan, L. S., and Chandler, A. M. (2001). Spatial bias in *b*-value of the frequency–magnitude relation for the Hong Kong region. *Journal of Asian Earth Sciences* 20 (1), 73–81. doi:10.1016/s1367-9120(01)00025-6

Gardner, J. K., and Knopoff, L. (1974). Is the sequence of earthquakes in Southern California with aftershocks removed, Poissonian? *Bulletin of the Seismological Society of America* 64, 1363–1367. doi:10.1785/bssa0640051363

Grimm, C., Käser, M., Hainzl, S., Pagani, M., and Kuchenhoff, H. (2021). Improving earthquake doublet frequency predictions by modified spatial trigger kernels in the Epidemic-Type Aftershock Sequence (ETAS) Model. *Bull. Seismol. Soc. Am.* 112 (1), 474–493. doi:10.1785/0120210097

Gulia, L., Rinaldi, A. P., Tormann, T., Vannucci, G., Enescu, B., and Wiemer, S. (2018). The effect of a mainshock on the size distribution of the aftershocks. *Geophys. Res. Lett.* 45, 13277–13287. doi:10.1029/2018GL080619

Gulia, L., and Wiemer, S. (2019). Real-time discrimination of earthquake foreshocks and aftershocks. *Nature* 574 (7777), 193–199. doi:10.1038/s41586-019-1606-4

Gulia, L., Wiemer, S., and Vannucci, G. (2020). Pseudoprospective evaluation of the foreshock traffic-light system in Ridgecrest and implications for aftershock hazard assessment. *Seismological Research Letters* 91 (5), 2828–2842. doi:10.1785/0220190307

Gutenberg, R., and Richter, C. F. (1944). Frequency of earthquakes in California. *Bulletin of the Seismological Society of America* 34, 185–188. doi:10.1785/bssa0340040185

Huang, F. Q., Li, M., Ma, Y. C., Han, Y., Tian, L., Yan, W., et al. (2017). Studies on earthquake precursors in China: A review for recent 50 years. *Geodesy and Geodynamics* 8 (1), 1–12. doi:10.1016/j.geog.2016.12.002

Iwata, T. (2013). Estimation of completeness magnitude considering daily variation in earthquake detection capability. *Geophysical Journal International* 194 (3), 1909–1919. doi:10.1093/gji/ggt208

Jiang, C., Qiu, Y., Jiang, C. S., Yin, X. X., Zhai, H. Y., Zhang, Y. B., et al. (2021a). A new method for calculating *b*-value of time sequence based on data-driven (TbDD): A case study of the 2021 yangbi M_S6.4 earthquake sequence in yunnan. *Chinese Journal of Geophysics (in Chinese)* 64 (9), 3126–3134. doi:10.6038/cjg2021P0385

Jiang, C., Jiang, C. S., Yin, F. L., Zhang, Y. B., Bi, J. M., Long, F., et al. (2021b). Traffic light system (TLS) for risk control of earthquake induced by industrial activities: Problem and prospects. *Progress in Geophysics* (in Chinese) 36 (6), 2320–2328. doi:10.6038/pg2021EE0495

Jiang, C. S., Bi, J. M., Wang, F. C., et al. (2018). Application of the Omi-R-J method for forecast of early aftershocks to the 2017 Jiuzhaigou, Sichuan, M_S7.0 earthquake. *Chinese Journal of Geophysics* (in Chinese) 61, 2099–2110. doi:10.6038/cjg2018M0113

Jiang, C. S., Han, L. B., Long, F., Lai, G., Yin, F., Bi, J., et al. (2021). Spatiotemporal heterogeneity of *b* values revealed by a data-driven approach for June 17, 2019 M_S 6.0, Changning Sichuan, China earthquake sequence. *Nat. Hazards Earth Syst. Sci.* 21, 2233–2244. doi:10.5194/nhess-21-2233-2021

Kagan, Y. Y., and Jackson, D. D. (1995). New seismic gap hypothesis: Five years after. *J. Geophys. Res.* 100 (B3), 3943–3959. doi:10.1029/94jb03014

Lippiello, E., Giacco, F., Marzocchi, W., Godano, G., and Arcangelis, L. d. (2017). Statistical features of foreshocks in instrumental and ETAS catalogs. *Pure Appl. Geophys.* 174 (4), 1679–1697. doi:10.1007/s00024-017-1502-5

Liu, Z. R., Qian, Z. X., and Wang, W. Q. (1979). Decay in earthquake frequency, an indicator of foreshocks. *Journal of Seismological Research* (in Chinese) 2 (4), 1–9.

Lv, X. J., Gao, M. T., Gao, Z. W., and Mi, S. T. (2007). Comparison of the spatial distribution of ground motion between mainshocks and strong aftershocks. *Acta Seismologica Sinica* (in Chinese) 29 (3), 295–301. doi:10.1007/s11589-007-0312-8

Matsu'ura, R. S. (1986). Precursory quiescence and recovery of aftershock activities before some large aftershocks. *Bulletin of the Earthquake Research Institute* 61, 1–65.

Mignan, A., Jiang, C. S., Zechar, J. D., Wiemer, S., Wu, Z., and Huang, Z. (2013). Completeness of the mainland China earthquake catalog and implications for the setup of the China earthquake forecast testing center. *Bulletin of the Seismological Society of America* 103 (2A), 845–859. doi:10.1785/0120120052

Mignan, A., and Woessner, J. (2012). Estimating the magnitude of completeness for earthquake catalogs. *CORSSA Community Online Resource for Statistical Seismicity Analysis*. doi:10.5078/corssa-00180805

Nandan, S., Ouillon, G., Wiemer, S., and Sornette, D. (2017). Objective estimation of spatially variable parameters of epidemic type aftershock sequence model: Application to California. *J. Geophys. Res. Solid Earth* 122 (7), 5118–5143. doi:10.1002/2016JB013266

Nanjo, K. Z., Izutsu, J., Orihara, Y., and Kamogawa, M. (2022). Changes in seismicity pattern due to the 2016 Kumamoto earthquake sequence and implications for improving the foreshock traffic-light system. *Tectonophysics* 822, 229175. doi:10.1016/j.tecto.2021.229175

Nanjo, K. Z., Tsuruoka, H., Yokoi, S., Ogata, Y., Falcone, G., Hirata, N., et al. (2012). Predictability study on the aftershock sequence following the 2011 Tohoku-Oki, Japan, earthquake: First results. *Geophys. J. Int.* 191, 653–658. doi:10.1111/j.1365-246X.2012.05626.x

Ogata, Y., and Katsura, K. (1993). Analysis of temporal and spatial heterogeneity of magnitude frequency distribution inferred from earthquake catalogues. *Geophys. J. Int.* 113 (3), 727–738. doi:10.1111/j.1365-246x.1993.tb04663.x

Ogata, Y., Katsura, K., Falcone, G., Nanjo, K., and Zhuang, J. (2013). Comprehensive and topical evaluations of earthquake forecasts in terms of number, time, space, and magnitude. *Bulletin of the Seismological Society of America* 103 (3), 1692–1708. doi:10.1785/0120120063

Ogata, Y. (2001). Increased probability of large earthquakes near aftershock regions with relative quiescence. *J. Geophys. Res.* 106, 8729–8744. doi:10.1029/2000jb900400

Ogata, Y. (2006). Monitoring of anomaly in the aftershock sequence of the 2005 earthquake of M7.0 off coast of the Western Fukuoka, Japan, by the ETAS model. *Geophys. Res. Lett.* 33, L01303. doi:10.1029/2005GL024405

Ogata, Y. (1989). Statistical model for standard seismicity and detection of anomalies by residual analysis. *Tectonophysics* 169 (1/2/3), 159–174. doi:10.1016/0040-1951(89)90191-1

Omi, T., Ogata, Y., Hirata, Y., and Aihara, K. (2013). Forecasting large aftershocks within one day after the main shock. *Sci. Rep.* 3, 2218. doi:10.1038/srep02218

Omi, T., Ogata, Y., Hirata, Y., and Aihara, K. (2015). Intermediate-term forecasting of aftershocks from an early aftershock sequence: Bayesian and ensemble forecasting approaches. *J. Geophys. Res. Solid Earth* 120 (4), 2561–2578. doi:10.1002/2014JB011456

Omi, T., Ogata, Y., Shiomi, K., Enescu, B., Sawazaki, K., and Aihara, K. (2016). Automatic aftershock forecasting: A test using real-time seismicity data in Japan. *Bulletin of the Seismological Society of America* 106 (6), 2450–2458. doi:10.1785/0120160100

Omori, F. (1894) Tokyo, Japan. Imperial University of Tokyo, 111–200.On aftershocks of earthquakes, Doctoral dissertation.

Reasenberg, P. A., and Jones, L. M. (1989). Earthquake hazard after a mainshock in California. *Science* 243, 1173–1176. doi:10.1126/science.243.4895.1173

Scholz, C. H. (2015). On the stress dependence of the earthquake *b*-value. *Geophys. Res. Lett.* 42 (5), 1399–1402. doi:10.1002/2014GL062863

Scholz, C. H. (1968). The frequency-magnitude relation of microfracturing in rock and its relation to earthquakes. *Bulletin of the Seismological Society of America* 58 (1), 399–415. doi:10.1785/bssa0580010399

Schorlemmer, D., Gerstenberger, M. C., Wiemer, S., Jackson, D. D., and Rhoades, D. A. (2007). Earthquake likelihood model testing. *Seismological Research Letters* 78, 17–29. doi:10.1785/gssrl.78.1.17

Schorlemmer, D., Werner, M. J., Marzocchi, W., Jordan, T. H., Ogata, Y., Jackson, D. D., et al. (2018). The collaboratory for the study of earthquake predictability: Achievements and priorities. *Seismological Research Letters* 89 (4), 1305–1313. doi:10.1785/0220180053

Schwarz, G. (1978). Estimating the dimension of a model. *Ann. Statist.* 6 (2), 461–464. doi:10.1214/aos/1176344136

Shcherbakov, R. (2021). Statistics and forecasting of aftershocks during the 2019 Ridgecrest, California, earthquake sequence. *J. Geophys. Res. Solid Earth* 126, e2020JB020887. doi:10.1029/2020JB020887

Si, Z. Y., and Jiang, C. S. (2019). Research on parameter calculation for the Ogata-Katsura 1993 model in terms of the frequency-magnitude distribution based on a data-driven approach. *Seismological Research Letters* 90 (3), 1318–1329. doi:10.1785/0220180372

Trevlopoulos, K., Guéguen, P., Helmstetter, A., and Cotton, F. (2020). Earthquake risk in reinforced concrete buildings during aftershock sequences based on period elongation and operational earthquake forecasting. *Structural Safety* 84, 101922. doi:10.1016/j.strusafe.2020.101922

Utsu, T. (1961). A statistical study of on the occurrence of aftershocks. *Geophysical Magazine* 30, 521–605.

Villiger, L., Gischig, V. S., Doetsch, J., Krietsch, H., Dutler, N. O., Jalali, M., et al. (2020). Influence of reservoir geology on seismic response during decameter-scale hydraulic stimulations in crystalline rock. *Solid Earth* 11 (2), 627–655. doi:10.5194/se-11-627-2020

Woessner, J., Hainzl, S., Marzocchi, W., Werner, M. J., Lombardi, A. M., Catalli, F., et al. (2011). A retrospective comparative forecast test on the 1992 Landers sequence. *J. Geophys. Res.* 116, B05305. doi:10.1029/2010JB007846

Yang, H. F., Wang, D., Guo, R. M., Xie, M., Zang, Y., Wang, Y., et al. (2022). Rapid report of the 8 january 2022 menyuan *Ms*6.9 earthquake, Qinghai, China. *Earthquake Research Advances* 2 (1), 100113–100114. doi:10.1016/j.eqrea.2022.100113

Zechar, J. D. (2010). "Evaluating earthquake predictions and earthquake forecasts: A guide for students and new researchers, *Community online resource for statistical seismicity analysis* 126. doi:10.5078/corssa-77337879

Zhang, C. J., Hou, Y. Y., Hu, B., Xu, H. H., and Wang, D. B. (2011). Analysis on the seismic activities and hazards of M7.1 earthquake, 2010 and M6.3 earthquake, 2011 in New Zealand. *Recent Developments in World Seismology* 1 (4), 44–51. doi:10.3969/j.issn.0235-4975.2011.04.010

Zorn, E., Kumar, A., Harbert, W., and Hammack, R. (2019). Geomechanical analysis of microseismicity in an organic shale: A West Virginia marcellus shale example. *Interpretation* 7 (1), T231–T239. doi:10.1190/int-2018-0072.1

frontiers | Frontiers in Earth Science

TYPE Original Research
PUBLISHED 23 January 2023
DOI 10.3389/feart.2023.1043468

OPEN ACCESS

EDITED BY
Giovanni Martinelli,
National Institute of Geophysics and Volcanology, Italy

REVIEWED BY
Mikhail Rodkin,
Institute of Earthquake Prediction Theory and Mathematical Geophysics (RAS), Russia
Yan Xue,
China Agricultural University, China

*CORRESPONDENCE
Yingfeng Ji,
yingfengji@itpcas.ac.cn

SPECIALTY SECTION
This article was submitted to Solid Earth Geophysics, a section of the journal Frontiers in Earth Science

RECEIVED 13 September 2022
ACCEPTED 03 January 2023
PUBLISHED 23 January 2023

CITATION
Gao J, Zhu Y, Ji Y, Zhu W, Qu R, Li J, Xu L and Xie C (2023), Low-intensity anomaly involving ML≥4 events preceding strong earthquakes in Tibet.
Front. Earth Sci. 11:1043468.
doi: 10.3389/feart.2023.1043468

Low-intensity anomaly involving ML≥4 events preceding strong earthquakes in Tibet

Jinrui Gao[1,2], Ye Zhu[1,3], Yingfeng Ji[1,3]*, Weiling Zhu[1,3], Rui Qu[1,3], Jiaji Li[2], Liang Xu[2] and Chaodi Xie[4]

[1]State Key Laboratory of the Tibetan Plateau Earth System, Environment and Resources (TPESER), Institute of Tibetan Plateau Research, Chinese Academy of Sciences, Beijing, China, [2]Seismological Bureau of the Tibet Autonomous Region, Lasha, China, [3]University of the Chinese Academy of Sciences, Beijing, China, [4]Department of Geophysics, Yunnan University, Kunming, China

Seismic quiescence or enhanced phenomena are anomalous changes against the background of normal seismic activity. Preliminary studies have found that earthquakes with a magnitude of ML≥4 often occur at a low occurrence frequency before giant earthquakes in Tibet. This study analyzed the catalog of ML≥4 earthquakes from 2008 to 2022 and examined the anomalous occurrence of ML≥4 earthquakes preceding most ML≥6 earthquakes. When the monthly occurrence frequency of ML≥4 earthquakes was lower than 4 times over six consecutive months, the subsequent occurrence of ML≥6 earthquakes was highly likely as evidenced by observations. The anomalous characteristics of low-intensity activities were analyzed as a medium- and short-term forecasting index for large earthquakes in the Tibetan area.

KEYWORDS

Tibet, seismic quiescence, low-frequency, anomaly, earthquake forecasting

1 Introduction

Statistical analysis of quiescent seismic activity anomalies constitutes one of the methods used in seismological forecasting (e.g., Mogi, 1969; Huang et al., 2001; Wyss et al., 2004; Gentili et al., 2017; Gentili et al., 2019; Shi, 2020; Liu, 2021). The seismic quiescence area reflects the accumulation of regional strain during a certain period and thus is meaningful (Sobolev et al., 2002; Zöller et al., 2002; Chen et al., 2005; Wu and Chiao, 2006; Huang, 2008; Qin et al., 2015; Wen et al., 2016). Obvious moderate earthquake quiescence before many large earthquakes has been suggested and considered a precursor of strong earthquakes with physical significance as an important basis for earthquake forecasting (e.g., Huang et al., 2001; Zhang, 2001; Di Giovambattista and Tyupkin, 2004; Wyss et al., 2004; Zhu et al., 2012; Wang et al., 2014; Gentili et al., 2017; Wang et al., 2017; Chen, 2018; Zhang et al., 2018; Gentili et al., 2019; Katsumata and Nakatani, 2021). The seismic activity in mainland China indicates the alternation of strong and weak segments and associated fluctuations (e.g., Su, 1996), and the accumulated seismic data for northern China and southwestern China (Yunnan) suggest an appropriate minimum limit of the magnitude and quiescence period for seismic forecasting using the optimal parameter combination (e.g., Han, 1998; Han et al., 2006a; 2006b).

Although the Tibetan Plateau is vast and sparsely populated, earthquakes of magnitude six and above are highly destructive and can easily result in casualties and property losses (Tillotson, 1951; Liu et al., 2014; Liu et al., 2015). The destructive earthquakes caused direct economic losses of approximately 1,280 billion Yuan from 1993 to 2016, nearly equal to 80% of China's fiscal revenue in 2016 (e.g., Li et al., 2018). For instance, the 2020 Yutian earthquakes affected an area of approximately 128,310 km^2 with

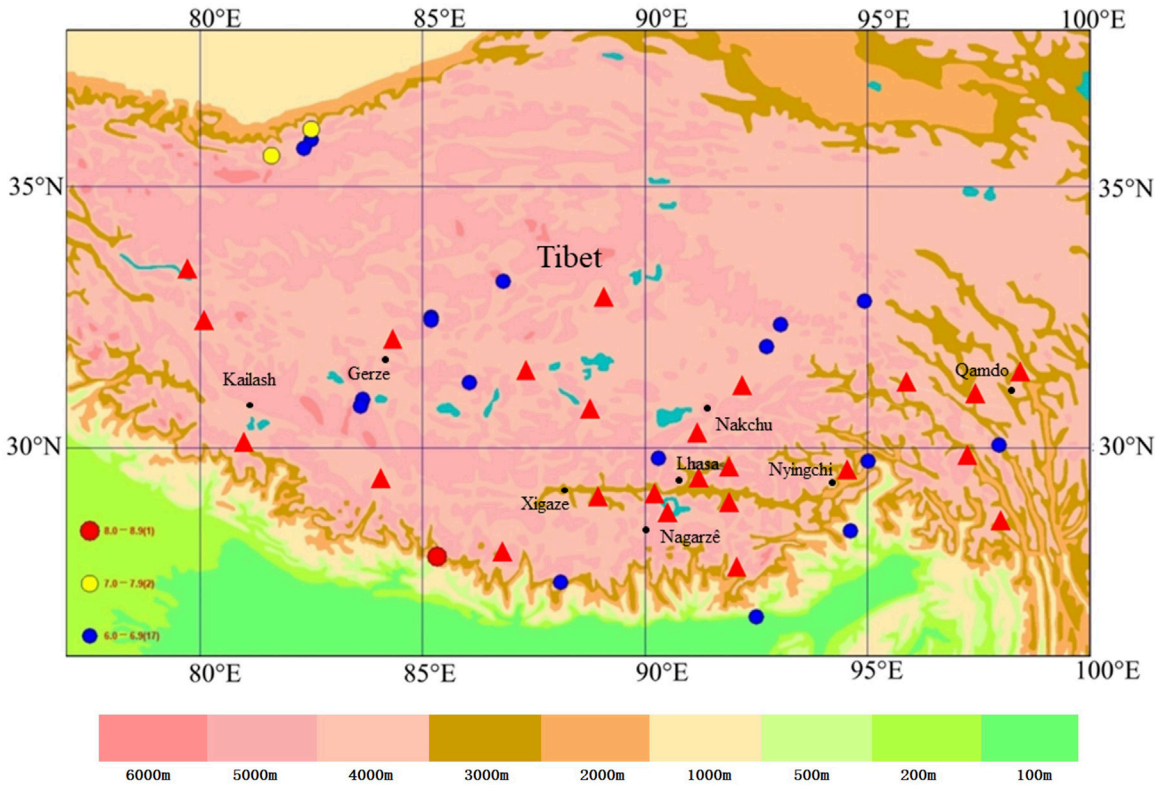

FIGURE 1
Epicenter distribution of ML≥6 earthquakes in Tibet since 2008. The background color indicates the height. The colored circles indicate the epicenters of the ML≥6 earthquakes recorded by the China Earthquake Network Center. The red triangles indicate the seismic stations in Tibet in 2018.

455,000 inhabitants, causing direct economic losses of 1,080 million Yuan, and 2,970,054 m^2 of houses in rural residential areas were completely destroyed or seriously damaged (e.g., Ni and Hong, 2014). From the perspective of reducing earthquake disasters, it is of great significance to explore and study forecasting methods for large earthquakes. Previous studies have also suggested that before the occurrence of M>6 earthquakes in Tibet (e.g., Chen, 2007; Liu et al., 2008; Yu et al., 2013; Tian et al., 2021), the epicenter and surrounding regions of earthquakes with a magnitude of ML≥4 were characterized by a large quiescent area (Chen et al., 2014). To further explore the relationship between low-intensity activity anomalies of ML≥4 earthquakes and large earthquakes, we conducted spatiotemporal scans of ML≥4 earthquakes in the Tibet Autonomous Region and adjacent areas (hereafter referred to as Tibet), performed statistical analysis of low-intensity anomalies to predict their significance and criteria, and determined medium- and short-term predictors of ML≥6 earthquakes with satisfactory regularity and reliability.

2 Data and methods

Regarding the sparse earthquake monitoring network in Tibet and because the magnitude of completeness is the ML≥3 level, the lower limit of the magnitude in this study was selected as ML=4.0. The catalog of M<5 earthquakes used in this study was a catalog of monthly earthquake reports obtained from the Tibet Regional Seismological Network from 1987 to 2022 (Seismological Bureau of the Tibet Autonomous Region), and the catalog of earthquakes of ML≥5 was compiled by the China Earthquake Network Center (China Earthquake Administration). The magnitude completeness for the regional catalog over running time windows has been checked to be ML≥3.0 and confirmed not to influence the ML≥4 earthquake occurrence frequency change. During daily earthquake forecasting, we adopted a very convenient statistical method to track this anomaly. We defined the occurrence frequency of fewer than 24 ML≥4 earthquakes over half a year in Tibet as a low-intensity anomaly and conducted time scans for the ML≥4 earthquake low-intensity occurrence within a 6-month window and 1-month steps. In this study, we focus on the Tibetan region because a great number of multidisciplinary studies have been conducted on forecasting methods for larger earthquakes, and the Tibetan Plateau has one of the highest seismic hazards in the world, such as the 1950 Assam M8.6 earthquake (e.g., Tillotson, 1951).

The study area was selected in the Tibet Autonomous Region and adjacent areas within 50 km around the Tibet Autonomous Region, covering the majority of the Tibetan Plateau (Figure 1). Considering the occurrence frequency of ML≥4 earthquakes in Tibet and adjacent areas, there is a notable difference before and after 2008 (Figure 2). From 1987 to 2007, the average annual recurrence frequency was 19 times, but from 2008 to 2022, the average annual recurrence frequency increased to >50 times. This could be explained by the rapid construction of the seismic monitoring network in 2008, namely, the 10th Five-Year Plan project. Before 2007, there were only five

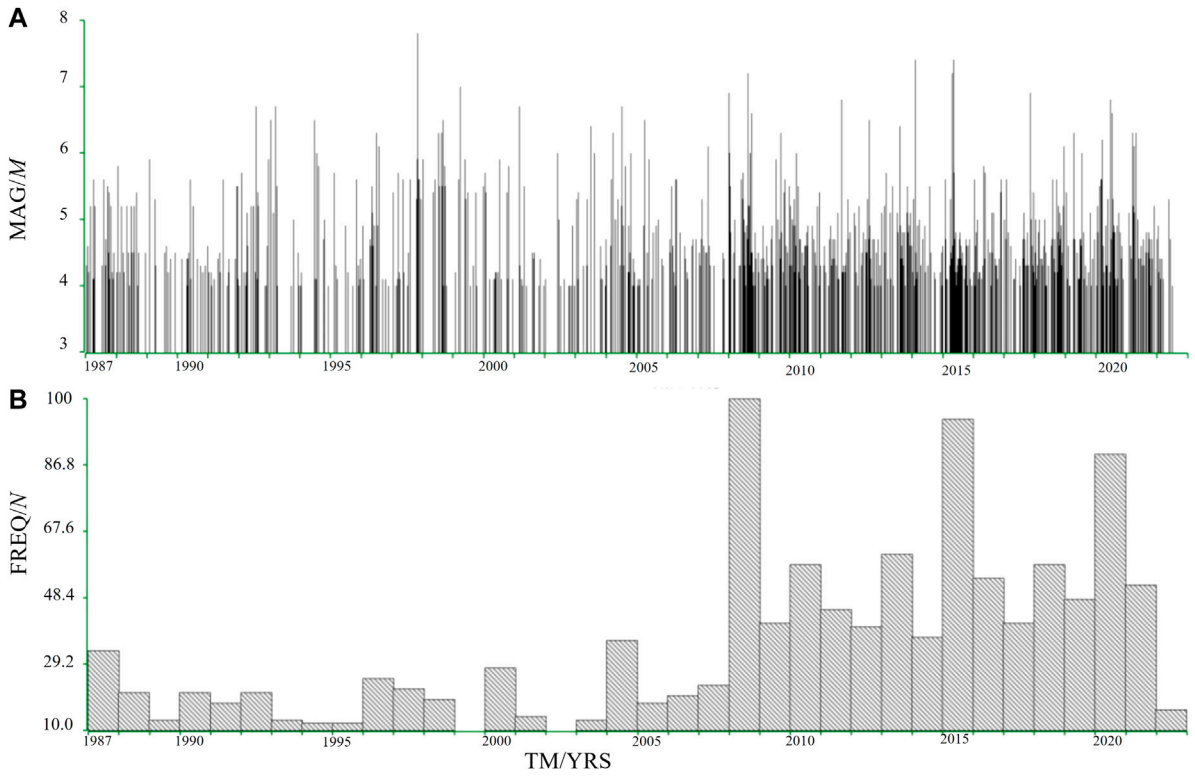

FIGURE 2
Magnitude (MAG)-time (TM) and occurrence frequency (FREQ)-time diagrams of the ML≥4 earthquake occurrences from 1987 to 2022. The unit of time is years (YRS) **(A)** The earthquake magnitude adopts the ML scale according to the local network **(B)** The occurrence frequency uses the number (N) of times per year as a unit.

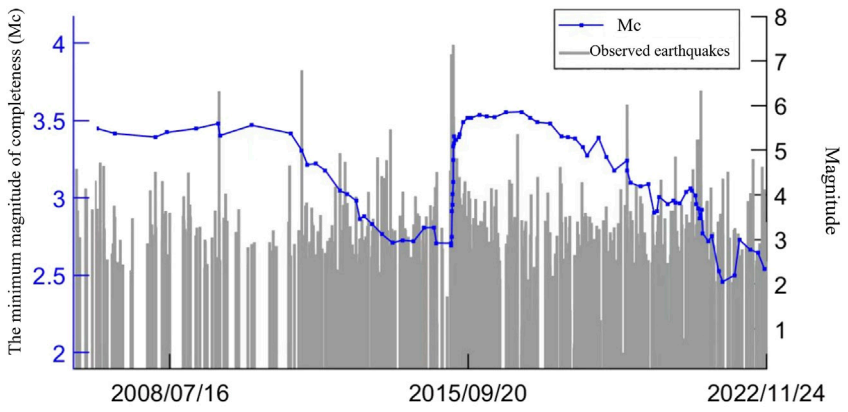

FIGURE 3
Variation in the minimum magnitude of completeness (Mc, blue curve) over 14 years in this study based on the MAXC and GFT methods using the software package of ZMAP (Stefan Wiemer, ETH).

seismic stations in Tibet, and the recorded ML≥4 earthquake catalog was incomplete (Gao et al., 2015). However, after 2008, the number of seismic stations in the Tibetan region significantly increased, and the monitoring capacity was greatly improved (e.g., Gao et al., 2015).

The minimum magnitude of completeness (Mc) in earthquake catalogs plays an important role in studying seismicity and assessing seismic hazards (e.g., Feng et al., 2010; Jiang and Wu, 2011; Yu et al., 2020). The specific calculation methods for Mc are the maximum curvature method (MAXC; Woessner et al., 2004) and the goodness-of-fit method (GFT; Wiemer and Wyss, 2000), or the entire magnitude range method (EMR; Woessner and Wiemer, 2005). Another method for calculating Mc is based on non-G-R relationships, such as the magnitude sequence (Schorlemmer and Woessner, 2008). In this study, we use the combination of MAXC, GFT and magnitude-

TABLE 1 Parameters of the ML≥6 earthquakes in Tibet from 2008 to 2022.

Number	[a]Date	Latitude (N°)	Longitude (E°)	Depth (km)	Magnitude (ML)	[b]Epicenter	ML≥4 foreshocks (months, times/m)	[c]Poisson possibility
1	2008-01-09	32.50	85.20	24	6.9	Gaize, Tibet AR	7, 0.9	2.13%
	2008-01-16	32.45	85.20	15	6.0	Gaize, Tibet AR	7, 0.9	2.13%
2	2008-03-21	35.60	81.60	33	7.3	Yutian, Xinjiang	7, 0.9	2.13%
3	2008-08-25	31.00	83.60	10	6.8	Zhongba, Tibet AR	6, 3.3	20.23%
	2008-09-25	30.80	83.60	10	6.0	Zhongba, Tibet AR	6, 3.3	20.23%
4	2008-10-06	29.80	90.30	8	6.6	Dangxiong, Tibet AR	6, 3.3	20.23%
5	2009-07-24	31.25	86.05	13	6.0	Nima, Tibet AR	8, 3.6	20.23%
6	2010-03-24	32.36	93.05	7	6.1	Nie Rong, Tibet AR	8, 3.9	20.23%
7	2011-09-18	27.42	88.10	11	6.8	Sikkim, India	13, 3.2	20.23%
8	2012-08-12	35.90	82.50	30	6.2	Yutian, Xinjiang	10, 3.1	20.23%
9	2013-08-12	30.04	97.96	15	6.1	Zuogong, Tibet AR	11, 3.1	20.23%
10	2014-02-12	36.10	82.50	12	7.3	Yutian, Xinjiang	—	—
11	2015-04-25	27.91	85.33	12	8.1	Nepal	12, 2.2	15.76%
12	2016-10-17	32.81	94.93	9	6.2	Zaduo, Qinghai	—	—
13	2017-11-18	29.75	95.02	10	6.9	Milin, Tibet AR	12, 2.2	15.76%
14	2019-04-24	28.40	94.61	10	6.3	Medog, Tibet AR	—	—
15	2020-06-26	35.73	82.33	10	6.4	Yutian, Xinjiang	6, [d]2.3	15.76%
16	2020-07-23	33.19	86.81	10	6.6	Nima, Tibet AR	6, [d]2.3	15.76%
17	2021-03-19	31.94	92.74	10	6.1	Tibet AR	6, 2.5	15.76%
18	2021-04-28	26.76	92.50	10	6.2	India	6, 2.5	15.76%

[a]The data format follows the yyyy-mm-dd format in this study.
[b]Tibet AR, denotes the Tibet Autonomous Region in this study.
[c]The expectation value of Poisson possibility is 3.85 times per month for the ML≥4 foreshock events in this study (Supplementary Table S2).
[d]The period calculated is from 2019 to 09 to 2020–02 due to the occurrence of M≥5 earthquakes in 2020–03 and 2020-05, respectively.

sequence methods based on the software package ZMAP (Stefan Wiemer, ETH) according to the G-R law and the maximum curvature of logN-M correlation analysis (Figure 3; Supplementary Table S1). The advantage of complementing the earthquake-sequence method is that it can avoid the significant reduction in seismic monitoring capability in the aftershock area or even in a larger area after a strong earthquake (Aki, 1965). The observed earthquakes were randomly sampled, and the statistics were calculated after each sampling. The standard variance of each statistic was estimated as ΔMc (Yu et al., 2020). For these reasons, this study considered the period from 2008 to 2022, during which the minimum magnitude of the Tibetan network could reach 2.5–3.5 and

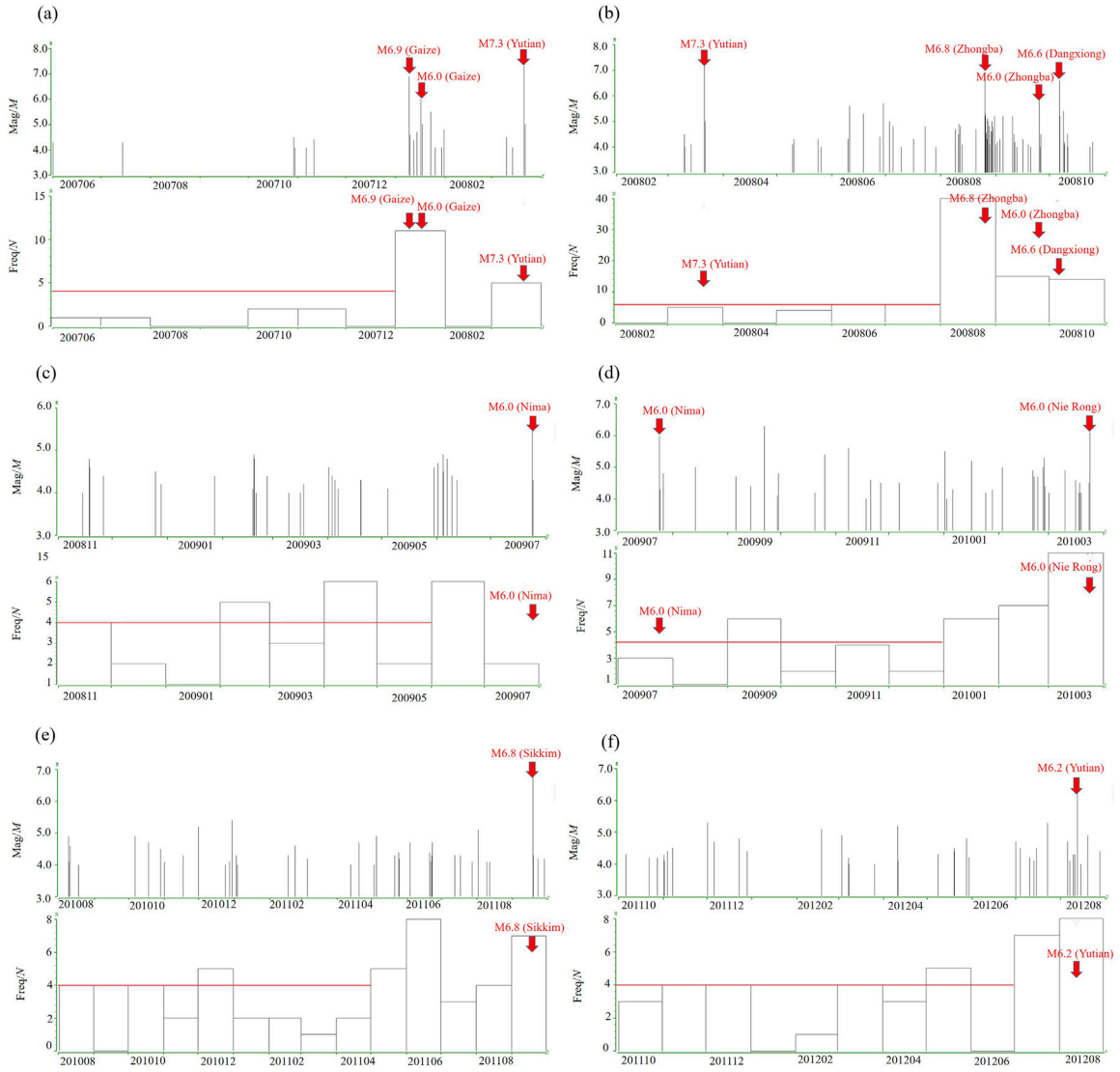

FIGURE 4
Magnitude–time and occurrence frequency–time diagrams of the ML≥4 earthquakes during the different periods **(A)** from June 2007 to March 2008 **(B)** from February 2008 to October 2008 **(C)** from November 2008 to July 2009 **(D)** from July 2009 to March 2010 **(E)** from August 2010 to September 2011 **(F)** from October 2011 to August 2012.

an average of <3.5 (Figure 3; Table 1 and Supplementary Table S1). By scanning the activity of ML≥4 earthquakes from 2008 to 2022, we found that the monthly occurrence frequency of M≥4 earthquake activity was than a certain value (e.g., 4–8 times per month), concordant with the subsequently occurring M>6 earthquakes. This type of forecasting index can hardly be applied in forecasting because the time length of each seismic quiescence period differs. For instance, the earthquake quiescence phenomena before a strong earthquake and the quiescence interval between two strong earthquakes notably differ, which must be solved before using the seismic quiescence period as an effective earthquake forecasting index (e.g., Ping et al., 2001; Zhuang et al., 2002; Console et al., 2010; Zhu et al., 2014). The identification of spontaneous and triggered earthquakes is performed statistically. We applied the method to the seismicity of Tibet, analyzed the sensitivity of the results and mapped the background seismicity in Tibetan seismic areas (Figure 2). In addition, the aftershock elimination method was not incorporated to this study because the removal of aftershocks reduces the event number and thus enhances the observed seismic quiescence, which remains within the range of low-intensity anomalies and follows our estimates.

3 Results

3.1 Statistics of the low-intensity occurrence of ML≥4 earthquakes immediately before strong earthquakes

The formation of the Tibetan Plateau had a profound effect on geological and geophysical evolution (e.g., Lei and Zhao, 2016). The eastern Tibetan region is composed of several tectonic blocks and separated by several very long active faults, such as the Kunlun fault,

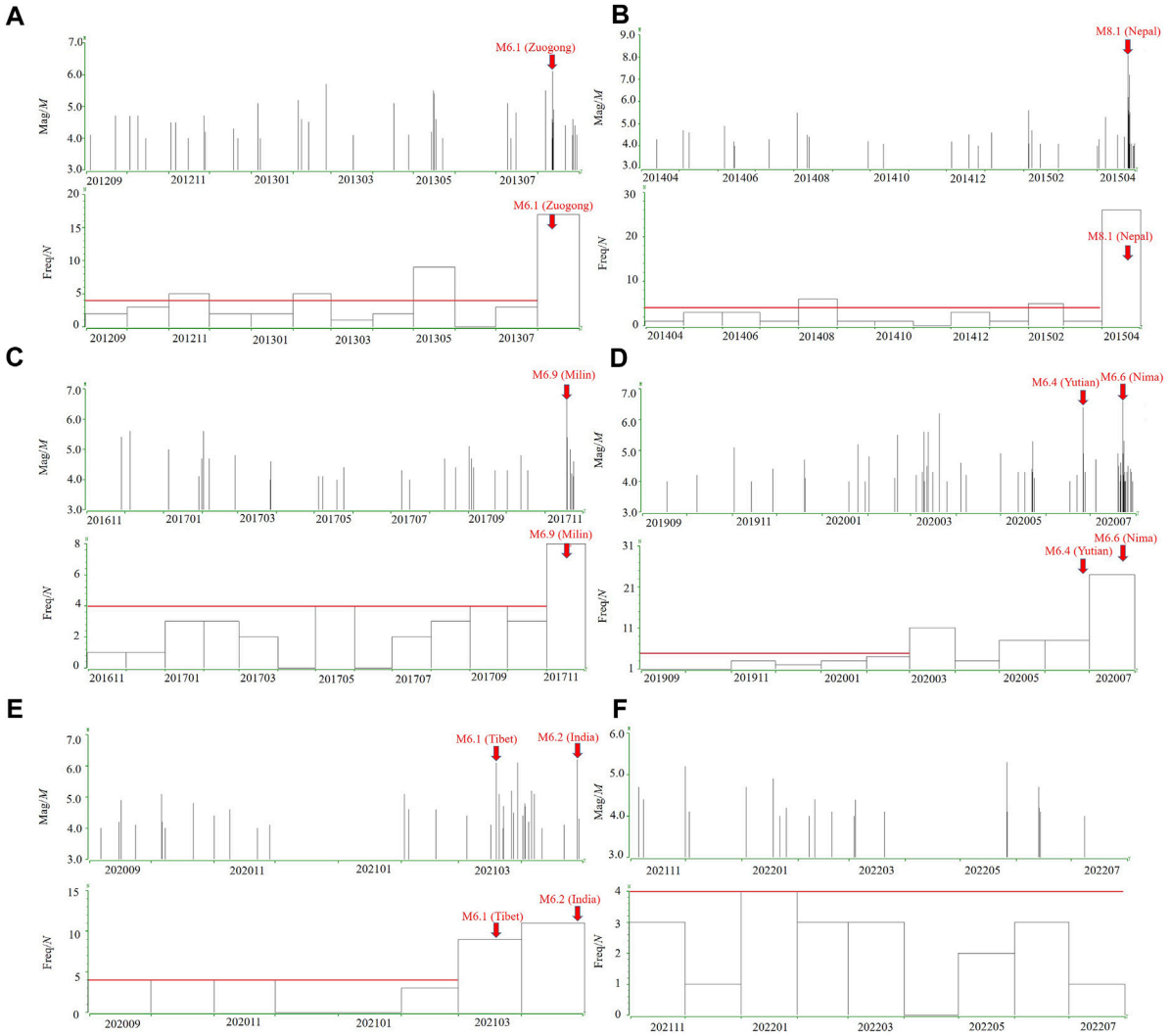

FIGURE 5
Magnitude-time and occurrence frequency-time diagrams of the ML≥4 earthquakes occurring during the different periods **(A)** from September 2012 to August 2013 **(B)** from April 2014 to April 2015 **(C)** from November 2016 to November 2017 **(D)** from September 2019 to July 2020 **(E)** from September 2020 to April 2021 **(F)** from November 2021 to June 2022.

the Longmenshan (LMS) fault, the Xianshuihe fault, the Xiaojiang fault, and the Red River fault (Lei and Zhao, 2016). Along these faults, numerous large earthquakes have occurred frequently. Tibet upper crustal faulting is currently active throughout the orogen, with exceptions along a few north-trending rifts in southern Tibet, where earthquakes may have occurred within the lower crust or upper mantle lithosphere (e.g., Taylor and Yin, 2009).

From 2008 to 2022, a total of nearly twenty earthquakes of magnitude ML≥6 occurred in the study areas (Figure 1; Table 1), of which three earthquakes exhibited magnitude ML≥7, including two earthquakes of magnitude 7.3 in Yutian and Xinjiang and one earthquake of magnitude 8.1 in Nepal (within 50 km from the border). The minimum magnitude of completeness (Mc) in the study area has been decreasing since 2008 (Figure 3), with the highest Mc close to 3.5 from 2008 to 2011 and between 3.5 and 2.8 from 2011 to 2015, and the overall decrease in Mc from 2015 to 2021, with a minimum value of roughly 2.3 (Figure 3). The decrease in Mc value with time reflects the increase in seismic monitoring capability in the study area with time (e.g., Long et al., 2009). Then, the monthly occurrence frequency characteristics of ML≥4 earthquakes before ML≥6 earthquakes and the temporal correlation between fore- and mainshocks were analyzed (e.g., Guo, 2019). We calculate the expectation values of ML≥4 events times per month preceding the ML≥6 earthquakes in the study period (Supplementary Table S2) and further analyze the variation in the Poisson possibility distribution of the ML≥4 foreshock occurrence over the entire 14 years. The ML≥4 foreshocks exhibited Poisson probability of >10% in the consecutive months preceding the ML≥6 events (Fig. S1).

During data analysis, we found that the monthly occurrence frequency of ML≥4 earthquakes was greatly affected by the aftershocks of M≥5 earthquakes. In January 2008, two consecutive earthquakes of magnitude ML≥6 occurred in Gaize, and the activity characteristics of ML≥4 earthquakes from June 2007 to January

TABLE 2 Correspondence of the low-intensity M_L≥4 earthquakes to the M_L≥6 mainshocks.

Area	[a]Period	[b]Months	[c]Actual earthquake occurrence (M_L≥6)	Intervals (/month)	[d]Correspondence
Gaize, Tibet AR	2007-06-2007-12	7	2008-01-09 (M6.9)	0	Y
			2008-01-16 (M6.0)		
Yutian, Xinjiang	2007-06-2008-02	8	2008-03-21 (M7.3)	0	Y
Zhongba, Tibet AR	2008-02-2008-07	6	2008-08-25 (M6.8)	0	Y
			2008-09-25 (M6.0)		
Dangxiong, Tibet AR	2008-02-2008-07	6	2008-10-06 (M6.6)	2	Y
Nima, Tibet AR	2008-11-2009-05	7	2009-07-24 (M6.0)	1	N
Nie Rong, Tibet AR	2009-07-2010-02	8	2010-03-24 (M6.1)	0	Y
Sikkim, India	2010-08-2011-04	9	2011-09-18 (M6.8)	4	Y
Yutian, Xinjiang	2011-10-2012-06	9	2012-08-12 (M6.2)	1	Y
Zuogong, Tibet AR	2012-09-2013-07	11	2013-08-12 (M6.1)	0	Y
Yutian, Xinjiang	Not applicable	None	2014-02-12 (M7.3)		Y
Nepal	2014-04-2015-03	12	2015-04-25 (M8.1)	0	Y
Zaduo, Qinghai	Not applicable	None	2016-10-17 (M6.2)		Y
Milin, Tibet AR	2016-11-2017-10	12	2017-11-18 (M6.9)	0	N
Medog, Tibet AR	Not applicable	None	2019-04-24 (M6.3)		Y
Yutian, Xinjiang	2019-09-2020-02	6	2020-06-26 (M6.4)	3	Y
Nima, Tibet AR	2019-09-2020-02	6	2020-07-23 (M6.6)	4	Y
Tibet AR	2020-09-2021-02	6	2021-03-19 (M6.1)	0	Y
India	2020-09-2021-02	6	2021-04-28 (M6.2)	1	Y

[a]The period of the low-intensity M_L≥4 earthquakes.
[b]The number of months matching the low-intensity M_L≥4 earthquake period.
[c]The occurrence time and magnitude of the subsequent M_L≥6.0 earthquakes.
[d]Whether M_L≥6.0 earthquakes occurred in the previous M_L≥4 earthquake quiescence zone, which was determined by the Seismological Bureau of the Tibet Autonomous Region monthly.

2008 were used for analysis. Figures 4, 5 show the time series and monthly occurrence frequency of earthquakes of magnitude ML≥4 from 2008 to 2022. Among the listed groups of M≥6 earthquakes and their foreshocks, we found no anomaly before the subsequent M6.0 earthquake (the 2009 Nima earthquake), which likely contained undetected events. The remaining earthquakes corresponded well to the quiescence phenomenon of ML≥4 earthquakes with a monthly occurrence frequency of ≤4 times over six consecutive months. Before the M6.6 earthquake in Dangxiong on 6 October 2008, affected by the M6.8 earthquake in Zhongba on 25 August 2008, and the M6.0 earthquake in Zhongba on 25 September 2008, the monthly occurrence frequency of ML≥4 earthquakes was high, and this could be regarded as an anomaly corresponding to strong earthquakes. Based on the above analysis, the monthly occurrence frequency of ML≥4 earthquakes was generally low before the occurrence of ML≥6 earthquakes in Tibet, e.g., at most 4 ML≥4 earthquakes over six consecutive months. The potential correspondence between the monthly occurrence frequency of the time series of ML≥4 events and distributed ML≥6 events was visualized (Figures 4, 5).

Accordingly, in recent decades, the average monthly occurrence frequency of ML≥4 earthquakes in Tibet has remained above 4.2, and the meaningful low-intensity seismic activity for ML≥6 event forecasting indicates that the monthly occurrence frequency should decrease to <4 over >4 consecutive months (e.g., Li and Li, 1999; Ma et al., 2017). In detail, we noted that low-intensity earthquake activities corresponded to the subsequent occurrence of 15 ML≥6 events (>83% in total), as shown in the subfigures. For example, the low-intensity events between June 2007 and July 2008 exhibited a suitable agreement with the Gaize M6.9 (2008-01-09, Figure 4A), Yutian M7.3 (2008-03-21, Figure 4B), Zhongba M6.8 (2008-08-25, Figure 4B), Zhongba M6.0 (2008-09-25, Figure 4B), and Dangxiong M6.6 (2008-10-06, Figure 4B) earthquakes; the low-intensity events between November 2008 and May 2009 corresponded with the Nima M6.0 earthquake (2009-07-24) (Figures 4C, D). A similar correspondence is shown in Figures 4C–F, Figures 5A–F until 2022. However, there were still 3 ML≥6 earthquakes without the aforementioned low-intensity precursor of ML≥4 events before strong earthquakes, i.e., the Yutian M7.3 (2014-02-12), Zaduo M6.2 (2016-10-17), and Medog M6.3 (2019-04-24) earthquakes, which could be attributable to unclear mechanisms.

The statistical results revealed that 15 of the 18 ML≥6 earthquakes exhibited low-intensity activity of ML≥4 earthquakes lasting for more than 6 months before earthquake occurrence, accounting for >83% of the total number, and these strong earthquakes occurred within 4 months after the end of the low-intensity events. Among them,

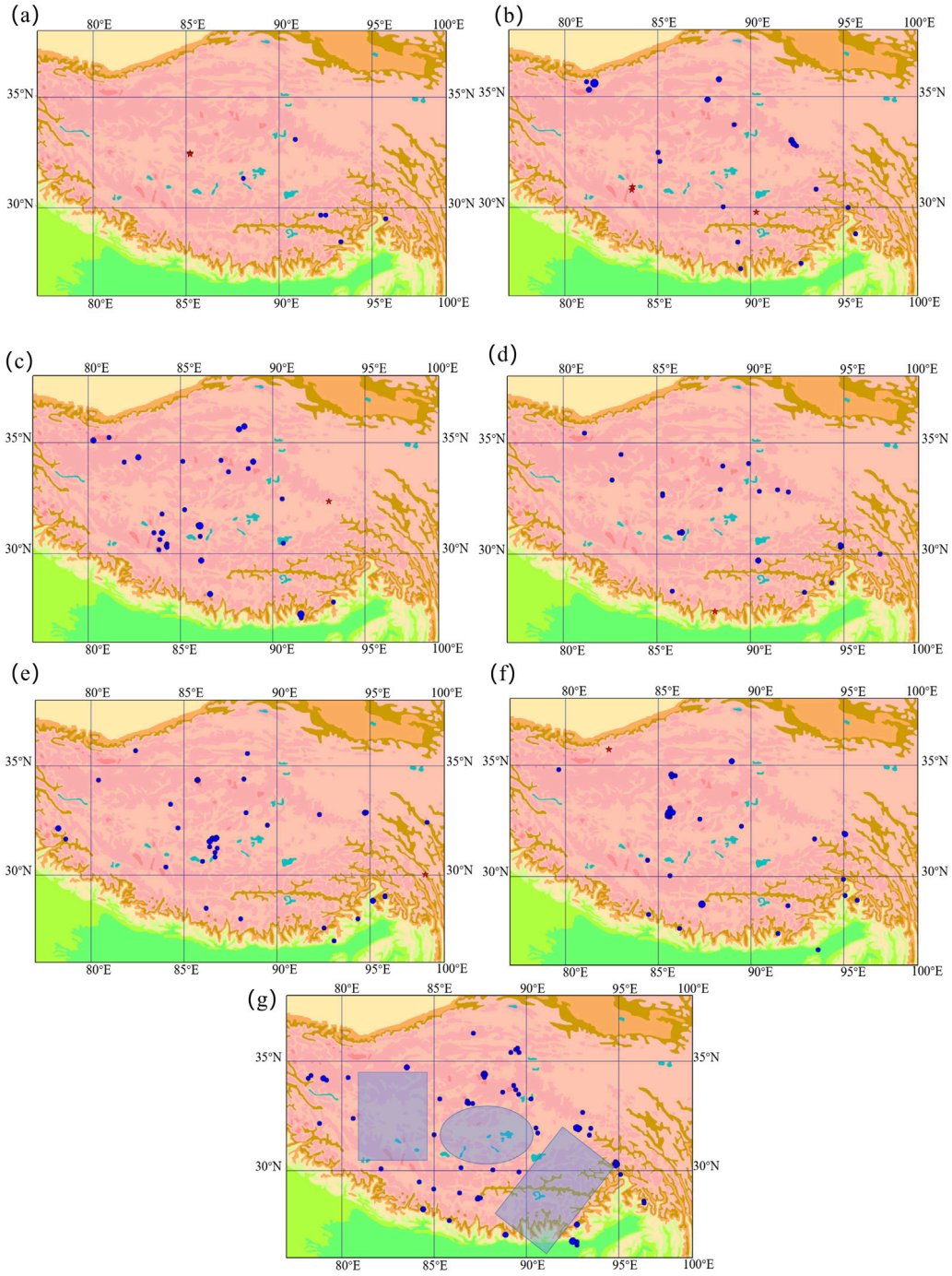

FIGURE 6
Distribution of the ML≥4 earthquakes and subsequent ML≥6 earthquakes. The blue solid circles indicate the ML≥4 foreshocks. The red stars represent the ML≥6 mainshocks **(A)** Gaize M6.9 (2009-01-09) and Gaize M6.0 earthquakes (2008-01-16) **(B)** Zhongba M6.8 (2008-08-25), Zhongba M6.0 (2008-09-25), and Dangxiong M6.6 earthquakes (2008-10-06) **(C)** Nie Rong M6.1 earthquake (2010-03-24) **(D)** Sikkim M6.8 earthquake (2011-09-18) **(E)** Zuogong M6.1 earthquake (2013-08-12) **(F)** Yutian M6.4 earthquake (2020-06-26) **(G)** Schematic illustration of estimating the loci of impending ML≥6 earthquakes based on ML≥4 foreshocks from November 2021 to July 2022.

8 ML≥6 earthquakes occurred during the continuous low-intensity activity period, 4 ML≥6 earthquakes occurred within 1–2 months after the low-intensity activity ended, and 3 ML≥6 earthquakes occurred within 3–4 months. Before the occurrence of large earthquakes, the monthly occurrence frequency of ML≥4 earthquakes was low on average, but the low-intensity period was not proportional to the magnitude of large earthquakes, and the low occurrence frequency did not significantly increase before large earthquakes, similar to short-term enhancement, which may be one of the characteristics of local seismicity in Tibet (Chen and Sun, 2004).

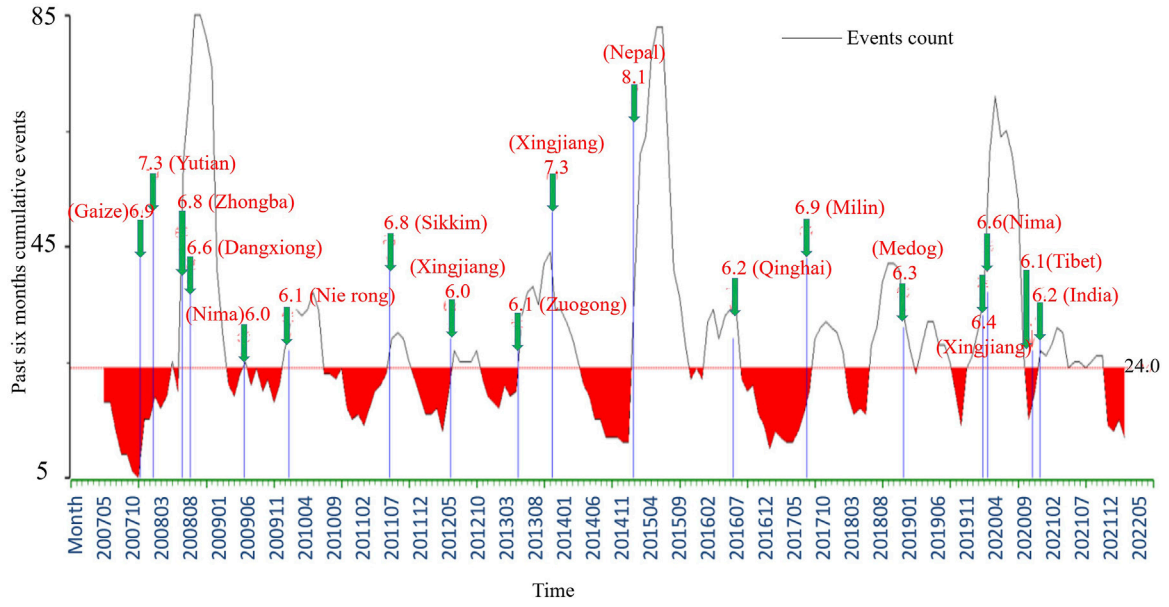

FIGURE 7
Occurrence frequency–time diagram of the ML≥4 earthquakes in Tibet from 2008 to 2022. The black curve indicates the cumulative events in the past 6 months. The red threshold line indicates the occurrence frequency of fewer than 24 ML≥4 earthquakes over half a year in Tibet, and the green arrows indicate ML≥6 earthquakes.

3.2 Spatial location analysis of large earthquakes

Seismic quiescence before large earthquakes has been found and demonstrated in several regions of the world, such as the 1995 M7.2 Kobe (Japan) earthquake (Huang et al., 2001), 2000 Mw 6.8 Uglegorskoe (Russia) earthquake (Wyss et al., 2004), 2016 Mw 6.0 Amatrice (Italy) earthquake (Gentili et al., 2017), 2017 Mw 7.3 Sarpol Zahab (Iran) earthquake (Gentili et al., 2019). Wyss and Habermann (1988) defined the above precursory seismicity quiescence as a statistically significant reduction in the activity rate before mainshock occurrence compared to the background rate within the same study area. Chen et al. (Chen et al., 2014) studied the moderate seismic activity in the surrounding areas of M>6.5 mainshocks in western China since 1970 and found that precursor large-scale seismicity quiescence occurred at the epicenter and surrounding areas of the mainshock. Spatially, a rate decrease occurred in the main shock source region and its vicinity. Currently, the detection of seismic quiescence before a major earthquake remains an exciting new possibility in earthquake physics (Chen et al., 2005) and represents a new and promising method to realize earthquake forecasting (Kisslinger, 1988; Wyss et al., 1997; Hainzl et al., 2000; Rundle et al., 2000; Keilis-Borok, 2002; Zöller et al., 2002; Turcotte et al., 2003; Takahashi and Kasahara, 2004).

We analyzed the spatial distribution of the abovementioned 15 ML≥6 large earthquakes corresponding to low-intensity precursory anomalies and found that most of these large earthquakes occurred in the quiescence area of ML≥4 earthquakes. Among them, 13 earthquakes (86%) occurred within the quiescence area, and two earthquakes did not occur in the quiescence area (Table 2). Here, we compare the location of the epicenters of the fore- and mainshocks (Figure 6). Since November 2021, low-intensity anomalies of ML≥4 earthquakes have again occurred, and ML≥4 earthquake quiescence areas have been formed in western, central and southeastern Tibet. These areas are high-risk areas for future ML≥6 earthquakes after July 2022.

4 Discussion

Earthquake quiescence or enhancement represents an anomalous change against the background of normal activity, and this anomaly could provide a certain predictive significance for the time and location of strong earthquakes (e.g., Ping et al., 2000; Ma and Chen, 2011; Chen et al., 2013). From the perspective of reducing earthquake disasters, it is important to improve the forecasting methods for M>6 earthquakes. In Tibet, there is no systematic study of the forecasting performance of the earthquake quiescence anomaly due to technical and instrumental limits, but based on a recently greatly improved seismic network, we found that the ML≥4 seismic activity in Tibet was consistently associated with a low monthly occurrence frequency and moderate intensity in this region.

Earthquake occurrence imposes a certain effect on forecasting (Zhang et al., 2019). Subsequently, it is necessary to determine the anomalous characteristics of ML≥4 seismic activities to further explore the relationship between low-intensity ML≥4 seismic activity anomalies and strong earthquakes and to determine additional short-term forecasting indicators for strong earthquakes. The period of low-intensity seismicity is related to the magnitude of earthquakes above M6. However, there exists no direct proportional relationship between the period of low-intensity seismicity and subsequent strong earthquake magnitude according to our current study (Figures 4, 5), and more comprehensive

evaluation research should be performed for hazardous earthquake forecasting.

Through analysis, we found that there occurred a suitable correspondence between strong earthquakes and the low-intensity activities of ML≥4 earthquakes, lasting for more than 6 months (e.g., Yan et al., 2012). The average monthly frequency of ML≥4 earthquakes in Tibet and neighboring areas since 2007 is 4.71 times, and the monthly frequency is generally considered low when it is less than 4 (Supplementary Table S2). In this study, the cumulative semiannual frequency of ML≥4 earthquakes in Tibet and neighboring areas is defined as low-frequency anomalies when the semiannual frequency is less than 24. However, sometimes influenced by aftershocks of large earthquakes or ML4 clusters, there are individual months with more than four earthquakes of ML≥4 during the duration of low frequency. The statistics of this study find that better correspondence with earthquakes of M≥ 6 is a period of sustained weak ML ≥ 4 seismic activity, and these occasional slightly higher frequencies have less impact. We compared different time windows to assess the low-intensity activity of events and found that the time window of the month range is one of the most effective and convenient windows for analyzing the event occurrence frequency, possibly due to the triggering effect of short-period Earth tides, including semidiurnal and diurnal tides (e.g., Klein, 1976). In this study, we counted the low-intensity anomalies from January 2007 to July 2022, with a window length of 6 months, in sequence, as shown in Supplementary Table S3. Since 2007, a total of 12 low-intensity anomalies have occurred, and except for the ongoing anomalies indicating subsequent corresponding earthquakes, nine of the previous 11 anomalies corresponded to ML≥6 earthquakes, with a corresponding rate of 82%. After eight low-intensity anomalies ended, ML≥6 earthquakes occurred within 2 months, accounting for 73% of the total number (Figure 7). To scientifically and objectively evaluate the effectiveness of this method for forecasting earthquakes, this study uses the R-value calculation method proposed by Xu (1993) in the evaluation of forecast effectiveness: $R = c - b$, $c = n_1^1 - N_1$, $d = n_0^0 - N_0$, where n_1^1 denotes the number of correctly forecasted earthquakes, N_1 denotes the total number of earthquakes that should be forecasted, n_0^0 denotes the forecast occupation time, and N_0 denotes the total forecast study time. In this study, the total forecast study time is from January 2007 to March 2022, for a total of 182 months. During this period, 18 earthquakes of magnitude six or higher occurred. The forecast occupation time is 6 months from the beginning to the end of the anomaly, and the forecast occupation time for 11 anomalies is 143 months. The earthquakes that occurred during this period, called correctly forecasted earthquakes, are 16 in total. It is calculated that R = .1 > 0, indicating that the method is more effective than random forecasting and has predictive significance. Therefore, we suggest using this low-intensity anomaly as a short-term forecasting index for earthquakes of magnitude six or above. The forecasting threshold of the low-intensity anomaly is half a year, the predicted occurrence time of impending ML≥6 earthquakes is less than 2 months, and the earthquake location is within the quiescence zone of the ML≥4 foreshocks. The catalog and monthly count of the ML≥4 events used in this study are shown in Supplementary Table S4 and the supplemental dataset.

5 Conclusion

In this study, spatial and temporal scanning analysis of ML≥4 earthquakes and subsequent ML≥6 earthquakes in Tibet and adjacent areas was conducted *via* statistical test methods, and the following conclusions could be drawn: (Katsumata, 2011; Traitangwong and Pailoplee, 2017).

1) The low-intensity occurrence (≤24 times every 6 months) of ML≥4 earthquakes lasting for more than 6 months from 2008 to 2022 corresponded well to the subsequent occurrence of ML≥6 earthquakes in Tibet.
2) ML≥6 mainshocks preferentially occurred in the quiescent area of the epicenters of ML≥4 foreshocks. This anomalous feature could be used to predict the location of strong earthquakes in Tibet.
3) The period of low-intensity ML≥4 earthquakes was not proportional to the magnitude of subsequent strong earthquakes.

Data availability statement

The original contributions presented in the study are included in the article/Supplementary Material, further inquiries can be directed to the corresponding author.

Author contributions

JG performed the observation analysis and interpreted the results. YZ, YJ, and WZ elaborated the study and wrote the manuscript. RQ, JL, LX, and CX provided comments to improve the manuscript. All authors examined the results and interpretations and participated in manuscript writing. All authors have read and agreed to the published version of the manuscript.

Funding

This study benefited from financial support provided by the Chinese Academy of Sciences (CAS) Pioneer Hundred Talents Program and the Second Tibetan Plateau Scientific Expedition and Research Program (2019QZKK0708).

Acknowledgments

We are thankful to three reviewers for their constructive comments allowed to improve our manuscript. We thank China Earthquake Administration and the Seismological Bureau of the Tibet Autonomous Region for sharing the data used in this study. We are also obliged to Mengyu Xie from the China Earthquake Networks Center for sharing the software package of ZMAP (Stefan Wiemer, ETH).

Conflict of interest

The authors declare that the research was conducted in the absence of any commercial or financial relationships that could be construed as a potential conflict of interest.

Publisher's note

All claims expressed in this article are solely those of the authors and do not necessarily represent those of their affiliated organizations, or those of the publisher, the editors and the reviewers. Any product that may be evaluated in this article, or claim that may be made by its manufacturer, is not guaranteed or endorsed by the publisher.

Supplementary material

The Supplementary Material for this article can be found online at: https://www.frontiersin.org/articles/10.3389/feart.2023.1043468/full#supplementary-material

References

Aki, K. (1965). Maximum likelihood estimate of b in the formula logN= a-bM and its confidence limits. *Bull. Earthq. Res. Inst. Univ. Tokyo* 43, 237–239.

Chen, C., Rundle, J., Holliday, J. R., Nanjo, K. Z., Turcotte, D. L., Li, S. C., et al. (2005). The 1999 Chi-Chi, Taiwan, earthquake as a typical example of seismic activation and quiescence. *Geophys. Res. Lett.* 32 (22). doi:10.1029/2005GL023991

Chen, L. (2018). Analysis of quiescence anomalies of MS4 earthquake in Keping block, Xinjiang. *Inland Earthq. (in Chin.* 32, 370–378. doi:10.16256/j.issn.1001-8956.2018.04.009

Chen, X. (2007). Analysis of relationship between quiescence of earthquakes with Ms≥6 and occurrence of earthquakes with Ms≥7. *Prog. Earthq. Sci. (in Chinese)* 1, 12–15.

Chen, Y., Yao, J., Li, G., Yu, N., Liu, W., Wang, P., et al. (2013). Analysis of earthquake group activity and foreshock sequences in the Qinghai region since 1980. *Earthquake Research In China (in Chinese)* 29, 489–500. doi:10.3969/j.issn.1001-4683.2013.04.009

Chen, Y., and Sun, H. (2004). Study on one of index of strong earthquakes with Ms≥6.5-middle earthquake quiescence in Western Chi-na mainland. *Plateau Earthquake Research* 4, 8–12. doi:10.3969/j.issn.1005-586X.2004.04.002

Chen, Y., Yao, J., and Ma, Y. (2014). Research on quiescence anomaly of ML ≥ 4 earthquakes before M6.0~6.9 earthquakes in Qinghai-Tibet Plateau. *Journal of Seismological Research (in Chinese)* 37, 1–7.

Console, R., Jackson, D., and Kagan, Y. (2010). Using the ETAS model for catalog declustering and seismic background assessment. *Pure and applied geophysics* 167 (6), 819–830. doi:10.1007/s00024-010-0065-5

Di Giovambattista, R., and Tyupkin, Y. S. (2004). Seismicity patterns before the M= 5.8 2002, Palermo (Italy) earthquake: Seismic quiescence and accelerating seismicity. *Tectonophysics* 384 (1-4), 243–255. doi:10.1016/j.tecto.2004.04.001

Feng, J., Jiang, C., Han, L., and Chen, J. (2012). Analysis on the monitoring capability of seismic networks and completeness of earthquake catalogues in Gansu region. *Acta Seismologica Sinica* 34 (05), 646–658+727+15.

Gao, J., NimaWen, S., and Zhang, J. (2015). Characteristics of seismic damage by the Nepal M8.1 earthquake in the Tibet area of chi-na. *Technology For Earthquake Disaster Prevention (in Chinese)* 10, 961–968. doi:10.11899/zzfy20150414

Gentili, S., Di Giovambattista, R., and Peresan, A. (2017). Seismic quiescence preceding the 2016 central Italy earthquakes. *Phys. Earth Planet. Inter.* 272, 27–33. doi:10.1016/j.pepi.2017.09.004

Gentili, S., Peresan, A., Talebi, M., Zare, M., and Di Giovambattista, R. (2019). A seismic quiescence before the 2017 Mw 7.3 Sarpol Zahab (Iran) earthquake: Detection and analysis by improved RTL method. *Phys. Earth Planet. Inter.* 290, 10–19. doi:10.1016/j.pepi.2019.02.010

Guo, Y. (2019). Monthly occurrence frequency distribution characteristics of small earthquakes in the middle Tianshan mountains, Xinjiang. *Inland Earthquake (in Chinese)* 33, 296–305. doi:10.16256/j.issn.1001-8956.2019.04.002

Hainzl, S., Zöller, G., Kurths, J., and Zschau, J. (2000). Seismic quiescence as an indicator for large earthquakes in a system of self-organized criticality. *Geophys. Res. Lett.* 27 (5), 597–600. doi:10.1029/1999GL011000

Han, W. (1998). Overview of the concept of three kinds of seismic quiescence and its significance in earthquake forecasting. *Progress in Earthquake Sciences (in Chinese)* 1998, 9–13.

Han, W., Xin, H., and Jiang, G. (2006a). Researching on the seismic quiescence index and forecasting efficient in Sichuan and its three re-gions:Predicting researching of the seismic quiescence precursor with the different seismic magnitudes(Part1). *Earthquake Research in Sichuan (in Chinese)* 10, 1–6.

Han, W., Xin, H., and Jiang, G. (2006b). Seismic quiescence index to the regions of mainland, North China and Yunnan (part2). *Earthquake Research in Sichuan* 21, 1–3. (in Chinese).

Huang, Q. (2008). Seismicity changes prior to the Ms8. 0 wenchuan earthquake in sichuan, China. *Geophys. Res. Lett.* 35 (23)–L23308. doi:10.1029/2008GL036270

Huang, Q., Sobolev, G. A., and Nagao, T. (2001). Characteristics of the seismic quiescence and activation patterns before the M= 7.2 Kobe earthquake, January 17, 1995. *Tectonophysics* 337 (1-2), 99–116. doi:10.1016/S0040-1951(01)00073-7

Jiang, C., and Wu, Z. (2011). Intermediate-term medium-range accelerating moment release (AMR) priori to the 2010 yushu Ms7.1 earthquake. *Chinese Journal of Geophysics* 54 (6), 1501–1510+110.

Katsumata, K. (2011). A long-term seismic quiescence started 23 years before the 2011 off the Pacific coast of Tohoku Earthquake (M= 9.0). *Earth, planets and space* 63 (7), 709–712. doi:10.5047/eps.2011.06.033

Katsumata, K., and Nakatani, M. (2021). Testing the seismic quiescence hypothesis through retrospective trials of alarm-based earthquake forecasting in the Kurile–Japan subduction zone. *Earth, Planets and Space* 73 (1), 100–119. doi:10.1186/s40623-021-01418-z

Keilis-Borok, V. (2002). Earthquake forecasting: State-of-the-Art and emerging possibilities. *Annu. Rev. Earth Planet. Sci.* 30, 1–33. doi:10.1146/annurev.earth.30.100301.083856

Kisslinger, C. (1988). An experiment in earthquake forecasting and the 7 May 1986 Andreanof Islands earthquake. *Bull. Seismol. Soc. Am.* 78 (1), 218–229. doi:10.1785/BSSA0780010218

Klein, F. W. (1976). Earthquake swarms and the semidiurnal solid Earth tide. *Geophysical Journal of the Royal Astronomical Society* 45, 245–295. doi:10.1111/j.1365-246X.1976.tb00326.x

Lei, J., and Zhao, D. (2016). Large earthquakes and structural heterogeneity in Eastern Tibetan Plateau. *Plate Boundaries and Natural Haz-ards* 12, 167–191. doi:10.1002/9781119054146.ch8

Li, X., and Li, G. (1999). Monthly occurrence frequency of comprehensive precursors: Application and implication. *Earthquake (in Chinese)* 4, 323–330.

Li, X., Li, Z., Yang, J., Liu, Y., Fu, B., Qi, W., et al. (2018). Spatiotemporal characteristics of earthquake disaster losses in China from 1993 to 2016. *Natural Hazards* 94 (2), 843–865. doi:10.1007/s11069-018-3425-6

Liu, J., Guo, T., Yang, L., Su, Y., and Liu, G. (2008). Follow-up forecast study on the exceeding long quiescence of the earthquake with M>6 in China mainland during 2005-2007. *Journal of Seismological Research (in Chinese)* 31, 324–329.

Liu, M., Fu, B., and Dong, Y. (2015). Neotectonics of NE-striking fault zones and earthquake risk in the Yunnan-Myanmar block, south-eastern margin of the Tibetan plateau. *Chinese Journal of Geophysics (in Chinese)* 58, 4174–4186. doi:10.6038/cjg20151124

Liu, Y., Zhao, G., Wu, Z., Li, Y., Ma, D., and Jiang, Y. (2014). Application of spatial database technology and seismic gap method to seismic hazard analysis around south-eastern Tibetan plateau. *Journal of Geomechanics (in Chinese)* 20 (3).

Liu, Z. (2021). Analysis of the spatial distribution characteristics of the first strong earthquakes after the long-term quiescence of moderate earthquakes in Yunnan. *Seismological and Geomagnetic Observation and Research (in Chinese)* 42 (S1), 26–28. doi:10.3969/j.issn.1003-3246.2021.S1.009

Long, F., Wen, X., and Ni, S. (2009). Determination of temporal-spatial distribution of the regional minimum magnitudes of completeness:application to the longmenshan fault zone. *Earthquake* 29 (3), 27–36.

Ma, R., Wang, P., and Su, W. (2017). The implication of seismic quiescence on moderately strong earthquakes in northern Qinhai and adijacent areas. *China Earthquake Engineering Journal (in Chinese)* 39, 088–093. doi:10.3969/j.issn.1000-0844.2017.Supp.088

Ma, Y., and Chen, Y. (2011). Study on the characteristics of anomaly before the April 14,2010 Yushu Ms7.1 earthquake and its dynamic relationship. *Earthquake Research in China (in Chinese)* 27, 136–146. doi:10.3969/j.issn.1001-4683.2011.02.003

Mogi, K. (1969). Laboratory study of elastic shocks prior to rock failure. *Eos Transactions American Geophysical Union* 50, 401. doi:10.1029/EO050i005p00401-01

Ni, H., and Hong, H. (2014). The yutian earthquake of 12 february 2014. *Geomatics, Natural Hazards and Risk* 5 (3), 185–189. doi:10.1080/19475705.2014.937774

Ping, J., Luo, L., and Cao, S. (2000). Study on the evolutional characteristics of earthquake anomalous precursory information field and its relation with seismicity in north China. *Earthquake Research in China (in Chinese) 2000* 3. doi:10.3969/j.issn.1001-4683.2000.03.004

Ping, J., Zhang, Q., Cao, S., and Bian, Q. (2001). The quiescence of earthquakes with M L≥4.0 as an important precursory characteristic prior to strong shocks in North China region. *Acta Seismologica Sinica* 14 (4), 471–480. doi:10.1007/s11589-001-0126-z

Qin, S., Li, P., Xue, L., Wu, X., and Yang, B. (2015). A prospective forecasting of major earthquakes for the eurasian seismic belt(ii): In-traplate seismogenic zones. *Progress In Geophysics* 30 (4), 1625–1652. doi:10.6038/pg20150417

Rundle, J. B., Klein, W., Turcotte, D. L., and Malamud, B. D. (2000). "Precursory seismic activation and critical-point phenomena," in *Microscopic and macroscopic simulation: Towards predictive modelling of the earthquake process* (Basel: Birkhäuser), 2165–2182. doi:10.1007/978-3-0348-7695-7_19

Schorlemmer, D., and Woessner, J. (2008). Probability of detecting an earthquake. *Bulletin of the Seismological Society of America* 98 (5), 2103–2117. doi:10.1785/0120070105

Shi, X. (2020). Study on Ms≥4.0 earthquake quiescence anomaly in Xinyuan-Korla area. *Inland Earthquake (in Chinese)* 34, 388–394. doi:10.16256/j.issn.1001-8956.2020.04.08

Sobolev, G., Huang, Q., and Nagao, T. (2002). Phases of earthquake's preparation and by chance test of seismic quiescence anomaly. *J Geodyn* 33 (4-5), 413–424. doi:10.1016/S0264-3707(02)00007-8

Su, L. (1996). The relation between the quiescence of M≥5 shocks and the M≥7 earthquakes in China continent. *Northwestern Seis-mological Journal (in Chinese)* 18, 36–41.

Takahashi, H., and Kasahara, M. (2004). The 2003 Tokachi-oki earthquake, off Southeastern Hokkaido, Japan: Seismic activities from the former 1952 Tokachi-oki earthquake, foreshock, mainshock, aftershocks, and triggered earthquakes. *Jishin* 57 (2), 115–130. doi:10.4294/zisin1948.57.2_115

Taylor, M., and Yin, A. (2009). Active structures of the Himalayan-Tibetan orogen and their relationships to earthquake distribution, contemporary strain field, and Cenozoic volcanism. *Geosphere* 5 (3), 199–214. doi:10.1130/GES00217.1

Tian, L., Zhang, X., Xie, M., Jiang, X., Wang, Y., Deng, G., et al. (2021). Summary of the biru MS 6.1 earthquake in Tibet on March 19, 2021. *Seismological and Geomagnetic Observation and Research* 42 (2). (in Chinese). doi:10.3969/j.issn.1003-3246.2021.02.005

Tillotson, E. (1951). The great Assam earthquake of August 15, 1950. *Nature* 167 (4239), 128–130. doi:10.1038/167128a0

Traitangwong, P., and Pailoplee, S. (2017). Precursory seismic quiescence along the Sagaing fault zone, Central Myanmar–application of the region-time-length algorithm. *Geosciences Journal* 21 (4), 543–552. doi:10.1007/s12303-016-0068-z

Turcotte, D. L., Newman, W. I., and Shcherbakov, R. (2003). Micro and macroscopic models of rock fracture. *Geophysical Journal Interna-tional.* 152 (3), 718–728. doi:10.1046/j.1365-246X.2003.01884.x

Wang, X., Wang, Y., Gong, M., Guo, L., and Wang, X. (2017). Comprehensive judgment of quiescence anomaly under the background of the quiet time of the fifth activity in North China. *Seismological and Geomagnetic Observation and Research (in Chinese)* 3, 21–27. doi:10.3969/j.issn.1003-3246.2017.01.004

Wang, Y., Liu, X., Wang, X., and Gong, M. (2014). The analysis of ML4 earthquake quiescence in north China. *North China Earthquake Sciences (in Chinese)* 32, 55–61. doi:10.3969/j.issn.1003-1375.2014.02.011

Wen, Y., Song, Z., Yu, H., and Huang, K. (2016). Current large earthquake risk on the eastern himalayan belt and compared to the seismicities before 1950 motuo M 8.6 earthquake. *Progress In Geophysics* 31 (1), 103–109. doi:10.6038/pg20160112

Wiemer, S., and Wyss, M. (2000). Minimum magnitude of completeness in earthquake catalogs: Examples from Alaska, the Western United States, and Japan. *Bulletin of the Seismological Society of America* 90 (4), 859–869. doi:10.1785/0119990114

Woessner, J., Hauksson, E., Wiemer, S., and Neukomm, S. (2004). The 1997 kagoshima (Japan) earthquake doublet: A quantitative analysis of aftershock rate changes. *Geophysical research letters* 31 (3)–L03605. doi:10.1029/2003gl018858

Woessner, J., and Wiemer, S. (2005). Assessing the quality of earthquake catalogues: Estimating the magnitude of completeness and its uncertainty. *Bulletin of the Seismological Society of America* 95 (2), 684–698. doi:10.1785/0120040007

Wu, Y. M., and Chiao, L. Y. (2006). Seismic quiescence before the 1999 chi-chi, taiwan, M W 7.6 earthquake. *Bull. Seismol. Soc. Am.* 96 (1), 321–327. doi:10.1785/0120050069

Wyss, M., Habermann, R., Bodin, P., Kisslinger, C., Burford, R., Klein, F., et al. (1997). Case 23 nomination of pre-cursory seismic quiescence as a significant precursor. *Pure and applied geophysics* 149 (1), 79–113. doi:10.1007/BF00945162

Wyss, M., and Habermann, R. E. (1988). Precursory quiescence before the August 1982 stone canyon, san andreas fault, earthquakes. *Pure and Applied Geophysics* 126, 333–356. doi:10.1007/BF00879002

Wyss, M., Sobolev, G., and Clippard, J. D. (2004). Seismic quiescence precursors to two M7 earthquakes on Sakhalin Island, measured by two methods. *Earth, planets and space* 56 (8), 725–740. doi:10.1186/BF03353081

Xu, S. (1993). Seismic activity forecasting methods. *Acta Seismologica Sinica* 2, 239–252+121.

Yan, Z., Zhang, H., Fan, X., Du, X., and Shi, Y. (2012). Comparative analysis on the characteristics of low-frequency energy released by the wenchuan earthquake and Kunlun mountains earthquake. *Chinese Journal of Geophysics* 55, 719–732. doi:10.1002/cjg2.1766

Yu, H., Cheng, J., Zhang, X., Zhang, L-P., Liu, J., and Zhang, Y. (2013). Multi-methods combined analysis of future earthquake potential. *Pure and Applied Geophysics* 170, 173–183. doi:10.1007/s00024-011-0408-x

Yu, N., Zhang, X., and Yang, X. (2020). Analysis of minimum magnitude of completeness for earthquake catalog in qinghai region. *Earthquake* 40 (4), 23–32.

Zhang, G. (2001). *Introduction to earthquake forecasting*. Beijing: Science Press.

Zhang, G., Yin, X., Wang, P., and Shao, Z. (2019). Low seismicity anomaly and its efficiency in mid-term earthquake forecasting in Chinese mainland. *Earthquake (in Chinese)* 39 (2). doi:10.3969/j.issn.1000-3274.2019.02.001

Zhang, S., Wang, X., Wang, Y., Gong, M., Chen, T., and Guo, L. (2018). The relationship between seismic quiescence in hebei and its adjacent areas and several great earthquakes. *North China Earthquake Sciences (in Chinese)* 36, 38–42. doi:10.3969/j.issn.1003-1375.2018.02.006

Zhu, H., Li, H., Wu, M., and Yue, X. (2014). Quiescence-seismic-quiescence evolution of medium-earthquakes before moderate-strong shocks in junction region of Shanxi, Hebei and Neimenggu. *Progress in Geophysics (in Chinese)* 29, 1114–1120. doi:10.6038/pg20140314

Zhu, H., Yue, X., Wu, M., Li, H., and Lin, X. (2012). The Abnormally Quiescence of medium-earthquakes before moderate-strong shocks in the central and northern of Fenwei seismic belt. *Progress in Earthquake Sciences* 42. (in Chinese).

Zhuang, J., Ogata, Y., and Vere-Jones, D. (2002). Stochastic declustering of space-time earthquake occurrences. *J. Am. Stat. Ass.* 97 (458), 369–380. doi:10.1198/016214502760046925

Zöller, G., Hainzl, S., Kurths, J., and Zschau, J. (2002). A systematic test on precursory seismic quiescence in Armenia. *Natural Hazards* 26 (3), 245–263. doi:10.1023/A:1015685006180

frontiers | Frontiers in Earth Science

TYPE Original Research
PUBLISHED 23 January 2023
DOI 10.3389/feart.2022.1049911

OPEN ACCESS

EDITED BY
Huajian Yao,
University of Science and Technology of China, China

REVIEWED BY
Vasileios Karakostas,
Aristotle University of Thessaloniki, Greece
Alessandro Vuan,
Istituto Nazionale di Oceanografia e di Geofisica Sperimentale, Italy
Jianshe Lei,
China Earthquake Administration, China

*CORRESPONDENCE
Yi Guixi,
yigx64@163.com

SPECIALTY SECTION
This article was submitted to Solid Earth Geophysics,
a section of the journal
Frontiers in Earth Science

RECEIVED 21 September 2022
ACCEPTED 13 December 2022
PUBLISHED 23 January 2023

CITATION
Feng L, Chang H, Guixi Y, Xiaohui H, Li L, Fuqiang S, Yue G and Liyuan P (2023), Seismogenic structures and spatiotemporal seismicity patterns of the 2022 *Ms*6.0 Maerkang earthquake sequence, Sichuan, China.
Front. Earth Sci. 10:1049911.
doi: 10.3389/feart.2022.1049911

Seismogenic structures and spatiotemporal seismicity patterns of the 2022 *Ms*6.0 Maerkang earthquake sequence, Sichuan, China

Long Feng[1], He Chang[1], Yi Guixi[1]*, He Xiaohui[2], Li Li[3], Shi Fuqiang[4], Gong Yue[1] and Peng Liyuan[1]

[1]Sichuan Earthquake Agency, Chengdu, China, [2]Guangdong Provincial Key Laboratory of Geodynamics and Geohazards, School of Earth Science and Engineering, Sun Yat-Sen University, Zhuhai, China, [3]Shanxi Earthquake Agency, Taiyuan, China, [4]Shaanxi Earthquake Agency, Xi'an, China

The 2022 Ms6.0 Maerkang earthquake sequence, Sichuan, China, occurred in an unexpected area with historically rare seismicity in the Bayan Har block. Here we relocated the earthquake sequence, inverted for the focal mechanisms of the larger events, and calculated the rupture directivity of the earthquake sequence to reveal the seismogenic structures and mechanisms of this sequence. The high-precision relocations indicate that the seismogenic structures consist of several clusters that are generally parallel to the nearby NW-trending Songgang fault, and relatively small-scale conjugate faults are also identified. The seismicity migrated from cluster one in the south to cluster two in the north during the sequence. Furthermore, the hypocenters were largely located at 5–10 km depth, thereby highlighting that the seismogenic structures are buried. The vertical fault planes of the seismogenic structures are consistent with the high-dip focal mechanism solutions from seven events. A stress field inversion based on the focal mechanisms indicates that the sequence occurred in a strike-slip environment that was controlled by a NNW–SSE-striking principal compressive stress. The different rupture directivities of the *Ms*5.8 (southwestward) and *Ms*6.0 (southeastward) events prove the existence of conjugate faults. The *Ms*5.8 event induced a coseismic Coulomb stress change of 1.6 MPa where the *Ms*6.0 event subsequently occurred, thereby highlighting that the *Ms*5.8 event triggered the *Ms*6.0 event and produced the spatiotemporal seismicity pattern of the sequence. We therefore conclude that the seismogenic structures of the 2022 *Ms*6.0 Maerkang earthquake sequence are previously unknown concealed conjugate structures associated with the main Songgang fault. The complex seismogenic structures and their potential to generate large earthquakes warrant the need to better understand the seismogenesis of this area and the seismic risks that may be present.

KEYWORDS

Maerkang earthquake sequence, seismogenic structure, spatiotemporal pattern, focal mechanism, Coulomb stress change

Introduction

An earthquake sequence that contained three *Ms* > 5.0 earthquakes (the largest of which was a *Ms*6.0 event) occurred in Maerkang City, Aba Tibetan and Qiang Autonomous Prefecture, Sichuan Province, southwestern China, beginning in the early morning of June 10, 2022 [China Standard Time (CST)]. A NW-trending seismicity belt with a maximum intensity of VIII was identified during the post-earthquake investigation. The initial earthquake locations were scattered in the inner Bayan Har block in an area adjacent to the northern segment of the NW-trending Songgang fault. Previous studies have revealed that most of the *Ms* ≥ 6 events that had occurred in the Bayan Har block since 2007, including the 2008 *Ms*7.3 Yutian (Wang et al., 2009; Ji et al., 2014), 2008 *Mw*7.9 Wenchuan (Wei et al., 2008; Shen et al., 2009; Yu et al., 2010; Hartzell et al., 2013), 2010 *Ms*7.1 Yushu (Chen et al., 2010; Wang et al., 2012), 2013 *Ms*7.0 Lushan (Xu et al., 2013; Long et al., 2015), 2013 *Ms*6.3 Knagding (Fang et al., 2015; Yi et al., 2015), and 2017 *Ms*7.0 Jiuzhaigou (Yi et al., 2017; Long et al., 2019; Wu et al., 2020; Hu et al., 2022) earthquakes, were located along boundaries of the block, whereas the 2021 *Ms*7.4 Maduo earthquake (Wang et al., 2021; Yue et al., 2022) and the *Ms*6.0 event in this sequence occurred in the block's interior. Furthermore, the evolution of this sequence followed a foreshock–mainshock–aftershock pattern that was similar to the 2021 *Ms*6.4 Yangbi sequence in Yunnan Province (Long et al., 2021), thereby providing an additional reason to study this earthquake sequence.

It is well known that the precise location and focal mechanism solutions of an earthquake sequence play significant roles in determining its seismogenic structures and tectonic stress features (Michael, 1988; Shearer, 1997; Presti et al., 2008). We therefore relocated the sequence using a hybrid multi-stage method (Long et al., 2015) and inverted the focal mechanism solutions using the CAP (Zhao and Helmberger, 1994; Zhu and Helmberger, 1996) and HASH (Hardebeck and Shearer, 2002, 2003) methods. We then determined the rupture directivity of the two largest events to determine the fault planes and extracted the local stress map from the focal mechanisms to constrain the geodynamic source of these earthquakes. We also delineated the rupture processes of three $M \geq 5.0$ events to deduce the causation of the seismicity transmission revealed by the Coulomb failure stress change. Our study may provide a reference for both investigating the geodynamic environment and earthquake nucleation process in this region and evaluating the potential risk of subsequent strong earthquakes.

Geological setting and historical earthquakes

The Bayan Har block, which is one of the main tectonic units that formed during the eastward movement of the Qinghai–Tibet Plateau. Its movement mode is controlled by the East Kunlun and Ganzi Yushu-Xianshuihe fault belts, two significant strike-slip faults on the northern and southern boundaries of the block, respectively (Xu et al., 2008). This area is also one of the most tectonically complex and active regions for strong earthquakes in Mainland China. The five *Ms* ≥ 7.0 earthquakes that have occurred in Mainland China since 2007 were all located in the boundary and internal areas of the block (Figure 1A).

The nearest known tectonic structure to the Maerkang earthquake sequence is the Songgang fault (F1 in Figure 1B), an ~103-km-long, NW-striking fault that dips 50°–70° toward the NE (Sun et al., 2010). Its slickensides and geomorphic features indicate mainly left-lateral movement along the fault. The Longriba fault intersects the Songgang fault, dividing it into northern and southern segments. In particular, the southern segment may have experienced a period of strong activity during the middle Pleistocene, followed by another episode in the late Pleistocene, whereas the northern segment records no apparent signs of activity at the surface since the late Pleistocene. Sun et al. (2010) suggested that only two *Ms* ≥ 5 earthquakes have occurred along the Songgang fault over the past 100 years, the 1932 *Ms*5.0 Maerkang and 1941 *Ms*6.0 Heishui earthquakes, both of which ruptured the southern segment.

The NW-trending Fubianhe fault (F2 in Figure 1B) forms the southeastern extension of the Songgang fault, and the two faults are en-echelon structures. Geological surveying has indicated that the Fubianhe fault became active during the late Pleistocene and has been dominated by sinistral strike-slip movement with a specific dip-slip component and an average horizontal slip rate of ~1.3 ± 0.1 mm/a since the late Quaternary (Zhou et al., 1999). Several strong historical events such as the 1928 *Ms*5¾, 1989 *Ms*5.0, 1989 *Ms*6.0, and 1991 *Ms*5.0 Xiaojin earthquakes have indicated that the Fubianhe fault has been more seismically active than the Songgang fault over the past 100 years (Zhou et al., 1999).

The NE-trending Longriba fault is a boundary structure that divides the two secondary Aba and Longmenshan blocks within the Bayan Har block (F3 in Figure 1B) (Xu et al., 2008; Ren et al., 2013). This 300-km-long fault is strongly segmented, with thrust and strike-slip faulting along different fault segments. Although a *Ms* ≥ 5 event has not been recorded along the Longriba fault, Xu et al. (2008) proposed that this fault may be a highly active thrust–strike-slip fault zone that formed during the late Quaternary, based on field

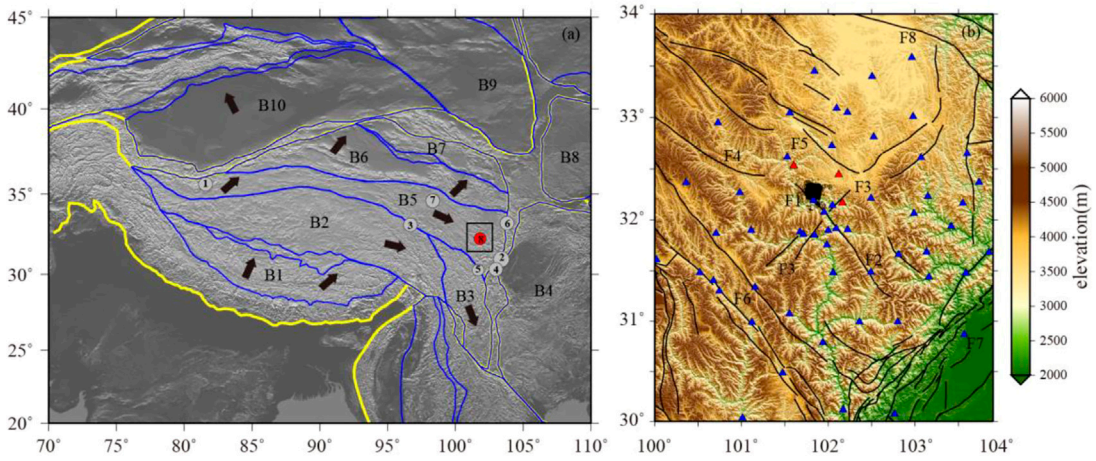

FIGURE 1
(A) Geological setting of the Qinghai–Tibet plateau and the surrounding region. Solid yellow and blue lines indicate the block and sub-block boundaries, respectively, and the blue polygon B5 defines the bayan har block (Zhang et al., 2003). Numbered circles denote the *Ms* ≥ 6 earthquakes that have occurred in the region since 2007, which are described in the introduction orderly. The solid black arrows represent the movement directions of the blocks. The black box indicates the study region, which is shown in **(B)**. B1: Lhasa block. B2: Qiangtang block. B3: Sichuan–Yunnan block. B4: South China block. B5: Bayan Har block. B6: Qaidam block. B7: Qilian block. B8: Ordos block. B9: Alashan block. B10: Tarim block. **(B)** Active faults and seismicity associated with the 2022 *M*s6.0 Maerkang earthquake sequence in the study region. Black circles denote earthquakes that occurred during the Maerkang *M*s6.0 earthquake sequence. Blue and red triangles represent the permanent and temporary (portable) seismometer locations. F1: Songgang fault. F2: Fubianhe fault. F3: Longriba fault. F4: Dari fault. F5: Aba fault. F6: Xianshuihe fault. F7: Longmenshan fault. F8: eastern Kunlun fault.

investigations, geomorphologic fault measurements. Global positioning system (GPS) measurements have determined a fracture deformation rate of ~5 mm/a (Shen et al., 2005; Wang et al., 2008), which indicates that a *M*s ≥ 7 earthquake risk exists along this fault zone.

The Dari fault (F4 in Figure 1B) is one of several large NW-trending, left-lateral strike-slip faults within the Bayan Har block and has been tectonically active during the Holocene. Liang et al. (2022) estimated an average horizontal slip rate of 20 ± 0.3 mm/a since the late Quaternary based on a joint interpretation of high-resolution seismic images, field investigations, and trench excavations.

The Aba fault (F5 in Figure 1B) is the main structural control on the Aba basin. It generally presents a sinistral strike-slip dislocation, as observed along other NW-trending faults in the region. The Abe fault is also strongly segmented. Geological surveying has indicated weak fault activity along its southern segment, with no dislocation of the Quaternary overburden visible at the surface, whereas intense activity has occurred along the middle segment during the Quaternary, with prominent normal fault movement. The fault plane for this middle segment is inclined to the south at 56°, and many graben structures have formed owing to extension along this segment (Cui, 2020). Fault activity in the northern segment is dominated by low-angle thrust faulting, which initiated during the late Pleistocene (Cui, 2020).

Earthquake sequence relocation and spatiotemporal distribution characteristics

We detected 4,200 events that were associated with the Maerkang earthquake sequence during the June 9–23, 2022, period using a seismometer array that consisted of 57 permanent and three portable stations. Table 1 lists the locations and deployment times of the three portable stations; their locations are also marked as red triangles in Figure 1B. We double-checked the phase arrival information and relocated the earthquakes in the sequence that were detected during this time period. There was excellent station coverage for this earthquake sequence (Figure 1B), with almost all seismometers being within an epicentral distance of 150 km, such that clear upper-crustal compressional (Pg) and shear (Sg) phases were recorded. The magnitude–time (*M*–*t*) diagram (Figure 2A) indicates that this sequence consisted of many events, with four foreshocks recorded during the 4-h period before the *M*s5.8 event at 00: 03 CST on June 10. No events were recorded before June 9 in this region. We estimated the magnitude of completeness (*Mc*) of the sequence using the entire magnitude range algorithm (Woessner and Wiemer, 2005), and *Mc* was estimated to 1.4 for our dataset. We also fitted the Gutenberg–Richter (G–R) relationship, $\log10\ N = a - bM$ (Gutenberg and Richter, 1944), using the maximum-likelihood method (Aki, 1965), where *M* is the

TABLE 1 Locations and deployment times for the three portable stations.

NO.	Name	Lat (°N)	Lon (°E)	Elevation (m)	Deployment time (YYYY-MM-DD HH:MM CST)
1	L5133	32.5305	101.6026	3,025	2022-06-10 22:12
2	L5134	32.4425	102.1191	3,519	2022-06-11 19:27
3	L5135	32.1666	102.1636	2,755	2022-06-12 19:23

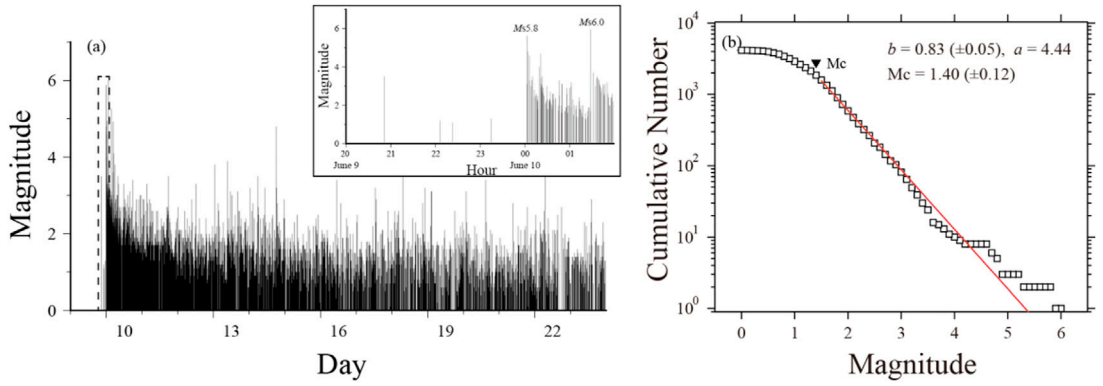

FIGURE 2
(A) *M*–*t* diagram of the Maerkang earthquake sequence during June 9–23, 2022. The dashed box highlights the early stage of the sequence, with its *M*–*t* diagram enlarged in the upper-right corner. **(B)** Frequency–magnitude distribution of the 2022 *Ms*6.0 Maerkang earthquake sequence. Each square indicates the cumulative earthquake frequency at a given magnitude, and the red line is the best-fit line to the G–R relationship (Gutenberg and Richter, 1944).

magnitude, *N* is the cumulative number of earthquakes that are larger than or equal to *M*, and a and b are constants. The regression parameters were 4.44 and 0.83 for a and b, respectively. The sequence exhibited a significant trend for the higher-magnitude events: the observed frequency of the $M_L \geq 4.0$ events was higher than the synthetic value (Figure 2B).

We used a hybrid multi-stage method (Long et al., 2015) to relocate the earthquake sequence. The sequence was first located using HYPOINVERSE (Klein, 2014) based on a prior seismic velocity model estimated from local phase travel times in the eastern Qinghai–Tibet Plateau (Zhao and Zhang, 1987), wheras the Moho depth and compressional-to-shear seismic velocity ratio (*Vp*/*Vs*.) were fiexed at 61 km and 1.71, respectively, based on the *H*–κ stacking (Zhu and Kanamori, 2000) results from a regional receiver function analysis (Yang, 2014). We then selected the events that were recorded by more than eight stations and possessed a maximum azimuthal gap of <120° for a one-dimensional (1-D) velocity model inversion (Kissling, 1988; Kissling et al., 1994, 1995). The process was conducted 200 times by randomly resampling 80% of the selected events to obtain the best-fit local 1-D velocity model (Table 2) and station corrections. Lastly, we applied the hypoDD double-difference algorithm (Waldhauser and Ellsworth, 2000; Waldhauser, 2001), with a 5-km search radius applied to the travel-time-corrected earthquake sequence using the newly inverted velocity model. We relocated 3,800 events, as some events were eliminated owing to either weak links or air quakes. We applied a bootstrap procedure to estimate the location errors by repeating hypoDD 200 times using phase arrival times with Guassian noise. The standard errors were set to 0.15 and 0.25 s for the *p* and S phases, respectively, following Long et al. (2018). The average errors estimated from the 90% confidence interval contours were 520, 530, and 960 m in the E–W, N–S, and vertical directions, respectively, and the root mean square (RMS) error was 0.12 s.

The relocated epicentral map (Figure 3) shows that the entire sequence is located on the eastern border of a NW–SE-trending valley between Caodeng and Mori towns. The nearest active tectonic structure consists of three branches of the NW-trending Songgang fault, which are located to the west of the sequence. The sequence exhibits strong segmentation characteristics, and three distinguishable earthquake clusters are identified. The two more significant clusters (clusters 1 and 2 in Figure 3B) are parallel, NW-trending features, which are consistent with the main characteristics of the Songgang fault. Cluster 1 is positioned in the southwestern portion of the study region, whereas cluster

TABLE 2 Local 1-D velocity model for the study region.

Top depth (km)	0.00	0.50	1.50	2.00	3.00	5.00	8.00	15.0	20.0	27.0	40.0	61.0
Vp (km/s)	4.64	4.66	5.32	5.45	5.69	5.89	6.00	6.14	6.24	6.58	7.06	7.84

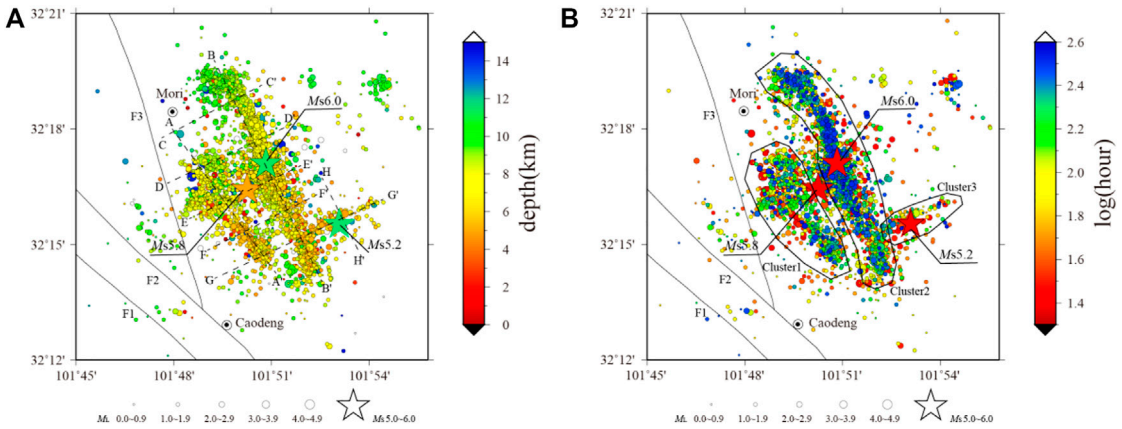

FIGURE 3
Relocated epicenters of the *Ms*6.0 Maerkang earthquake sequence. **(A)** Color-coded by depth. Dashed lines indicate the positions of the profiles, which are shown in Figures 4, 8. **(B)** Color-coded by occurrence time. Black polygons denote the three earthquake clusters discussed in the text. F1–F3: branches of the Songgang fault.

2 is much larger and located in the northeast. Clusters 1 and 2 are separated by ~2 km, which is greater than the location errors. The *Ms*5.8 event occurred between these two clusters. The *Ms*6.0 event occurred in the central to northern part of cluster 2, whereas the *Ms*5.2 event occurred within cluster 3 (Figure 3B), a small NE-trending branch in the south. Furthermore, there appears to be a N–S trend in the depth distribution of the sequence, with the events along the northern segments of clusters 1 and 2 being much deeper than those along the other segments (Figure 3A), as well as a spatiotemporal seismicity pattern, with the seismicity migrating from cluster 1 to cluster 2 during the sequence (Figure 3B). We created a series of vertical profiles through the study region to characterize the seismogenic structures that were activated by the sequence (Figure 3A).

The AA′ profile (Figure 4A) was along the long axis of the southwestern cluster of the sequence (Cluster 1 in Figure 3B), with a 1.5-km projection width on each side to ensure that only the events within this cluster were plotted. The same projection width was set to create the other profiles. The area with a high aftershock density highlights a 6-km-long, NW-dipping rupture plane. Stratified seismicity along three semi-parallel planes is also observed along the southeastern end of the rupture area, illustrating a stress trigger effect. The BB′ profile (Figure 4B) was positioned along the long axis of the northeastern cluster of the sequence (Cluster 2 in Figure 3B), and a 12-km-long, NW-dipping rupture and stratified seismicity were observed along the southeastern end of

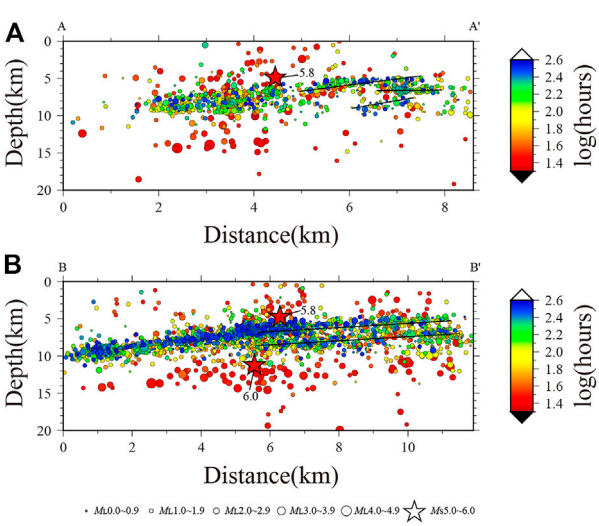

FIGURE 4
Focal depth projections along profiles **(A)** AA′ and **(B)** BB′. Solid lines indicate seismicity stratification along distinct rupture planes. Profile locations are shown in Figure 3A.

the rupture area. The structural characteristics of profile BB′ are similar to those of profile AA′. The *Ms*6.0 event was positioned at ~12 km depth in profile BB′, slightly below the lower boundary of the dense aftershock area.

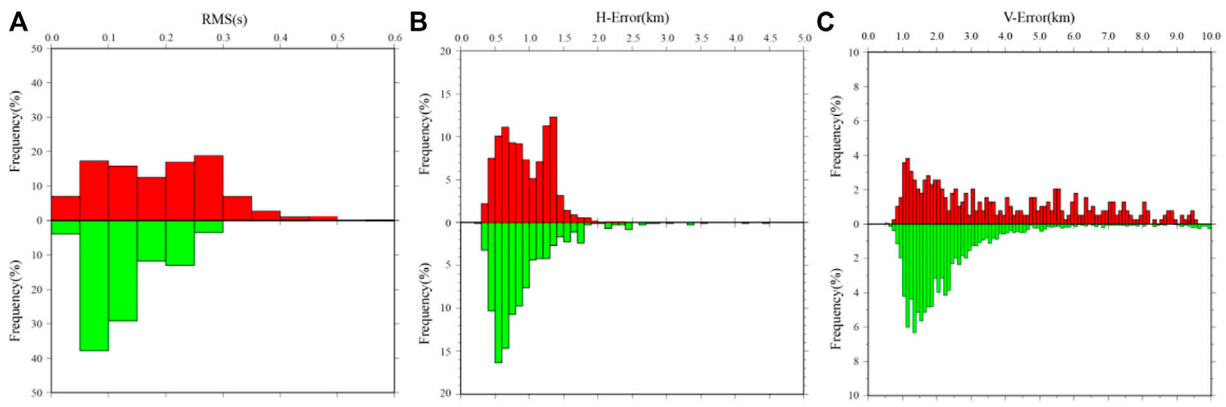

FIGURE 5
Histograms of the earthquake location **(A)** RMS error, **(B)** horizontal error, and **(C)** vertical error before (red) and after (green) deployment of three portable stations.

The relocated *M*s5.8 event was at ~5 km depth in the AA′ and BB′ profiles, along the upper boundary of the dense aftershock area, which is contrary to our understanding of large earthquakes often occurring along the lower boundary of an earthquake sequence. The earthquake depths are heavily scattered during the early stage of the sequence (red circles in Figure 4A, which span the first 46 h of the sequence, or up to ~1.65 on the logarithm scale) compared with the later earthquakes, which may indicate that the near-field portable station deployment significantly improved the precision of the focal depths. We compared the HYPOINVERSE inversion RMS error (Figure 5A), horizontal error (Figure 5B), and vertical error (Figure 5C) before and after the portable station deployment and found that the portable stations significantly reduced the location errors. The events in the early stage of the sequence, including the *M*s5.8 event, may therefore have significant focal depth uncertainties. The focal depths from the early part of the sequence are expected to converge along more defined rupture planes if additional constraints are supplied.

The subsurface lengths of clusters 1 and 2 are 6 and 12 km, which correspond to predicted magnitudes of 5.4 and 5.9, respectively, based on the Wells and Coppersmith, (1994) relationship. The down-dip rupture widths were also measured from the dense aftershock areas of clusters 1 and 2, with widths of 4 and 6 km corresponding to predicted magnitudes of 5.4 and 5.8, respectively. The predicted magnitudes for cluster 2 are very similar to the observed *M*s6.0 (or *M*w5.87 from the focal mechanism analysis below) event that occurred within cluster 2, whereas no $M > 5$ event occurred within cluster 1.

The near-field observations also significantly improved the seismic monitoring limitation. The *M*c decreased from 1.8 to 1.3 after the portable station deployment, and the *b*-value from the G–R relationship increased from 0.72 to 0.97 (Figure 6). We selected the $M_L \geq 1.8$ events (upper *M*c bound for the two stages) to fit the modified Omori law (Utsu, 1961):

$$N(t) = k(t + c)^{-p} \quad (1)$$

where N is the aftershock frequency, t is the time since the triggering event, k is the productivity of the aftershock sequence, p is the power law exponent, and c is the time delay before the onset of the power-law aftershock decay rate. The p-values were 0.41 and 0.66 before and after the portable station deployment, respectively, which indicates that the sequence decayed slowly. However, the near-field observations yielded a faster decay rate (Figure 7).

Profiles CC′ to GG′ intersected clusters 1 and 2 from north to south. Profile CC′ (Figure 8A) highlights that the earthquakes in the northwestern part of cluster 2 lie along a listric fault surface that is vertical above 9 km depth and dips toward the southwest below 9 km depth. Profiles DD′–GG′ (Figures 8B–E) indicate that clusters 1 and 2 lie along almost vertical faults above 8 km depth that then start to slope toward each other, intersecting at 10 km depth. The parallel branches of seismogenic structures often show independence on shallow part, while they are connected at deep part, such as the Longquan shan fault (Zhao et al., 2021). The same distribution pattern showed by the cluster 1 and 2 of the Maerkang earthquake sequence highlighted they come from a unified seismogenic structure. Profile HH′ (Figure 8F) indicates that cluster 3 lies along an almost vertical fault plane.

Focal mechanisms

The focal mechanism solutions for most of the *M*w ≥ 4.0 events in this sequence that possessed high signal-to-noise ratios were determined *via* the CAP method (Zhao and

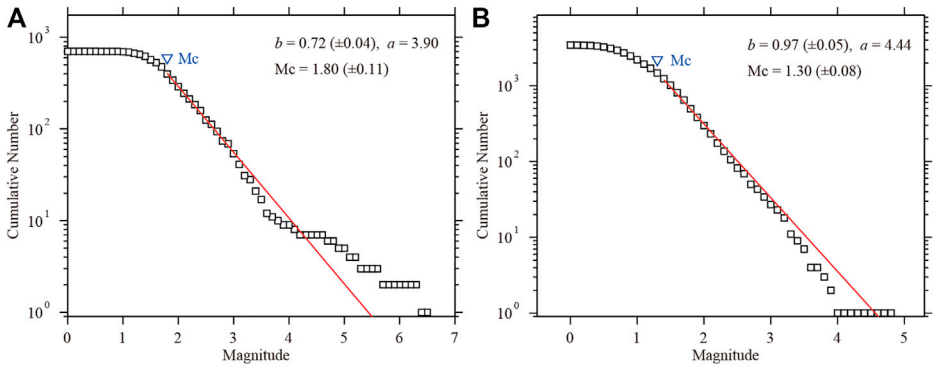

FIGURE 6
Frequency–magnitude distributions **(A)** before and **(B)** after the deployment of three portable stations.

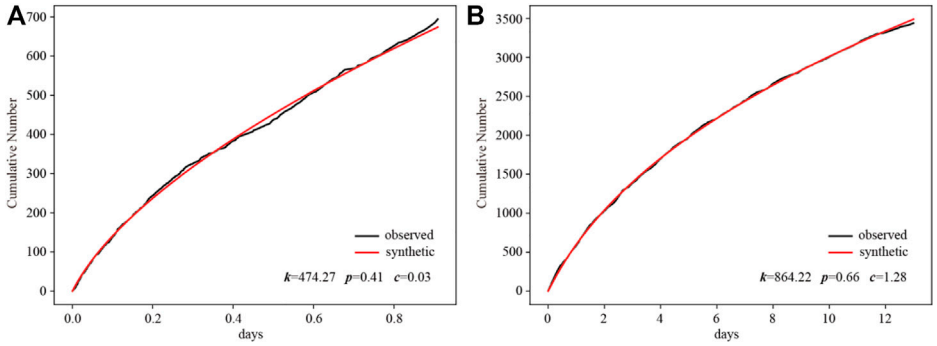

FIGURE 7
Fit of the modified Omori's law to the earthquake sequence **(A)** before and **(B)** after the deployment of three portable stations.

Helmberger, 1994; Zhu and Helmberger, 1996). The method has been proven to yield robust and well-constrained results (Tan et al., 2006; Zheng et al., 2009). We divided the waveform into two parts, extended *p* waves (Pnl), which are long-period body waves after the P-wave onset (first two columns of Figures 10A,B) and surface waves, and time-shifted the synthetic waveforms along the observed waveforms until the maximum cross-correlation coefficient (CC) was obtained. A grid-search algorithm was applied to calculate the best-fit focal mechanism parameters in five dimensions: strike, dip, rake, moment magnitude, and centroid depth.

The waveforms from the broadband stations within an epicentral distance of 350 km were used to invert for the focal mechanisms, and the Green functions were calculated using the frequency–wavenumber method (Zhu and Rivera, 2002) based on the newly inverted local velocity model in Table 2. We specified window lengths of 30 and 60 s for Pnl and surface waves, respectively, and filtered them using 0.05–0.2 and 0.05–0.1 Hz bandpass filters, respectively. The source time duration was set to 5 s when the magnitude was ~6, and 1 s when the magnitude was less than 5.0.

The RMS error–focal depth diagrams indicate that the respective best-fit depths of the *M*s5.8 and *M*s6.0 events are 8.0 km (Figure 9A) and 8.5 km (Figure 9B), respectively, which are about ~4 km from the relocated depths in Figure 4. We believe that the CAP results may therefore be more reliable for constraining the focal depths of these events due to the lack of near-field constraints during the early stage of the sequence. The fits between the observed and synthetic waveforms yielded CC > 0.8 for >70% of the Pnl and surface-wave components (Figure 10), which indicate that the new 1-D model is accurate for the study region. We computed the focal mechanisms for six events in the earthquake sequence *via* the CAP method and found that they were all strike-slip events with centroid depths between 4.5 and 8.5 km (Table 3).

The focal mechanism solution for the *M*s5.2 event at 03:27 CST on June 10, 2022, could not be determined *via* the CAP

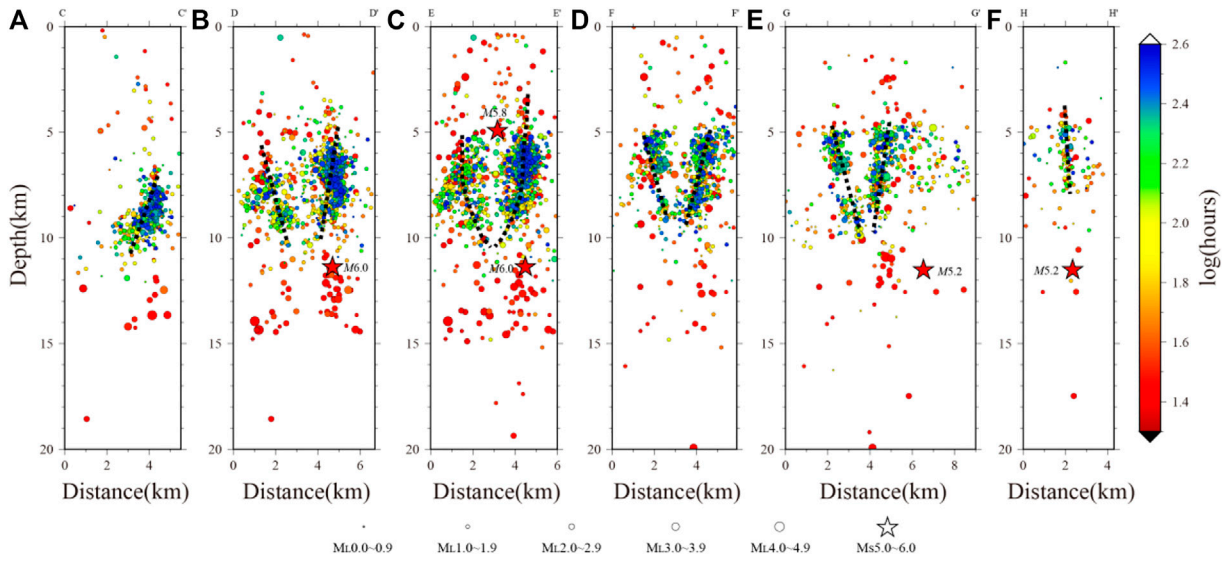

FIGURE 8
Focal depth projection along profiles CC′–HH′. Dashed lines indicate inferred seismogenic structures. **(A)**: profile AA′, **(B)**: profile DD′, **(C)**: profile EE′, **(D)**: profile FF′, **(E)**: profile GG′, **(F)**: profile HH′.

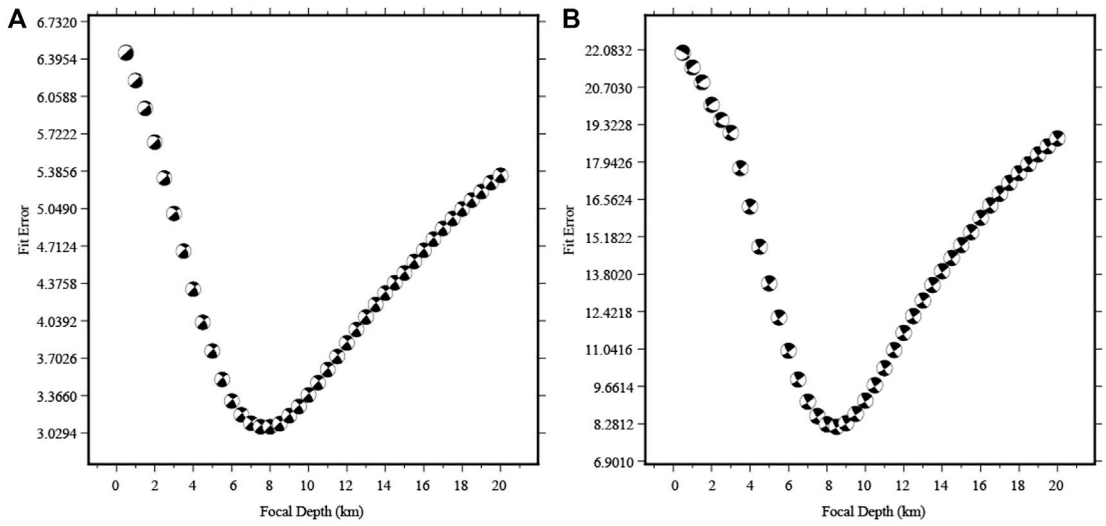

FIGURE 9
Variations in RMS error with focal depth during the focal mechanism inversion for the **(A)** *M*s5.8 and **(B)** *M*s6.0 Maerkang earthquakes.

method owing to waveform superposition from a smaller event (Figure 11). We therefore applied the HASH method (Hardebeck and Shearer, 2002, 2003) to obtain the focal mechanism for this event. We only used the P-wave onset polarities from the vertical component within an epicentral distance of 300 km and estimated the take-off angles using a simplified two-layer crust velocity model (Zhu, 1988). The results yielded a nearly pure strike-slip-type focal mechanism, which is very similar to the other focal mechanisms determined *via* the CAP method (Table 3; Figure 12).

The stress field was obtained *via* the SSI method (Michael, 1985; Michael, 1991) using the focal mechanisms of seven *M*s > 4 events in the sequence (Table 3; Figure 13A), yielding strike-slip faulting along the seismogenic structures (Figure 13B). The NWW-trending principal stress is consistent with the local stress map (Wang et al., 2015) and

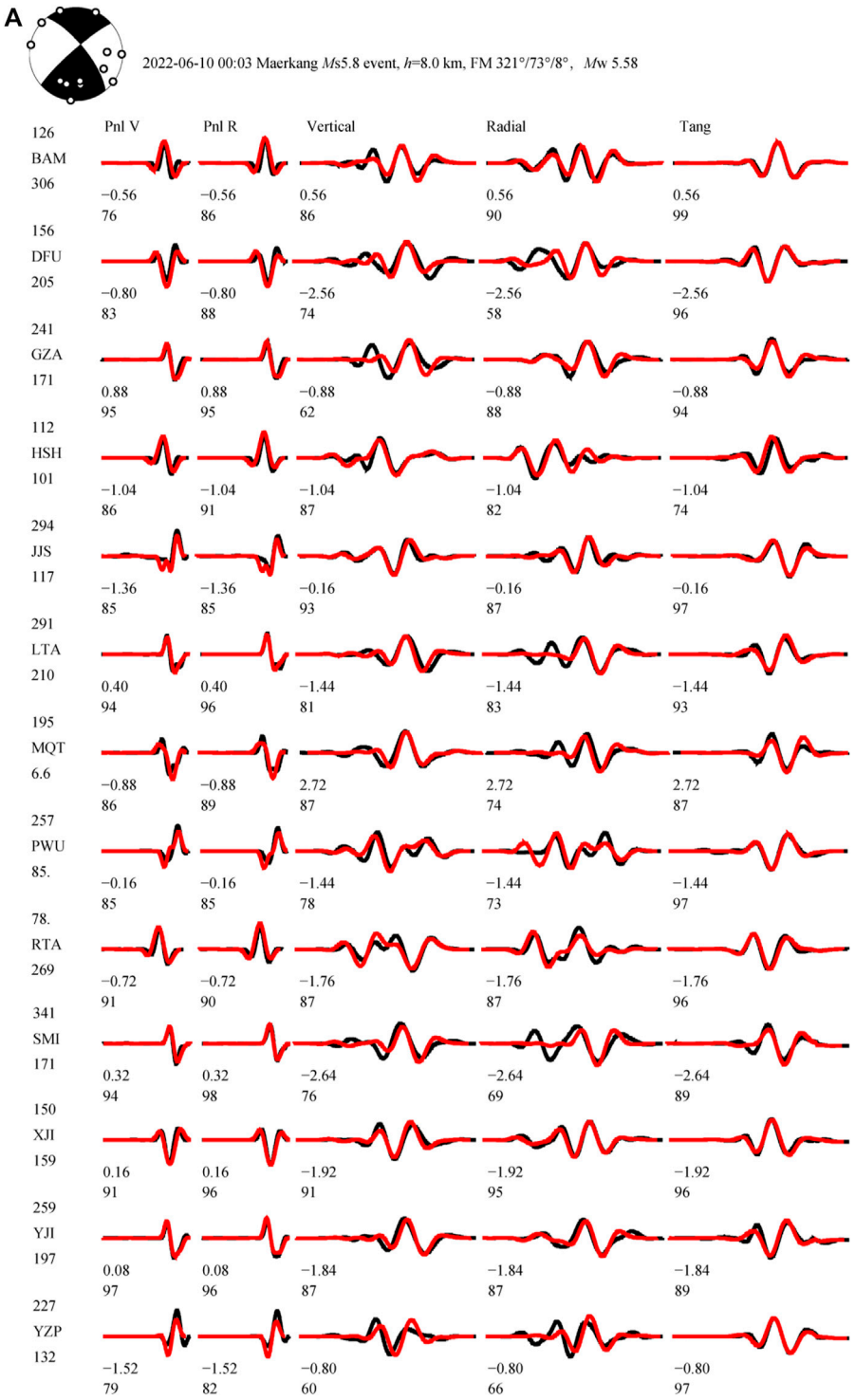

FIGURE 10
(Continued).

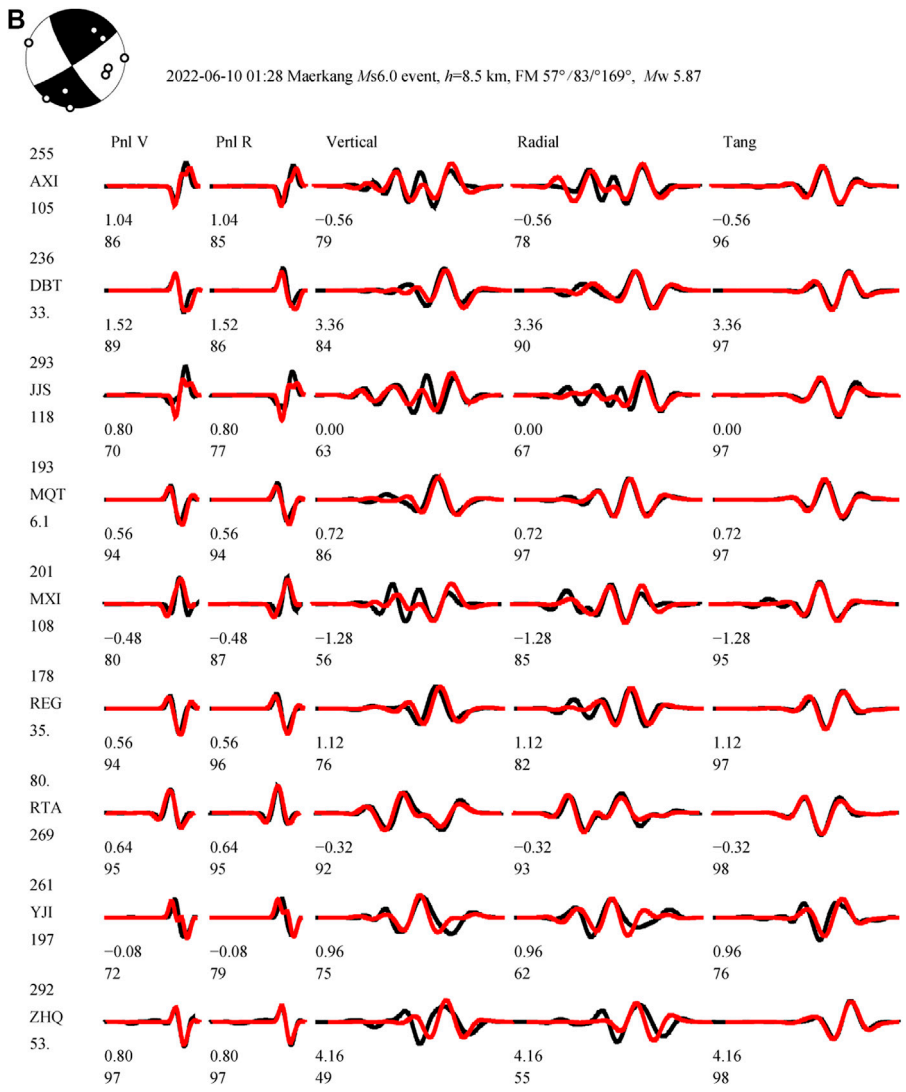

FIGURE 10
(Continued). Observed (black) and synthetic (red) waveforms for the station observations that were used to constrain the focal mechanisms for the **(A)** *Ms*5.8 and **(B)** *Ms*6.0 Maerkang earthquakes. Letters on the left represent station names. Numbers above and below the station names are the epicentral distance (in km) and azimuth (in degrees), respectively. Numbers below the waveforms are the time shifts (in s) in the synthetic waveforms relative to the observed waveforms (upper) and the cross-correlation coefficients (in %; lower).

GPS-derived block movement (Wang and Shen, 2020). Therefore, we suggest that the regional tectonic stress field may have controlled this earthquake sequence.

Rupture directivity of the two mainshocks

The different trends of the relocated clusters (Figure 2) indicate varying rupture patterns during this sequence. Although the focal mechanisms can provide nodal plane information, it is difficult to determine the true ruptured fault plane due to ambiguities in the focal mechanism solutions (Shearer, 2009). We further explored the complexity of the source process of this sequence using the relative centroid location approach (He et al., 2015; He et al., 2018) to determine the rupture directivities of the *Ms*5.8 and *Ms*6.0 events (det1 and det2, respectively, in Table 4). The relative location between the centroid and hypocenter indicates the rupture direction and half of the rupture length when a unilateral rupture is assumed, where the hypocenter is usually determined using P-wave arrival times and the centroid can be

TABLE 3 Focal mechanism solutions for the maerkang earthquake sequence.

Time	Location		Nodal plane 1			Nodal plane 2			*p*		*T*		*B*		*Mw*	Depth/km	Method
YYYY-MM-DD HH:MM (CST)	Lon/°E	Lat/°N	Strike/°	Dip/°	rake/°	Strike/°	Dip/°	rake/°	az/°	pl/°	az/°	pl/°	az/°	pl/°			
2022-06-10 00:03	101.837	32.273	229	82	163	321	73	8	276	6	184	18	25	71	5.58	8.0	CAP/det1
2022-06-10 00:21	101.809	32.279	55	63	178	146	88	27	277	17	14	20	149	63	4.61	5.5	CAP/ref1
2022-06-10 01:28	101.847	32.285	57	83	169	148	79	7	103	3	12	13	205	77	5.87	8.5	CAP/det2
2022-06-10 03:27	101.884	32.259	251	84	−175	160	85	−6	116	8	206	1	301	82	5.2[a]	11.5[b]	HASH
2022-06-10 04:37	101.868	32.250	241	81	163	334	73	9	288	5	196	18	34	71	4.56	7.0	CAP
2022-06-10 04:54	101.834	32.310	61	71	168	155	79	19	287	5	19	22	184	68	4.02	8.0	CAP
2022-06-14 18:11	101.824	32.267	53	67	−173	320	84	−23	274	30	8	12	126	66	4.38	4.5	CAP/ref2

[a]*Ms*,

[b]Depth determined by phase arrival time. az and pl are the azimuth and plunge, respectively. det1 and det2 are the events whose rupture directivities are being determined. ref1 and ref2 are the reference events, which are described in the RUPTURE DIRECTIVITY OF THE TWO, MAINSHOCKS, section.

10.3389/feart.2022.1049911

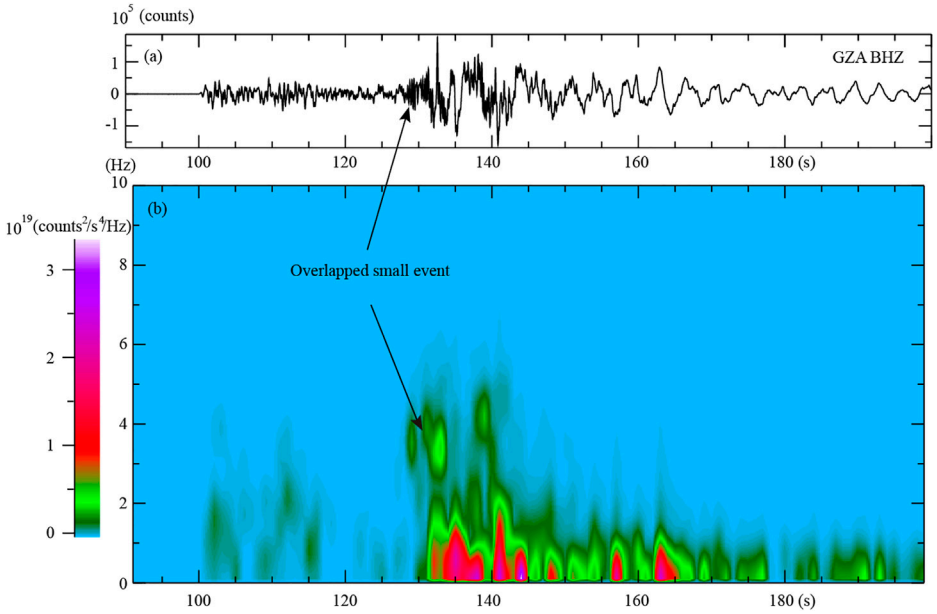

FIGURE 11
(A) Original waveform and **(B)** spectrogram of the *M*s5.2 event, recorded at station GZA, with the high-frequency energy signal detected before the S phase indicating an overlapping small event.

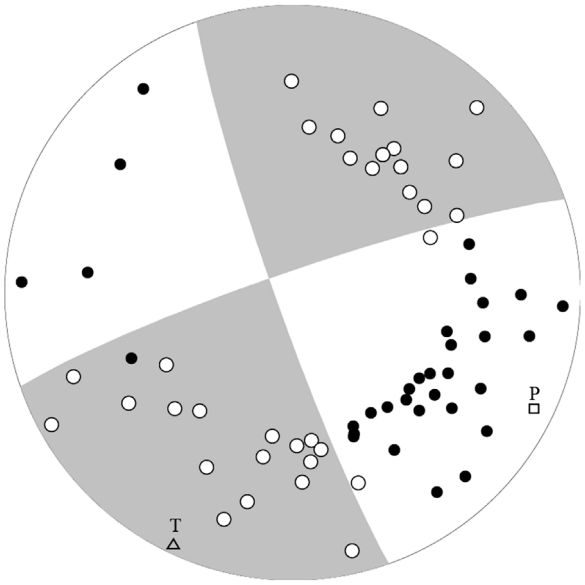

FIGURE 12
Focal mechanism beach ball solution for the *M*s5.2 event. Solid and hollow circles indicate downward and upward polarities, respectively.

resolved using a long-period waveform cross-correlation approach. This method allows a smaller event near the master event (the reference event) to be applied to suppress the path effect.

We selected two small events with high signal-to-noise ratios near the *M*s5.8 and *M*s6.0 events as reference events (ref1 and ref2, respectively, in Table 4) and used the hypocenter locations and focal mechanisms for both the *M*s5.8 and *M*s6.0 events and the reference events to determine the rupture directivity. The synthetic waveforms in the CAP method are calculated for a given reference velocity model, with the event located at the hypocenter. The time shifts for the Pnl and surface waves that are output in the CAP inversion are mainly attributed to two parameters: the location difference between the centroid and hypocenter and the difference between the real crustal structure and reference velocity model. We assume that the hypocenter and reference event are located close to each other, such that the time shifts of the reference event can be applied as the path calibration factor and the time shifts of the master event can be corrected by subtracting the path calibration factor. The differential time shifts can then be fit using a cosine function (Eq. 2) by assuming that the master event ruptures either parallel or perpendicular to the strike of either nodal plane:

$$dt = t_0 + \frac{L}{2v} \times \cos(az - stk) \quad (2)$$

where dt is the differential time shift, t_0 is the source time duration difference between the master event and the reference event, v is the apparent velocity of the selected seismic phase (generally assumed to be 6.0 km/s for Pnl waves, 3.1 km/s for Rayleigh waves, and 3.5 km/s for Love waves), L is the rupture length, and az and stk are the

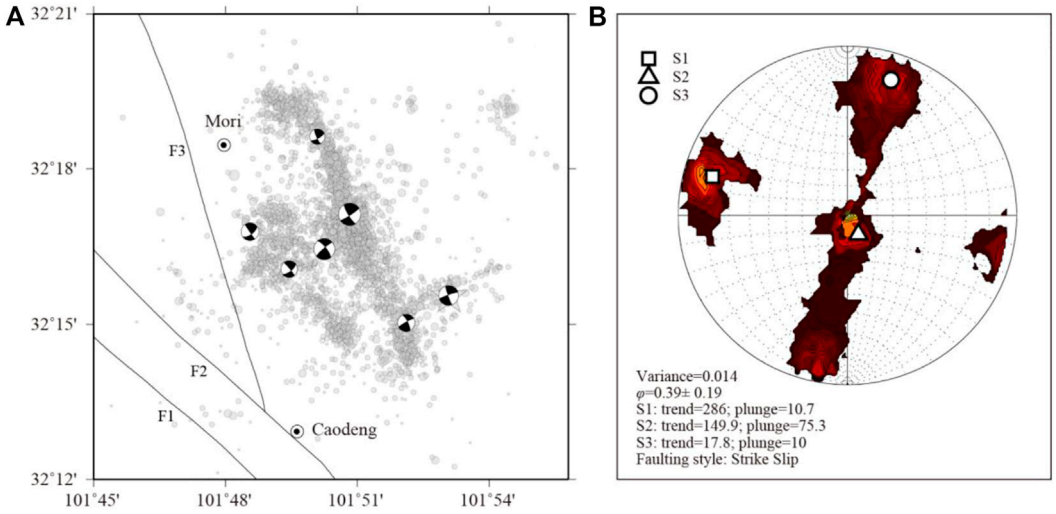

FIGURE 13
(A) Focal mechanisms for the events that were analyzed in this study. **(B)** Stress field that was inverted *via* the SSI method using the focal mechanisms in **(A)**. The other symbols in **(A)** are the same as those in Figure 3. S1, S2, and S3 are the principal stresses, ordered from most compressional to most dilatational, and contours indicate the uncertainty range of each axis at the 95% confidence interval and the variance and φ representing the solution misfit and relative stress size, respectively [see Michael (1991) for further details of the SSI method].

azimuth and strike of the rupture plane. t_0 and L can be resolved *via* a least-squares approach, with the sign of L representing rupture perpendicular (positive) or parallel (negative) to the strike of the rupture plane. We used the time shift differences that were measured from the Love waves with CC > 0.9 for the *Ms*5.8 and *Ms*6.0 events and then fit the time shifts using Eq. 2, and the rupture directivity and length estimates are listed in Table 4. The *Ms*5.8 event (det1) ruptured toward the southwest for 3 km (Figure 14), and the *Ms*6.0 event (det2) ruptured toward the southeast for 3-4 km (Figure 15). The rupture lengths of both events were much shorter than the 9-km rupture length that was determined *via* the empirical scale law (Wells and Coppersmith, 1994), thereby suggesting the potential of bilateral rupture.

Discussion

Seismogenic structures of the 2022 *Ms*6.0 maerkang earthquake sequence

Although the focal mechanisms indicate that the 2022 *Ms*6.0 Maerkang earthquake sequence was controlled by a consistent tectonic movement that was induced by a horizontal, approximately E–W-oriented principal compressive stress, both the relocated sequence and the rupture directivity illustrate that more complex seismogenic structures may be associated with this sequence. The different trends of the three clusters, stratified seismicity, and various rupture directions all indicate that at least four different-scale faults ruptured during the sequence (Figure 16). The rupture directivity of the *Ms*5.8 event suggests that there may be another SW-trending fault where the *Ms*5.8 event occurred that is perpendicular to clusters 1 and 2. However, there is no sign of a corresponding relocated earthquake distribution.

Although the inferred fault planes of this sequence do not align with the local branches of the Songgang fault, their vertical orientations and proximity to each other suggest that these seismogenic structures may be associated with the Songgang fault. The fact that these structures are buried and only active at 5–10 km depth, as indicated by the relocated sequence (Figure 3), is a key reason why they have not been identified during previous geological surveys (Sun et al., 2010).

Similar to the 2021 *Ms*6.4 Yangbi earthquake sequence in Yunnan Province, China (Long et al., 2021), clusters one and two, or inferred faults one and two (if1 and if2 in Figure 16), may have been generated by the dragging effect of large-scale strike-slip faults, as these structures are approximately parallel to the Songgang fault, which is the main fault in the area. This interpretation would mean that cluster three (or if3 in Figure 16) and inferred fault four (if4 in Figure 16) are likely conjugate faults (Figure 13B). Under the control of the unified tectonic stress field, conjugate faults are usually perpendicular to the main fault, and they form an angle of 45° with the principal stress axis (Bretan et al., 1996).

TABLE 4 Rupture directivity of the *Ms*5.8 (det1) and *Ms*6.0 (det2) events.

Event	References event	Station NO.	Rupture directivity	Rupture length (km)	Fit error Nodal plane 1/Nodal plane 2
*Ms*5.8 (det1)	ref1	23	SW	3.0	0.33/0.43
	ref2	25	SW	3.0	0.26/0.37
*Ms*6.0 (det2)	ref1	25	SE	3.0	0.36/0.20
	ref2	24	SE	3.8	0.43/0.17

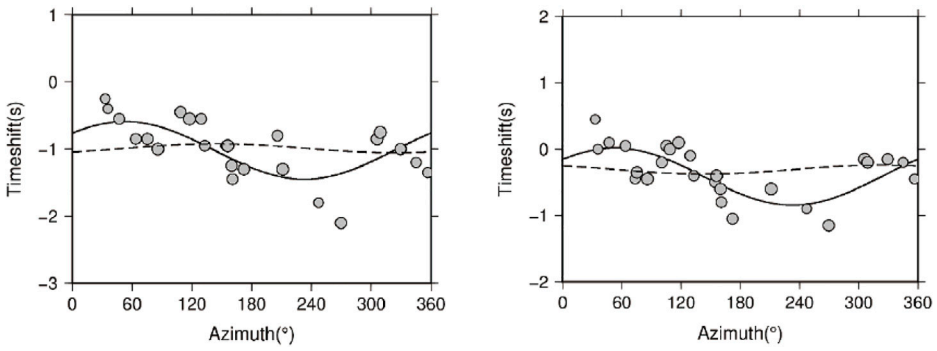

FIGURE 14
Rupture directivity fitting of the *Ms*5.8 event (det1). Two reference events are used (left: ref1; and right: ref2). Dots denote the time shift differences at each station (CC ≥ 0.9), and the lines denote the predicted time shifts of nodal planes 1 (solid) and 2 (dashed) listed in Table 3. The results indicate ~3 km of rupture to the southwest.

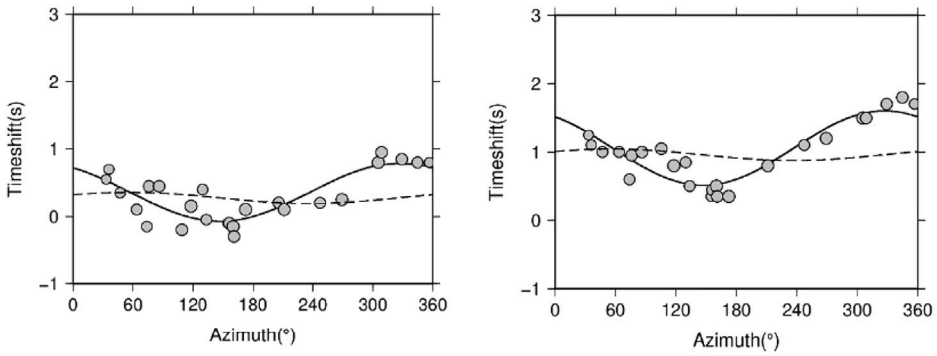

FIGURE 15
Rupture directivity fitting of the *Ms*6.0 event (det2). Two reference events are used (left: ref1; right: ref2). Dots denote the time shift differences at each station (CC ≥ 0.9), and lines denote the predicted time shifts of nodal planes 1 (dashed) and 2 (solid) listed in Table 3. The results indicate 3–4 km of rupture to the southeast.

Coseismic stress triggering of the earthquake sequence

The coseismic stress transfer produced by large earthquakes has a profound impact on the occurrence of successive earthquakes (Stein, 2003). A number of prior studies have successfully applied the Coulomb failure stress model to explain aftershock distributions (Deng and Sykes, 1997a, b; King et al., 1994; Stein, 1999, 2003; Yadav et al., 2011), earthquake sequences (Stein et al., 1994; Nalbant et al.,

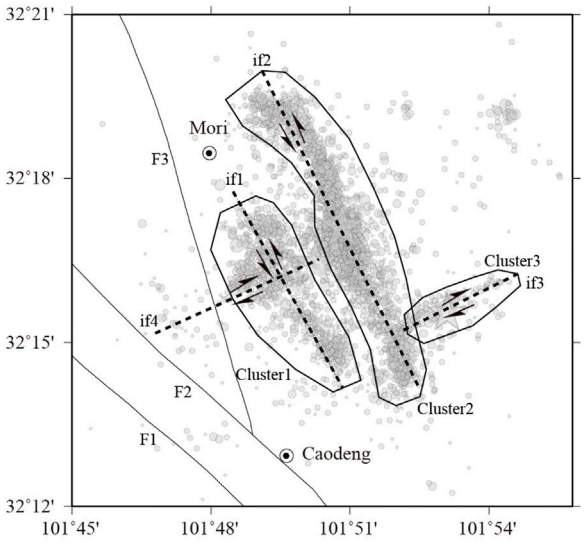

FIGURE 16
Rupture pattern of the 2022 *Ms*6.0 Maerkang earthquake sequence. F1–F3 are branches of the Songgang fault. Clusters 1–3 are the same earthquake clusters in Figure 2B if1–if4 are the inferred faults that were activated by the sequence, and arrows indicatie the relative movement directions. The other symbols are the same as those in Figure 3.

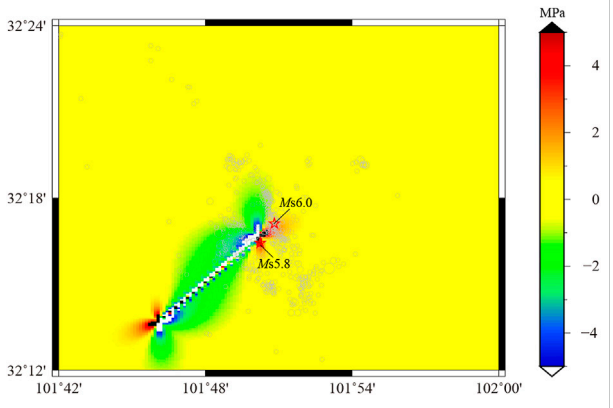

FIGURE 17
Coulomb failure stress changes (ΔCFS) due to the *Ms*5.8 event.

1998; Xiong et al., 2010), and the triggering of moderate-to-strong earthquakes (Harris et al., 1995; Deng and Sykes, 1996; Jaume and Sykes, 1996). We calculated the coseismic Coulomb failure stress changes (ΔCFS) of the *Ms*5.8 event using the PSGRN and PSCMP tools (Wang, 2003; Wang et al., 2006) to determine if there was a stress transfer effect on the spatiotemporal evolution of this sequence. The positions of the main faults were defined by the relocated earthquake locations and their associated rupture directivities, and the fault lengths were estimated from the empirical relationship of Wells and Coppersmith (1994). The slip amount on the fault planes, D, was then evaluated using the $M_0 = \mu DA$ formula (Aki, 1966), where M_0 is the seismic moment (determined *via* the CAP method), μ is the shear modulus (reasonable estimation of 3×10^{11} dyn/cm^2 applied), and A is the fault area (measured from the relocated cross sections). We defined if2 as the receiver fault, as the *Ms*6.0 event occurred along this fault, and we specified the fault occurrence based on the focal mechanism of the *Ms*6.0 event in Table 3. Our analysis indicates that the *Ms*6.0 event occurred in a highly stressed area that possessed a ΔCFS value of 1.6 MPa (Figure 17), which is well above the trigger threshold of 0.01 MPa (Toda et al., 1998; Stein, 1999). It could therefore be inferred that the *Ms*5.8 event along fault if4 triggered the *Ms*6.0 event along fault if2, which constituted the spatiotemporal pattern of the earthquake sequence.

Characteristics of the complex faults of the seismogenic structures

The interconnectivity of the earthquake clusters and inferred faults highlights that the 2022 *Ms*6.0 Maerkang earthquake sequence occurred along complex seismogenic faults, which are a rare tectonic phenomenon. This is due to the problem of linking the complex seismogenic structures of multiple faults at depth through geometric and mechanical relationships. Parallel clusters 1 and 2 in the Maerkang sequence appear to be connected at 10 km depth (Figure 8), which illustrates that they are the branches of another main fault. Chamberlain et al. (2021) carefully studied the 2016 Kaikōura earthquake on the South Island of New Zealand, which generated the significant rupture of at least 21 crustal faults, and they found that the offshore faults provided a link between the southern faults where the earthquake initiated and the northern faults where the largest amount of slip occurred. Ross et al. (2019) pointed out that these types of earthquakes, which present complex seismogenic structures, often occur in immature fault zones and activate many orthogonal structures during their analysis of the 2019 Ridgecrest sequence. The migration of seismicity early in the earthquake sequence is a significant characteristic. The Maerkang earthquake sequence migrated from cluster 1 to 2 during the early stage of the sequence, similar to the migration of seismicity during the 2012 Emilia seismic sequence, Italy, which Sugan et al. (2019) interpreted as a fingerprint of an early afterslip that was triggered by the first mainshock.

Conclusion

We revealed the seismogenic structures and mechanism of the 2022 *Ms*6.0 Maerkang earthquake sequence, Sichuan Province, southwestern China, by relocating the earthquake

sequence, inverting for the focal mechanisms, and calculating the rupture directivity of the earthquake sequence to better understand the seismogenesis of this earthquake sequence and the potential seismic risks it may pose. We conclude that:

1. The seismogenic structures of the Maerkang earthquake sequence are buried faults that may be linked to the nearby Songgang fault, as opposed to the Songgang fault itself. There was a strong spatiotemporal segmentation of the sequence that could be separated into several clusters that were generally parallel to the NW-trending Songgang fault, and a conjugate structure was also identified. The fault planes were vertical at shallow depths but appeared to be connected at ~10 km depth. The fault planes associated with the two major clusters also dip toward the NW.
2. The focal mechanisms for seven $M > 4.0$ events (Table 3) in the sequence were similar and indicated a stress field with strike-slip faulting, which is consistent with the local stress map (Wang et al., 2015). We determined the rupture plane using the directivity effect to avoid the ambiguity of the two nodal planes of the focal mechanisms. We confirmed that the *Ms*6.0 event ruptured to the southeast, which is consistent with the dominant distribution of the sequence, whereas the *Ms*5.8 ruptured to the southwest. This latter rupture direction suggests that additional conjugate faults may be present in the area.
3. Four inferred seismogenic faults were identified. Furthermore, the spatiotemporal pattern of the sequence was due to coseismic stress transfer, with the seismicity migrating from cluster 1 to cluster two.
4. Similar to the *Ms*6.4 Yangbi (Long et al., 2021) and *Ms*6.0 Changning (Yi et al., 2019) earthquakes, the associated structures of the active faults may generate strong earthquakes, such that the potential seismic risks in these areas need to be seriously considered.

Data availability statement

The raw data supporting the conclusion of this article will be made available by the authors, without undue reservation.

Author contributions

LF: Conceptualization, methodology, software, visualization, formal analysis, writing–original draft. HC: Conceptualization, writing–reviewing and editing; YG: conceptualization, visualization, formal analysis. HX: Conceptualization, methodology, software, visualization. SF: Methodology, software, visualization. LL: Writing–reviewing and editing. GY: Writing–reviewing and editing. PL: Writing–reviewing and editing.

Funding

This study was supported by the National Key R&D Program of China (Nos. 2020YFA0710603-01, 2021YFC3000702-05), National Science Foundation of China (No. 41574047), Science and Technology Program of Guangzhou (No. 202102020003), Natural Science Foundation of Shanxi Province (No. 201901D211549), and Sichuan Science and Technology Program (No. 2020YJ0475).

Acknowledgments

We thank Professor Fang Lihua and Peng Zhigang for useful discussions on the earthquake sequence analysis, and Wang Meng for helpful suggestions regarding this manuscript. The digital seismic signals were all processed using SAC 2000 (Goldstein et al., 2003), the stress tensor was inverted using zmap (Wiemer, 2001), and most of the figures were plotted using GMT (Wessel and Smith, 1998).

Conflict of interest

The authors declare that the research was conducted in the absence of any commercial or financial relationships that could be construed as a potential conflict of interest.

Publisher's note

Supplementary material

The Supplementary Material for this article can be found online at: https://www.frontiersin.org/articles/10.3389/feart.2022.1049911/full#supplementary-material

References

Aki, K. (1966). Earthquake generating stress in Japan for the years 1961 to 1963 obtained by smoothing the first motion radiation patterns. *Bull. Earthq. Res. Inst.* 44, 447–471.

Aki, K. (1965). Maximum likelihood estimate of *b* in the formula $\log_{10}N=a-bM$ and its confidence limits. *Bull. Earthq. Res.* 43, 237–239.

Bretan, P., Nicol, A., Walsh, J. J., and Watterson, J. (1996). Origin of some conjugate or "X" fault structures. *Geophysics* 15, 812–816. doi:10.1190/1.1437367

Chamberlain, C. J., Frank, W. B., Lanza, F., Townend, J., and WarrenSmith, E. (2021). Illuminating the pre-co-and post-seismic phases of the 2016 M7.8 Kaikōura earthquake with 10 years of seismicity. *J. Geophys. Res. Solid Earth* 126, e2021JB022304. doi:10.1029/2021JB022304

Chen, L., Wang, H., Ran, Y., Sun, X., Su, G., Wang, J., et al. (2010). The *Ms*7.1 Yushu earthquake surface rupture and large historical earthquakes on the Garzê-Yushu Fault. *Chin. Sci. Bull.* 55, 3504–3509. doi:10.1007/s11434-010-4079-2

Chen, Y., Liu, J., and Ge, H. (1999). Pattern characteristics of foreshock sequences. *Pure Appl. Geophys.* 155 (2/4), 395–408. doi:10.1007/s000240050271

Christophersen, A., and Smith, E. G. C. (2008). Foreshock rates from aftershock abundance. *Bull. Seismol. Soc. Am.* 96, 2133–2148. doi:10.1785/0120060143

Cui, B. (2020). *Geological tectonic features and activity analysis of Aba fault in west Sichuan*. Master Dissertation (in Chinese). Chengdu: Chengdu University of Technology.

Deng, J., and Sykes, L. R. (1997a). Evolution of the stress field in southern California and triggering of moderate-size earthquakes: A 200-year perspective. *J. Geophys. Res.* 102, 9859–9886. doi:10.1029/96jb03897

Deng, J., and Sykes, L. R. (1997b). Stress evolution in southern California and triggering of moderate-small-and micro-size earthquakes. *J. Geophys. Res.* 102, 24411–24435. doi:10.1029/97jb02127

Deng, J., and Sykes, L. R. (1996). Triggering of 1812 santa barbara earthquake by a great san andreas shock: Implications for future seismic hazards in southern California. *Geophys. Res. Lett.* 23, 1155–1158. doi:10.1029/96gl00738

Fang, L., Wu, J., Liu, J., Cheng, J., Jian, C., Han, L., et al. (2015). Preliminary report on the 22 november 2014 *Mw* 6.1/*ms* 6.3 kangding earthquake, western sichuan, China. *Seismol. Res. Lett.* 86 (6), 1603–1613. doi:10.1785/0220150006

Felzer, K. R. (2004). A common origin for aftershocks, foreshocks, and multiplets. *Bull. Seismol. Soc. Am.* 96, 88–98. doi:10.1785/0120030069

Goldstein, P., Dodge, D., Firpo, M., and Minner, L. (2003). "SAC2000: Signal processing and analysis tools for seismologists and engineers," in *The IASPEI international handbook of earthquake and engineering seismology, Part B*. Editors W. H. K. Lee, P. Jennings, C. Kisslinger, and H. Kanamori (New York: Elsevier). chapter 85.5.

Gulia, L., and Wiemer, S. (2019). Real-time discrimination of earthquake foreshocks and aftershocks. *Nature* 574 (7777), 193–199. doi:10.1038/s41586-019-1606-4

Gutenberg, R. C., and Richter, F. (1944). Frequency of earthquakes in California. *Bull. Seismol. Soc. Am.* 34, 185–188. doi:10.1785/bssa0340040185

Hardebeck, J. L., and Shearer, P. M. (2002). A new method for determining first-motion focal mechanisms. *Bull. Seismol. Soc. Am.* 92, 2264–2276. doi:10.1785/0120010200

Hardebeck, J. L., and Shearer, P. M. (2003). Using S/P amplitude ratios to constrain the focal mechanisms of small earthquakes. *Bull. Seismol. Soc. Am.* 93, 2434–2444. doi:10.1785/0120020236

Harris, R. A., Simpson, R. W., and Reasenberg, P. A. (1995). Influence of static stress changes on earthquake locations in southern California. *Nature* 375, 221–224. doi:10.1038/375221a0

Hartzell, S. H., Mendoza, C. I., Ramírez-Guzmán, L., Zeng, Y. J., and Mooney, W. D. (2013). Rupture history of the 2008M_w 7.9 wenchuan, China, earthquake: Evaluation of separate and joint inversions of geodetic, teleseismic, and strong-motion data. *Bull. Seismol. Soc. Am.* 103 (1), 353–370. doi:10.1785/0120120108

He, X. H., Ni, S. D., and Liu, J. (2015). Rupture directivity of the august 3rd, 2014 ludian earthquake (yunan, China). *Sci. China Earth Sci.* 58 (5), 795–804. doi:10.1007/s11430-015-5053-2

He, X. H., Ni, S. D., Zhang, P., and Freymueller, J. T. (2018). The 1 May 2017 British Columbia-Alaska earthquake doublet and implication for complexity near southern end of Denali fault system. *Geophys. Res. Lett.* 45 (12), 5937–5947. doi:10.1029/2018gl078014

Helmstetter, A., Sornette, D., and Grasso, J-R. (2003). Mainshocks are aftershocks of conditional foreshocks: How do foreshock statistical properties emerge from aftershock laws. *J. Geophys. Research-Solid Earth* 108 (B1), 1–20. doi:10.1029/2002jb001991

Hu, M., Wu, Y., Hao, H., Wang, J., Wang, J., and Li, Z. (2022). Lithospheric flexural isostasy background of the 2017 *Ms*7.0 Jiuzhaigou earthquake and its implications on material extrusion in the northeastern Bayan Har Block. *Tectonophysics*. doi:10.1016/j.tecto.2022.229209

Ishimoto, M., and Iida, K. (1939). Observations of earthquakes registered with the microseismograph constructed recently. *Bull. Earthq. Res. Inst.* 17, 443–478.

Jaume, S. C., and Sykes, L. R. (1996). Evolution of moderate seismicity in the san francisco bay region, 1850 to 1993: Seismicity changes related to the occurrence of large and great earthquakes. *J. Geophys. Res.* 101, 765–789. doi:10.1029/95jb02393

Ji, Z., Zhao, C., Wang, Q., and LiWang, Z. H. (2014). Source rupture process of yutian, xinjiang, M_S7.3 earthquake on 21 march 2008. *Acta Seismol. Sin.*, 339–349. (in Chinese). doi:10.3969/j.issn.0253-3782.2014.03.001

King, G. C. P., Stein, R. S., and Lin, J. (1994). Static stress changes and the triggering of earthquakes. *Bull. Seismol. Soc. Am.* 84, 935–953. doi:10.1785/BSSA0840030935

Kissling, E., Ellsworth, W., Eberhart-Phillips, D., and Kradolfer, U. (1994). Initial reference models in local earthquake tomography. *J. Geophys. Res.* 99, 19635–19646. doi:10.1029/93jb03138

Kissling, E., Kradolfer, U., and Maurer, H. (1995). VELEST user's guideshort introduction, Tech. rep. Institute of Geophysics, ETH Zurich, kiss@tomo.ig.erdw.ethz.ch.

Kissling, E. (1988). Geotomography with local earthquake data. *Rev. Geophys.* 26 (4), 659–698. doi:10.1029/rg026i004p00659

Klein, F. W. (2014). *User's guide to HYPOINVERSE-2000, a Fortran program to solve for earthquake locations and magnitudes*. Menlo Park: U.S. Geological Survey Open-File. Report 02–171.

Liang, M. J., Wu, W. W., Yang, Y., Du, F., Zhou, W. Y., Zuo, H., et al. (2022). Late quaternary fault activity and deformation mechanism in the eastern Tibet Plateau (Dari fault, bayan har block). *Quat. Int.* doi:10.1016/j.quaint.2022.09.009

Lippiello, E., Petrillo, G., and Godano, C. (2020). Recognizing the waveform of a foreshock. *Res. Square*. doi:10.21203/rs.3.rs-57209/v1

Long, F., Jiang, C. S., Qi, Y. P., Liu, Z. F., and Fu, Y. (2018). A joint probabilistic approach for merging earthquake catalogs of two neighboring seismic networks: An example of the 2014 Ludian sequence catalog. *Chin. J. Geophys. (in Chinese)* 61 (7), 2815–2827. doi:10.6038/cjg2018L0593

Long, F., Qi, Y. P., Yi, G. X., Wu, W. W., Wang, G. M., Zhao, X. Y., et al. (2021). Relocation of the *Ms*6.4 Yangbi earthquake sequence on May 21, 2021 in Yunnan province and its seismogenic structure analysis. *Chinese Journal of Geophysics (in Chinese)* 64 (08), 2631–2646.

Long, F., Wen, X., Ruan, X., Zhao, M., and Yi, G. (2015). A more accurate relocation of the 2013 Ms7.0 Lushan, Sichuan, China, earthquake sequence, and the seismogenic structure analysis. *Journal of Seismology* 19, 653–665. doi:10.1007/s10950-015-9485-0

Long, F., Yi, G. X., Wang, S. W., Qi, Y. P., and Zhao, M. (2019). Geometry and tectonic deformation of the seismogenic structure for the 8 August 2017 M_S7.0 Jiuzhaigou earthquake sequence, northern Sichuan, China. *Earth Planetary Physics* 3 (3), 253–267. doi:10.26464/epp2019027

Michael, A. J. (1988). Effects of three-dimensional velocity structure on the seismicity of the 1984 Morgan Hill, California, aftershock sequence. *Bulletin of the Seismological Society of America* 78, 1199–1221. doi:10.1785/BSSA0780031199

Michael, A. J. (1985). *Regional stress and large earthquakes: An observational study using focal mechanisms*. Ph.D. Dissertation. Stanford, Calif: Stanford Univ., 156.

Michael, A. J. (1991). Spatial variations in stress within the 1987 whittier narrows, California, aftershock sequence: New techniques and results. *Journal of Geophysical Research* 96 (B4), 6303–6319. doi:10.1029/91jb00195

Molchan, G. M., Konrod, T. L., and Nekrasova, A. K. (1999). Immediate foreshocks: Time variation of the *b*-value. *Phys. Earth Planet. Inter* 111, 229–240. doi:10.1016/s0031-9201(98)00163-0

Nalbant, S. S., Hubert, A., and King, G. C. P. (1998). Stress coupling between earthquakes in northwest Turkey and the north Aegean Sea. *Journal of Geophysical Research* 103, 24469–24486. doi:10.1029/98jb01491

Peng, Z., Vidale, J. E., Ishii, M., and Helmstetter, A. (2007). Seismicity rate immediately before and after main shock rupture from high-frequency waveforms in Japan. *Journal of Geophysical Research-Solid Earth* 112, B03306–B03315. doi:10.1029/2006jb004386

Presti, D., Orecchio, B., Falcone, G., and Neri, G. (2008). Linear versus non-linear earthquake location and seismogenic fault detection in the southern Tyrrhenian Sea, Italy. *Geophysical Journal International* 172, 607–618. doi:10.1111/j.1365-246x.2007.03642.x

Reasenberg, P. A. (1999). Foreshock occurrence before large earthquakes. *Journal of Geophysical Research Solid Earth* 104 (B3), 4755–4768. doi:10.1029/1998jb900089

Ren, J., Xu, X., Yeats, R. S., and Zhang, S. (2013). Latest quaternary paleoseismology and slip rates of the Longriba fault zone, eastern Tibet: Implications for fault behavior and strain partitioning. *Tectonics* 32, 216–238. doi:10.1002/tect.20029

Ross, E., Idini, B., Jia, Z., Stephenson, O. L., Zhong, M., Wang, X., et al. (2019). Hierarchical interlocked orthogonal faulting in the 2019 Ridgecrest earthquake sequence. *Science* 366 (6463), 346–351. doi:10.1126/science.aaz0109

Shearer, P. M. (2009). *Introduction to seismology*. Cambridge: Cambridge University Press. doi:10.1017/CBO9780511841552

Shearer, P. (1997). Improving local earthquake locations using the L1 norm and waveform cross correlation: Application to the whittier narrows, California, aftershock sequence. *Journal of Geophysical Research* 102, 8269–8283. doi:10.1029/96jb03228

Shen, Z. K., Lü, J. N., Wang, M., and Bürgmann, R. (2005). Contemporary crustal deformation around the southeast borderland of the Tibetan Plateau. *J. Geophys. Res.* 110, B11409. doi:10.1029/2004JB003421

Shen, Z. K., Sun, J., Zhang, P., Wan, Y., Wang, M., Burgmann, R., et al. (2009). Slip maxima at fault junctions and rupturing of barriers during the 2008 Wenchuan earthquake. *Nature Geoscience* 2, 718–724. doi:10.1038/ngeo636

Stein, R. S. (2003). Earthquake conversations. *Scientific American* 288, 72–79. doi:10.1038/scientificamerican0103-72

Stein, R. S., King, G. C. P., and Lin, J. (1994). Stress triggering of the 1994 *M*=6.7 Northridge, California, earthquake by its predecessors. *Science* 265 (5177), 1432–1435. doi:10.1126/science.265.5177.1432

Stein, R. S. (1999). The role of stress transfer in earthquake occurrence. *Nature* 402, 605–609. doi:10.1038/45144

Sugan, M., Vuan, A., Kato, A., Massa, M., and Amati, G. (2019). Seismic evidence of an early afterslip during the 2012 sequence in Emilia (Italy). *Geophysical Research Letters* 46 (2), 625–635. Portico. doi:10.1029/2018gl079617

Sun, D., Wang, D. Y., Wu, D. C., Zhao, D. J., and Huang, C. (2010). Activity and effect of main faults in near field of Bala Hydro power station in Maerkang. *J. Engineer. Geol. (in Chinese)* 18 (6), 940–949.

Tamaribuchi, K., Yagi, Y., Enescu, B., and Hirano, S. (2018). Characteristics of foreshock activity inferred from the JMA earthquake catalog. *Earth, Planets and Space* 70, 90–13. doi:10.1186/s40623-018-0866-9

Tan, Y., Zhu, L., Helmberger, D. V., and Saikia, C. K. (2006). Locating and modeling regional earthquakes with two stations. *Journal of Geophysical Research* 111 (B1), B013061029. doi:10.1029/2005jb003775

Toda, S., Stein, R. S., Reasenberg, P. A., Dieterich, J. H., and Yoshida, A. (1998). Stress transferred by the 1995 *M*w= 6.9 Kobe, Japan, shock: Effect on aftershocks and future earthquake probabilities. *Journal of Geophysical Research Solid Earth* 103 (B10), 24543–24565. doi:10.1029/98jb00765

Utsu, T. (1961). A statistical study on the occurence of aftershocks. *Geophys. Mag.* 30, 521–605.

Waldhauser, F., and Ellsworth, W. L. (2000). A double-difference earthquake location algorithm: Method and application to the northern hayward fault, California. *Bulletin of the Seismological Society of America* 90, 1353–1368. doi:10.1785/0120000006

Waldhauser, F. (2001). *HypoDD: A computer program to compute double-difference earthquake locations*. Menlo Park: USGS Open File Rep., 01–113.

Wang, M., and Shen, Z. K. (2020). Present-day crustal deformation of continental China derived from GPS and its tectonic implications. *Journal of Geophysical ResearchSolid Earth* 125 (2), e2019JB018774. doi:10.1029/2019JB018774

Wang, Q., Wang, H., and Xia, A. (2009). Features of seismicity in Xinjiang and its possible reason after the Yutian M_S7.4 earthquake, 2008. *Earthquake. Science (in Chinese)* 22, 615–622. doi:10.1007/s11589-009-0615-z

Wang, R., (2003). Computation of deformation induced by earthquakes in a multi-layered elastic crust - FORTRAN programs EDGRN/EDCMP. *Computer and Geosciences* 29 (2), 195–207. doi:10.1016/s0098-3004(02)00111-5

Wang, R., Lorenzo-Martin, F., and Roth, F. (2006). PSGRN/PSCMP - a new code for calculating co- and post-seismic deformation, geoid and gravity changes based on the viscoelastic-gravitational dislocation theory. *Computers and Geosciences* 32, 527–541. doi:10.1016/j.cageo.2005.08.006

Wang, W., Fang, L., Wu, J., Tu, H., Chen, L., Lai, G., et al. (2021). Aftershock sequence relocation of the 2021 MS7.4 Maduo earthquake, Qinghai, China. *Science China Earth Sciences* 64, 1371–1380. doi:10.1007/s11430-021-9803-3

Wang, W. L., Wu, J. P., Fang, L. H., and Wang, C. Z. (2012). Relocation of the Yushu M_S7.1 earthquake and its aftershocks in 2010 from HypoDD. *Science China Earth Sciences* 56, 182–191. doi:10.1007/s11430-012-4450-z

Wang, X. S., Lü, J., Xie, Z. J., Long, F., Zhao, X. Y., and Zheng, Y. (2015). Focal mechanisms and tectonic stress field in the North-South Seismic Belt of China. *Chinese Journal of Geophysics (in Chinese)* 58 (11), 4149–4162. doi:10.6038/cjg20151122

Wang, Y. Z., Wang, E. N., Shen, Z. K., Wang, M., Gan, W. J., Qiao, X. J., et al. (2008). GPS-constrained inversion of present-day slip rates along major faults of the Sichuan-Yunnan region, China. *Science in China (Ser D)* 51 (9), 1267–1283. doi:10.1360/zd2008-38-5-582

Wei, Z., Yang, S., and Chen, X. F. (2008). Numerical simulation of strong ground motion for the M s8.0 Wenchuan earthquake of 12 May 2008. *Science in China Series D Earth Sciences* 51, 1673–1682. doi:10.1007/s11430-008-0130-4

Wells, D., and Coppersmith, K. (1994). New empirical relationships among magnitude, rupture length, rupture width, rupture area, and surface displacement. *Bulletin of the Seismological Society of America* 84, 974–1002.

Wessel, P., and Smith, W. H. F. (1998). New, improved version of generic mapping tools released. *AGU* 79, 579. doi:10.1029/98eo00426

Wiemer, S. (2001). A software package to analyze seismicity: Zmap. *Seismological Research Letters* 72 (3), 373–382. doi:10.1785/gssrl.72.3.373

Woessner, J., and Wiemer, S. (2005). Assessing the quality of earthquake catalogues: Estimating the magnitude of completeness and its uncertainty. *Bulletin of the Seismological Society of America* 95 (2), 684–698. doi:10.1785/0120040007

Wu, W. W., Wei, Y. L., Long, F., Liang, M. J., Chen, X. F., Sun, W., et al. (2020). Study on source parameters of the 8 August 2017 *M*7.0 Jiuzhaigou earthquake and its aftershocks, northern Sichuan. *Seismology and Geology (in Chinese)* 42 (02), 492–512. doi:10.3969/j.issn.0253-4967.2020.02.015

Xiong, X., Shan, B., Zheng, Y., and Wang, R. J. (2010). Stress transfer and its implication for earthquake hazard on the Kunlun Fault, Tibet. *Tectonophysics* 482, 216–225. doi:10.1016/j.tecto.2009.07.020

Xu, X. W., Wen, X. Z., Chen, G. H., and Yu, G. H. (2008). Discovery of the Longriba faults, eastern part of the Bayankela tectonic block and its geodynamic implications. *Sciences in China (Series-D) (in Chinese)* 38 (5), 529–542. doi:10.1360/zd2008-38-5-529

Xu, X. W., Wen, X. Z., Han, Z. J., Chen, G. H., Li, C. Y., Zheng, W., et al. (2013). Lushan M_S7.0 earthquake: A blind reserve-fault event. *Chinese Science Bulletin (in Chinese)* 58, 3437–3443. doi:10.1007/s11434-013-5999-4

Yadav, R., Papadimitriou, E. E., Karakostas, V., Shanker, D., Rastogi, B. K., Chopra, S., et al. (2011). The 2007 talala, Saurashtra, Western India earthquake sequence: Tectonic implications and seismicity triggering. *Journal of Asian Earth Sciences* 40, 303–314. doi:10.1016/j.jseaes.2010.07.001

Yang, Y. H. (2014). *Application of receiver function method for crust and upper mantle structure beneath sichuan and yunnan region*. Master Dissertation (in Chinese). Chengdu: Chengdu University of Technology.

Yi, G. X., Long, F., Liang, M. J., Zhang, H. P., Zhao, Min, Ye, Y. Q., et al. (2017). Focal mechanism solution and seismogenic structure of the 8 August 2017 M7.0 Jiuzhaigou earthquake and its aftershocks, nortthern Sichuan. *Chinese Journal of Geophysics (in Chinese)* 60 (10), 4083–4097. doi:10.6038/cjg20171033

Yi, G. X., Long, F., Liang, M. J., Zhao, M., Wang, S. W., Gong, Y., et al. (2019). Focal mechanism solutions and seismogenic structure of the 17 June 2019 M_S6.0 Sichuan Changning earthquake sequence. *Chinese Journal of Geophysics (in Chinese)* 62 (9), 3432–3447. doi:10.6038/cjg2019N0297

Yi, G. X., Long, F., Wen, X. Z., Liang, M. J., and Wang, S. W. (2015). Seismogenic structure of the *M*6.3 kangding earthquake sequence on 22 nov. 2014, southwestern China. *Chinese Journal of Geophysics (in Chinese)* 58 (4), 1205–1219. doi:10.6038/cjg20150410

Yu, G., Xu, X., Klinger, Y., Diao, G., Chen, G., Feng, X., et al. (2010). Fault-scarp features and cascading-rupture model for the *M*w 7.9 Wenchuan earthquake, eastern Tibetan Plateau, China. *Bulletin of the Seismological Society of America* 100, 2590–2614. doi:10.1785/0120090255

Yue, H., Shen, Z., Zhao, Z., Wang, T., Cao, B., Li, Z., et al. (2022). Rupture process of the 2021 *M*7.4 Maduo earthquake and implication for deformation mode of the Songpan-Ganzi terrane in Tibetan Plateau. *Proc. Natl. Acad. Sci. U. S. A.* 119 23 (2022), e2116445119. doi:10.1073/pnas.2116445119

Zhang, P. Z., Deng, Q. D., Zhang, G. M., Ma, J., Gan, W. J., Min, W., et al. (2003). Active tectonic-block and Strong earthquakes in the continent of China. *Science in China Series D Earth Sciences* 46, 13–20.

Zhao, L. S., and Helmberger, D. V. (1994). Source estimation from broadband regional seismograms. *Bulletin of the Seismological Society of America* 84 (1), 91–104. doi:10.1785/BSSA0840010091

Zhao, M., Long, F., Yi, G. X., Liang, M. J., Xie, J. T., and Wang, S. W. (2021). Focal mechanism and seismogenic structure of the MS 5.1 qingbaijiang earthquake on february 3, 2020, southwestern China. *Frontiers in Earth Science* 9. doi:10.3389/feart.2021.644142

Zhao, Z., and Zhang, R. S. (1987). The compilation of regional travel time table in Sichuan. *Earthquake Research in Sichuan* 2, 29–35. (in Chinese with English abstract).

Zheng, Y., Ma, H., Lü, J., Ni, S., Li, Y., and Wei, S. (2009). Source mechanism of strong aftershocks ($M_S \geq 5.6$) of the 2008/05/12 Wenchuan earthquake and the implication for seismotectonics. *Science in China Series D Earth Sciences* 52 (6), 739–753. doi:10.1007/s11430-009-0074-3

Zhou, R. J., He, Y. L., Ma, S. H., and Li, X. G. (1999). Late quaternary active characteristics of Fubianhe fault in Sichuan's Xiaojin. *J. Seismol. Res. (in Chinese)* 22 (4), 376–381.

Zhu, J. S. (1988). *The computational methods in the Seismology*. Beijing: Seismological Press. (in Chinese).

Zhu, L., and Kanamori, H. (2000). Moho depth variation in southern California from teleseismic receiver functions. *J Geophys Res* 105, 2969–2980. doi:10.1029/1999jb900322

Zhu, L. P., and Rivera, L. A. (2002). A note on the dynamic and static displacements from a point source in multilayered media. *Geophysical Journal International* 148, 619–627. doi:10.1046/j.1365-246x.2002.01610.x

Zhu, L., and Helmberger, D. V. (1996). Advancement in source estimation techniques using broadband regional seismograms. *Bulletin of the Seismological Society of America* 86, 1634–1641. doi:10.1785/bssa0860051634

frontiers | Frontiers in Earth Science

TYPE Original Research
PUBLISHED 25 January 2023
DOI 10.3389/feart.2023.1081605

OPEN ACCESS

EDITED BY
Hongfeng Yang,
The Chinese University of Hong Kong, China

REVIEWED BY
Gaohua Zhu,
Institute of Oceanology (CAS), China
Fatih Bulut,
Boğaziçi University, Türkiye

*CORRESPONDENCE
Lian-Feng Zhao,
zhaolf@mail.iggcas.ac.cn

SPECIALTY SECTION
This article was submitted to Solid Earth Geophysics,
a section of the journal
Frontiers in Earth Science

RECEIVED 27 October 2022
ACCEPTED 11 January 2023
PUBLISHED 25 January 2023

CITATION
He X, Zhao L-F, Xie X-B, Zhang L and Yao Z-X (2023), Eastward expansion of the Tibetan plateau: Insights from stress drops of the 2021 Ms 6.4 Yangbi, Yunnan and Ms 7.4 Maduo, Qinghai earthquake sequences in China.
Front. Earth Sci. 11:1081605.
doi: 10.3389/feart.2023.1081605

Eastward expansion of the Tibetan plateau: Insights from stress drops of the 2021 Ms 6.4 Yangbi, Yunnan and Ms 7.4 Maduo, Qinghai earthquake sequences in China

Xi He[1], Lian-Feng Zhao[1,2]*, Xiao-Bi Xie[3], Lei Zhang[1,4] and Zhen-Xing Yao[1]

[1]Key Laboratory of Earth and Planetary Physics, Institute of Geology and Geophysics, Chinese Academy of Sciences, Beijing, China, [2]Heilongjiang Mohe Observatory of Geophysics, Institute of Geology and Geophysics, Chinese Academy of Sciences, Beijing, China, [3]Institute of Geophysics and Planetary Physics, University of California, Santa Cruz, Santa Cruz, CA, United States, [4]School of Earth and Space Sciences, Peking University, Beijing, China

The eastward expansion of the Tibetan Plateau has resulted in extensive seismic activities in the eastern Tibetan Plateau, along with various types of faulting processes across this region. However, the crustal stress status related to these phenomena remains unclear. On 21 May 2021, the Ms 6.4 Yangbi and Ms 7.4 Maduo earthquakes with diverse focal mechanisms occurred consecutively in the Chuandian and Bayan Har blocks in the southern and northern parts of the eastern Tibetan Plateau, providing a distinct opportunity to directly compare the stresses in both flanks of the laterally expanding plateau. In this study, we estimate the stress drops of the Yangbi and Maduo earthquake sequences for all $M \geq 3.0$ events from the Lg-wave spectra. Both the path attenuation and site effect are properly removed based on an established broadband Lg-wave attenuation model. Then, the distribution of the stress drops is refined through high-precision earthquake relocation. Quick decays in stress drops were observed after both mainshocks. The Yangbi sequence has a relatively high median stress drop value, with significantly high stress drops for some foreshocks that possibly indicate a cascade triggering mechanism for the nucleation of the mainshock. In comparison, the Maduo sequence is characterized by a higher stress drop for the mainshock and sustained large fluctuation in stress drops for aftershocks. The Maduo aftershocks extend both the eastern and western directions from the mainshock, with relatively low stress drops in the east, suggesting a large amount of energy has been spent to drive the supershear rupture during the mainshock. We also find that the stress drops are associated with fault junctions for the Yangbi sequence, and are associated with variations in strength along the fault for the Maduo sequence, which are very likely linked with patterns of crustal motion and deformation in the eastern Tibetan Plateau.

KEYWORDS

stress drop, Lg source spectra, Yangbi earthquake sequence, Maduo earthquake sequence, eastern Tibetan plateau

1 Introduction

The geological evolution of the Tibetan Plateau during the Cenozoic is accompanied by well-developed fault systems and seismic activities (Figure 1); therefore, explorations into present-day seismicity and source parameters can shed light on structures and properties of the seismogenic layers, advancing our understanding of the growing process of the plateau (Molnar and Lyoncaen, 1989). In the southern and northern Tibetan Plateau, significant thrusting indicates the uplift of the Tibetan Plateau in response to the continued north-south convergence between the Indian and Eurasian plates (Yin and Harrison, 2000). Since the middle Miocene, north–south-trending normal faulting began to develop in the central Tibetan Plateau, signifying the east-west expansion of the high-rising plateau crust (e.g., Yin and Harrison, 2000; Blisniuk et al., 2001). The resulting eastward movements of crustal blocks, including the Bayan Har and Chuandian, led to reverse faulting on the Longmanshan faults that mark the eastern boundary of the Tibetan Plateau (e.g., Zheng et al., 2017) and devastating earthquakes, including the Wenchuan earthquake in 2008 and the Lushan earthquake in 2013 (Wang et al., 2015). In addition, significant strike-slip motions were also produced on the boundaries of the extruding blocks. In particular, on 21 May 2021, within ~4.3 h, the Yangbi Ms 6.4 earthquake occurred in the Chuandian block, and the Maduo Ms 7.4 earthquake occurred in the Bayan Har block, both with primarily strike-slip faulting. However, the faulting behaviors vary across the southern boundaries of the Chuandian block and the northern boundaries of the Bayan Har block. Right-lateral strike-slip plus normal faulting and left-lateral strike-slip plus reverse faulting were obtained for the mechanism solutions of the Yangbi and Maduo earthquakes, respectively (Long et al., 2021; Zhang J. Y. et al., 2022). The various focal mechanisms may reflect intricate fault morphology and probably a complicated regional stress setting, yet the stress distributions within the fault system and related tectonic attributions remain unclear. Exploring the stress release of these earthquakes can shed light on the localized stress variability within seismogenic faults and improve our understanding of the nature of plateau expansion (Holt et al., 1991; Zhang et al., 2010; Sun et al., 2018).

The stress drop is defined as the difference between the average stresses on a fault before and after an earthquake (e.g., Shearer et al., 2006). It is one of the fundamental source-scaling parameters, providing information on the rupture processes and underlying tectonics controlling them (e.g., Allmann and Shearer, 2009; Abercrombie, 2014). The stress drop of earthquakes can be an indicator of the localized stress variability of the seismogenic fault (e.g., Allmann and Shearer, 2007; Yamada et al., 2010), whereas it is not equivalent to the overall stress levels of faults. Rupture simulations demonstrated that keeping the same stress drop at different stress levels can produce identical synthetic waveforms, even in near field (Weng and Yang, 2018; Yao and Yang, 2020). Since both Yangbi and Maduo earthquake sequences were primarily strike-slip faulting, it is not necessary to attribute the difference in stress drop to focal mechanisms and we can explore the localized stress variability in the eastern Tibetan Plateau by straightforward comparison of the stress drops between the two earthquake sequences. However, the stress drop is calculated based on reliable restoration of the earthquake source spectrum, which can be easily distorted by seismic attenuation and shallow structures beneath stations. Several methods have been developed to solve this, including the empirical Green's function method (Shearer et al., 2006) and the generalized joint inversion method to solve for both the source and path attenuation (Oth et al., 2011). However, the rapid development in attenuation tomography over recent years has inspired us with a novel approach to directly remove the attenuation and site effects from the observed spectra based on the established attenuation model (He et al., 2020). Zhao et al. (2010) developed a broadband Lg-wave attenuation tomography scheme that utilized both source-station amplitudes and interstation amplitude ratios to obtain the high-resolution broadband Lg-

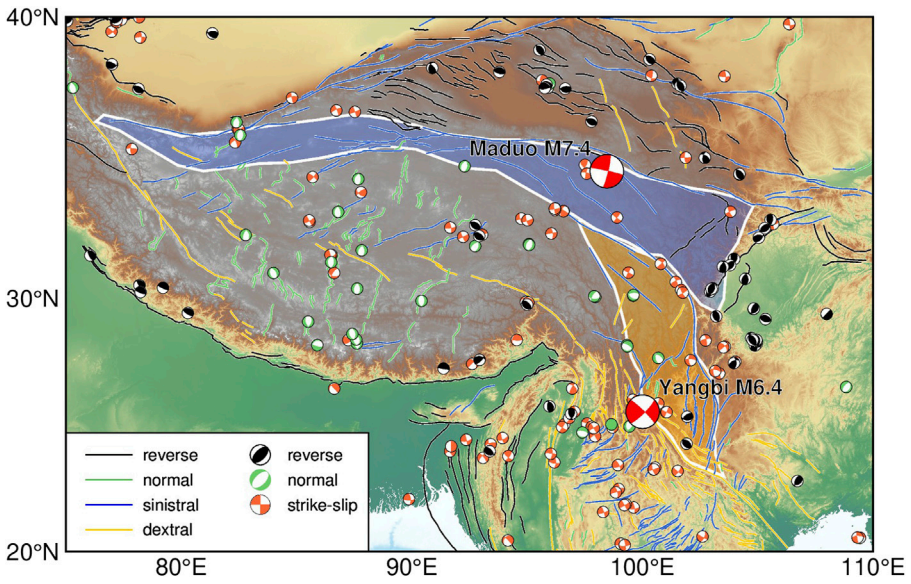

FIGURE 1
Map showing active faults (lines) and moderate to large earthquakes (beach balls) on the Tibetan Plateau, with their kinematic types coded by colors. Geological blocks filled with blue and yellow are the Bayan Har and Chuandian blocks, respectively. Locations and focal mechanisms of the 2021 May Yangbi and Maduo earthquakes are indicated by red beach balls.

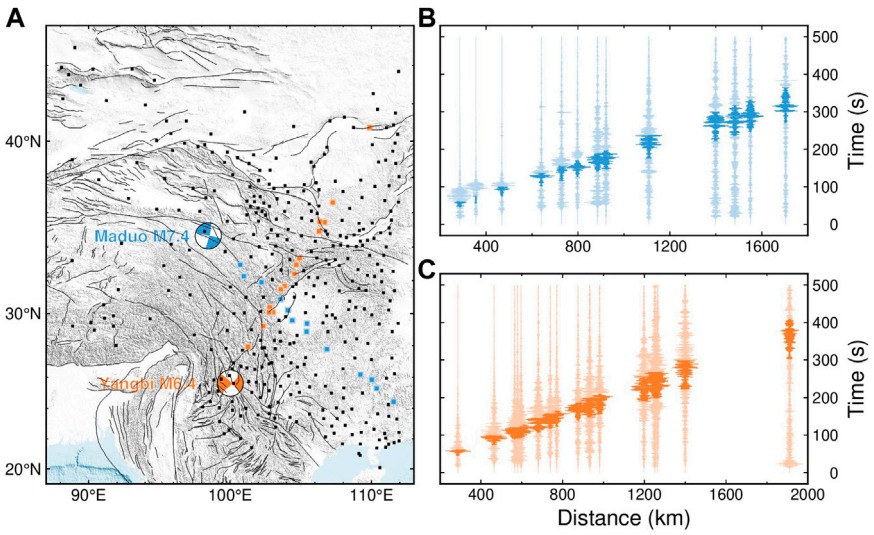

FIGURE 2
Map of the distribution of stations used in this study **(A)** and illustrations of seismograms **(B,C)**. **(A)** Stations are represented by filled squares. Locations and focal mechanisms of the 2021 May Yangbi and Maduo earthquakes are indicated by orange and blue beach balls, respectively. Orange and blue squares represent stations selected to show their recordings for the Yangbi and Maduo mainshocks, respectively. **(B,C)** Waveforms are filtered between 0.5 and 1.0 Hz to improve the Lg demonstrations and are aligned with a reduced velocity of 8.4 km/s. Typical group velocities of the Lg phase, 3.6–3.0 km/s, are highlighted. The Lg-wave group velocity window can be slightly adjusted for each trace to capture the maximum energy arrival.

wave Q model. This method was then improved to incorporate the interevent amplitude ratios thus the site response for each station could also be inverted (Zhao and Xie, 2016). By using the this method, a high-resolution broadband Lg-wave Q model was obtained for China, which is consistent with geological features (Zhao et al., 2010; 2013b; Zhao et al., 2013a; He X. et al., 2021). The site responses were also obtained for relevant stations. Taking advantage of attenuation and site response dataset, the accurate of the stress drop estimates for the 21 May 2021 Yangbi and Maduo earthquake sequences can be achieved.

In this study, we retrieve Lg-wave source spectra for earthquakes with magnitudes ≥3.0 for both Yangbi and Maduo earthquake sequences. The effects of attenuation along the propagation path and site response are removed using the established broadband regional Lg-wave attenuation model and regional site response data. Based on the reliable source spectra and assuming a generalized source model (Boatwright, 1980), the seismic moment, corner frequency and high-frequency falloff rate are estimated for each event. The stress drop is then calculated for both the Yangbi and Maduo earthquake sequences. To investigate the temporal and spatial evolutions of these stress drops, we relocated earthquakes to refine their source locations. Finally, we discuss the tectonic implications of these stress drops and their relations with the eastward expansion of the Tibetan Plateau.

2 Data and method

2.1 Regional dataset

In this study, 105 earthquakes were selected from the catalog of the China Earthquake Network Center (CENC), including the 21 May 2021 Yangbi mainshock, with 11 foreshocks after 13 May and 39 aftershocks before 1 June, and the Maduo mainshock, with 53 aftershocks before 1 June. These earthquakes were selected according to magnitudes ≥3.0 to improve the quality of Lg recordings, and their locations and origin times were obtained from the catalog. We collected more than 42 thousand vertical-component seismograms recorded by 376 permanent seismic stations to investigate the source properties of the 2021 Yangbi and Maduo earthquake sequences. These stations have good azimuthal coverage and were within epicentral distances between 200–3,000 km to ensure well developed Lg waves (Figure 2).

2.2 Lg-wave preprocessing

The seismic Lg-wave, developed from a reverberated S-wave in the continental crust, is one of the prominent seismic phases in regional seismograms and often used in amplitude analysis (Furumura and Kennett, 1997; Fisk, 2006; Pasyanos et al., 2009). To analyze the arrival times and frequency contents of different regional phases, illustrated in Figure 3A is a regional waveform, and in Figure 3B is the corresponding spectrogram. The spectrogram was obtained using the short-time Fourier transform, where the window was determined to be consistent with the regular Lg-extraction length, according to the velocity window with a length of 0.6 km/s. Due to the changing length of the window, we regularized the spectrogram at 58 frequencies within 0.05–10.0 Hz, and then normalized the spectrogram at each frequency. The first arrival in the spectrogram was Pn at ~2–5 Hz, followed by Pg over ~0.3–4 Hz. The Sn was very weak compared with other regional phases. Lg could be recognized as a prominent patch with a longer duration and dominating energy within ~0.2–2.0 Hz. Based on the spectrogram, the velocity window is 3.6–3.0 km/s. We followed the procedure of Zhao et al. (2010) to process the Lg amplitudes. First, instrument responses were removed,

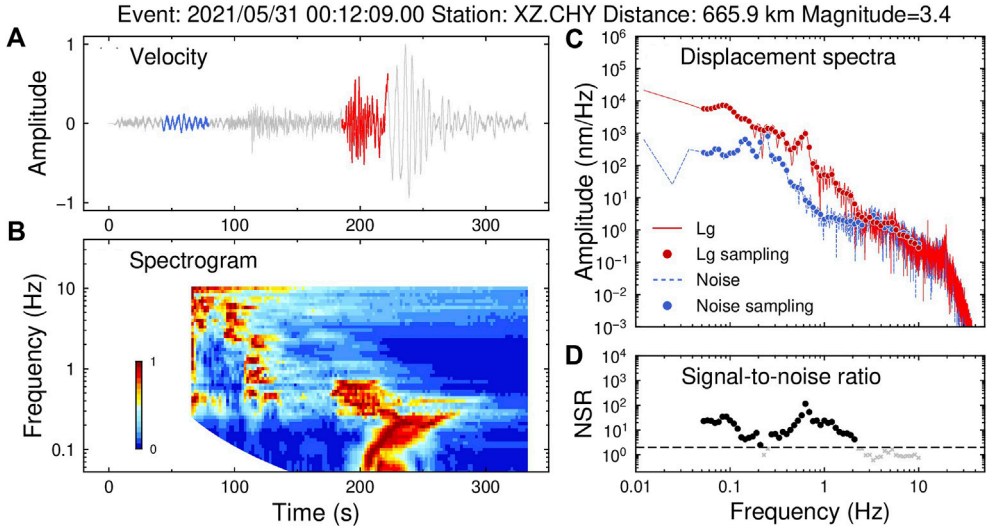

FIGURE 3
(A) Sample seismogram of the Yangbi aftershock recorded at station XZ. CHY. The Lg waveform and pre-event noise are highlighted in red and blue, respectively. **(B)** Time-frequency spectrogram of the sample seismograms. **(C)** Spectra of Lg and pre-event noise. **(D)** Signal-to-noise ratio. The SNR threshold of 2.0 is adopted and illustrated by a dashed line. Data points with SNRs lower than 2.0 are discarded and represented by gray crosses.

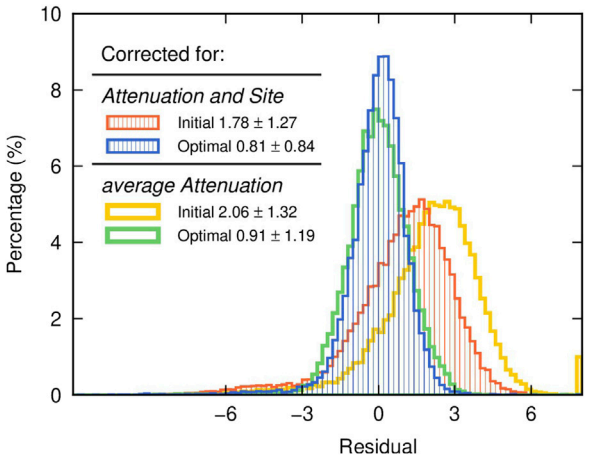

FIGURE 4
Histogram comparing the amplitude residuals. Red and blue histograms represent the distributions of residuals between the observed and predicted Lg spectra before and after inversion based on both attenuation and site corrections. Yellow and green histograms represent the distributions of residuals between the observed and predicted Lg spectra before and after inversion based on constant attenuation. The initial and final rms residual and deviation are labeled for both inversion schemes.

and Lg waveforms were cut using the velocity window of 3.6–3.0 km/s (Figure 3B). The window can be slightly adjusted to capture the maximum Lg energy. The waveforms immediately before the first p arrivals were defined as noise (Figure 3B). Then, the spectra of Lg and corresponding noise were calculated by applying a cosine taper and fast Fourier transformation and were sampled at 58 frequency points between 0.05 and 10.0 Hz to obtain the spectral amplitudes A_{obs} and A_{noise} of Lg and noise, respectively (Figure 3C). Next, the signal-to-noise ratio (SNR) was calculated by $A_{obs}(f)/A_{noise}(f)$ at each frequency point f. We set the SNR threshold of 2.0, in consideration of the trade-off between the quality and amount of available data, to select the data to be used (Figure 3D). The quality control resulted in, for example, 18,039, 18,070 and 10,179 valid Lg spectral measurements at 0.5, 1.0 and 2.0 Hz, respectively. Finally, by assuming that the noise is not correlated with the Lg wave, the true Lg spectral amplitudes were obtained by $\sqrt{A^2_{obs}(f) - A^2_{noise}(f)}$.

2.3 Lg spectra modeling and source spectra retrieval

According to Aki (1967), we modeled the Lg spectral amplitude $A(f,\Delta)$ as

$$A(f,\Delta) = S(f)G(\Delta)\Gamma(f,\Delta)P(f)R(f) \quad (1)$$

where Δ is the epicentral distance, S is the source spectrum, G is the geometrical spreading term, Γ is the attenuation term, P is the site response and R is the term containing modeling errors. The geometrical spreading term can be written as $(\Delta_0\Delta)^{-\frac{1}{2}}$, where Δ_0 is the reference distance to be fixed at 100 km (Street et al., 1975). The attenuation term has the form

$$\Gamma(f,\Delta) = \exp\left[\frac{-\pi f}{v}\int\frac{ds}{Q(x,y,f)}\right] \quad (2)$$

where the symbol $\int$ denotes the integral along the source-station ray path and Q can be obtained from the established high-resolution broadband Lg-wave Q models (Zhao et al., 2013a; Zhao et al., 2013b; He X. et al., 2021). To compute the attenuation term, we mapped the ray path onto the Q model and split it into N segments with a length of ds; then, Eq. 2 can be discretized and rewritten as summation

$$\Gamma(f,\Delta) = \exp\left[\frac{-\pi f}{v}\sum_{n=1}^{N}\frac{ds}{Q_n}\right] \quad (3)$$

where n denotes the n th segment of the ray, and Q_n is the average Q within this segment. It is frequency-dependent and can be obtained from the broadband Lg-wave attenuation model. In previous studies, the relative site response has been determined in conjunction with attenuation (He X. et al., 2021) and is available for 375 stations in this study. For the only station without an available site term, we assigned it with a unit amplification. The Q model and site response dataset used are illustrated in Supplementary Figures S1, S2.

With known geometrical spreading, attenuation, and site response, we linearized Eq. 1 to relate source perturbations with the residuals between the observed and predicted Lg spectra (Zhao et al. (2010). The least squares QR (LSQR) factorization algorithm (Paige and Saunders, 1982) was used to obtain the source perturbations by minimizing the L2 norm of the residual. The source terms, starting with the unit source function, were iteratively updated until convergence. Based on the attenuation, site response and restored source terms, the synthetic Lg spectral amplitudes fit well to the observations. For example, the mean absolute error between synthetic and observed Lg amplitudes at 1 Hz decreased from 1.78 to 0.81 and the deviation from 1.27 to 0.84 (red and blue histograms in Figure 4). We also tested a constant Q to restore the source terms (yellow and green histograms in Figure 4), and found that Lg spectra can also be fitted to a certain degree, but not as good as that based on both laterally-varying Q model and site response.

2.4 Source parameter estimation

After retrieving the source spectra $S(f)$ for each earthquake at 58 individual frequencies, we estimate the scalar seismic moment M_0 and the corner frequency f_c based on the source model

$$S(f) = \frac{M_0}{4\pi\rho v^3\left[1+\left(\frac{f}{f_c}\right)^{\gamma n}\right]^{1/\gamma}} \quad (4)$$

where n is the high-frequency falloff rate, γ controls the sharpness of the spectral corner, and ρ and v are the density and shear wave velocity in the source region, respectively. Typical values of $\rho = 2.7\ kg/m^3$ and $v = 3.5\ km/s$ were used. Generally, γ can be set to 1, although a larger value of $\gamma = 2$ was also used for some studies (Boatwright, 1980). Letting $\gamma = 1$ and $n = 2$ yields the commonly used Brune (1970) model. However, in this study, the high-frequency spectra often fall faster than 2. Therefore, we treated n as a variable to be estimated as well. By fitting the theoretical source model to the retrieved source spectrum using the annealing simulation algorithm (Kirkpatrick et al., 1983), M_0, f_c and n can be determined for each earthquake. The above results were also compared to those using other source models, including the Brune model ($\gamma = 1$; $n = 2$), the ω^{-3} model ($\gamma = 1$; $n = 3$) and the Boatwright model ($\gamma = 2$; n as variable) (refer to Supplementary Figure S3)

The ideal scenario is that the source spectrum has a flat low-frequency asymptote and a high-frequency descending portion, permitting to accurately estimate M_0 and f_c. In practice, our analysis showed that for small earthquakes, the Lg source spectra at frequencies lower than ~0.2 Hz were sometimes raised, possibly by ambient noise or surface waves generated by preceding earthquakes. Although not apparent for larger earthquakes because their source spectra were significantly higher than the noise level, the contaminated step-like spectrum would possibly result in an underestimated corner frequency and overestimated seismic moment for small earthquakes, introducing large errors into the following analysis. To suppress these effects and improve the reliability of parameter estimation, we set the fitting band truncations for small earthquakes and then screened problematic estimations based on comparisons of magnitude measurements. First, for $M \leq 3.5$ earthquakes, we fitted the retrieved source spectra within only 0.3–10.0 Hz because the observed noise level is high at approximately 0.2 Hz and the corner frequencies for earthquakes with magnitudes between 3.0 and 3.5 are generally higher than 0.3 Hz (e.g., Madariaga, 1976). The fitting band of 0.3–10.0 Hz could generally exclude the noise spectrum and retain the high-frequency portion of source spectra as much as possible to estimate the corner frequencies. Such a magnitude-dependent fitting band strategy was also used in previous source analysis studies (Abercrombie, 1995; Allmann and Shearer, 2007; Allmann and Shearer, 2009). Although effective in finding M_0 and f_c for small earthquakes, such rough truncation would sometimes omit all of the flat portion, leading to a problematic estimation. Therefore, next, we screened these problematic results based on the obtained seismic moment M_0. The moment magnitude M_W can be calculated from M_0 using the China Earthquake Administration scaling relationship $M_W = \frac{2}{3}(\log M_0 - 9.1)$ (M_0 is in the unit of N m). Magnitude scaling analysis based on earthquakes in Switzerland demonstrated that the difference between M_W and the local magnitude M_L, $M_W - M_L$ generally ranged from −1.0 to 0.5 (Goertz-Allmann et al., 2011). Considering the geological settings and algorithm used to calculate M_0, we set a broader threshold and discard earthquakes with $|M_L - M_W| > 1.0$ (Figure 5). In total, 17 earthquakes were discarded due to

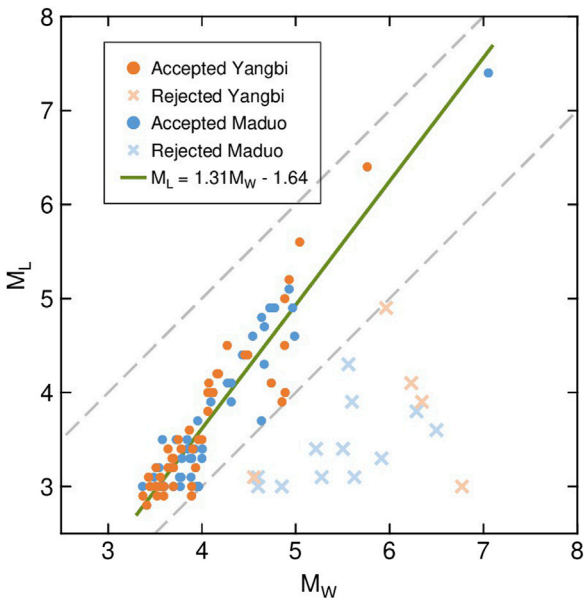

FIGURE 5
Comparison between the retrieved moment magnitude and catalog magnitude. Two gray dashed lines represent $M_L - M_W = \pm 1.0$, which are used to screen the retrieved source spectra with unusually large uncertainties (Goertz-Allmann et al., 2011).

abnormally high M_0 values. The remaining earthquakes yielded a linear relationship $M_L = 1.31(\pm 0.02)M_W - 1.64(\pm 0.12)$. The slope was in agreement with previous studies (e.g., Bethmann et al., 2011), whereas slight differences could result from geological settings, algorithms to calculate the M_W or the uncertainty in the catalog magnitude.

Based on a circular fault model (Eshelby, 1957), the stress drop can be calculated using

$$\Delta\sigma = \frac{7M_0}{16}\left(\frac{f_c}{kv}\right)^3 \quad (5)$$

where the constant k is 0.21 by assuming a rupture velocity of 0.9 shear wave velocity (Madariaga, 1976). The constant k was also suggested to be 0.29 and 0.37, depending on specific source model used (Brune, 1970; Sato and Hirasawa, 1973). We also tested the effects of using different k values, and found that the absolute stress drop values may vary with k, but their relative relationships are kept unchanged among events (Supplementary Figure S4). For simplicity, stress drops for all events were calculated based on same assumptions, including using the circular fault model, although it may be improper for large earthquakes with excessive long ruptures. Therefore, the mainshock stress drops will not be compared with aftershock stress drops.

2.5 Earthquake relocation

To refine the spatial distribution of the stress drop, we relocated the 2021 Yangbi and Maduo earthquake sequences for all earthquakes with local magnitudes greater than 3.0 using the HypoDD program, which allows for simultaneous accurate relocation of clusters of earthquakes based on double-difference travel times (Waldhauser and Ellsworth, 2000). Earthquake relocation and stress drop calculation based on consistent catalog avoid possible errors of assigning the calculated stress drops to incorrect events. We first visually inspected first P-wave arrivals automatically picked by the deep-learning-based PickNet program (Left panels in Figure 6) (Wang et al., 2019). This program can offer better picks at regional distances and was previously trained by the travel-time dataset from earthquakes in the Myanmar region (Wang et al., 2019). Then, we further processed the picked arrival times to calculate the double-difference first-P travel times of earthquake pairs at their common stations and only those pairs observed by more than eight stations were used. For the Yangbi earthquake sequence, a total of 1,493 first arrival P-wave travel times with epicentral distances less than 5° generated 20,124 P-phase pairs. The earthquake pairs had a separation of less than 10 km. For the Maduo earthquake sequence, a total of 2,594 first arrival P-wave travel times at 214 stations were used to generate 3,872 P-phase pairs. When processing the Maduo earthquake sequence, the performance of PickNet significantly reduced the amount of available data, and therefore, we allowed larger observation distances of 10°. Due to its ~150-km-long aftershock zone, we also allowed a larger spatial separation of 20 km within each earthquake pair so to include as many earthquakes as possible into the relocation clusters. The station distributions have relatively good azimuthal coverage for both earthquake sequences (Supplementary Figure S5). Proper parameters were chosen through several trials to control the initial conditions, clustering of earthquakes and data weighting in the HypoDD program. During relocation, local 1D crustal structures for the source regions of Yangbi and Maduo sequences were extracted from the USTClitho1.0 model (Right panels in Figure 6) (Xin et al., 2018). The relocation results were obtained using the LSQR factorization algorithm (LSQR, Paige and Saunders, 1982) with eight iterations. For convergence purpose, in each iteration, the data outside of 3 times the standard deviation of the RMS residual were treated as outliers and dropped. The iterations updated epicenter locations. Meanwhile, the rms travel time residuals were reduced from 0.49 s to 0.28 s and from 0.67 s to 0.25 s for Yangbi and Maduo sequences, respectively (Supplementary Figure S6). To assess relocation errors, we relocated the events for 100 times, in each time, with only 80% randomly-selected double-different travel times being used. For the Yangbi sequence, the mean errors were 245, 200 and 558 m in the east-west, north-south and vertical directions, respectively (Supplementary Figure S7). For the Maduo sequence, the mean errors were 812, 667 and 1,053 m in the east-west, north-south and vertical directions, respectively (Supplementary Figure S8). The errors were comparable to those of previous studies (Long et al., 2021; Xu et al., 2021; Zhang J. Y. et al., 2022; Zhu et al., 2022). The accuracy and reliability of earthquake relocation could be further improved by incorporating the cross-correlation double-different travel times, which is, however, out of the scope of this study.

3 Results

In this study, we retrieved the source spectra for earthquakes with local magnitudes greater than 3.0 for both the Yangbi and Maduo earthquake sequences and estimated the seismic moment, corner frequency and high-frequency falloff rate for the 81 earthquakes with reliable Lg-wave source spectra (Figure 7; Supplementary Table S1). The obtained seismic moment ranged from 1.42×10^{14} to 4.76×10^{19} N · m, corresponding to the moment magnitude M_W between 3.4 and 7.1. The corner frequency ranged from 0.08 to 1.61 Hz, within the band limitation of 0.05–10.0 Hz in this study. The corner frequencies obtained in this study from Lg waves are generally consistent with previous studies using body waves, although there appears slight systematic difference (Supplementary Figure S9). The high-frequency falloff rate was between 2.1 and 3.6, with a mean value of 2.8, which was a value higher than 2.0 for the ω^{-2} model (Brune, 1970), demonstrating the necessity of setting this parameter as a variable. The stress drop was calculated for each earthquake through the seismic moment and corner frequency. Large variability in the stress drop is observed, with the value ranging from 0.08 to 22.59 MPa and a logarithmic standard deviation of 0.48 for Yangbi sequence, and with the value ranging from 0.05 to 28.31 MPa and a logarithmic standard deviation of 0.54 for Maduo sequence. The logarithmic standard deviation was used to quantify the variability of the stress drop, and recent studies found values generally between ~0.35 and 0.45 (e.g., Trugman, 2020). The notably higher values obtained in this study indicate large variations in stress that may happen over short distances and thus could be related to the very complicated tectonics in both areas. To estimate the reliability of the result, the bootstrap method was used to assess the obtained Lg source spectra parameters (Efron, 1983). We repeat the Lg source calculation for 50 times, with each time involving randomly-sampled 80% of the observed displacement spectra (Figure 7). The seismic moment, corner frequency, high-frequency falloff rate and stress drop are calculated for each time, and we estimate errors in these parameters based on their standard deviations. The stress drop calculation is sensitive to the

10.3389/feart.2023.1081605

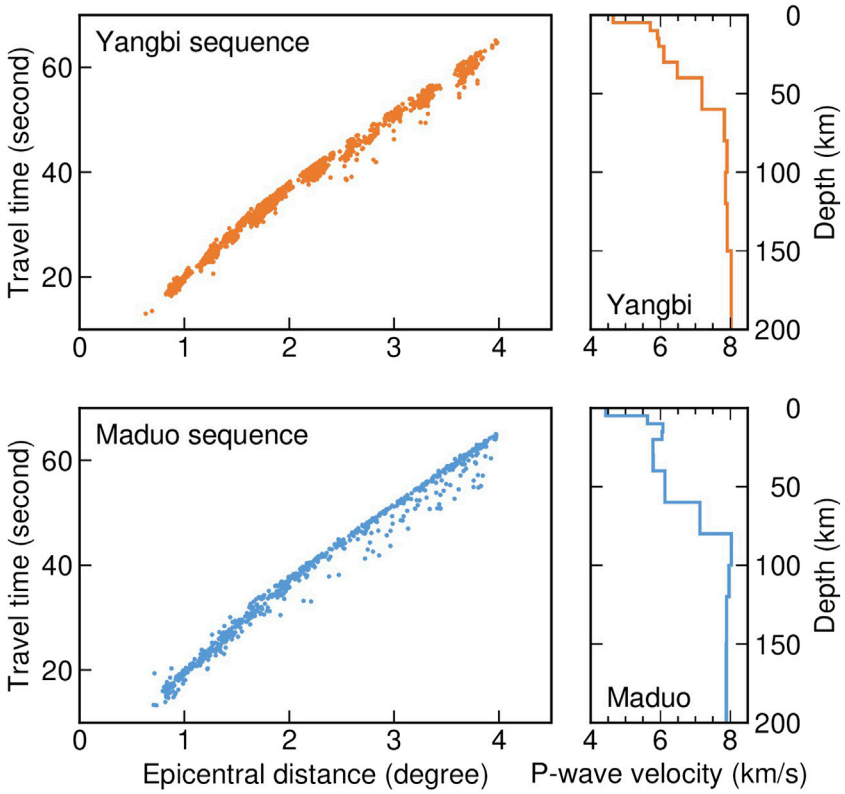

FIGURE 6
Left, travel times picked using the PickNet, and right, the USTClitho1.0 1D velocity models used in relocation calculations. The upper and lower panels are for Yangbi and Maduo sequences, respectively.

methods and source models (e.g., Shearer et al., 2006), and therefore, we mainly focus on relative variations within the May 2021 Yangbi and Maduo earthquake sequences. The logarithmic scale was used for the time axes to better demonstrate the temporal variations in stress drops for the early aftershocks. We also plotted trendlines to show the general temporal variations in stress drops (Figure 8). The trendlines were obtained by first resampling the time series of the stress drop with nearest point interpolation and an increment of 0.1 log(T) and then filtering using a low-pass Gaussian filter with a width of 0.5 log(T), where T denotes the time in days before or after the mainshock. The spatial distributions of the stress drop were investigated for both the Yangbi and Maduo earthquake sequences based on the epicenters relocated using the *HypoDD* program (Figures 9, 10). We also investigated the relationship between the stress drop and focal depth, and found no significant correlation, with correlation coefficients of 0.08 and 0.33 for Yangbi and Maduo sequences, respectively (Supplementary Figure S10).

3.1 Stress drops for the Yangbi and Maduo earthquake sequences

The stress drop of the Yangbi mainshock is 22.59 ± 4.85 MPa. For the foreshocks, the stress drops range from 0.44 to 11.56 MPa, with a median value of 0.59 MPa, and for aftershocks ranged from 0.08 to 5.55 MPa, with a median value of 0.75 MPa (Figures 8A,B). The foreshocks emerged on 18 May, with their stress drops exhibiting a general decrease from the initial value, until foreshocks became active again on 19 May. After that, a gradual increase in stress drop was visible, followed by two earthquakes, including the largest Ms 5.6 one, characterized by a significantly higher stress drops of ~10 MPa occurring ~25–27 min before the mainshock. In the aftershock sequence, the stress drops were relatively fluctuated and decreased gradually along with the decrease of seismicity. The minimum stress drop appeared ~26 min after the mainshock, indicating of a great amount of stress was released by the mainshock. The stress drop was again increased along with several strong aftershocks, including the largest Ms 5.2 aftershock occurring ~43 min after the mainshock, with the highest stress drop among all aftershocks. After strong fluctuation lasting for approximately 1 day, the stress drop values remained around the median value, which could indicate the stress adjustment following the mainshock.

For the Maduo earthquake sequence, the stress drop of the mainshock is 28.31 ± 3.92 MPa, and the stress drops of aftershocks range from 0.05 to 3.21 MPa, with a median value of 0.51 MPa (Figure 8C). The values of the stress drop for the Maduo aftershock sequence are generally lower than those for the Yangbi sequence in terms of their maximum, minimum and median values, suggesting a possibly lower stress level on the Maduo seismogenic fault after the mainshock. The Maduo aftershock sequence is characterized by more scattered stress drop values undulated for ~9 days after the mainshock. For example, several large aftershocks occurred ~8 h

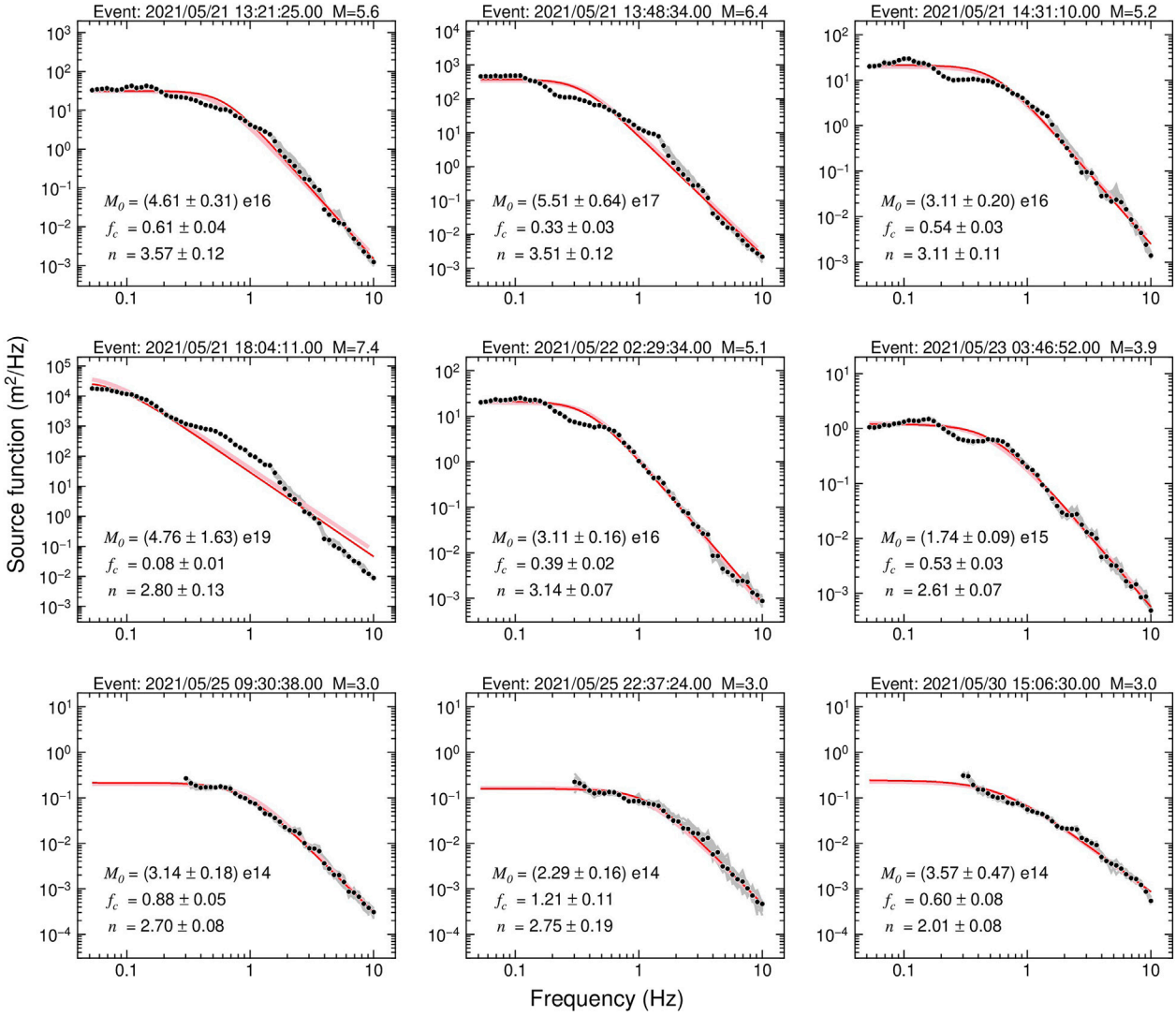

FIGURE 7
Illustrations of retrieved source spectra (black circles) and estimated source models (red lines). For earthquakes with magnitudes less than 3.5, the source models fit only the spectra above 0.3 Hz. Gray and pink lines represent the source spectra obtained using 80% randomly sampled data and corresponding source models, respectively. In each panel, the earthquake information, scalar seismic moment, corner frequency, and high-frequency falloff rate are labeled.

and ~8 days after the mainshock, with their stress drops greater than 1.5 MPa. Compared with the Yangbi sequence, the prolonged undulation in the stress drop and late occurrence of the minimum value nearly 3 days after the mainshock probably indicate a relatively long stress repartition process, which could be related to the longer seismogenic fault involved in the Maduo sequence.

3.2 Relocations of the Yangbi and Maduo earthquake sequences with stress drop estimated

Based on the first *P* arrivals picked by the *PickNet* program, we used the double-difference earthquake relocation program *HypoDD* to refine the locations of the calculated stress drop. The results were generally consistent to previous studies (e.g., Long et al., 2021; Xu et al., 2021; Zhang et al., 2021; Zhang J. Y. et al., 2022). For the May 2021 Yangbi earthquake sequence, we relocated 51 epicenters (Figure 9; Supplementary Table S1). The Yangbi earthquake sequence was generally distributed along a northwest–southeast trend and extended for approximately 21 km. Although roughly parallel to regional tectonics, e.g., the northwest–southeast-trending Red River fault and Jinshajiang fault, the distribution of the Yangbi earthquake sequence appeared not directly linked to any known faults, including the Weishan–Qiaohou fault ~10 km to the northeast. The foreshock activities migrated back and forth within the epicentral area, including the largest M5.6 foreshock near the center and the M4.5 foreshock near the southeastern end occurring ~2 min later. The Yangbi mainshock was located at 99.8635°E and 25.7039°N, with a depth of 9.090 km at the northwestern end of the epicentral area, suggesting a unilateral rupture toward the southeast. For the aftershocks, their epicenters extended further southeast and gradually scattered to a wider area, possibly indicating secondary structures with variable orientations. An M4.1 event was located

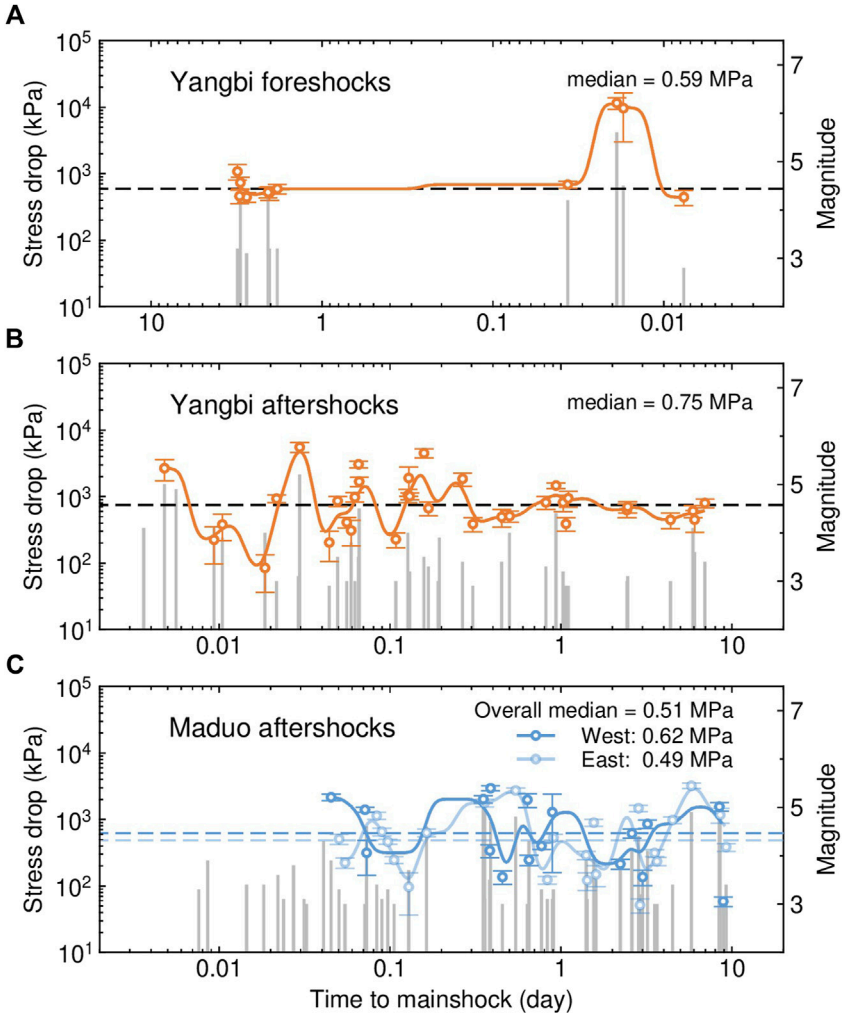

FIGURE 8
Temporal variations in the stress drop for the **(A)** Yangbi foreshock sequence, **(B)** Yangbi aftershock sequence and **(C)** Maduo aftershock sequence. The stress drop estimates are represented by open circles. Solid trendlines are obtained by applying a low-pass Gaussian filter. The seismicity of earthquakes with magnitudes greater than 3.0 is shown by vertical gray lines, with their heights corresponding to magnitudes. Error bars indicate the standard deviations of stress drops measurements, with their stress drop values indicated by dashed lines. Aftershocks in Maduo sequence are grouped according to their locations east (light blue) or west (blue) to the mainshock.

notably off the primary aftershock trend to the northeast, which may indicate a cluster of earthquakes on an activated secondary fault (Zhang et al., 2021). The sources of the Yangbi earthquake sequence were mostly located in the upper crust at approximately 10 km depths.

By relocation, we obtained the fine distribution of the stress drop. The highest stress drop in the foreshock sequence was observed for a M5.6 event located near the center of the foreshock zone, where foreshock activities had been initiated since 18 May. Another significantly high stress drop was linked to the M4.5 foreshock, occurred at the southeast end of the foreshock area. The mainshock and the largest aftershock were located at the northwestern and southeastern ends of the epicentral zone, respectively, both with notably high stress drops.

We relocated 54 earthquakes in the Maduo sequence (Figure 10; Supplementary Table S1). The results demonstrate that the mainshock was located at 98.3641°E and 34.6656°N, with a depth of 21.909 km. The epicenter of the mainshock was ~5 km northeast to the mapped trace of the Kunlunshankou–Jiangcuo fault (KJF). The aftershocks were nearly linearly distributed on both sides of the mainshock, extending approximately 170 km along a northwest–west trends and generally consisting with the KJF. Gaps with absent or sparse aftershocks are visible, for example, at sections ~40–60 km (gap 1), ~15–20 km northwest (gap 2), and ~30–50 km southeast (gap 3) of the mainshock (Figure 10B). The aftershock zone intersected with the Maduo–Gande fault (MGF) near its southeast end, with the strike turning from northwest–west to west–east. The relocated focal depths in the Maduo sequence mainly ranged between ~5–15 km, which were generally deeper than those in the Yangbi sequence and appeared more scattered. Except for the mainshock, which has the highest stress drop, other events with significantly high stress drops (e.g., >103.5 kPa) in the Maduo sequence can be generally associated with the aftershock gaps, especially the cluster ~30 km northwest of the mainshock (gap 1). The cluster of high stress drops

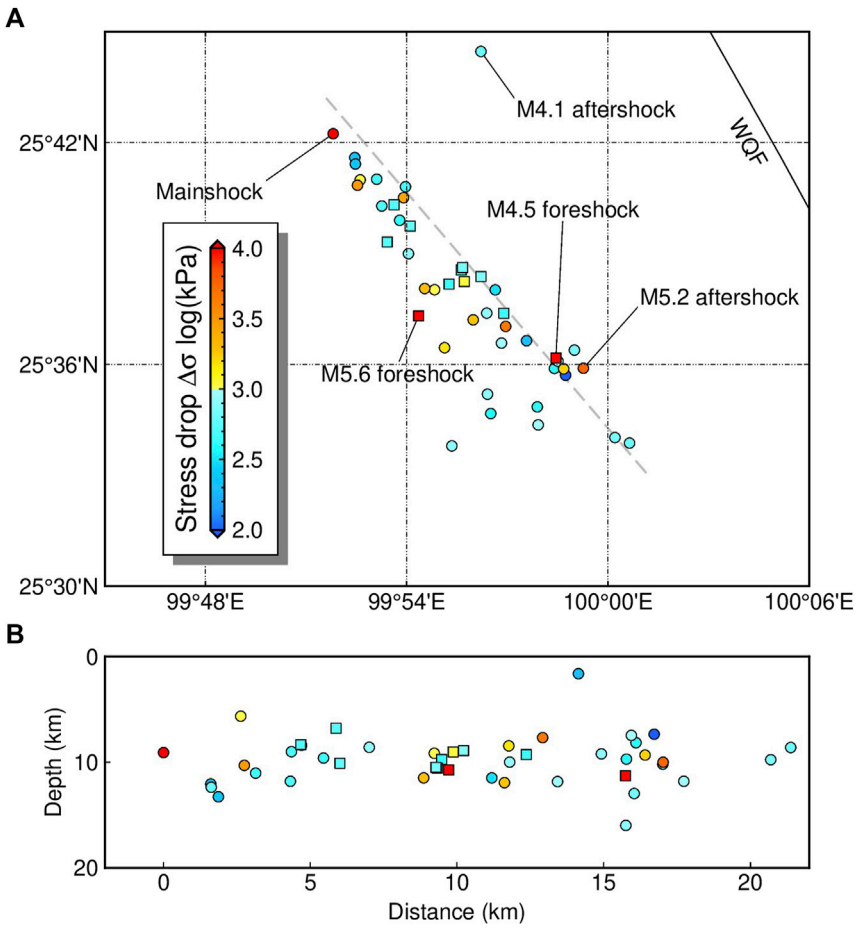

FIGURE 9
(A) Map view and **(B)** depth cross-section of stress drops for the 21 May 2021 Yangbi earthquake sequence. The filled symbols illustrate the relocated sources, with their stress drops coded by colors. The squares represent the foreshocks, and the circles represent the mainshock and aftershocks. The Weixi–Qiaohou fault (WQF) is represented by a black lines. The mainshock is located at distance=0 in the depth cross-section. Gray dashed line shows the location of the cross-section.

~60 km southeast of the mainshock may also be related to the intersection with the MGF.

4 Discussion

4.1 Earthquake stress drop and stress distributions on faults

The earthquake stress drop can be related to the localized stress variability on a seismogenic fault. Larger stress drop variations could result from fault plane heterogeneities (Kirkpatrick et al., 2020), e.g., a rougher fault plane may cause higher stress drops due to its additional resistance to slip (Fang and Dunham, 2013). Allmann and Shearer (2009) observed higher overall stress drops for strike-slip earthquakes at a global scale, which is consistent with previous findings of increased apparent stress for strike-slip events. However, at local scales, the dependence on the focal mechanism is less significant, and stress drops appear more dominated by the local tectonics (Shearer et al., 2006; Goebel et al., 2015; Boyd et al., 2017). Therefore, investigating stress drops in the Yangbi and Maduo earthquake sequences may reveal stress variations in the related seismogenic zones.

In the Yangbi sequence, the stress drops of foreshocks may suggest the accumulation of stress and hint the stress variation that led to the nucleation of the mainshock. The pre-slip mechanism is one of the popular explanations for how an earthquake initiates, in which concentrated and repeated seismicity is expected (Zhu et al., 2022). However, the relocated foreshock sequence revealed a back-and-forth migration pattern. In addition, high-stress-drop foreshocks, including the first and the largest ones, have their stress drops significantly higher than the median value of the entire sequence, implying the potential to trigger earthquake. By modeling the cumulative static stress change from large foreshocks, Zhu et al. (2022) found that the local shear stress at the Yangbi mainshock epicenter was increased by major foreshocks. Therefore, our results of foreshock relocation and stress drops were consistent with the cascade triggering process during the nucleation of the Yangbi mainshock (Long et al., 2021; Zhang et al., 2021; Zhu et al., 2022). For the aftershock sequence, fluctuations of stress drops including many significantly high and low stress drop events may be related to the stress adjustment and continually release of the local stress field disturbed by the mainshock. Similar stress

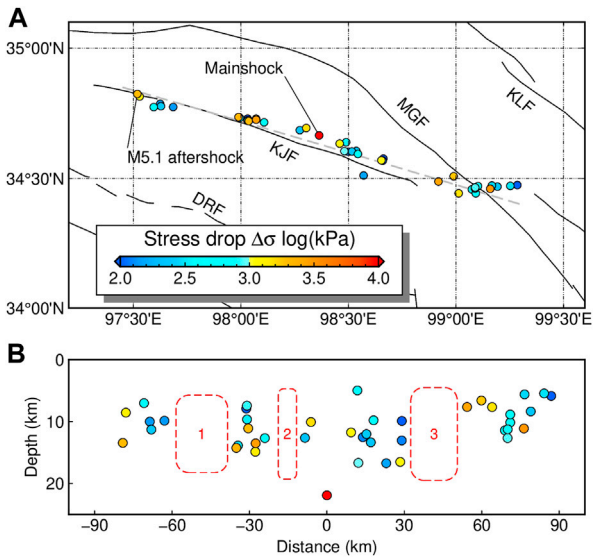

FIGURE 10
(A) Map view and **(B)** depth cross-section of the stress drops for the 21 May 2021 Maduo earthquake sequence. The filled circles illustrate the relocated epicenters, with their stress drops coded by colors. The active faults are indicated by black lines, with their names labeled in abbreviations: DRF, Dari fault; KJF, Kunlunshankou–Jiangcuo fault; MGF, Maduo–Gande fault; and KLF, Eastern Kunlun fault. The mainshock is located at distance=0 in the depth cross-section. Gray dashed line shows the location of the cross-section. Three aftershock gaps are marked in the depth profile with red dashed rectangles.

development pattern were also suggested by the observed b-values, which demonstrated long-term low values before 20 May 2021, showed abrupt reductions before the Ms 5.6 foreshock and the Ms 6.4 mainshock, then demonstrated large fluctuations around their mean value after the mainshock (Duan et al., 2021; Jiang et al., 2021). The b-value measures the distribution of earthquakes with different sizes in the recurrence relation of Gutenberg and Richter (1941) and is found to be reversely related to the differential stress within the crust (Schorlemmer et al., 2005). A low b-value and high stress were also observed preceding the M6.4 and M7.1 Ridgecrest, California earthquakes in 2019 (Nanjo, 2020).

In the Maduo sequence, the aftershocks were distributed on both the northwest and southeast sides of the mainshock along the Kunlunshankou–Jiangcuo fault. For aftershocks to the east and west of the mainshock, our results showed their median stress drops were 0.49 MPa and 0.62 MPa, respectively. The difference probably suggested differentiated rupture processes between the east- and west-sections. Previous studies have suggested that the eastward rupture of the Maduo mainshock propagated at a speed exceeding 3.5 km/s S-wave velocity, i.e., supershear rupture (Zhang X. et al., 2022; Li et al., 2022; Lyu et al., 2022; Yue et al., 2022). The back-projection imaging technique is commonly used to obtain large earthquake rupture kinematics. With this method, the Maduo mainshock was found ruptured toward the east and west, with velocities of 3–5 km/s and 2–3 km/s, respectively (Zhang X. et al., 2022; Li et al., 2022; Yue et al., 2022). Zhang X. et al. (2022) further confirmed the eastward supershear rupture by recognizing far-field Love Mach waves. Joint analysis using Global Positioning System, Interferometric Synthetic Aperture Radar, and teleseismic data determined the westward and eastward rupture velocities to be 2.0 and 4.6 km/s, respectively (Yue et al., 2022). Near-field Global Navigation Satellite Systems recordings demonstrated significant sensitivity to determine rupture velocities and confirmed sub- and supershear ruptures on the west and east sections of the mainshock fracture, respectively (Lyu et al., 2022). We suggest that the lower aftershock stress drops on the east section can be related to the larger stress release due to the supershear rupture. Yue et al. (2022) pointed out that the coseismic slip east of the mainshock was concentrated in seismogenic layers, in which rate-weakening friction law might support instability failure to facilitate the supershear rupture. Since a large amount of energy was consumed to feed the supershear rupture, the remaining stress was low, resulting in low stress drops for the aftershocks to the east of the mainshock. The relatively high aftershock stress drops observed on the west section of the mainshock fracture suggest there were more strain stored within this part of the crust. This energy can be further released by later aftershocks or interseismic creeping.

4.2 Earthquake stress drop and fault complexity

In this study, stress drops from the relocated earthquake sequences demonstrated that high stress drops were often related to fault junctions or earthquake gaps, suggesting stress concentrations at these locations.

The relocated sources of the Yangbi sequence suggested a complicated fault system with a northwest–southeast-trending major fault, which may split into multiple branches in the southeast section. This is consistent with previous earthquake relocations; however, a detailed fault structure can be suggested by relocation for a larger number of small earthquakes. Long et al. (2021) relocated more than 1,000 Yangbi events with local magnitudes greater than 1.0 based on the seismic phase bulletin, suggesting a northwest–

southeast-trending primary fault, with northeast–southwest-trending conjugate faults in its northwestern segment, and multiple secondary faults along the primary fault and gradual turning toward the south in the southeast. The multiscale en echelon structures were further revealed by high-resolution catalogs built using a deep-learning phase picker (Su et al., 2021; Liu et al., 2022). Combining the fault structures with our relocation results, high-stress-drop events in the Yangbi sequence were generally related to fault junctions and tips. For example, the M4.5 and M5.6 foreshocks with significantly high stress drops were located around the middle of the epicentral zone, where the south-trending en echelon faults intersect with the primary fault; several aftershocks with high stress drops could be found near fault junctions and tips, including the M5.2 and M4.1 aftershocks. Simulations suggested significantly increased stress localized at the junctions of branching faults (e.g., Ando et al., 2018). Therefore, the high stress drops in the Yangbi sequence may result from the stress concentrations near the fault junctions and tips and may in turn indicate the precise locations of sophisticated fault branches.

In the Maduo sequence, the stress drops demonstrated a more fluctuating pattern than in the Yangbi sequence. The prolonged stress drop variations could be related to the fault properties. The cross-section view reveals that the clusters of earthquakes with significantly high-stress-drop values were generally associated with the earthquake gaps along the fault. These gaps should be robust features despite a magnitude threshold 3.0 was used for earthquake relocation in this study. In previous studies that relocated more than 1,300 earthquakes with magnitudes greater than 0, reduced seismicity was still pronounced at these locations, and in particular, few aftershocks occurred ~50 km northwest and ~30 km southeast of the mainshock (Wang W. L. et al., 2021; Xu et al., 2021) (corresponding to the gaps 1 and 3 in Figure 10B). The correspondence between high stress drops and aftershock gaps probably indicated redistributed stress following the mainshock. Geodetic observations revealed coseismic slip on the seismogenic fault following the mainshock. They varied significantly along the fault strike and concentrated at several localized segments with maximum slips of ~3–4 m (He K. et al., 2021). These high-slip patches may represent the asperities where stresses were released by significant rupture during the mainshock, resulting in localized reduced or lack of aftershock activities. Since the asperities are generally related to variations in strength or friction properties due to the changes of fault geometry, and result in stress concentration (Mildon et al., 2019), we propose that the stress remaining on the fault was redistributed and concentrated near the edges of fault asperities, thus leading to the occurrence of larger aftershocks with high stress drops. A similar complementary correspondence between the stress drop and mainshock slip was also suggested for the 1992 Landers earthquake in southern California (Shearer et al., 2006).

4.3 Implications for the eastward expansion of the Tibetan plateau

The stress drops of the Yangbi, Yunnan and Maduo, Qinghai earthquake sequences in May 2021 demonstrated different temporal and spatial patterns, which reflected varying localized crustal stress variability and deformations across the eastern Tibetan Plateau. A deformation field recently constructed from GPS data revealed predominantly continuous strains inside the eastern Tibetan Plateau, with significant shear associated with large strike-slip faults to accommodate the eastward extrusion of geological blocks (Wang and Shen, 2020). On the southern flank of the extrusion, the Chuandian block represents the majority of the escaping crustal material from the interior plateau. Wang and Shen (2020) found that the translation of the Chuandian block was accompanied by notable clockwise rotation at a rate of ~2.9°/Myr around the Eastern Himalayan syntax and widespread dilatation at 10–20 nanostrain/yr. The dilatation should be responsible for the normal component obtained in the focal mechanism solutions of the Yangbi earthquake sequence. The complicated combination of southeastward translation, clockwise rotation and interior deformations requires a large number of active faults to accommodate, possibly resulting in the multiscale en echelon faults and conjugate faults that inherited motions of the associated large strike-slip faults. Therefore, these small faults could also generate large earthquakes, including the 2021 Yangbi Ms 6.4 earthquake, with the repartitioned stress concentration subject to the geometric complexity of the fault systems, for example, the fault junctions and tips, giving rise to several high stress drops in the Yangbi earthquake sequence. The local stress field inverted from focal mechanisms suggested a change in the orientation of the horizontal maximum principal stress from near north–south to nearly east–west in the southernmost epicentral zone, coincident with the regional stress and possibly reflecting the tectonic rotation of the Chuandian block (Wang Y. et al., 2021).

In contrast, the focal mechanism of the Maduo earthquake sequence demonstrated a consistent northwest–southeast orientation of maximum principal stress, corresponding to the movement of the Bayan Har block (Xu et al., 2021). The Bayan Har block is bounded in the north by the Kunlun fault, with significant left-lateral strike-slip, to accommodate the northeastward expansion of the eastern Tibetan Plateau. The slip rate on the Kunlun fault shows a west–east decrease from ~12.5 mm/yr to less than 3 mm/yr, which was suggested to be decomposed to slips on several secondary faults subparallel to and south of the Kunlun fault (Kirby et al., 2007), including the Kunlunshankou–Jiangcuo fault, which was the seismogenic fault of the 2021 Maduo earthquake sequence. The slip around the middle segment of the Kunlun fault, which is faster than that near the northern segment of the Red River fault, is more likely to result in a concentration of shear strain (Zheng et al., 2017; Wang and Shen, 2020). Localized variations in crustal strength could occur due to shear heating and increased crustal temperature (Leloup et al., 1999; Bao et al., 2012). As a consequence, large earthquakes would rupture the high-strength asperities, and the perturbed stresses were likely to be repartitioned around the asperities and lead to larger variability in the stress drops of aftershocks. Therefore, the stress drops of the Yangbi and Maduo earthquake sequences were controlled by the eastward expansion of the Tibetan Plateau, and the differences in their patterns showed varying impacts on the seismogenic environment.

Conclusion

In this study, the temporal and spatial variations in stress drop were investigated for Yangbi and Maduo earthquake sequences in May 2021, including all foreshocks, mainshocks and aftershocks with magnitudes greater than 3.0. The results reveal that the stress drop for Yangbi mainshock was relatively low than Maduo mainshock. Comparing with the Yangbi sequence, the Maduo sequence was characterized by stress drops of relatively low median value and rather scattered values for individual events. For stress drops in both sequences, no apparent depth

dependency was found. The temporal-spatial pattern in stress drop for Yangbi sequence can be related to geometric complexity of the fault systems, which were resulted from the tectonic movement of the Chuandian block incorporating translation, rotation, and interior deformation. The Bayan Har block is regarded as another component in the eastward expansion of the Tibetan Plateau. Fast slip and high shear strain rate around its northern boundary may cause localized variations in fault strength, which controls the temporal-spatial pattern in the stress drop of Maduo sequence.

Data availability statement

Publicly available datasets were analyzed in this study. This data can be found here: https://data.earthquake.cn/yhsj/info/2016/5596.html.

Author contributions

XH: Conceptualization, formal analysis, writing—original draft, writing—review and editing, funding acquisition. L-FZ: Conceptualization, methodology, formal analysis, writing—review and editing, funding acquisition. LZ: Formal analysis. X-BX: Writing—review and editing. Z-XY: Funding acquisition, supervision.

Funding

This research was supported by the National Natural Science Foundation of China (U2139206, 42104055, 41974054, and 41974061) and the Special Fund of China Seismic Experimental Site (2019CSES0103).

Acknowledgments

The waveforms used in this study were collected from the National Earthquake Data Center (NEDC) at https://data.earthquake.cn/yhsj/info/2016/5596.html (in Chinese, last accessed August 2022) and the Incorporated Research Institutions for Seismology Data Management Center (IRIS-DMC) at https://ds.iris.edu/wilber3/find_event (last accessed August 2022). Researchers can register for an account to apply for the NEDC data. Some figures were generated using Generic Mapping Tools (GMT; https://www.generic-mapping-tools.org/).

Conflict of interest

The authors declare that the research was conducted in the absence of any commercial or financial relationships that could be construed as a potential conflict of interest.

Publisher's note

All claims expressed in this article are solely those of the authors and do not necessarily represent those of their affiliated organizations, or those of the publisher, the editors and the reviewers. Any product that may be evaluated in this article, or claim that may be made by its manufacturer, is not guaranteed or endorsed by the publisher.

Supplementary material

The Supplementary Material for this article can be found online at: https://www.frontiersin.org/articles/10.3389/feart.2023.1081605/full#supplementary-material

References

Abercrombie, R. E. (1995). Earthquake source scaling relationships from −1 to 5$M_L$using seismograms recorded at 2.5-km depth. *J. Geophys Res.* 100 (B12), 24015–24036. doi:10.1029/95JB02397

Abercrombie, R. E. (2014). Stress drops of repeating earthquakes on the san andreas fault at parkfield. *Geophys Res. Lett.* 41, 8784–8791. doi:10.1002/2014GL062079

Aki, K. (1967). Scaling law of seismic spectrum. *J. Geophys Res.* 72 (4), 1217–1231. doi:10.1029/JZ072i004p01217

Allmann, B. P., and Shearer, P. M. (2009). Global variations of stress drop for moderate to large earthquakes. *J. Geophys Res.* 114 (B1). doi:10.1029/2008jb005821

Allmann, B. P., and Shearer, P. M. (2007). Spatial and temporal stress drop variations in small earthquakes near Parkfield, California. *J. Geophys Res.* 112 (B4). doi:10.1029/2006JB004395

Bao, X. Y., Sandvol, E., Chen, Y. S. J., Ni, J., Hearn, T., and Shen, Y. (2012). Azimuthal anisotropy of Lg attenuation in eastern Tibetan Plateau. *J. Geophys Res.* 117 (B10). doi:10.1029/2012jb009255

Bethmann, F., Deichmann, N., and Mai, P. M. (2011). Scaling relations of local magnitude versus moment magnitude for sequences of similar earthquakes in Switzerland. *Bull. Seismol. Soc. Am.* 101 (2), 515–534. doi:10.1785/0120100179

Blisniuk, P. M., Hacker, B. R., Glodny, J., Ratschbacher, L., Bi, S. W., Wu, Z. H., et al. (2001). Normal faulting in central Tibet since at least 13.5 Myr ago. *Nature* 412 (6847), 628–632. doi:10.1038/35088045

Boatwright, J. (1980). A spectral theory for circular seismic sources; simple estimates of source dimension, dynamic stress drop, and radiated seismic energy. *Bull. Seismol. Soc. Am.* 70 (1), 1.

Boyd, O. S., McNamara, D. E., Hartzell, S., and Choy, G. (2017). Influence of lithostatic stress on earthquake stress drops in North America. *Bull. Seismol. Soc. Am.* 107 (2), 856–868. doi:10.1785/0120160219

Brune, J. N. (1970). Tectonic stress and the spectra of seismic shear waves from earthquakes. *J. Geophys Res.* 75 (26), 4997–5009. doi:10.1029/JB075i026p04997

Duan, M., Zhao, C., Zhou, L., Zhao, C., and Zuo, K. (2021). Seismogenic structure of the 21 May 2021 M(s)6. 4 Yunnan Yangbi earthquake sequence. *Chin. J. Geophys (in Chin.* 64 (9), 3101–3115. doi:10.6038/cjg2021P0423

Efron, B. (1983). Estimating the error rate of a prediction rule: Improvement on cross-validation. *J. Am. Stat. Assoc.* 78 (382), 316–331. doi:10.1080/01621459.1983.10477973

Eshelby, J. D. (1957). The determination of the elastic field of an ellipsoidal inclusion, and related problems. *Proc. R. Soc. Lon Ser-A* 241 (1226), 376–396. doi:10.1098/rspa.1957.0133

Fang, Z., and Dunham, E. M. (2013). Additional shear resistance from fault roughness and stress levels on geometrically complex faults. *J. Geophys Res.* 118, 3642–3654. doi:10.1002/jgrb.50262

Fisk, M. D. (2006). Source spectral modeling of regional P/S discriminants at nuclear test sites in China and the former Soviet Union. *Bull. Seismol. Soc. Am.* 96 (6), 2348–2367. doi:10.1785/0120060023

Furumura, T., and Kennett, B. L. N. (1997). On the nature of regional seismic phases-II. On the influence of structural barriers. *Geophys J. Int.* 129 (2), 221–234. doi:10.1111/j.1365-246X.1997.tb01577.x

Goebel, T. H. W., Hauksson, E., Shearer, P. M., and Ampuero, J. P. (2015). Stress-drop heterogeneity within tectonically complex regions: A case study of san gorgonio pass, southern California. *Geophys J. Int.* 202 (1), 514–528. doi:10.1093/gji/ggv160

Goertz-Allmann, B. P., Edwards, B., Bethmann, F., Deichmann, N., Clinton, J., Fäh, D., et al. (2011). A new empirical magnitude scaling relation for Switzerland. *Bull. Seismol. Soc. Am.* 101 (6), 3088–3095. doi:10.1785/0120100291

Gutenberg, B., and Richter, C. F. (1941). Seismicity of the Earth seismicity of the Earth. *Geol. Soc. Am.* 34

He, K., Wen, Y., Xu, C., and Zhao, Y. (2021a). fault geometry and slip distribution of the 2021 Mw 7.4 Maduo, China, earthquake inferred from InSAR measurements and relocated aftershocks. *Seismol. Res. Lett.* 93, 8–20. doi:10.1785/0220210204

He, X., Zhao, L.-F., Xie, X.-B., Shen, L., Wang, W.-M., and Yao, Z.-X. (2020). Stress drop assessment of the August 8, 2017, Jiuzhaigou earthquake sequence and its tectonic implications. *Earthq. Sci.* 33 (4), 161–176. doi:10.29382/eqs-2020-0161-01

He, X., Zhao, L.-F., Xie, X.-B., Tian, X., and Yao, Z.-X. (2021b). Weak crust in southeast Tibetan Plateau revealed by Lg-wave attenuation tomography: Implications for crustal material escape. *J. Geophys Res.* 126, e2020JB020748. doi:10.1029/2020JB020748

Holt, W. E., Ni, J. F., Wallace, T. C., and Haines, A. J. (1991). The active tectonics of the eastern Himalayan syntaxis and surrounding regions. *J. Geophys Res.* 96 (B9), 14595–14632. doi:10.1029/91JB01021

Jiang, C., Jiang, C. S., Yin, F. L., Zhang, Y. B., Bi, J. M., Long, F., et al. (2021). A new method for calculating b-value of time sequence based on data-driven (TbDD): A case study of the 2021 Yangbi M(s)6. 4 earthquake sequence in yunnan. *Chin. J. Geophys (in Chin.* 64 (9), 3116–3124. doi:10.6038/cjg2021P0385

Kirby, E., Harkins, N., Wang, E., Shi, X., Fan, C., and Burbank, D. (2007). Slip rate gradients along the eastern Kunlun fault. *Tectonics* 26. No.2). doi:10.1029/2006tc002033

Kirkpatrick, J. D., Edwards, J. H., Verdecchia, A., Kluesner, J. W., Harrington, R. M., and Silver, E. A. (2020). Subduction megathrust heterogeneity characterized from 3D seismic data. *Nat. Geosci.* 13 (5), 369–374. doi:10.1038/s41561-020-0562-9

Kirkpatrick, S., Gelatt, C. D., Jr., and Vecchi, M. P. (1983). Optimization by simulated annealing. *Science* 220 (4598), 671–680. doi:10.1126/science.220.4598.671

Leloup, P. H., Ricard, Y., Battaglia, J., and Lacassin, R. (1999). Shear heating in continental strike-slip shear zones: Model and field examples. *Geophys J. Int.*, 136(1), 19–40. doi:10.1046/j.1365-246X.1999.00683.x

Li, Q., Wan, Y., Li, C., Tang, H., Tan, K., and Wang, D. (2022). Source process featuring asymmetric rupture velocities of the 2021 Mw 7.4 Maduo, China, earthquake from teleseismic and geodetic data. *Seismol. Res. Lett.* 93 (3), 1429–1439. doi:10.1785/0220210300

Liu, M., Li, H., Li, L., Zhang, M., and Wang, W. (2022). Multistage nucleation of the 2021 Yangbi MS 6.4 earthquake, Yunnan, China and its foreshocks. *J. Geophys Res.* 127 (5), e2022JB024091. doi:10.1029/2022JB024091

Long, F., Qi, Y., Yi, G., Wu, W., Wang, G., Zhao, X., et al. (2021). Relocation of the MS6.4 Yangbi earthquake sequence on May 21,2021 in Yunnan Province and its seismogenic structure analysis. *Chin. J. Geophys.* 64 (8), 2631–2646.

Lyu, M., Chen, K., Xue, C., Zang, N., Zhang, W., and Wei, G. (2022). Overall subshear but locally supershear rupture of the 2021 Mw 7.4 Maduo earthquake from high-rate GNSS waveforms and three-dimensional InSAR deformation. *Tectonophysics* 839, 229542. doi:10.1016/j.tecto.2022.229542

Madariaga, R. (1976). Dynamics of an expanding circular fault. *Bull. Seismol. Soc. Am.* 66 (3), 639–666. doi:10.1785/bssa0660030639

Mildon, Z. K., Roberts, G. P., Walker, J. P. F., and Toda, S. (2019). Coulomb pre-stress and fault bends are ignored yet vital factors for earthquake triggering and hazard. *Nat. Commun.* 10, 2744. doi:10.1038/s41467-019-10520-6

Molnar, P., and Lyoncaen, H. (1989). Fault plane solutions of earthquakes and active tectonics of the Tibetan Plateau and its margins. *Geophys J. Int.* 99 (1), 123–154. doi:10.1111/j.1365-246X.1989.tb02020.x

Nanjo, K. Z. (2020). Were changes in stress state responsible for the 2019 Ridgecrest, California, earthquakes? *Nat. Commun.* 11 (1), 3082. doi:10.1038/s41467-020-16867-5

Oth, A., Bindi, D., Parolai, S., and Di Giacomo, D. (2011). Spectral analysis of K-NET and KiK-net data in Japan, Part II: On attenuation characteristics, source spectra, and site response of borehole and surface stations. *Bull. Seismol. Soc. Am.* 101, 667–687. doi:10.1785/0120100135

Paige, C. C., and Saunders, M. A. (1982). Lsqr: An algorithm for sparse linear equations and sparse least squares. *ACM Trans. Math. Softw.* 8 (1), 43–71. doi:10.1145/355984.355989

Pasyanos, M. E., Matzel, E. M., Walter, W. R., and Rodgers, A. J. (2009). Broad-band Lg attenuation modelling in the Middle East. *Geophys J. Int.* 177 (3), 1166–1176. doi:10.1111/j.1365-246X.2009.04128.x

Sato, T., and Hirasawa, T. (1973). Body wave spectra from propagating shear cracks. *J. Phys. Earth* 21 (4), 415–431. doi:10.4294/jpe1952.21.415

Schorlemmer, D., Wiemer, S., and Wyss, M. (2005). Variations in earthquake-size distribution across different stress regimes. *Nature* 437 (7058), 539–542. doi:10.1038/nature04094

Shearer, P. M., Prieto, G. A., and Hauksson, E. (2006). Comprehensive analysis of earthquake source spectra in southern California. *J. Geophys Res.* 111 (B6). doi:10.1029/2005jb003979

Street, R. L., Herrmann, R. B., and Nuttli, O. W. (1975). Spectral characteristics of the Lg wave generated by central United States earthquakes. *Geophys J. Int.* 41 (1), 51–63. doi:10.1111/j.1365-246X.1975.tb05484.x

Su, J. B., Liu, M., Zhang, Y. P., Wang, W. T., Li, H. Y., Yang, J., et al. (2021). High resolution earthquake catalog building for the 21 May 2021 Yangbi, Yunnan, M-S 6. 4 earthquake sequence using deep-learning phase picker. *Chin. J. Geophys (in Chin.* 64 (8), 2647–2656. doi:10.6038/cjg2021O0530

Sun, J., Yue, H., Shen, Z.-K., Fang, L., Zhan, Y., and Sun, X. (2018). The 2017 jiuzhaigou earthquake: A complicated event occurred in a young fault system. *Geophys Res. Lett.* 45, 2230–2240. doi:10.1002/2017gl076421

Trugman, D. T. (2020). Stress drop and source scaling of the 2019 Ridgecrest, California, earthquake sequence. *Bull. Seismol. Soc. Am.* 110 (4), 1859–1871. doi:10.1785/0120200009

Waldhauser, F., and Ellsworth, W. L. (2000). A double-difference earthquake location algorithm: Method and application to the northern Hayward fault, California. *Bull. Seismol. Soc. Am.*, 90(6), 1353–1368. doi:10.1785/0120000006

Wang, J., Xiao, Z., Liu, C., Zhao, D., and Yao, Z. (2019). Deep learning for picking seismic arrival times. *J. Geophys Res.* 124 (7), 6612–6624. doi:10.1029/2019JB017536

Wang, M., and Shen, Z.-K. (2020). Present-day crustal deformation of continental China derived from GPS and its tectonic implications. *J. Geophys Res.* 125 (2), e2019JB018774. doi:10.1029/2019JB018774

Wang, W. L., Fang, L. H., Wu, J. P., Tu, H. W., Chen, L. Y., Lai, G. J., et al. (2021a). Aftershock sequence relocation of the 2021 M(S)7.4 Maduo earthquake, Qinghai, China. *Sci. China-Earth Sci.* 64 (8), 1371–1380. doi:10.1007/s11430-021-9803-3

Wang, Y., Hu, S., He, X., Guo, K., Xie, M., Deng, S., et al. (2021b). Relocation and focal mechanism solutions of the 21 May 2021 MS6.4 Yunnan Yangbi earthquake sequence. *Chin. J. Geophys. Chin.* 64 (12), 4501–4525. doi:10.6038/cjg2021P0401

Wang, Z., Su, J., Liu, C., and Cai, X. (2015). New insights into the generation of the 2013 lushan earthquake (M_s7.0), China. *J. Geophys Res.* 120 (5), 3507–3526. doi:10.1002/2014jb011692

Weng, H., and Yang, H. (2018). Constraining frictional properties on fault by dynamic rupture simulations and near-field observations. *J. Geophys Res.* 123 (8), 6658–6670. doi:10.1029/2017JB015414

Xin, H., Zhang, H., Kang, M., He, R., Gao, L., and Gao, J. (2018). High-resolution lithospheric velocity structure of continental China by double-difference seismic travel-time tomography. *Seismol. Res. Lett.* 90 (1), 229–241. doi:10.1785/0220180209

Xu, Z., Liang, S., Zhang, G., Liang, J., Zou, L., Li, X., et al. (2021). Analysis of seismogenic structure of Madoi, Qinghai M(s)7. 4 earthquake on May 22, 2021. *Chin. J. Geophys (in Chin.* 64 (8), 2657–2670. doi:10.6038/cjg2021P0390

Yamada, T., Okubo, P. G., and Wolfe, C. J. (2010). Kiholo Bay, Hawai'i, earthquake sequence of 2006: Relationship of the main shock slip with locations and source parameters of aftershocks. *J. Geophys Res.* 115, B08304. doi:10.1029/2009jb006657

Yao, S., and Yang, H. (2020). Rupture dynamics of the 2012 nicoya M_w 7.6 earthquake: Evidence for low strength on the megathrust. *Geophys Res. Lett.* 47 (13), e2020GL087508. doi:10.1029/2020GL087508

Yin, A., and Harrison, T. M. (2000). Geologic evolution of the Himalayan-Tibetan orogen. *Annu. Rev. Earth Planet Sci.* 28, 211–280. doi:10.1146/annurev.earth.28.1.211

Yue, H., Shen, Z.-K., Zhao, Z., Wang, T., Cao, B., Li, Z., et al. (2022). Rupture process of the 2021 M7.4 Maduo earthquake and implication for deformation mode of the Songpan-Ganzi terrane in Tibetan Plateau. *Proc. Natl. Acad. Sci.*, 119(23), e2116445119. doi:10.1073/pnas.2116445119

Zhang, J. Y., Wang, X., Chen, L., and Liu, J. (2022a). Seismotectonics and fault geometries of the Qinghai Madoi M(s)7. 4 earthquake sequence: Insight from aftershock relocations and focal mechanism solutions. *Chin. J. Geophys (in Chin.* 65 (2), 552–562. doi:10.6038/cjg2022P0516

Zhang, P. Z., Wen, X. Z., Shen, Z. K., and Chen, J. H. (2010). "Oblique, high-angle, listric-reverse faulting and associated development of strain: The Wenchnan earthquake of May 12, 2008, Sichuan, China," in *Annu. Rev. Earth Planet. Sci.* Editors R. Jeanloz and K. H. Freeman (Palo Alto: Annual Reviews), 3838, 353.

Zhang, X., Feng, W., Du, H., Samsonov, S., and Yi, L. (2022b). Supershear rupture during the 2021 MW 7.4 Maduo, China, earthquake. *Geophys Res. Lett.* 49 (6), e2022GL097984. doi:10.1029/2022GL097984

Zhang, Y., An, Y., Long, F., Zhu, G., Qin, M., Zhong, Y., et al. (2021). Short-term foreshock and aftershock patterns of the 2021 Ms 6.4 Yangbi earthquake sequence. *Seismol. Res. Lett.* 93, 21–32. doi:10.1785/0220210154

Zhao, L. F., Xie, X. B., He, J. K., Tian, X. B., and Yao, Z. X. (2013a). Crustal flow pattern beneath the Tibetan Plateau constrained by regional Lg-wave Q tomography. *Earth Planet Sci. Lett.* 383, 113–122. doi:10.1016/j.epsl.2013.09.038

Zhao, L. F., and Xie, X. B. (2016). Strong Lg-wave attenuation in the Middle East continental collision orogenic belt. *Tectonophysics* 674, 135–146. doi:10.1016/j.tecto.2016.02.025

Zhao, L. F., Xie, X. B., Wang, W. M., Zhang, J. H., and Yao, Z. X. (2013b). Crustal Lg attenuation within the north China craton and its surrounding regions. *Geophys J. Int.* 195 (1), 513–531. doi:10.1093/gji/ggt235

Zhao, L. F., Xie, X. B., Wang, W. M., Zhang, J. H., and Yao, Z. X. (2010). Seismic lg-wave Q tomography in and around northeast China. *J. Geophys Res.* 115 (B08), B08307. doi:10.1029/2009jb007157

Zheng, G., Wang, H., Wright, T. J., Lou, Y., Zhang, R., Zhang, W., et al. (2017). Crustal deformation in the India-Eurasia collision zone from 25 years of GPS measurements. *J. Geophys Res.* 122 (11), 9290–9312. doi:10.1002/2017jb014465

Zhu, G., Yang, H., Tan, Y. J., Jin, M., Li, X., and Yang, W. (2022). The cascading foreshock sequence of the Ms 6.4 Yangbi earthquake in Yunnan, China. *Earth Planet Sci. Lett.* 591, 117594. doi:10.1016/j.epsl.2022.117594

frontiers | Frontiers in Earth Science

TYPE Original Research
PUBLISHED 26 January 2023
DOI 10.3389/feart.2023.1078796

OPEN ACCESS

EDITED BY
Giovanni Martinelli,
National Institute of Geophysics and Volcanology, Italy

REVIEWED BY
Vlad Constantin Manea,
National Autonomous University of Mexico, Mexico
Rolando Carbonari,
Hebrew University of Jerusalem, Israel

*CORRESPONDENCE
Bin Zhou,
dztzb@163.com
Yan Zhan,
zhanyan66@vip.sina.com

†These authors have contributed equally to this work and share first authorship

SPECIALTY SECTION
This article was submitted to Solid Earth Geophysics, a section of the journal Frontiers in Earth Science

RECEIVED 24 October 2022
ACCEPTED 10 January 2023
PUBLISHED 26 January 2023

CITATION
Yan C, Li S, Zhou B, Zhan Y, Sun X, Liu X, Su S, Liang F and Zhao L (2023), Deep electrical structure of the hinterland of Yunkai magmatic arc in South China and the seismogenic environment of the 2019 Beiliu earthquake.
Front. Earth Sci. 11:1078796.
doi: 10.3389/feart.2023.1078796

Deep electrical structure of the hinterland of Yunkai magmatic arc in South China and the seismogenic environment of the 2019 Beiliu earthquake

Chunheng Yan[1†], Sha Li[1†], Bin Zhou[1*], Yan Zhan[2*], Xiangyu Sun[2], Xuehua Liu[2], Shan Su[1], Fei Liang[1] and Lingqiang Zhao[3]

[1]Earthquake Agency of Guangxi Zhuang Autonomous Region, Nanning, China, [2]State Key Laboratory of Earthquake Dynamics, Institute of Geology, China Earthquake Administration, Beijing, China, [3]The Second Monitoring and Application Center, China Earthquake Administration, Xi'an, China

The Yunkai Magmatic Arc (YKMA) is located southwest of the South China Block. It has experienced the amalgamation, splitting, and intracontinental orogeny caused by multistage tectonic thermal events. It is also a concentrated area of strong earthquakes in South China. On 12 October 2019, the Beiliu M5.2 earthquake occurred in the hinterland of the YKMA. To reveal the deep electrical structure of the YKMA and the seismogenic environment of the Beiliu earthquake, 101 high-quality data from the magnetotelluric (MT) survey points were acquired. The deep electrical structure images were obtained by three-dimensional electromagnetic inversion imaging. The results indicated that the deep part of the hinterland of the YKMA is characterized by a mushroom-shaped electrical structure composed of ultra-high resistance (R1, with a resistivity value exceeding 10,000 Ωm) and sub-high resistance (R2, with a resistivity value of about 1,000–10,000 Ωm) bodies. The epicenter of the Beiliu M5.2 earthquake was located in R1, close to the contact region between R1 and R2. There are broad low resistivity zones on the southeast and northwest sides of the YKMA. The low resistivity zones is considered to be correspond to the deep extension of the Wuchuan-Sihui and Hepu-Beiliu brittle-ductile shear zones, respectively. The brittle-ductile shearing of the boundary zones and the oblique upwelling of deep mantle-derived magma from the Leiqiong region are the main reasons for the activation of faults and the activity of moderate and strong earthquakes in the YKMA. In this geodynamic environment, local stress and strain accumulation easily occur in the brittle high resistivity body (R1). When the strain energy accumulation exceeded the threshold value that the rock could withstand, new fracture dislocations occurred in the weak region where R1 and R2 contact, which finally resulted in the 2019 Beiliu M5.2 earthquake.

KEYWORDS

Yunkai magmatic arc in South China, three-dimensional magnetotelluric imaging, resistivity structure, 2019 Beiliu earthquake, deep seismogenic environment

1 Introduction

Magmatic arc is where magma upwelling, emplacement and eruption occur when the oceanic crust subducts under the continental crust. Now the major island arcs around the Pacific are magmatic arcs, which are prone to volcanoes and strong earthquakes (Hall, 2002). After a long history of geological evolution, most of the ancient magmatic arcs have not been the

scene of the past intense volcanic eruption and seismic activity. However, if the ancient magmatic arcs are affected by the current regional dynamic thermal events to activate the crustal tectonic, they will certainly become a zone of strong earthquake activity. The region of Yunkai Great Mountain in the South China block may be a window to explore the activation of ancient magmatic arcs. Yunkai Great Mountain starts from the South bank of the Xijiang River at the junction of Guangxi and Guangdong provinces in the North and reaches Lianjiang City in Guangdong Province in the South. It stretches for more than 200 km from northeast to southwest. Structurally, Yunkai Great Mountain is located in the South China Block at the southeast edge of the Eurasian continental plate, close to the southern end of the tectonic junction zone of the Yangtze and Cathaysia blocks (Qin-Hang tectonic junction zone, QHTJZ; Qin et al., 2017; Yan et al., 2019). It was called the Yunkai Magmatic Arc (YKMA; Figures 1A, B) by Pan et al. (2009). YKMA was formed during the Late Proterozoic to Caledonian. It belongs to the multi-island arc basin system in the southeast margin of the Pan-Cathaysian continent and has experienced the amalgamation, fragmentation, and two significant intracontinental orogenic events which originated from multiple tectonic-thermal events during the Early Paleozoic to Mesozoic (Qiu and Liang, 2006; Shu, 2006; Yu et al., 2006; Zhang et al., 2013; Qin et al., 2017; Wang et al., 2020). Since the Late Cenozoic, the Leiqiong area in the South of YKMA has experienced multi-cycle volcanic eruption (Zhou and Armstrong, 1982; Flower et al., 1992; Zou and Fan., 2010). The geothermal flow, seismological, and geochemical multi-disciplinary studies showed that the upwelling of deep mantle-derived magma in the Leiqiong area may have reached YKMA (Lebedev and Nolet, 2003; Yuan et al., 2006; Lei et al., 2009; Wang and Huang, 2012; Yan et al., 2014; Huang et al., 2015; Wei and Chen, 2016; Xia et al., 2016; Yan et al., 2018; Ge et al., 2022). Compared with the overall low level of modern seismicity of the South China Block, YKMA and the Leiqiong area are the concentrated areas of strong earthquakes in South China. Over the past 400 years, more than eleven

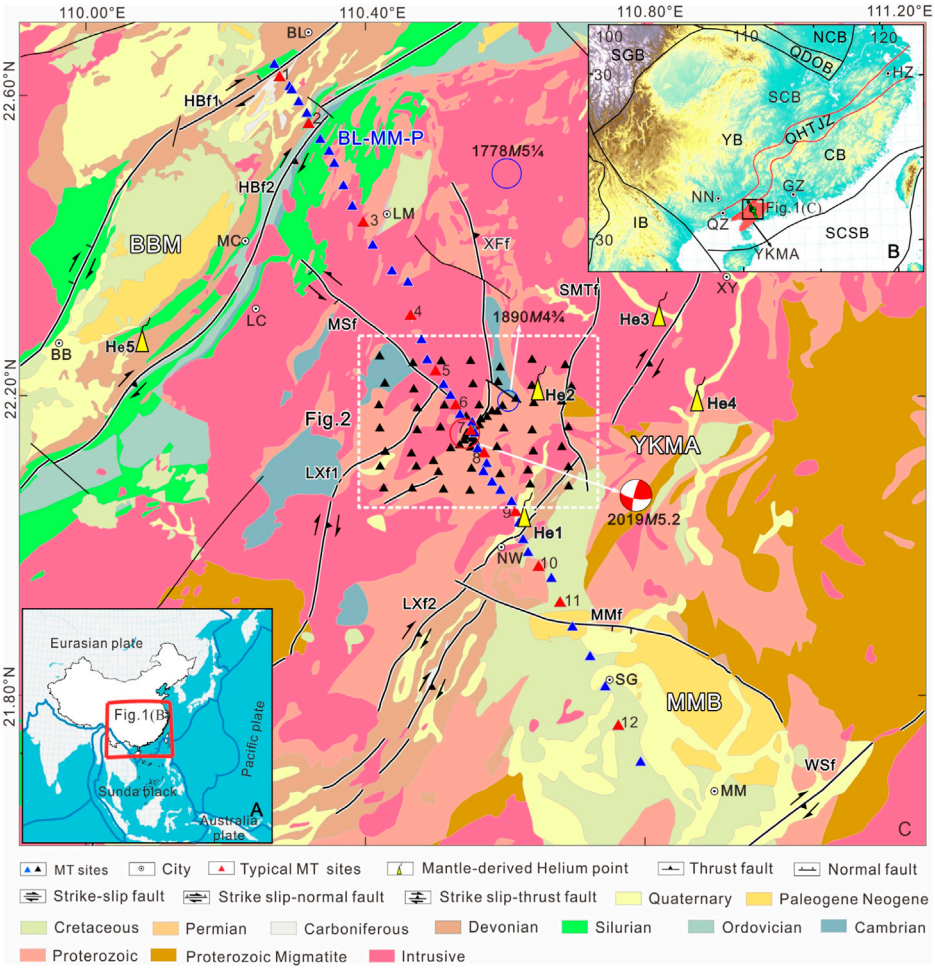

FIGURE 1
(A) Simplified map shows the location of the **(B)** in East Asia; **(B)** Simplified map of the South China Block (modified from Yan et al., 2002; Yan et al., 2019); **(C)** Geology map of the Yunkai magmatic Arc, South China (modified from China Regional Geology Guangxi Chronicle, 2016). NCB, North China Block; SCB, South China Block; YB, Yangtze Block; CB, Cathaysia Block; SGB, Songpan-Ganzi Block; IB, Indosinian Block; SCSB, South China Sea Block; QDOB, Qinling-Dabie Orogen belt; QHTJZ, Qin-Hang tectonic Junction zone; BBM, Bobai Massif; YKMA, Yunkai magmatic Arc; MMB, Maoming Basin; HBf1, Western Hepu-Beiliu fault; HBf2, Eastern Hepu-Beiliu fault; MSf, Michang-Shiwo fault; XFf, Xinfeng fault; LXf1, Western Lianjiang-Xinyi fault; LXf2, Eastern Lianjiang-Xinyi fault; SMTf, Simentang fault; MMf, Northern Maoming basin fault; WSf:Wuchuan-Sihui fault. HZ, Hangzhou; GZ, Guangzhou; NN, Nanning; QZ, Qinzhou; BB, Bobai; BL, Beiliu; LC, Luchuan; MM, Maoming; LJ, Lianjiang; XY, Xinyi; MC, Michang; LM, Liuma; NW, Nawu; SG, Shigu. He1, Xinshidai thermal spring; He2, Wentang thermal spring; He3, XiJiang thermal spring; He4, Reshuiwo thermal spring; He5, Jiatang thermal spring (Zhao et al., 2021).

earthquakes above M6 have been recorded, including the 1890 Guangxi Luchuan M6 earthquake in the hinterland of YKMA (Zhou et al., 2021). The above evidence suggests that the YKMA and its adjacent area have currently become the concentrated zone of strong earthquake activity, which may be related to the upwelling of deep mantle-derived magma in the Leiqiong area. The lack of detailed historical seismic data and deep exploration results makes it impossible for us to further research.

On 12 October 2019, another M5.2 earthquake occurred in Beiliu City, located in the Guangxi Zhuang Autonomous Region, in the hinterland of YKMA, with a focal depth of about 10 km. Owing to the increase in the density of the regional seismic monitoring network in recent years and the erection of six mobile observation stations after the earthquake, the activity of this earthquake sequence was completely recorded. Overall, 165 aftershocks above M_L0.0 were recorded. After the M5.2 earthquake, numerous studies have been carried out regarding the earthquake sequence, focal mechanism, seismogenic structure, and earthquake occurrence mechanism. For example, Li et al. (2019) conducted investigations about surface geology and tectonic geomorphology and concluded that the seismogenic structure was the NW-trending Michang-Shiwo Fault (MSf), but no fault outcrops or surface fractures were found near the epicenter. Yan et al. (2019) achieved the same result based on the integration of focal mechanism solution, precise earthquake location, and seismic intensity distribution. He et al. (2021) studied the rupture directions of the M5.2 earthquake and the M4.2 foreshock, and suggested that these earthquakes resulted from the conjugate activities of the NW-trending MSf and the near SN-trending Xinfeng Fault (XFf). Fan et al. (2022), Huang et al. (2022), and Wen et al. (2022) obtained the velocity structure of the upper crust in the seismic region according to short-period dense array noise imaging and broadband receiver function, and concluded that the strike-slip movement of MSf was blocked by high-speed bodies, resulting in stress accumulation, which finally led to the earthquake. Zhao et al. (2021) observed a high mantle-derived helium anomaly in the earthquake region before the earthquake, and concluded that the earthquake may be related to the upwelling of deep mantle-derived magma in the nearby Leiqiong area. In summary, abundant monitoring data related to the Beiliu earthquake have been acquired, and some understandings of the seismogenic structure and earthquake genetic mechanism have also been attained, but there are still some controversies. In particular, the movement mode of the focal mechanism solution surface of the Beiliu M5.2 earthquake is opposite to the sinistral strike-slip movement of the NW-trending faults and the dextral strike-slip movement of the NE-trending faults in this region (Yan et al., 2019; Figure 1C). The incompatibility of the fault movement mode and deformation behavior may be related to the unique deep seismogenic environment of the Beiliu M5.2 earthquake region. Therefore, to reveal the details of the deep seismogenic environment of the Beiliu earthquake region, to find the evidence that the upwelling of deep mantle-derived magma has affected the earthquake region, and to uncover the mystery of the activation of the ancient YKMA fault structure, profound scientific understanding of the seismogenic structure of the Beiliu M5.2 earthquake is required which itself depends on the high-precision deep detection results.

The existence, transport, and interconnection of fluids can cause a significant increase in the conductivity values of rock masses within a fault zone. Changes in their pressure or slip rates can lead to changes in fault activity (Bürgmann, 2018). The MT method is a geophysical exploration method that uses natural electromagnetic fields as the source. It is the most sensitive method to detect the conductivity of rock masses and is, therefore, commonly used in the detection studies of seismogenic structures (Unsworth and Bedrosian, 2004; Becken et al., 2011; Zhao et al., 2012; Zhang et al., 2016; Zhan et al., 2017; Wang et al., 2018; Ye et al., 2018; Ye et al., 2020). The results of three-dimensional MT exploration in recent years suggest that moderate and strong earthquakes and aftershocks are closely related to the resistivity structure of underground media (Zhao et al., 2012; Zhan et al., 2013; Mohan et al., 2015; Aizawa et al., 2017; Arora et al., 2017; Cai et al., 2017; Sun et al., 2019; Ye et al., 2020; Zhao et al., 2019; Peng et al., 2022). Some moderate and strong earthquakes have occurred near the boundary between high and low resistivity structure of underground media. Earthquakes always occurred in the transition zone of high and low resistivity structures, mainly close to the high resistivity side (Ye et al., 2021; Zhan et al., 2021; Yu et al., 2022; Zhao et al., 2022). In recent years, magnetotelluric exploration aimed at mineral resources has obtained a large-scale deep electrical structure framework of the South China Block (Yan et al., 2019; Xu et al., 2019; Hu et al., 2020; Mao et al., 2021), but the deep electrical structure exploration of the Beiliu M5.2 earthquake region is still lacking.

In this study, we obtained an MT profile and array across the YKMA and Beiliu earthquake region, respectively. The results of the three-dimensional magnetotelluric sounding array in the Beiliu earthquake region are displayed in Figure 1C. Based on the results of seismology, geochemistry, and geothermal flow, the deep electrical structure of YKMA and the deep seismogenic environment of the Beiliu M5.2 earthquake were revealed. The research results are significant for understanding the activation of the ancient YKMA fault structure and the genesis of intraplate earthquakes in South China.

2 Regional geological structure and magnetotelluric profile

There are three groups of NE-trending fault zones in the study area, including the western branch (HBf1) and eastern branch (HBf2) of the Hepu-Beiliu fault zone, the western branch (LXf1) and eastern branch (LXf2) of the Lianjiang-Xinyi fault zone, and the Wuchuan-Sihui fault zone (WSf) from northwest to southeast (China Regional Geology Guangxi Chronicle, 2016; Figure 1C). HBf1 is a normal strike-slip fault dipping NW. HBf2 is a reverse strike-slip fault dipping SE. LXf1 and LXf2 are reverse strike-slip faults dipping SE. WSf is a reverse strike-slip transcrust fault dipping SE, and it is also a large brittle-ductile shear zone with intensive dynamic thermal metamorphism (Peng and Wu, 1994). Besides, there is an NWW-trending fault (MMf) on the northern edge of the Maoming Basin, which has controlled the evolution of this basin (Ye, 2008). The topographic and geological features of the Beiliu M5.2 earthquake region are shown in Figure 2. The Beiliu M5.2 earthquake region is at a low elevation region, with an average elevation of about 100 m, but the northwest side of the Beiliu seismic area shows a southwest-northeast spreading mountain, with an elevation of more than 300 m. The Beiliu earthquake occurred in the area where the mountain meets the plain (Figure 2A). The survey area is characterized by typical conjugate structural systems, including the NE-trending LXf1 and LXf2, NW-trending MSF, and near SN-trending XFf and SMTf. The surface

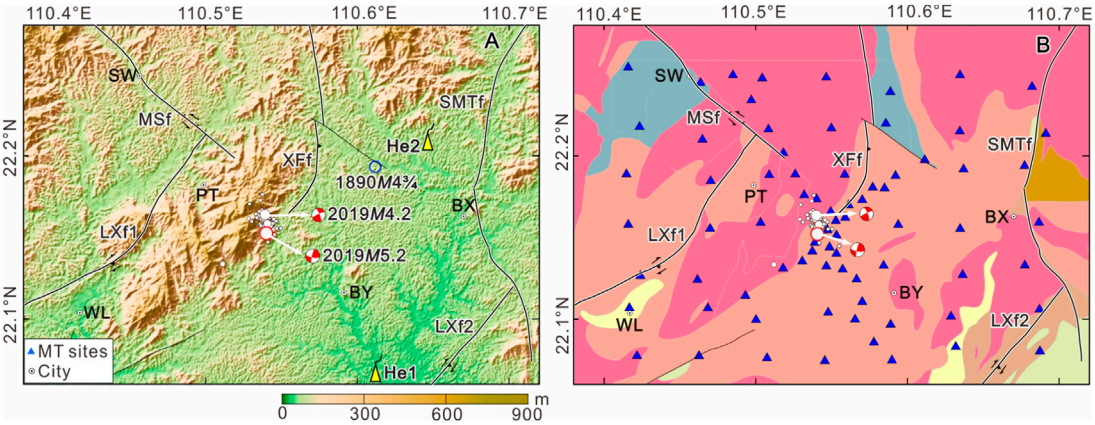

FIGURE 2
(A) Topographic map in Beiliu M5.2 earthquake region; **(B)** Geology map and distribution of MT sites in Beiliu M5.2 earthquake region. SW, Shiwo; WL, Wenlou; PT, Pingtian; BY, Boyang; BX, Baoxu. The names of faults, stratum and mantle-derived Helium of thermal spring gas are consistent with those in Figure 1.

trajectories of MSF and XFf near the epicenter meet but do not intersect (Li et al., 2019).

The study area is divided into the Bobai Massif (BBM) and YKMA by HBf1 (China Regional Geology Guangxi Chronicle, 2016; Figure 1C). BBM is sandwiched between the eastern and western branches of the Hepu-Beiliu fault zone. It is a large collision zone and brittle-ductile shear zone (Huang, 2000; Qin et al., 2008). The outcropped rocks include the Cretaceous-Paleogene glutenite and the Devonian sandstone, mudstone, and limestone. Ordovician-Silurian siltstone and shale are exposed near HBf2. YKMA is located between HBf2 and WSf. Precambrian crystalline basement, shallow metamorphic folded basement, and multistage granitoids are distributed in this region. The Beiliu earthquake region is dominated by shallow metamorphic folded basement granitic plutons (Zhong et al., 1996; Wang et al., 1998; Figure 2B). The Bobai Massif (MMB) in YKMA is covered with Cretaceous-Paleogene red clastic rocks (Ye, 2008).

In this research, the Beiliu-Maoming Magnetotelluric Profile (BL-MM-P) stretched across BBM, YKMA, and MMB from northwest to southeast. The profile began from Beiliu in Guangxi Province, through the Beiliu earthquake region, to about 10 km northwest of Maoming in Guangdong Province, with a total length of about 115 km. We obtained 43 survey points, with an average point distance of 2.5 km (Figure 1C). Given the characteristics of the conjugate tectonic system and the mixed distribution of intrusive rocks and metamorphic rocks in the Beiliu earthquake area, the magnetotelluric sounding array was arranged around the epicenter of the Beiliu earthquake. We obtained a total of 58 survey points. The distance between the survey points in the epicenter area was smaller than 1 km (Figure 2).

3 Acquisition, processing, analysis, and inversion of electromagnetic data

3.1 Data acquisition and processing

From December 2020 to March 2021, the MTU-5A magnetotelluric observation system was used for magnetotelluric data acquisition. The electric field components in the SN and EW directions, and the magnetic field components in the SN, EW, and vertical directions were observed. To obtain high-quality electromagnetic data, the recording time of each survey point included two nights, and that of the survey points near strong electromagnetic interference sources included three nights. Meanwhile, a remote reference station (YCK in Supplementary Figure S1.1, about 150 km away from the northwest end and 270 km away from the southeast end of the BL-MM-P profile) was set up for synchronous observation in Xiangzhou County, located in Laibin City, northeast of the study area, to eliminate the strong near-field electromagnetic interference. After processing the data using the remote reference and without robust technologies (Gamble et al., 1979; Egbert and Booker, 1986; Han et al., 2022), the data quality was greatly improved and the continuity of apparent resistivity and phase curve was improved (Supplementary Figures S1.2, S1.3). Finally, 101 MT survey points were obtained.

The apparent resistivity and impedance phase curves of 12 typical survey points distributed in BBM, YKMA, and MMB on the BL-MM-P profile are shown in Figure 3. The apparent resistivity curve of each survey point in BBM is characterized by high-low-sub high values with the increase in frequency, indicating that there is a high-resistance layer in the shallow part of this sectionas well as a low-resistance body with a certain thickness in the deep part. The apparent resistivity of each survey point in YKMA is larger than 100 Ω·m in almost all frequency bands, and the curve is characterized by low-high-sub low values with the increase of frequency. These suggest that there are low-resistance layers in the shallow part and high-resistance bodies in the deep part, which are the manifestations of crystalline metamorphic rocks and granitic intrusive rocks. The resistivity tends to decrease further with depth. The apparent resistivity values of the survey points in MMB are generally below hundreds of Ω·m. The apparent resistivity values of No. 5–7 survey points in the Beiliu earthquake region are relatively high, especially in the middle frequency band such that the apparent resistivity reaches 1,000–10,000 Ω·m, and the apparent resistivity tends to decrease in the low-frequency band, indicating that there is a high-resistance body in the middle and deep parts of the earthquake region.

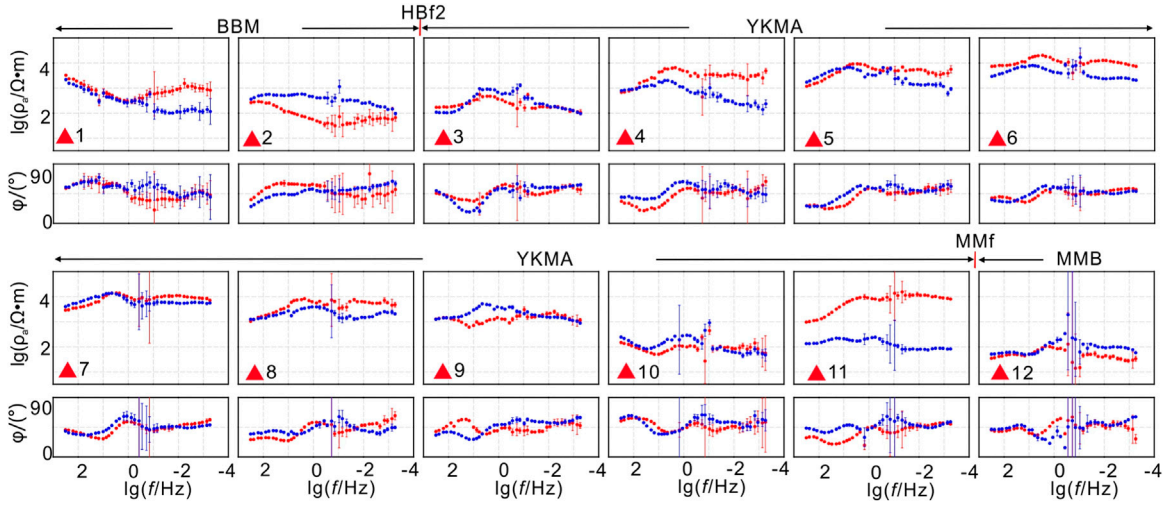

FIGURE 3
Apparent resistivity and impedance phase curves of typical MT sites. Red dots denote XY mode, blue dots denote YX mode. The names of faults, BBM, YKMA, and MMB are consistent with those in Figure 1.

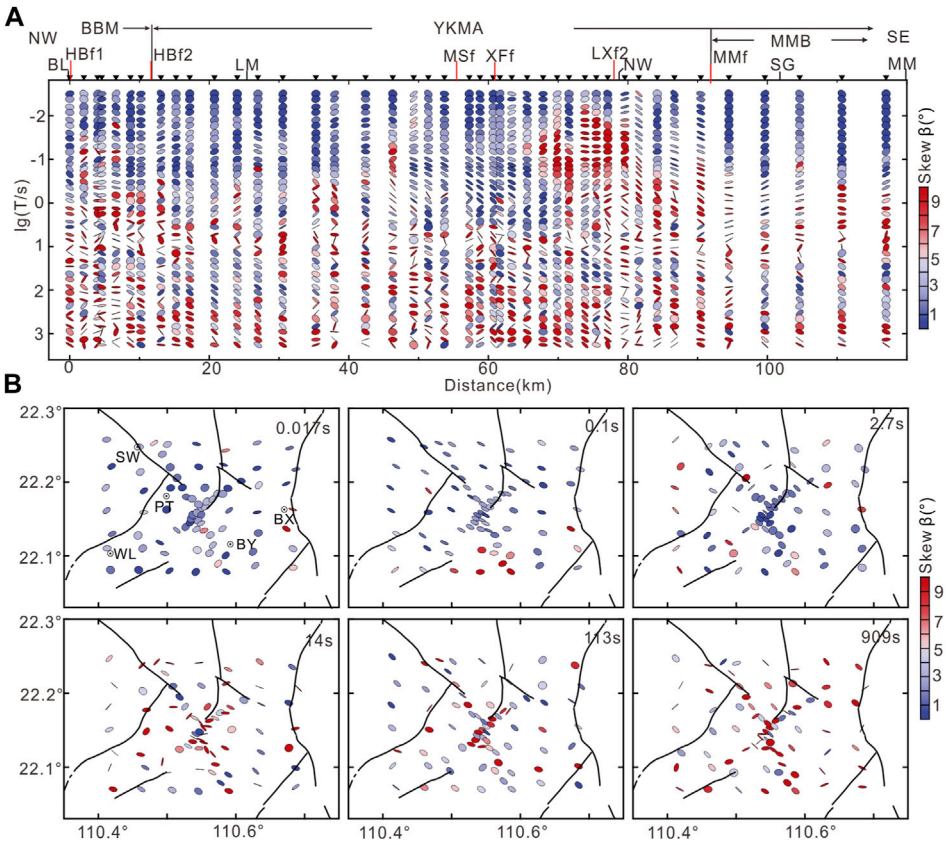

FIGURE 4
(A) Phase tensor ellipses filled with the absolute value of skew angle β along the profiles (upper); **(B)** Phase tensor ellipses in Beiliu M5.2 earthquake region filled with the absolute value of skew angle β for six periods (bottom). The names of faults, city, BBM, YKMA, and MMB are consistent with those in Figure 1.

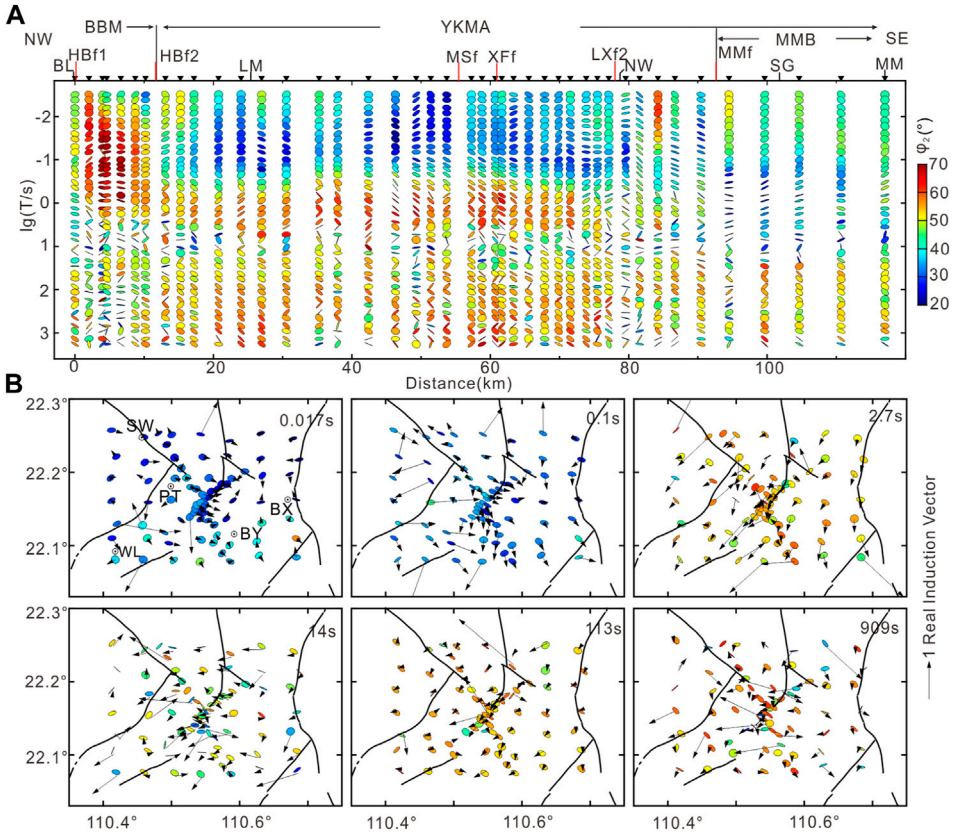

FIGURE 5
(A) Phase tensor ellipses filled with the phase tensor invariant along the profiles (upper); **(B)** Phase tensor ellipses in Beiliu M5.2 earthquake region filled with the phase tensor invariant for six periods (bottom). The names of faults, city, BBM, YKMA, and MMB are consistent with those in Figure 1.

3.2 Regional dimensional analysis

The phase tensor decomposition technology is one of the important tools for the qualitative analysis of electromagnetic data. The two-dimensional deviation degree of the phase tensor (β) can be employed to determine the dimensional characteristics of underground structures (Caldwell et al., 2004; Bibby et al., 2005). Considering the errors of data in the study area, it is suggested that the three-dimensional property of the deep structure is strong when $|\beta|$ is greater than 5 (Booker, 2014; Cai et al., 2017). The variation of the two-dimensional deviation value of phase tensor decomposition of each survey point on the BL-MM-P profile with the period is shown in Figure 4A. According to the change of $|\beta|$ with the period, the values of $|\beta|$ in the middle- and high-frequency bands over 10 seconds are all smaller than 5. As the period increases, the $|\beta|$ value of many survey points in the southeast of XFf becomes greater than 5, suggesting that the shallow structure of the study area is simple, while the middle and deep structures are complex, displaying obvious three-dimensional characteristics. The two-dimensional deviation plan of the phase tensor of six periods in the Beiliu earthquake region is exhibited in Figure 4B. It can be observed that the $|\beta|$ value in the high-frequency band with a period of smaller than 2.7 s is generally smaller than 5, and the principal axis directions of the phase tensor ellipses are similar, demonstrating that the shallow structure in the Beiliu earthquake region is characterized by strong two-dimensional characteristics. In the middle- and low-frequency bands with a period of more than 2.7 s, the $|\beta|$ values of sporadic survey points are initially greater than 5, and then those of most survey points become greater than 5. The $|\beta|$ values of survey points in the epicenter area of the Beiliu earthquake are even greater, indicating that the three-dimensional nature of the Beiliu earthquake region is very strong. Therefore, to achieve an effective and reliable BL-MM-P profile and a deep electrical structure in the Beiliu earthquake region, it is necessary to perform a three-dimensional magnetotelluric inversion simulation.

3.3 Analysis of regional electrical differences

The geometric mean of the maximum and minimum phases in the phase tensor (i.e., the phase tensor invariance) is used as a parameter to measure the trend of resistivity with depth (Heise et al., 2008). When the φ_2 is greater than 45°, it indicates that the resistivity structure decreases with increasing depth. Conversely, when the φ_2 is smaller than 45°, the resistivity structure increases with depth in the deep. The phase tensor invariance can be employed to qualitatively analyze the resistivity trend in the deep subsurface with depth. The distribution feature of the phase invariant value of the BL-MM-P profile increases with the period, demonstrating that the deep structures of the three tectonic units across the profile are characterized by unique electrical distribution characteristics (Figure 5A). YKMA has a low phase in the high-frequency band above a few seconds, and a high phase in the high-frequency band

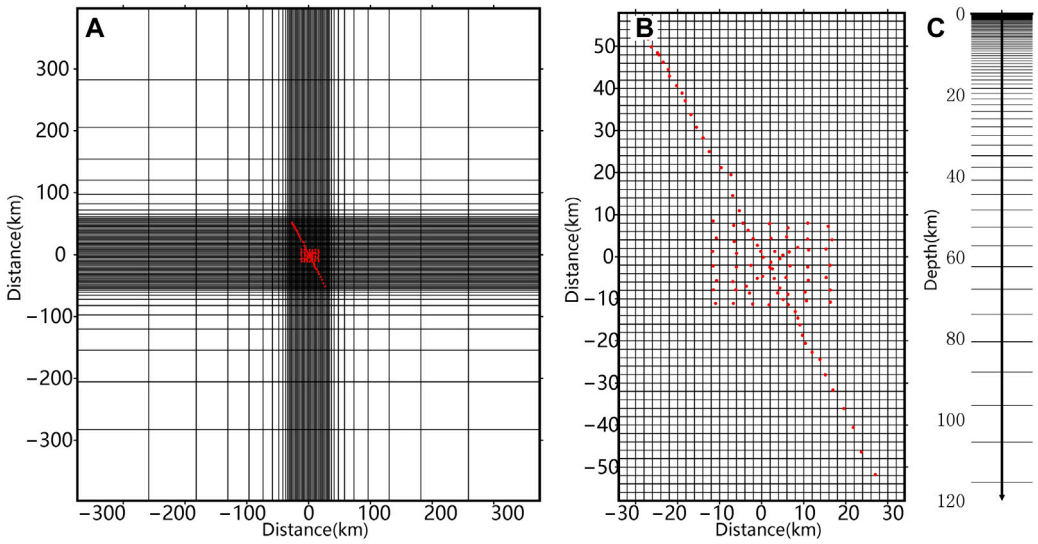

FIGURE 6
Grid used for the 3D inversion in the first step; **(A)** Horizontal grid; **(B)** Horizontal grid of central part; **(C)** Vertical grid; The red dotes denote MT stations.

below a few seconds, suggesting that the deep structure is characterized by high-resistance in the middle and shallow parts and sub-low resistance in the middle and deep parts. BBM shows a sub-high phase in the high-frequency band above tens of hertz, a low phase in the frequency band of about 10 s, and a sub-high phase in the lower frequency band, suggesting that this section is characterized by a three-layer resistivity structure. A thin sub-high resistance layer is developed on the shallow part, the resistivity in the lower part is low, and the resistivity increases in the deeper part. MMB displays a sub-low phase in the high-frequency band above 10 Hz, a sub-high phase in the frequency band from below to more than 10 s, and a sub-low phase in the frequency band below 10 s, indicating that the deep part of this section is characterized by a low-high-low three-layer resistivity structure. The distribution characteristics of the six-period phase invariants in the Beiliu earthquake region are consistent with the profile which passes through YKMA. The φ_2 value is large in the high-frequency band of more than a few seconds, and is small in the lower frequency band, demonstrating that the shallow to middle parts have high resistance, and the middle to deep parts have a sub-low resistance (Figure 5B). The six-period magnetic real induction vector pattern is also superimposed in Figure 5B, showing that the magnetic real induction vector of the central survey point in the high-frequency measuring area with a period of more than 2.7 s points to the periphery, indicating that the resistivity in the center of the measuring area is the largest within a certain depth range.

4 Three-dimensional inversion

Among the 101 survey points obtained along the BL-MM-P profile and the Beiliu earthquake region, the effective frequency band of most of the survey points was 320 Hz to 5,500 s. The outliers, or disturbed data, of each survey point were added with errors to reduce their weight in the inversion. The ModEM (Egbert and Kelbert, 2012) three-dimensional electromagnetic imaging system was employed for the inversion. The apparent resistivity and impedance phase data were utilized, and the error floor was 10% and 5% (2.84°), respectively.

The three-dimensional inversion was carried out in two steps. First, the BL-MM-P profile and 92 survey point data in the Beiliu earthquake region were integrated at an interval of 2 km to perform a three-dimensional inversion. The size of the SN and EW horizontal grid in the central area of the dataset was 2 km × 2 km, and the number of grids was 40 × 58. There were ten expanded grids with a scale factor of 1.5 in each of the four directions outside the central area, and the final number of grids was 60 × 74. The thickness of the first layer of the vertical grid was 20 m, and the grid thickness increased in different proportions in downward segments. The growth factors within 0.5, 0.5–1, 1–15, 15–150, and 150–500 km were 1.2, 1.1, 1.05, 1.1, and 1.2, respectively. Finally, a total of 87 layers were divided (Figure 6). A uniform half space of 500 Ω·m was employed as the initial model. The automatically updated regularization factor was adopted. The initial value of the regularization factor was 5,000. When the inversion was no longer convergent, the regularization factor was updated to one-tenth of the initial value to continue the inversion. After 90 iterations of inversion, the root mean square error (RMS) of the model was 2.51 (Supplementary Figure S2.1). The responses obtained by the three-dimensional inversion were well consistent with the measured apparent resistivity and impedance phase data (Supplementary Figure S2.2).

Second, the inversion of the electromagnetic array in the Beiliu earthquake region was performed. The area contained 76 survey points with a spacing of about 1 km. The size of the SN and EW horizontal grid in the central area of the dataset was 0.6 km × 0.6 km, and the number of grids was 40 × 58. There were 10 expanded grids with a scale factor of 1.5 in each of the four directions outside the central area. The final number of grids was 60 × 74. The vertical grid division was consistent with the large area (Figure 7). Using the model obtained in the first step as the initial model, after 90 iterations of inversion, the RMS of the model was 1.79 (Supplementary Figure S3.1). The responses obtained by the three-dimensional inversion were well consistent with the measured apparent resistivity and impedance

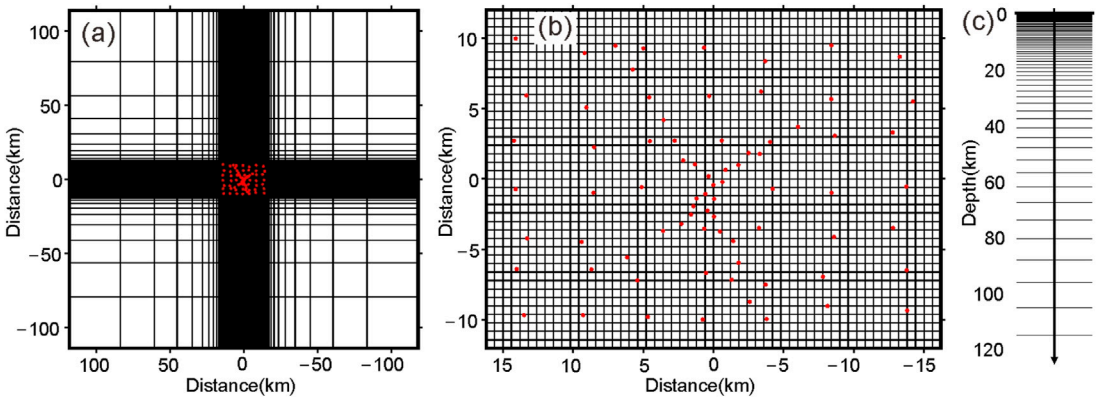

FIGURE 7
Grid used for the 3D inversion in the second step; **(A)** Horizontal grid; **(B)** Horizontal grid of central part; **(C)** Vertical grid; The red dotes denote MT stations.

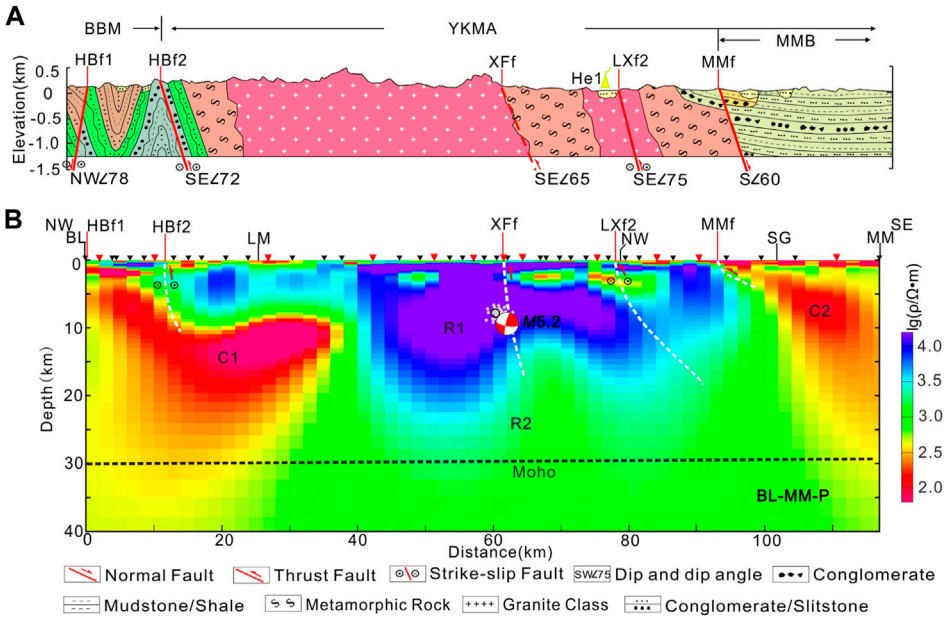

FIGURE 8
(A) Geological cross-section along the BL-MM-P; **(B)** Electrical structure obtained from 3D inversion of the BL-MM-P. The white dotted lines indicate the inferred extension pattern of the faults in the crust, and the black dotted line indicates the buried depth of the Moho surface along the MT profile. The names of faults, city, BBM, YKMA, and MMB are consistent with those in Figure 1.

phase data (Supplementary Figure S3.2). To assess the robustness of the major model features, sensitivity tests of C1 and C2 were carried out (Supplementary Figure S4).

5 Deep electrical structure of YKMA and Beiliu earthquake region

The deep electrical structure along the BL-MM-P profile is depicted in Figure 8. The depth of Moho near the profile is about 29.5 km (Shen et al., 2013). The geological profile along the BL-MM-P profile was obtained based on the 1:500 000 geological map (China Regional Geology Guangxi Chronicle, 2016), and it was displayed above the electrical structure profile (Figure 8A). The profile crossed BBM, YKMA, and MMB from northwest to southeast, and the main faults included HBf1, HBf2, LXf2, and MMf. Combined with the surface geological outcrops, the electrical structure of the tectonic unit and the deep extension of the main faults are explained in the following.

Figure 8 shows that there are differential zones with high and low resistances in the lower parts of HBf2 and MMf, representing the main tectonic boundary. The electrical difference zone extends shallowly below LXf2. Accordingly, the deep and shallow electrical structures along the profile can be divided into three segments bounded by HBf2 and MMf. In the northwest of HBf2 in the BBM in the northwest section of the BL-

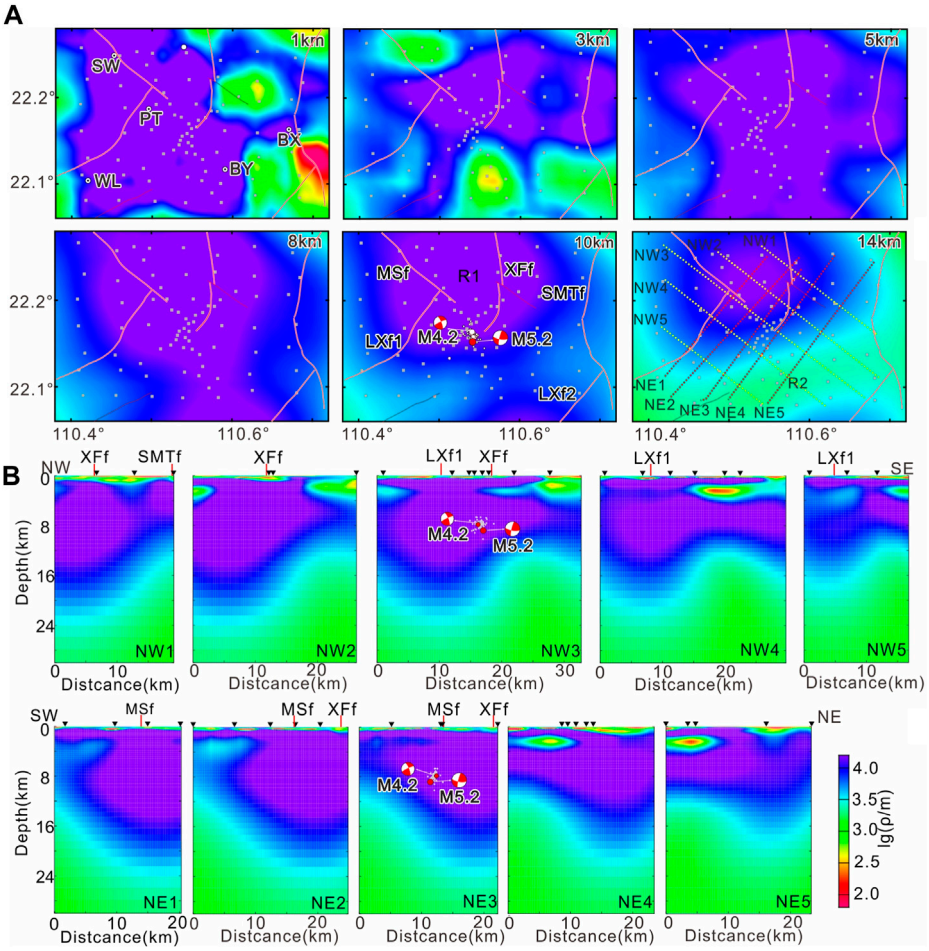

FIGURE 9
Mapview **(A)** and cross sections **(B)** of the electrical structure beneath the Beiliu earthquake region. The names of faults, city, BBM, YKMA, and MMB are consistent with those in Figure 1.

MM-P profile, a high-resistance layer is covered at a depth of 1 km, corresponding to the Paleozoic glutenite, sandstone, and shale. The downward zone is a low-resistance zone (C1) inclined to SE with a resistivity of 100–300 Ω·m, which gradually deepens to below 10 km and is buried under the high resistivity body (R1) in the upper crust of YKMA. The YKMA in the middle section of the BL-MM-P profile is dominated by Precambrian shallow metamorphic folded basement and multistage granitoids. From the shallow surface to the depth of about 20 km, there is a high-resistance body (R1) with a resistivity of thousands or even ten thousands of Ω·m. It covers a wide area in the NW-SE direction between HBf2 and MMf. From the depth of 20 km to the Moho surface, the resistivity decreases to about 1,000 Ω·m (R2). The high-sub-high-resistance structure (R1 and R2) is like a "mushroom" that is wide at the top and narrow at the bottom. The upper high-resistance body (R1) and the lower sub-high-resistance body (R2) are intertwined. The top surface of R2 is undulating like a "hump." The XFf is located near the "hump"-shaped uplift, where the top surface of the sub-high resistance body (R2) is uplifted to a shallow depth of 13 km. The epicenter of the 2019 Beiliu M5.2 earthquake was located near the high- and low-resistance boundary in the high-resistance area towards the northwest. In the MMB of the southeast section of the BL-MM-P profile, within a depth of about 1 km, there is a low-resistance layer with a resistivity of several hundreds of Ω·m, corresponding to the Quaternary and Cretaceous sandstone and siltstone. The 1–3 km depth is dominated by a medium resistivity layer with a resistivity of about 1,000 Ω·m. The resistivity decreases to several hundreds of Ω·m below 3 km.

To observe the more detailed characteristics of the deep resistivity structure in the Beiliu earthquake region, the cross sections at six depths and the deep electrical structure profile in the NE and NW directions were drawn (Figure 9). According to the cross sections, the ultra-high-resistance block (R1) is located to the west of XFf at the depth of less than 3 km, and its resistivity reaches ten thousands of Ω·m, which is attributed to the widely distributed intrusive rocks in the earthquake region. The northeast and southwest corners of the study area displayed sub-high resistivity, which may be related to the sandstone and siltstone existing in small basins along LXf2 and SMTf. At the depth of 4–10 km, the ultra-high resistivity structure almost covers the whole study area. At the depth of 10–14 km, the ultra-high resistivity body (R1) still exists in the Beiliu earthquake region and the northwest side, while the southeast side of the earthquake region shows a sub-high resistivity structure (R2), with a resistivity close to 1,000 Ω·m. From the NW- and NE-trending profiles, it can be seen more clearly that R1 is deeper in the northwest of the Beiliu

earthquake region and shallower in the southeast. The NW-trending profile suggests that R1 is deeply buried in the northwest of the epicenter, and the top interface of R2 in the southeast is convex, just like the "hump" shape in Figure 8B. In the NW- and NE-trending profiles, there is no significant difference between the deep electrical structure of MSF and XFf. The area where MSF and XFf meet but do not intersect in the upper crust is a completely rigid high-resistance body, but the middle and lower crustal materials below XFf show obvious upward convexity.

6 Discussion

The large brittle-ductile shear zones near paleo-orogenic belts and the boundaries of active plates or blocks are generally the products of the oblique convergence of plates or blocks, and they play a significant role in regulating the tectonic deformation between plates or blocks (Means, 1995; Jiang et al., 2001; Zhu et al., 2004). Based on geological surveys and geochemical studies, the Wuchuan-Sihui fault zone (WSf) and Hepu-Beiliu fault zone (HBf) on the East and west sides of YKMA are is large subduction and collision zones originating from amalgamation, splitting, and multistage orogeny of the Yangtze and Cathaysia blocks (Peng and Wu, 1994; Huang, 2000). In addition, mylonite belts with different degrees of ductile deformation emerged along the two fault zones, and caused the Indosinian strata and geological bodies to be involved in deformation (Liu et al., 2005; China Regional Geology Guangxi Chronicle, 2016; Guo et al., 2020). These indicate that the two fault zones have experienced large-scale brittle-ductile shear deformation since Indosinian orogeny. The MT exploration results show that the Lithosphere brittle-ductile shear zone corresponds to the variation zone of deep electrical structure or the low resistivity zone, which cuts the Moho surface (Yoshimura, et al., 2008; Yu et al., 2017; Cai et al., 2018; Martí et al., 2020). At the depth below 5 km in BBM, there is a low-resistance zone (C1) that slopes toward SE and extends below the Moho surface. C1 may be a broad brittle-ductile shear zone with low rheological strength and viscosity. The shallow part of the zone corresponds to the morphology of HBf which extends in the upper crust. Although the BL-MM-P profile does not cross WSf (the southeast survey point of the profile is about 18 km away from WSf), there is also a low-resistance zone (C2) below the depth of 5 km under MMB. By comparing with the relatively wide lateral distribution characteristics of the Hepu-Beiliu brittle-ductile shear zone in the middle to lower crust, it is inferred that C2 is the horizontal extension of the Wuchuan-Sihui brittle-ductile shear zone on the southeast side in the middle to lower crust. WSf and HBf are not only the concentrated areas of hot springs but also the NE-trending high thermal abnormal belts with a beaded distribution (Yuan et al., 2006; China Regional Geology Guangxi Chronicle, 2016). Hot springs and high thermal anomalies may be related to the melting of deep crustal materials. Before the Beiliu M5.2 earthquake, Zhao et al. (2021) conducted a survey of helium and carbon isotopes of hot spring gas in the Leiqiong area and YKMA. They found that mantle-derived helium constituted the largest percentage (15.23%, He5 in Figure 1C) in Jiatang Hot Spring located in HBf, and helium anomalies were also present in Wentang Hot Spring (10.01%), Xijiang Hot Spring (2.05%), Reshuiwo Hot Spring (3.17%), and Xinshidai Hot Spring (0.97%) near the Beiliu M5.2 earthquake area in the hinterland of YKMA (He1-He4 in Figure 1C). These results indicated that there was mantle-derived magmatic activity below YKMA, and its boundary fault zone played an important role in the upwelling and intrusion of mantle-derived magma. Since the late Cenozoic, the Leiqiong area in the south of YKMA has undergone multi-cycle volcanic eruptions (Zhou and Armstrong, 1982; Flower et al., 1992; Zou and Fan., 2010). According to rock geochemical studies and seismological studies, the magmatism in the Leiqiong area originated from the mantle transition zone or even the core-mantle boundary, and the upwelling of mantle-derived magma was the deep driving force in Leiqiong and its adjacent areas (Lebedev and Nolet, 2003; Lei et al., 2009; Wang and Huang, 2012; Yan et al., 2014; Huang et al., 2015; Wei and Chen, 2016; Xia et al., 2016; Yan et al., 2018; Ge et al., 2022). The low-resistance zone extending deep from the boundary of YKMA, the "hump"-shaped sub-high-resistance body (R2) in the middle and lower crust of YKMA, and the strong earthquake activities in YKMA and its southern Leiqiong area, may all be related to the mantle-derived magmatic activities in the Leiqiong area. The brittle-ductile shearing of the boundary fault zone and the deep thermodynamic action provide the deep dynamic source for the activation of fault structures and seismic activities in YKMA.

The studies on focal mechanism solution (Jiang et al., 1992; Wan, 2010), GPS (Wang and Shen, 2020), and water system statistics (Ai et al., 1982) have indicated that the principal compressive stress direction in the southwest of the South China Block is generally NW-SE, and the dip angle is close to horizontal. Such a tectonic environment is favorable for the sinistral strike-slip movement of the NW-trending faults and the dextral strike-slip movement of NE-trending faults. This is also confirmed by the occurrence of destructive earthquakes since the regional seismic monitoring network was established in 1970, such as the 1977 Guangxi Pingguo M5.0 earthquake, 1994 Beibuwan M6.1 and M6.2 earthquakes, and 2016 Guangxi Cangwu M5.4 earthquake (Zhao, 1983; Yin et al., 1996; Zhou et al., 2019). The focal mechanism solution of the Beiliu M5.2 earthquake suggests that the NWW- and NNE-trending nodal planes are characterized by dextral strike-slip and sinistral strike-slip (Yan et al., 2019; Figure 1C), respectively. This is opposite to the sinistral strike-slip movement of NW-trending faults and dextral strike-slip movement of NE-trending faults in the southwest of the South China Block. Seismologists have been puzzled by the inconsistency between the mode of fault movement and deformation behavior. As mentioned above, the geothermal flow, seismological, and geochemical studies show that the upwelling of deep mantle-derived magma in the Leiqiong area may have reached YKMA. The HBf and WSf at the boundary of YKMA have become the preferred channel and the most significantly affected zone for the upwelling of deep mantle-derived magma. Therefore, the strength of the rocks is reduced, the rheology is enhanced, and the local strain rate is increased. Under the coupling effect of deep thermal and regional tectonic stress, the two boundary faults regulated the tectonic deformation in YKMA in the form of brittle-ductile shear. Moreover, the deep mantle-derived magma in the Leiqiong area upwelled obliquely from south to north, reaching the deep part of YKMA, which led to the transformation of YKMA. They gradually evolved in the upper and middle crust to form the intertwined interface of the sub-high-resistance body (R2) and the high-resistance body (R1). Local stress and strain accumulations were easy to occur in the brittle high-resistance body (R1). When the conditions for rock fracture and instability were reached, the pre-existing or newly formed NW-trending faults would exhibit dextral strike-slip dislocation, and the near SN-trending faults would show sinistral strike-slip dislocation (Figure 10). The Beiliu M5.2 earthquake occurred in the area where the NW-trending MSF and the NE-trending XFf meet but do not intersect. No fault outcrop and seismic surface fracture zone were found during the surface geological

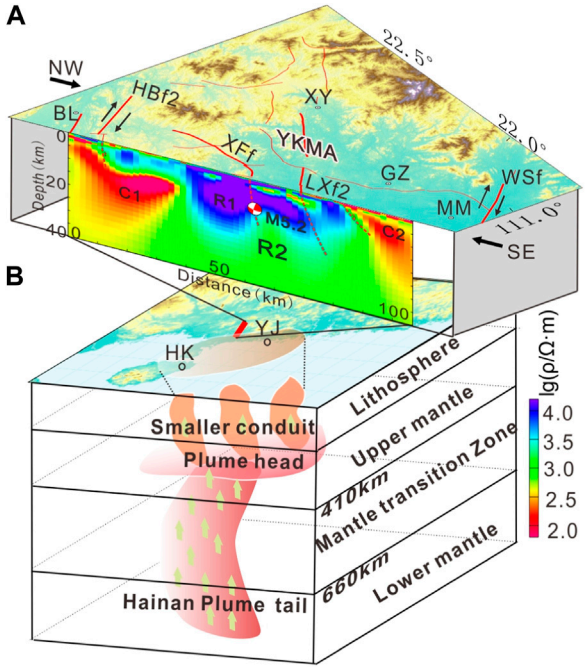

FIGURE 10
(A) Three-dimensional structure of BL-MM-P; **(B)** Hainan mantle plume modified from Wei and Chen (2016). HK, Haikou; YJ, Yangjiang. Other names of faults, city, BBM, YKMA, and MMB are consistent with those in Figure 1.

survey. We speculated that the earthquake was induced by the new fracture in the conjugate tectonic area.

The seismogenic structure and environment of the Beiliu earthquake are similar to those of the 1998 Zhangbei M6.2 earthquake in the Zhangbo seismic belt of North China. The Zhangbei earthquake occurred in the Hannuoba high-resistance basalts (Peng et al., 2022). The surging of deep thermal materials resulted in the activity of conjugate faults, which triggered the earthquake. The 2019 M_w6.4-7.1 Ridgecrest earthquake sequence in eastern California of the USA occurred in the distribution area of immature orthogonal strike-slip faults with a low deformation rate. It was caused by the joint rupture of multiple faults under the action of regional tectonic stress (Goldberg et al., 2020; Jia et al., 2020; Fialko and Jin, 2021). These earthquakes indicate that the region with existing conjugate faults is more prone to moderate and strong earthquakes when the stable block is subjected to deep dynamic and/or regional tectonic stress. The occurrence of moderate and strong earthquakes in YKMA may be attributed to the brittle-ductile shear of the boundary fault zone as well as the mantle-derived magmatic activity. This is of great significance for the understanding of the genesis of intraplate earthquakes in South China.

7 Conclusion

According to the data of 101 broadband MT survey points in the hinterland of YKMA in South China and based on the 2019 Guangxi Beiliu M5.2 earthquake area, the deep electrical structure images were obtained by three-dimensional electromagnetic inversion imaging. The results indicated that there are low-resistance zones on the East and West sides of YKMA, corresponding to the deep extension of the Wuchuan-Sihui and Hepu-Beiliu brittle-ductile shear zones, respectively. The deep part of the hinterland of YKMA is characterized by a mushroom-shaped electrical structure composed of ultra-high resistance (R1) and sub-high resistance (R2) bodies. We speculated that this has likely resulted from the brittle-ductile shearing of the boundary zone and the oblique upwelling of the mantle-derived materials in the Leiqiong area. The top interface of R2 is undulating like a "hump." The 2019 Beiliu M5.2 earthquake occurred near the boundary between high resistance and low resistance in the sub-high resistance uplift and was inclined to the northwest high-resistance body.

The brittle-ductile shearing of the boundary fault zone of YKMA and the deep mantle-derived magmatic action provide the dynamic source for the activation of fault structures and seismic activities in YKMA. Local stress and strain accumulations are easy to occur in the brittle high-resistance body (R1). When the conditions for rock fracture and instability were reached, the pre-existing or newly formed NW-trending faults would exhibit dextral strike-slip dislocation, and the near SN-trending faults would show sinistral strike-slip dislocation. No fault outcrop was found near the epicenter of the Beiliu M5.2 earthquake, thus, we speculated that the earthquake was caused by the new fracture in the conjugate tectonic area. The occurrence of moderate and strong earthquakes in YKMA may be attributed to the brittle-ductile shear of the boundary fault zone as well as the deep mantle-derived magmatic activity, which is of great significance for the understanding of the genesis of intraplate earthquakes in South China.

Data availability statement

The original contributions presented in the study are included in the article/Supplementary Material, further inquiries can be directed to the corresponding authors.

Author contributions

CY, SL, BZ, YZ, XS, XL, and SS completed the field data acquisition, and the data analyses, and wrote the article. BZ, CY, and SL provided funding for the study. XL, FL, and LZ assisted in data acquisition. All authors contributed to the manuscript revision and discussion and approved the submitted version.

Funding

This paper was supported by the Guangxi Scientific Research and Technology Development Plan Project (1377002, 14124004-4-8), Earthquake Prediction Open Fund Project (2021EF0F02), and Science for Earthquake Resilience (XH22004YA) of China Earthquake Administration.

Acknowledgments

We appreciate the access to the computing resources of the Computer Network Information Center at the Institute of Geology, China Earthquake Administration. Some figures were prepared using GMT (Wessel et al., 2013).

Conflict of interest

The authors declare that the research was conducted in the absence of any commercial or financial relationships that could be construed as a potential conflict of interest.

Publisher's note

All claims expressed in this article are solely those of the authors and do not necessarily represent those of their affiliated organizations, or those of the publisher, the editors and the reviewers. Any product that may be evaluated in this article, or claim that may be made by its manufacturer, is not guaranteed or endorsed by the publisher.

Supplementary material

The Supplementary Material for this article can be found online at: https://www.frontiersin.org/articles/10.3389/feart.2023.1078796/full#supplementary-material

References

Ai, N., Liang, G., and Scheidegger, A. (1982). The valley trends and neotectonic stress field of Southeast China. *Acta Geogr. Sin.* 37 (2), 111–122. (in Chinese).

Aizawa, K., Asaue, H., Koike, K., Takakura, S., Utsugi, M., Inoue, H., et al. (2017). Seismicity controlled by resistivity structure: The 2016 kumamoto earthquakes, kyushu island, Japan. *Earth Planets Space* 69, 4. doi:10.1186/s40623-016-0590-2

Arora, B., Bansal, B., Prajapati, S., Sutar, A., and Nayak, S. (2017). Seismotectonics and seismogenesis of M_w7.8 Gorkha earthquake and its aftershocks. *J. Asian Earth Sci.* 133, 2–11. doi:10.1016/j.jseaes.2016.07.018

Becken, M., Ritter, O., Bedrosian, P., and Weckmann, U. (2011). Correlation between deep fluids, tremor and creep along the central San Andreas fault. *Nature* 480, 87–90. doi:10.1038/nature10609

Bibby, H., Caldwell, T., and Brown, C. (2005). Determinable and non-determinable parameters of galvanic distortion in magnetotellurics. *Geophys. J. Int.* 163, 915–930. doi:10.1111/j.1365-246X.2005.02779.x

Booker, J. (2014). The magnetotelluric phase tensor: A critical review. *Surv. Geophys* 35, 7–40. doi:10.1007/s10712-013-9234-2

Bürgmann, R. (2018). The geophysics, geology and mechanics of slow fault slip. *Earth Planet. Sci. Lett.* 495, 112–134. doi:10.1016/j.epsl.2018.04.062

Cai, J., Chen, X., Xu, X., Tang, J., Wang, L., Guo, C., et al. (2017). Rupture mechanism and seismotectonics of the M_s6.5 Ludian earthquake inferred from three-dimensional magnetotelluric imaging. *Geophys. Res. Lett.* 44, 1275–1285. doi:10.1002/2016GL071855

Cai, X., Cao, J., Zhu, J., and Cheng, X. (2018). System of crust-mantle ductile shear zone in the continental lithosphere in China. *Earth Sci. Front.* 15 (3), 36–54. (in Chinese). doi:10.1016/s1872-5791(08)60061-5

Caldwell, T., Bibby, H., and Brown, C. (2004). The magnetotelluric phase tensor. *Geophys. J. Int.* 158, 457–469. doi:10.1111/j.1365-246X.2004.02281.x

China Regional Geology Guangxi Chronicle (2016). *Guangxi regional geological survey area summary and service product development ("China regional geology · Guangxi Chronicle") project*. Geological Publishing House. (in Chinese).

Egbert, G., and Booker, J. (1986). Robust estimation of geomagnetic transfer functions. *Geophys. J. R. Astr. Soc.* 87, 173–194. doi:10.1111/j.1365-246X.1986.tb04552.x

Egbert, G., and Kelbert, A. (2012). Computational recipes for electromagnetic inverse problems. *Geophys. J. Int.* 189, 251–267. doi:10.1111/j.1365-246X.2011.05347.x

Fan, P., Shen, X., and Huang, Q. (2022). Crust structures beneath M_s5.2 Beiliu earthquake focal region in Guangxi province constrained by receiver functions and surface wave dispersion. *Geotect. Metallogenia* 46 (3), 633–644. (in Chinese). doi:10.16539/j.ddgzyckx.2022.03.016

Fialko, Y., and Jin, Z. (2021). Simple shear origin of the cross-faults ruptured in the 2019 Ridgecrest earthquake sequence. *Nat. Geosci.* 14, 513–518. doi:10.1038/s41561-021-00758-5

Flower, M., Zhang, M., Chen, C., Tu, K., and Xie, G. (1992). Magmatism in the South China basin. *Chem. Geol.* 97, 65–87. doi:10.1016/0009-2541(92)90136-S

Gamble, T., Goubau, W., and Clarke, J. (1979). Error analysis for remote reference magnetotellurics. *Geophysics* 44 (5), 959–968. doi:10.1190/1.1440988

Ge, T., Chen, Y., and Zhang, C. (2022). Study of hainan mantle plume based on shear wave splitting method. *Acta Sci. Nat. Univ. Pekin.* 58 (2), 261–270. (in Chinese). doi:10.13209/j.0479-8023.2022.014

Goldberg, D., Melgar, D., Sahakian, V., Thomas, A., Xu, X., Crowell, B., et al. (2020). Complex rupture of an immature fault zone: A simultaneous kinematic model of the 2019 ridgecrest, ca earthquakes. *Geophys. Res. Lett.* 47, e2019GL086382. doi:10.1029/2019GL086382

Guo, S., Huang, X., Nong, J., He, Z., Sun, M., Li, W., et al. (2020). Deformation characteristics and ^{40}Ar-^{39}Ar age of the sanbao ductile shear zone on the northwestern margin of Yunkai block, south China. *Geotect. Metallogenia* 44 (3), 357–366. (in Chinese). doi:10.16539/j.ddgzyckx.2020.03.003

Hall, R. (2002). Cenozoic geological and plate tectonic evolution of SE Asia and the SW pacific: Computer-based reconstructions, model and animations. *J. Asian Earth Sci.* 20 (4), 353–431. doi:10.1016/S1367-9120(01)00069-4

Han, J., Zhan, Y., Sun, X., Zhao, G., Liu, X., Bao, Y., et al. (2022). Characteristics and processing of magnetotelluric data under strong electromagnetic interference environment. *Seismol. Geol.* 44 (3), 736–752. (in Chinese). doi:10.3969/j.issn.0253–4967.2022.03.011

He, X., Liang, H., Zhang, P., and Wang, Y. (2021). The 2019 M_s4.2 and 5.2 Beiliu earthquake sequence in South China: Complex conjugate strike-slip faulting revealed by rupture directivity analysis. *Seismol. Res.Lett.* 92 (6), 3327–3338. doi:10.1785/0220210008

Heise, W., Caldwell, T., Bibby, H., and Bannister, S. (2008). Three-dimensional modelling of magnetotelluric data from the Rotokawa geothermal field, Taupo Volcanic Zone, New Zealand. *Geophys. J. Int.* 173, 740–750. doi:10.1111/j.1365-246X.2008.03737.x

Hu, X., Lin, W., Yang, W., and Yang, B. (2020). A review on developments in the electrical structure of craton lithosphere. *Sci. China Earth Sci.* 63 (11), 1661–1677. (in Chinese). doi:10.1007/s11430-019-9653-2

Huang, H., Tosi, N., Chang, S., Xia, S., and Qiu, X. (2015). Receiver function imaging of the mantle transition zone beneath the South China B lock. *Geochem, Geophys, Geosyst* 16, 3666–3678. doi:10.1002/2015GC005978

Huang, Q., Shen, X., Wang, W., Xu, X., Zhou, Q., Huang, H., et al. (2022). Short-period dense array ambient noise imaging in the source area of the Guangxi Beiliu earthquake. *Chin. J. Geophys.* 65 (8), 2917–2930. (in Chinese). doi:10.6038/cjg2022P0221

Huang, Q. (2000). The characteristics of some important basic geology in Guangxi. *Guangxi Geol.* 13 (3), 3–12. (in Chinese).

Jia, Z., Wang, X., and Zhan, Z. (2020). Multifault models of the 2019 Ridgecrest sequence highlight complementary slip and fault junction instability. *Geophys. Res. Lett.* 47, e2020GL089802. doi:10.1029/2020GL089802

Jiang, D., Lin, S., and Williams, P. (2001). Deformation path in high-strain zones, with reference to slip partitioning in transpressional plate-boundary regions. *J. Struct. Geol.* 23, 991–1005. doi:10.1016/S0191-8141(00)00170-X

Jiang, W., Lin, J., and Zhao, Y. (1992). Focal mechanism of small earthquakes and characteristics of tectonic stress field in South China. *Earth. Res. China.* 8 (1), 36–42. (in Chinese).

Lebedev, S., and Nolet, G. (2003). Upper mantle beneath Southeast Asia from S velocity tomography. *J. Geophys. Res.* 108 (B1), 2048. doi:10.1029/2000JB000073

Lei, J., Zhao, D., Steinberger, B., Wu, B., Shen, F., and Li, Z. (2009). New seismic constraints on the upper mantle structure of the Hainan plume. *Earth Planet. Sci. Lett.* 173, 33–50. doi:10.1016/j.pepi.2008.10.013

Li, B., Li, X., Nie, G., Zhao, X., Wei, W., Zhong, D., et al. (2019). Seismogenic structure of the Beiliu M_s5.2 earthquake in Guangxi. *North. earth. scie.* 37 (S), 17–23. (in Chinese). doi:10.3969/j.issn.1003-1375.2019.S.004

Liu, H., Guo, L., and Hong, Y. (2005). Showing of continental ductile strike slipping: An attempt on Genesis of gneissosity of plutonic rocks in Yunkai area, Western Guangdong. *Mineral Resour. Geol.* 5, 533–536. (in Chinese).

Mao, X., Ye, G., Zhang, Y., Jin, S., and Wei, W. (2021). Electric structure of the southern section of the Jiangnan orogenic belt and its tectonic implications. *Chin. J. Geophys.* 64 (11), 4043–4059. (in Chinese). doi:10.6038/cjg2021O0424

Martí, A., Queralt, P., Marcuello, A., Ledo, J., Rodríguez-Escudero, E., Martínez-Díaz, J., et al. (2020). Magnetotelluric characterization of the Alhama de Murcia Fault (Eastern Betics, Spain) and study of magnetotelluric interstation impedance inversion. *Earth Planets Space* 72, 16. doi:10.1186/s40623-020-1143-2

Means, W. (1995). Shear zones and rock history. *Tectonophysics* 247 (1-4), 157–160. doi:10.1016/0148-9062(96)89824-x

Mohan, K., Rastogi, B., and Chaudhary, P. (2015). Magnetotelluric studies in the epicenter zone of 2001, Bhuj earthquake. *J. Asian Earth Sci.* 98, 75–84. doi:10.1016/j.jseaes.2014.10.019

Pan, G., Xiao, Q., Lu, S., Deng, J., Feng, Y., Zhang, K., et al. (2009). Subdivision of tectonicunits in China. *Chin. Geol.* 36 (1), 1–28. (in Chinese).

Peng, S., and Wu, G. (1994). Tectonic evolution of wuchuan-sihui fault zone and its relationship with gold mineralization. *J. Shenyang Inst. Gold Technol.* 13 (2), 109–115. (in Chinese).

Peng, Y., Sun, X., Zhan, Y., Zhao, L., Luo, Q., Liu, X., et al. (2022). 3D deep electrical structure and seismogenic environment in the Western section of the Zhangjiakou-Bohai fault zone. *Front. Earth Sci.* 10, 966192. doi:10.3389/feart.2022.966192

Qin, X., Li, J., Li, R., et al. (2008). *Formation and evolution of the Bobai-Cenxi orogenic belt in the northern margin of the Yunkai block*. Beijing: China Land Press. (in Chinese).

Qin, X., Wang, Z., Gong, J., Zhao, G., Shi, H., Zhan, J., et al. (2017). The confirmation of caledonian intermediate-mafic volcanic rocks in northern margin of Yunkai block: Evidence for early paleozoic paleo-ocean basin in southwestern segment of qinzhou-hangzhou joint belt. *Acta. Pet. Sin.* 33 (3), 791–809. (in Chinese).

Qiu, Y., and Liang, X. (2006). Evolution of basin-range coupling in the Yunkai dashan-shiwan dashan area, Guangdong and Guangxi: With a discussion of several tectonic problems of south China. *Geol. Bull. China.* 25 (3), 340–347. (in Chinese).

Shen, Y., Kang, Y., and Xu, G. (2013). The crustal thickness and Poisson's ratio distribution in Guangdong and its adjacent areas. *Earth. Res. China.* 29 (2), 210–218. (in Chinese).

Shu, L. (2006). Pre-devonian tectonic evolution of South China: From cathaysian block to caledonian foled orogenic belt. *Geol. J. China Univ.* 12, 418–431. (in Chinese).

Sun, X., Zhan, Y., Unsworth, M., Egbert, G., Zhang, H., Chen, X., et al. (2020). 3-D Magnetotelluric imaging of the easternmost Kunlun fault: Insights into strain partitioning and the seismotectonics of the Jiuzhaigou M_s7.0 earthquake. *J. Geophys. Res.* 125, e2020JB019731. doi:10.1029/2020JB019731

Sun, X., Zhan, Y., Zhao, L., Chen, X., Sun, J., Li, C., et al. (2019). Electrical structure of the Kunlun–Qinling fault system, northeastern Tibetan Plateau, inferred from 3-D inversion of magnetotelluric data. *J. Asian Earth Sci.* 181, 103910. doi:10.1016/j.jseaes.2019.103910

Unsworth, M., and Bedrosian, P. (2004). On the geoelectric structure of major strike-slip faults and shear zones. *Earth Planets Space* 56, 1177–1184. doi:10.1186/bf03353337

Wan, Y. (2010). Contemporary tectonic stress field in China. *Earthq. Sci.* 23, 377–386. doi:10.1007/s11589-010-0735-5

Wang, C., and Huang, J. (2012). Mantle transition zone structure around Hainan by receiver function analysis. *Chin. J. Geophys.* 55 (4), 1161–1167. (in Chinese). doi:10.6038/j.issn.0001-5733.2012.04.012

Wang, M., and Shen, Z. (2020). Present-day crustal deformation of continental China derived from GPS and its tectonic implications. *J. Geophys. Res. Solid Earth.* 125 (2), e2019JB018774. doi:10.1029/2019JB018774

Wang, X., Xu, D., Wang, L., Zhou, D., Hu, J., and Ke, X. (2020). Reworking of indosinian tectono-thermal events in the Yunkai massif:gneissic multi-mineral U-Pb geochronological evidence. *Earth Sci.* 45 (5), 1653–1675. (in Chinese). doi:10.3799/dqkx.2019.151

Wang, X., Zhang, G., Zhou, J., Li, D., Luo, W., Hu, Y., et al. (2018). Crust and upper mantle electrical resistivity structure in the Longmenshan tectonic belt and its relationship with Wenchuan and Lushan earthquake. *Chin. J. Geophys.* 61 (5), 1984–1985. (in Chinese). doi:10.6038/cjg2018M0233

Wang, Z., Zhou, Y., Zhang, H., and Zhou, H. (1998). The basement evolution and mineralization of Yunkai Massif, South China. *Prog. Precam Res.* 21 (1), 45–53. (in Chinese).

Wei, S., and Chen, Y. (2016). Seismic evidence of the Hainan mantle plume by receiver function analysis in southern China. *Geophys. Res. Lett.* 43, 8978–8985. doi:10.1002/2016GL069513

Wen, X., Shen, X., and Zhou, Q. (2022). Study on the characters of the aftershocks of Beiliu 5.2 earthquake using machine learning method and dense nodal seismic array. *Chin. J. Geophys.* 65 (9), 3297–3308. (in Chinese). doi:10.6038/cjg2022P0430

Wessel, P., Smith, W., Scharroo, R., Luis, J., and Wobbe, F. (2013). Generic mapping tools: Improved version released. *Eos Trans. AGU.* 94, 409–410. doi:10.1002/2013eo450001

Xia, S., Zhao, D., Sun, J., and Huang, H. (2016). Teleseismic imaging of the mantle beneath southernmost China: New insights into the Hainan plume. *Gondwana Res.* 36, 46–56. doi:10.1016/j.gr.2016.05.003

Xu, S., Unsworth, M., Hu, X., and Mooney, W. (2019). Magnetotelluric evidence for asymmetric simple shear extension and lithospheric thinning in south China. *J. Geophys. Res. Solid Earth.* 124, 104–124. doi:10.1029/2018JB016505

Yan, C., Xiang, W., Su, S., Zhou, B., Huang, H., Pan, Y., et al. (2019). Consistency analysis of seismic records and strong motion records in Guangxi taking the Guangxi Beiliu M_s5.2 earthquake as an example. *North. earth. scie.* 37 (S), 12–16. (in Chinese). doi:10.3969/j.issn.1003-1375.2019.S.003

Yan, D., Zhou, M., Song, H., and Malpas, J. (2002). Where was South China located in the reconstruction of Rodinia? *Earth Sci. Front.* 9 (4), 249–256. (in Chinese).

Yan, J., Lü, Q., Luo, F., Chen, A., Ye, G., Zhang, Y., et al. (2019). Where is qinzhou-hangzhou juncture belt? Evidence from integrated geophysical exploration. *Chin. Geol.* 46 (4), 690–703. (in Chinese). doi:10.12029/gc20190402

Yan, Q., Shi, X., and Castillo, P. (2014). The late mesozoic- cenozoic tectonic evolution of the South China Sea: A petrologic perspective. *J. Asian Earth Sci.* 85, 178–201. doi:10.1016/j.jseaes.2014.02.005

Yan, Q., Shi, X., Metcalfe, L., Liu, S., Xu, T., Kornkanitnan, N., et al. (2018). Hainan mantle plume produced late Cenozoic basaltic rocks in Thailand, Southeast Asia. *Sci. Rep.* 8, 2640–2714. doi:10.1038/s41598-018-20712-7

Ye, G. (2008). Discussion on the formation mechanism of Maoming Basin in Guangdong province. *West-china Explor. Eng.* 2008(7), 141–144. (in Chinese).

Ye, T., Chen, X., Huang, Q., and Cui, T. (2021). Three-dimensional electrical resistivity structure in focal area of the 2021 Yangbi M_s6.4 Earthquake and its implication for the seismogenic mechanism. *Chin. J. Geophys.* 64 (7), 2267–2277. (in Chinese). doi:10.6038/cjg2021O0523

Ye, T., Chen, X., Huang, Q., Zhao, L., Zhang, Y., and Uyeshima, M. (2020). Bifurcated crustal channel flow and seismogenic structures of intraplate earthquakes in Western Yunnan, China as revealed by three-dimensional magnetotelluricimaging. *J. Geophys. Res.* 125, e2019JB018991. doi:10.1029/2019JB018991

Ye, T., Huang, Q., Chen, X., Zhang, H., Chen, Y. J., Zhao, L., et al. (2018). Magma chamber and crustal channel flow structures in the Tengchong volcano area from 3-D MT inversion at the intracontinental block boundary southeast of the Tibetan Plateau. *J. Geophys. Res.* 123, 11112–11126. doi:10.1029/2018JB015936

Yin, K., Wu, S., and Wang, L. (1996). Focal mechanism and seismic geologic conditions of the Beibuwan earthquakes. *South China J. Seismol.* 16 (3), 77–81. (in Chinese).

Yoshimura, R., Oshiman, N., Uyeshima, M., Ogawa, Y., Mishina, M., Toh, H., et al. (2008). Magnetotelluric observations around the focal region of the 2007 noto hanto earthquake (M_j6.9), central Japan. *Earth Planet Sp.* 60, 117–122. doi:10.1186/BF03352771

Yu, C., Zhang, G., Wang, X., Luo, W., Li, D., Cai, X., et al. (2017). Deep electrical resistivity structure of Sanjiang Area of west Yunnan and its significance. *Chin. J. Geophys.* 60 (6), 2385–2396. (in Chinese). doi:10.6038/cjg20170628

Yu, J., Wei, Z., Wang, L., Shu, L., and Sun, T. (2006). Cathaysia block: A young continent composed of ancient materials. *Geol. J. China Univ.* 12 (4), 440–447. (in Chinese).

Yu, N., Wang, X., Li, D., Li, X., Wang, E., Kong, W., et al. (2022). The mechanism of deep material transport and seismogenic environment of the Xiaojiang fault system revealed by 3-D magnetotelluric study. *Sci. China Earth Sci.* 65 (6), 1128–1145. doi:10.1007/s11430-021-9914-3

Yuan, Y., Ma, Y., Hu, S., Guo, D., and Fu, X. (2006). Present-day geothermal characteristics in South China. *Chin. J. Geophys.* 49 (4), 1005–1014. (in Chinese). doi:10.1002/cjg2.922

Zhan, Y., Liang, M., Sun, X., Huang, F., Zhao, L., Gong, Y., et al. (2021). Deep structure and seismogenic pattern of the 2021.5. 22 Madoi (Qinghai) M_s7.4 earthquake. *Chin. J. Geophys.* 64 (7), 2232–2252. (in Chinese). doi:10.6038/cjg2021O0521

Zhan, Y., Yang, H., Zhao, G., Zhao, L., and Sun, X. (2017). Deep electrical structure of crust beneath the Madongshan step area at the Haiyuan fault in the northeastern margin of the Tibetan plateau and tectonic implications. *Chin. J. Geophys.* 60 (6), 2371–2384. (in Chinese). doi:10.6038/cjg20170627

Zhan, Y., Zhao, G., Unsworth, M., Wang, L., Chen, X., Li, T., et al. (2013). Deep structure beneath the southwestern section of the Longmenshan fault zone and seimogenetic context of the 4.20 Lushan M_s7.0 earthquake. *Chin. Sci. Bull.* 58 (28), 3467–3474. doi:10.1007/s11434-013-6013-x

Zhang, G., Guo, A., Wang, Y., Li, S., Dong, Y., Liu, S., et al. (2013). a1Tectonics of South China continent and its implications. *Sci. China Earth Sci.* 56, 1804–1828. (in Chinese). doi:10.1007/s11430-013-4679-1

Zhang, H., Huang, Q., Zhao, G., Guo, Z., and Chen, Y. (2016). Three-dimensional conductivity model of crust and uppermost mantle at the northern Trans North China Orogen: Evidence for a mantle source of Datong volcanoes. *Earth Planet. Sci. Lett.* 453, 182–192. doi:10.1016/j.epsl.2016.08.025

Zhao, C., Hu, J., Zhou, Y., and Guo, M. (2021). The deep seismogenic environment of Beiliu M_s5.2 earthquake in yulin, Guangxi on october 12, 2019. *Sei. Geo. Obser. Resarch.* 42 (2), 116–118. (in Chinese). doi:10.3969/j.issn.1003-3246.2021.02.022

Zhao, G., Unsworth, M. J., Zhan, Y., Wang, L., Chen, X., Jones, A. G., et al. (2012). Crustal structure and rheology of the Longmenshan and Wenchuan M_w7.9 earthquake epicentral area from magnetotelluric data. *Geology* 40 (12), 1139–1142. doi:10.1130/G33703.1

Zhao, L., Sun, X., Zhan, Y., Yang, H., Wang, Q., Hao, M., et al. (2022). The seismogenic model of the Menyuan M_s6.9 earthquake on January 8, 2022, Qinghai Province and segmented extensional characteristics of the Lenglongling fault. *Chin. J. Geophys.* 65 (4), 1536–1546. (in Chinese). doi:10.6038/cjg2022Q0051

Zhao, L., Zhan, Y., Sun, X., Hao, M., Zhu, Y., Chen, X., et al. (2019). The hidden seismogenic structure and dynamic environment of the 21 January Menyuan, Qinghai,

M_s6.4 earthquake derived from magnetotelluric imaging. *Chin. J. Geophys.* 62 (6), 2088–2100. (in Chinese). doi:10.6038/cjg2019M0204

Zhao, Y. (1983). Focal mechanism of Pingguo M5.0 earthquake 19 october 1977. *South China J. Seismol.* 3 (S1), 78–80. (in Chinese). doi:10.13512/j.hndz.1983.s1.012

Zhong, Z., You, Z., Zhou, H., and Han, Y. (1996). Composition, evolution and basic structural framework of basement of Yunkai uplift between Guangxi and Guangdong Provinces. *Regional Geol. China* 14 (1), 36–43. (in Chinese).

Zhou, X. H., and Armstrong, R. (1982). Cenozoic volcanic rocks of eastern China-secular and geographic trends in chemistry and strontium isotopic composition. *Earth Planet. Sci. Lett.* 58 (3), 301–329. doi:10.1016/0012-821X(82)90083-8

Zhou, Y., Yan, C., Xiang, W., Zhou, B., and Wen, X. (2019). Source parameter of the Cangwu M_s5.4 earthquake' 31 july' 2016. *Seismol. Geol.* 41 (1), 150–161. (in Chinese). doi:10.3969/j.issn.0253-4967.2019.01.010

Zhou, Z., Lv, J., and Zhou, B. (2021). *Earthquake prediction index system in SouthSouth China*. Beijing: Seismological Press. (in Chinese).

Zhu, G., Liu, G., Dunlap, W., Teyssier, C., Wang, Y., and Nie, M. (2004). $^{40}Ar/^{39}Ar$ chronological evidence of synorogenic strike-slip movement in the Zhenglu Fault Zone. *Chin. Sci. Bull.* 49 (2), 191–198. (in Chinese).

Zou, H., and Fan, Q. (2010). U-Th isotopes in hainan basalts: Implications for sub-asthenospheric origin of EM2 mantle endmember and the dynamics of melting beneath hainan island. *Lithos* 116, 145–152. doi:10.1016/j.lithos.2010.01.010

frontiers | Frontiers in Earth Science

TYPE Original Research
PUBLISHED 26 January 2023
DOI 10.3389/feart.2022.992858

OPEN ACCESS

EDITED BY
Giovanni Martinelli,
National Institute of Geophysics and Volcanology, Italy

REVIEWED BY
Yaxin Bi,
Ulster University, United Kingdom
Danhua Xin,
Southern University of Science and Technology, China
Zhenguo Zhang,
Southern University of Science and Technology, China

*CORRESPONDENCE
Fenghe Ding,
dingfenghe@126.com

SPECIALTY SECTION
This article was submitted to Solid Earth Geophysics, a section of the journal Frontiers in Earth Science

RECEIVED 13 July 2022
ACCEPTED 01 December 2022
PUBLISHED 26 January 2023

CITATION
Luo G, Ding F, Ma H and Yang M (2023), Pre-quake frequency characteristics of *Ms* ≥7.0 earthquakes in mainland China. *Front. Earth Sci.* 10:992858. doi: 10.3389/feart.2022.992858

Pre-quake frequency characteristics of *Ms* ≥7.0 earthquakes in mainland China

Guofu Luo, Fenghe Ding*, Heqing Ma and Mingzhi Yang

Seismological Bureau of the Ningxia Hui Autonomous Region, Yinchuan, China

In this study, natural orthogonal expansion was performed on earthquake frequencies to compute the pre-quake frequency fields of 9 *Ms* ≥7.0 earthquakes in mainland China from 1980 to 2020. The temporal and spatial pre-quake anomalies of these earthquakes were extracted from their frequency fields. We found that the majority of pre-quake temporal anomalies (i.e., variations exceeding two-times the absolute mean square error) of a strong earthquake are condensed within the first four frequency fields, and typically comprise multiple components. The temporal factor of the first frequency field usually accounts for the largest proportion of these anomalies (40%–60% of the entire field). Most *Ms* ≥7.0 earthquakes exhibited long-term anomalies 5–8 years before their occurrence; some presented medium-term anomalies 1–2 years prior to the quake, and only a few presented short-term and imminent anomalies (≤3 months before the quake). Anomalous seismic hazard zones have high-gradient turning points in regional frequency-field contour maps, and the epicenters of strong earthquakes are often located in areas containing active faults that have contour values. Through the comparison of seismic frequency field and the traditional method of regional seismic activity frequency (3 months), it is shown that the frequency-field time factor has the advantages of diversified and rich abnormal information. The slope comparison between the frequency field and the cumulative frequency curve shows that the frequency anomaly time of the two is consistent, and the conclusion is reliable. Therefore, the seismic frequency method can predict the occurrence time and location of strong earthquakes, which is closer to the predictable seismic model.

KEYWORDS

earthquake frequency field, temporal factor, contour line, cumulative frequency, earthquakes with a magnitude of 7 or above in mainland China

1 Introduction

Before a strong earthquake there is an abnormal frequency of seismic activity around the source, wherein the frequency of seismic activity increases or decreases significantly compared with the normal level (Mei, 1996; Wyss and Habermann, 1998). Mogi (1969) studied the seismic activities around the focal area before the strong earthquake in Japan, and proposed for the first time that the frequency of earthquakes might increase or decrease significantly. Many subsequent studies have shown that there are frequent anomalous seismic signs around the focal points before most strong earthquakes, such as the 1988 Armenia Spitak *Ms*7.0 earthquake (Wyss and Habermann, 1998), 1992 US Landers *M*s 7.3 earthquake (Wiemer and Wyss, 1994), 2011 Japan *M*s 9.0 earthquake (Katsumata, 2011), 2014 Chile Iquique M_W 8.1 earthquake (Aden-Antoniow et al., 2020) and the 2015 Chile Illapel M_W 8.3 earthquake (Jarmolowski et al., 2021). Therefore, it is of great significance to study the abnormal variation characteristics of earthquake frequency for the development of earthquake prediction.

Some researchers have begun to study the anomaly of regional seismic activity frequency before strong earthquakes by using the traditional method of regional seismic variation over time. For instance, Feng et al. (2009) studied 22 moderate-to-strong earthquakes that occurred in the northeastern margin of the Qinghai–Tibet Block from 1980 to 2008, and found that 17 of these earthquakes were preceded by significant increases in the frequency of small earthquakes. Li et al. (2017) analyzed the data from the seismograph network around the Sichuan–Yunnan rhombic block and found significant anomalous increases in the local earthquake frequency prior to the 2013 *M*s 7.0 Lushan Earthquake and 2014 *M*s 6.5 Ludian Earthquake. This was an important result in terms of recognizing the precursors of strong earthquakes. Ma et al. (2008) studied the cumulative number of small earthquakes in the Qilian Mountain fault zone and variations in the earthquake frequency fields of *M*s ≥6.0 earthquakes that occurred in China. Zhang and Li (2021) noted that the activity of small earthquakes around the focal point of the Maduo *M*s 7.4 earthquake in Qinghai province increased significantly before the earthquake, and that the Luqu earthquake swarm was formed. They theorized that the Luqu area is a stress-sensitive area, which has a good corresponding relationship to the Maduo *M*s 7.4 earthquake. Ma et al. (2022) studied 15 *M*s ≥7.0 earthquakes in mainland China, and the cumulative frequency of earthquakes showed exponential growth. They found that at the annual scale non-linear growth characteristics are present in a cumulative number of small earthquakes before Ms ≥7.0 earthquakes. They also demonstrated that the gradient of the cumulative earthquake frequency graph changes prior to a moderate or strong earthquake owing to the formation of a seismogenic stress state in the region. The research methods of these scholars are effectively similar, in that they are one-dimensional images of earthquake frequency variable with time, which can predict the occurrence time of strong earthquakes.

The application of field theory to study anomalies before strong earthquakes is relatively new, having only been developed in recent years. The natural orthogonal expansion method (Ma et al., 1993) is used to calculate the energy field or frequency field before a strong earthquake. Two-dimensional images of the time and space of typical fields are studied, so as to predict the time and location of strong earthquakes. In particular, seismic energy fields have been studied intensively by several authors. For example, energy field theory was used for the first time by Yang and Ma (2004) to study how temporal anomalies in seismic energy are related to strong earthquakes in Ningxia. Luo and Yang (2005) conducted a systematic analysis of the relationship between spatial and temporal seismic energy field anomalies and moderate-to-strong earthquakes in Yunnan based on the seismic energy field in the region since 1975. Luo et al. (2011a) extracted spatiotemporal anomalies from the seismic energy field of the northwest Yunnan to south Yunnan region and accurately predicted the strong earthquakes that occurred in this region over the next 3 years. Luo et al. (2011b) and Yang and Ma (2011), Yang and Ma (2012) discovered medium- and short-term temporal and spatial anomalies in the seismic energy field of Wenchuan prior to the 2008 *M*s 8.0 Wenchuan Earthquake that corresponded closely to the earthquake event. Ma and Yang (2012) analyzed the pre-quake temporal changes in the seismic energy field of the area around the epicenter of the 2010 *M*s 7.1 Yushu Earthquake and the Yushu Fault and found that spatiotemporal energy-field anomalies preceded the earthquake by approximately half a year. Yang and Ma (2013) reviewed the pre-quake temporal factors of seismic activity fields around the epicenters of 30 *M*s ≥6.0 earthquakes in China and found that most of these earthquakes were preceded by significant temporal anomalies. Luo et al. (2014) studied pre-quake spatiotemporal anomalies in the seismic energy field of the epicenter of the 2013 *M*s 6.6 Minxian Earthquake and analyzed the correspondence between the evolution of spatiotemporal anomalies in the pre-quake seismic energy field and the epicenter of the *M*s 6.6 earthquake. Yang et al. (2017) studied the strain fields of *M*s ≥6.0 earthquakes in China and found that the temporal anomalies of such fields are more useful as earthquake predictors than those of seismic energy fields. Luo et al. (2018) studied the pre-quake seismic strain field of the 2017 *M*s 7.0 Jiuzhaigou Earthquake and compared the temporal evolution of the strain anomalies of this earthquake with that of the 1976 *M*s 7.2 Songpan–Pingwu Earthquake. Luo et al. (2019a) studied the pre-quake spatiotemporal anomalies of seismic strain fields around the epicenter of large earthquakes with an emphasis on their relationship to the mainshock. Luo et al. (2019b) studied how the seismic strain field of the *M*s 8.0 Wenchuan Earthquake affected the subsequent *M*s ≥6.0 earthquakes in the Longmenshan Fault and other nearby faults by investigating the interactions between strong earthquakes from the perspective

of seismic strain evolution. Ma et al. (2020) applied a natural orthogonal function to study the variation of frequency field time factor of 7 *Ms* 7 earthquakes and 8 *Ms* 6 earthquakes and found that frequency field anomalies before strong earthquakes mainly concentrated in the first and second typical fields.

On the basis of the above research, we extracted the spatial isoline anomalies of the frequency field, studied the spatiotemporal abnormal variation characteristics of the frequency field of seismic activity before strong earthquakes in mainland China, and considered the abnormal variation rules of *Ms* ≥7.0 earthquakes. Next, through the comparison of seismic frequency field and the traditional method of regional seismic activity frequency (3 months), it was found that the frequency field time factor has the advantages of diversified and rich abnormal information. A slope comparison between the frequency field and the cumulative frequency curve then revealed that the frequency anomaly time of the two is consistent, and the conclusion is reliable. Lastly, the seismic frequency method was used to predict the occurrence time and location of strong earthquakes, and was found to be closer to the predictable seismic model.

2 Data and methods

2.1 Convolution regression method

The earthquake frequencies of a region are random variables that can be decomposed *via* natural orthogonal expansion into spatial and temporal functions. These functions comprise the earthquake frequency field, *N*. A random field can then be created by gridding the study area according to its local earthquake frequencies, that is, by dividing the study area, ΔN, into *n* elements of equal areas such that $\Delta N = \Delta x \times \Delta y$. The central coordinates of each element are $(x_j, y_j)(j = 1, 2, \ldots, n)$. The observation time, t_i, is then divided into m intervals of length Δt such that $t_i = \Delta t \times I(i = 1, 2, \ldots, m)$. The observed seismic activity frequency of each element during each time interval is then calculated and recorded as N_{ij}; these values constitute the function field of the spatiotemporal coordinates $(x_i, y_i, t_j)(i, j = 1, 2, \ldots, n)$.

We herein express *N*, the frequency of the seismic activity applied in the gridding of the study area, as $N = \sum_i N_{ij}$, which has the following matrix representation:

$$N = \begin{bmatrix} N_{11} & N_{12} & \cdots & N_{1n} \\ N_{21} & N_{22} & \cdots & N_{2n} \\ \vdots & \vdots & \vdots & \vdots \\ N_{m1} & N_{m2} & \cdots & N_{mn} \end{bmatrix}, \tag{1}$$

where $N_{ij}(i = 1, 2, \ldots, m, j = 1, 2, \ldots, n)$ is the cumulative earthquake frequency of the *j*-th grid (spatial factor) during the *i*-th time interval (temporal factor). A natural orthogonal expansion is then performed on *N* by decomposing the matrix into the sum of the products of the orthogonal spatial functions *x* and orthogonal temporal functions *T*, that is,

$$N_{ij} = \sum_{p=1}^{n} T_{ip} X_{pj} \begin{cases} i = 1, 2, \cdots, m \\ j = 1, 2, \cdots, n \end{cases}. \tag{2}$$

These functions are orthogonal and normalized and satisfy the conditions

$$\sum_{j=1}^{n} x_{kj} x_{lj} = \begin{cases} 0 & k \neq l \\ 1 & k = l \end{cases}, \tag{3}$$

$$\sum_{i=1}^{m} T_{ik} T_{il} = \begin{cases} 0 & k \neq l \\ \lambda_k & k = l \end{cases}. \tag{4}$$

We can then define the matrix $R = N'N$ and solve for the characteristic equation of *R*, that is,

$$\begin{bmatrix} R_{11} & R_{12} & \cdots & R_{1n} \\ R_{21} & R_{22} & \cdots & R_{2n} \\ \cdots & \cdots & \cdots & \cdots \\ R_{n1} & R_{n2} & \cdots & R_{nn} \end{bmatrix} \begin{bmatrix} x_1 \\ x_2 \\ \cdots \\ x_n \end{bmatrix} = \lambda \begin{bmatrix} x_1 \\ x_2 \\ \cdots \\ x_n \end{bmatrix}, \tag{5}$$

from which we obtain the eigenvectors $\vec{x}_k$ and eigenvalues $\lambda_k (k = 1, 2, \ldots, n)$. The temporal factors can then be expressed as

$$\vec{T}_k = N\vec{x}_k \quad k = 1, 2, \cdots n. \tag{6}$$

The eigenvectors $\vec{x}_k$ (frequency field) represent the spatial distribution of earthquake frequencies in each field, and the temporal factor $\vec{T}_k$ represents the time dependence of the frequency field $\vec{x}_k$ as well as reflecting the dynamics of each time-frequency field. The eigenvectors corresponding to the first few eigenvalues of *R* (which are arranged in decreasing order) are sufficiently precise to fit the entire frequency field. In other words, we can approximate the entire frequency field by superimposing the first few eigenvectors (frequency fields), with the changes that occur in these first fields representing the spatiotemporal characteristics of the frequency field corresponding to the study area. If the sum of all *n* eigenvalues is b_0, the precision of fit between the first *l* frequency fields and the entire field is

$$r_l = \sum_{p=1}^{l} \lambda_p / b_0, \tag{7}$$

where λ_p is the *p*-th characteristic root.

In summary, natural orthogonal expansion condenses most of the information carried by an earthquake frequency field into the "primary" frequency fields that correspond to its largest eigenvalues. Frequency fields that are either invariant or poorly correlated with large quakes can then be excluded, thus simplifying the problem to the anomalies of the first few frequency fields.

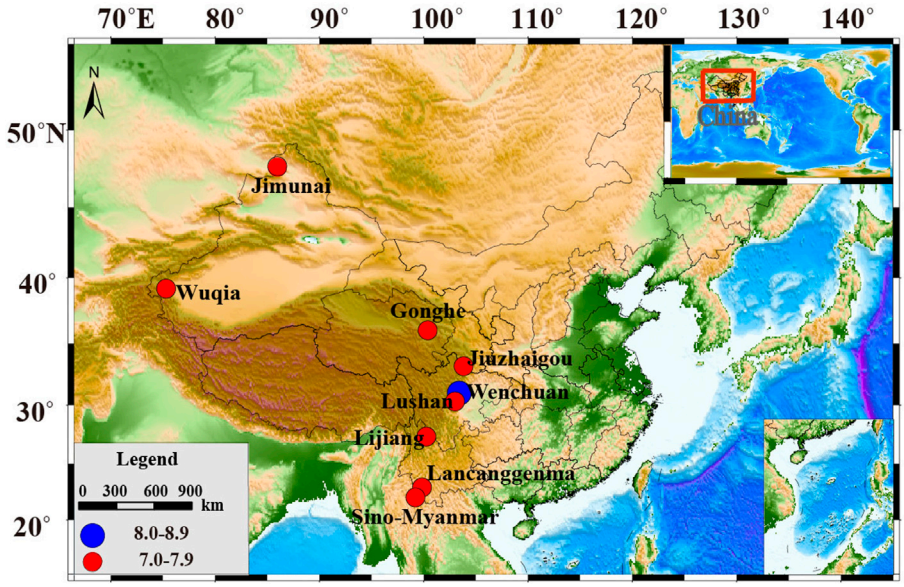

FIGURE 1
Locations of 9 *Ms* ≥7.0 earthquakes in mainland China. Red circles represent magnitude-7.0–7.9 earthquakes, and blue circles represent magnitude-8.0–8.9 earthquakes, the spatial distribution of epicenters in the Chinese mainland from 1980 to 2022.

2.2 Data and case examples

The earthquake data used in this study were obtained from the official national earthquake catalog provided by the China Earthquake Networks Center. The b-values of the study areas that correspond to the epicenters of 9 *Ms* ≥7.0 earthquakes were estimated from the earthquake catalog and their minimum magnitudes of completeness, *Mc*. One of the considerations in this study was the difference between frequency and energy fields. Small earthquakes (*Ms* 2-3) reflect the background seismicity of each region and have a significant effect on the earthquake frequency fields; large earthquakes, which are primarily controlled by seismogenic mechanisms, have a stronger effect on the energy field. To ensure that the selected dataset adequately reflected the background seismicity of a region as well as the seismogenic processes of large earthquakes, earthquakes between *Mc* and M_L 5.4 (*Ms* 5.0) were included in the dataset. In principle, the aftershocks of each study area should also be included in the dataset. However, for cases in which the study areas of *Ms* ≥7.0 earthquakes overlapped, it was necessary to eliminate the aftershocks of the earlier earthquake to avoid affecting the later earthquake. For example, the study areas of the 2008 *Ms* 8.0 Wenchuan Earthquake and 2013 *Ms* 7.0 Lushan Earthquake overlapped; in this case, it was necessary to omit the aftershocks of the *Ms* 8.0 Wenchuan Earthquake from the dataset. The grid was divided into square cells of 1.0°x1.0°, and the time interval was selected as 3 months. The data were discretized and calculated, and the specific spatiotemporal scale was discussed in the following paper. Earthquake frequency matrices, *N*, were constructed for each study area using Eq. 1. These matrices were then analyzed by natural orthogonal expansion and the corresponding *R* matrices were solved to obtain the eigenvalues of the frequency field, primary fields that correspond to these eigenvalues, temporal factors of these primary fields, and frequencies of the spatial grids of each study area.

Natural orthogonal expansion was used to analyze the pre-quake local frequency fields of all *Ms* ≥7.0 earthquakes in mainland China from 1980 to 2020 (Figure 1). However, based on Wang et al. (2017) studies of the disparities in the precision and sensitivity of the national seismograph network (especially in Tibet and parts of Qinghai, where the network is poorly developed), the seismic observation data of the following earthquakes were found to be insufficiently complete for the purposes of this study: the *Ms* 7.5 Earthquake in Mani, Tibet, on 8 November 1997; the *Ms* 8.1 earthquake to the west of the Kunlun Pass on 14 November 2001; and the *Ms* 7.1 earthquake in Yushu Tibetan Autonomous Prefecture on 14 April 2010. Therefore, the frequency fields of these earthquakes were not computed in this study.

2.3 Earthquake parameters and computational accuracy

The proposed method was first tested on the *Ms* 7.1 Wuqia Earthquake that occurred on 23 August 1985. The coordinates of

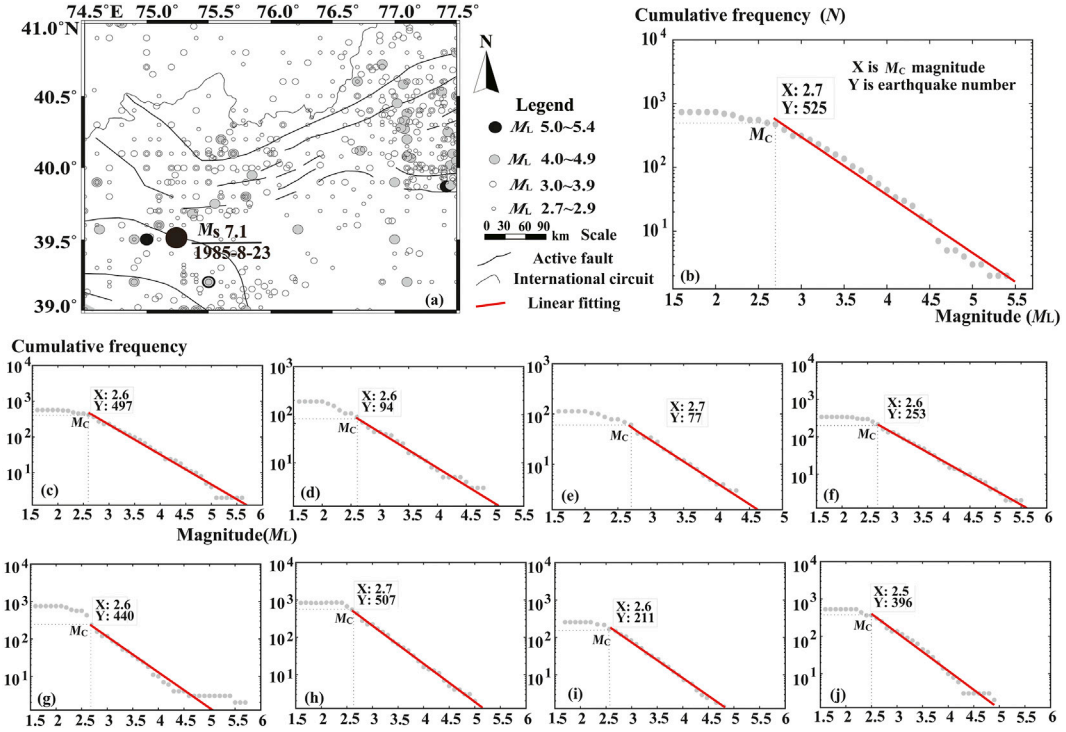

FIGURE 2
Spatial distribution of *Ms* 7.1 Wuxia earthquake epicenters, The gray circles represent earthquakes of magnitude 2.7 to 5.4 **(A)**.The G-R relationship of 9 earthquake cases above *Ms* 7 in the study area, the gray dot represents the cumulative number of earthquakes, and the red line represents the linear fit **(B–J)**. **(B)** 1985 *Ms* 7.1 Wuxia earthquake; **(C)** 1988 *Ms* 7.6 Lancang–Gengma earthquake; **(D)** 1990 *Ms* 7.0 Gonghe earthquake; **(E)** 1990 *Ms* 7.2 Jeminay earthquake; **(F)** 1995 *Ms* 7.3 Myanmar–China earthquake; **(G)** 1996 *Ms* 7.0 Lijiang earthquake; **(H)** 2008 *Ms* 8.0 Wenchuan earthquake; **(I)** 2013 *Ms* 7.0 Lushan earthquake; **(J)** 2017 *Ms* 7.0 Jiuzhaigou earthquake.

its study area are (74.5°–77.5°*E*, 39°–41°*N*) and the *b*-value of this area was estimated using the seismic data from January 1975 to July 1985. The *Mc* of this area was determined to be M_L = 2.7 according to the G-R equation (Figure 2). The study area was divided into 1.0°×1.0°grids, with a time interval of Δt = 1/4 years (3 months). The earthquake frequency field of the n grids (n = 6) and m time intervals (m = 42) was then computed. When l = 4, the first four frequency fields encompass 88.91% of the entire frequency field, which is equivalent to all of the pre-quake frequency field anomalies of the *Ms* 7.1 Wuqia Earthquake being condensed within these four primary frequency fields. In other words, the anomalies in the first four frequency fields were equivalent to all of the anomalies of the study area. The parameters of the other 8 *Ms* ≥7.0 earthquakes and their computed results are listed in Table 1. This table includes the selected earthquakes and their spatial and temporal ranges, the magnitudes of the weak earthquakes included in the frequency field, the number of computational grids and time intervals, the magnitudes of the first four eigenvalues, and the accuracy of fit between the first four frequency fields and the entire field. It is seen from the table that the study areas of most of the *Ms* ≥7.0 earthquakes were larger than 3°×3° and spanned ten years or more (Yang et al., 2017) except in a few special cases. For instance, the spatial and temporal ranges of the 2017 *Ms* 7.0 Jiuzhaigou Earthquake had to be selected in a different manner to account for the influence of the 2008 *Ms* 8.0 Wenchuan Earthquake. The accuracy of fit between the entire frequency field and first four frequency fields was always greater than 70%, and the fit was 100% for the 1988 *Ms* 7.6 Lancang–Gengma Earthquake. Therefore, most of the anomaly data carried by the earthquake frequency fields (regardless of location) have been condensed within the first four frequency fields, and the anomalies of the first four frequency fields are representative of all anomalies in the study areas. The temporal changes in the pre-quake frequency fields of the aforementioned earthquakes are shown in Figure 3. All changes in the temporal factors that were greater than two times the magnitude of the pre-quake mean square error were deemed to be anomalies. The anomalies were then classified as long-term, medium-term, short-term, or imminent anomalies and the primary frequency fields that induced these anomalies are identified in Table 2. These results served as a guide for subsequent comparisons between the pre-quake anomalies of each frequency field.

TABLE 1 Parameters and computed frequency fields of 9 *Ms* ≥7.0 Earthquakes in mainland China.

No	Earthquake	Number of grids,n and time intervalsm (n,m)	Number of earthquakes in dataset	Anomaly centroid (°N, °E)	Anomalous amplitude	Coordinates of the study area lat. (°) and long. (°)	Time span of the data	Range of seismic magnitudes (M_L)	First four eigenvalues	Accuracy *r*
1	1985-8-23 Wuqia (Xinjiang), M_s 7.1	(6,42)	525	(39.5,75.2) (40.2,76.0) (38.7,76.2)	1.1	39.0°–41.0°, 74.5°–77.5°	1975-01–1985-06	2.7–5.4	177.6046 72.4315 45.0674 25.8071	0.8891
2	1988-11-6 Lancang–Gengma (Yunnan)M_s 7.4	(4,55)	277	(23.0,100.0) (23.7,99.3)	1.4	21.5°–23.5°, 99.0°–101.0°	1975-01–1988-10	2.7–5.4	370.8477 133.8201 108.5304 90.9299	1.0000
3	1990-4-26 Gonghe (Qinghai), M_s 7.0	(6,41)	94	×	0.2	35.0°–38.0°, 99.0°–101.0°	1980-01–1990-03	2.6–5.4	42.8715 10.1152 6.7076 4.5336	0.9548
4	1990-6-14 Jeminay (Xinjiang), M_s 7.2	(6,42)	77	×	0.2	46.5°–48.5°, 84.0°–87.0°	1980-01–1990-05	2.7–5.4	18.2853 12.0240 8.9396 6.3606	0.8307
5	1995-7-12 China–Myanmar border, M_s 7.3	(6,42)	195	(22.0,99.5)	0.9	20.0°–23.0°, 98.5°–100.5°	1985-01–1995-06	2.7–5.4	119.8241 81.4368 27.2826 16.4039	0.9934
6	1996-2-3 Lijiang (Yunnan), M_s 7.0	(4,44)	440	(27.5,100.2)	1.7	26.5°–28.5°, 99.0°–101.0°	1985-01–1996-01	2.6–5.4	196.6908 75.8525 36.3662 15.8406	1.0000
7	2008-5-12 Wenchuan (Sichuan), M_s 8.0	(12,41)	507	(31.0,103.5) (30.0,102.5) (31.5,101.5)	1.3	30.0°–33.0°, 101.5°–105.5°	1998-01–2008-04	2.7–5.4	90.7340 65.7430 45.2748 40.3907	0.6755
8	2013-4-2 Lushan (Sichuan), M_s 7.0	(9,53)	211	(31.0,103.5) (30.2,103.0)	1.0	29.0°–32.0°, 102.0°–105.0°	2000-01–2013-03	2.7–5.4	273.45571 137.7011 90.7523 70.1106	0.8021
9	2017-8-8 Jiuzhaigou (Sichuan), M_s 7.0	(9,34)	408	(33.0,104.2)	0.9	32.0°–34.0°, 102.0°–105.0°	2009-01–2017-07	2.6–5.4	142.0628 39.3225 27.8213 16.2313	0.8482

Note: The earthquake time in the table is Beijing time in China. Anomaly zones are areas with frequency-field contours greater than 0.9 (blue zones); anomalous amplitude is the value of the contour closest to the epicenter of the mainshock; "×" indicates that the anomalies cannot be deemed significant owing to a lack of samples.

10.3389/feart.2022.992858

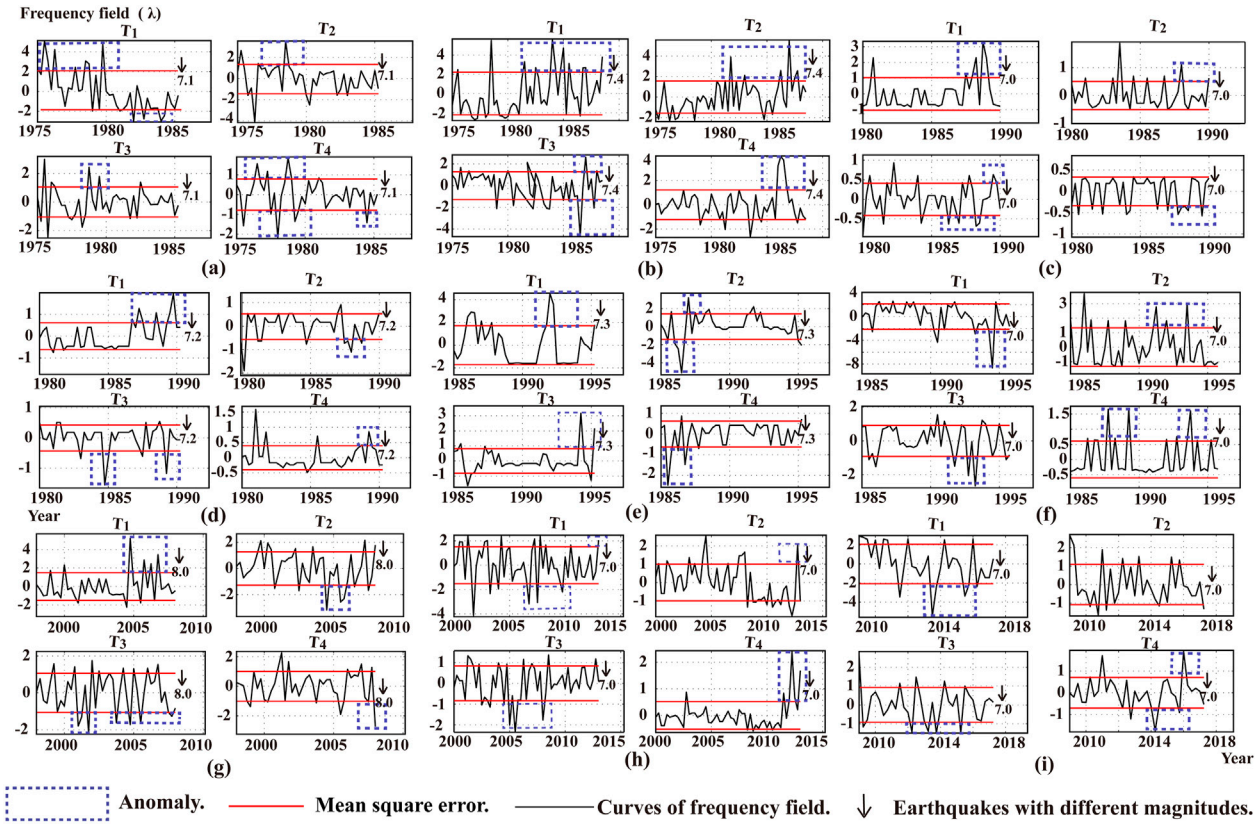

FIGURE 3
Temporal factors of the first four frequency fields of 9 *Ms* ≥7.0 earthquakes, The green dotted line represents the anomaly, The red line is two times the mean square error, The black arrow represents the magnitude of a *Ms* ≥7.0 earthquake. **(A)** 1985 *Ms* 7.1 Wuxia earthquake; **(B)** 1988 *Ms* 7.6 Lancang–Gengma earthquake; **(C)** 1990 *Ms* 7.0 Gonghe earthquake; **(D)** 1990 *Ms* 7.2 Jeminay earthquake; **(E)** 1995 *Ms* 7.3 Myanmar–China earthquake; **(F)** 1996 *Ms* 7.0 Lijiang earthquake; **(G)** 2008 *Ms* 8.0 Wenchuan earthquake; **(H)** 2013 *Ms* 7.0 Lushan earthquake; **(I)** 2017 *Ms* 7.0 Jiuzhaigou earthquake.

2.4 Changes in temporal factors of the frequency fields

The temporal factor anomalies that appeared in the frequency fields of the 9 *Ms* ≥7.0 earthquakes shown in Table 2 reveal that, in each of these earthquakes, the temporal factors of the first four frequency fields (T_1–T_4) exhibited one or more anomalies at different times. For each earthquake, the anomalous amplitude is taken as the largest value between several consecutive anomalies, and a change is deemed anomalous if it is larger than twice the absolute mean square error. Under the earthquake forecasting standards of the China Earthquake Administration, anomalies that appear 10 years, 1–2 years, 3 months, and a few to tens of days before a mainshock are called long-term, medium-term, short-term, and imminent anomalies, respectively. The vast majority of the 9 *Ms* ≥7.0 earthquakes exhibited long-term and medium-term anomalies, such as the 2008 *Ms* 8.0 Wenchuan and 2013 *Ms* 7.0 Lushan Earthquakes, and also showed short-term and imminent anomalies. Overall, the T_1–T_4 graphs of the *Ms* ≥7.0 earthquakes always exhibit large and complex fluctuations and contain many anomalies that exceed the anomaly determination threshold (the range of the mean square error is indicated by red lines in Figure 3). Some of these earthquakes exhibited extremely significant imminent anomalies, which are useful as earthquake predictors.

2.5 Changes in contours of frequency fields

The frequency-field contour maps of the areas that correspond to the 9 *Ms* ≥7.0 earthquakes that occurred in mainland China from 1980 to 2020 are shown in Figure 4. These maps were computed using Eq. 6 based on the weak-earthquake data described in Table 1. It is seen that the locations of the mainshocks coincide with high-density gradient turning points (locations where the blue zones turn into red zones, which

TABLE 2 Parameters of the frequency field temporal factors of 9 *Ms* ≥7.0 earthquakes in mainland China.

No.	Earthquake	Temporal factor	Time of anomaly (year-month)	Anomalous amplitude	Mean square error	Type of anomaly	Proportion of anomalous frequency fields in all fields
1	1985-8-23 Wuxia (Xinjiang), M_s 7.1	1	1979-10-12	4.7400	±2.0813	Long and medium term	0.4920
			1984-01-06	−2.9761			
		2	1976-04-09	4.0877	±1.3291	Long and medium term	0.2007
			1978-07-09	3.4967			
		3	1978-10-1979-03	2.4285	±1.0484	Long and medium term	0.1249
			1982-04-09	1.3962			
		4	1978-01-03	−2.1664	±0.7934	Long and medium term	0.0715
			1984-07-09	−1.4225			
2	1988-11-6 Lancang–Gengma (Yunnan), M_s 7.4	1	1986-01-1987-12	−4.2504	±1.6088	Long-to-medium term	0.3723
		2	1978-07-09	4.3942	±1.3869	Long and medium term	0.2767
			1988-01-03	2.1328			
		3	1985-01-03	2.9369	±1.2848	Short-to-imminent, medium and long term	0.2375
			1987-10-12	−1.9242			
			1988-07-10	1.9193			
		4	1982-10-1983-03	−1.6735	±0.8883	Short-to-imminent, medium and long term	0.1135
			1986-10-12	1.3008			
			1988-04-10	2.8872			
3	1990-4-26 Gonghe (Qinghai), M_s 7.0	1	1980-10-12	1.3020	±1.0353	Long-to-medium term	0.6373
			1988-01-1989-03	3.2967			
		2	1983-07-09	1.8698	±0.5029	Long term	0.1504
			1987-01-03	1.1038			
		3	1987-04-09	−0.6848	±0.4095	Long term	0.0997
		4	1984-01-06	−0.5432	±0.3367	Long-to-medium term	0.0674
			1987-10-1988-09	−0.4545			
			1989-07-09	−0.5759			
4	1990-6-14 Jeminay (Xinjiang), M_s 7.2	1	1987-07-09	1.5919	±0.6678	Short-to-medium term and long term	0.3330
			1989-04-1990-03	2.2373			
		2	1988-01-03	0.8137	±0.5415	Long-to-medium term	0.2190
			1988-07-12	−1.7110			
		3	1988-07-12	1.0586	±0.4669	Long-to-medium term	0.1628
			1989-10-12	0.7609			
		4	1986-10-1987-06	−0.7909	±0.3939	Long-to-medium term	0.1158
			1988-10-12				

(Continued on following page)

TABLE 2 (*Continued*) Parameters of the frequency field temporal factors of 9 *Ms* ≥7.0 earthquakes in mainland China.

No.	Earthquake	Temporal factor	Time of anomaly (year-month)	Anomalous amplitude	Mean square error	Type of anomaly	Proportion of anomalous frequency fields in all fields
5	1995-7-12 China–Myanmar border, M_s 7.3	1	1986-01-09	2.9845	±1.7095	Long-to-medium term	0.4860
			1991-01-06	4.5031			
		2	1985-07-1986-09	−5.0412	±1.4093	Short-to-imminent, medium term and long term	0.3303
			1995-04-07	−2.0745			
		3	1994-04-06	3.1704	±0.8157	Short-to-imminent and medium term	0.1106
			1995-01-06	2.1671			
		4	1985-07-09	−2.4894	±0.6325	Long term	0.0665
6	1996-2-3 Lijiang (Yunnan), M_s 7.0	1	1994-04-12	−8.6238	±2.1387	Medium term	0.6057
		2	1986-01-03	3.6841	±1.3282	Long-to-medium term	0.2336
			1993-07-09	2.9939			
		3	1992-10-1993-06	−2.6703	±0.9196	Medium term	0.1120
		4	1987-10-12	1.6602	±0.6069	Long-to-medium term	0.0488
			1993-10-12	1.6085			
7	2008-5-12 Wenchuan (Sichuan), M_s 8.0	1	2004-10-12	5.2214	±1.5061	Long-to-medium term	0.2531
			2006-10-12	3.4450			
		2	2004-07-09	−3.1590	±1.2820	Long-to-medium term	0.1834
			2005-07-12	−2.5542			
		3	2004-10-2005-09	−1.7189	±1.0639	Long-to-medium term	0.1263
		4	2008-01-04	−2.7228	±1.0049	Short-to-imminent	0.1127
8	2013-4-20 Lushan (Sichuan), M_s 7.0	1	2011-07-2013-03	8.8316	±2.2932	Medium-to-imminent	0.3834
		2	2012-07-2013-03	3.4351	±1.6273	Medium-to-imminent	0.1931
		3	2012-01-2013-03	−4.4865	±1.3211	Medium-to-imminent	0.1273
		4	2006-07-2007-12	2.9353	±1.1612	Long term	0.0983
9	2017-8-8 Jiuzhaigou (Sichuan), M_s 7.0	1	2013-07-12	−5.4744	±2.0748	Medium term	0.5345
		2	2017-04-06	−1.3303	±1.0916	Short-to-imminent	0.1479
		3	2015-07-12	−1.4614	±0.9182	Medium term	0.1047
		4	2014-04-06	−1.7373	±0.7013	Medium term	0.0611
			2016-01-03	1.8994			

have gradients greater than 0.9) in seven out of the nine earthquakes. The mainshocks typically occur near the turning points rather than the maximum contour values. In two other earthquakes (the 1990 *Ms* 7.0 Gonghe Earthquake and *Ms* 7.2 Jimenay Earthquake), the contours are relatively sparse and small in number and do not exhibit any significant anomalies. This is potentially related to the low earthquake monitoring ability and low earthquake frequency in the study area. Generally, high-gradient turning points appear when the values of the frequency-field contour lines become large, and an

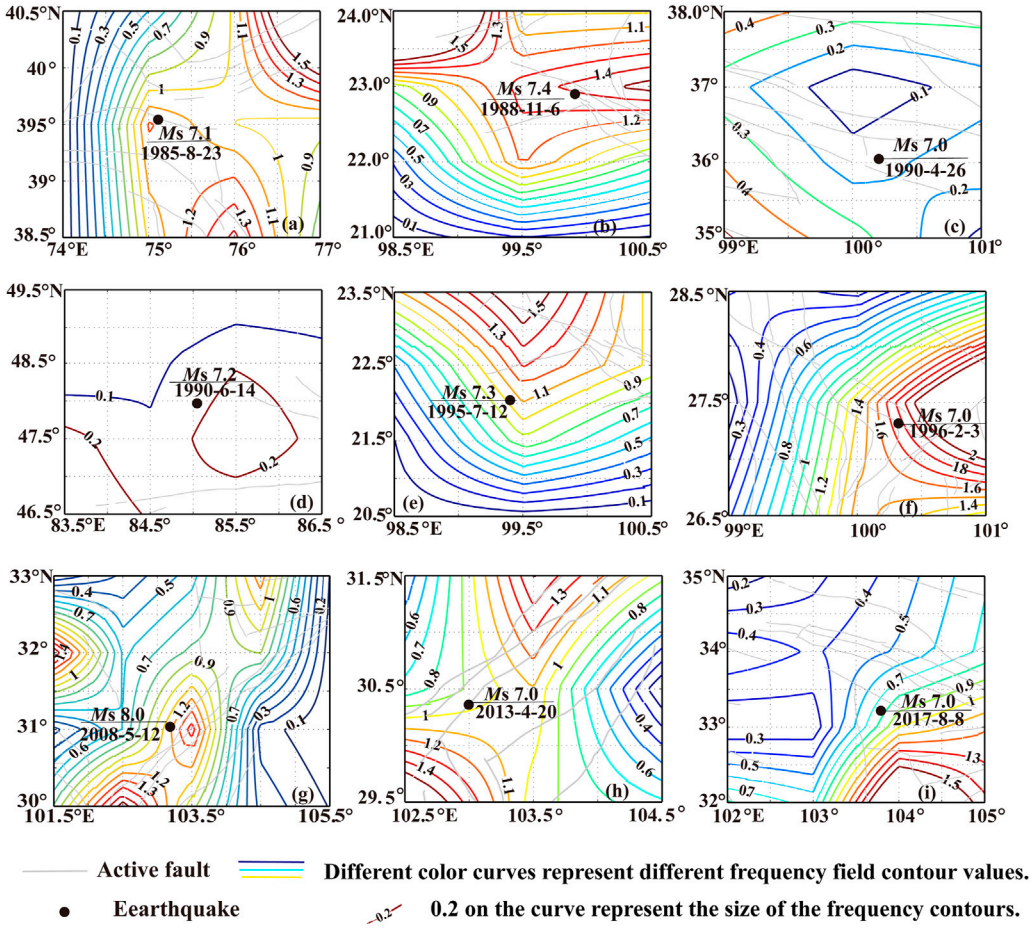

FIGURE 4
Frequency field contour maps of 9 *Ms* ≥7.0 earthquakes that occurred in mainland China, the black dots represent earthquakes, the blue, green, orange and red lines represent frequency field contours, and the gray lines represent active faults. **(A)** 1985 *Ms* 7.1 Wuxia earthquake; **(B)** 1988 *Ms* 7.6 Lancang–Gengma earthquake; **(C)** 1990 Ms 7.0 Gonghe earthquake; **(D)** 1990 Ms 7.2 Jeminay earthquake; **(E)** 1995 Ms 7.3 Myanmar–China earthquake; **(F)** 1996 *Ms* 7.0 Lijiang earthquake; **(G)** 2008 *Ms* 8.0 Wenchuan earthquake; **(H)** 2013 *Ms* 7.0 Lushan earthquake; **(I)** 2017 *Ms* 7.0 Jiuzhaigou earthquake.

area can exhibit one or more of these anomalous zones. Anomalous zones that occur near an active fault are often the epicenters of *Ms* ≥7.0 earthquakes; other anomalous zones can become the epicenter of strong earthquakes in the future.

It may be possible to preliminarily locate the epicenter of future *Ms* ≥7.0 earthquakes in a study area by studying the variations of its frequency-field contours. The January 1998–April 2008 frequency-field contour map of the 2008 *Ms* 8.0 Wenchuan Earthquake (Table 1; Figure 4G) exhibits three vortex-like isocratic anomalies (areas with high densities of contours with values greater than 0.9). The anomalies centered around (31.0°N, 103.5°E) and (30.0°N, 102.5°E) correspond to the epicenters of the 2008 *Ms* 8.0 Wenchuan Earthquake and 2013 *Ms* 7.0 Lushan Earthquake, respectively, whereas the anomaly centered around (31.5°N, 101.5°E) might be related to the 2014 *Ms* 6.3 Kangding Earthquake. The strong earthquakes that occurred persistently around the Longmenshan Fault after 2009 might have been triggered by the frequency field anomalies of the 2008 *Ms* 8.0 Wenchuan Earthquake. For brevity, we will simply describe the pre-quake frequency-field contour anomalies associated with the eight other *Ms* ≥7.0 earthquakes in Table 1 instead of providing a detailed analysis of each earthquake.

3 Discussion

3.1 Comparison between regional earthquake frequency graphs and earthquake frequency fields

Several scholars (Feng et al., 2009; Li et al., 2017; Zhang and Li, 2021) took the area around the epicenter of a strong

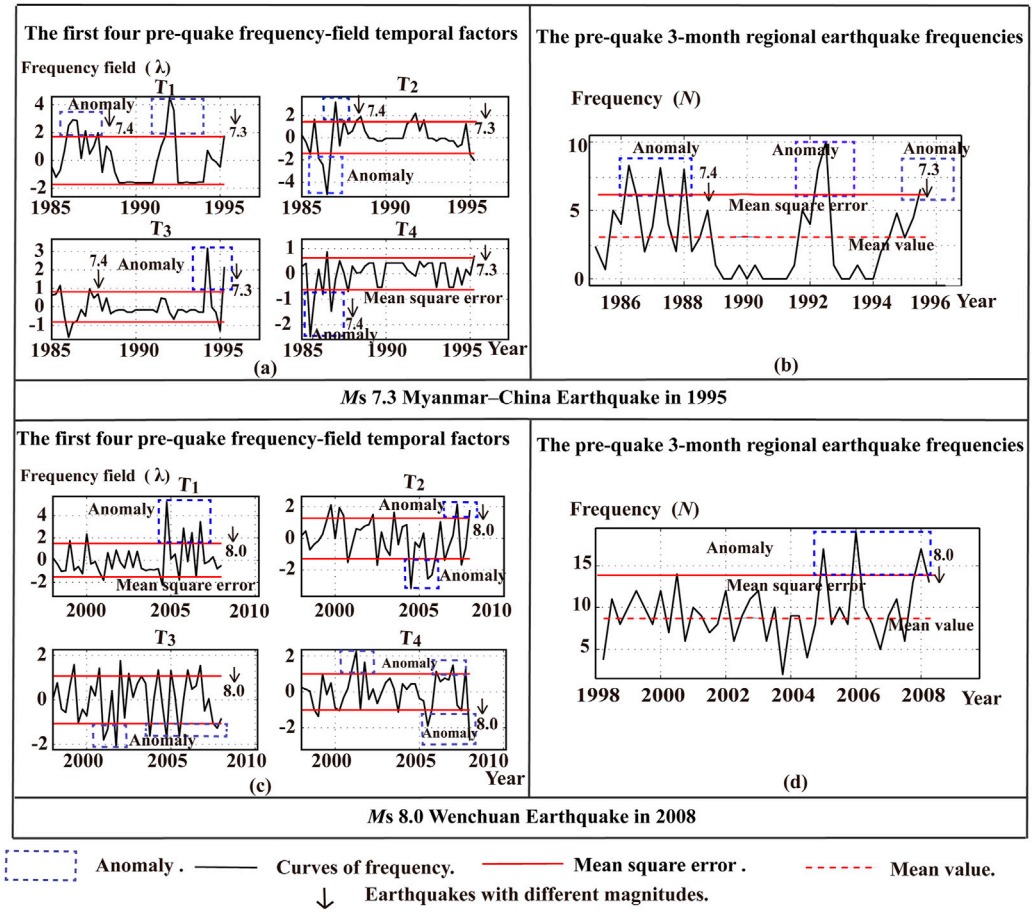

FIGURE 5
Comparison between frequency-field temporal factors and regional earthquake frequency graphs, the green dotted line represents the anomaly, the red line is two times the mean square error, the black arrow represents the magnitude of a *Ms* ≥7.0 earthquake, the red dotted line is the mean line **(A,B)**the 1995 *Ms* 7.3 Myanmar–China earthquake (top), **(C,D)** the 2008 *Ms* 8.0 Wenchuan earthquake (bottom).

earthquake as the research area to study the frequency anomaly of regional seismic activity before a strong earthquake. In this paper, the natural orthogonal expansion method is mainly used to study the typical frequency field in the strong earthquake area. The regional earthquake frequency graphs of 9 *Ms* ≥7.0 earthquakes (with 3-month frequencies) were compared with their T_1–T_4 graphs; the use of frequency graphs is a conventional seismological method, whereas the use of T_1–T_4 graphs is the method proposed in this paper. Owing to length constraints, this comparison was limited to the 1995 *Ms* 7.3 Myanmar–China Earthquake and the 2008 *Ms* 8.0 Wenchuan Earthquake. The earthquake frequency graph of the 1995 *Ms* 7.3 Myanmar–China Earthquake strongly resembles its T_1 graph (Figure 5 top). Based on Tables 1, 2, the accuracy of T_1–T_4 for this earthquake is 99.34% and the fit of T_1, which is the primary field of the frequency field, is 48.6%. Therefore, the earthquake frequency graph is simply a part of T_1–T_4 and the information carried by the former is contained within the latter. The earthquake frequency graph of the 2008 *Ms* 8.0 Wenchuan Earthquake also closely resembles the T_1 graph, which is the primary field of the frequency field (Figure 5 bottom); the information within the earthquake frequency graph is effectively contained in the T_1 graph. The same relation was observed for all other *Ms* ≥7.0 earthquakes.

Table 1 shows a partial overlap between the study areas of the 1995 *Ms* 7.3 Myanmar–China Earthquake (20.0°N–23.0°N, 98.5°E–100.5°E) and 1988 *Ms* 7.4 Lancang–Gengma Earthquake (21.5°N–23.5°N, 99.0°E–101.0°E). It is seen that the temporal spans of these earthquakes also overlap, with temporal spans of January 1985—June 1995 and January 1975—October 1988, respectively. As a result, both Figures 5A, B exhibit medium and short-term pre-quake anomalies prior to the earthquake and high-value anomalies that always correspond to strong earthquakes. The T_2, T_3, and T_4 graphs in Figure 5A also contain the short-term and imminent anomalies of the 1995 *Ms* 7.3 Myanmar–China earthquake and are more

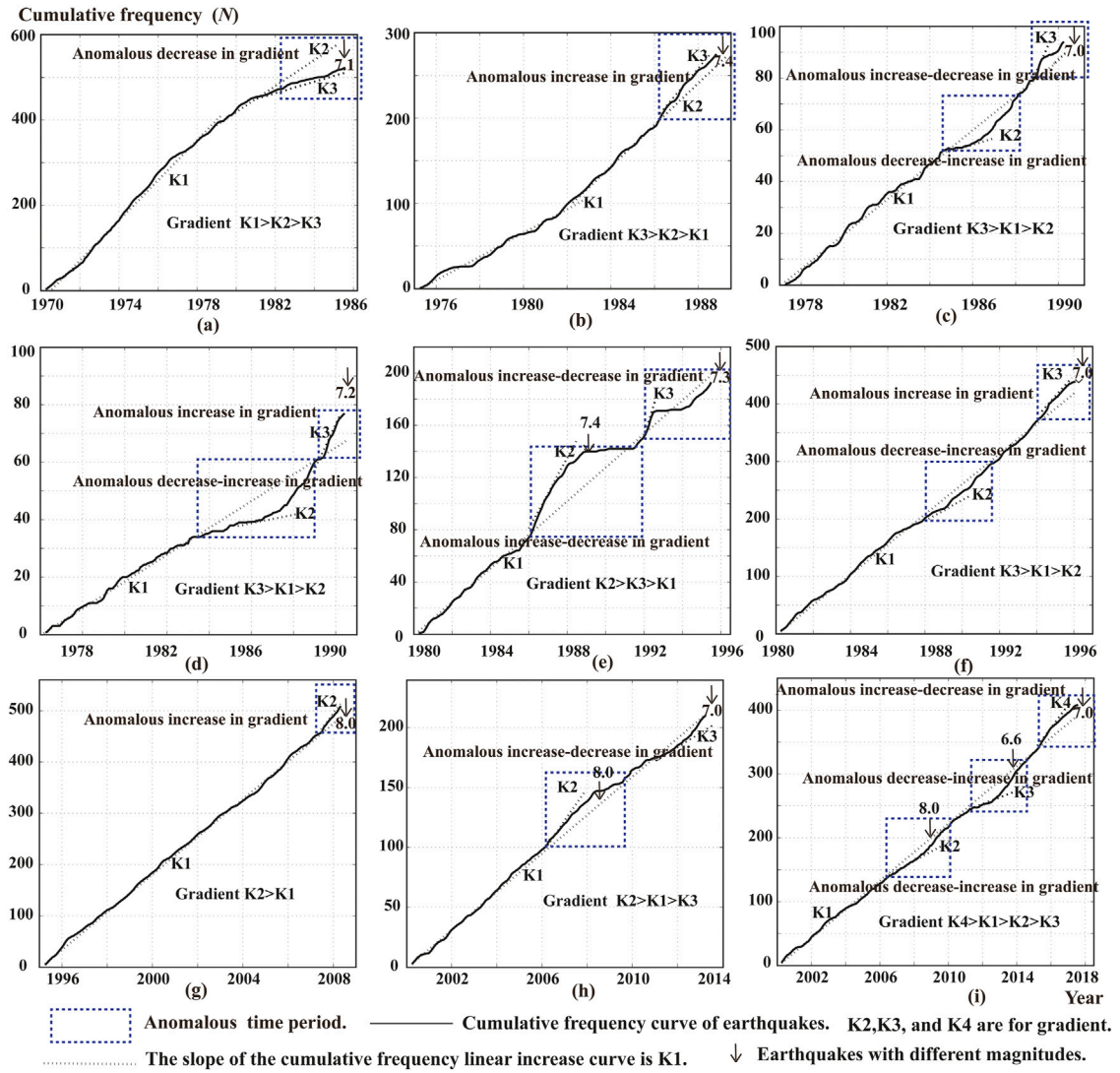

FIGURE 6
Cumulative frequency graphs of 9 *Ms* ≥7.0 earthquakes, the green dotted line represents the anomaly, the black arrow represents the magnitude of a *Ms* ≥7.0 earthquake, the dashed line represents the slope of a linear increase in cumulative frequency, K1, K2, K3, and K4 are for gradient. **(A)** 1985 *Ms* 7.1 Wuxia earthquake; **(B)** 1988 *Ms* 7.6 Lancang–Gengma earthquake; **(C)** 1990 *Ms* 7.0 Gonghe earthquake; **(D)** 1990 *Ms* 7.2 Jeminay earthquake; **(E)** 1995 *Ms* 7.3 Myanmar–China earthquake; **(F)** 1996 *Ms* 7.0 Lijiang earthquake; **(G)** 2008 *Ms* 8.0 Wenchuan earthquake; **(H)** 2013 *Ms* 7.0 Lushan earthquake; **(I)** 2017 *Ms* 7.0 Jiuzhaigou earthquake.

accurate than the regional earthquake frequency graph. This result highlights the advantage of using natural orthogonal expansion to study earthquake frequency fields.

3.2 Comparison between cumulative earthquake frequency graphs and earthquake frequency fields

The seismic activities that occur in the study area of an *Ms* ≥7.0 earthquake include its background seismicity, which comprises small random quakes, and strong earthquake precursors that manifest as small anomalous quakes. These seismic activities are controlled by different stress mechanisms. Background seismicity is controlled by stable long-term and region-wide stresses and is a relatively stable process. The cumulative earthquake frequency owing to background seismicity generally increases linearly over time, with small fluctuations, and it represents the equilibrium state of the region. By contrast, small anomalous quakes are caused by localized short-range stresses in the vicinity of seismic sources or fault junctions. They typically occur in highly seismic-sensitive

TABLE 3 Comparison between the cumulative earthquake frequency graphs and frequency field anomalies of 9 M_s ≥7.0 earthquakes in China.

No.	Earthquake	Parameters of the cumulative earthquake frequency graphs				Spatiotemporal parameters of the earthquake frequency fields		Comparison between spatiotemporal anomalies
		Changes in gradient, K	Time and nature of anomaly	Corresponding earthquake	Cumulative number of earthquakes	Time span of anomaly	Centroid of anomaly (°N, °E)	
1	1985-8-23 Wuxia (Xinjiang), M_s 7.1	Continuous decrease, K1 > K2 > K3	1981–1985 medium-short-imminent	1985 Wuxia M_s 7.1	525	1978–1979	39.5,75.2	Consistent temporal anomalies. significant spatial anomaly
						1982–1984	40.2,76.0	
							38.7,76.2	
2	1988-11-6 Lancang–Gengma (Yunnan), M_s 7.4	Continuous increase, K3 > K2 > K1	1986–1988 medium-short-imminent	1988 Lancang–Gengma M_s 7.4	277	1985–1988	23.0,100.0	Consistent temporal anomalies. significant spatial anomaly
							23.7,99.3	
3	1990-4-26 Gonghe (Qinghai), M_s 7.0	Decrease followed by increase, K3 > K1 > K2	1985–1988 medium-long; 1989–1990 medium-short-imminent	1990 Gonghe M_s 7.0	94	1983–1989	×	Consistent temporal anomalies. insignificant spatial anomaly
4	1990-6-14 Jimenay (Xinjiang), M_s 7.2	Decrease followed by increase, K3 > K1 > K2	1984–1989 medium-long; 1989–1990 medium-short-imminent	1990 Jimenay M_s 7.2	77	1987–1989	×	Consistent temporal anomalies. insignificant spatial anomaly
5	1995-7-12 Myanmar–China border, M_s 7.3	Increase to a flat, followed by increase to a plateau, and then a decrease, K2 > K3 >K1	1986–1991 medium-short-imminent; 1992–1995 medium-short-imminent	1988 Lancang M_s 7.4; 1995 Myanmar–China M_s 7.3	195	1985–1995	22.0,99.5	Consistent temporal anomalies. significant spatial anomaly
6	1996-2-3 Lijiang (Yunnan), M_s 7.0	Decrease followed by increase, K3 > K1 > K2	1988–1991 long-term; 1994–1996 medium-short-imminent	1996 Lijian M_s 7.0	440	1987–1994	27.5,100.2	Consistent temporal anomalies. significant spatial anomaly
7	2008-5-12, Wenchuan (Sichuan), M_s 8.0	Increase, K2 > K1	2007–2008 medium-short-imminent	2008 Wenchuan M_s 8.0	507	2004–2008	31.0,103.5 30.0,102.5 31.5,101.5	Consistent temporal anomalies. significant spatial anomaly
8	2013-4-20 Lushan (Sichuan), M_s 7.0	Increase followed by decrease K2 > *K1* > *K3*	2006–2009 medium-short-imminent; 2011–2013 medium-short-imminent	2008 Wenchuan M_s 8.0; 2013 Lushan M_s 7.0	211	2006–2007 2011–2013	31.0,103.5 30.2,103.0	Consistent temporal anomalies. significant spatial anomaly
9	2017-8-8 Jiuzhaigou (Sichuan), M_s 7.0	Decrease to a plateau, followed by another decrease to a plateau, and then an increase, K4 > K1 > K2 > K3	2007–2009 medium-short-imminent; 2011–2014 medium-short-imminent; 2015–2017 medium-short-imminent	2008 Wenchuan M_s 8.0; 2013 Dingxi M_s 7.0; 2017 Jiuzhaigou M_s 7.0	408	2013–2017	33.0,104.2	Consistent temporal anomalies. significant spatial anomaly

Note: × indicates that no anomalous zones were detected.

10.3389/feart.2022.992858

regions; once their mechanical equilibrium is disrupted, the cumulative earthquake frequency will decrease or increase significantly over time owing to tectonic stress, thus causing the cumulative earthquake frequency graph to become non-linear (Figure 6).

Application of earthquake cumulative frequency method (Ma et al., 2008; Ma et al., 2022) The study of the non-linear variation law of regional seismic activity before strong earthquakes can better explain the seismic frequency field anomalies in this paper. The pre-quake cumulative earthquake frequency graphs of the 9 *M*s ≥7.0 earthquakes are shown in Figure 6. In the normal state, the cumulative earthquake frequency graph will extend linearly over time. If a significant decrease or increase in seismic activity occurs, the gradient of the graph will decrease or increase significantly, which is indicative of seismic locking around the seismic source zone or fault as well as enhanced seismic activity. In the pre-quake cumulative earthquake frequency graph of the 2017 *M*s 7.0 Jiuzhaigou Earthquake (Table 3), it is seen that the graph is linear from January 2000—July 2006 with a gradient of K1. The gradient of the graph decreases significantly (to K2) from August 2006, indicating an abnormal seismic state. This is quickly followed by the medium-to-imminent anomalies of the 2008 *M*s 8.0 Wenchuan Earthquake, after which the graph returns to its equilibrium state (K1). The cumulative earthquake frequency graph decreases to K3 in October 2011 and then exhibits the medium-to-short term anomalies of the 2013 *M*s 6.6 Gansu Earthquake before returning to the equilibrium state. In June 2015, the gradient of the cumulative earthquake frequency graph rises to K4, where it remains until the 2017 *M*s 7.0 Jiuzhaigou Earthquake; this increase in gradient is the medium-to-short term anomaly that precedes the 2017 *M*s 7.0 Jiuzhaigou Earthquake. Long-term or medium-to-imminent anomalies in the pre-quake cumulative earthquake frequency graph always precede the occurrence of a strong earthquake in all other *M*s ≥7.0 earthquakes (Table 3).

The timing and nature of the anomalies in the cumulative earthquake frequency graphs are listed in Table 3. The nature of each anomaly was determined with respect to its corresponding earthquake and the cumulative earthquake frequency graphs were calculated using the same number of samples as were used to create the contours in Figure 4. It is seen from the table that the spatial anomalies of the frequency-field contours appear to be insignificant if an insufficient number of samples are available. In each study area, the temporal anomalies of the cumulative earthquake frequency graph and frequency field generally agree in terms of time span. By comparing the cumulative earthquake frequency graphs and frequency fields of the 9 *M*s ≥7.0 earthquakes, we found that the frequency-field temporal anomalies and spatial contours calculated *via* natural orthogonal expansion are highly accurate and reliable. This result is consistent with the spatiotemporal anomaly of the magnitude frequency distribution inferred by Ogata and Katsuta (1993).

3.3 Comparison between strain fields and frequency fields

The seismic strain field method (Yang et al., 2017; Luo et al., 2018; Lu et al., 2019a) is the same as the frequency field method, except that the parameter variables are different. The seismic strain field takes the seismic strain as the independent variable, and the frequency field takes the frequency as the independent variable. A comparison between the frequency and strain fields of the 1995 *M*s 7.3 Myanmar–China Earthquake and the 2008 *M*s 8.0 Wenchuan Earthquake is shown in Figure 7. It is seen that the frequency-field temporal factors are highly sensitive to seismic anomalies, as they exhibit large fluctuations and complex anomaly patterns. Conversely, the strain-field temporal factors are largely noiseless and exhibit clear and distinct pre-quake anomalies. However, the frequency-field temporal factors can reflect the anomaly patterns of multiple *M*s ≥7.0 earthquakes if they have overlapping study areas (Figure 7A). Conversely, the strain field can only reflect pre-quake anomalies associated with large accumulations (or releases) of strain energy, as smaller anomalies are masked in the strain-field temporal factors (Figure 7B). The results are consistent with the cumulative growth anomaly results of non-linear earthquakes Ma et al. (2022).

3.4 Discussion on the rationality of the selection of time interval and space scale

In the selection of seismic spatial scale, the seismicity statistical area related to large earthquakes and the grid cell are determined separately. Mei (1997) studied an *M*s ≥7.0 earthquake in the North China Plain and found that its seismic activity occurred in three stages: an initial low level, a gradually increasing phase, and a final weakening phase. The statistical area over which the earthquake occurred changed over time from 500 to 400 km; as seismic activity developed, the area was gradually reduced. Further measurements taken from 20 *M*s 6.0–6.9 earthquakes occurring in China revealed pre-earthquake activity enhancement areas ranging from 180 to 390 km. Based on these data, we applied a natural orthogonal function expansion to select a range of 3° in both longitude and latitude around the epicenter as the study area. The grid cells calculated using this approach reflected the distribution characteristics of regional seismic frequency but were too densely clustered. If 0.5°×0.5°grid cells were used, the frequency field curves would be averaged and the abnormal characteristics of the main frequency fields would not be effectively highlighted. If instead a 1.5°×1.5°grid cell was selected, the grid could be too large and the primary anomaly would be concentrated in the first frequency field in a manner similar to the results for the overall study area (Figure 4B), losing the multi-component characteristics of the results. In our paper,

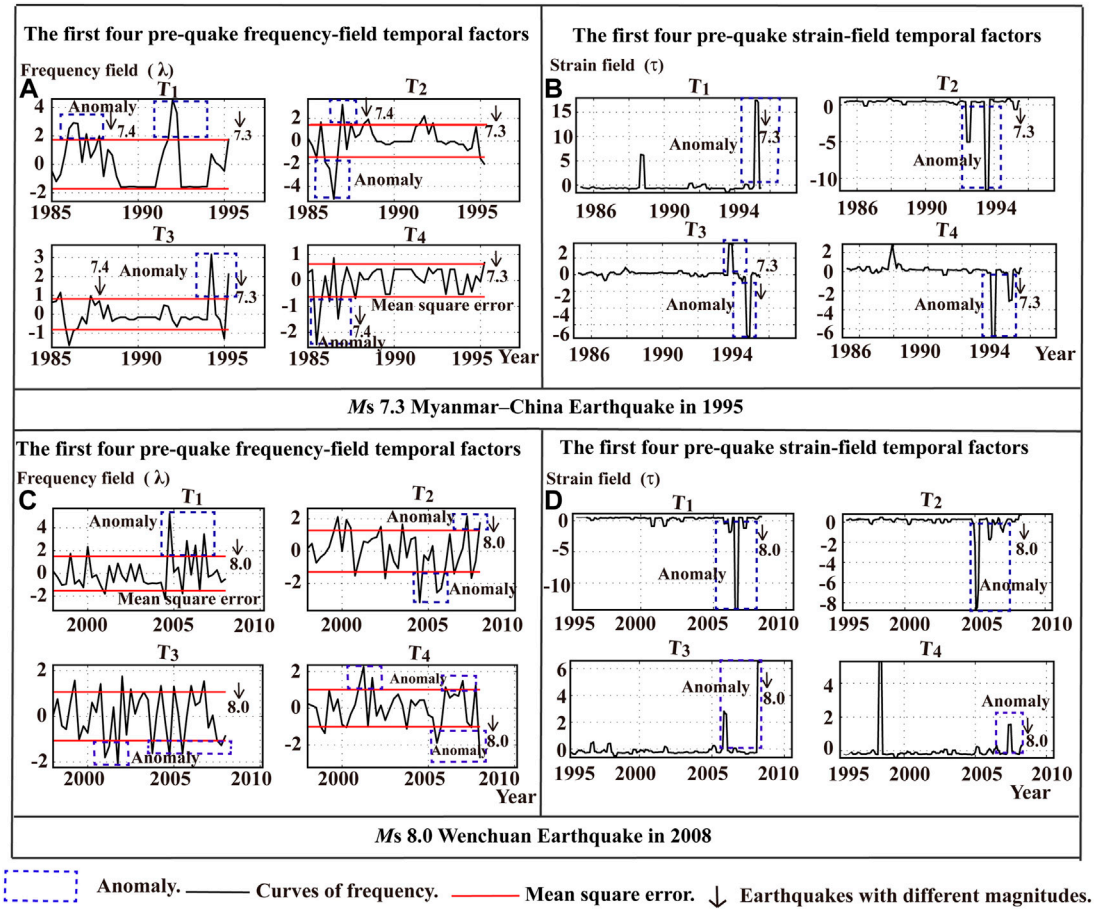

FIGURE 7
Comparison between frequency-field and strain-field temporal factors, the green dotted line represents the anomaly, the red line is two times the mean square error, the black arrow represents the magnitude of a *Ms* ≥7.0 earthquake **(A,B)** the 1995 *Ms* 7.3 Myanmar–China earthquake (top) and **(C,D)**the 2008 *Ms* 8.0 Wenchuan earthquake (bottom).

we reference Ma et al. (2020) discussion of these specific factors; we directly cite their research results and optimize the grid cell to 1.0°×1.0°.

The time interval is taken as a sliding calculation over 3 months because an interval of two or 4 months would have a negative influence on the sliding calculation results. If the time interval were too short, there would be more data, making anomalies more prominent, but the calculation speed would be slow. Increasing the time interval would speed up the computation but reduce the amount of data, masking anomalies. Thus, we followed the detailed discussion by Ma et al. (2020) and set a sliding of window of 3 months to obtain the best calculation results.

4 Conclusion

In this study, we analyzed the anomalies in the frequency-field temporal factors and spatial contours that preceded 9 *Ms* ≥7.0 earthquakes in mainland China. The following conclusions were drawn from the results of this analysis:

Prior to an *Ms* ≥7.0 earthquake, three to four of the first four frequency fields always exhibit anomalous changes in their temporal factors. The vast majority of these temporal anomalies are concentrated in the first four frequency fields and the anomalies appear to comprise multiple components. The contribution of T_1 to these anomalies is the largest among all temporal factors (typically 40%–60%) and the T_1 graph strongly resembles the regional (3-month) earthquake frequency graph. The proposed natural orthogonal expansion-based frequency field approach is more accurate than the conventional method and can be used to detect short-term and imminent seismic anomalies.

Frequency-field temporal factors are highly sensitive to seismic anomalies, as their graphs exhibit large fluctuations and complex anomaly patterns (rising, falling, fluctuating, rising and then falling, falling and then rising, etc.). This is

because the frequency-field temporal factors depend only on the number of small earthquakes within a region. For instance, the contribution of an M_L 2.7 earthquake to the frequency field is identical to that of an M_L 5.3 earthquake. The strain field (seismic energy field) graph is much more "noiseless," which results in highly distinct anomaly peaks. This is because the strain field depends on the cumulative seismic strain (or energy) of the quake; a difference of one in magnitude corresponds to a 33-times difference in strain (energy). Therefore, the contribution of an M_L 2.7 quake to a strain field graph is much smaller than that of an M_L 5.3 quake, and the signals of smaller strains are often masked by those of larger strains. The frequency field is more adept than the strain field at highlighting the pre-quake temporal anomalies of different *M*s ≥7.0 earthquakes if there is some overlap in their affected areas, as these anomalies are usually masked in strain fields.

High-gradient turning points are present in the spatial contours of pre-quake frequency fields of *M*s ≥7.0 earthquakes. Areas that have high densities of contour lines and contour values greater than 0.9 (where the blue lines change into red lines in Figure 4) are high-risk zones for strong earthquakes as they have the potential to generate large events. The detection of danger zones using frequency-field spatial contours is strongly dependent on the number of earthquake samples in the dataset; generally, increasing the number of earthquakes increases the reliability of forming contour danger zone.

If the seismic stresses of a region are in a normative state, the cumulative earthquake frequency curve of the region should increase linearly over time and its seismic events should be normally distributed. An anomalous increase or decrease in the gradient of the cumulative earthquake frequency graph is indicative of a significant calming of or increase in the seismic activity around a seismic source zone or fault junction. The anomalies of the cumulative earthquake frequency graph and frequency-field temporal factors are generally consistent with each other in terms of their time spans. Therefore, the temporal factor anomalies that are computed using the proposed method are reliable.

The natural orthogonal expansion calculation method proposed in this study is novel and abandons the use of the conventional earthquake region as the research object. In the proposed approach, the natural frequency orthogonal field expansion method is used to calculate the typical frequency fields related to larger earthquakes occurring in an area, from which points can be extracted from the characteristics of short and intermediate anomalies in primary seismic frequency that precede earthquakes with magnitudes greater than 7. This provides a reference for the prediction of large earthquakes occurring on the Chinese mainland. This study had the following limitations: the time factor used to describe the typical frequency field is sensitive; in addition, the curves generated using the proposed approach fluctuate significantly and have an abnormal shape that is complex and difficult to identify.

Data availability statement

The original contributions presented in the study are included in the article/supplementary material, further inquiries can be directed to the corresponding author.

Author contributions

All authors contributed to the conception and design of this study. GL, FD, and MY prepared the material, collected the data, and performed the analysis. The first draft of the manuscript was written by GL, and all authors provided their feedback on previous versions of the manuscript. All authors have read and approved the final manuscript. Sincerely, GL, FD, HM, MY Seismological Bureau of NH Autonomous Region.

Funding

This work was supported by the Earthquake Science and Technology Spark Plan Project (XH18052) and the Ningxia Natural Science Foundation Project (2021AAC03483).

Acknowledgments

We are very thankful for the guidance and help of Puqiong Huang of the seismic network center of China Seismological Bureau. Thanks to the reviewers for their valuable revision suggestions, and especially thanks to the responsible editors for their patient answers and help.

Conflict of interest

The authors declare that the research was conducted in the absence of any commercial or financial relationships that could be construed as a potential conflict of interest.

Publisher's note

References

Aden-Antóniow, F., Satriano, C., Bernard, P., Poiata, N., Aissaoui, E.-M., Vilotte, J.-P., et al. (2020). Statistical analysis of the preparatory phase of the M_W 8.1 Iquique earthquake, Chile. *JGR Solid Earth* 125, e2019JB019227. doi:10.1029/2019JB019337

Feng, J. G., Zhou, L. Q., Yang, L. M., and Dai, W. (2009). Anomaly of small earthquake activities before medium to strong earthquakes in the northeast margin of the Qinhai-Tibe block. *Earthq. (in Chin.* 29 (3), 19–26.

Jarmolowski, W., Belehaki, A., Hernandez, P. M., Schmidt, M., Goss, A., Wielgosz, P., et al. (2021). Combining swarm Langmuir probe observations, LEO-POD-based and ground-based GNSS receivers and ionosondes for prompt detection of ionospheric earthquake and tsunami signatures: Case study of 2015 Chile-Illapel event. *J. Space Weather Space Clim.* 11, 58. doi:10.1051/SWSC/2021042

Katsumata, K. (2011). A long-term seismic quiescence started 23 years before the 2011 off the Pacific coast of Tohoku earthquake (*M*=9.0). *Earth Planets Space* 63, 709–712. doi:10.5047/eps.2011.06.033

Li, Y. E., Chen, L. J., and Chen, X. Z. (2017). Enhancement of seismicity recorded by the Qiaojia seismic network before the 2013 Lushan and 2014 Ludian earthquakes. *Earthq. (in Chin.* 37 (3), 95–105.

Luo, G. F., Liu, Z. W., Ding, F. H., Ma, H. Q., and Yang, M. Z. (2018). Research on the seismic strain field prior to the 2017 Jiuzhaigou, Sichuan *Ms*7.0 earthquake. *China Earthq. Eng. J.* 40 (6), 1322–1330. doi:10.3969/j.issn.1000-0844.2018.06.1322

Luo, G. F., Liu, Z. W., Luo, H. Z., and Ding, F. H. (2019b). Effect of the strain field of Wenchuan 8 earthquake on the strong earthquake around the epicenter. *Prog. Geophys. (in Chinese)* 34 (3), 908–918. doi:10.6038/pq.2019CC0454

Luo, G. F., Tu, H. W., and Ding, F. H. (2019a). Spatio-temporal anomaly characteristics of regional seismic strain field before large earthquakes. *Earthquake (in Chinese)* 39 (2), 63–76.

Luo, G. F., Tu, H. W., Ma, H. Q., and Yang, M. Z. (2011b). Analysis on energy field of the seismic activity in earthquake hazard area from the northwest to the south of Yunnan. *Journal of Seismological Research (in Chinese)* 34 (4), 285–291.

Luo, G. F., Yang, M. Z., Ma, H. Q., and Xu, X. Q. (2011a). Intermediate and short-term anomalies of seismic activity energy field before the Wenchuan *Ms* 8.0 earthquake. *Earthquake (in Chinese)* 31 (3), 135–142.

Luo, G. F., and Yang, M. Z. (2005). Space-time distributed characteristics on energy field of earthquake in the Yunnan region. *Earthquake Research in China* 21 (3), 13–18.

Luo, G. F., Zeng, X. W., Ma, H. Q., and Yang, M. Z. (2014). Analysis of energy field of seismic activity before the minxian-zhangxian *Ms*6.6 earthquake in China. *Earthquake Engineering Journal (in Chinese)* 36 (2), 314–319. doi:10.3969/j.issn.1000-0844.2014.02.0314

Ma, H. Q., Yang, M. Z., Ding, F. H., and Luo, G. F. (2022). Nonlinear analysis on seismic activity before *Ms* ≥7.0 earthquakes occurred in Chinese mainland. *Earthquake Research in China* 38 (1), 42–51.

Ma, H. Q., Yang, M. Z., and Li, C. G. (2008). The theory explanation and application examples concerning the changes of small earthquake occurrence rate and accumulation time. *Earthquake (in Chinese)* 28 (1), 57–64.

Ma, H. Q., Yang, M. Z., and Luo, G. F. (2020). Study on frequency field of seismic activity. *Earthquake (in Chinese)* 40 (3), 99–111. doi:10.12196/j.issn.1000-3274.2020.03.008

Ma, H. Q., and Yang, M. Z. (2012). Research on the energy field about Yushu *ms* 7.1 earthquake in Qinghai in 2010. *Journal of Seismological Research (in Chinese)* 35 (4), 487–490.

Ma, K. Y., Ding, Y. G., and Tu, Q. (1993). *Principles and methods of climate statistics*. China: Beijing Press Meteorological.

Mei, S. R. (1997). *General characteristics of long term evolution of seismicity before strong earthquakes in North China//Theory and method of short impending earthquake prediction*. China: Beijing Press Seismological.

Mei, S. R. (1996). On the physical model of earthquake precursor fields and the mechanism of precursors' time-space distribution (III) — Anomalies of seismicity and crustal deformation and their mechanisms when a strong earthquake is in preparation. *Acta Seismologica Sinica* 9 (2), 223–234. doi:10.1007/bf02651066

Mogi, K. (1969). Some features of recent seismic activity in and near Japan (2) : Activity before and after great earthquakes. *Bull. Earthquake. Res. Inst. Univ. Tokyo* 47, 395–417.

Ogata, Y., and Katsuta, K. (1993). Analysis of temporal and spatial heterogeneity of magnitude frequency distribution inferred from earthquake catalogues. *Geophysical Journal International* 113 (3), 727–738. doi:10.1111/j.1365-246x.1993.tb04663.x

Wang, Y. W., Jiang, C. S., Liu, F., and Bi, J. M. (2017). Assessment of earthquake monitoring capability and score of seismic station detection capability in China Seismic Network (2008-2015). *Chinese J. Geophys (in Chinese)* 60 (7), 2767–2778. doi:10.6038/cjg20170722

Wiemer, S., and Wyss, M. (1994). Seismic quiescence before the Landers (*M*=7.3) and big bear (*M*=6.5) 1992 earthquakes. *Bull. Seismic. Soc. Am.* 84, 900–916.

Wyss, M., and Habermann, R. E. (1998). Precursory seismic quiescence. *Pageoph* 126 (2), 319–332. doi:10.1007/bf00879001

Yang, M. Z., and Ma, H. Q. (2013). Features of time factor anomalies of regional energy field before large earthquake. *Earthquake (in Chinese)* 33 (3), 107–115.

Yang, M. Z., and Ma, H. Q. (2012). Analysis of regional seismic energy field before Wenchuan *Ms* 8.0 earthquake. *Progress in Geophysics (in Chinese)* 27 (3), 0872–0877. doi:10.6038/j.issn.1004-2903.2012.03.006

Yang, M. Z., Ma, H. Q., Luo, G. F., and Xu, X. Q. (2017). Research on the seismic strain field before strong earthquakes above *Ms*6 in Chinese mainland. *Chinese Journal of Geophysics* 60 (10), 3804–3814. doi:10.6038/cjg20171010

Yang, M. Z., and Ma, H. Q. (2004). Statistical analysis of seismic activity energy field in Ningxia and its adjacent areas. *Journal of Earthquake (in Chinese)* 26 (5), 516–522.

Yang, M. Z., and Ma, H. Q. (2011). Variation of energy field of Longmenshan fault zone before the Wenchuan M_S 8.0 earthquake. *Earthquake Research in China* 27 (3), 260–267.

Zhang, B., and Li, M. J. (2021). Characteristics of seismicity anomalies before the 2021 *Ms* 7.4 earthquake in Qinghai Province. *China Earthquake Engineering Journal (in Chinese)* 43 (4), 826–833. doi:10.3969/j.issn.1000-0844.2021.04.826

frontiers | Frontiers in Earth Science

TYPE Original Research
PUBLISHED 30 January 2023
DOI 10.3389/feart.2022.1069046

OPEN ACCESS

EDITED BY
Fuqiong Huang,
China Earthquake Networks Center, China

REVIEWED BY
Dan Ma,
China University of Mining and Technology, China
Shunyun Chen,
China Earthquake Administration, China

*CORRESPONDENCE
Runhai Yang,
runhaiyang@163.com

SPECIALTY SECTION
This article was submitted to Solid Earth Geophysics, a section of the journal Frontiers in Earth Science

RECEIVED 13 October 2022
ACCEPTED 09 December 2022
PUBLISHED 30 January 2023

CITATION
Zhang S, Yang R, Tan J, Zhang Y and Jiang J (2023), The evolution characteristics of rock fracture instability under cyclic loading on the basis of the enhanced LURR. *Front. Earth Sci.* 10:1069046. doi: 10.3389/feart.2022.1069046

The evolution characteristics of rock fracture instability under cyclic loading on the basis of the enhanced LURR

Shuai Zhang[1], Runhai Yang[1]*, Junqing Tan[2], Yan Zhang[1] and Jinzhong Jiang[1]

[1]Kunming Earthquake Prediction Research Institute, Yunnan Earthquake Agency, Kunming, Yunnan, China, [2]Department of Earth and Space Sciences, Southern University of Science and Technology, Shenzhen, Guangzhou, China

Prospective discrimination of rock instability and fracture is a key problem in mining, slope stability, earthquake triggering, and other research fields. Through the rock fracture experiment, scientists put forward the load unload response ratio (referred to as LURR) to detect the non-linear deformation process of the strain stress curve, judge the degree of rock damage and instability fracture, which is accepted worldwide and has been widely used in seismic risk assessment. But, the extraction of response parameters (including strain, energy, well water level, etc.) are faced with many difficulties in actual observation, which makes the application of results uncertain. In this paper, the change of relative wave velocity is proposed as the loading unloading response parameter. Through rock mechanics experiments, a prospective discrimination method of rock instability and fracture process is constructed. The change characteristics of the LURR in the process of rock instability and fracture under stress are studied, the experiment result show that: when approaching the main fracture, the LURR calculated by taking the transverse strain energy as the response quantity obviously rises and fall back, the acoustic emission energy release rate and event rate are close to exponential acceleration process; The LURR by taking the change of relative wave velocity as the response parameter, first decreases, then fluctuates near zero, and rapidly decreases to below zero when it reaches the critical failure. The change combination of the above parameters' response ratio can effectively judge the process of rock deformation, instability and fracture under stress. Moreover, this study of the load unload response ratio which takes the change of relative wave velocity as the response parameter, makes up the deficiency of the traditional load unload response ratio method in judging the rock instability of the medium under stress.

KEYWORDS

rock experiment, cyclic loading, instability fracture, measurement of wave velocity, loading and unloading response ratio

1 Introduction

Study on the process of rock instability and fracture is the core content of rock mechanic. Reveal the evolution process of rock instability and fracture is of great significance to the prediction of dynamic disasters of rock mass, such as: earthquake mechanism, stability of roadway engineering, mining and slope instability. In order to reveal the seismic physical process, many scholars have carried out a large number of experimental studies on rock instability by using different observation measures and different observation conditions, exploring the process of rock instability and fracture under different loading modes, many results of predicting the precursor characteristics of rock instability and fracture have been obtained (Ma et al., 2019; Kwiatek G et al., 2014; Yamashita F et al., 2021; Ma et al., 2022a; Ma et al., 2022b; Li and Ma, 2021; Chen et al., 2009; Lei et al., 2000).

However, the preparation process of the rock instability and fracture is extremely complicated, but its physical essence lies in the deformation, instability and fracture process of the medium. Just because the rock instability prediction is extremely complicated and difficult, it is necessary to vigorously look for physical parameters that can essentially reflect the instability process. At the same time, it must be physically related to the local instability and rupture of the medium (Yin et al., 1994; Yin et al., 1995). The theory of loading and unloading response ratio that can quantitatively describe the damage degree and instability failure of rock, and is often used to detect the deformation stage before the peak value of strain stress curve (Yin, 1987). Yin et al. (2004) and Wang (1998) tested a large number of earthquake cases on the variation law of loading and unloading response ratio before moderate earthquakes, and the results showed that more than 80% of the earthquake cases had loading and unloading response ratios significantly greater than 1 before earthquakes, so it can be applied to earthquake prediction (Liu et al., 2012). With the development of more than 30 years, it has been widely used in the field of earthquake prediction. Many scholars use different geophysical parameters as responses, and have carried out a large number of experimental studies at different scales, including physical mechanism, experimental studies, numerical simulation and earthquake prediction practice (Yu, 2004; Yu et al., 2006; Yu et al., 2010; Yin et al., 2013; Yin et al., 2002; Zhang H et al., 2005a; Zhang W et al., 2006a; Zhang Y et al., 2006b), and made a series of progress. Experiments and numerical simulations also confirm the correctness of the theory of loading-unloading response ratio (Yin et al., 1995; Zhang et al., 2013). But, in the actual field observation, it is difficult to measure the stress and strain of the block, so it is equally difficult to measure the deformation modulus during loading and unloading (Yin et al., 2017). The response change based on magnitude energy depends heavily on seismic activity, and many earthquake source faults are locked for a long time, so it is impossible to obtain the relevant response from seismic activity itself (Lei and Wang, 2022). Moreover, the response based on other geophysical parameters (water level, temperature, etc.) is limited by the scale of observation and the density of observation points, so it is difficult to apply it to field regional scale observation.

Therefore, it is an important research direction to develop the loading/unloading response ratio method with the wave velocity change rate as the response. Considering the impenetrability of the Earth's interior and the observation problem of regional scale. Because, among the information parameters of seismic waves, the seismic wave velocity is the most accurate and reliable parameter, the measurement method is relatively mature. A large number of laboratory experiments show that the wave velocity of rocks will change with the change of stress (Birch, 1990; Nur et al., 1971). It increases with the increase of wave velocity pressure and is related to loading and unloading cycles (Yang and Shi, 2004). Therefore, the continuous and accurate measurement of wave velocity can be used as a "stress meter" to reflect the state change of stress field in underground media. After years of development, the observation method based on wave velocity measurement has been preliminarily applied and developed in the laboratory ultrasonic scale observation research (Yang et al., 2020; Song et al., 2012). Xie et al. (2017) even obtained the observation accuracy of relative wave velocity change as high as 10^{-6} by using the observation method of coda interference. Moreover, more importantly, it can be used to monitor the change of medium wave velocity at field scale. For example, the air gun seismic source detection technology in land water has the characteristics of environmental protection, high repeatability, etc. It can spread hundreds of kilometers through superposition, and the measurement accuracy of relative wave velocity change is 10^{-4}~10^{-3}. It can observe diurnal and semidiurnal changes caused by atmospheric pressure or solid tide. This high-precision wave velocity measurement provides a reliable technical means for responding to the state and change of weak stress field in underground media (Wang et al., 2016).

Based on the active ultrasonic source, this paper carried out experimental research before and after rock fracture under cyclic loading. An important highlight of the paper is that developed the new LURR could make up for the lack of general LURR, and has theoretical significance for the study of earthquake prediction methods since instability of fault occurs after the peak point of strain-stress curve. At the same time, it is possible to use the wave velocity change under small stress disturbance to detect the stability of rock or engineering structure in the future, which shows a potential engineering significance of the results of this paper.

2 Experiment introduction

2.1 Experimental system

The system includes: loading and unloading operation system, signal excitation system, acoustic emission waveform acquisition

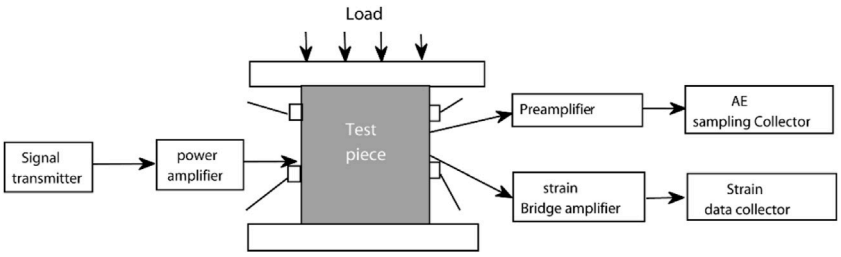

FIGURE 1
Schematic diagram of experimental system.

system and strain acquisition system as shown in Figure 1. In the experiment, CTM microcomputer servo-controlled hydraulic universal testing machine of Institute of Geology, Seismological Bureau of China was used, with a maximum loading capacity of 1000 kN. The signal generator continuously excited two sinusoidal signals (100 s/s) with an interval of 10 m, a transmission frequency of 100 KHz, a voltage of 2 Vpp and a preamplifier of 40 dB, which were amplified to 40 V by a power amplifier (Yang et al., 2020). The AE probe model is RS-2A, its frequency range is 50–400 KHz, and its center frequency is 150 KHz. The AE waveform acquisition system with 16 AE probes is used for recording. The AD conversion resolution is 16 Bit, the sampling frequency is 3MHz, and the sampling frequency of LB-V multi-channel digital strain gauge is 100 Hz.

Before loading, the clocks of the press operating system, acoustic emission data acquisition and strain observation system should be networked and synchronized to avoid the clock error affecting the calculation accuracy of the subsequent wave velocity change. The signal generator continuously excites two sinusoidal signals, which are amplified to 40Vpp by a power amplifier. The received signals are recorded in a 16-bit precision data collector at a sampling rate of 3 m/s, and the time length of the received waveform is 10 m. Each probe has 969 s continuous seismic records, and there are 3 million sampling points in 1s data. In this paper, the data is processed according to the data format with a time resolution of 1 s.

2.2 Sample and observation system

Granite samples with pre-cracks are used in the experiment. The sample size is 99.48 mm × 98.04 mm × 146.50 mm, as shown in Figure 2. The physical and mechanical properties of marble materials are as follows: compressive strength is 162 MPa, Young's modulus is 72.7 GMa, Poisson's ratio is 0.21, p-wave velocity is 5 km/s. The specimen is oblique cut in echelon in 45° axial direction, and macro fault zone is prefabricated for rock specimen by mechanical cutting method to simulate the geometric structure of tensile echelon fault. The cutting tool is a high-speed electric cutting machine. The upper fault is about 5.3 cm, and the lower fault is about 5.0 cm, all of which are cut through. The wheel blade of the cutting machine is an ultra-thin diamond saw blade. The width of the fault zone is about 3 mm and the depth of the fault zone is about 42 mm. The prepared sample is mixed with 1:1 gypsum and water and then filled into the crack to simulate the fault zone with low strength. It is placed for 24 h for the test after solidification. The test rock samples are processed according to the international rock mechanics test method.

The experimental system consists of 13 piezoelectric ceramic sensors (AE probe CH3-CH16) and one excitation probe (S) to excite ultrasonic waves. Piezoelectric ceramic sensors (14 AE probes in total, as shown in Figure 2) are installed on the rock samples. Nine red five-pointed probes are distributed on the first surface, one purple five-pointed probe is distributed on the second surface, three black five-pointed probes are distributed on the third surface, and one green five-pointed probe is distributed on the fourth surface. The center dot S is the position of the excitation probe. Before installation, wipe the contact surface between the probe and the rock with paper towel dipped in absolute ethanol to remove the dust on the sample surface. Apply honey evenly on the contact surface of the probe with the rock to ensure the coupling. The active excitation system is excited by double-pulse sine wave, and the acoustic emission data acquisition system is used to continuously record the active excitation ultrasonic wave and acoustic emission waveform. At the same time, six groups of strain gauges are deployed on the four surfaces of the rock sample, and each group includes longitudinal, transverse and oblique strain records. The strain data acquisition system is used to record the strain, and the whole process of rock failure is recorded by strain gauges.

2.3 Experimental process

The rock pattern is fixed on the servo-controlled hydraulic universal testing machine, and the loading system is used for cyclic loading and unloading at the loading speed of 2 kn/s and

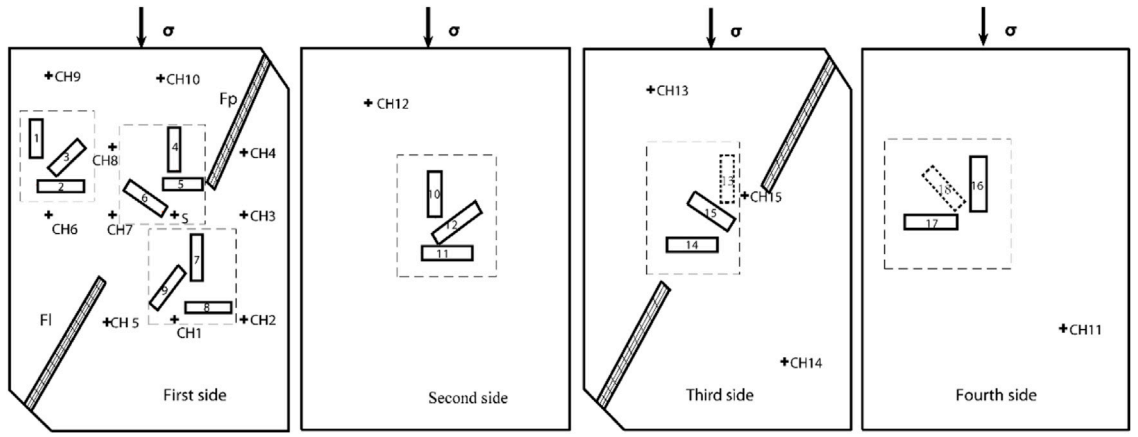

FIGURE 2
Sample model and observation system.

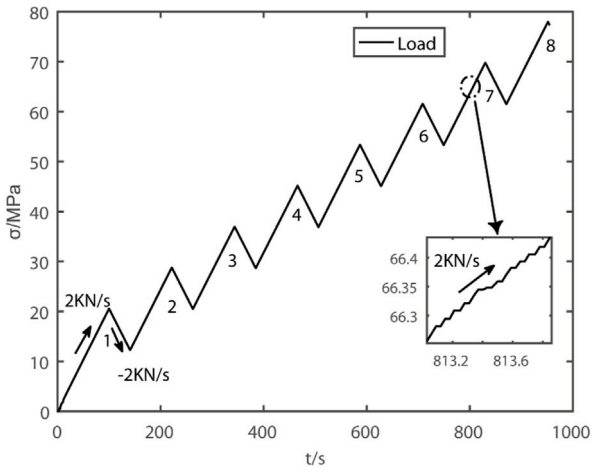

FIGURE 3
Loading and unloading curve.

the unloading speed of−2 kn/s. As shown in Figure 3, there are eight stages of cyclic loading and unloading, with each loading lasting about 80 s (the first loading lasting 100 s) and unloading lasting about 40 s. The whole cycle loading time lasts for 960 s. According to the empirical formula (p=F/S), in the first stage, the stress drops by 20.5 MPa in the loading section and 8 MPa in the unloading section. And the stress drops in the subsequent loading and unloading sections (2–7) are 16.4 and 8.2 MPa respectively. This loading method can simulate the effect of the tidal force of the Sun and the Moon, and the correlation of its response can be used as the response of the loading and unloading stages, respectively, and the sample reaches shear failure in the last stage of (~78 MPa) loading.

3 Theory and results

3.1 Loading and unloading response ratio theory

The theory of loading and unloading response ratio describes the evolution process of earthquakes with the Y value of loading and unloading response ratio in source areas, and the Y value can quantitatively measure the source process of the medium in source areas to a certain extent, so it is possible to predict earthquakes (Mora et al., 2002).

The theoretical principle is as follows: Assuming that the system is loaded and unloaded, $X+$ and the $X-$ response rates of the loading and unloading periods are divided, the loading and unloading response ratio Y is defined as when the medium is in the elastic deformation stage $X+ = X- = C$, therefore, $Y = 1$.At the stage of damage $X+ > X-$.When $Y > 1$ the medium is about to be destroyed, Y the value becomes larger and larger, reaching its peak value. Taking different physical quantities as responses, X the expressions are different. Taking seismic energy as the response, the loading and unloading response ratio is expressed as:Y_m

$$Y_m = \frac{\left(\sum_{i=1}^{N+} E_i^m\right)+}{\left(\sum_{i=1}^{N-} E_i^m\right)-}. \quad (1)$$

In Eq. 1: E represents seismic energy, and "+"and "-"represent loading and unloading, respectively (Liu and Yin, 2013). M is a constant between 0 and 1. When m=1, it means energy, m=1/2, it means energy Benioff strain, and m=1/3 or 2/3, it means the line scale and plane scale of the source area. M=0 indicates the earthquake frequency. $N+$ And $N-$ the

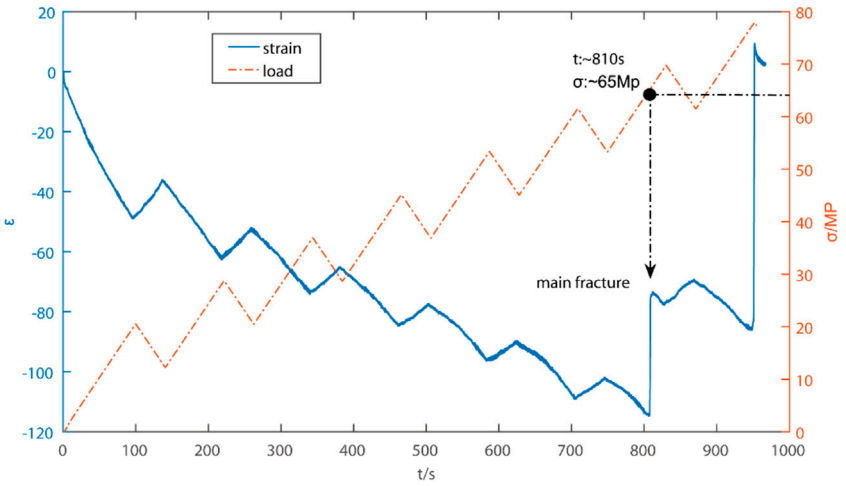

FIGURE 4
Strain-stress curve.

number of earthquakes loaded and unloaded in the study period respectively (Yin et al., 2000).

3.2 Strain energy response results

The stress-strain relationship (curve) shows the whole process of rock failure, as shown in Figure 4. At the initial stage of rock loading, the cracks in the rock closed elastically, and the strain curve showed strong consistency with the stress loading and unloading curve, and the strain increased linearly with the stress. When the extreme stress reaches ~65 MPa, the main crack occurs, and the strain gauge 5 records the occurrence time of the main crack to ~810 s, and the main crack occurs near the bottom area of the precast crack *Fp*, which is mainly because the sensitivity of axial stiffness to crack initiation and penetration is weaker than the non-linear lateral deformation (Zhang et al., 2017), and the stress accumulation of the precast crack structure is concentrated and the brittleness is weak. At the same time, the rock cracks spread unsteadily along the transverse direction, and the strain curve suddenly changes abnormally, and the deformation is large, which indicates that the occurrence time of the main rock fracture can be defined at this time.

Although the loading and unloading time in this paper is different, when the response quantity takes the average strain energy of each loading and unloading interval, it accords with the loading and unloading theory (Yin, 2004; Wang et al., 2004). Firstly, taking the strain energy as the response quantity, the Y value of the loading and unloading ratio response in all directions is calculated. As shown in Figures 5A–C. It is found that the loading and unloading curves basically coincide with the strain curves in the low stress stage, especially in the elastic stage, so the Y value of the loading and unloading response ratio is approximately 1. However, as the extreme stress approaches, more strain energy will be converted into permanent deformation of rock every time it is unloaded. Moreover, this change is getting bigger and bigger. Therefore, with approaching the extreme stress, before the main fracture occurs, the loading and unloading response ratios of strain gauges 5 and 14 near the rock bridge area are obviously inconsistent, and the values of the loading and unloading response ratios are obviously increased and decreased, indicating that the initiation and penetration of rock cracks mainly extend along the vertical axis. At the same time, the time series of the loading and unloading response ratio of the rock increased obviously before it became unstable, and the loading and unloading response ratio was abnormal. Before the rock was fundamentally damaged, the loading and unloading response ratio in many directions showed synchronous response.

3.3 Acoustic emission response results

Studying the evolution law of acoustic emission activities can characterize the whole process of rock damage and instability. Acoustic emission testing is a method to study the evolution process of rock damage from meso-fracture scale (Zhang H et al., 2005b). During the test process, the micro-fracture signal inside the rock was recorded by acoustic emission monitoring system, and the variation law of acoustic emission characteristic parameters was obtained by post-processing. The records of acoustic emission event release rate and acoustic emission energy release rate in the experimental process are shown in Figures 6A, B. The results show that in the initial loading stage, there are very few acoustic emission events in the rock, and only a

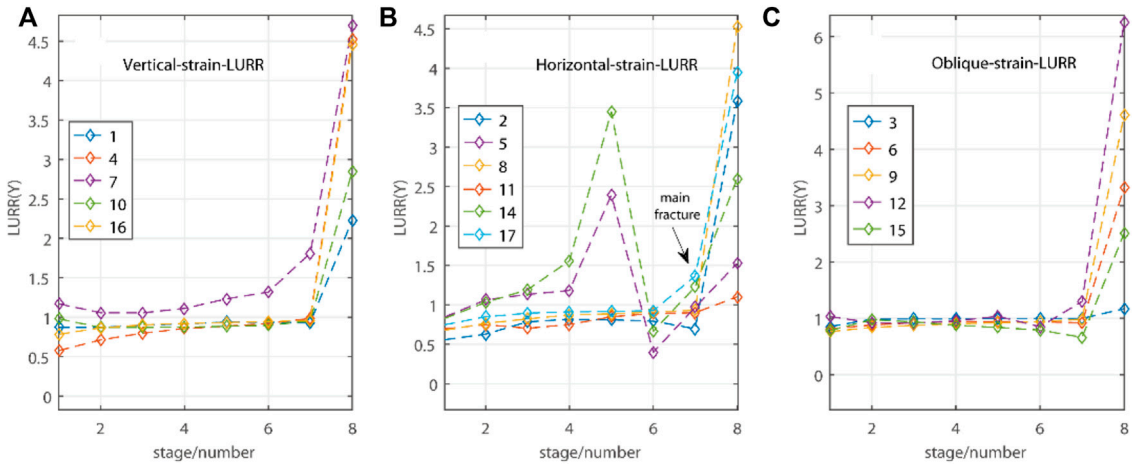

FIGURE 5
Load unload response ratio of strain energy in three directions **(A–C)**.

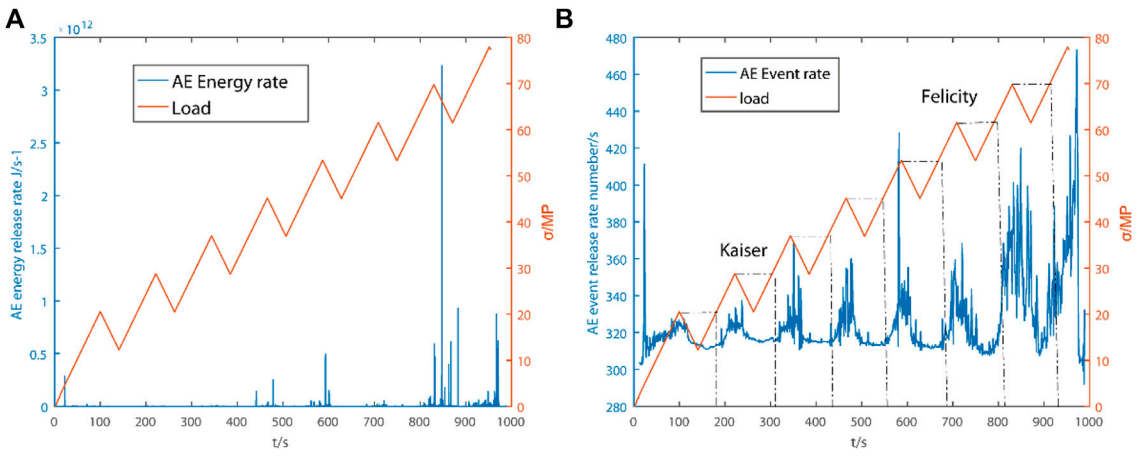

FIGURE 6
AE energy release rate **(A)** and event release rate **(B)**.

few acoustic emission events occur when the stress reaches about 10 MPa. At this time, acoustic emission phenomena occur at intervals, and the event rate and energy release rate are low. When the stress exceeds 28 MPa, the AE event rate gradually increases, but it is far less than that near the peak value. The AE events generated at this time are mostly due to the collision and friction between particles radiating elastic waves during the initial micro-crack closing process under external load. When the stress increases to 40 MPa, the AE event rate increases rapidly, and the first peak appears. Here, the stress is regarded as the crack initiation stress, and the AE event propagation rate gradually increases linearly. At this time, the crack is still in a stable propagation stage. When the stress reaches 60 MPa, the main fracture occurs, and the AE event rate increases non-linearly. At this time, the AE event rate has developed rapidly at a certain rate.

When rock is subjected to repeated loading and unloading experiments, only when the load reaches the previous maximum load will obvious acoustic emission occur. This “memory” phenomenon of materials is called Kaiser effect (Kaiser, 1950). The loading and unloading stages in this paper meet Kaiser effect law from 1 to 4. Subsequently, the Kaiser effect was also confirmed in the compression experiments of sandstone and quartzite (Goodman, 1963). The discovery of Kaiser effect

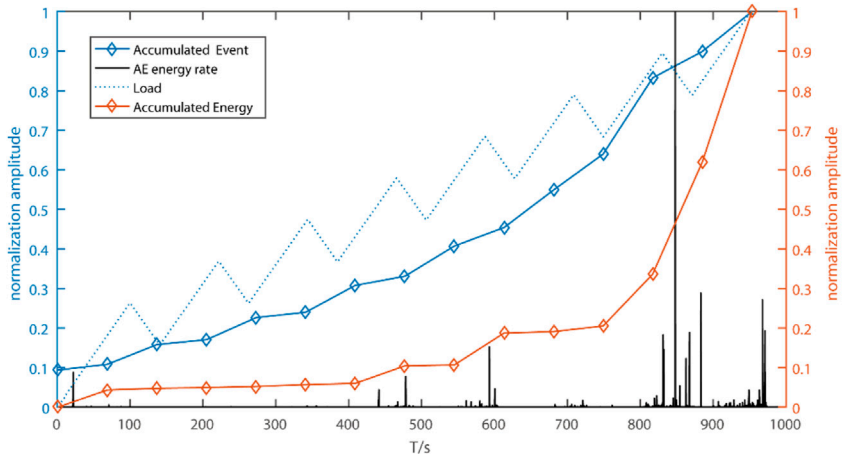

FIGURE 7
Acoustic emission energy release and cumulative event rate.

provides a new method to solve the problem of medium damage estimation in rock mechanics. However, when there is damage inside the rock, when the load is less than the highest stress level experienced in the previous period, the acoustic emission begins to increase significantly. This phenomenon is called Felicity effect (Fowler, 1986), as shown in Figures 6A, B. Felicity effect appears in the acoustic emission activity in the 5–8 stages, which indicates that with the continuous accumulation of stress, the rock has been damaged, and the acoustic emission activity has obviously intensified.

The energy of acoustic emission events recorded in the experiment reflects the elastic energy released when microcracks in rocks are generated or expanded. Therefore, by analyzing the acoustic emission energy, we can study the evolution law of elastic energy release of rocks. Let the energy of acoustic emission events recorded in the time t_k be:

$$E(t_k) = \sum_{t<t_k} e(t)(k = 1, 2, \ldots, t_k \le t_c), \tag{2}$$

Where: t_c is the critical moment, $e(t)$ is the energy of acoustic emission events, and the number of acoustic emission events recorded in the moment t_k is:

$$N(t_k) = \sum_{t<t_k} n(t)(k = 1, 2, \ldots, t_k \le t_c). \tag{3}$$

t_c is the critical moment and $n(t)$ is the number of acoustic emission events.

As shown in Figure 7, the energy release law of acoustic emission and the cumulative law of acoustic emission events are in good agreement with the cumulative law of the number of events. At the initial loading stage, the energy release of acoustic emission in rock is relatively stable, and the closer the energy release is to the linear process, the energy release does not

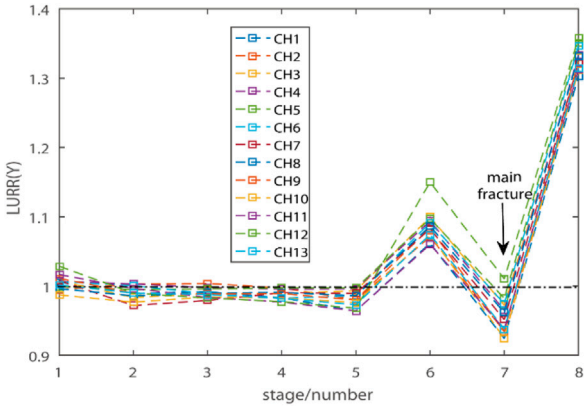

FIGURE 8
change of energy loading and unloading response ratio.

obviously accelerate. When the time reaches about 400 s, the release degree of acoustic emission energy is obviously enhanced, and the inside of the rock changes dramatically. The inside of the rock is in the process of initial microcracks closing under external load, and the mutual collision and friction between particles are intensified. When the time reaches about 810 s, the rock is in a high stress state, and the main rock fracture occurs, and the AE energy release is closer to the exponential acceleration process. The changes of the above acoustic emission characteristic parameters are directly related to the development and evolution of the internal damage of rocks, and the sudden increase of energy and events can be used as precursors of the catastrophic failure of rocks.

Meanwhile, according to the loading and unloading theory, any geophysical quantity that can reflect the instability process of the system can be taken as the response quantity (Yin et al., 2013). In seismology, the energy E of seismic waves and its related quantities are often used as response quantities, because they can directly carry the media information of the source area. In the experiment, a large number of acoustic emission events were recorded during loading and unloading. According to Eq. 1, take m =1, that is, use energy as the response, and get the change of Y value of loading and unloading response ratio with time, as shown in Figure 8.

From the experimental results, the loading and unloading response ratios of all channels reflect basically the same law, that is, when the load level is low and the damage degree of rock is small, the value of loading and unloading response ratio Y fluctuates around 1, and the rock is relatively stable. When the load level is high and close to the critical load of main fracture, the value of loading and unloading response ratio Y increases briefly, and the damage degree of rock is large. Then, the value of loading and unloading response ratio Y decreased briefly, and the main rupture occurred during the decline of loading and unloading response ratio. When the critical load is reached or exceeded, and before the rock is fundamentally damaged, the degree of rock damage is greater, and the value of the loading and unloading response ratio Y will increase sharply. The above experimental results are consistent with the discussion on the relationship between material failure, earthquake occurrence and critical sensitivity in statistical meso-damage mechanics (Bai et al., 2004; Zhang et al., 2004). At the same time, these results also show that the loading and unloading response ratio Y can be used as an important precursor to reflect rock instability and earthquake occurrence.

3.4 LURR based on wave velocity change

3.4.1 Principle of methods

According to the theory of loading and unloading response ratio, it can be known that the loading and unloading response ratio Y is a parameter that can quantitatively reflect the approaching instability degree of non-linear system, and it can be defined as

$$Y_k = \frac{K_+}{K_-}. \tag{4}$$

Equation 4: K^+ indicates the relative wave velocity response rate in loading stage K^- indicates the relative wave velocity response rate in unloading stage.

$$K = \frac{dv/v}{\Delta\sigma}. \tag{5}$$

Equation 5: $\Delta\sigma$ represents the variation of stress load, dv/v Indicates the change of wave velocity, the variation of K wave velocity and the linear relationship between two physical quantities. K value is used to quantitatively express the change rate of wave velocity with stress, and Fit value is used to characterize the coincidence degree between scatter value and fitting curve.

The accuracy of wave velocity measurement is the key to construct the loading and unloading response observation method with the relative wave velocity change as the response quantity, and the high-precision wave velocity measurement results can better respond to the stress state and change in the rock medium (Wang et al., 2020). Assuming that the time delay is caused by the relative velocity that changes uniformly in space, the relative wave velocity change in the medium can be expressed as:

$$\frac{dv}{v} = -\frac{dt}{t}. \tag{6}$$

In Eq. 6, v represents the wave velocity in the medium, dv represents the wave velocity change in the medium, dt represents the arrival time difference of some coda windows, and t represents the arrival time difference. By measuring the linear change relationship of the arrival time difference with time at different times, the wave velocity change in the medium can be obtained. The specific steps are as follows:

Assuming that the ultrasonic coda signal received by the probe is sum before and after, two active ultrasonic coda excitations are x_1 and x_2, two columns of Green's functions are sum after cross-correlation with the excitation wavelet are r_1 and r_2, and their velocities are v_1 and v_2 respectively. By stretching parameter τ compressing r_1 along the time axis, by the expansion factor $r_1[t-\tau]$, the wave velocity variation from v_1 to $v_1[t-\tau]$ can be obtained. By cross-correlation analysis with r_2 and $r_1[t-\tau]$, when the coefficient reaches the maximum value by Eq. 7, the more accurate travel time variation can be obtained, and then the wave velocity variation of medium can be calculated by Eq. 8.

$$RR^{t1,t2}_{r1,r2}(\tau) = \frac{\int_{t1}^{t2} r_1[t(1-\tau)]^* r_2(t)dt}{\sqrt{\int_{t1}^{t2} r_1^2[t(1-\tau)]\mathrm{d}t \int_{t1}^{t2} r_2^2(t)dt}}. \tag{7}$$

When a certain value τ of the expansion $\tau_{\max}$ factor is $RR(\tau)$ taken to maximize, the wave velocity variation of the r_1 and r_2, two series of signals can be obtained.

$$\frac{dv}{v} = \frac{(v_1 - v_2)}{v_1}. \tag{8}$$

The waveform analysis $t1, t2$ windows of the direct wave and the coda wave are respectively represented in the above Eq. 7, and the measured time change can be carried out in time domain or frequency domain (Zhang J, 2014). As shown in Figure 9A. In addition, the requirement of sufficient scattering (≥4 times the average free path) should be considered when measuring the coda wave, and in order to keep the stability of the results, the

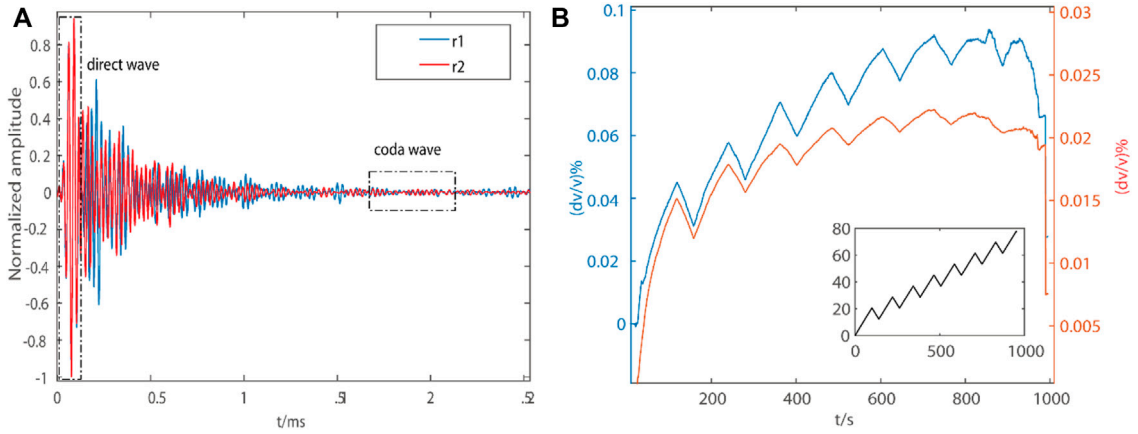

FIGURE 9
measurement window **(A)** and change of average relative wave velocity **(B)**.

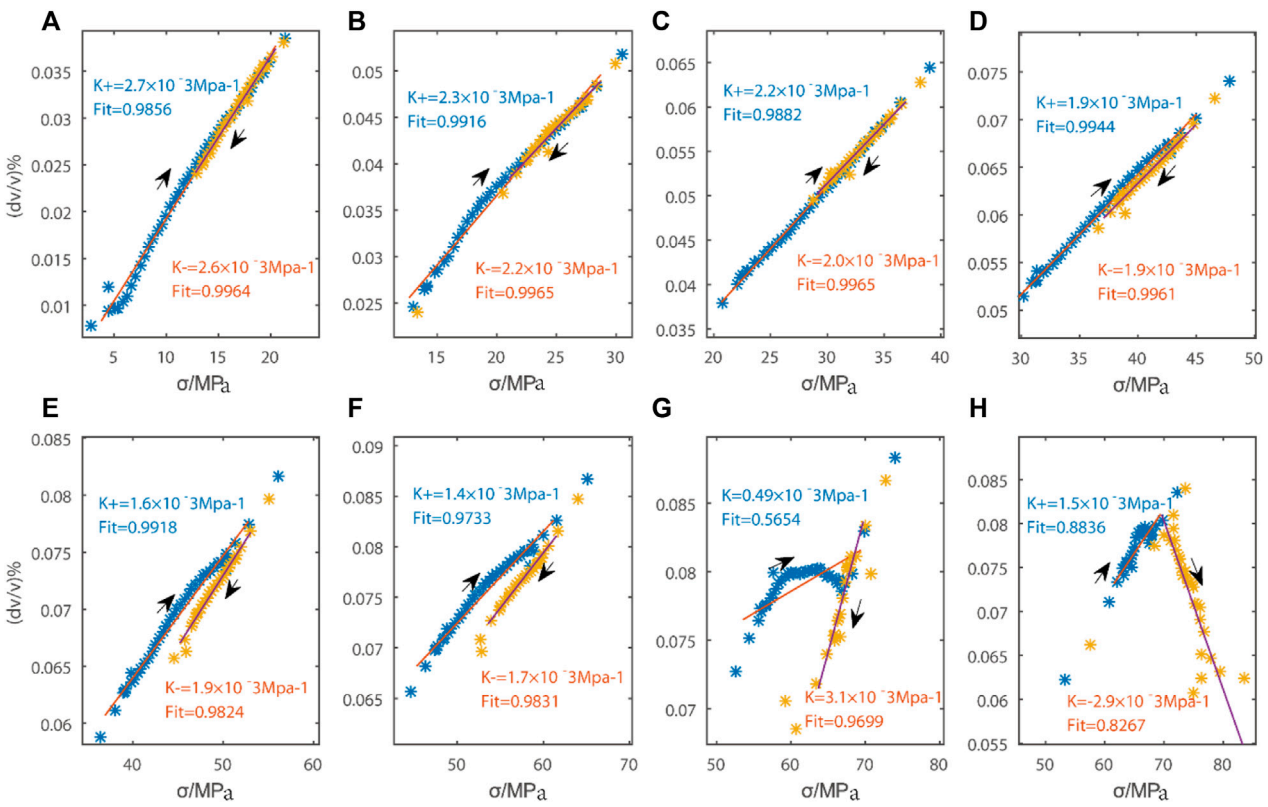

FIGURE 10
Rate of change of direct wave velocity in each loading and unloading stage **(A–H)**.

appropriate coda wave measurement window should be selected. Through continuous attempts, the window of coda signal selected in this experiment is 1.7–2.2 m.

Through the wave velocity measurement method, the average direct wave velocity and the relative variation of the wake wave velocity of 13 AE sensors are obtained as shown in Figure 9B. It is

TABLE 1 Parameter changes at different stages.

Direct wave	K value (load)	K value (unload)	LURR(Y)	Code wave	K value (load)	K value (unload)	LURR(Y)
1	2.7×10^{-3} Mpa^{-1}	2.6×10^{-3} Mpa^{-1}	1.038	1	0.51×10^{-3} Mpa^{-1}	0.41×10^{-3} Mpa^{-1}	1.243
2	2.3×10^{-3} Mpa^{-1}	2.2×10^{-3} Mpa^{-1}	1.045	2	0.37×10^{-3} Mpa^{-1}	0.28×10^{-3} Mpa^{-1}	1.321
3	2.2×10^{-3} Mpa^{-1}	2.0×10^{-3} Mpa^{-1}	1.100	3	0.24×10^{-3} Mpa^{-1}	0.22×10^{-3} Mpa^{-1}	1.090
4	1.9×10^{-3} Mpa^{-1}	1.9×10^{-3} Mpa^{-1}	1.000	4	0.18×10^{-3} Mpa^{-1}	0.18×10^{-3} Mpa^{-1}	1.000
5	1.6×10^{-3} Mpa^{-1}	1.9×10^{-3} Mpa^{-1}	0.842	5	0.14×10^{-3} Mpa^{-1}	0.15×10^{-3} Mpa^{-1}	0.9330
6	1.4×10^{-3} Mpa^{-1}	1.7×10^{-3} Mpa^{-1}	0.823	6	0.12×10^{-3} Mpa^{-1}	0.13×10^{-3} Mpa^{-1}	0.9231
7	0.5×10^{-3} Mpa^{-1}	3.1×10^{-3} Mpa^{-1}	0.258	7	0.006×10^{-3} Mpa^{-1}	0.16×10^{-3} Mpa^{-1}	0.0375
8	1.5×10^{-3} Mpa^{-1}	-2.9×10^{-3} Mpa^{-1}	-0.517	8	0.03×10^{-3} Mpa^{-1}	-0.11×10^{-3} Mpa^{-1}	−0.272

found that the two wave velocity curves are in good agreement with the loading curve, and the relative change of the direct wave velocity is obviously higher than that of the coda wave. As the stress increases, the increase of relative wave velocity decreases. After the main rupture, the wave velocity decreased obviously, but the decrease was small. When the critical load is reached, the change of relative wave velocity decreases in a cliff-like way.

3.4.2 Calculation results

The least square method (LSQ) is used to fit the K value. As shown in Figures 10A–H. The calculation results of the K value of the relationship between the relative wave velocity change and the stress quantitative change show that there is a high linear relationship in the initial stage of loading. The wave velocity increases with the increase of stress. The relative wave velocity change rate decreases with the increase of stress (K value), and the K+ value of the loading interval is slightly higher than the K- value of unloading, as shown in Table 1. As the stress increases, new cracks are generated in the rock, and the damage degree increases. When unloading, some cracks open with the stress decreasing, which leads to the wave velocity in the unloading process being smaller than that in the loading process. When the stress reaches ~50 MPa, the rock is damaged, and the change of K value in each loading and unloading interval is obviously inconsistent. A large number of cracks enter the compaction stage, and the wave velocity during unloading is larger than that during loading, and the K value during loading is lower than that during unloading. With the continuous loading of the stress, the increase of the wave velocity began to decrease from ~68 MPa, and the variation trend of the average wave velocity curve was inconsistent with that of the stress curve, showing a discrete stage deviating from linearity. This is mainly because after loading to the damage stress, the microcracks continue to increase, the microcracks gradually penetrate, and the expansion of rock samples accelerates, which leads to the rapid decline of wave velocity and amplitude. This feature can be regarded as a sign of approaching the main fracture. So, the change of wave velocity during repeated loading can be used as an evaluation method of rock damage.

As shown in Figures 11A–H, the calculation result of the K value of the quantitative relationship between the relative wave velocity change of the wake wave and the stress shows that the curve is highly consistent with that of the direct wave. But there are some differences between them. In the initial loading elastic stage, due to the compression closure of the initial micro-cracks, the wave velocity increases with the increase of stress, but the increasing amplitude gradually decreases. This is because with the increase of stress, the closing degree of the initial micro-cracks gradually increases, and the closing degree of the micro-cracks decreases under the same stress increment, which leads to the decrease of the increasing amplitude of the wave velocity. When the crack closing stress reaches ~60 MPa, the relative wave velocity basically reaches the peak, and the relative wave velocity changes by 2.3%. The increase of wave velocity decreases significantly faster than the direct wave, mainly because the coda wave is more sensitive to the change of the medium after multiple reflections and refractions in the medium. Moreover, it can also be observed from Figure 7 in this paper, the acoustic emission events at this stage begin to increase and the energy release intensifies. It can be seen that in a certain period of time, the fault has been in an unstable stage. Compared with the wave velocity change in the initial stage, the wave velocity change of rock medium is obviously abnormal at this stage, and the relationship between the wave velocity change and the stress change is obviously deviated from the non-linear state. With the continuous accumulation of stress and reaching the stress peak value of ~70 MPa, the fault enters the sub-instability stage, at which time the observation accuracy can reach 2.9125×10^{-8}, and the wave velocity change suddenly drops. The wave velocity change curve and the stress loading curve show a linear negative correlation, that is, when loading, the wave velocity change decreases, indicating that they are in a strongly discrete non-linear state. At this time, the value of k is -2.9×10^{-3} Mpa^{-1},

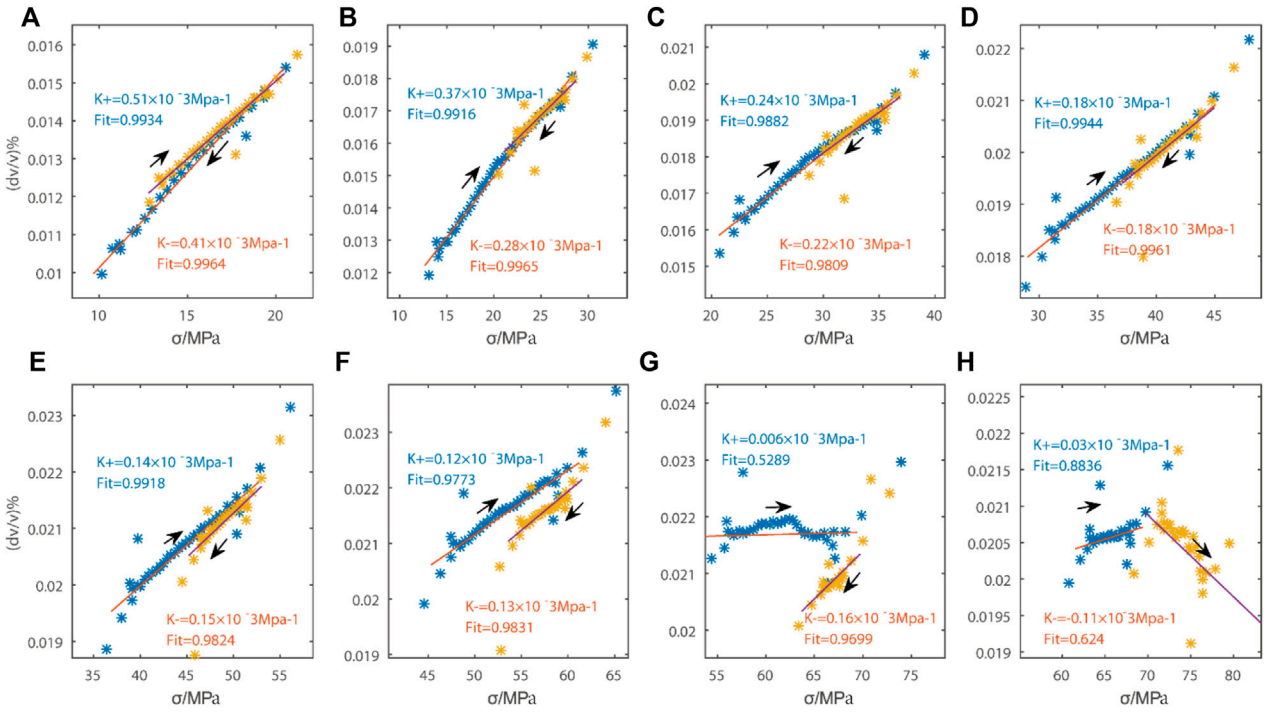

FIGURE 11
Change rate of coda wave velocity in each loading and unloading stage **(A–H)**.

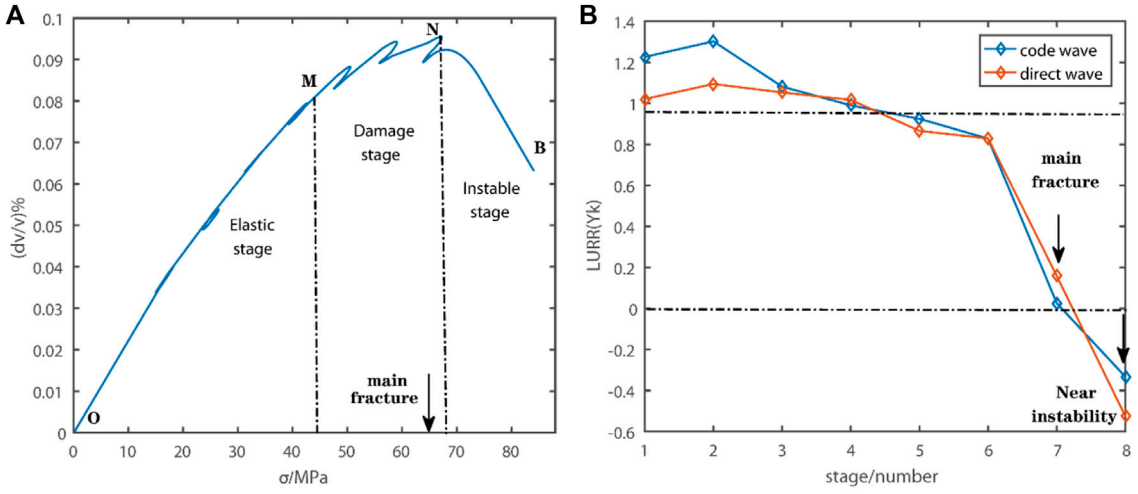

FIGURE 12
Relationship between relative wave velocity change and stress **(A)** and LURR of direct wave and coda wave **(B)**.

which means that the change of relative wave velocity at this time shows a cliff-like decline with the increase of stress.

According to Figure 12A of the relationship between average wave velocity change and stress, it is observed that in the elastic stage, the wave velocity change and stress can keep a good linear relationship, and the accumulation and release of stress are relatively stable. In the damage stage, the relationship between stress and relative wave velocity is in a non-linear state

before the main fracture occurs and the internal damage of rock occurs. In the stage of rock instability, the stress is negatively correlated with the change of relative wave velocity, that is, when the stress increases, the wave velocity decreases in a cliff-like manner, which reflects the drastic changes in the medium at the later stage of loading, which can be used as an important precursor before rock fracture.

According to the loading and unloading theory and the theoretical formula with relative wave velocity as the response, the loading and unloading response ratios of the two wave velocities are calculated respectively. Figure 12B shows the changes of LURR with the relative wave velocity changes of the direct wave and the code wave as the response during the rupture incubation process. In the initial stage, the response ratio of loading and unloading is close to 1. As the main rupture approaches, the corresponding ratio of loading and unloading fluctuates around zero, and decreases rapidly and becomes negative, then the main rupture comes. The results show that when the rock approaches the main fracture, the response ratio of loading and unloading decreases sharply, and then there is a minimum value, and even a negative value when the rock is unstable, the result is more consistent with the loading and unloading obtained in response to the P-wave travel time in the process of rock fracture preparation (Xu et al., 2002). Therefore, this feature can be regarded as a sign of rock near instability fracture.

4 Discussion

Whether the response ratio is negative or not is related to the stress state at the lowest point of the stress cycle after the peak value. The degree of bearing capacity reduction or energy release. The stress at the lowest point is larger, and its response wave velocity variation is larger than the wave velocity variation corresponding to the highest stress. When the bearing capacity decreases or the energy release exceeds the energy reduced by external force unloading, the response ratio will be negative. When the stress at the lowest point is smaller, the response wave velocity variation is smaller than the wave velocity variation corresponding to the highest stress, the bearing capacity decreases or the energy release is less than the energy reduced by external force unloading, then the response ratio may not be negative, but it may be the smallest. Therefore, the minimum value (even negative value) after the rapid decrease of loading and unloading response ratio can be used as a sign of approaching instability and rupture.

5 Conclusion

The experimental study of rock instability and fracture under cyclic loading was carried out, and the following conclusions were obtained:

When the cyclic loading reaches the 7th stage, the loading time reaches ~810 s, and the stress reaches ~65 MPa, the main fracture occurs. The main fracture point is near the bottom area of Fp, which is mainly caused by the concentrated stress accumulation and weak brittleness in the pre-crack position. With the approach of main rupture, the response ratio of loading and unloading calculated by taking transverse strain energy as the response quantity increases and decreases obviously. Before the occurrence of main fracture, the rock is relatively stable, the value of loading and unloading response ratio Y fluctuates around 1. When the load level is high, close to the critical load of the main fracture, the Y value of the loading and unloading response ratio rises briefly and then falls back, the main fracture occurs during the falling of the loading and unloading response ratio. When the load level is high and exceeds the critical load, and before the rock is fundamentally failure, the value of the loading-unloading response ratio Y will increase sharply, the energy release of acoustic emission is closer to the exponential acceleration process. The sudden increase of energy/event can be used as a precursor to the catastrophic failure of rock. Based on the results of constructing the loading and unloading response ratio in response to the change of relative wave velocity, it is found that the corresponding loading and unloading ratio fluctuates around zero as the main rupture approaches. When the critical load (~68 MPa) is reached, it decreases rapidly and becomes negative before the rock fundamentally failure, which is consistent with the change pattern of the wave velocity ratio in the process of fracture incubation. This feature can be regarded as a sign of approaching instability.

Data availability statement

The original contributions presented in the study are included in the article/supplementary material, further inquiries can be directed to the corresponding author.

Author contributions

SZ: Participation, conceptualization, data processing, writing—original, draft, visualization. RH: Methodology, participation, guide experiment, discussion. JQ: Participation, data processing. YZ: Participation, data processing. JZ: Discussion.

Funding

This study was Supported jointly by the Open Fund of the State Key Laboratory of Seismic Dynamics (LED 2016B06), the National Natural Science Foundation (41574059, 41174043, 42104060), Key Research and Development Plan of Yunnan Province (No. 202203AC100003), Sichuan Science and Technology Program (2020YJ0184), Innovation team of Yunnan earthquake agency for "research on earthquake mechanism and earthquake-generating environment".

Acknowledgments

We sincerely thank the reviewers and the editor for providing useful comments and suggestions, which greatly improved the quality of this manuscript. Nan Song took part in the whole process of the experiment, and thanks Associate Professor Peixun Liu, Yanshuang Guo and Guoqiang Chen for their strong support and guidance during the implementation of the experiment.

Conflict of interest

The authors declare that the research was conducted in the absence of any commercial or financial relationships that could be construed as a potential conflict of interest.

Publisher's note

All claims expressed in this article are solely those of the authors and do not necessarily represent those of their affiliated organizations, or those of the publisher, the editors and the reviewers. Any product that may be evaluated in this article, or claim that may be made by its manufacturer, is not guaranteed or endorsed by the publisher.

References

Bai, Y., Jia, Z., Zhang, X., Ke, F., and Xia, M. (2004). Long-range stress redistribution resulting from damage in heterogeneous media. *Pure Appl. Geophys.* 161 (9-10), 1841–1852. doi:10.1007/s00024-004-2535-0

Birch, F. (1990). The velocity of compressional waves in rocks to 10 kilobars:1. *J. Geophys. Res.* 65 (4), 1083–1102. doi:10.1029/JZ065i004p01083

Chen, S. Y., Liu, L. Q., Liu, P. X., Ma, J., and Chen, G. (2009). Theoretical and experimental study on relationship between stress strain and temperature variation. *Sci. China (Ser D)* 52 (11), 1825–1834. doi:10.1007/s11430-009-0183-z

Fowler, T. J. (1986). Experience with acoustic emission monitoring of chemical process industry vessels, in Proceedings of the Eight International Acoustic Emission Symposium, Tokyo: Progress AE III, 150–162.

Goodman, R. E. (1963). Subaudible noise during compression of rocks. *Geol. Soc. Amer. Bull.* 74 (3), 487. doi:10.1130/0016-7606(1963)74

Kaiser, J. (1950). *An investigation into the occurrence of noises in tensile tests or a study of acoustic phenomena in tensile tests*. Munich, Germany: Tech. Hosch.

Kwiatek, G., Goebel, T., and Dresen, G. (2014). Seismic moment tensor and b value variations over successive seismic cycles in laboratory stick-slip experiments. *Geophys. Res. Lett.* 41 (1), 5838–5846. doi:10.1002/2014GL060159

Lei, X., Kusunose, K., Rao, M., and Satoh, T. (2000). Quasi-static fault growth and cracking in homogeneous brittle rock under triaxial compression using acoustic emission monitoring. *J. Geophys. Res. Solid Earth* 105 (B3), 6127–6139. doi:10.1029/1999jb900385

Lei, X. L., and Wang, G. M. (2022). Is clustered seismicity an indicator of regional stress? Insights from earthquake sequences in yongning-luguhu faulted basin, southwest China. *Earthq. Res. Adv.* 2 (3), 100138. doi:10.1016/j.eqrea.2022.100138

Li, Q., Ma, D., Yandong, Z., Yong, L., and Yingjian, M. (2021).Insights into controlling factors of pore structure and hydraulic properties of broken rock mass in a geothermal reservoir. *Lithosphere*, 2022, 3887832. doi:10.2113/2022/3887832

Liu, Y., and Yin, X. C. (2013). A plate model for the damage of a crustal block induced by earthquake and the new definition for the load/unload response ratio. *Earth Sci. Front.* 20 (6), 067–072.

Liu, Y., Yin, X. C., Yuan, S., and Zhang, L. P. (2012). Exploration study of dimension analysis applying to earthquake prediction. *Chin. J. Geophys.* 55 (9), 3043–3050. doi:10.6038/j.issn.0001-5733.2012.09.022

Ma, D., Duan, H., Zhang, J., Liu, X., and Li, Z. (2022b). Numerical simulation of water-silt inrush hazard of fault rock: A three-phase flow model. *Rock Mech. Rock Eng.* 12, 5163–5182. doi:10.1007/s00603-022-02878-9

Ma, D., Duan, H., and Zhang, J. (2022a). Solid grain migration on hydraulic properties of fault rocks in underground mining tunnel: Radial seepage experiments and verification of permeability prediction. *Tunn. Undergr. Space Technol.* 126, 104525. doi:10.1016/j.tust.2022.104525

Ma, D., Wang, J., Cai, X., Ma, X., Zhang, J., Zhou, Z., et al. (2019). Effects of height/diameter ratio on failure and damage properties of granite under coupled bending and splitting deformation. *Eng. Fract. Mech.* 220, 106640. doi:10.1016/j.engfracmech.2019.106640

Mora, P., Wang, Y. C., Yin, X. C., and Place, D. (2002). Simulation of the load-unload response ratio and critical sensitivity in the lattice solid model. *Pure Appl. Geophys.* 159, 2525–2536. doi:10.1007/978-3-0348-8197-5_18

Nur, A. (1971). Effects of stress on velocity anisotropy in rocks with cracks. *J. Geophys. Res.* 76 (8), 2022–2034. doi:10.1029/JB076i008p02022

Song, L. L., Ge, H. K., Guo, Z. W., and Wang, X. Q. (2012). Experimental study of variation of media properties monitoring using multiple scattering waves. *Chin. J. Rock Mech. Eng.* 31 (04), 713–722. doi:10.3969/j.issn.1000-6915.2012.04.009

Wang, B. S., Li, X. B., Liu, Z. F., Yang, J., and Yang, R. H. (2016). The source and observation system of binchuan earthquake signal transmitting seismic station and its preliminary observation results. *Earthq. Res. China* 30 (3), 316–325.

Wang, B. S., Yang, W., Wang, W. T., Yang, J., Li, X., and Ye, B. (2020). Diurnal and semidiurnal P-and S-wave velocity changes measured using an air gun source. *J. Geophys. Res. Solid Earth* 125 (1). doi:10.1029/2019JB018218

Wang, Y. C., Mora, P., Yin, C., and David, P. (2004). Statistical tests of load-unload response ratio signals by lattice solid model: implication to tidal triggering and earthquake prediction. *Pure Appl. Geophys.* 161 (9-10), 1829–1839. doi:10.1007/s00024-004-2534-1

Wang, Y. C. (1998). The simulation of rock experiment on load/unload response ratio earthquake prediction. *Earthq. Res. China* 14 (02), 28–32. doi:10.1088/0256-307X/15/11/025

Xie, F., Ren, Y. Q., and Wang, B. S. (2017). Observation of stick-slips on a 1.5 m-long granite fault using ultrasonic coda waves. *J. Geophys.* 60 (04), 1470–1478. doi:10.ssss/j.issn.0001-5733.2017.4.019

Xu, Z. Y., Yang, R. H., Wang, B., Zhao, J. m., Wang, Y. y., and Mei, S. r. (2002). Physical meaning and prediction efficiency of the load/unload response ratio of rocks in strain-weakening phase before failure. *Acta Seismol. Sin.* 24 (1), 47–55. doi:10.1007/s11589-002-0046-6

Yamashita, F., Fukuyama, E., Xu, S., Kawakata, H., Mizoguchi, K., and Takizawa, S. (2021). Two end-member earthquake preparations illuminated by foreshock

activity on a meter-scale laboratory fault. *Nat. Commun.* 12 (1), 4302–4311. doi:10.1038/s41467-021-24625-4

Yang, H. F., and Shi, X. J. (2004). Experimental research on wave velocity under axial pressure. *Prog. Geophys.* 19 (2), 481–485. doi:10.3969/j.issn.1004-2903.2004.02.043

Yang, H. M., Chen, S. Y., Liu, P. X., Guo, Y. S., Zhuo, Y. Q., and Qi, W. B. (2020). Exeperimental study on the changes of ultrasonic coda wave and acoustic emission during rock loading and deformation. *Seismol. Geol.* 42 (3), 715–731. doi:10.3969/j.issn.02534967.2020.03.012

Yin, X. C. (2004). The new approach of earthquake prediction. *Earthq. Res. China* 3 (1), 3–10.

Yin, X. C., Chen, X. Z., Song, Z. P., and Yin, C. (1995). A new approach to earthquake prediction-the load/unload response ratio (LURR) theory. *Pure Appl. Geophys.* 145 (3), 701–715. doi:10.1007/bf00879596

Yin, X. C., Chen, X. Z., Song, Z. P., and Yin, C. (1994). The load-unload response ratio theory and its application to earth-quake prediction. *J. Earthq. Predict. Res.* 3 (3), 325–333.

Yin, X. C., Chen, X. Z., Wang, Y. C., Bai, Y., and Wang, H. (2000). Development of a new approach to earthquake prediction: Load/Unload Response Ratio(LURR) theory. *Pure Appl. Geophys.* 1 57 (11-12), 2365–2383. doi:10.1007/PL00001088

Yin, X. C., Liu, Y., Mora, P., Yuan, S., and Zhang, L. p. (2013). New progress in LURR: Integrating with the dimensional method. *Pure Appl. Geophys.* 170 (1), 229–236. doi:10.1007/s00024-012-0453-0

Yin, X. C., Liu, Y., Zhang, L. P., Li, W. J., Yuan, S., and Zhang, X. T. (2017). LURR anomaly, prediction and tracking of large earthquakes in the pan-southwestern region. *Earthquake* 37 (04), 37–49. doi:10.3969/j.issn.1000-3274.2017.04.004

Yin, X. C., Mora, P., Peng, K. Y. T., Wang, Y. C., and Weatherley, D. (2002). Load-unload response ratio and accelerating moment/energy release critical region scaling and earthquake prediction. *Pure Appl. Geophys.* 159 (10), 2511–2523. doi:10.1007/s00024-002-8745-4

Yin, X. C. (1987). The new approach of earthquake prediction. *Earthq. Res. China* 3 (1), 3–10.

Yin, X. C., Yu, H. Z., Kukshenko, V., Xu, Z. Y., Wu, Z., Li, M., et al. (2004). Load-unload response ratio (LURR), accelerating moment/energy release (AM/ER) and state vector saltation as precursors to failure of rock specimens. *Pure Appl. Geophys.* 161 (11-12). doi:10.1007/s00024-004-2572-8

Yu, H. Z., Cheng, J., and Wan, Y. G. (2010). Load-unload response ratio and stress accumulation model before large earthquake. *Acta Seismol. Sin.* 32 (5), 517–528. doi:10.3969/j.issn.0253-3782.2010.05.002

Yu, H. Z. (2004). *Experimental research on pre-cursors of brittle heterogeneous media and earthquake prediction methods*. Beijing, China: Institute of Mechanics, Chinese Academy of Science.

Yu, H. Z., Shen, Z. K., Wan, Y. G., Zhu, Q. Y., and Yin, X. c. (2006). Increasing critical sensitivity of the load/unload response Ratio before large earthquakes with identified stress accumulation pattern. *Tectonophysics* 428 (1-4), 87–94. doi:10.1016/j.tecto.2006.09.006

Zhang, G. K., Li, H. B., Xia, X., Chen, Q. Y., Liu, J. S., and Huang, Z. H. (2017). Experiment study on acoustic emission and wave propagation in granite under uniaxial compression. *Chin. J. Rock Mech. Eng.* 36 (05), 1133–1144. doi:10.13722/j.cnki.jrme.2017.0849

Zhang, H. H., Yan, Y. D., Yu, H. Z., and Yin, X. C. (2005b). Experimental study of rock failure precursor using simulated tide stress-load/unload response ratio (LURR) and accelerating energy release (AER). *Chin. J. Rock Mech. Eng.* 24 (17), 3172–3179.

Zhang, H. H., Yin, X. C., and Liang, N. G. (2005a). Statistic study of LURR anomaly temporal scale before moderately strong earthquakes on the Chinese mainland. *Earthq. Res. China* 21 (4), 486–495. doi:10.3969/j.issn.1001-4683.2005.04.005

Zhang, J. C. (2014). "The study of media changes caused by the reservoir storage with coda wave interferometry," in *Institude of earthquake science* (Beijing, China: China Earthquake Administration).

Zhang, L. P., Yu, H. Z., and Yin, X. C. (2013). Failure potential evaluation in engineering experiments using load/unload response ratio method. *Pure Appl. Geophys.* 170 (1-2), 237–245. doi:10.1007/s00024-011-0370-7

Zhang, W. J., Chen, Y. M., and Zhan, L. T. (2006a). Loading/Unloading response ratio theory applied in predicting deep-seated landslides triggering. *Eng. Geol.* 82 (4), 234–240. doi:10.1016/j.enggeo.2005.11.005

Zhang, X. H., Xu, X., Wang, H., Xia, M., Ke, F., and Bai, Y. (2004). Critical sensitivity in driven nonlinear threshold systems. *Pure Appl. Geophys.* 161 (9-10), 1931–1944. doi:10.1007/s00024-004-2540-3

Zhang, Y. X., Yin, X. C., Peng, K. Y., Wang, H. T., Zheng, J. C., Wu, Y. J., et al. (2006b). LURR and the san simeon M6.5 earthquake in 2003 and the seismic tendency in CA. *Pure Appl. Geophys.* 163 (11-12), 2343–2351. doi:10.1007/s00024-006-0125-z

frontiers | Frontiers in Earth Science

TYPE Original Research
PUBLISHED 01 February 2023
DOI 10.3389/feart.2023.1110061

OPEN ACCESS

EDITED BY
Paolo Capuano,
University of Salerno, Italy

REVIEWED BY
Iván Cabrera-Pérez,
Instituto Volcanológico de Canarias (INVOLCAN), Spain
Yunfeng Chen,
Zhejiang University, China
Mario La Rocca,
University of Calabria, Italy

*CORRESPONDENCE
Lingli Li,
heartkey@mail.ustc.edu.cn

SPECIALTY SECTION
This article was submittedto Solid Earth Geophysics, a section of the journal Frontiers in Earth Science

RECEIVED 28 November 2022
ACCEPTED 19 January 2023
PUBLISHED 01 February 2023

CITATION
Li L, Yao H, Zhang B, Li J, Shu P, Yang Y, Wang X, Zhou D, Zhao P and Luo J (2023), High resolution upper crustal velocity and seismogenic structure of the Huoshan "seismic window" in the Dabie orogenic belt.
Front. Earth Sci. 11:1110061.
doi: 10.3389/feart.2023.1110061

High resolution upper crustal velocity and seismogenic structure of the Huoshan "seismic window" in the Dabie orogenic belt

Lingli Li[1,2]*, Huajian Yao[3,2], Bing Zhang[1,2], Junhui Li[1,2], Peng Shu[1,2], Yuanyuan Yang[1,2], Xiaoli Wang[1,2], Dongrui Zhou[1,2], Peng Zhao[1,2] and Jiaji Luo[1,2]

[1]Anhui Earthquake Administration, Hefei, China, [2]Anhui Mengcheng National Geophysical Observatory, Mengcheng, Anhui, China, [3]Laboratory of Seismology and Physics of Earth's Interior, School of Earth and Space Sciences, University of Science and Technology of China, Hefei, China

Huoshan "seismic window" is located in the northern margin of the Dabie Orogen belt, the contact zone between North China and the Yangtze plate, where the seismic activity is mainly concentrated in this area. Small earthquake swarms in this region often appear before significant moderate-strong earthquakes in East China. To reveal the fine structures of several faults and discuss their correlation with the seismic activity, a seismic array composed of 136 sets of short period seismometers was deployed in the Huoshan region and its surrounding areas. Ambient noise data were recorded for 1 month, and a 3-D velocity structure model of the upper crust was constructed. The results show that with the Meishan-Longhekou and Qingshan-Xiaotian faults as the boundary, the Dabie Mountain, Hefei Basin, North Dabie and North Huaiyang show exhibit obvious high and low velocity variation characteristics. The shallow crust along the NW-trending, normal Qingshan-Xiaotian fault, presents a high velocity zonal distribution, which is related to the large number of magmatic and metamorphic rocks exposed under the strong metamorphic power in this region. The NE-trending Tudiling-Luoerling fault comprised three groups of parallel and nearly vertical en echelon secondary faults in the upper crust, which control most of the seismic activities. A relatively low velocity anomaly is observed in the seismic concentrated occurrence layer near the intersection of the fault. It suggests that this area inherits the property of the low velocity detachment zone of the middle crust in the wing of the Dabie Mountain dome structure, and a relatively broken weak structural zone form near the intersection of the fault, which leads to the release of small strain accumulation, thus enriching small earthquake activities. The focal depth of earthquakes above ML3 mainly distribute along the Tudiling-Luoerling fault plane, which is indicated this fault is the main seismogenic fault of greater seismicity in Huoshan "seismic window". This study provides an important model basis for reliable earthquake location, focal mechanism and the determination of possible earthquake risk sites, and provides a reference for the further study of small earthquake activity mechanism of other "seismic windows" in China.

KEYWORDS

shallow velocity structure, dense seismic array, seismicity, Huoshan "seismic window", seismogenic structure

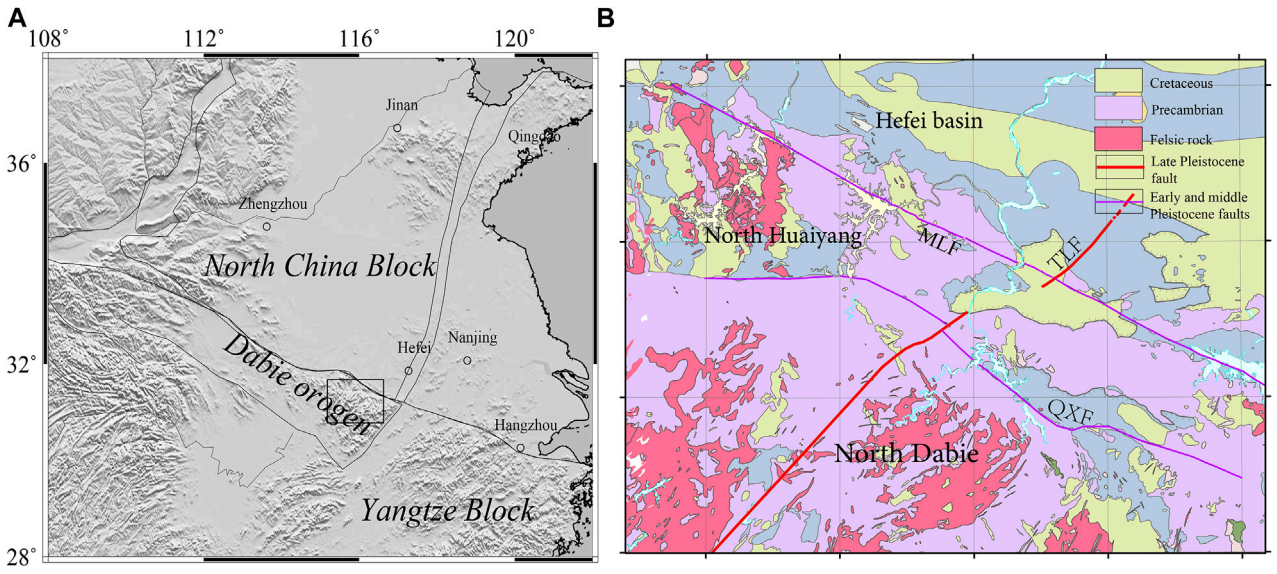

FIGURE 1
Topography **(A)** and Geological structure **(B)** of Dabie orogenic belt and its adjacent areas (MLF:Meishan-Longhekou Fault; QXF:Qingshan-Xiaotian Fault; TLF:Tudiling-Luoerling Fault).

1 Introduction

There are some regions in mainland China where small and medium-sized earthquakes are very active, and the frequency of their seismic activity over time is indicative of moderate-to-strong earthquakes in the corresponding regions, so they are called “seismic windows”. For many years, the statistical characteristics of the seismic activity of “seismic windows” have become one of the main indicators for the assessment of seismic hazard (routine work) in mainland China. However, the seismogenic mechanism, subsurface tectonic characteristics and velocity structure of the “seismic window” have not been studied in depth, and the physical significance of the seismic activity of the “seismic window” cannot be deeply understood. The Huoshan area studied in this paper is such a “seismic window".

The Huoshan area is located in the northeastern margin of the Dabie Mountains and is adjacent to the Tanlu Fault Zone in the east. It is the most concentrated and active area of seismic activity in the Dabie Mountains and surrounding areas. Many groups of crisscross faults exist in the area, the most important of which are the NE-trending Tudiling-Luoerling fault (TLF) and the NW-trending Qingshan-Xiaotian fault (QXF; Figure 1) Small earthquakes (below ML3) have been very active in the modern era (since 1970) since instrumental records were available and have repeatedly shown near-periodic small-earthquake swarm activity before the occurrence of medium-strong earthquakes in East China (l_1). It is suggested that the eastward extrusion of crustal materials caused by the convergence of tectonic plates, with the consequence of strong seismic activity in western China. The driving force of the crustal extrusion also can be transmitted to eastern China along the Qinling-Dabie orogenic belt As a result, in the Huoshan area where is the intersection of multiple groups of faults, small eartthquke swarms are active, and small earthquakes swarms are active before the occurrences of some moderate-strong earthquakes in eastern China (Hong et al., 2013; Miao et al., 2014). In earthquake prediction research (Routine work in China Earthquake Administration), the cumulative frequency of Huoshan “seismic window” earthquake activity with ML1.0 or above in 3 months has reached more than 40, which is often used as an index for earthquake prediction within a certain range.

In addition to the active concentration of small earthquakes, the spatial characteristics of historical earthquakes of magnitude 5 or higher in the region are also obvious, mostly spreading along the Tudiling-Luoerling fault, with the maximum magnitude of 6.25 in 1917. However, there are few earthquakes with the magnitude above 5 in the concentrated area of small earthquakes. A remarkable characteristic of seismic activity is that the spatial distribution of historically strong earthquakes is quite different from that of modern small earthquakes, which is closely related to the characteristics and control of the regional fault structure. Therefore, in-depth research on the seismotectonic characteristics of the Huoshan “seismic window” and the correlation with seismic activity is important for understanding the causes of small earthquake swarms and the mechanism of fault inception and earthquake risk prediction in the Dabie orogenic belt.

Geological researches show that the Tudiling-Luoerling fault has been an active fault since the early Late Pleistocene in the Dabie area (Yao et al., 2003; Shu et al., 2018), with a tectonic background of strong earthquake activity. However, because the historical earthquakes are only written records, there is no evidence of surface rupture even for the 6.25 strong earthquake in 1917. Therefore, the research on the seismogenic structure of the fault is insufficient. An Ms4.3 earthquake struck the Huoshan area in 2014, with the epicenter close to the southern side of the Qingshan-Xiaotian fault. This is the largest earthquake in the region in the past 50 years. The focal mechanism solution results show that the earthquake occurred due to a typical right-lateral strike-slip movement of the tectonic plates, which is related to the horizontal compression in the east-west direction and the horizontal tension in the north-south direction in the Huoshan area (Liu et al., 2015). However, the two nodal results of the focal mechanism solution cannot determine which fault is the main seismogenic structure. Cui et al. (2020) believed that the seismogenic fault of the earthquake was the Tudiling-Luoerling fault through the

electrical structure, but the resolution of the Qingshan-Xiaotian fault was not sufficient. Xu et al. (2022) used the regional stress field to simulate and calculate three NE-trending seismic sections and suggested that the main earthquake-controlling fault in the region is the NE-trending Tuling-Luoerling fault. However, detailed fine structural differences between the two faults in the Huoshan area and their relation with seismic activity require more geophysical observation evidence.

Seismotectonic characteristics affect the preparation and occurrence of earthquakes. Therefore, the fine geometric shape of faults needs to be studied to provide an important modeling basis for accurate localization of regional earthquakes, research on seismogenic mechanisms, and determination of earthquake hazard locations. The main body of small and medium earthquakes is concentrated in the intersection of the two faults, and the focal depth is mostly shallow than 10 km. Therefore, the study of the fine velocity structure of the upper crust can provide a reference for the seismogenic mechanism in this area.

Previous studies have obtained the high-resolution structural model of the Chinese mainland by the joint inversion of seismic body waves and surface waves (Xin et al., 2019; Han et al., 2022) and of the region around the Dabie Mountains (Luo et al., 2013; Ye, et al., 2015; Xiong et al., 2019), providing important deep velocity structure information for determining the tectonic evolution dynamics of the Dabie orogenic belt. Early studies of several artificial seismic deep reflection profiles and other geophysical data have also systematically revealed the dynamic characteristics of the crust-mantle structure and the deep tectonic evolution beneath the Dabie Mountains (Dong, 1999; Dong et al., 2005; Zhang et al., 2000; Yang, 2003; Xu et al., 2000; Xiao et al., 2007; Liu et al., 2003; Yuan et al., 2003). However, for studying the small-scale structure of the Huoshan seismic zone in the northern margin of the Dabie Mountain, data on the fine structure characteristics of multiple sets of faults are still lacking, especially on the seismogenic environment associated with seismic activity. In terms of the detection method of the regional fine velocity structure, currently, through dense array observation, a fault-scale fine model of fault scale can be constructed. Consequently, the lateral resolution of inversion can reach the order of several kilometers or even hundreds of meters (Yao, 2020), which provides more constraints for the fine structure of the upper crust seismogenic layer and reveals the control effect of the regional faults on seismic activity.

To elucidate the structural characteristics of the possible seismogenic layer beneath the two main faults in Huoshan area and study its tectonic correlation with seismic activity, this study uses the ambient noise data recorded by a dense array of 136 short-period seismometers in the Huoshan area to construct a high-resolution velocity structure of the upper crust at the depths of 1–7.5 km, improving the resolution accuracy of the seismic concentration area. Furthermore, combined with the results of the small earthquake relocation, the seismogenic structure and seismogenic environment in the deep crust beneath the Huoshan "seismic window" are discussed.

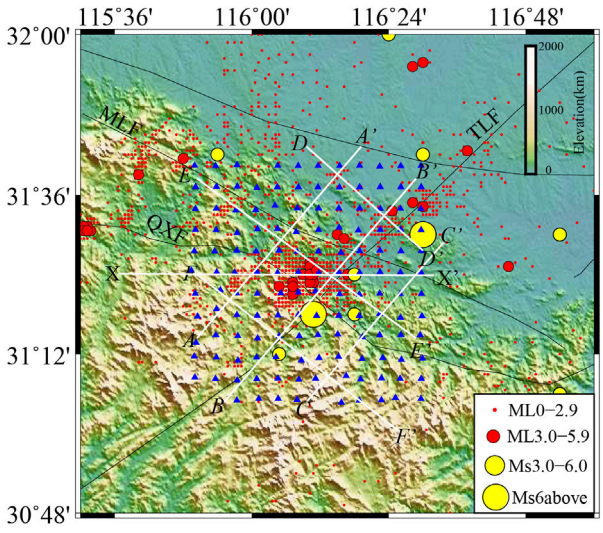

FIGURE 2
Distribution of short period temporary stations and main faults in the Huoshan area and its adjacent areas (Red dots and circles represent earthquakes (ML0 above)after 1970s by instrumental records; yellow circles are the earthquakes have been occurred before 1970s. The white lines AA′ to FF′ are the Vs. profiles in Figure 9; the lines XX′ is the vertical profile in Figure 6).

2 Data and methods

2.1 Data processing and dispersion measurements

The data used in our study comprise continuous data records of the vertical component of ambient noise collected from 26 April 2021 to 6 June 2021 by 136 short-period temporary seismometers deployed around Huoshan and the adjacent areas (Figure 2). The data were classified into daily records and then subjected to various forms of data processing, which aims to improve the signal-to-noise ratio (SNR) or suppress strong instantaneous signals. The entire date processing process can be found in Bensen et al. (2007). The daily data of each station were decimated and re-sampled at 20 Hz before detrending and demeaning. Then, to eliminate the influences of fixed noise sources, the data were segmented into multiple time series in three connecting period bands (0.5–2, 2–5, 5–10 s) and temporal normalization was performed for each band. The different period bands were finally stacked to afford normalized daily broadband (0.5–10 s) waveforms for the daily station-pair cross-correlation. Finally, the noise cross-correlation functions (NCFs) were obtained from 9180 station pairs, and EGFs were computed from the NCFs (NCFs between station 136 and others shown in Figure 3A).

The image transforms analysis technique of Yao et al. (2006,2011) was employed to extract the fundamental mode Rayleigh wave group and phase velocity dispersion curves from the EGF of every station pair. About 4244 phase dispersion curves were selected following several quality control criteria: 1) The SNR>4; 2) deviation greater than 2.5; and 3) small differences on similar paths. Subsequently, 4242 reliable phase dispersion curves were finally selected for direct inversion for this study. Figure 3B shows that the phase velocity varies significantly from 2.2 km/s to 3.2 km/s in the period band of 0.6–2 s, revealing the strong lateral heterogeneity of the shallow crust. Due to the small changes of dispersion in the long period, the short period instrument may have poor sensitivity. Thus, reliable phase velocity dispersion curves with a period of 0.8–4.6 s were selected for the direct inversion for the high-resolution three-dimensional (3D) tomography (Figure 3B).

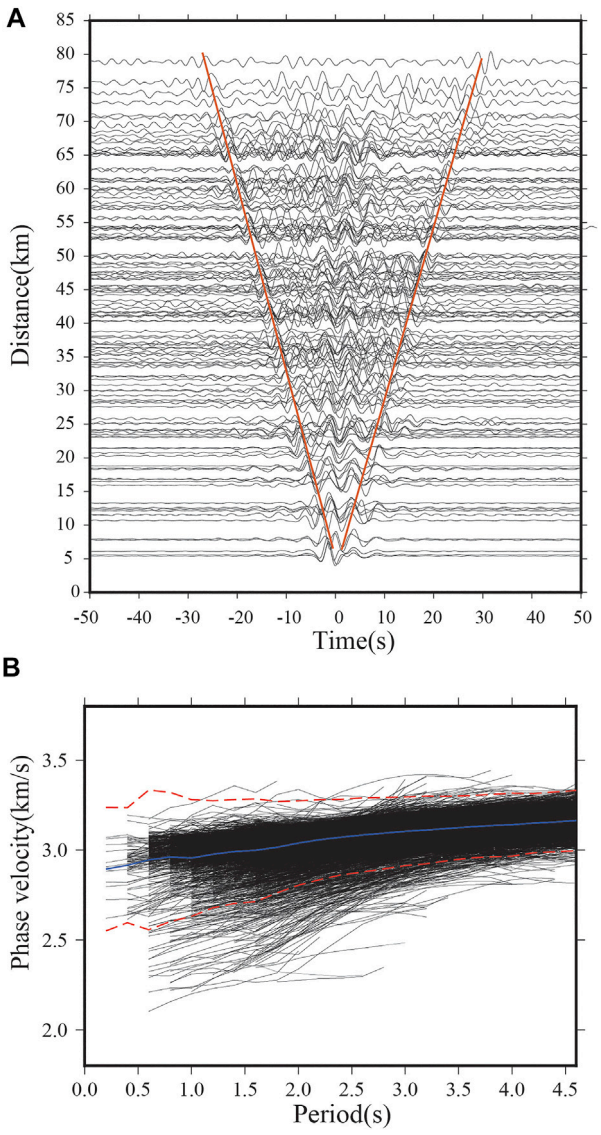

FIGURE 3
(A) The plot of cross-correlation functions of station HS136 with the period-band of 0.5–10 s (orange lines represent the average velocity with 2.6 km/s) **(B)** All phase velocity dispersion curves from 0.8 to 4.6 s obtained after quality control. The blue line shows the mean Rayleigh wave phase velocity; two red lines give the lower and upper boundaries of ±2.5 times the standard deviation.

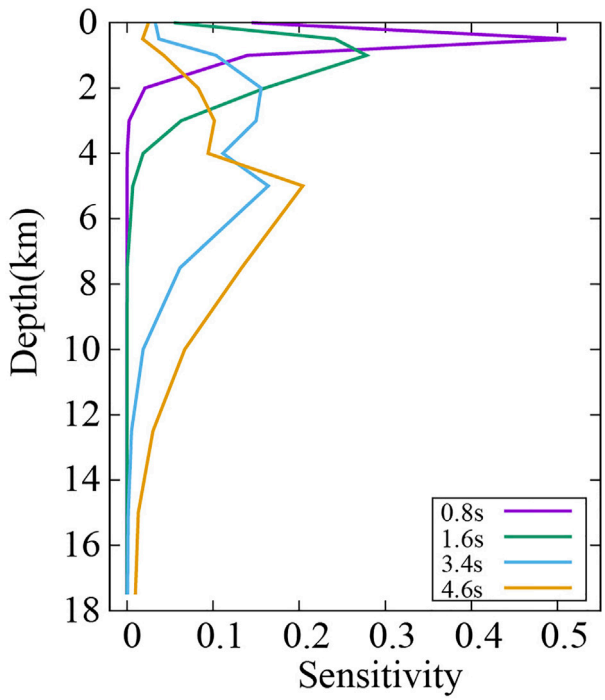

FIGURE 4
1-D depth sensitivity kernels to Vs. for the Rayleigh wave fundamental phase velocity at different periods using the average velocity.

2.2 Inversion method for 3-D vs. structure

In this study, the direct surface wave tomography method (DSurfTomo) of Fang et al. (2015) was employed to obtain a fine 3-D shear wave velocity model of the upper crust in the Huoshan area and adjacent areas. Considering the influence of bending rays of complex medium paths with smaller scales in the Huoshan area, the inversion problem was solved using the ray fast tracing method (Paige and Saunders, 1982; Rawlinson and Sambridge, 2005). This method skips the intermediate step of computing two-dimensional phase velocity maps that are based on the assumption of a great circle distance between the stations.

The average one-dimensional shear velocity model was fabricated from all the dispersion data from the depths of 0–5 km, and Luo's crustal velocity model (Luo et al., 2019) from the dispersion data from the depths of 5–15 km was constructed as an initial velocity model. A 0.04°×0.04°grid interval in the horizontal directions was employed, yielding 16×13 and 11 depth grid points. The depth grid intervals were kept constant at 0.5 km from the surface to 2 km and increased to 1 km and 2.5 km at the depthsof 2–5 km and 5–15 km, respectively. The checkboard test was used to access the model resolution in 3D. First, a synthetic model was generated, producing positive and negative checkerboard anomalies with a size of 0.08°×0.08°. Second, 2% Gaussian random noise was considered for the synthetic travel time data and inverted using exactly the same parameters and the number of iterations as those used for the inversion of the real data. After five iterations, the inversion results tended to stabilize, and the RMS decreased from 0.48 to 0.192 (Supplementary Figure S1). We rely on the Rayleigh wave depth sensitivity kernels of the periods from 0.8 to 4.6 s to constrain the reliable depth range for our results. Such depth sensitivity information is often obtained from the 1-D depth sensitivity kernels for Rayleigh waves. The kernels for some periods (0.6 s,1.6 s,3.4 s, 4.6 s) (Figure 4) show that the depth sensitivity increasing with increasing periods. The shallow part of the uppermost crust (<2 km) is constrained by the 0.8 s period, while the 4.6 s period is mainly sensitive to the lower brittle part of the upper crust (5–8 km). The sensitivity kernels reveal that our dataset is capable of resolving features in upper crust in this study.

The results are shown as horizontal slices in Figure 5 and vertical slices (herein, only the vertical profile (shown in Figure 2 X-X') for the latitude equals to 31.4°was tested in Figure 6. The velocity anomalies are well resolved by the dense crisscrossing ray paths (Figure 7) in the depth range of 1–7.5 km.

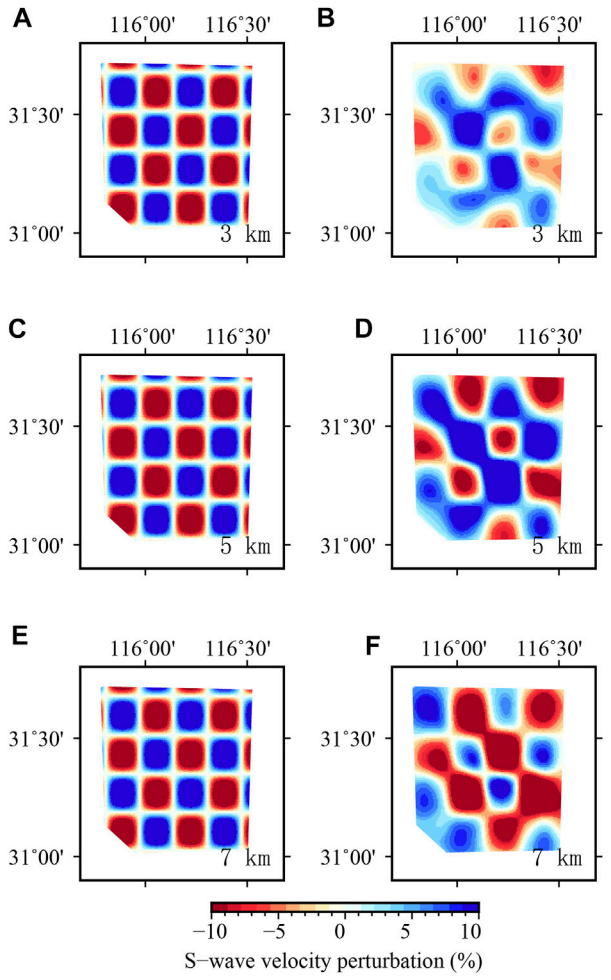

FIGURE 5
Theoretical results of Checkerboard test in horizontal slices **(A, C, E)**: Real model; **(B, D, F)**: Inverted model.

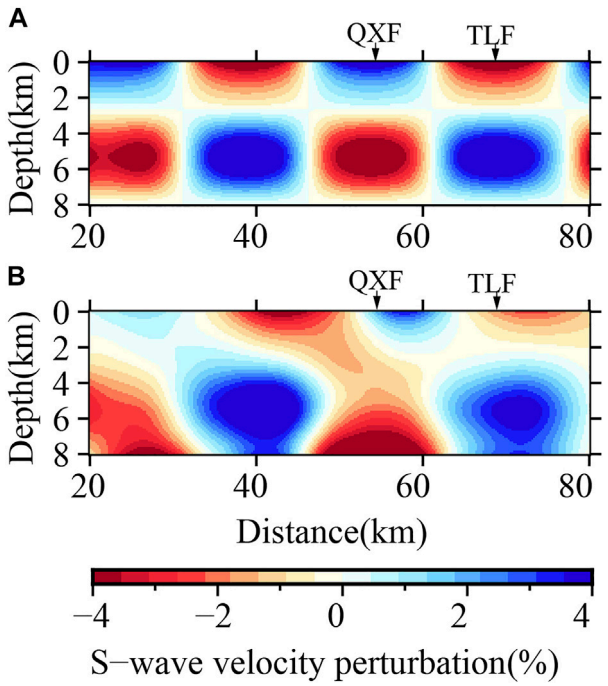

FIGURE 6
Theoretical results of checkerboard test in vertical slices XX′ (shown in Figure 2; **(A)**: Real model; **(B)**: Inverted model.

3 Results

Figure 8 displays the shear wave velocities at different depths (1–7.5 km) in the Huoshan earthquake area and adjacent areas (31–31.7°N, 115.8–116.5°E). Slices with different depths reveal the obvious high and low velocity conversions of the Dabie Mountains and Hefei Basin. The velocity structures relatively correspond to the geological and geomorphic characteristics of known tectonic units, which is consistent with the large-scale results of the region obtained by Luo et al. (2019). However, the results of this study depict more detailed information of multiple groups of faults. The details are as follows:

3.1 The NW-trending high velocity anomaly on the northern edge of the Dabie mountains

The northern edge of the Dabie Mountains has a high velocity anomaly in the shallow crust (Figure 8A, B), and has a relatively obvious zonal distribution along the NW direction, which is consistent with the trend of the Meishan-Longhekou and Qingshan-Xiaotian faults in this area, indicating the structural characteristics of the northern border fault of the Dabie Mountains. This figure shows that the NW-trending fractures have a certain control over the linear distribution of several high-velocity anomaly bodies. The value in the high velocity region is more than 3.6 km/s near the surface, which is similar to the velocity value obtained by Luo et al. (2012, 2013) in the shallow crust. The Qingshan-Xiaotian fault is the northern boundary of the North Dabie with complex rocks (Wang et al., 2009), and weak Quaternary development. The Yuexi-Yingshan area to the south is a concentrated zoneof high/ultrahigh pressure metamorphic rocks (Xiao et al., 2007). The North Dabie comprises complex metamorphic rocks and abundant Yanshanian granites (Jiang et al., 2000). Strong magnetic intrusive rocks and pyroclastic sedimentary rock series are developed on the surface of the North Huaiyang (Du and Zhang, 1999; Liu et al., 2010; Wang et al., 2012), which is consistent with the high anomaly features near the faults in this area. From the surface to 2 km depth, the NW-trending high velocity is more prominent in the shallow crust, which is consistent with the geomorphic features (Zhao et al., 2018) of the broken rock mass exposed along the Qingshan-Xiaotian fault, as well as the shallow metamorphic rocks of the Foziling Group in the Huoshan area (Liu Y C et al., 2013; Wang Y S et al., 2020). At the depth of 5 km, the NE direction is also characterized by high velocity zonation, which is related to the possible existence of high velocity rock mass in the upper crust near the Tudiling-Luoerling fault.

3.2 Low velocity anomaly and seismicity distribution at the intersection of different faults

At the depth of 5–7 km, the intersection of Tudiling-Luoerling and Qingshan-Xiaotian faults presents a relatively low velocity anomaly, and it is concentrated with medium and small earthquakes. The earthquake relocation results (TomoDD, Zhang and Thurber, 2003) show that small earthquakes in the Huoshan area exhibit obvious NE

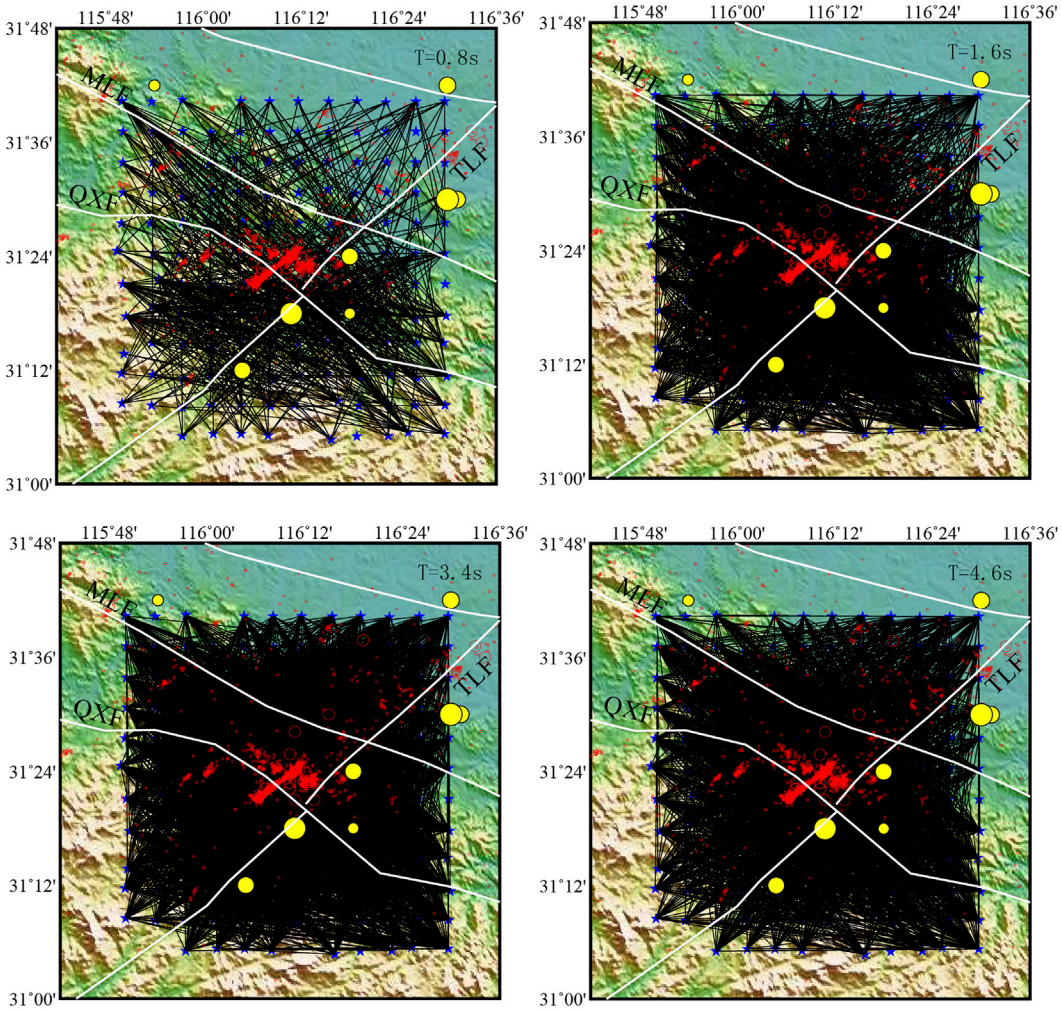

FIGURE 7
Distribution of the ray-path covered in Huoshan and adjacent area (T = 1,2,3,4,5,7 s). Red dots and circles represent the relocated earthquakes have been occurred during 2010–2022 and yellow circles are the same shown in Figure 2.

and NW banded distribution (Figures 8A, F). The dominant depth after positioning is mainly 5–10 km, which is basically located in the low velocity area. The NE-trending strip has a high degree of seismic concentration, and its strike is similar to that of the Tudiling-Luoerling fault. The NW-trending strip is along the strike direction of the Qingshan-Xiaotian fault and perpendicular to the Tudiling-Luoerling fault. The figure shows that the two fractures in different directions play an important role in controlling the spatial distribution of earthquakes in the Huoshan area. The relatively broken faults near the intersection area form a tectonic weak zone and extend to the surface, which is consistent with the concentrated small earthquakes.

4 Discussion

4.1 Deep characteristics of main faults on the northern edge of Dabie orogenic belt

Many groups of NW trending faults are present on the northern edge of the Dabie orogenic belt, which intersect with NE-trending faults and form complex structure features on the surface. The NW-trending faults mainly include the Meishan-Longhekou, Jinzhai-Shucheng, and Qingshan-Xiaotian faults, which are mainly exposed to the surface, and their active age is probably in the early Middle Pleistocene (Zhao et al., 2018). The NE-trending Tudiling-Luoerling fault is a relatively new active fault, and the latest active time is from Pleistocene to early Late Pleistocene (Shu et al., 2018). Figure 9 displays the six vertical profiles along NW and NE directions in the study area, revealing that the crustal velocity structure on the northern edge of the Dabie orogenic belt is closely related to the fault properties.

4.1.1 Qingshan-xiaotian fault

The three vertical velocity profiles of AA', BB' and CC' (Figures 9A–C) along the Dabie orogenic belt from the south to north exhibit obvious boundary characteristics of high and low velocity anomalies at the junction of the mountain and basin. The AA' and BB' profile reveal that the large velocity variation in the shallow crust corresponds to the location of the Qingshan-Xiaotian and Meishan-Longhekou faults. The most significant velocity contrast is argubaly observed beneath the

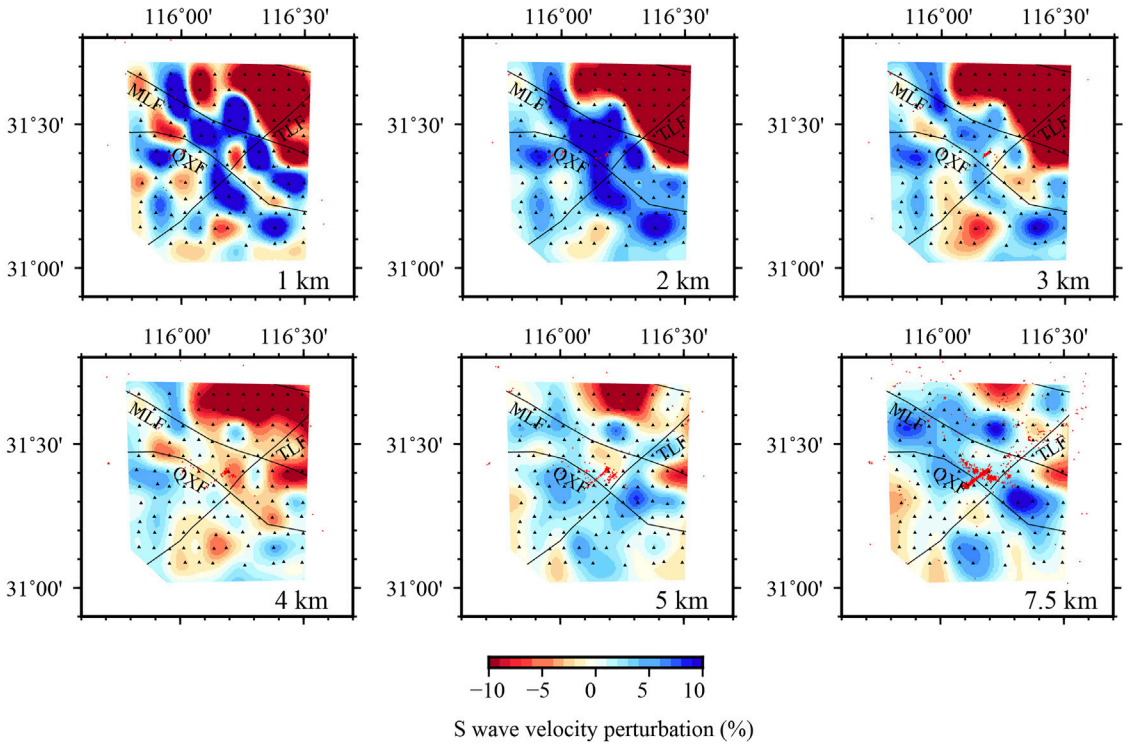

FIGURE 8
Slices of shear wave velocity at the depths of 1–7.5 km (Red dot represents the re-locations of earthquakes below magnitude 3).

Meishan-Longhekou faultand Meishan-Longhekou fault is also known as Jinzhai-Shucheng fault in some geological researches. It is considered that the extensional structure of the Qingshan-Xiaotian fault and the thrust nappe structure with the Jinzhai-Shucheng fault as the front edge have the same shear direction, which is part of the extensional structure during the exhumation of the ultrahigh-pressure metamorphic rocks in the Dabie Mountains (Jiang et al., 2003). This fault separated the Hefei Basin and Dabie mountains (Figure 8, and Figures 9A, C, E), and delineates nicely the northern boundary of the seismogenic zone in Figure 2.

The Qingshan-Xiaotian fault has an anti "S" shape, and the velocity map shows that different sections exhibit different tendencies (Figures 9A, B). The AA' profile shows that the northwest section of the fault under the surface dips toward the northeast and that the high velocity anomaly on both sides is discontinuous (black dash line in Figure 9A). The BB' profile shows that the middle section of the fault tends to be nearly vertical and that the velocity structure on both sides has a slight gradient difference (Figure 9B). The electrical structure of the Dabie orogenic belt shows that (Xiao et al., 2007), under the north inclined and normal Qingshan–Xiaotian fault (Xiang et al., 2008), a relatively high resistivity and conductivity change occurs in the middle and upper crust, which is a boundary fault separating the North Dabie and North Huaiyang massifs. This has been verified by other geophysical integrated explorations (Liu et al., 2003; Yang, 2003; Zhang et al., 2012). Significant velocity variation beneath the north edge of Dabie mountain in this study confirm that the Qingshan–Xiaotian fault and Meishan-Longhekou fault dislocated different strata in the upper crust of the Huoshan area.

According to the research on deep structural characteristics, due to the subduction and collision between the Yangtze plate and North China plate, and due to the strong compression deformation environment in the orogenic process, the dislocation of the Moho under the Qingshan-Xiaotian fault has reached 4.5 km (Wang et al., 1997; Liu et al., 2003). The suture zone between the Yangtze plate and the North China plate may be located below this fault (Yang, 2003; Yuan et al., 2003; Xu et al., 2008). Although the surface location of the suture zone cannot be determined from the shallow crustal structure, the AA 'and BB' profiles still reveal that the Qingshan–Xiaotian fault presents a high shear wave velocity, especially at a depth of 6–8 km where the value is as high as 3.8 km/sThe high velocity structure from the deep suture zone may be related to the upwelling of the upper mantle magma, the remelting of the crustal material, and the local intrusion, occurring during the collision of the two large blocks of the Yangtze and North China.

4.1.2 Tudiling-luoerling fault

Figures 9D–F reveals relatively obvious high and low velocity changes, showing that the dip angle of the Tudiling-Luoerling fault is nearly vertical. The DD ' (Figure 9D) and EE' (Figure 9E) profiles show that the velocity of different sections has significantly changed. The DD' profile reveals that the northeastern segment of the Tudiling-Luoerling fault gradually hides in the Hefei basin at a depth of about 4 km. The EE' profile shows that an obvious low velocity area exists in the fault intersection area, extending to a depth of about 8 km. Projection of the relocated earthquakes on to the velocity profile shows that there are three groups of very close parallel faults existing near the high and low velocity gradient zone

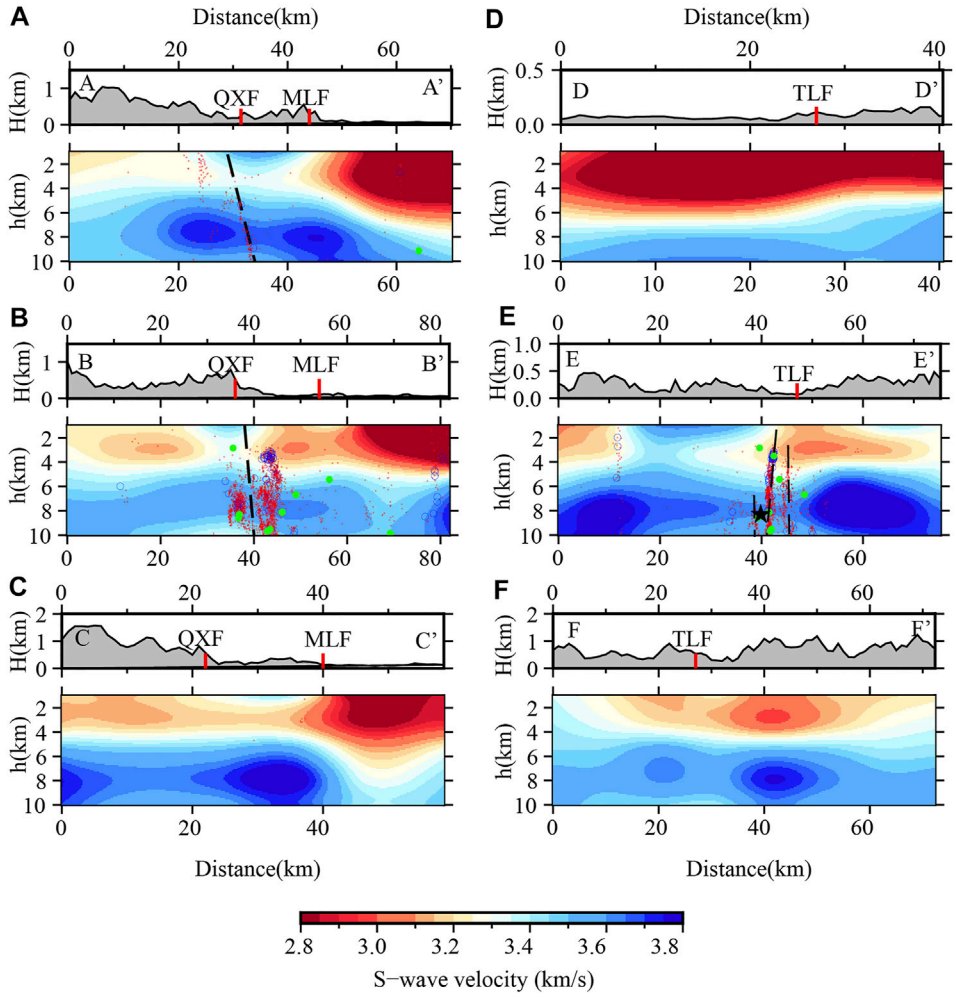

FIGURE 9
Shear wave velocity structure in different vertical profile **(A–F)** shown in Figure 2 (The red and blue circles are the small earthquakes of ML0-1.9, 1.9–2.9, respectively; the green dots represent earthquakes above ML3. The black star represents the 2014 Huoshan M4.3 earthquake. Black dashed lines represent the inferred fault under the surface).

(Figure 9E) and that the seismic concentration of the middle fault is the highest. It is indicated that Tudiling-Luoerling faults is composed of multiple secondary faults in th shallow crust. Xu et al. (2022) used the regional stress field to simulate and calculate the sliding properties of three NE-trending seismic sections in the Huoshan area, which is consistent with the trend of the Tudiling–Luoerling fault andmatches the results of this study. In the late period of the Dabie orogen, a series of extensional faults formed in the Dabie Mountains due to the extensional action in the NS direction (Ma et al., 2003). The NE-trending Tudiling–Luoerling fault inherited the tectonic weak zone of the early Qingshan–Xiaotian fault in the shallow crust in the way of the right-lateral strike–slip (Cui et al., 2020) and formed numerous fault planes with an echelon parallel arrangement with different depths in the low velocity area at the intersection. Xu et al. (2022) suggested that this was related to the pull apart produced by the right-lateral right step of the Tanlu fault zone and the Shangcheng-Macheng fault. By the convergence of the tectonic force, it forms multiple faults and cause large amounts of small earthquakes in the Huoshan area.

4.2 Low velocity and fault seismogenic environment in shallow crust of Huoshan "seismic window"

The main earthquakes in Huoshan "seismic window" are distributed in the low velocity area at a depth of 5–8 km. The deep seismic wide-angle reflection/refraction results of the eastern Dabie (Liu et al., 2003) reveal the high-velocity dome structure in the Dabie Mountains, and a low velocity layer exists in the middle and upper crusts on its wings. Moreover, the tomography results (Xu et al., 2000) reveal that the middle and upper crustal tectonic detachment zone in the Dabie Mountains is the main tectonic reason for the existence of low velocity layers, which is closely related to the deep subduction of the Yangtze Block as well as the collision orogeny and compression uplift of the North China Block. The Qingshan–Xiaotian fault is a large-scale boundary fault that cuts through the crust inside the Dabie Mountains. The profiles across the Qingshan-Xiaotian fault exhibit obvious discontinuous high velocity in the upper crust (Figures 9A, B), inferring the location of the north detachment of the dome wing of the Dabie Mountains is near the Qingshan-Xiaotian fault, which is

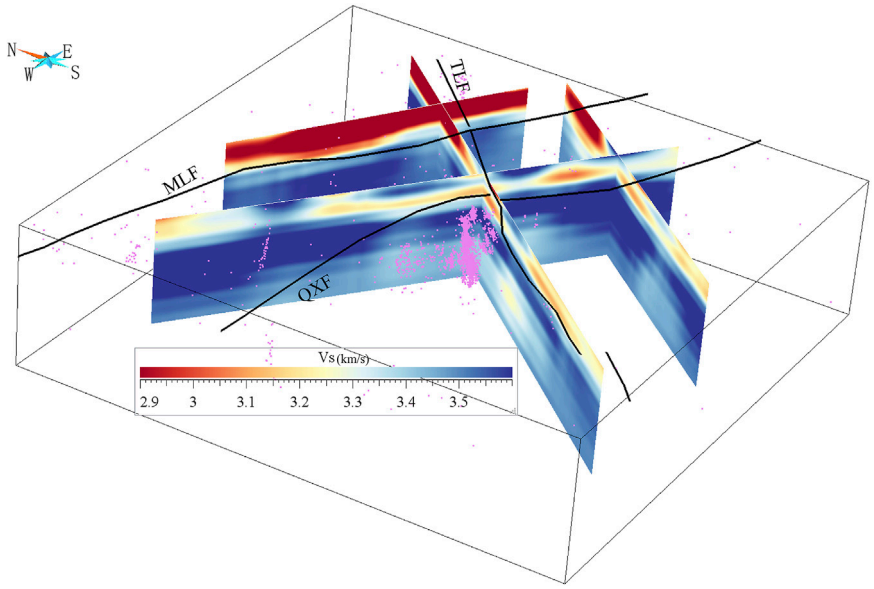

FIGURE 10
3-Dimensional map of the upper crust structure with the distribution of small earthquakes in Huoshan "seismic window" (Black lines on the surface are the known faults, and pink dots are the earthquake swarm).

consistent to the observation of the seismic wide-angle reflection/refraction (Liu et al., 2003).

Figure 10 displays multiple profiles of the earthquakes by combining multiple profiles. The relatively low velocity zone to the north at the intersection of the Tudiling-Luoerling fault and the Qingshan-Xiaotian faults is also a concentrated area of earthquakes. The electrical structure suggests that the earthquake cluster area is located in a relatively high conductivity area, which is related to the truncation of the fluid in the high conductivity layer of the middle and lower crust, migration to both sides under the compression environment, rising through the fault, and weakening of the stress conditions (Xiao et al., 2007; Cui et al., 2020). From the position of the low-velocity body, this area may be interpreted as the low velocity detachment zone at the wing of the Dabieshan dome. A structural weak zone formed under the action of multiple sets of faults. Since large amounts of strain cannot be accumulated, small earthquakes are active and concentrated. Multiple en echelon parallel secondary faults (black dashed lines in Figure 9E) of the Tudiling-Luoerling fault zone in the upper crust are all near the low velocity zone, which plays a major role in controlling the concentrated activity of NE-trending small earthquakes.

Historical earthquakes with magnitudes of over 5 are mainly distributed along the Tudiling-Luoerling fault in the NE direction, which is different from the concentrated distribution of small earthquakes at the fault intersections. This study discussed the reasons for the difference of spatial distribution between historical and modern small earthquakes. The BB' section (Figure 9B) shows that small earthquakes below ML3 are mostly concentrated on both sides of the Qingshan-Xiaotian fault, forming two obvious clusters of seismic activity. One of the main fault planes to the north side controls most of the seismic activity. However, the seismicity above ML3 is not concentrated, and it is scattered along the Tudiling-Luoerling fault to the northeast, denoting that the Qingshan-Xiaotian fault mainly controls the microseismicity below ML3. Moreover, the surface topography shows that the distribution width of this fault is wide. Considering the distribution of the relocated earthquakes, it can be deduced that there exists several secondary faults in this area. Field geological investigations have determined that the Qingshan-Xiaotian fault leads to ductile shear zones and brittle faults, with the widest ductile shear zone up to 2 km (Wang et al., 2009). The abundant micro-seismic activities below ML1 (Stanek F, et al., 2014) are more likely related to shear slips on micro-fractures on multiple fault planes (Hubbert and Rubey, 1959). The focal depth of earthquakes above ML3 is generally 6–10 km, which is obviously different from the distribution depth of with ML1 and ML2 earthquakes. These larger earthquakes mainly distribute far away from the low velocity weak zone (Figure 9C), which is believed that these areas can accumulate more strain. Figure 9E shows that compared to the more divergent microseismic activity near the Qingshan-Xiaotian fault, the earthquakes especially the larger earthquakes above ML3, are more concentrated on the multiple parallel secondary faults of the Tudiling-Luoerling fault, indicating that the control effect isstronger.

In 2014, an Ms 4.3 earthquake (black star show in Figure 9E occurred in the Huoshan area, with the epicenter located south of the Qingshan–Xiaotian fault, slightly away from the main area of the small earthquake activity. Although the main earthquake was very close to the fault from the surface projection, the EE' profile showed that it was close to the main fault plane of the Tudiling-Luoerling fault; therefore, the seismogenic structure of this earthquake was the Tudiling-Luoerling fault. The Tudiling-Luoerling fault is an active strike-slip fault that exists since the late Pleistocene, which may be the reason why the historically strong earthquake activities have been mainly distributed along the NE direction and are not concentrated in a certain area.

5 Conclusion

In this study, the fine velocity structure of the upper crust in the Huoshan area was obtained using the continuous ambient noise data procured from a dense array. Furthermore, along with the relocated small seismic events, the fine structural characteristics of the upper crust and the relation of the main faults and their correlation with seismic activity were discussed. The following conclusions were obtained:

(1) A significant high velocity belt anomaly exists in the shallow crust in Huoshan "seismic window", which is consistent with the trend of the NW-trending Qingshan-Xiaotian fault, reflecting that numerous high velocity magmatic rocks and metamorphic rocks ascended and were exposed on the surface under the action of strong metamorphic dynamics in this area. As the boundary fault between the North Dabie and North Huaiyang, the Qingshan-Xiaotian fault dislocated different strata, providing an important channel for the upwelling of the upper mantle magma, the remelting of the crustal granite, and the *in-situ* intrusion under the action of strong extrusion deformation environment in the collision process of the Dabie orogenic belt.
(2) At a depth of 5–7 km in the upper crust, the intersection of the Qingshan–Xiaotian and Tudiling–Luoerling exhibits relatively low velocity characteristics. The high and low velocity gradient zone shown in the velocity profile corresponds to the lower part of the Qingshan–Xiaotian fault, revealing the shape of the detachment zone in the wing of the Dabie dome structure. The shallow low velocity of the north of the fault is believed to inherit the low velocity from the middle crust detachment zone, which is closely related to the deep subduction of the Yangtze block as well as the collision orogeny and compression uplift of the North China block.
(3) The low velocity zone of the upper crust in Huoshan "seismic window" is consistent with the main distribution layer of small earthquake activity. The relocated earthquakes exhibit a concentrated and orthogonal zonal distribution on the surface, which is obviously controlled by the NW-trending Qingshan-Xiaotian fault and the NE-trending Tuling-Luoerling fault. Along with the velocity structure and positioning results, the two fault zones are believed to be composed of multiple secondary faults, which are distributed at different depths in the shallow crust. Among them, three parallel and nearly vertical en echelon secondary faults are present in the Tudiling-Luoerling fault zone, which control the occurrence of most earthquakes in Huoshan "seismic window".

Data availability statement

The raw data supporting the conclusion of this article will be made available by the authors, without undue reservation.

Author contributions

LL completed the main part of the paper, HY provide important suggestions in inversion calculation and result discussion, BZ completed earthquake relocated work, JuL and JiL completed array layout, XW and DZ participated in part of the calculation, and PS, YY and PZ participated in result discussion and map drawing.

Funding

This study is funded by the National Natural Science Foundation of China (NSFC) Project (4212540, 42104023), the Earthquake Prediction Open Fund of China Earthquake Administration (XH22026D), the Open Fund of Anhui Mengcheng National Geophysical National Observatory (MEMGO-202212, MENGO-202213), and the Earthquake Science and Technology Innovation Team of Anhui Earthquake Agency.

Acknowledgments

The authors are grateful for the use of field instruments and some data pre-processing provided by the Institute of Geology and Geophysics, Chinese Academy of Sciences.

Conflict of interest

The authors declare that the research was conducted in the absence of any commercial or financial relationships that could be construed as a potential conflict of interest.

Publisher's note

Supplementary material

The Supplementary Material for this article can be found online at: https://www.frontiersin.org/articles/10.3389/feart.2023.1110061/full#supplementary-material

SUPPLEMENTARY FIGURE S1
The standard deviation of residuals obtained after 5 iterations is given 686 by the red lines in **(A)**, with a significant convergence after the first 2 iteration and reduction of 687 standard deviations of residuals from 0.48 s to 0.192 s **(B)**.

References

Bensen, G. D., Ritzwoller, M. H., Barmin, M. P., Levshin, A. L., Lin, F., Moschetti, M. P., et al. (2007). Processing seismic ambient noise data to obtain reliable broad-band surface wave dispersion measurements. *Geophys. J. Int.* 169 (3), 1239–1260. doi:10.1111/j.1365-246x.2007.03374.x

Cui, T. F., Cen, X. B., Zhan, Y., Zhao, L. Q., and Liu, Z. Y. (2020). Characteristics of deep electrical structure and seismogenic structure beneath Anhui Huoshan earthquake area. *Chin. J. Geophys. (in Chinese)* 63 (1), 256–269. doi:10.6038/cjg2019M0458

Dong, S. W., Gao, R., Li, Q. S., Liu, X. C., Qian, G. H., Huang, D. D., et al. (2005). A deep seismic reflection profile across a foreland of the Dabie orogen. *Acta Geological Sinica (in Chinese)* 79 (5), 595–601. doi:10.3321/j.issn:0001-5717.2005.05.003

Du, J. G., and Zhang, P. (1999). Mesozoic volcanic rocks in northern part of Dabie orogenic belt. *Geoscience*, 57–65.

Fang, H., Zhang, H. H., Huang, Y. C., and van der Hilst, R. D. (2015). Direct inversion of surface wave dispersion for three-dimensional shallow crustal structure based on ray tracing: Methodology and application. *Geophys. J. Int.* 201, 1251–1263. doi:10.1093/gji/ggv080

Han, S., Zhang, H., Xin, H., Shen, W., and Yao, H. (2022). USTClitho2. 0: Updated unified seismic tomography models for continental China lithosphere from joint inversion of body-wave arrival times and surface-wave dispersion data. *Seismological Research Letters* 93 (1), 201–215. doi:10.1785/0220210122

Hong, D. Q., Wang, X. Z., ChengX, et al. (2013). Study on variation of seismic coda Qc value of repeating earthquake series in Anhui "Huoshan Seismic Window". *Chinese Journal of Geophysics (in Chinese)* 56 (10), 3416–3424. doi:10.6038/cjg20131017

Hubbert, M. D., and Rubey, W. W. (1959). Role of fluid pressure in mechanics of over thrust faulting. *Geological Society of America Bulletin* 70, 115–205. doi:10.1130/0016-7606(1959)70[115:rofpim]2.0.co;2

Jiang, L. L., Wu, W. P., Chu, D. R., Liu, Y. C., and Zhang, Y. (2003). Extension-thrust nappe structure in the northern Dabie mountains after the plates collision of mesozoic crustal transition from compression to extension in the Dabie mountains: Evidence from granite. *Chin. Sci. Bull.* 48 (14), 1557–1563. doi:10.1360/csb2003-48-14-1557

Jiang, L. L., Wu, W. P., Hu, L. J., Liu, Y. C., and Su, W. (2000). Tectonic setting of the north Dabie complex in the Dabie mountains. *Geoscience, Journal of Graduate School, China University of Geosciences* 14 (1), 29–36.

Liu, F. T., Xu, P. F., Liu, J. S., Yin, Z. X., Qin, J. Y., Zhang, X. K., et al. (2003). The crustal velocity structure of the continental deep subduction belt: Study on the eastern Dabie orogen by seismic wide-angle reflection/refraction. *Chinese Journal of Geophysics (in Chinese)* 46 (3), 366–372. doi:10.3321/j.issn:0001-5733.2003.03.014

Liu, Y. C., Li, Y., Liu, L. X., Gu, X. F., Deng, L. P., and Liu, J. (2013). Neoproterozoic igneous rocks of triassic low-grade metamorphism in the Dabie orogenic belt: Sheets detached and exhumed from the surface of subducted continental crust. *Chinese Science Bulletin* 58 (23), 2330–2337. doi:10.1360/972013-581

Liu, Y. C., Liu, L. X., Gu, X. F., Li, S. G., and Liu, J. (2010). Discovery of neoproterozoic epimetamorphic granites in the western part of the North Huaiyang belt of the Dabie mountains and its tectonic significance. *Chinese Science Bulletin* 55 (24), 2391–2399. doi:10.1360/csb2010-55-24-2391

Liu, Z. M., Huang, X. L., and Ni, H. Y. (2015). Seismogenic structure of the 20, April, 2014Huoshan Ms4.3 earthquake in auhui region. *Acta Seismologica Sinica* 37 (3), 402–410. doi:10.11939/jas.2015.03.003

Luo, S., Yao, H. Y., Li, Q., Wang, W., Wan, K., Meng, Y., et al. (2019). High-resolution 3D crustal S-wave velocity structure of the Middle-Lower Yangtze River Metallogenic Belt and implications for its deep geodynamic setting. *Science China Earth Sciences* 62 (9), 1361–1378. doi:10.1007/s11430-018-9352-9

Luo, Y., Xu, Y., and Yang, Y. (2013). Crustal radial anisotropy beneath the Dabie orogenic belt from ambient noise tomography. *Geophysical Journal International* 195 (2), 1149–1164. doi:10.1093/gji/ggt281

Luo, Y., Xu, Y., and Yang, Y. (2012). Crustal structure beneath the Dabie orogenic belt from ambient noise tomography. *Earth and Planetary Science Letters* 313, 12–22. doi:10.1016/j.epsl.2011.11.004

Ma, C. Q., Yang, K. G., Ming, H. L., and Lin, G. C. (2003). Time of mesozoic crustal transition from compression to extension in the dabie mountains: Evidence from granite. *Sci. Chi.(Series D)* 33 (9), 817–827.

Miao, P., Hong, D. Q., Wang, X. Z., Liu, Z. M., and Wang, J. (2014). Dynamic backgrounds of the "huoshan seismic window" and its implications. *Earthquake Research in China* 30 (4), 534–542.

Paige, C. C., and Saunders, M. A. (1982). LSQR: An algorithm for sparse linear equations and sparse least squares. *ACM Transactions on Mathematical Software (TOMS)* 8 (1), 43–71. doi:10.1145/355984.355989

Rawlinson, N., and Sambridge, M. (2005). The fast marching method: An effective tool for tomographic imaging and tracking multiple phases in complex layered media. *Exploration Geophysics* 36 (4), 341–350. doi:10.1071/eg05341

Shu, P., Lu, S., Fang, L. H., Zheng, Y. P., and Shong, F. M. (2018). Preliminary study on geometry structure and activity features of Luo'erling tudiling fault in late quaternary. *Technology for Earthquake Disaster Prevention* 13 (1), 87–97. doi:10.11899/zzfy20180108

Stanek, F., Eisner, L., and Moser, T. J. (2014). Stability of source mechanisms inverted from P-wave amplitude microseismic monitoring data acquired at the surface. *Geophysical Prospecting* 62 (3), 475–490. doi:10.1111/1365-2478.12107

Wang, C. Y., Zheng, J. H., Hu, H. X., Lou, H., Zhang, X. K, Song, S. Y., et al. (1997). The study on the crustal structure of Dabie orogenic belt. *Sci. China* 27 (3), 221–226.

Wang, Y. S., Bai, Q., Tian, Z. Q., and Du, H. (2020). Dating of clastic rocks in the southern margin of hefei basin and its implications for the exhumation of ultrahigh pressure rocks in the Dabie orogenic belt. *Sci. China Earth Sci.* 50 (07), 921–935.

Wang, Y. S., Sheng, Y., Xiang, B. W., and Zhang, C. Y. (2012). Metamorphic pressure of the luzhenguan group in the North Huaiyang low-grade metamorphic belt and its indication for evolution of the Dabie mountains. *Geological review* 58 (05), 865–872. doi:10.16509/j.georeview.2012.05.014

Wang, Y. S., Xiang, B. W., Zhu, G., Chen, W., and Wei, X. (2009). 40Ar-39Ar geochronology. *records for post-orogenic extension of the Xiaotian-Mozitan fault* 38 (5), 458–471.

Xiang, B. W., Wang, Y. S., Li, C. C., Zhu, G., and Shi, Y. (2008). Evolution of the Xiaotian-Mozitan fault and its implications for exhumation of Dabie HP–UHP rocks. *Progress in Natural Science* 18 (6), 713–722. doi:10.1016/j.pnsc.2007.11.020

Xiao, Q. B., Zhao, G. Z., Zhan, Y., Chen, X. B., Tang, J., and Wang, J. J. (2007). A preliminary study on electrical structure and dynamics of the ultra-high pressure metamorphic belt beneath the Dabie Mountains. *Chinese Journal of Geophysics* 50 (3), 812–822.

Xin, H., Zhang, H., Kang, Gao, L., and Gao, J. (2019). High-resolution lithospheric velocity structure of continental China by double-difference seismic travel time tomography. *Seismological Research Letters* 90 (1), 229–241. doi:10.1785/0220180209

Xiong, C., Xie, Z. J., Zheng, Y., Xiong, X., Ai, S. X., and Xie, R. X. (2019). Rayleigh wave tomography in the crust and upper mantle of the Dabie-Tanlu orogenic zone. *Seismology and Geology* 41 (1), 1–20. doi:10.3969/j.issn.0253-4967.2019.01.001

Xu, P. F., Liu, F. T., Wang, Q. C., Cong, B. L, Chen, H., and Sun, R. M. (2000). Seismic tomography beneath the Dabie-Sulu collision orogen-3D velocity structures of lithosphere. *Chinese Journal of Geophysics(in Chinese)* 43 (3), 377–385. doi:10.3321/j.issn:0001-5733.2000.03.011

Xu, S. T., Yuan, X. C., and Wu, W. P. (2008). New geological interpretation of the seismic reflection profile from Huangshi to Liu'an across the Dabie Mountains, China. *Geological Bulletin of China* 27 (1), 19–26.

Xu, X., Wan, Y. G., Feng, G., Li, X., Liu, Z. M., and He, J. (2022). Study on three seismic fault segments and their sliding properties revealed by clustered seismic events in Huoshan area, Anhui province. *Chinese Journal of Geophysics* 65 (5), 1688–1700. doi:10.6038/cjg2022P0768

Yang, W. C. (2003). Deep structures of the east Dabie ultrahigh pressure metamorphic belt. *East China. Science in China Series D-Earth Science* 2003 (06), 183–194. doi:10.6038/cjg2022P0768

Yao, D. Q., Liu, J. C., Li, J., and Zhai, H. T. (2003). Seismic activities and structures of the Lu'an-Huoshan seismic risk area. *Seismology and Geology* 25 (2), 211–219. doi:10.3969/j.issn.0253-4967.2003.02.005

Yao, H., Gouedard, P., Collins, J. A., McGuire, J. J., and van der Hilst, R. D. (2011). Structure of young East Pacific Rise lithosphere from ambient noise correlation analysis of fundamental- and higher-mode Scholte-Rayleigh waves. *Comptes Rendus Geoscience* 343 (8-9), 571–583. doi:10.1016/j.crte.2011.04.004

Yao, H. (2020). Building the community velocity model in the Sichuan-Yunnan region, China: Strategies and progresses.2020. *Science China Earth Science* 63, 1425–1428. doi:10.1007/s11430-020-9645-3

Yao, H., van der Hilst, R. D., and de Hoop, M. V. (2006). Surface-wave array tomography in SE tibet from ambient seismic noise and two-station analysis: I - phase velocity maps. *Geophys.J. Int.* 166, 732–744. doi:10.1111/j.1365-246X.2006.03028.x

Ye, Q. D., Ding, Z. F., Zheng, C., Lu, M. M., Wu, P. P., and Chen, H. P. (2015). Phase velocity tomography of Rayleigh and Love waves in Dabie-Sulu and its adjacent areas from ambient seismic noise. *Acta Seismologica Sinica* 37 (1), 29–38. doi:10.11939/jass.2015.01.03

Yuan, X. C., Klemperer, S. L., Teng, W. B., Lai, X. L., and Chetwin, E. (2003). Crustal structure and exhumation of the DabieShan ultra-high pressure oroge, eastern China, from seismic reflection profiling. *Geology* 31 (5), 435–438.

Zhang, H., and Thurber, C. H. (2003). Double-difference tomography: The method and its application to the hayward fault, California. *Bulletin of the Seismological Society of America* 93, 1875–1889. doi:10.1785/0120020190

Zhang, J. D., Yang, X. Y., Liu, C. Z., Zhang, L. L., Li, B., Xu, Y., et al. (2012). The fine deep structure of the northern margin of the Dabie Orogenic Belt from gravity-magnetic-electrical-seismic combination survey. *Chinese Journal of Geophysics (in Chinese)* 55 (07), 2292–2306. doi:10.6038/j.issn.0001

Zhang, Z., Li, Y. K., Lu, D. Y., Teng, J., and Wang, G. (2000). Velocity and anisotropy structure of the crust in the Dabieshan orogenic belt from wide-angle seismic data. *Physics of the Earth and Planetary Interiors* 122 (1), 115–131. doi:10.1016/s0031-9201(00)00190-4

Zhao, P., Li, G., Zhai, H., Tong, Y. L., Zheng, Y. P., and Yang, Y. Y. (2018). A preliminary study on quaternary activity of Qingshan-Xiaotian fault zone in east Dabie area. *Plateau Earthquake Research* 30 (03), 11–16.

Zheng, Z. B., Qing, M., and Li, M. L. (1999). Study on correlation between Huoshan seismic window and occurrence of moderate earthquake of East China. *Journal of Seismology* 1999 (2), 1–9.

frontiers | Frontiers in Earth Science

TYPE Original Research
PUBLISHED 03 February 2023
DOI 10.3389/feart.2023.1082680

OPEN ACCESS

EDITED BY
Fuqiong Huang,
China Earthquake Networks Center, China

REVIEWED BY
Lihua Fang,
Institute of Geophysics, China Earthquake Administration, China
Guixi Yi,
Sichuan Earthquake Administration, China

*CORRESPONDENCE
Xianwei Zeng,
zeng_xw@126.com

SPECIALTY SECTION
This article was submitted to Solid Earth Geophysics,
a section of the journal
Frontiers in Earth Science

RECEIVED 28 October 2022
ACCEPTED 23 January 2023
PUBLISHED 03 February 2023

CITATION
Zeng X, Li X, Li M and Li W (2023), Investigation of the 2015 M_s5.8 Alxa Left Banner earthquake sequence: Aftershock evolution and seismogenic structure. *Front. Earth Sci.* 11:1082680.
doi: 10.3389/feart.2023.1082680

Investigation of the 2015 M_s5.8 Alxa Left Banner earthquake sequence: Aftershock evolution and seismogenic structure

Xianwei Zeng*, Xinyan Li, Mengya Li and Wenjun Li

Earthquake Administration of Ningxia Hui Autonomous Region, Yinchuan, China

Introduction: The 2015 M_s5.8 Alxa Left Banner earthquake (Alxa M_s 5.8 eathquake) struck a sparsely inhabited area of Inner Mongolia, northwestern China. However, as first > M_s 5 event on the Ningxia–Inner Mongolia segment of the North–South seismic zone for 24 years, the earthquake is of considerable scientific interest.

Methods: In this study, the seismic distribution of the Alxa M_s 5.8 earthquake sequence was redetermined *via* the analysis of data from permanent and campaign seismic stations using the double-difference (DD) method. To improve the completeness of the earthquake catalog, the match and locate (M&L) method was then used to detect micro-earthquakes.

Results: The mainshock rupture started at the eastern end of the fault, propagating east-to-west and deep-to-shallow. Aftershocks were distributed in a NEE trending (N70°–75°E), with a 12-km length and a dominant depth of 15–25 km. Moreover, the aftershocks formed two distinct segments (the eastern and western segments). The mainshock and early aftershocks were primarily located on the eastern segment and relatively fewer aftershocks occurred on the western segment.

Discussion: Subsequently, from March to June 2016, three earthquakes of > M_L3.0 occurred in the seismic gap between the eastern and western segments, releasing stress that was not released by the mainshock. According to the aftershock evolution, the seismogenic fault of Alxa M_s 5.8 eathquake associated with a NEE-striking blind fault that becomes steeply dipping toward the south. Furthermore, the seismogenic fault is a western branch fault of the Dengkou–Benjing blind fault (DBF). The aftershock evolution and inferred seismogenic structure provide a reference for further research in the study area.

KEYWORDS

double-difference (DD) location, match and locate (M&L) method, aftershock evolution, barrier, seismogenic structure

1 Introduction

During the morning (UTC 07:39) of 15 April 2015, an M_s5.8 [or *M*w 5.4, United States Geological Survey (USGS)] earthquake occurred in Alxa Left Banner, Inner Mongolia, northwestern China. The epicenter was located at the junction of Bayanmuren Sumu and Jilantai Town. The earthquake struck a sparsely inhabited area and caused few casualties; however, it ended 24-years of seismic quiescence along the Ningxia–Inner Mongolia segment of the North–South seismic zone. As the first > M_s 5 earthquake in this region for quarter of a century, numerous studies of the earthquake have been reported. Focal mechanism solutions of the mainshock and locations of early aftershocks show a nearly pure left-lateral strike-slip

faulting mechanism of the mainshock (Han et al., 2015). The earthquake was affected by NW tensile stress and NE compressive stress (Li et al., 2020), and the seismogenic structure has been inferred as a blind strike-slip fault with E–W trending (Song and Ge, 2018; Liu et al., 2020). Nevertheless, in the previous reports, the velocity structure inversion were mostly employed *via* the earthquake relocation and micro-earthquake detection, with little attention paid to aftershock evolution and seismogenic structure. Furthermore, only six permanent seismic stations are within 200 km of the epicenter, of which five are located south of the epicenter with azimuth angle range of 60°. The small number and limited distribution of permanent stations limited the monitoring capability, resulting in poor location accuracy for the mainshock and aftershocks. Moreover, a lack of locatable aftershocks has increased the difficulty in analyzing the aftershocks process and seismogenic structure associated with the earthquake.

The temporal and spatial evolution of aftershocks offers the potential determine the possibility of relatively large magnitude earthquakes, and is critical for determining seismogenic faults, stress fields, and the evolution of seismicity and seismic properties (Syracuse et al., 2012). The aftershocks distribution of the 2021 M_s 6.4 Yangbi earthquake revealed a predominantly unilateral rupture to the southeast, while a cluster of off-fault aftershocks indicated a nearly vertical dipping fault (Zhang et al., 2021; Tang et al., 2022). Aftershocks of the 1999 Izmit earthquake delineated the fault rupture from on-shore, through the Hersek Delta, and into the Marmara Sea (Gulen et al., 2002). Aftershocks of the 2011 Oklahoma earthquake helped to reveal subsurface geologic units and fault structures, including a previously unknown fault, and also provided insight on the second largest earthquake after the mainshock (McMahon et al., 2017). However, an adequate number of aftershocks are needed for aftershocks analysis. The early aftershock catalog around the mainshock rupture zone of the Alxa Left Banner M_s 5.8 earthquake (Alxa M_s 5.8 earthquake) has suffered from incompleteness; in particular, small earthquakes with low signal-to-noise ratios (SNRs) are missing from the main catalog.

The Alxa M_s 5.8 earthquake occurred in the Jilantai Basin, which is bound by the Dengkou–Benjing blind fault to the east and piedmont fault of Bayanwula Mountain to the west. The northern and southern boundaries of the basin are not clearly defined. To date, the internal structure of the Jilantai Basin remains poorly constrained owing to poor data coverage and limited outcrops; however, the basin is known to have a complex internal structure containing a series of small topographical prominences and depressions separated by NW-, NE-, and E-trending secondary faults (Research Group of Active Fault System around the Ordos Massif, 1988). The Alxa M_s5.8 earthquake occurred close to the Dengkou–Benjing blind fault (DBF), a blind fault of ~120 km in length based on aeromagnetic data (Research Group of Active Fault System around the Ordos Massif, 1988). The extent and Quaternary activity of this fault remain unknown owing to a lack of surface expression. Furthermore, the dominant spread direction of the Alxa M_s 5.8 earthquake sequence is ambiguous; nodal plane focal mechanism solutions (Han et al., 2015) and long-axis directions of intensity differ from the strike of the DBF. Accordingly, an integrated interpretation of its seismogenic structure has not been achieved to date.

Campaign seismic arrays with a mean inter-station distance of 35 km were deployed by the China Seismic Array Exploration Program between 2014 and April 2016. The epicenter region of the Alxa M_s 5.8 earthquake was fully covered by one such array at the time of the earthquake. Among the campaign stations, five stations were located within 50 km of the epicenter and 24 stations were located within 100 km of the epicenter, with a uniform distribution. In this study, data from these stations and from the six permanent seismic stations within 200 km of the epicenter were used to relocate the events of the Alxa M_s 5.8 earthquake sequence using the double-difference (DD) location algorithm (Waldhause and Ellsworth, 2000). In addition, micro-earthquake events were detected using the match and locate (M&L) method (Zhang and Wen, 2015a). The detailed aftershock evolution

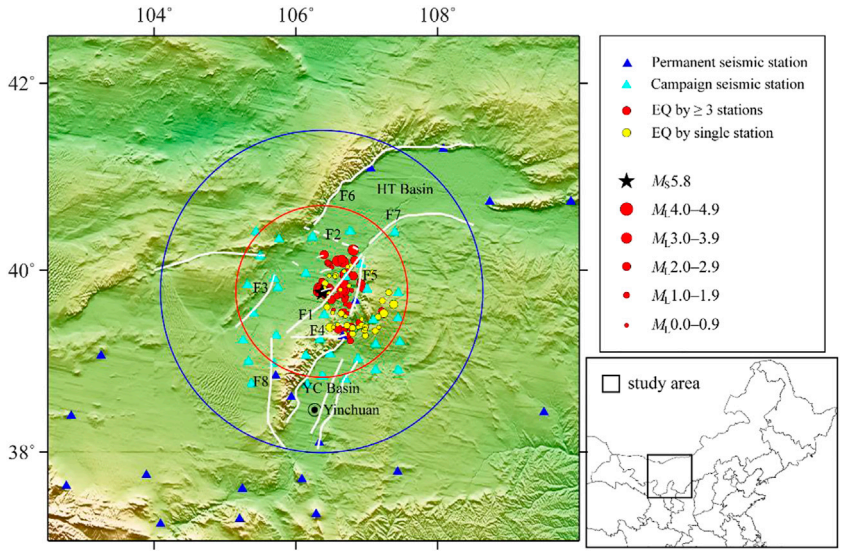

FIGURE 1
Distribution of seismic stations in the study area and epicenter of the Alxa Left Banner M_s 5.8 earthquake sequence. White solid lines represent faults and white dotted lines represent inferred faults. The red and blue circles represents areas of 100 and 200 km radius around the epicenter. F1: Dengkou–Benjing Fault, F2: Dengkou–Xulisitewula Fault, F3: Eastern Piedmont Fault of Bayanwula Mountain, F4: Zhengyiguan Fault, F5: Western Piedmont Fault of Zhuozi Mountain, F6: Piedmont Fault of Lang Mountain, F7: North Fringe Fault of Ordos, F8: Bayanhaote Fault, YC Basin: Yinchuan Basin, HT Basin: Hetao Basin.

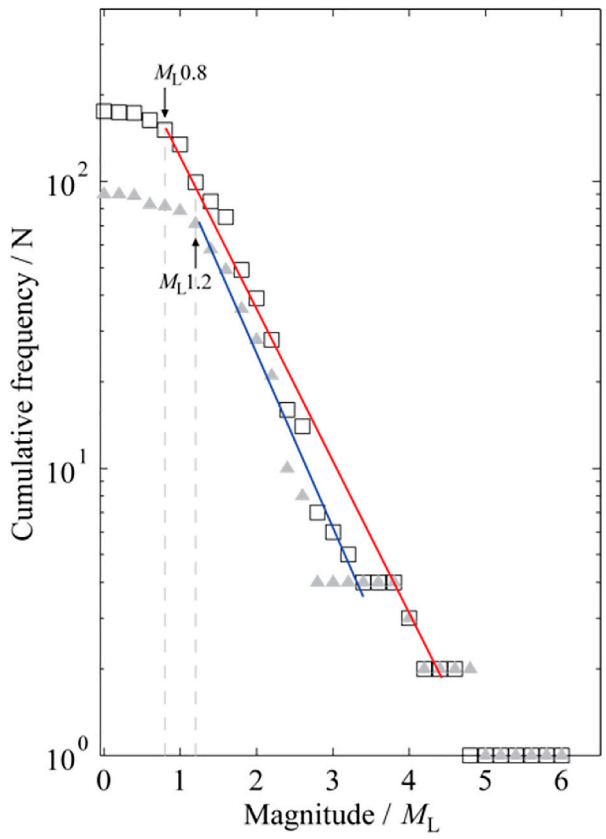

FIGURE 2
Cumulative frequency and magnitude of events in the Alxa Left Banner M_s 5.8 earthquake sequence. Triangles represent earthquakes located using data from permanent seismic stations; squares represent earthquakes located using data from both permanent and campaign seismic stations.

process and seismogenic structure of the earthquake were determined by combining the spatial distribution of the relocated earthquake sequence, the focal mechanism solutions, and the results of previous studies.

In conclusion, the Jilantai Basin has little knowledge of its internal active structure, and it has rarely recorded earthquakes of magnitude 5 or greater. The Alxa M_s 5.8 earthquake presents a good opportunity to study the active structure and seismogenic process inside the basin. Moreover, it has been concluded that there are differences between the fault–plane solution of this earthquake, the long axis of seismic intensity and the strike of the DBF. In this way, no unified seismogenic structure of this earthquake has been characterized, and the strike, dip, dip angle of the DBF remain unclear. Therefore, a detailed investigation of the aftershock evolution and seismogenic structure of the Alxa M_s 5.8 earthquake based on the analysis of data from permanent and campaign seismic stations play an essential role in understanding the seismogenic process and seismic hazard in the Jilantai Basin.

2 Methods, data, and velocity model

Location methods

The HYPOINVERSE-2000 (HYPO 2000) location algorithm was adopted to determine the absolute position of the master event (Klein, 2002); this approach has been successfully applied to multiple earthquake sequences (Langin, 2003; Clinton et al., 2006; Konstantinou et al., 2006; 2009a; 2009b; Choi and Noh, 2010; Hauksson et al., 2012; Caciagli et al., 2015; Schoenball and Ellsworth, 2017; Yao et al., 2021). In the DD earthquake location algorithm, developed by Waldhause and Ellsworth (2000), the relative positions of event pairs are determined through minimum residuals between observed and theoretical travel-time differences (or double-difference). The DD method has been widely used to improve earthquake locations (Waldhauser and Ellsworth, 2002; Hauksson and Shearer, 2005; Mandal and Horton, 2007; Waldhauser and Schaff, 2008; Mottaghi et al., 2010; Zhao et al., 2013; Fang et al., 2015; Kato et al., 2016; Sippl et al., 2018; Fan et al., 2022).

In the M&L method, the DD travel-time is used to detect micro-earthquakes; the detection depends only weakly on the accuracy of the velocity model. A brief description of the M&L detection algorithm applied in this study is as follows (Zhang and Wen, 2015a). First, seismic events located by the DD method were chosen as template events with low SNR. The study area was then gridded in longitude, latitude, and depth with the positions of template events used as centers. The travel-time difference of the reference phases (S waves) between each potential small event (i.e., grid point) and template event at each station was calculated. Subsequently, based on travel-time differences of multiple stations, sliding window cross-correlation was performed between reference phases of the template events and the continuous data stream at each station and data component. Finally, the mean correlation coefficient (CC) and SNR after the stacking cross-correlation were calculated. When the mean CC and SNR exceeded defined thresholds, a small event was deemed to be a positive detection, and its position was determined as the grid point with the maximum mean CC. The magnitudes of the detected small events were determined based on the median of the amplitude ratios for the reference phases in all station components (Peng and Zhao, 2009).

Data selection

Continuous waveform data recorded by 24 stations (Figure 1) within 100 km of the Alxa M_s 5.8 earthquake (i.e., mainshock) epicenter were selected. The study period was from 1 January 2015, to 28 February 2016 (i.e., 3 months before and 10 months after the mainshock). In order to obtain accurate arrival-times and reliable earthquake locations, event waveforms recorded clearly by at least four stations were first selected and the arrival-times of the direct P and S seismic phases were picked manually. The arrival-time data for each earthquake event were checked and corrected using the Wadati diagram, and data that greatly deviated from the fitting line were removed based on regional-phase travel-time curves for Pg and Sg.

Based on the observation data from permanent seismic stations, 90 localizable earthquakes in the Alxa M_s 5.8 (i.e., mainshock) earthquake sequence were obtained using the HYPO2000 method. After the inclusion of data from the campaign arrays, 175 localizable earthquakes were obtained (i.e., the number of localizable earthquakes almost doubled), the minimum complete magnitude decreased from M_L1.2 to M_L0.8 (Figure 2), and the completeness of the earthquake catalog was significantly improved.

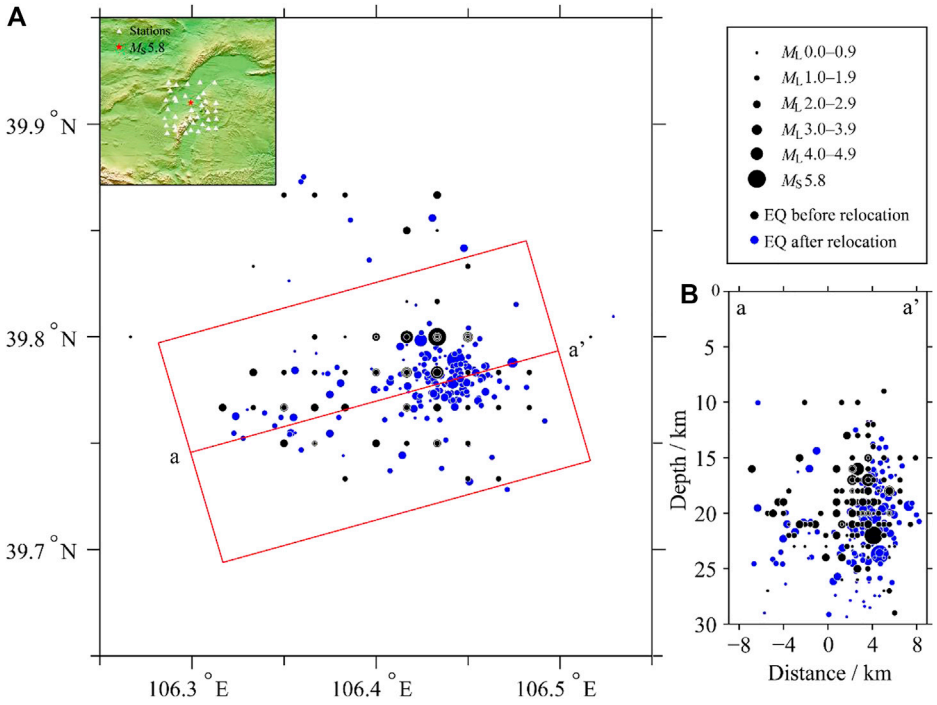

FIGURE 3
Distribution of the **(A)** epicenters (from 1 January 2015, to 28 February 2016) and **(B)** focal depths of the studied earthquakes before and after relocation.

Velocity model

The study area was located in the Hetao Basin. Velocity data for the area are available in the CRUST1.0 velocity model (Laske et al., 2013); however, these data are low resolution. Based on the results of previous research into the one-dimensional crustal velocity structure in Alxa, the subsurface structure of the study area was divided into four layers (Song and Ge, 2018).

3 Results

Earthquake relocation

Based on corrected seismic phase data and uniform station coverage, reliable hypocenter positions can be obtained using the HYPO2000 method. The horizontal and vertical position errors of the mainshock are 0.25 and 0.83 km, respectively. For the earthquake sequence, the horizontal position errors of nearly 95% of earthquakes are within 1 km; the vertical position errors of more than 95% of earthquakes are within 3 km; the arrival residuals of ~95% earthquakes are within 0.3 s. The average values of horizontal and vertical position errors and arrival residual are 0.55 km, 1.53 km, and 0.175 s, respectively. Thus, the hypocenter position of the Alxa M_s 5.8 earthquake sequence obtained by the HYPO2000 method is reliable.

The HYPO2000 location parameters were taken as input parameters for the DD method. The relative location accuracy of earthquake source was improved and the directional distribution of the occurrence of earthquakes was clearer, representing a difference from the disordered distribution before relocation (Figure 3). The spatial distribution of aftershocks appears to be very similar before and after relocation. In comparison, it was found that the hypocenters of most earthquakes were very close before relocation, and the hypocenters is layered distribution, as shown in Figure 3B. After the relocation, the linear distribution characteristics of the hypocentres became more obvious, as well as the seismic gap.

Earthquakes at the eastern end of the aftershock zone were found to have undergone an eastward shift after relocation, with an increased spread length of aftershocks (Figure 3A). The focal depths mainly ranged between 16 and 22 km before relocation, while after relocation, the depth spread increased to 15–25 km (Figure 3B). The dominant distribution of the focal depth of the Alxa M_s 5.8 earthquake sequence shows that the seismogenic layer was located in the middle–upper crust.

Micro-earthquake detection

Under the premise of uniform azimuthal distribution of stations and waveforms with high SNR, the number of stations used for micro-earthquake detection should be appropriate, and stations close to the epicenter should be selected to the extent possible. Therefore, six stations were selected for micro-earthquake detection, and 25 earthquakes of > M_L2.5 with high SNR waveforms were selected as template events (Table 1); waveforms 1 s before and 3 s after the Sg seismic phases of the template events were chosen as template waveforms. Wave filtering at 2–8 Hz was then performed for the template and continuous waveform data. In accordance with the M&L method, the study area was gridded at 0.01° × 0.01° × 0.5 km (longitude, latitude, depth), with the positions of the template earthquakes used as the centers. Finally, the origin times, seismic-

TABLE 1 Parameters of template events.

Template earthquake	Earthquake origin time (Beijing time)	Longitude (°N)	Latitude (°E)	Depth (km)	Magnitude (M_L)
	Month/Day/Year Hour/Minute				
d_1	01/27/2015 15/25	39.8485	106.7285	11.0	2.8
d_2	01/27/2015 19/02	40.1344	106.3192	21.8	3.1
d_3	02/05/2015 02/52	39.8547	106.2348	25.5	2.5
d_4	02/06/2015 09/27	40.1113	106.5525	24.4	2.6
d_5	04/15/2015 15/39	39.7820	106.4451	22.6	M_s5.8
d_6	04/15/2015 15/44	39.7920	106.4271	19.2	4.6
d_7	04/15/2015 15/55	39.7868	106.4284	19.0	3.3
d_8	04/15/2015 16/01	39.7786	106.4424	20.0	2.5
d_9	04/15/2015 18/49	39.7751	106.4313	20.4	3.8
d_{10}	04/15/2015 19/25	39.7712	106.4194	22.1	2.8
d_{11}	04/16/2015 03/12	39.7825	106.4490	19.7	2.8
d_{12}	04/16/2015 04/40	39.7793	106.4207	19.9	2.6
d_{13}	04/16/2015 17/16	39.7808	106.4517	22.9	4.1
d_{14}	04/18/2015 16/38	39.7674	106.3572	23.9	2.7
d_{15}	04/21/2015 00/26	40.1266	106.3155	22.0	3.1
d_{16}	04/29/2015 14/28	39.7626	106.3699	23.3	2.8
d_{17}	05/02/2015 18/28	39.7862	106.4060	24.9	2.9
d_{18}	05/10/2015 09/01	40.1337	106.3185	21.9	2.6
d_{19}	05/20/2015 09/18	39.7794	106.4297	23.1	2.5
d_{20}	05/24/2015 18/18	39.7783	106.4496	23.7	2.6
d_{21}	06/06/2015 23/19	39.7752	106.4184	21.3	2.6
d_{22}	10/16/2015 20/01	39.8557	106.4402	20.5	2.9
d_{23}	11/22/2015 22/53	39.9838	106.5828	26.7	4.1
d_{24}	12/10/2015 05/55	40.0824	106.4545	31.8	3.5
d_{25}	12/28/2015 00/21	39.8699	106.8592	16.4	2.6

Note: d_i indicates the results of the double-difference (DD) location.

source locations, and magnitudes of the micro-earthquakes were determined using a grid search method. In this study, the average CC threshold value was set as 0.3 (Zhang and Wen, 2015a; 2015b; 2015c) based on existing studies, and the event magnitude was decided based on the median of the amplitude ratios for the reference seismic phases in all station components. When the S wave amplitude is barely above the noise level, the principal component fit method can be used to calibrate the magnitude (Shelly et al., 2016; Meng et al., 2018; Yao et al., 2020; Daniels and Peng, 2022). The Sg seismic phase parameters were calculated using the TauP Toolkit (Crotwell et al., 1999) based on the Preliminary Reference Earth Model (Dziewonski and Anderson, 1981). The event with the largest CC in each 6-s time window was chosen as the detected earthquake to avoid duplicate detection.

A total of 803 micro-earthquakes (including 208 DD-located earthquakes) were detected using the M&L method (Figure 4); these were mainly distributed near the mainshock. In addition, two areas of micro-earthquakes were concentrated ~30 km north of the mainshock. The number of earthquakes showed a sharp increase to nearly four times the number of events before micro-earthquake detection.

After micro-earthquake detection using the M&L method, the minimum complete magnitude decreased from M_L0.8 to M_L0.6 (Figure 5), and the seismic gap of the earthquake catalog was improved. The resultant richer aftershocks provided an improved basis for detailed analysis of aftershock evolution and seismogenic structure.

Effectiveness of micro-earthquake detection

After micro-earthquake detection using the M&L method, 25 template events were all self-detected, with CCs of 1.0. Figure 6A shows the self-detected result of the mainshock, and Figure 6B shows the detection result of a single M_L0.3 micro-earthquake with an average CC of 0.3259.

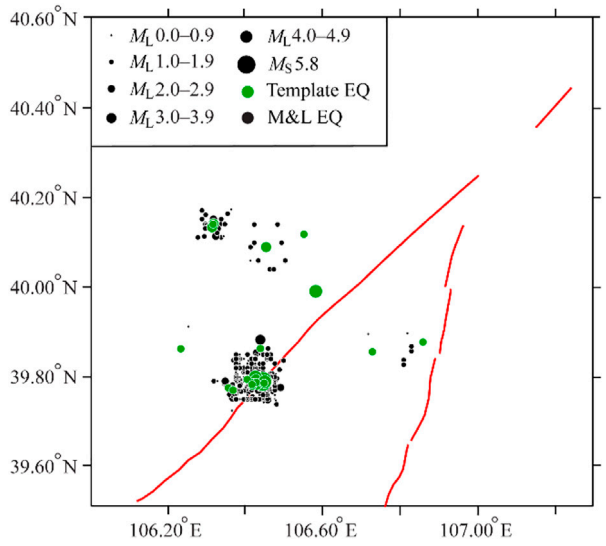

FIGURE 4
Distribution of template earthquakes and detected micro-earthquakes.

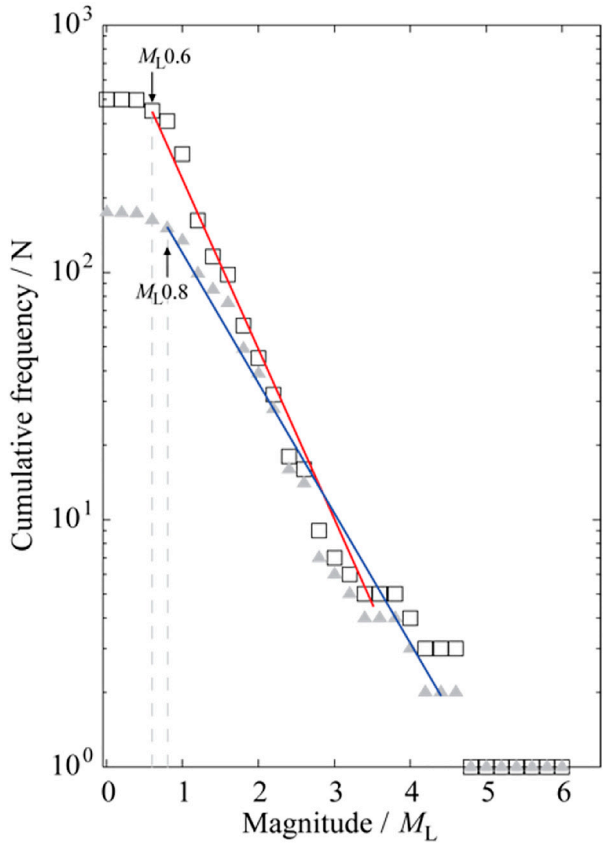

FIGURE 5
Cumulative frequency–magnitude distribution before and after micro-earthquake detection. Triangles represent earthquakes before micro-earthquake detection; squares represent earthquakes after micro-earthquake detection.

The results of the 208 DD-located earthquakes were compared with those of the M&L method for the same earthquake to illustrate the effectiveness of micro-earthquake detection (Figure 7). More than 70% of earthquakes (i.e., 155 events) had an origin time difference of <0.5 s, and >92% of earthquakes (i.e., 195 events) had a magnitude difference of <0.3. In addition, the distance between epicenter positions was <3 km for >95% of earthquakes (i.e., 201 events), while the focal depth difference of >95% of earthquakes (i.e., 199 events) was <4 km. In general, the detection results are similar to the DD location of the same earthquake, confirming the reliability of the micro-earthquake detection.

Focal mechanism solutions

The Cut and Paste (i.e., CAP) method (Zhao and Helmberger, 1994; Zhu and Helmberger, 1996) was applied to invert focal mechanism solutions for the mainshock and the four aftershocks of > M_L4.0. The focal mechanism parameters are shown in Table 2.

The focal mechanism solution and waveform fitting results were analyzed by taking the mainshock as an example. As shown in Figure 8, the phases and amplitudes of the theoretical and observed seismic waveforms at different stations had a good fit. The nodal plane solution of the focal mechanism of the mainshock was characterized by 86° strike, 84° dip, and −9° rake; the strike, dip, and rake of the alternative nodal plane solution were 177°, 81°, and −174°, respectively. The azimuth and plunge of the P axis were 41° and 11°, whereas those of the T axis were 132° and 2°, respectively. The moment magnitude of the mainshock was M_w5.6. The fit errors corresponding to the mechanism solutions of the mainshock at different focal depths are shown in Figure 9A. The fit error was smallest for a focal depth of 21 km; the mechanism solutions were relatively stable within a depth range from 15km to 31 km and were dominated by strike-slip with some normal components.

The mechanism solutions of the four aftershocks of > M_L4.0 were also well fitted (Figures 9B–E). The mechanism solutions at different depths were relatively stable and primarily characterized by strike-slip with a smaller number of normal or thrust components. These results are consistent with the focal mechanism solution of the mainshock. Overall, the seismogenic structure of the mainshock was a strike-slip fault, which is consistent with the development of multiple strike-slip faults in the study area (Research Group of Active Fault System around the Ordos Massif, 1988).

4 Discussion

Mainshock depth

The focal mechanism solutions of the Alxa M_s 5.8 earthquake were determined using data from previous literature (Han et al., 2015; Wang et al., 2019) and several institutions, including GFZ, USGS, GCMT, Institute of Geophysics, China Earthquake Administration (CEA-IGP). Focal depths obtained through inversion ranged from 13 to 30 km, with the relocated focal depth of the mainshock being 22.7 km. This depth falls within the upper crust and is essentially consistent with the results of Wang et al. (2019) [20.597 km], but is significantly deeper than the inverted focal depth (18 km) of Song and Ge (2018), the focal depth determined by the China Earthquake

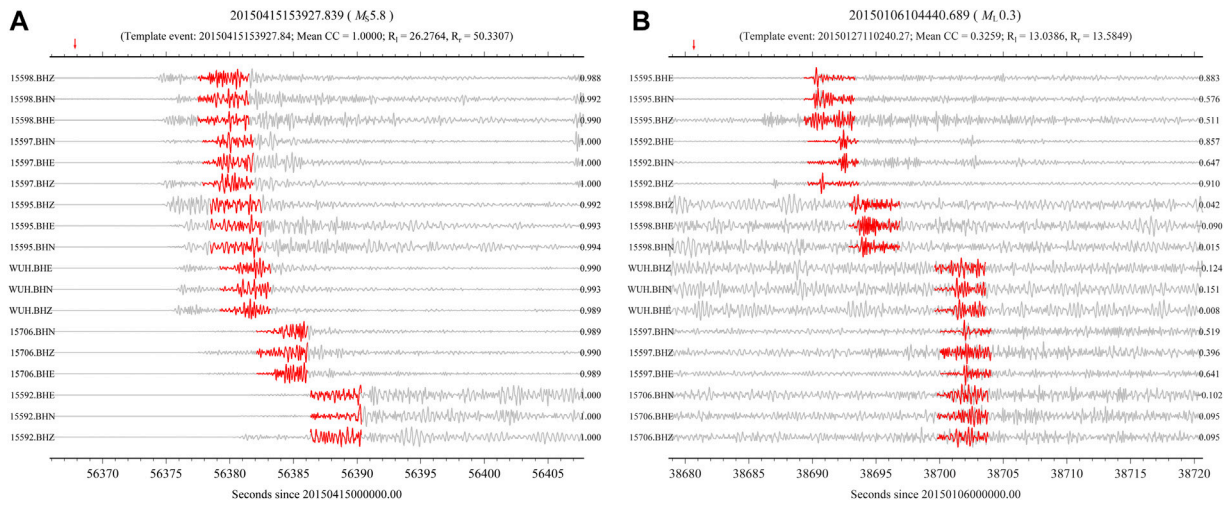

FIGURE 6
Detection results of the match and locate (M&L) method. **(A)** Self-detection results of the mainshock and **(B)** detection results of a single micro-earthquake. Red lines represent the waveforms of template earthquakes, gray lines represent the continuous waveforms of the detected earthquakes, and red arrows show the origin times of detected earthquakes. The left- and right-hand ends of the waveforms show the station components and correlation coefficient (CC), respectively. The template earthquake, average correlation coefficient, left and right signal-to-noise ratio (SNR), and magnitude of the detected earthquake are listed above each plot. The starting time of the waveforms is shown below each plot.

Network Center (10 km), the relocated depth (13.2 km) of Wei et al. (2017), and relocated depth (13 ± 1 km) of Han et al. (2015). However, the lack of significant ground surface rupture, major building damage, or casualties (Wang et al., 2019) is inconsistent with such shallow focal depths. Furthermore, the P wave velocity structure in the epicenter region, inverted by Wang et al. (2019) *via* the TomoDD method, shows a high- and low-velocity conversion zone at 20-km depth in the Alxa Left Banner focus region. Previous studies have shown that the presence of intracrustal high-velocity bodies is essential for high stress concentrations, and strong earthquakes are prone to occur in the transition zone between intracrustal high- and low-velocity zones or on the sides of high-velocity bodies (Lees and Malin, 1990; Zeng et al., 2014; 2017a; Wu et al., 2022). Thus, the above analysis and previous studies of seismogenic dynamics confirm that the focal depth of 22.7 km for the Alxa M_s 5.8 earthquake determined in this study is likely a realistic value.

Spatiotemporal distribution of the earthquake sequence

According to the *M*-t diagram and 2-day frequency diagram for the Alxa M_s 5.8 earthquake sequence (Figure 10), there were fluctuations in the development of the sequence. Aftershocks mainly occurred before 30 June 2015, followed by a rapid decrease in number. In December 2015, the number of aftershocks abruptly rose; however, these were mostly earthquakes with small magnitudes. Therefore, we selected only earthquakes from before 30 June 2015, for the analysis of aftershock evolution. Notably, after a period of quiescence following the aftershock decay, three larger aftershocks occurred between March and June 2016, including M_L4.2, M_L3.2 and M_L4.1 earthquakes.

From analysis of the distribution characteristics of the Alxa M_s 5.8 earthquake sequence from April 15 to 30 June 2015 (Figure 11), we found that the aftershock sequence extended in an NEE direction (N70°–75°E) with a length of 12 km, likely indicating the rupture length of the mainshock. The mainshock rupture started from the eastern end of the aftershock zone and gradually extended to the western end, suggesting unilateral rupture. Aftershock activity was segmented, with eastern and western segments separated by an area of low seismicity extending 5 km horizontally. Both the mainshock and two aftershocks of > M_L 4.0 occurred on the eastern segment, with significantly fewer aftershocks on the western segment. The aftershock zone was ~4 km wide on the western segment and 5 km wide on the eastern segment. From March to June 2016, M_L 4.2, M_L 3.2 and M_L 4.1 earthquakes occurred in the low-seismicity gap.

The NE-oriented DBF lies near the location of the Alxa M_s 5.8 earthquake, with an angle of ~15° between the spread direction of the earthquake sequence and the direction of the DBF. More, the strike of the DBF does not match the focal mechanism solution of the mainshock. Therefore, the earthquake sequence is tentatively determined to have occurred on an unknown blind fault to the west of the DBF.

Aftershock evolution

The mainshock epicenter (i.e., the starting point of earthquake rupture) was located at the eastern segment of the aftershock zone (Figure 12A), demonstrating a unilateral rupture of the main shock. In addition, it shows that the eastern segment of the aftershock zone should belong to the asperity zone on the seismogenic fault zone. The two largest aftershocks (>M_L4.0) also occurred on the eastern segment of the aftershock zone, indicating that mainshock did not release all of the strain in the main asperity zone. The focal depth profile (Figure 12B) illustrates that most aftershocks were shallower than the mainshock (22.7 km), which is consistent with the theory that strong earthquakes nucleation tend to the deeper and propagate

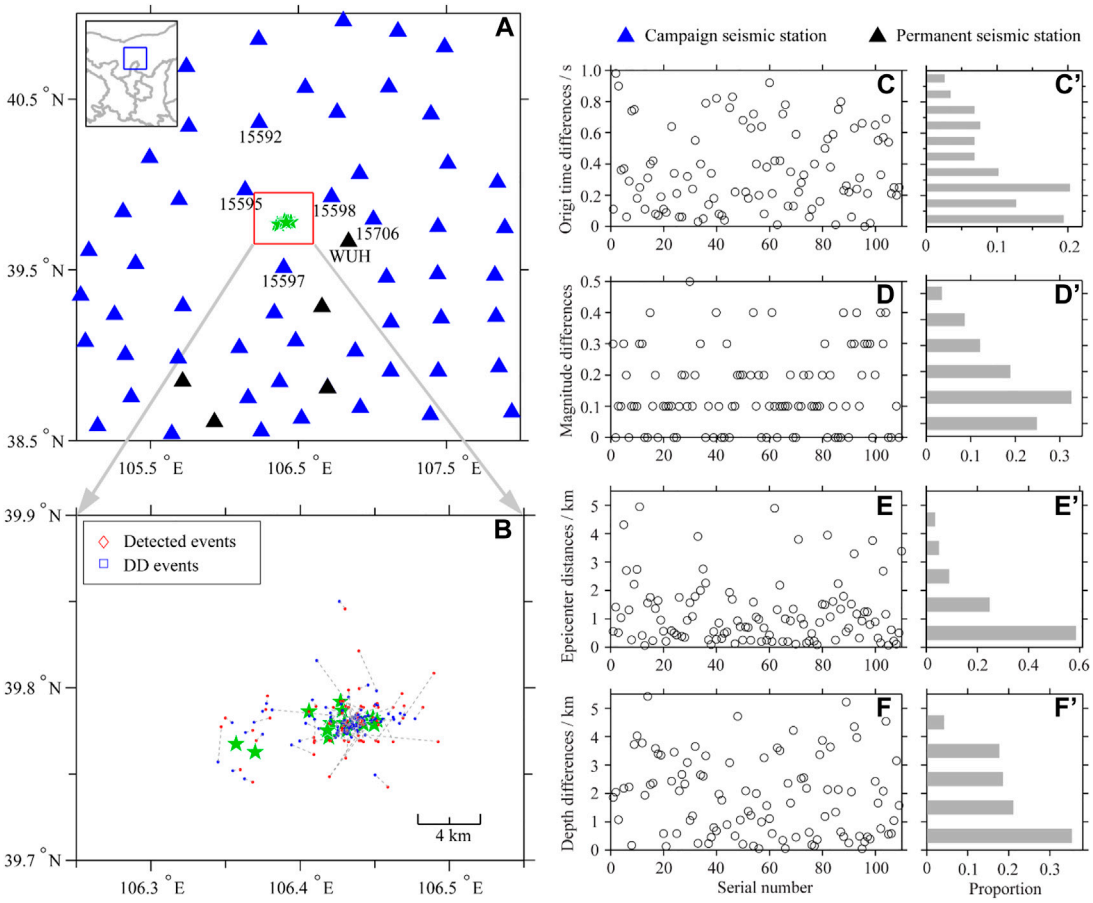

FIGURE 7
Station distribution and distributions of earthquakes from the double-difference (DD) and match and locate (M&L) methods. **(A)** Locations of permanent seismic stations (black triangles) and campaign seismic stations (blue triangles); the station codes of seismic stations used in the detection are shown; green stars indicate template events. The inset map in the upper left shows the eastern part of northwestern China, with the study area shown by a blue rectangle. **(B)** For each earthquake within the red rectangle in **(A)**, the detection results of the M&L (red points) and DD (blue points) methods are compared and connected by gray dotted lines. Raw plots and histograms for earthquake origin time differences **(C,C′)**, magnitude differences **(D,D′)**, epicenter distances **(E,E′)**, and depth differences **(F,F′)**.

TABLE 2 Focal mechanism solutions of > M_L4.0 events in the Alxa Left Banner M_s 5.8 earthquake sequence.

Order number	Earthquake origin time (Beijing time)	Epicenter position			*M*	Nodal plane I			Best fitting depth
	Month/Day/Year Hour/Minute	φ_N/°	λ_E/°	Depth/km		Strike/°	Dip/°	Rake/°	
1	04/15/2015 15/39	39.78	106.45	23	M_s5.8	86	84	−9	21 km
2	04/15/2015 15/44	39.79	106.43	19	M_L4.6	241	79	10	17 km
3	04/16/2015 17/16	39.78	106.45	23	M_L4.1	4	72	−177	18 km
4	03/24/2016 02/23	39.77	106.38	22	M_L4.2	65	80	15	20 km
5	06/14/2016 13/29	39.76	106.41	21	M_L4.1	84	90	−9	17 km

upwards (Scholz, 1990). Aftershocks predominantly occurred at depths of 15–25 km, largely consistent with the depth of the mainshock rupture from previous studies (Wang et al., 2019). Few aftershocks above 15 km is compatible with field survey findings that no significant surface rupture was found after the mainshock (Wang et al., 2019). Figure 12A shows an obvious area of low seismicity (~5 km^2 × 5 km^2) between the western and eastern segments of the aftershock zone, located at a depth of 20–25 km (Figure 12B). This zone potentially relates to a high strength barrier on the fault (Aki, 1979), and it was also consistent with an Coulomb stress triggering

10.3389/feart.2023.1082680

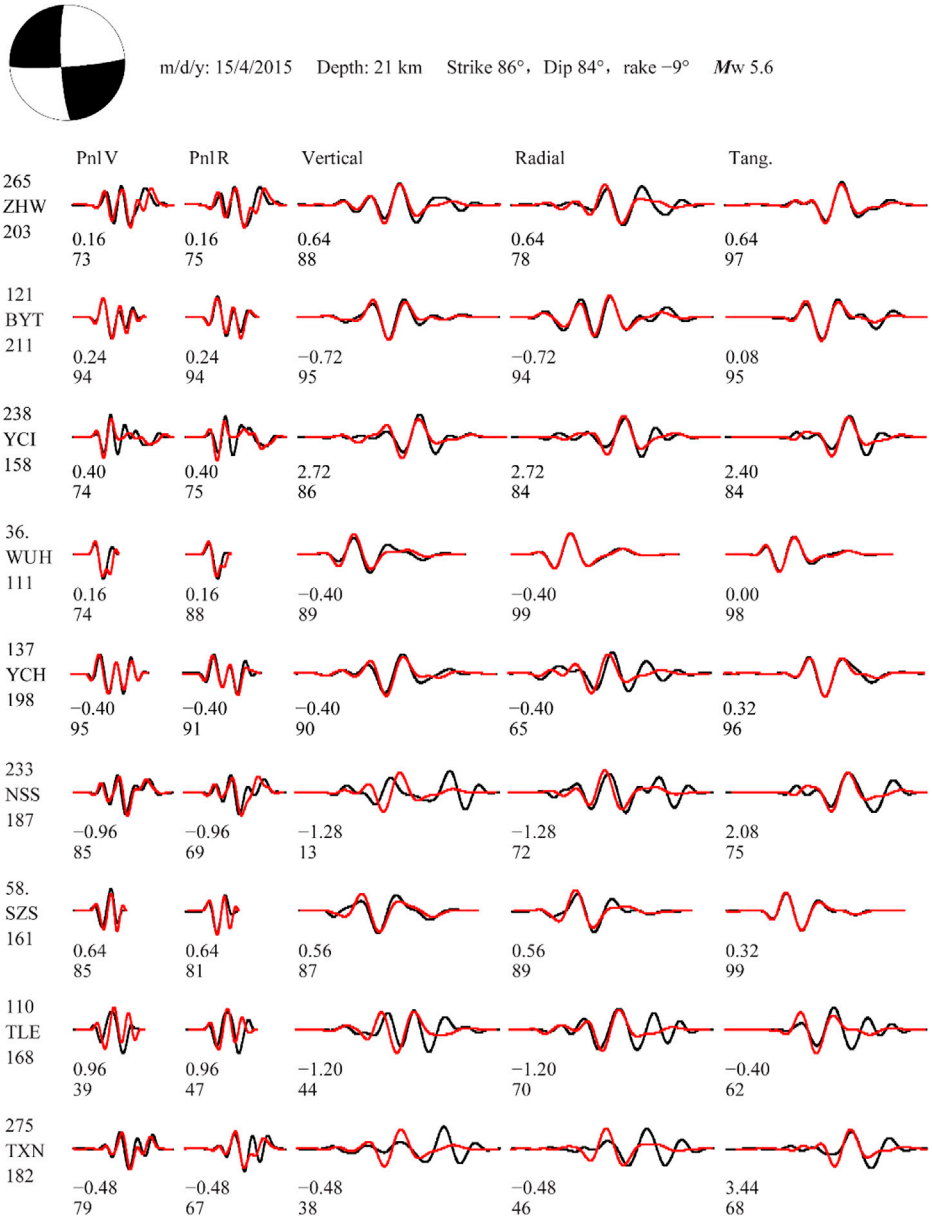

FIGURE 8
Selection of station focal mechanism solutions and waveforms for the Alxa Left Banner M_s5.8 earthquake on 15 April 2015. The lower-hemisphere beach ball focal mechanism, earthquake occurrence date, best fitting depth of the waveforms, mechanism solution, and moment magnitude are shown at the top of the figure. Black and red curves represent theoretical and observed seismograms, respectively. The numbers in the first line below each waveform represent the moving time (s) of the theoretical seismogram relative to the observed seismogram, and values in the second line indicate the correlation coefficient (%) between them. The epicenter distance (km), station name, and azimuth angle (°) are shown to the left of each set of waveforms.

area of the mainshock (Gao et al., 2015). From March to June 2016, three earthquakes of > M_L3.0, including two M_L4 earthquakes, occurred in a low seismicity zone, indicating that the three large aftershocks were caused by the rupture of this barrier.

In summary, the eastern segment of the aftershock zone formed the main asperity of the seismogenic fault zone. The main rupture was initiated at the eastern segment of the fault, and propagated west, before being blocked by a barrier in the western section of the fault zone. Subsequently, the rupture crossed the barrier and continued for another 2 km. Between the mainshock and February 2016, there were very few aftershocks in the low seismicity zone, and those earthquake that did occur had very low magnitudes. It suggested that the barrier zone remained in a state of high stress until 24 March 2016, after which M_L4.2, M_L3.2, and M_L4.1 earthquakes occurred. Therefore, the location and magnitude of larger aftershocks can be determined through the analysis of aftershock evolution.

Seismogenic structure

There is a significant lack of shallow seismic exploration and deep seismic reflection profiles in the study area. Moreover, the epicenter of the Alxa M_s 5.8 earthquake was located on the edge of a desert with no visible surface faults. As such, our results, which reveal the seismogenic

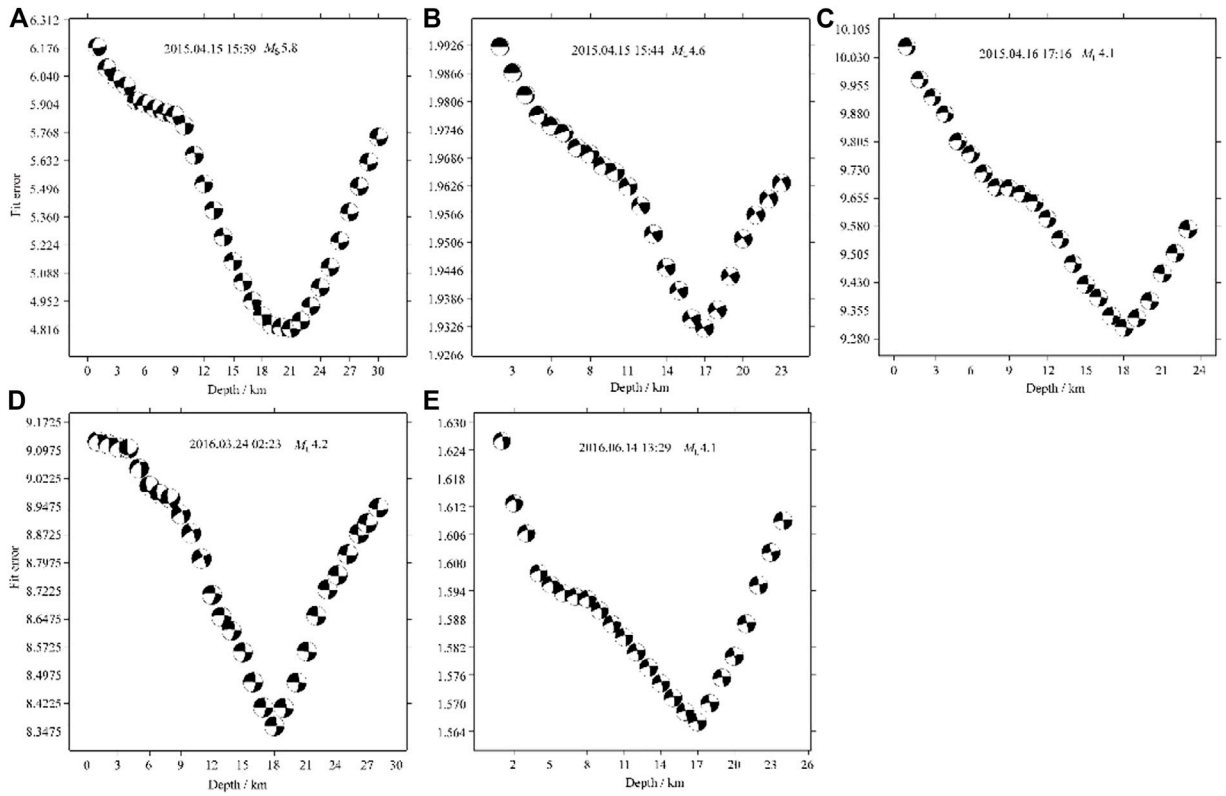

FIGURE 9
Fit errors of focal mechanism solutions of the Alxa Left Banner M_s 5.8 earthquake on 15 April 2015, and its four largest aftershocks.

structure of the Alxa M_s 5.8 earthquake sequence, offer a new basis data for further research in the study area.

Comprehensive analysis of cross-sectional focal depth profiles for the eastern and western fault segments (Figures 13A–C) was performed by combining the relocated earthquake locations, focal mechanism solutions (flat and profile projections), and fault interpretation results from adjacent profiles (Wen et al., 2011; Wen et al., 2013; Wen, 2014). The interpreted seismogenic structures of both segments generally show upward

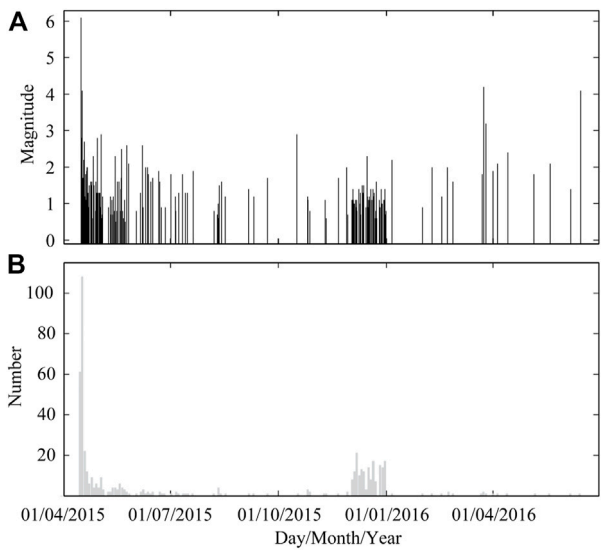

FIGURE 10
(A) M–t and **(B)** 2-day number N–t plots of $M_L > 0$ events in the Alxa Left Banner M_s 5.8 earthquake sequence.

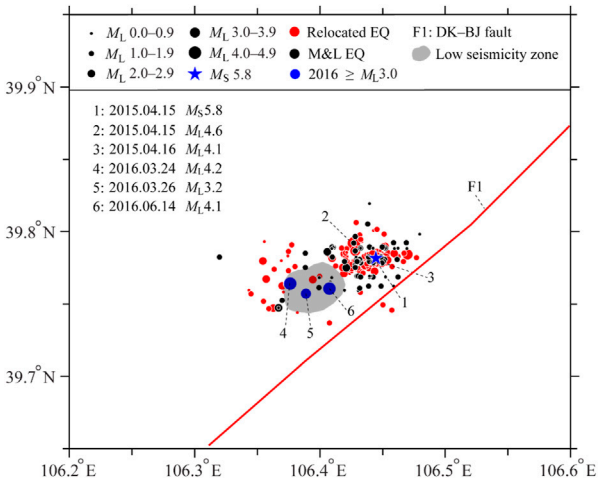

FIGURE 11
Epicenter distribution of the Alxa Left Banner M_s 5.8 earthquake sequence. Red and black dots represent relocated earthquakes (from April 15 to 30 June 2015) using the double-difference (DD) and match and locate (M&L) methods. Blue dots denote three large aftershocks that occurred from March to June 2016.

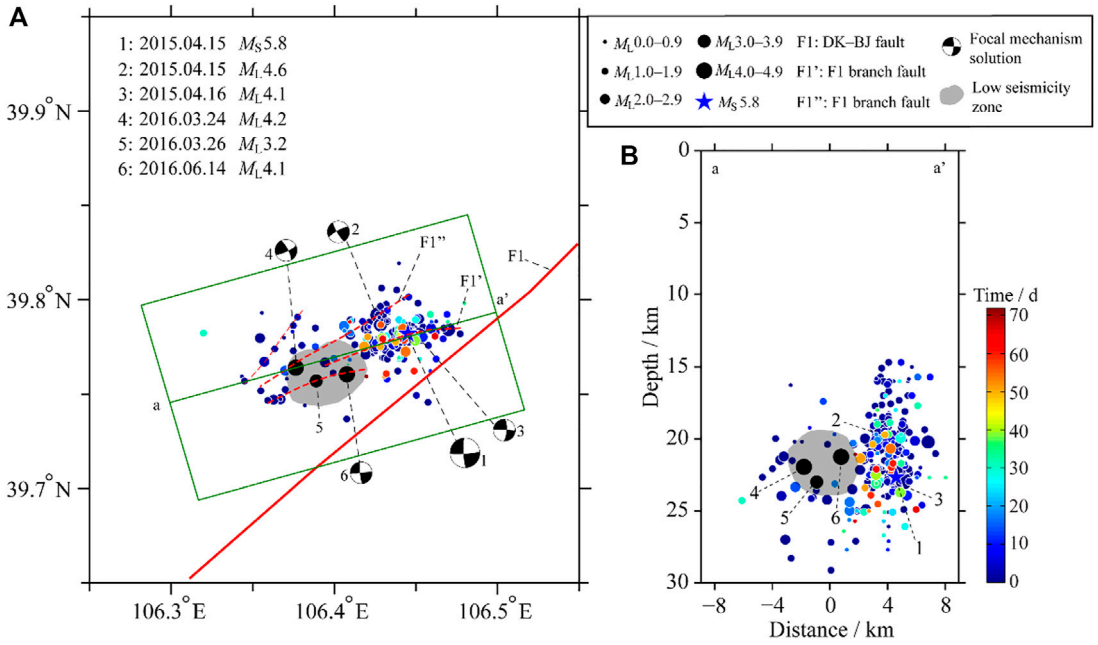

FIGURE 12
(A) Epicenter distribution of the Alxa Left Banner M_S 5.8 earthquake sequence and **(B)** distribution of the sequence along the a–a′ profile. Colored dots indicate earthquakes after the mainshock until 30 June 2015, where colors indicate time after the mainshock; black dots denote the three ≥ M_L3.0 earthquakes that occurred in the first half of 2016. F1: Dengkou–Benjing Fault, F1′: branch fault I of F1, F1″: branch fault II of F1.

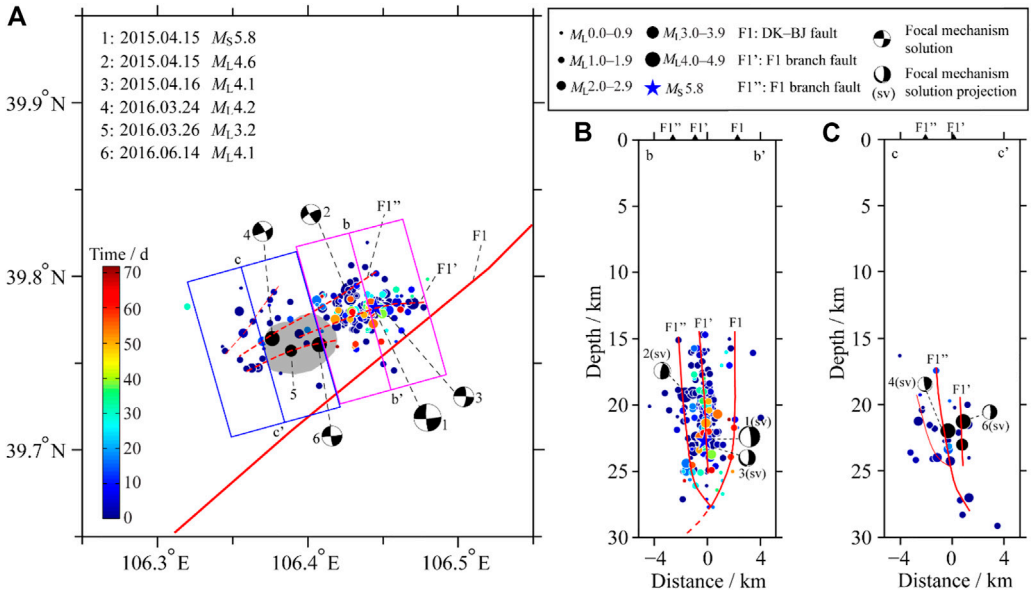

FIGURE 13
Epicenter distribution and segmentation structure of the seismogenic fault of the Alxa Left Banner M_S 5.8 earthquake sequence **(A)** Extent of two profiles across the seismogenic fault **(B,C)** Focal depths and interpreted profiles of b–b′ and c–c′, respectively. F1: Dengkou–Benjing fault, F1′: branch fault I of F1, and F1″: branch fault II of F1. Colored dots denote earthquakes from after the mainshock to 30 June 2015, where the color indicates the time after the mainshock; black dots indicate the three ≥ M_L3.0 earthquakes that occurred in the first half of 2016. F1′ and F1″ are seismogenic fault interpretation results of the earthquake locations, focal mechanism solutions, and interpretation results for adjacent profiles, which are inferred faults.

bifurcation, forming a negative flower structure that is commonly observed in strike-slip fault zones. This structure consists of the main seismogenic fault (F1'), the DBF (F1), and the main branch fault (F1″). F1′ is a blind fault trending N70°–75°E that dips steeply to the southeast. On the eastern segment of the aftershock zone (Figure 13B), there is an angle of ~15° between F1 and F1′, and a maximum horizontal distance of ~4 km was

estimated. F1′ and F1″ are sub-parallel, with a maximum horizontal distance of 2.5 km. The dip angle of the structures becomes more gentle below the sub-vertical parts of F1 and F1″ at a depth of 25 km, and F1″ intersects the primary fault at a depth of 27–28 km. In the western segment of the aftershock zone (Figure 13C), F1′ and F1″ also exhibit an upward-bifurcating structure above 24 km depth, and are separated by a distance of 4 km above 20 km depth. A smaller secondary fault along which some M_L2 aftershock activity occurred intersects with F1″ at ~25 km depth.

Profile b–b' (Figure 13B) illustrates that the mainshock and M_L4.1 aftershock on 16 April 2015, occurred on steeply dipping fault F1' (≥85°) at a depth of 22–23 km. The focal mechanism solutions of the two events are approximately consistent between one nodal plane and the F1′ fault surface at the corresponding seismic focus. The M_L4.6 aftershock on 15 April 2015 occurred at a depth of ~19 km on the F1″ fault; similarly, one nodal plane from this event's focal mechanism is approximately consistent with the F1″ fault surface.

Profile c–c' (Figure 13C) shows a small number of aftershocks along the main F1′ fault in the western segment of the aftershock zone. Due to the profile location within the low-seismicity barrier zone, only limited strain was released during the mainshock. This barrier zone was ultimately ruptured by the three large aftershocks. On 24 March 2016, an M_L4.2 aftershock occurred at a depth of ~22 km± on F1". The profile projection of its focal mechanism shows that one nodal plane had consistent alignment with the F1" fault plane at the corresponding seismic focus. The M_L4.1 aftershock on 14 June 2016, occurred at a depth of ~21 km on F1'; as above, one nodal plane of the focal mechanism for this event was approximately consistent with the F1' fault plane.

In summary, the mainshock rupture and aftershock activity of the Alxa M_s 5.8 earthquake were not controlled only by a single fault; activity was dominated by the main fault F1'; however, activity also occurred along branch fault F1" and other secondary faults. The seismogenic fault zone was a maximum of 4 km wide and 12 km long, with a complex structure. The main fault, F1′, is SE-striking, occurs at depths of 15–25 km, and forms an upward bifurcation structure (or a negative flower structure). During the mainshock, the fault moved predominantly in a strike-slip direction but with a component of oblique slip.

Very few large earthquakes have occurred in the study area and there are few supporting evidences of tectonic faults from deep seismic sounding or other studies; therefore, some uncertainties in the interpretation results of seismogenic structure could not be excluded; however, a M_s6.2 earthquake occurred in 1976 at a distance of 25 km from the Alxa M_s 5.8 epicenter. In future work, we plan to investigate the 1976 Bayinmuren M_s6.2 earthquake in more detail, including the relocation of small background earthquakes in order to improve our understanding of the seismogenic structure in this region.

5 Conclusion

In this study, data from permanent and campaign seismic arrays were used to examine the Alxa M_s 5.8 earthquake sequence. The number of earthquakes was dramatically increased compared with previous studies that used only data from permanent stations, and the completeness of the earthquake catalog was improved *via* the M&L method for micro-earthquake detection. An improved catalog provided a solid basis for a detailed study of this earthquake sequence.

The focal depth of the mainshock was 22.7 km, with aftershocks dominantly occurring between 15 and 25 km. The aftershock distribution spread in an NEE trending (N70°–75°E) over a length of 12 km. The aftershocks formed two distinct segments (the eastern and western segments). The mainshock and early aftershocks were mainly located on an eastern segment, while fewer aftershocks occurred on a western segment. Moreover, there was an area of low seismicity with a horizontal extent of ~5 km between two segments. Most aftershocks occurred before 30 June 2015, after which the number of aftershocks declined significantly. Three larger aftershocks (M_L4.2, M_L3.2, and M_L 4.1) occurred within the low-seismicity zone from March to June 2016.

The Alxa M_s 5.8 earthquake was caused by a blind, NEE-oriented western branch fault of the DBF. The eastern segment of the seismogenic fault zone formed the main asperity. The mainshock rupture started at the eastern end of the fault and propagated from east-to-west and from deep-to-shallow. There was an barrier zone in the western segment of the seismogenic fault zone with the low-seismicity region, illustrating that the rupture released only some of the accumulated stress. Subsequently, this barrier was ruptured on 24 March 2016, after which three successive large aftershocks occurred.

Data availability statement

The original contributions presented in the study are included in the article/supplementary material, further inquiries can be directed to the corresponding author.

Author contributions

XZ is the first author and the corresponding author. XL is contributed to the language improvement and the other coauthors contributed to the data calculation and analysis.

Funding

This work was supported by the Earthquake Science and Technology Spark Plan Project of China Earthquake Administration (XH21040, XH18053Y), Ningxia Natural Science Foundation Project (2022AAC03690) and the Innovative Teams of the Earthquake Agency of Ningxia Hui Autonomous Region [Grant number CX 2019-4(9)].

Acknowledgments

The earthquake catalog used in this paper comes from the China Seismic Networks Center, the waveform data was provided by China Seismic Array Data Management Center at Institute of Geophysics, China Earthquake Administration, and GMT software was used for data plotting.

Conflict of interest

The authors declare that the research was conducted in the absence of any commercial or financial relationships that could be construed as a potential conflict of interest.

Publisher's note

References

Aki, K. (1979). Characterization of barriers on an earthquake fault. *J. Geophys. Res.* 84 (B11), 6140–6148. doi:10.1029/jb084ib11p06140

Caciagli, M., Camassi, R., Danesi, S., Pondrelli, S., and Salimbeni, S. (2015). Can we consider the 1951 Caviaga (Northern Italy) earthquakes as noninduced events? *Seismol. Res. Lett.* 86 (5), 1335–1344. doi:10.1785/0220150001

Choi, H., and Noh, M. (2010). Source parameters of the may 2, 2009 andong earthquake in South Korea. *Geosci. J.* 14 (3), 269–276. doi:10.1007/s12303-010-0025-1

Clinton, J. F., Cua, G., Huerfano, V., Von Hillebrandt-Andrade, C. G., and Cruzado, J. M. (2006). The current state of seismic monitoring in Puerto Rico. *Seismol. Res. Lett.* 77 (5), 532–543. doi:10.1785/gssrl.77.5.532

Crotwell, H. P., Owens, T. J., and Ritsema, J. (1999). The Taup Toolkit: Flexible seismic travel-time and ray-path utilities. *Seismol. Res. Lett.* 70 (2), 154–160. doi:10.1785/gssrl.70.2.154

Daniels, C., and Peng, Z. (2022). Fault orientation and relocated seismicity associated with the 12 December 2018 *Mw* 4.4 Decatur, Tennessee, earthquake sequence. *Seismol. Res. Lett.* 93 (6), 3454–3467. doi:10.1785/0220220173

Dziewonski, A. M., and Anderson, D. L. (1981). Preliminary reference Earth model. *Phys. Earth Planet. Inter.* 25 (4), 297–356. doi:10.1016/0031-9201(81)90046-7

Fan, L. P., Li, B. R., Liao, S. R., Jiang, C., and Fang, L. H. (2022). High-precision relocation of the aftershock sequence of the January 8, 2022, M_S 6.9 Menyuan earthquake. *Earthq. Sci.* 35 (2), 138–145. doi:10.1016/j.eqs.2022.01.021

Fang, L. H., Wu, J. P., Wang, W. L., Yang, T., and Wang, C. Z. (2015). Relocation of the 2014 M_S7.3 earthquake sequence in yutian, xinjiang. *Chin. J. Geophys.* 58 (3), 802–808. (in Chinese). doi:10.6038/cjg20150310

Gao, X. W., Wan, Y. G., Huang, J. C., Li, X., and Cui, H. W. (2015). Tectonic stress field analysis and static coulmb stress changes of the *Ms*5.8 Inner Mongolias Alxa Left Banner earthquake. *North China Earthq. Sci.* 33 (2), 48–54. (in Chinese).

Gulen, L., Pınar, A., Kalafat, D., Özel, N., Horasan, G., Yılmazer, M., et al. (2002). Surface Fault breaks, aftershock distribution, and rupture process of the 17 august 1999 Izmit, Turkey, earthquake. *Bull. Seismol. Soc. Am.* 92 (1), 230–244. doi:10.1785/0120000815

Han, X. M., Liu, F., Zhang, F., Hu, B., and Chen, L. F. (2015). Source mechanism of the 2015 Alxa zuoqi *Ms*5.8 earthquake and its relocation. *Acta Seismol. Sin.* 37 (6), 1059–1063. (in Chinese). doi:10.11939/jass.2015.06.015

Hauksson, E., and Shearer, P. (2005). Southern California hypocenter relocation with waveform cross-correlation, Part 1: Results using the double-difference method. *Bull. Seismol. Soc. Am.* 95 (3), 896–903. doi:10.1785/0120040167

Hauksson, E., Yang, W., and Shearer, P. M. (2012). Waveform relocated earthquake catalog for southern California (1981 to June 2011). *Bull. Seismol. Soc. Am.* 102 (5), 2239–2244. doi:10.1785/0120120010

Kato, A., Fukuda, J., Nakagawa, S., and Obara, K. (2016). Foreshock migration preceding the 2016 *Mw* 7.0 Kumamoto earthquake, Japan. *Geophys. Res. Lett.* 43 (17), 8945–8953. doi:10.1002/2016GL070079

Klein, F. W. (2002). User's guide to HYPOINVERSE-2000, a fortran program to solve for earthquake locations and magnitudes. *U. S. Geol. Surv.* 171, 1–123. Open-File Rept. 02–.

Konstantinou, K. I., Kalogeras, I. S., Melis, N. S., Kourouzidis, M. C., and Stavrakakis, G. N. (2006). The 8 January 2006 earthquake (*Mw* 6.7) offshore Kythira Island, Southern Greece: Seismological, strong-motion, and macroseismic observations of an intermediate-depth event. *Seismol. Res. Lett.* 77 (5), 544–553. doi:10.1785/gssrl.77.5.544

Konstantinou, K. I., Lee, S. J., Evangelidis, C. P., and Melis, N. S. (2009a2009). Source process and tectonic implications of the 8 January 2006 (M_w 6.7) Kythira earthquake, southern Greece. *Phys. Earth Planet. Inter.* 175, 167–182. doi:10.1016/j.pepi.2009.03.010

Konstantinou, K. I., Melis, N. S., Lee, S. J., Evangelidis, C. P., and Boukouras, K. (2009b). Rupture process and aftershocks relocation of the 8 June 2008 M_w 6.4 earthquake in northwest Peloponnese, Western Greece. *Bull. Seismol. Soc. Am.* 99 (6), 3374–3389. doi:10.1785/0120080301

Langin, W. R. (2003). Seismicity of central Tibet from project INDEPTH III seismic recordings. *Bull. Seismol. Soc. Am.* 93 (5), 2146–2159. doi:10.1785/0120030004

Laske, G., Masters, G., Ma, Z. T., and Pasyanos, M. (2013)., Vol. 15. Vienna: EGU. EGU General Assembly.Update on CRUST1.0-A1-degree global model of Earth's crust

Lees, J. M., and Malin, P. E. (1990). Tomographic images of *P* wave velocity variations at Parkfield, California. *J. Geophys. Res.* 95 (B13), 21793–21804. doi:10.1029/JB095iB13p21793

Liu, M., Li, H. Y., Zhang, M., and Wang, T. L. (2020). Graphics processing unit-based Match and Locate (GPU-M&L): An improved match and locate method and its application. *Seismol. Res. Lett.* 91 (2A), 1019–1029. doi:10.1785/0220190241

Mandal, P., and Horton, S. (2007). Relocation of aftershocks, focal mechanisms and stress inversion: Implicaitons toward the seismo-tectonics of the causative fault zone of M_w7.6 2001 Bhuj earthquake (India). *Tectonophysics* 429, 61–78. doi:10.1016/j.tecto.2006.09.009

McMahon, N. D., Aster, R. C., Yeck, W. L., McNamara, D. E., and Benz, H. M. (2017). Spatiotemporal evolution of the 2011 Prague, Oklahoma, aftershock sequence revealed using subspace detection and relocation. *Geophys. Res. Lett.* 44 (14), 7149–7158. doi:10.1002/2017GL072944

Meng, X., Yang, H., and Peng, Z. (2018). Foreshocks, *b* value map, and aftershock triggering for the 2011 M_w 5.7 Virginia earthquake. *J. Geophys. Res. Solid Earth* 123, 5082–5098. doi:10.1029/2017JB015136

Mottaghi, A. A., Rezapour, M., and Yaminifard, F. (2010). Double-difference relocation of earthquake hypocenters along the southern flank of the central Alborz, Iran. *Bull. Seismol. Soc. Am.* 100 (5A), 2014–2023. doi:10.1785/0120090147

Peng, Z., and Zhao, P. (2009). Migration of early aftershocks following the 2004 Parkfield earthquake. *Nat. Geosci.* 2 (12), 877–881. doi:10.1038/ngeo697

Research Group of Active Fault System around the Ordos Massif (1988). *Active Fault System around Ordos Massif*. Beijing: Seismological Press. (in Chinese) 20–27.

Schoenball, M., and Ellsworth, W. L. (2017). Waveform-relocated earthquake catalog for Oklahoma and Southern Kansas illuminates the regional fault network. *Seismol. Res. Lett.* 88 (5), 1252–1258. doi:10.1785/0220170083

Scholz, C. H. (1990). *The mechanics of earthquakes and faulting*. New York: Cambridge University Press.

Shelly, D. R., Ellsworth, W. L., and Hill, D. P. (2016). Fluid-faulting evolution in high definition: Connecting fault structure and frequency-magnitude variations during the 2014 Long Valley Caldera, California, earthquake swarm. *J. Geophys. Res. Solid Earth* 121, 1776–1795. doi:10.1002/2015JB012719

Sippl, C., Schurr, B., Asch, G., and Kummerow, J. (2018). Seismicity structure of the northern Chile forearc from >100,000 double-difference relocated hypocenters. *J. Geophys. Res. Solid Earth* 123, 4063–4087. doi:10.1002/2017JB015384

Song, C., and Ge, Z. X. (2018). An iterative travel time inversion and waveform modeling method to determine the crust structure and the focal mechanism of 2015 Alxa Left Banner M_s5.8 earthquake. *Chin. J. Geophys.* 61 (4), 1225–1237. (in Chinese). doi:10.6038/cjg2018L0655

Syracuse, E. M., Holt, R. A., Savage, M. K., Hohnson, J. H., Thurber, C. H., Unglert, K., et al. (2012). Temporal and spatial evolution of hypocentres and anisotropy from the darfield aftershock sequence: Implications for fault geometry and age. *N. Z. J. Geol. Geophys.* 50 (3), 287–293. doi:10.1080/00288306.2012.690766

Tang, T., Li, B. R., Fang, L. H., Su, Y. J., Zhong, Y. S., Yang, J. Q., et al. (2022). Relocation of the foreshocks and aftershocks of the 2021 M_S 6.4 Yangbi earthquake sequence, Yunnan, China. *J. Earth Sci.* 33 (4), 892–900. doi:10.1007/s12583-021-1527-7

Waldhause, F., and Ellsworth, W. L. (2000). A double difference earthquake location algorithm: Method and application to the north Hayward fault, California. *Bull. Seismol. Soc. Am.* 90 (6), 1353–1368. doi:10.1785/0120000006

Waldhauser, F., and Ellsworth, W. L. (2002). Fault structure and mechanics of the Hayward fault, California, from double-difference earthquake locations. *J. Geophys. Res.* 107 (B3), ESE 3-1–ESE 3-15. doi:10.1029/2000jb000084

Waldhauser, F., and Schaff, D. P. (2008). Large-scale relocation of two decades of Northern California seismicity using cross-correlation and double-difference methods. *J. Geophys. Res.* 113 (B08311). doi:10.1029/2007JB005479

Wang, T. L., Liu, M., Li, H. Y., Cui, B. W., and Zhong, S. J. (2019). Relocation of the aftershock sequence and activity of the M_s 5.8 Alxa earthquake. *Chin. J. Geophys.* 62 (2), 2038–2047. (in Chinese). doi:10.6038/cjg2019N0024

Wei, J. M., Han, X. M., Zhang, F., and Li, T. (2017). The sequence character of alashan left banner M_s5.8 earthquake on April 15, 2015. *Seismol. Geomagnetic Observation Res.* 37 (1), 32–37. (in Chinese). doi:10.3969/j.issn.1003-3246.2017.01.006

Wen, X. Z., Du, F., Long, F., Fan, J., and Zhu, H. (2011). Tectonic dynamics and correlation of major earthquake sequences of the Xiaojiang and Qujiang-Shiping fault systems, Yunnan, China. *Sci. China Earth Sci.* 41 (5), 1563–1575. (in Chinese). doi:10.1007/s11430011-4231-0

Wen, X. Z., Du, F., Yi, G. X., Long, F., Fan, J., Yang, P. X., et al. (2013). Earthquake potential of the Zhaotong and Lianfeng fault zones of the eastern Sichuan-Yunnan border region. *Chin. J. Geophys.* 56 (10), 3361–3372. (in Chinese). doi:10.6038/cjg20131012

Wen, X. Z. (2014). Structures of source regions of the 1979 M_s6.0 wuyuan earthquake and the 1996 M_s6.4 baotou earthquake in inner Mongolia, China. *Seismol. Geol.* 36 (3), 586–597. (in Chinese). doi:10.3969/j.issn.0253-4967.2014.03.004

Wu, P. P., Chang, L. J., Lu, L. Y., Guo, H. L., Lv, M. M., and Ding, Z. F. (2022). Three-dimensional fine velocity structure of the upper crust of the 2021 Madoi M_s7.4 earthquake, Qinghai. *Chin. J. Geophys* 65 (6), 2006–2021. (in Chinese). doi:10.6038/cjg2022P0860

Yao, D. D., Huang, Y. H., Peng, Z. G., and Castro, R. R. (2020). Detailed investigation of the foreshock sequence of the 2010 M_w7.2 El Mayor-Cucapah earthquake. *J. Geophys. Res. Solid Earth* 124, e2019JB019076. doi:10.1029/2019jb019076

Yao, D., Huang, Y., and Fox, J. L. (2021). New insights into the Lake Erie fault system from the 2019 M_L 4.0 Ohio earthquake sequence. *Seismol. Res. Lett.* 92 (4), 2531–2539. doi:10.1785/0220200335

Zeng, X. W., Feng, J. G., Long, F., and Xin, H. L. (2017a). Research on mid-upper crustal velocity tomography of Pg wave in wstern margin of Ordos. *J. Seismol. Res.* 40 (2), 261–270. (in Chinese).

Zeng, X. W., Feng, J. G., and Lv, J. Q. (2014). Characteristics of lateral variation of Pg wave velocity before and after the 2003 Minle M_s6.1 earthquake. *Prog. Geophys.* 29 (4), 1601–1608. (in Chinese). doi:10.6038/pg20140415

Zhang, M., and Wen, L. X. (2015a). An effective method for small event detection: Match and locate (M&L). *Geophys. J. Int.* 200 (3), 1523–1537. doi:10.1093/gji/ggu466

Zhang, M., and Wen, L. X. (2015c). Earthquake characteristics before eruptions of Japan's Ontake volcano in 2007 and 2014. *Geophys. Res. Lett.* 42 (17), 6982–6988. doi:10.1002/2015gl065165

Zhang, M., and Wen, L. X. (2015b). Seismological evidence for a low-yield nuclear test on 12 May 2010 in North Korea. *Seismol. Res. Lett.* 86 (1), 138–145. doi:10.1785/02201401170

Zhang, Y., An, Y., Long, F., Zhu, G., Qin, M., Zhong, Y., et al. (2021). Short-term foreshock and aftershock patterns of the 2021 *Ms* 6.4 Yangbi earthquake sequence. *Seismol. Res. Lett.* 93, 21–32. doi:10.1785/0220210154

Zhao, B., Gao, Y., Huang, Z. B., Zhao, X., and Li, D. H. (2013). Double difference relocation, focal mechanism and stress inversion of Lushan M_s 7.0 earthquake sequence. *Chin. J. Geophys.* 56 (10), 3385–3395. (in Chinese). doi:10.6038/cjg20131014

Zhao, L. S., and Helmberger, D. V. (1994). Source estimation from broadband regional seismograms. *Bull. Seismol. Soc. Am.* 84 (1), 91–104. doi:10.1029/93JB02965

Zhu, L. P., and Helmberger, D. V. (1996). Advancement in source estimation techniques using broadband regional seismograms. *Bull. Seismol. Soc. Am.* 86 (5), 1634–1641. doi:10.1785/bssa0860051634

frontiers | Frontiers in Earth Science

TYPE Original Research
PUBLISHED 15 February 2023
DOI 10.3389/feart.2023.1091408

OPEN ACCESS

EDITED BY
Fuqiong Huang,
China Earthquake Networks Center, China

REVIEWED BY
Lingyuan Meng,
China Earthquake Networks Center, China
Yufang Rong,
FM Global Research, United States

*CORRESPONDENCE
Shi Chen,
chenshi@cea-igp.ac.cn

SPECIALTY SECTION
This article was submitted to Solid Earth Geophysics, a section of the journal *Frontiers in Earth Science*

RECEIVED 07 November 2022
ACCEPTED 23 January 2023
PUBLISHED 15 February 2023

CITATION
Zhang B, Chen S, Zhuang J, Zhang B, Wu X and Liang B (2023), Statistical evaluation of earthquake forecast efficiency using earthquake-catalog and fault slip rate in the Sichuan-Yunnan region, China. *Front. Earth Sci.* 11:1091408. doi: 10.3389/feart.2023.1091408

Statistical evaluation of earthquake forecast efficiency using earthquake-catalog and fault slip rate in the Sichuan-Yunnan region, China

Bo Zhang[1,2,3], Shi Chen[2,3]*, Jiancang Zhuang[4], Bei Zhang[2,3], Xu Wu[2,3] and Baojuan Liang[5]

[1]Liaoning Earthquake Agency, Shenyang, China, [2]Institute of Geophysics, China Earthquake Administration, Beijing, China, [3]Beijing Baijiatuan Earth Science National Observation and Research Station, Beijing, China, [4]The Institute of Statistical Mathematics, Research Organization of Information and Systems, Tokyo, Japan, [5]School of Electrical Control, Chang'An University, Xi'an, China

Epicenter locations are generally adjacent to active faults and past seismicity regions. Past earthquake catalogs and the geometry of the active faults can provide key prior knowledge concerning earthquake forecasts. In this study, we first introduce two straightforward dedicated models, the proximity-to-past-earthquakes (PPE) and proximity-to-mapped-faults (PMF) models, to fit the seismicity in the Sichuan-Yunnan region, China. The hybrid proximity-to-known-sources (PKS) model with the optimized model parameters is then used to estimate the probability of earthquake occurrence. Second, to compare the PKS forecast efficiency to those of different models, retrospective tests are applied to a dataset located in the Sichuan-Yunnan region. The results show that the probability maps derived from PPE, PMF, and PKS have non-uniform Poisson distribution features and that there is forecasting significance for past cases of moderate earthquakes in the test region. Finally, using Molchan error diagram tests, we find that the hybrid PKS model performs better than the other models in the testing region. The unsatisfactory performance of the PMF model for earthquake forecasting may lie both in the incompleteness of the fault database and the lack of consideration of co-seismic ruptures. Therefore, one of the three models can be used as a base model for comparing and evaluating earthquake forecast strategies.

KEYWORDS

earthquake catalog, Molchan error diagram, statistical evaluation, earthquake forecast, active fault

1 Introduction

More than one-third of the global population experiences earthquakes, with frequent slight or greater damage to lives and property from such events (Marti et al., 2019). However, at present, earthquake forecasting remains a major unsolved scientific problem and is not sufficiently reliable to rapidly predict earthquakes. Seismologists can also contribute to society by performing long-term probabilistic seismic hazard assessments. As a basic input for building codes, such assessments are crucial to ensure good building practices to save lives (Hiemer et al., 2013).

Mapped faults and past earthquakes have historically been the two main types of data used by seismic hazard models to estimate the likelihood of earthquake occurrence (Rhoades et al., 2017).

Some short-term models have been built using only cataloged earthquakes, including the short-term earthquake probability (STEP) (Gerstenberger et al., 2005) and epidemic-type aftershock sequence (ETAS) (Ogata, 1988; Ogata, 1998; Gerstenberger and Rhoades, 2010) models, which are based on the decay of aftershock rates and the Omori–Utsu law (Utsu, 1961). Other useful medium- or long-term models, such as the proximity-to-past-earthquakes (PPE) (Kagan and Jackson, 1994; Jackson and Kagan, 1999) and the every-earthquake-a-precursor-according-to-scale (EEPAS) (Rhoades and Evison, 2004; Rhoades and Evison, 2005; Rhoades, 2007) models, rely only on past earthquakes. Meanwhile, long-term models such as the proximity-to-mapped-faults (PMF) model (Rhoades and Stirling, 2012) often use mapped faults with their slip rates. In addition, the increasing availability of crustal movement observational data, such as Global Positioning System (GPS) network data and derived models of crustal strain rate (Bird et al., 2015; Rhoades et al., 2017) are important to estimate the earthquake occurrence rate (Rhoades et al., 2015).

A parallel development is that of hybrid methods, which combine two or more different models to gain predictive skills from a single idea or data source. The results of retrospective and pseudo-prospective analyses have shown that some multiplicative ensembles provide statistically better forecasts than their constituent forecasting models (Rhoades and Stirling, 2012; Rhoades 2013; Gerstenberger et al., 2014; Rhoades et al., 2015; Rhoades et al., 2016). Therefore, the international Collaboratory for the Study of Earthquake Predictability (CSEP) supports methods to evaluate combinations of two or more individual models or to assimilate new gridded covariates into existing models (Schorlemmer et al., 2018).

The robustness of various earthquake forecast models cannot be fully described without first being assessed in diverse regions with distinct seismic features. The Sichuan-Yunnan region provides a natural earthquake forecast experiment because, following the M_S 8.0 Wenchuan earthquake, it became more seismically active. For example, two earthquakes of magnitude ≥7.0, the M_S 7.0 Lushan and M_S 7.0 Jiuzhaigou earthquakes, have occurred in this region in the last 10 years since the M_S 8.0 Wenchuan earthquake; however, no earthquakes had occurred over the same time period before the M_S 8.0 Wenchuan earthquake. Moreover, substantial infrastructure, such as reservoirs, railway networks, and electricity grids, is spread throughout the Sichuan-Yunnan region. While earthquakes of great intensity occurring due to natural processes cannot be avoided, forewarning can help minimize their often catastrophic and damaging impacts (Herrera et al., 2022). Much work is required regarding probabilistic seismic hazard assessments in this area. Therefore, we introduce individual probabilistic models based on past earthquakes or mapped faults and a hybrid model based on both to estimate the probability of earthquake occurrence; we then take a statistical approach to evaluate the efficiency of earthquake forecasting in the Sichuan-Yunnan region.

Section 2 includes a full description of the mapped faults and cataloged earthquakes that were used in this study. The two individual models and the hybrid model are introduced in Section 3. Section 4 and Section 5 present, successively, the results of the estimated seismicity rate for each model, along with an evaluation of their predictive effectiveness.

2 Data

We chose the Sichuan-Yunnan region for testing because of the good monitoring capability in this region with respect to seismicity and fault movement. In the test area of the Sichuan-Yunnan region, which is marked in Figure 1, 1,234 earthquakes with magnitudes ≥4.0 and depth ≤50 km were recorded in the China Earthquake Networks Center (CENC) catalog from January 1, 1970, to September 10, 2022, including the M_S 8.0 Wenchuan earthquake, the largest earthquake in the test region. Of these, 14 target earthquakes in the test region with $M \geq 6.0$ and depth ≤ 50 km that occurred during the three periods of May 20, 2008–May 20, 2011; January 1, 2013–January 1, 2016; and September 10, 2019–September 10, 2022, listed in Table 1, were used to evaluate the forecast efficiency of the three different models. Figure 1 shows the epicenters of the earthquakes that occurred in the test region.

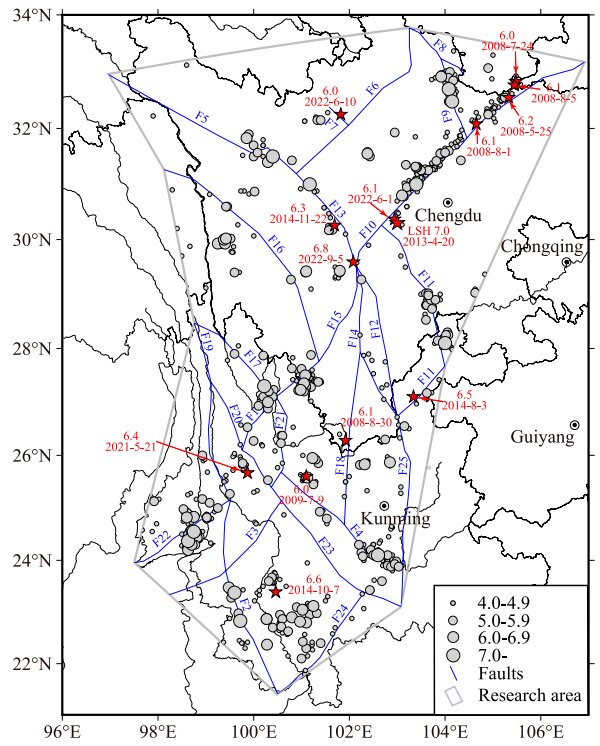

FIGURE 1
Epicenters of the earthquakes in the research area in the Sichuan-Yunnan region, China. The circle sizes represent the earthquake magnitudes. The red stars indicate the target earthquakes. The blue lines show the faults in the fault-model database. The gray line encloses the test area in the Sichuan-Yunnan region. Fault numbers F1–F25 indicate the Lijiang-Xiaojinhe, Hanmuba-Heihe-Mengzhe, Nandinghe, Chuxiong-Jianshui, Ganzi-Yushu, Longriba, Songgang, Tazang, Huya, Longmenshan, Mabian, Daliangshan, Xianshuihe, Anninghe, Jinpingshan, Litang, Deqin-Zhongdian-Daju, Yuanmou-Xigeda, Lancangjiang, Weixi-Qiaohou, Chenghai, Longling-Ruili, Honghe, Menglong, and Xiaojiang faults, respectively.

The Chinese Earthquake Administration (CEA) and other groups launched the Project Crustal Movement Observation Network of China (CMONC) to monitor the crust dynamics using various techniques including GPS. Based on the GPS measurements and the fault locations in the test region, the Second Monitoring and Application Center of CEA calculated the fault rates in the Sichuan-Yunnan region and provided the fault-model datasets for this study (Figure 2). Figure 2 shows the higher slip rates in the Ganzi-Yushu fault (F5), the fault intersection segment of the Xianshuihe fault (F13), the Longmenshan fault (F10), the Jinpingshan fault (F15), the

TABLE 1 Target earthquakes (M_S > 6.0) in the test area in the Sichuan-Yunnan region, China, during the three periods of May 20, 2008–May 20, 2011, January 1, 2013–January 1, 2016, and September 10, 2019–September 10, 2022.

No.	Date	Time	M_S	Location		Location name
				Long.	Lat.	
1	2008-05-25	16:21:49	6.2	105.33	32.55	Qingchuan, Sichuan
2	2008-07-24	15:09:28	6.0	105.48	32.83	Qingchuan, Sichuan
3	2008-08-01	16:32:42	6.1	104.65	32.08	Pingwu, Sichuan
4	2008-08-05	17:49:15	6.1	105.45	32.77	Qingchuan, Sichuan
5	2008-08-30	16:30:51	6.1	101.92	26.28	Panzhihua, Sichuan
6	2009-07-09	19:19:13	6.0	101.10	25.60	Yaoan, Yunnan
7	2013-04-20	08:02:46	7.0	103.00	30.30	Lushan, Sichuan
8	2014-08-03	16:30:10	6.5	103.34	27.10	Ludian, Yunnan
9	2014-10-07	21:49:39	6.6	100.46	23.39	Jinggu, Yunnan
10	2014-11-22	16:55:25	6.3	101.69	30.26	Kangding, Sichuan
11	2021-05-21	21:48:34	6.4	99.87	25.67	Yangbi, Yunnan
12	2022-06-01	17:00:08	6.1	102.94	30.37	Lushan, Sichuan
13	2022-06-10	01:28:34	6.0	101.82	32.25	Maerkang, Sichuan
14	2022-09-05	12:52:18	6.8	102.08	29.59	Luding, Sichuan

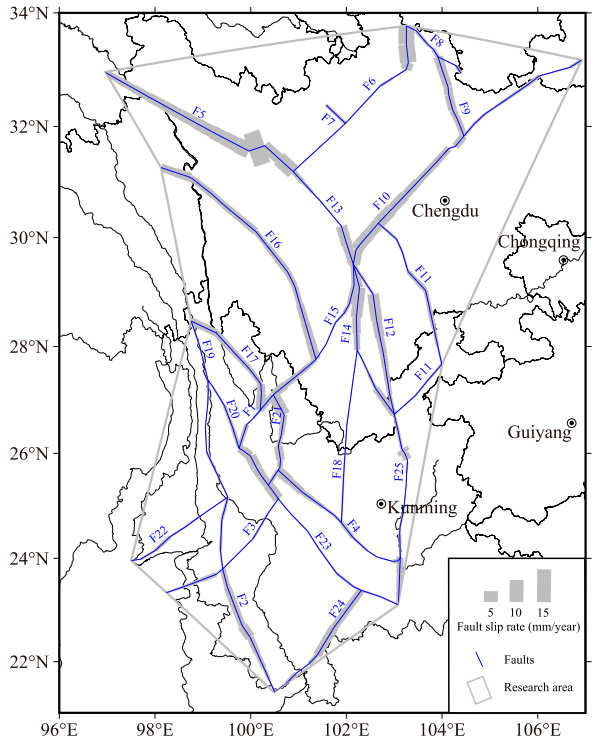

FIGURE 2
Fault slip rates. The blue lines indicate the faults in the fault-model database in the test area, with line thicknesses proportional to the fault slip rate. The gray line encloses the test area in the Sichuan-Yunnan region. The fault numbers are as indicated in Figure 1.

Anninghe fault (F14), and the Daliangshan fault (F12). The Qinghai-Tibet Plateau Block moves eastward continuously, blocked by the relatively stable Sichuan Basin, and the South China Block in the Sichuan-Yunnan region moves from east to south along these faults at a relatively high slip rate. In Figure 2, four aftershocks of the M_S 8.0 Wenchuan earthquake with magnitudes of M_S 6+ occurred near the northern segment (latitude >32°N) of the Longmenshan fault (F14), however, the segment of the fault does not have the expected relatively high slip rate (Shen et al., 2009; Xiong et al., 2021).

3 Method

3.1 Proximity-to-past-earthquakes model

According to the assumption that future earthquakes are more likely to occur near past earthquakes, Jackson and Kagan (1999) proposed the PPE forecasting model, in which the contribution from every earthquake is inversely proportional to the epicentral distance and is directly dependent on the earthquake magnitude.

Under the PPE model, the earthquake occurrence-rate density λ at time t and location (x, y) can be calculated from the earthquakes (t_i, m_i, x_i, y_i), where $i = 1, \ldots, n_{eq}$, in the catalog such that

$$\lambda_{PPE}(t,x,y) = \frac{1}{t-t_0}\sum_{i:\, t_i<t}\left(\frac{a_e}{d_e{}^2 + (x-x_i)^2 + (y-y_i)^2} + s_e\right) \quad (1)$$

where a is a normalization parameter, d is the smoothing distance, and s is a small spatially uniform background rate of earthquake occurrence per day per kilometer squared to allow for earthquakes far from past earthquakes. The seismicity rate $\lambda(t, x, y)$ is higher near past earthquakes of greater magnitude.

By maximizing the likelihood function, the three parameters (a_e, d_e, s_e) can be computed by fitting the model to the past earthquake catalog. We used earthquakes with magnitudes of M_S > 4.0 to compute the conditional density, using January 1, 1970, to January 1, 1990, as the learning period. The likelihood was only calculated for earthquakes with magnitudes of M_S > 6.0 over the learning period. The three parameters were optimized for target earthquakes with M_S > 6.0 over the forecast period from January 1, 1990, to May 20, 2008. Using the same parameters, the seismicity rates for January 1, 2013, and September 10, 2019, can also be estimated.

3.2 Proximity-to-mapped-faults model

The PMF model assumes that the mapped fault sources are frequently affected by earthquakes having the same characteristic magnitudes (Rhoades and Stirling, 2012). Under the PMF model, the mapped fault sources are composed of planar segments and each source has its own slip rate. Some long faults are divided into multiple segments, which are assigned their own slip rates. Because of earthquake depth estimation issues or because they are assigned a fixed depth, every fault is treated as if its dip angle were 90°; therefore, the distance between the faults and earthquakes has no relevance to the earthquake depths reported in the earthquake reports. The separated segments of the mapped faults and the individual associated slip rates

are used to fit the PMF model. The seismicity rate λ_{PMF} at time t and location (x, y) is of the form

$$\lambda_{PMF}(t,x,y) = \frac{1}{n_f}\sum_{i=1}^{n_f}\left(\frac{a_f r_i}{\pi\left[d_f^2 + (x-x_i)^2 + (y-y_i)^2\right]} + s_f\right) \quad (2)$$

where x_i and y_i are the locations of the individual point fault sources, n_f is the total number of points with associated slip rates r_i, and $i = 1, ..., n_f$. d_f is the space smoothing distance, which is not sensitive to the actual spacing between the individual points if it is much greater than d_f. s_f is a small spatially uniform background rate of earthquake occurrence per day per kilometer squared, which allows for earthquakes far from the mapped faults. Therefore, the seismicity rate $\lambda_{PMF}(t, x, y)$ is greater near mapped faults and lower far from mapped faults. In addition, the seismicity rate increases with the fault slip rate of the surrounding identified faults.

The test area of the Sichuan-Yunnan region has 25 mapped faults with known slip rates, as shown in Figure 2. Each mapped fault is separated into multiple point sources closely spaced at 0.01° intervals along the fault. To compare the earthquake forecast efficiency of the PMF model to that of the PPE model, we used the same learning and forecast periods as used in the PPE model. The three parameters were optimized for target earthquakes with magnitudes of $M_S > 6.0$ over the three periods of January 1, 1990–May 20, 2008; January 1, 1990–January 1, 2013; and January 1, 1990–September 10, 2019.

3.3 Proximity-to-known-sources model

Mapped faults and cataloged earthquakes can sometimes each contribute differently to the creation of conventional probabilistic seismic-hazard models. For short periods, the fault data may not play a worthwhile role in estimating the earthquake likelihood. Accordingly, Rhoades and Stirling (2012) proposed an optimal model for earthquake occurrence, called the proximity-to-known-sources (PKS) model, that combines the fault location and estimated slip rates with the cataloged earthquake locations and magnitudes. This model consists of a convex linear combination of the PPE and PMF models. The seismicity rate λ_{PKS} at time t and location (x, y) is of the form

$$\lambda_{PKS}(t,x,y) = \mu\lambda_{PMF}(t,x,y) + (1-\mu)\lambda_{PPE}(t,x,y) \quad (3)$$

where μ is an additional parameter to be estimated in the range of $0 \leq \mu \leq 1$, such that seven parameters are needed for the model.

Here, we provide three methods to combine the two models: 1) Based on the optimized parameters (a_e, d_e, s_e) of the PPE model and (a_f, d_f, s_f) of the PMF model, we calculated the seismicity rate λ_{PKS} on May 20, 2008; January 1, 2013; and September 10, 2019, using an empirically specified μ; i.e., μ = 0.1 and 0.9, and 2) μ is a liner dependent on magnitude, as proposed by Hiemer et al. (2013) and called PKS weighted model (PKSW) in this study. The form is

$$\mu\begin{cases}\dfrac{m_c - m}{m_c - 6} & for\ 6 \leq m \leq 7\\ 0 & for\ 7 < m \leq 9\end{cases} \quad (4)$$

where m_c is the upper corner magnitude of the Gutenberg-Richter relationship (Gutenberg and Richter, 1944). All m_c values over the three time intervals are M_S7.0. 3) All seven parameters of the hybrid model were optimized by maximizing the likelihood function over the same three time intervals. Finally, we compared the earthquake forecasting performances of the various parameter combinations.

4 Results

4.1 Results of the PPE model

Figure 3 shows the results of the fitted seismicity rates for the three different times: May 20, 2008; January 1, 2013; and September 10, 2019. The black stars represent earthquakes of M_S 6+ that occurred over the 3 years following the above three dates. The spatial inconsistency of the PPE model is due to its strong event location density concentration.

Some obvious differences along the Longmenshan fault between the exceptions of the earthquake occurrence are shown in Figures 3A, B. The M_S 8.0 Wenchuan earthquake and its aftershocks may be the dominant earthquake source locations contributing to the spatial variation differences in the rate density. The seismicity rate of the Lushan region in Figure 3C is higher than that in Figure 3B because of the M_S 7.0 Lushan earthquake. The PPE model gets its strength from its ability to use data from these huge earthquakes.

As shown in Figure 3, the M_S 6.1 Panzhihua, M_S 6.0 Maerkang, and M_S 6.8 Luding earthquakes are not located at locations of relatively higher seismicity rate, which indicates that no earthquake clustering occurred during the last several decades. This adds to the difficulty of forecasting earthquakes using the PPE model.

4.2 Result of the PMF model

Figures 4A–C show the spatial variation in seismicity rates at three different dates, May 20, 2008; January 1, 2013; and September 10, 2019, respectively. As shown in Figure 4, the location probability decreases with distance from the mapped faults. The spatial variations do not differ obviously in Figures 4A–C because the map of the seismicity rate is related to the locations of the mapped faults and their slip rates, which are static on decadal timescales.

As shown in Figure 4B, the seismicity rate at the location where the M_S 6.6 Jinggu earthquake occurred is low because the epicenter of the earthquake was far from the mapped faults. However, three of the M_S 8.0 Wenchuan aftershocks and the M_S 6.1 Panzhihua earthquake (Figure 4A) are not located in relatively high seismicity rate areas, even though they are near mapped fault sources. One possible explanation may be that the fault slip rate at these locations is small and that the seismicity rate did not benefit sufficiently from the fault slip rates, as seen in Figure 2.

4.3 Results of the PKS model

Based on the various μ values, the varying seismicity rates at the three dates, May 20, 2008; January 1, 2013; and September 10, 2019, are illustrated in Figure 5. All the graphs indicate that the rate density is highest near the greatest concentration of large earthquakes during the entire history of the catalog, as well as the mapped fault sources to different extents. The value of μ is related to the proportion of the contribution of the PPE model used to construct the PKS model.

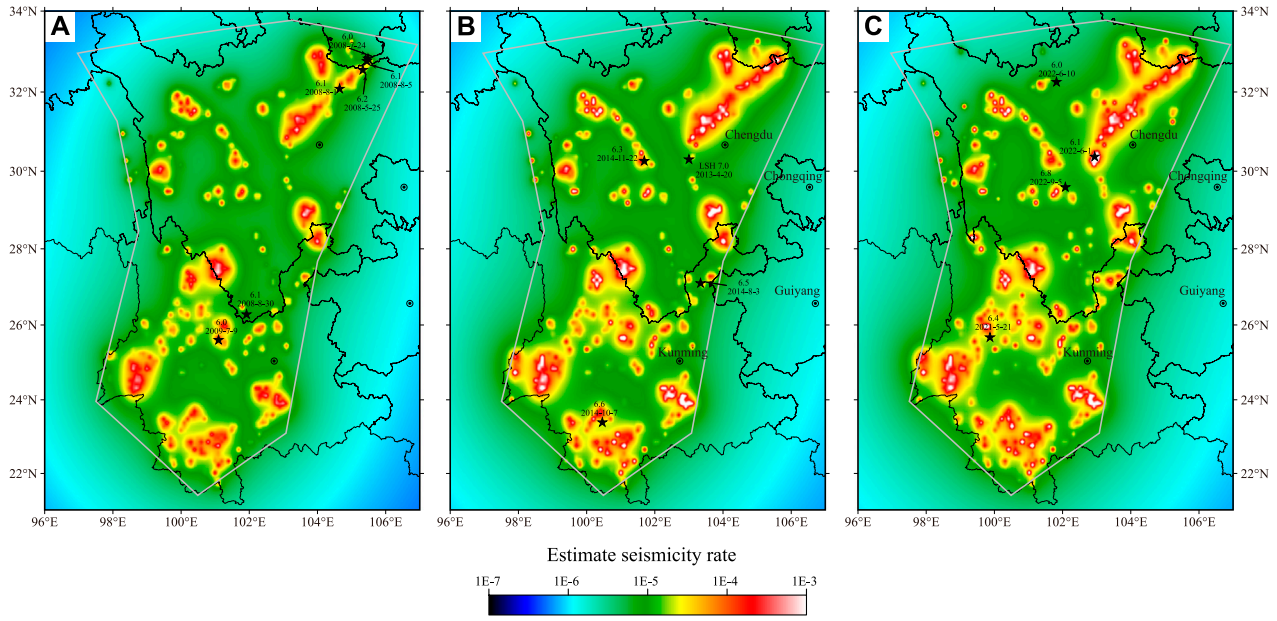

FIGURE 3
Estimated seismicity rate using earthquakes based on the China Earthquake Networks Center (CENC) catalog. The learning period was from January 1, 1970, to January 1, 1990, based on the proximity-to-past-earthquakes (PPE) model to calculate the conditional density. (A–C) Estimated results using data before May 20, 2008; January 1, 2013; and September 10, 2019, respectively. The black stars indicate the target earthquakes. The gray line encloses the test area in the Sichuan-Yunnan region.

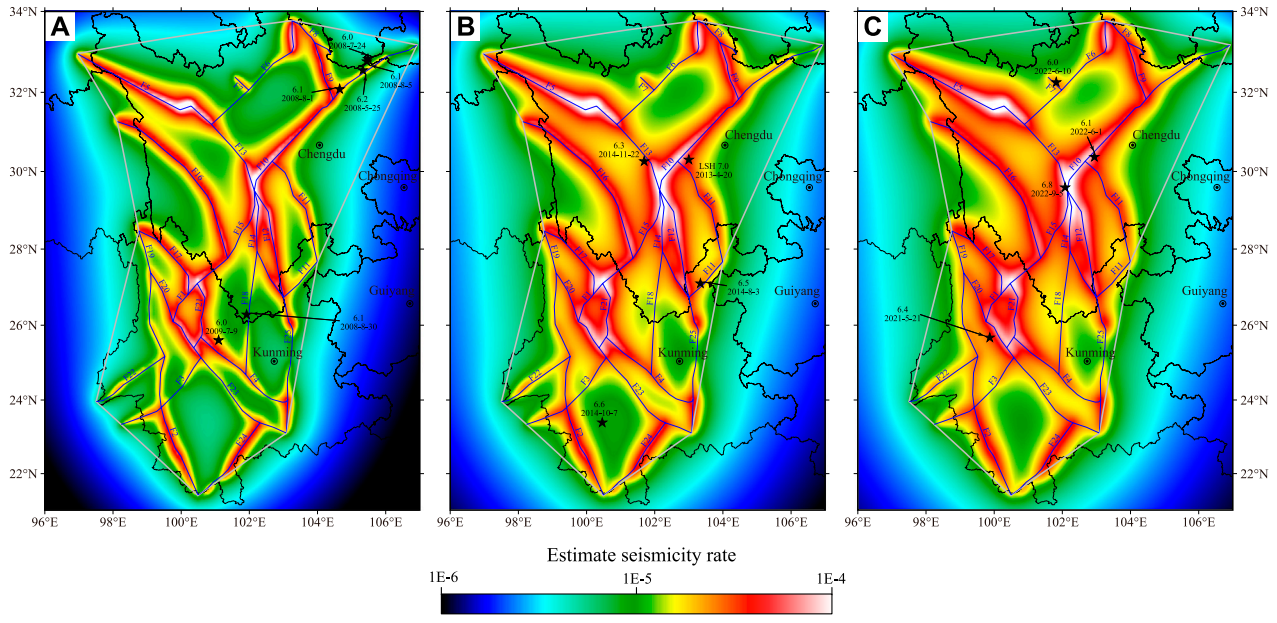

FIGURE 4
Estimated seismicity rate using earthquakes based on the CENC catalog and mapped faults. **(A–C)** Estimated results using data before May 20, 2008; January 1, 2013; and September 10, 2019, respectively. The black stars indicate the target earthquakes. The gray polygon encloses the test area in the Sichuan-Yunnan region. The fault numbers are as indicated in Figure 1.

Figure 5 illustrates that the smaller the μ value, the more "hot spots" with high seismicity rates will appear. The estimated seismicity rate of the PKS model looks like that for the μ value calculated using Eq. 4 at the three dates.

5 Discussion

A hybrid model may underperform in a separate testing period if the seismicity rates that contribute to it are not well correlated with the

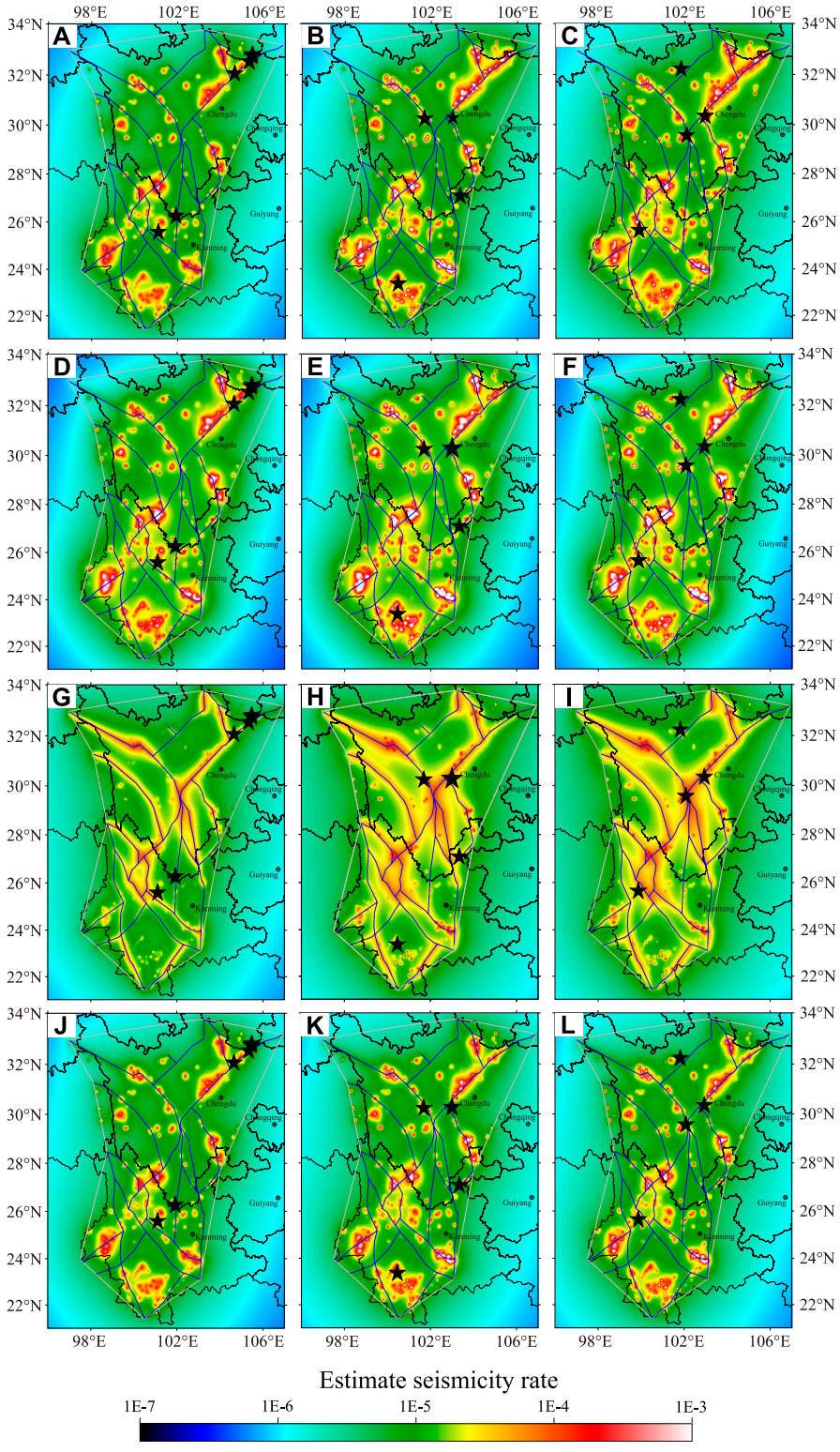

FIGURE 5
Estimated seismicity rate based on cataloged earthquakes and mapped faults, showing results for May 20, 2008 (left), January 1, 2013 (middle), and September 10, 2019 (right, **L**). **(A–C)** Spatial variations in estimated seismicity rates. **(D–F)** Seismicity rate with μ calculated using Eq. 4. Seismicity rate with μ set to **(G–I)** 0.9 and **(J–L)** 0.1. The black stars indicate the target earthquakes.

earthquake locations or if the model is overfitted to a training period in which the seismicity rates are more closely correlated with the earthquake locations than those in the testing period (Rastin et al., 2022). Unaffected by any model fitting, an error diagram is a valuable tool to illustrate the relationship between the seismicity rate and the earthquake occurrence during various time periods and is also

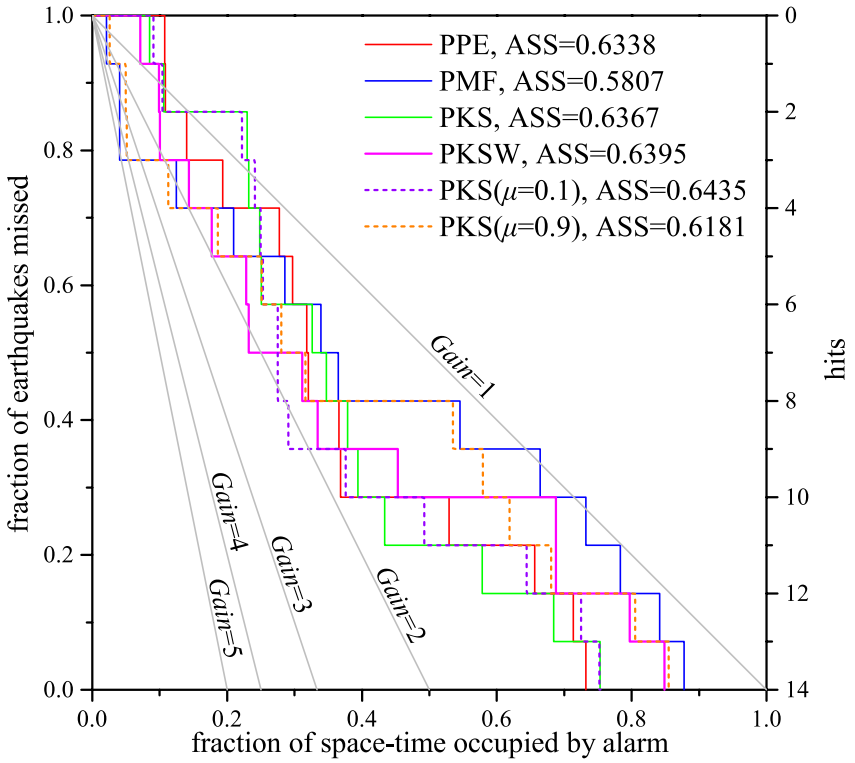

FIGURE 6
Molchan error diagram for the PPE (red curves), proximity-to-mapped-faults (PMF) (blue curves), and proximity-to-known-sources (PKS) models with different weighting schemes (green curves: μ value optimized by maximizing the likelihood function, pink curves: μ value calculated using Eq. 4; short purple and orange dashed curves: μ values manually specified at 0.1 and 0.9) at three different times: May 20, 2008; January 1, 2013; and September 10, 2019. The area skill score (ASS); that is, the area above the error diagram inside the unit square, is used to evaluate the efficiency of the earthquake forecast.

commonly used to evaluate earthquake forecast strategies (Molchan, 1991; Zechar and Jordan, 2008).

In this study, we defined the following earthquake forecast strategy: there will likely be earthquakes of $M_S \geq 6.0$ occurring in the subsequent 3-year period at locations with relatively high seismicity rates based on the PPE, PMF, and PKS models.

The testing region was divided into multiple cells $0.5^\circ \times 0.5^\circ$ in size. The seismicity rate of each cell was assigned the average of all the seismicity rates in the cells. A threshold was then specified and an alarm was generated if the seismicity rate of the cells was higher than the threshold. The fraction of the space-time occupied by the alarm (τ) of the Poisson is defined such that

$$\tau = \frac{\sum_{i=1,n} I(S(i) > slevel) A(i)}{\sum_{i=1,n} A(i)} \tag{4a}$$

The fraction of earthquakes missed (ν) is defined such that

$$\nu = \frac{\sum_{i=1,n} I(S(i) > slevel) E(i)}{\sum_{i=1,n} E(i)} \tag{5}$$

where $S(i)$ is the seismicity rate of the ith cell, *slevel* is the threshold value of the seismicity rate, $A(i)$ is the area of the ith cell, and $E(i)$ is the number of the targeted earthquakes at the ith alarm. We used the area skill score (ASS) and the probability gain to summarize the potential performance of the earthquake forecast strategy. The region above the error diagram inside the unit square, called ASS, serves as a summary of the prospective performance of the seismicity rate in alarm-based earthquake occurrence forecasting (Zechar and Jordan, 2008; Zechar and Jordan, 2010). The diagonal line indicates ASS = 0.5. A positive connection between the seismicity rate and the frequency of earthquakes is denoted by ASS >0.5, while ASS <0.5 denotes a negative correlation (Rhoades et al., 2017). The probability gain (*Gain*) is defined such that

$$Gain = \frac{1 - \nu}{\tau} \tag{6}$$

The sample value of *Gain* corresponds to the slope of the line connecting (0,1) to (τ, ν), as shown in Figure 6. The diagonal line corresponds to a completely random guess, and *Gain* = 1. A higher *Gain* value indicates that fewer cells are needed for the same "hits," which means better performance of the earthquake forecast strategy.

In Section 4, the spatial variation of the estimated seismicity rate under the PPE, PMF, and PKS models was calculated at three dates, May 20, 2008; January 1, 2013; and September 10, 2019. By adjusting the threshold of the seismicity rate from the highest to the lowest, the fraction of the space-time occupied by alarm and alarmed targeted earthquakes was obtained and their correlations are illustrated in a Molchan error diagram, as seen in Figure 6. All 14 targeted earthquakes during the three periods of May 20, 2008–May 20, 2011, January 1, 2013–January 1, 2016, and September 10, 2019–September 10, 2022, are included.

With respect to the individual models, the PPE model slightly outperforms the PMF model in the efficiency of earthquake forecast because the ASS value of the PPE model is higher than that of the PMF

model. However, the PMF model has a more informative probability gain than the PPE model because when $\tau < 0.3$ and the number of "alarmed" earthquakes is < 6, which indicates that less than six targeted earthquakes occur near the mapped faults having a relatively high slip rate, as seen in Figure 4. Conversely, when $\tau \geq 0.3$, the efficiency of PPE is better than that of PMF. The target catalogs include surprises; i.e., the M_S 8.0 Wenchuan aftershocks (Figure 4A) and the M_S 6.1 Panzhihua (Figure 4A) and M_S 6.6 Jinggu (Figure 4B) earthquakes, which did not correspond to previously mapped faults.

As shown in Figure 6, $ASS_{PMF} < ASS_{PPE}$; therefore, the PPE model is more informative than the PMF model. Meanwhile, $ASS_{PMF} < ASS_{PPE} \approx ASS_{PKS} \approx ASS_{PKSW} \approx ASS_{PKS(\mu=0.1)}$, which implies that, when we specify a low value of μ close to zero, the hybrid PKS model outperforms the PMF model in any combination but does not obtain a better forecast efficiency than the PPE model.

In addition, we obtained the performance for the two methods of combining the PMF model with the PPE model. A comparison of the results reveals that, according to the ASS value, there is no obvious difference between the two ensemble methods. However, the combination method in which μ is manually specified has a more informative gain when τ is in an appropriate range, as shown in Figure 6.

6 Conclusion

Predicting the time, location, and magnitude of future seismic events is possible using information from earthquakes in historical and instrumental catalogs and geologically mapped active faults, as proven in multiple studies (Rhoades and Stirling, 2012; Rhoades et al., 2015). In the present study, we applied the PPE and PMF models to fit the seismicity in the Sichuan-Yunnan region in China. Using the optimized parameters, we estimated the seismicity rates of the PPE and PMF models at three different times: May 20, 2008; January 1, 2013; and September 10, 2019. Retrospective synthetic testing has consistently shown that both independent and hybrid models can provide informative forecasts (Rhoades and Gerstenberger, 2009; Bayona et al., 2022). Next, we introduced the PKS model proposed by Rhoades and Stirling (2012) to fit the seismicity and to calculate the seismicity rate for the same dates using the PPE and PMF models. Finally, we collected the earthquakes with M_S 6.0+ in the test region during three time periods, May 20, 2008–May 20, 2011, January 1, 2013–January 1, 2016, and September 10, 2019–September 10, 2022, as target events for prospective testing. The Molchan error diagram method was used to evaluate the model performances with respect to earthquake forecasts. Based on our results, our main conclusions are as follows.

(1) The PPE, PMF, and PKS models show better forecast efficiency with respect to moderate earthquakes compared to a homogeneous Poisson distribution in the Sichuan-Yunnan test region. While the PPE model is straightforward, its earthquake forecast ability is significant. In some cases, the PMF model has a more informative probability gain than the PPE model when τ is below 0.3, which indicates that, in the Sichuan-Yunnan region, the earthquake forecast is more effective when assigning a relatively higher threshold. We obtained a poor performance with the PMF model when τ was high.

(2) The forecast efficiencies differed due to discrepancies in the prior information or precursors related to the earthquakes and active tectonic setting. The PMF model, which is derived from the time-independent slip rate of the active faults, represents features that are expected to affect the earthquake occurrence over a long-time frame. The results of the PMF model are also affected by the intrinsic incompleteness of the fault database (e.g., Basili et al., 2013), especially any unknown faults in the test region. However, it is impossible to obtain all of the existing faults. The missed earthquakes; e.g., the M_S 6.6 Jinggu earthquake, may have occurred in the vicinity of an unknown fault. Moreover, some large earthquakes can produce higher scaling co-seismic ruptures equal to thousands of times the slip displacement in a single year. The highest slip displacement, that of the M_S 8.0 Wenchuan earthquake, was 12–15 m (Li et al., 2009), located at Beichuan, where three aftershocks occurred that were missed in the forecast by the PMF model. The unsatisfactory performance of the PMF model may lie both in the incompleteness of the fault database and in the lack of consideration of co-seismic ruptures.

(3) The hybrid PKS model can incorporate information from the PPE and PKS models and consequently maintained the best performance over the three testing epochs. This is consistent with previous studies of hybrid short-, medium-, and long-term components (Rhoades et al., 2016; Christophersen et al., 2017; Rhoades et al., 2017). The key point may be that the hybrid model obtains a variety of strengths from the component in ways that other components do not. However, the PKS model, given any method of combination, did not outperform the PPE model, possibly due to the poor efficiency of the PMF model.

(4) Comparisons of the methods of hyper-parameter optimization in which the seven parameters are fit by maximizing the likelihood function, calculating the value of μ based on the linear function of magnitude, or by specifying the value of μ showed an efficiency difference in the PKS model performance. In particular, the optimization method with a manually specified μ potentially obtained a good informative gain for some particular seismic events, which implies that the earthquake forecast strategy could be adjusted using an appropriate specified threshold in the test region.

The retrospective tests in our study also had limitations; for instance, the earthquake forecast strategy was originally designed for a specified 3-year interval. The performance may change somewhat when applied to other periods because of the degree of time dependence in the data used to generate the models. In addition, we did not account for location uncertainties when estimating the seismicity rates of the three models. Because we calculated their seismicity rates on a rather coarse grid of $0.1^\circ \times 0.1^\circ$ cells, location errors can naturally be accommodated without significantly affecting the correlation with the earthquake locations (Rastin et al., 2022).

The Sichuan-Yunnan region is one of the most active seismic regions on the Chinese mainland, and various spatial parameters carrying different types of information have been used to analyze the seismic activity. The PPE model, which is straightforward, has good forecast efficiency and can be used as a base model to evaluate the effectiveness of various earthquake forecast methods. Moreover, the results of our study indicate that an approach to earthquake forecasting that is model-driven and hyper-parameter controlled could be a promising means to implement operational earthquake forecasting.

Data availability statement

The data analyzed in this study is subject to the following licenses/restrictions: The datasets used and/or analyzed during the current study are available from the corresponding author upon reasonable request. Requests to access these datasets should be directed to chenshi@cea-igp.ac.cn.

Author contributions

Study conception and design: SC and BoZ. Manuscript drafting: BoZ and SC. Data acquisition: SC and XW. Data interpretation: BoZ, SC, JZ, BeZ, XW, and BL. Manuscript revision critically for important intellectual content: JZ and SC.

Funding

This study was funded by the National Key R&D Program of China (2017YFC1500503) and the National Natural Science Foundation of China (U1839207 and U1939205).

Acknowledgments

The authors acknowledge the Second Monitoring and Application Center (TSMAC) and the China Earthquake Networks Center (CENC) for providing the data used in this study.

Conflict of interest

The authors declare that the research was conducted in the absence of any commercial or financial relationships that could be construed as a potential conflict of interest.

Publisher's note

References

Basili, R., Kastelic, V., Demircioglu, M. B., Garcia Moreno, D., Nemser, E. S., Petricca, P., et al. (2013). *The European database of seismogenic faults (EDSF) compiled in the framework of the Project SHARE*. Strasbourg, France: The European-Mediterranean Seismological Centre(EMSC). doi:10.6092/INGV.IT-SHARE-EDSF

Bayona, J. A., Savran, W. H., Rhoades, D. A., and Werner, M. J. (2022). Prospective evaluation of multiplicative hybrid earthquake forecasting models in California. *Geophys. J. Int.* 229, 1736–1753. doi:10.1093/gji/ggac018

Bird, P., Jackson, D. D., Kagan, Y. Y., Kreemer, C., and Stein, R. S. (2015). GEAR1: A global earthquake activity rate model constructed from geodetic strain rates and smoothed seismicity. *Bull. Seism. Soc. Am.* 105 (5), 2538–2554. doi:10.1785/0120150058

Christophersen, A., Rhoades, D. A., Gerstenberger, M. C., Bannister, S., Becker, J., Potter, S. H., et al. (2017). "Progress and challenges in operational earthquake forecasting in New Zealand," in New Zealand Society for Earthquake Engineering Annual Technical conference, Wellington, New Zealand, April, 2017, 27–29.

Gerstenberger, M. C., McVerry, G. H., Rhoades, D. A., and Stirling, M. W. (2014). Seismic hazard modeling for the recovery of christchurch. *Earthq. Spectra.* 30 (1), 17–29. doi:10.1193/021913eqs037m

Gerstenberger, M. C., and Rhoades, D. A. (2010). New Zealand earthquake forecast testing centre. *Pure Appl. Geophys.* 167, 877–892. doi:10.1007/s00024-010-0082-4

Gerstenberger, M., Wiemer, S., Jones, L. M., and Reasenberg, P. A. (2005). Real-time forecasts of tomorrow's earthquakes in California. *Nature* 435, 328–331. doi:10.1038/nature03622

Gutenberg, B., and Richter, C. (1944). Frequency of earthquakes in California. *Bull. Seismol. Soc. Am.* 34 (4), 185–188. doi:10.1785/bssa0340040185

Herrera, V. M. V., Rossello, E. A., Orgeira, M. J., Arioni, L., Soon, W., Velasco, G., et al. (2022). Long-term forecasting of strong earthquakes in north America, south America, Japan, southern China and northern India with machine learning. *Front. Earth Sci.* 10, 905792. doi:10.3389/feart.2022.905792

Hiemer, S., Jack, D. D., Wang, Q., Kagan, Y. Y., Woessner, J., Zechar, J. D., et al. (2013). A stochastic forecast of California earthquakes based on fault slip and smoothed seismicity. *Bull. Seism. Soc. Am.* 103 (2A), 799–810. doi:10.1785/0120120168

Jackson, D. D., and Kagan, Y. Y. (1999). Testable earthquake forecasts for 1999. *Seismol. Res. Lett.* 70 (4), 393–403. doi:10.1785/gssrl.70.4.393

Kagan, Y. Y., and Jackson, D. D. (1994). Long-term probabilistic forecasting of earthquakes. *J. Geophys. Res.* 99, 13685–13700. doi:10.1029/94jb00500

Li, H. B., Si, J. L., Fu, X. F., Qiu, Z. L., Li, N., Woerd, J. V., et al. (2009). Co-seismic rupture and maximum displacement of the 2008 Wenchuan earthquake and its tectonic implications. *Quat. Sci.* 29 (3), 387–402.

Marti, M., Stauffacher, M., and Wiemer, S. (2019). Difficulties in explaining complex issues with maps: Evaluating seismic hazard communication-the Swiss case. *Nat. Hazards Earth Syst. Sci.* 19 (12), 2677–2700. doi:10.5194/nhess-19-2677-2019

Molchan, G. M. (1991). Structure of optimal strategies in earthquake prediction. *Tectonophysics* 193, 267–276. doi:10.1016/0040-1951(91)90336-q

Ogata, Y. (1998). Space-time point process models for earthquake occurrences. *Ann. Inst. Stat. Math.* 50, 379–402. doi:10.1023/a:1003403601725

Ogata, Y. (1988). Statistical models for earthquake occurrences and residual analysis for point processes. *J. Am. Stat. Assoc.* 83, 9–27. doi:10.1080/01621459.1988.10478560

Rastin, S. J., Rhoads, D. A., Rollins, C., and Gerstenberger, M. C. (2022). How useful are strain rates for estimating the long-term spatial distribution of earthquakes? *Appl. Sci.* 12, 6804. doi:10.3390/app12136804

Rhoades, D. A. (2007). Application of the EEPAS model to forecasting earthquakes of moderate magnitude in southern California. *Seismol. Res. Lett.* 78, 110–115. doi:10.1785/gssrl.78.1.110

Rhoades, D. A., Christophersen, A., and Gerstenberger, M. C. (2015). Multiplicative earthquake likelihood models based on fault and earthquake data. *Bull. Seism. Soc. Am.* 105 (6), 2955–2968. doi:10.1785/0120150080

Rhoades, D. A., Christophersen, A., and Gerstenberger, M. C. (2017). Multiplicative earthquake likelihood models incorporating strain rates. *Geophys. J. Int.* 208, ggw486–1774. doi:10.1093/gji/ggw486

Rhoades, D. A., and Evison, F. F. (2004). Long-range earthquake forecasting with every earthquake a precursor according to scale. *Pure Appl. Geophys.* 161, 47–72. doi:10.1007/s00024-003-2434-9

Rhoades, D. A., and Evison, F. F. (2005). Test of the EEPAS forecasting model on the Japan earthquake catalogue. *Pure Appl. Geophys.* 162, 1271–1290. doi:10.1007/s00024-004-2669-0

Rhoades, D. A., and Gerstenberger, M. C. (2009). Mixture models for improved short-term earthquake forecasting. *Bull. Seism. Soc. Am.* 99 (2A), 636–646. doi:10.1785/0120080063

Rhoades, D. A., Liukis, M., Christophersen, A., and Gerstenberger, M. C. (2016). Retrospective tests of hybrid operational earthquake forecasting models for Canterbury. *Geophys. J. Int.* 204 (1), 440–456. doi:10.1093/gji/ggv447

Rhoades, D. A. (2013). Mixture models for improved earthquake forecasting with short-to-medium time horizons. *Bull. Seism. Soc. Am.* 103 (4), 2203–2215. doi:10.1785/0120120233

Rhoades, D. A., and Stirling, M. W. (2012). An earthquake likelihood model based on proximity to mapped faults and cataloged earthquakes. *Bull. Seism. Soc. Am.* 102 (4), 1593–1599. doi:10.1785/0120110326

Schorlemmer, D., Werner, M. J., Marzocchi, W., Jordan, T. H., Ogata, Y., Jackson, D. D., et al. (2018). The collaboratory for the study of earthquake predictability: Achievements and priorities. *Seismol. Res. Lett.* 89, 1305–1313. doi:10.1785/0220180053

Shen, Z. K., Sun, J. B., Zhang, P. Z. H., Wan, Y. G., Wang, M., Bürgmann, R., et al. (2009). Slip maxima at fault junctions and rupturing of barriers during the 2008 Wenchuan earthquake. *Nat. Geosci.* 2 (10), 718–724. doi:10.1038/ngeo636

Utsu, T. (1961). A statistical study on the occurrence of aftershocks. *Geophys. Mag.* 30, 521–605.

Xiong, Z. Y., Zhuang, J. C., Zhou, S. H. Y., MitsuhiroHao, M., and Wang, Q. L. (2021). Crustal strain-rate fields estimated from GNSS data with a Bayesian approach and its correlation to seismic activity in Mainland China. *Tectonophysics* 815, 229003. doi:10.1016/j.tecto.2021.229003

Zechar, J. D., and Jordan, T. H. (2008). Testing alarm-based earthquake predictions. *Geophys. J. Int.* 172 (2), 715–724. doi:10.1111/j.1365-246x.2007.03676.x

Zechar, J. D., and Jordan, T. H. (2010). The area skill score statistic for evaluating earthquake predictability experiments. *Pure Appl. Geophys.* 167 (8–9), 893–906. doi:10.1007/s00024-010-0086-0

frontiers | Frontiers in Earth Science

TYPE Original Research
PUBLISHED 20 April 2023
DOI 10.3389/feart.2023.1086854

OPEN ACCESS

EDITED BY
Fuqiong Huang,
China Earthquake Networks Center, China

REVIEWED BY
Chong Xu,
Ministry of Emergency Management, China
Biagio Giaccio,
Italian National Research Council, Italy
Xiwei Xu,
Ministry of Emergency Management, China

*CORRESPONDENCE
Yufa Liu,
lyfdreamer@aliyun.com

SPECIALTY SECTION
This article was submitted to Solid Earth Geophysics, a section of the journal Frontiers in Earth Science

RECEIVED 01 November 2022
ACCEPTED 18 January 2023
PUBLISHED 20 April 2023

CITATION
Ma C, Liu Y, An L, Yang X, Liu S and Zhang W (2023), Active faulting of the Nanhe Fault and relation to the Anninghe Fault zone in the late Quaternary, eastern Tibetan Plateau.
Front. Earth Sci. 11:1086854.
doi: 10.3389/feart.2023.1086854

Active faulting of the Nanhe Fault and relation to the Anninghe Fault zone in the late Quaternary, eastern Tibetan Plateau

Chao Ma[1], Yufa Liu[1]*, Like An[2], Xing Yang[1], Shao Liu[1] and Wei Zhang[1]

[1]Sichuan Earthquake Agency, Chengdu, China, [2]Department of Geophysics, Kyoto University, Kyoto, Japan

Faults along the boundaries of active tectonic blocks are the main structures that are responsible for major earthquakes in mainland China. Investigating the geometric distribution, rupture behavior, and paleoseismic history of these faults is the prerequisite for constraining geodynamic models and regional seismic hazard analyses. The Nanhe Fault, located at the eastern boundary of the Sichuan–Yunnan Block near Mianning County, has been paid less attention so far due to insufficient historical records of major earthquakes. In this paper, we focused on the Nanhe Fault and conducted satellite imagery interpretation, field investigations, and trench excavations. Our findings indicate that the Nanhe Fault initiates north of Mianning County; the north segment of the fault is connected with the Anninghe Fault; and it extends for about 70 km south-westward and terminates southwest of Ermaga Village. The fault has been faulting in the late Late Pleistocene with a left-lateral strike-slip rate of 2.40–2.56 mm/yr, while in the late Holocene, the left-lateral strike-slip and vertical slip rates are 2.50–2.60 mm/yr and about 0.60 mm/yr, respectively. Three paleoseismic events (5373–4525 BC, AD 1193–1576, and AD 1496–1843) were identified by excavating trenches at the Nanhe Fault. A comparative analysis of paleoseismic events between the Nanhe and the Anninghe fault indicates that both faults may have induced cascade rupture or triggered earthquakes—such related events may have occurred in 1496–1627. Additionally, by comparing the kinematic relationship of the faults at the eastern boundary of the Sichuan–Yunnan Block, we propose that the Nanhe Fault takes part in strain partitioning along the boundary. This interpretation reasonably explains the loss of the sliding rate between the Anninghe and Zemuhe faults, which also supports the GPS inversion results, and the discontinuous deformation model for the eastern margin of the Tibetan Plateau.

KEYWORDS

Anninghe Fault, Nanhe Fault, late Quaternary slip rate, paleoseismology, seismic hazard, Tibetan Plateau, Sichuan–Yunnan Block

1 Introduction

The ongoing collision of the Indian and Eurasian plates over the past 50 million years has caused the uplift of the Tibetan Plateau. The deformation mechanism of the eastern margin of the plateau is controversially discussed for decades (Tapponnier et al., 1982; Molnar and Qidong, 1984; Tapponnier et al., 1986; Peltzer et al., 1988;

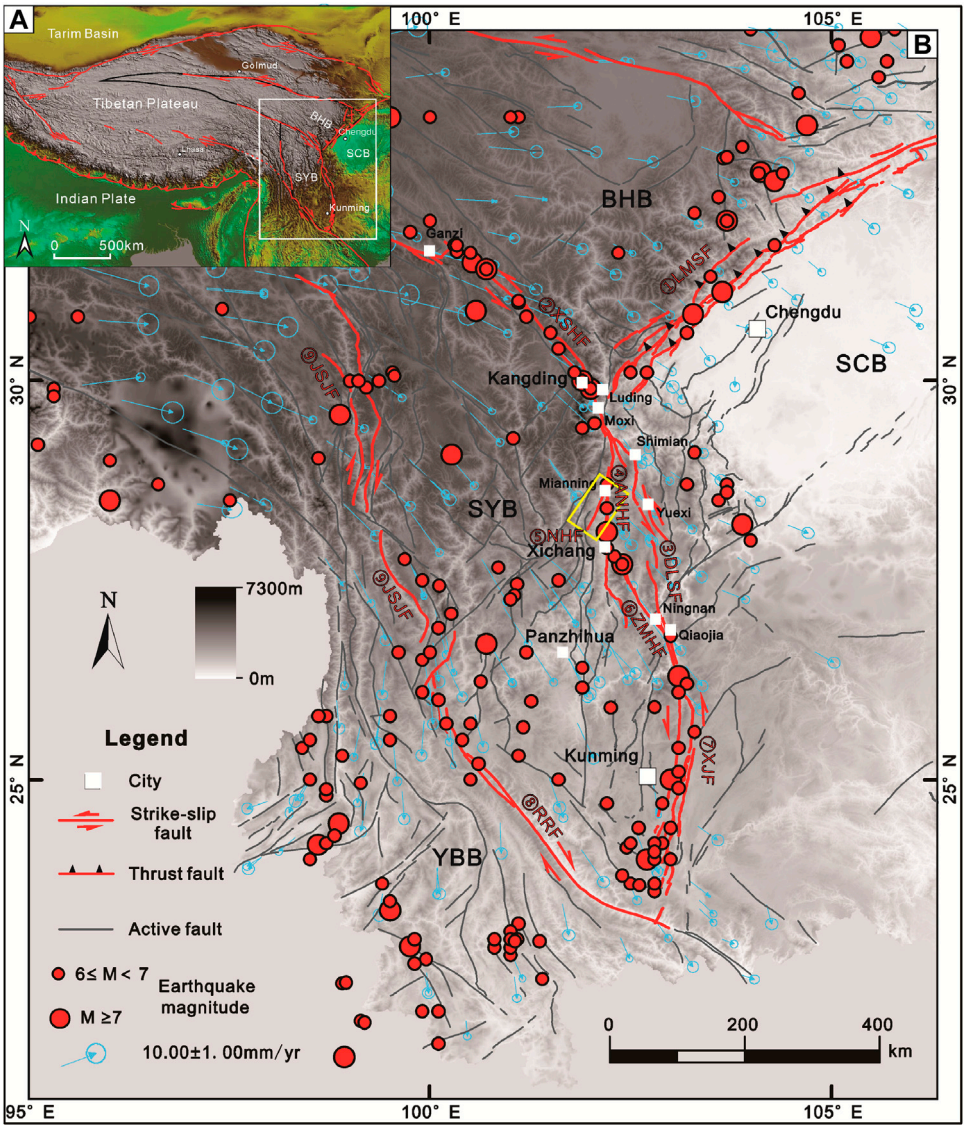

FIGURE 1
Tectonic setting at the southeastern Tibetan Plateau. **(A)** Regional tectonics of the Tibetan Plateau. **(B)** Tectonic setting at the eastern margin of the Sichuan–Yunnan Block. The distribution of the active faults is modified from Deng (2007). The yellow rectangle marks the study area which is shown in Figure 2 in more detail. Red circles show earthquakes recorded in this area, and the size of the circles represents different magnitudes. Blue arrows show GPS velocities of crustal motion of the southeastern Tibetan Plateau relative to Eurasia (Gan et al., 2007; Liang et al., 2013). The base map is the 3-arc-second SRTM digital elevation model (DEM). SCB, South China Block; BHB, Bayan Har Block; SYB, Sichuan–Yunnan Block; YBB, Yunnan–Burma Block; ①LMSFZ, Longmenshan Fault zone; ②XSHF, Xianshuihe Fault; ③DLSF, Daliangshan Fault; ④ANHF, Anninghe Fault; ⑤NHF, Nanhe Fault; ⑥ZMHF, Zemuhe Fault; ⑦XJF, Xiaojiang Fault; ⑧RRF, Red River Fault; ⑨JSJF, Jinshajiang Fault.

Tapponnier et al., 2001; Zhang et al., 2004). Two end-member hypotheses have been proposed to illustrate the deformation: 1) the continuous deformation model implies that the deformation is distributed over thousands of kilometers throughout the entire eastern Tibetan Plateau. Major faults played a negligible role in the eastward motion of the plateau. 2) On the contrary, the discontinuous deformation model considers that the deformation is mainly localized on the major faults along the margins of the active block. A way to explore the problem is to study the interaction of major fault systems in the eastern margin of the plateau, including the deformation decomposition of the slip rate and the interrelation of paleoseismicity.

Tectonically active blocks are the main geological units that are affected by deformation in mainland China nowadays and control the strong earthquake activity and distribution characteristics in this area (Deng, 1980; Ding, 1991; Zhang, 1999; Zhang et al., 2003). The hierarchy and classification of such active blocks can be considered a geological way of coupling the “continuous deformation model” with the “discontinuous deformation model.” Further refinement of active blocks can accurately analyze regional deformation modes more precisely

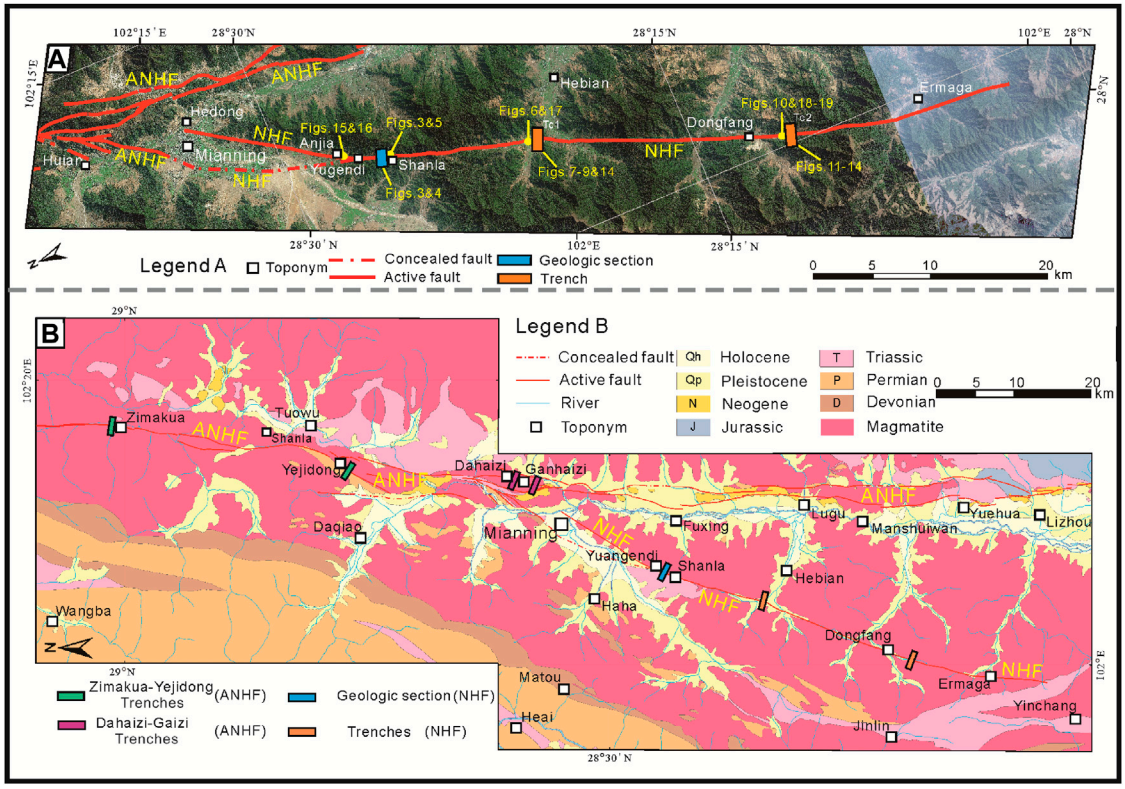

FIGURE 2
Satellite image (taken from Google Earth) and geologic map of the Nanhe Fault (NHF). **(A)** Satellite image illustrates the spatial distribution, structure, and intersecting relationship of the NHF and ANHF. The yellow dots represent the other images in this study. **(B)** Map of the surface geology of the study area, showing local geology and location of towns, trenches, and geological sections.

(Gao, 2021). Previous studies, including the block division at the regional level in mainland China (Zhang et al., 2003), the block division at the Tibetan Plateau level, and the detailed block division in the Sichuan–Yunnan region (Xu et al., 2003; Xu et al., 2013), have further documented the important role of the boundary faults in the areas of active blocks. The NW-NS-striking Xianshuihe–Anninghe Fault zone, a major left-lateral strike fault along the eastern boundary of the Sichuan–Yunnan Block, has a complex structure and is connected with a series of NE-NNW-trending faults. In the past 150 years before 1973, 10 major earthquakes occurred along the Xianshuihe and Anninghe faults (XSHF and ANHF) with magnitudes ≥7. On 5 September 2022, an M 6.8 earthquake occurred along the southeast section of the XSHF near Luding County in Sichuan Province, China. A total of 93 people died during the earthquake which furthermore caused numerous casualties and heavy property losses. This earthquake indicates that the Xianshuihe–Anninghe Fault zone still represents a major seismic hazard. Several detailed studies on the Xianshuihe–Anninghe Fault zone segmentation, slip rate, deformation history, and other aspects of the fault zone have been conducted (Qian et al., 1988; Wen, 1989; Allen et al., 1991; Wen et al., 2000a; Wen, 2000b; Wen et al., 2001; Zhou et al., 2001; Wen et al., 2007; Ran et al., 2008a; Ran et al., 2008b; Chen et al., 2011; Wang et al., 2018). These studies focused on the main faults. However, the secondary branch fault on the side of the main faults also plays an important role in the regional tectonic deformation. For instance, the Tazang Fault, the southern segment of the East Kunlun Fault, and the Diebu–Bailongjiang Fault together form a large strike-slip fault series with a NW parallel distribution, which jointly bears the structural deformation from the west side.

The Nanhe Fault (NHF) is an active fault, and the north segment of the fault is connected with the Anninghe Fault (ANHF) near Mianning County (Figures 1, 2). The NHF extends for about 70 km south-westward and terminates southwest of Ermaga Village (Figure 2). Due to the absence of major earthquakes records and low slip rate, the NHF has been poorly studied so far, and its characteristics and evolution are hardly known. Therefore, the study of the slip rate and paleoseismic events of the NHF is of major significance for understanding the strain distribution in the ANHF and for evaluating the regional seismic hazard related to this fault.

In this study, we conducted remote sensing, field investigations, unmanned aerial vehicle (UAV) mapping, and trench excavations on the NHF. Based on the new data, we constrained the fault characteristics, slip rate, and paleoseismic

history of the NHF, and we discussed the possible max potential magnitudes in the future of the fault. By analyzing the structural characteristics of the NHF and ANHF, along with their paleoseismic histories, we discussed the ruptured relationship between the NHF and ANHF and the role of the NHF in the regional tectonic model.

2 Geological setting

Since 70–34 Ma, the Tibetan Plateau was strongly uplifted as a response to the continuous collision between the Eurasian and Indian plates (Kirby et al., 2002; Wan et al., 2002; Clark et al., 2005; Aitchison et al., 2007). Due to the northward movement of the Indian Plate during the collision, tectonic blocks that were initially situated at the eastern Qinghai–Tibetan Plateau, including the Bayan Har Block (BYB), the South China Block (SCB), and the Sichuan–Yunnan Block (SYB), started to be pushed eastwards, along the direction of a large-scale strike-slip fault zone (Xu et al., 2003; Xu et al., 2013). Brittle deformation within this strike-slip fault zone caused the occurrence of earthquakes in China mainly along the block boundary faults (Xu et al., 2003; Zhang et al., 2003).

The SYB is located to the southeast of the Qinghai–Tibetan Plateau, which is mainly bounded by several major faults, including the XSHF, ANHF, Daliangshan Fault (DLSF), Zemuhe Fault (ZMHF), Xiaojiang Fault (XJF), Red River Fault (RRF), and Jinshajiang Fault (JSJF), from east to west (Figure 1). Among the tectonic blocks, the SYB is one of the best studied blocks, as it is one of the most seismic active blocks in the SW China. The eastern boundary of the SYB is characterized by four left-lateral strike-slip faults, namely, (from north to south) the XSHF, ANHF, DLSF, and ZMHF (Xu et al., 2003; Xu et al., 2005; Zhang et al., 2002; Zhang et al., 2004).

The overall moving direction of the SYB, as revealed by the GPS velocity, is south–southeast (150°–160°). In the Xianshuihe area, the moving direction of the northern SYB is SE120°, while in the Kunming area, the southern SYB is moved toward SE165° (Figure 1) (Wang et al., 2001; Zhang et al., 2002; Xu et al., 2003; Xu et al., 2005; Zhang et al., 2004; Gan et al., 2007). The GPS velocity tangential documents strong left-lateral shear along the XSHF–ANHF–ZMHF–XJF fault system (Wang and Shen, 2020). The moving velocity on the southern side of the XSHF is higher than that on the northern side, inducing the left-lateral strike-slip movement of the fault. In the area where the ANHF and DLSF intersect, the GPS velocity vector to the east of the Anning River deflects more eastward and increases, causing the maintenance of the dominant left-lateral strike-slip with a minor amount of a thrust component. On both sides of the ZMHF, the direction of the GPS velocity vector is almost parallel to the strike of the fault, causing the predominance of the left-lateral strike-slip movement of the ZMHF (Zhang et al., 2002; Xu et al., 2003).

The XSHF can be divided into northwest and southeast segments, concerning the Huiyuansi pull-apart basin. The northwest segment is about 200 km long and is a single fault with a left-laterally horizontal slip rate of 10.00–15.00 mm/yr (Qian et al., 1988; Wen, 1989; Allen et al., 1991). The structure of the southeast segment is more complex. Between Qianning and Kangding, the southeast segment of the XSHF is characterized by three parallel secondary faults. To the south of Kangding City, the XSHF manifests as a single fault and is named the Moxi Fault (MXF), with a sliding rate of about 9.00–10.00 mm/yr (Wen et al., 2001; Zhou et al., 2001). The MXF is the most critical component of the southeast segment of the XSHF and strikes N20°–30°W and starts close to the small village Yuejinping. Heading to the south, the MXF passes through Moxi, Tianwan, and Anshun. Further south, evidence of recent seismic activity of the MXF gradually diminishes (Zhou et al., 2001). The left-lateral displacement of MXF in an abandoned channel ditch on the Moxi platform shows a late Holocene sliding rate of 9.40 ± 1.70 mm/yr for MXF (Wen et al., 2001). According to trench analysis and carbon dating, the latest major earthquake in the southeastern segment of the XSHF, the Moxi M_w 7.75 earthquake, occurred in 1786 (Chen et al., 2011).

The ANHF is exposed to the south of XSHF and is one of the most active faults in the east of the SYB. The ANHF commences at Shimian and continues southward through Zimakua, Yejidong, Mianning, Lugu, and Dechang. Further south, the ANHF gradually disappears at Huili. The overall direction of the ANHF is approximately north–south, and its total length is approximately 150–160 km (Ran et al., 2008a; Ran et al., 2008b). The ANHF can be subdivided into three segments based on fault structure, geomorphology, and paleoseismicity (Wen et al., 2000a; Wen, 2000b; Wen et al., 2007; Ran et al., 2008a; Ran et al., 2008b). The two boundaries of these three segments of ANHF are located close to the cities of Mianning and Xichang. The northern segment of the ANHF is situated in Mianning. The central segment of the ANHF occurs between Mianning and Xichang, and the southern segment is exposed to the south of Xichang. The horizontal component of the slip rate from the late Holocene is 6.20 mm/yr for the northern segment of ANHF, and the vertical component is 1.40 mm/yr (Ran et al., 2008a; Ran et al., 2008b). Based on a block model, Wang et al. (2008) calculated a slip rate of about 5.10 ± 2.50 mm/yr for the entire ANHF. Several major paleoseismic events on the northern segment of the ANHF have been revealed (Wen et al., 2000a; Wen, 2000b; Wen et al., 2007; Ran et al., 2008a; Ran et al., 2008b). The southern segment of the ANHF is about 175 km long, and seismic activity since the late Quaternary is not recorded.

Near Xichang, the DLSF is situated to the east of the ANHF, and the DLSF is composed of six secondary faults. Major earthquakes were not recorded for these faults in recent times. The total length of the DLSF is about 280 km. The northern segment of the DLSF forms a left stage *en échelon* with the XSHF (Zhou et al., 2003) through Haitang, Yuexi, Puxiong, Zhuhai, Butuo, Jiaojihe, and Qiaojia. Continuing further south, it forms a right-stage *en échelon* with the XJF. The overall horizontal slip rate of the DLSF since the Holocene is 3.00–4.00 mm/yr (Zhang, 2008), and it is 3.10 mm/yr for its southern segment (Shen et al., 2005; He and Oguchi, 2008; Wei et al., 2012; Sun et al., 2015). Many paleoseismic events have been identified on the secondary faults of the DLSF (Song et al., 2002; Zhou et al., 2003; Gao et al., 2016). Recent paleoseismic studies have been focused on the southern segment of the DLSF (Gao et al., 2016; Sun et al., 2019) and have documented the potential for the generation of M6.5+ earthquake in this segment (Sun et al., 2019).

TABLE 1 Equations for the calculation of the maximum magnitude of an earthquake potentially generated by a specific fault (Bonilla et al., 1984; Deng et al., 1992; Wells and Coppersmith, 1994; Wen, 1995) (M, maximum earthquake magnitude; L, fault length; U, fault displacement in one earthquake).

Article	Equation	Accuracy (δ)	Suitable area	Suitable scenario
Bonilla et al. (1984)	M = 4.94 + 1.296logL	δ = 0.19	U.S. and China	Independent earthquake
Wells and Coppersmith (1994)	M = 5.16 + 1.12logL	δ = 0.29	Global	Independent earthquake
Wen (1995)	M = 5.117 + 0.579lnL	δ = 0.21	SW China	Independent earthquake
Deng et al. (1992)	M = 5.92 + 0.88logL	δ = 0.37	Tibetan Plateau	Independent earthquake
Wells and Coppersmith (1994)	M = 7.02 + 0.89logU			Triggered earthquake

TABLE 2 Equations for the calculation of the maximum fault displacement potentially produced by a specific earthquake (Bonilla et al., 1984; Deng et al., 1992; Wells and Coppersmith, 1994; Wen, 1995) (D_{max}, maximum fault displacement; M, earthquake magnitude; L, fault length).

Method 1: compare NHF with other faults.					
	Time	Suitable area	Magnitude	Maximum displacement (m)	Reference
1	1988.11.06	Yunnan, China	7.6	2.2	Deng et al. (1992)
2	1952.08.18	Tibet, China	7.5	5	Deng et al. (1992)
3	1944.01.02	Turkey	7.5	3.6	Wells and Coppersmith (1994)
4	1970.01.04	Tonghai, China	7.5	2.7	Wells and Coppersmith (1994)
5	1978.09.16	Iran	7.5	3.0	Wells and Coppersmith (1994)
6	1895.07.05	Tashikuergan	7.5	3.9	Wells and Coppersmith (1994)
7	1967.07.22	Turkey	7.4	2.6	Wells and Coppersmith (1994)
8	1973.02.06	Luhuo, Sichuan, China	7.6	3.6	Li et al. (1997)
Method 2:					
	Suitable area	Accuracy	Equation	Reference	
1	Global	δ = 0.26	logDmax = 0.481 × M-3.09	Bonilla et al. (1984)	
2	Global	δ = 0.34	logDmax = 1.03 × M-7.03	Wells and Coppersmith (1994)	
3	SW China	δ = 0.30	lnDmax = 1.372 × M-8.978	Wen (1995)	
4	Tibet	δ = 0.33	logDmax = 0.53 × M-3.37	Deng et al. (1992)	
Method 3:					
	Suitable area	Accuracy	Equation	Reference	
1	Global	δ = 0.36	logDmax = 1.16 × logL-1.69	Wells and Coppersmith (1994)	
2	SW China	δ = 0.317	lnDmax = 0.862 × lnL-2.21	Wen (1995)	
3	Tibet	δ = 0.338	logDmax = 0.72 × logL-0.72	Deng et al. (1992)	

The northern end of the ZMHF is connected to the ANHF at Xichang. The deformation of the ZMHF is also dominated by a left-lateral strike-slip movement since the late Quaternary, thus resembling the movement of the ANHF and the XSHF (Wang et al., 2014). The overall length of the ZMHF is roughly 140 km, and it passes through Xichang, Puge, Ningnan, and Qiaojia from north to south where it intersects with the XJF (Huang and Tang, 1983). Recent studies on the ZMHF have focused on the characterization of the surface rupture caused by the M_w7 earthquake in 1850 (Ren and Li, 1993; Ren, 1994; Feng and Du, 2000; Yu et al., 2001; He and Oguchi, 2008; Ren et al., 2010; Wang et al., 2011; Wang et al., 2013). Analyses of the paleoseismic events in the northern segment of the ZMHF have indicated an average recurrence interval of about 2,300 years for large-magnitude earthquakes in this area (Du, 2000; He and Ren, 2003; Tian et al., 2008; Ren et al., 2010). The slip rate of the ZMHF, estimated through geological and geomorphological analyses, is 2.40–3.60 mm/yr with an average of 3.00 mm/yr (Wang, 2012; Wang et al., 2013; Wang et al., 2017). Wang et al. (2008) calculated a left-lateral strike-slip rate of 2.80 ± 2.30 mm/yr for the ZMHF zone using a tectonic block model.

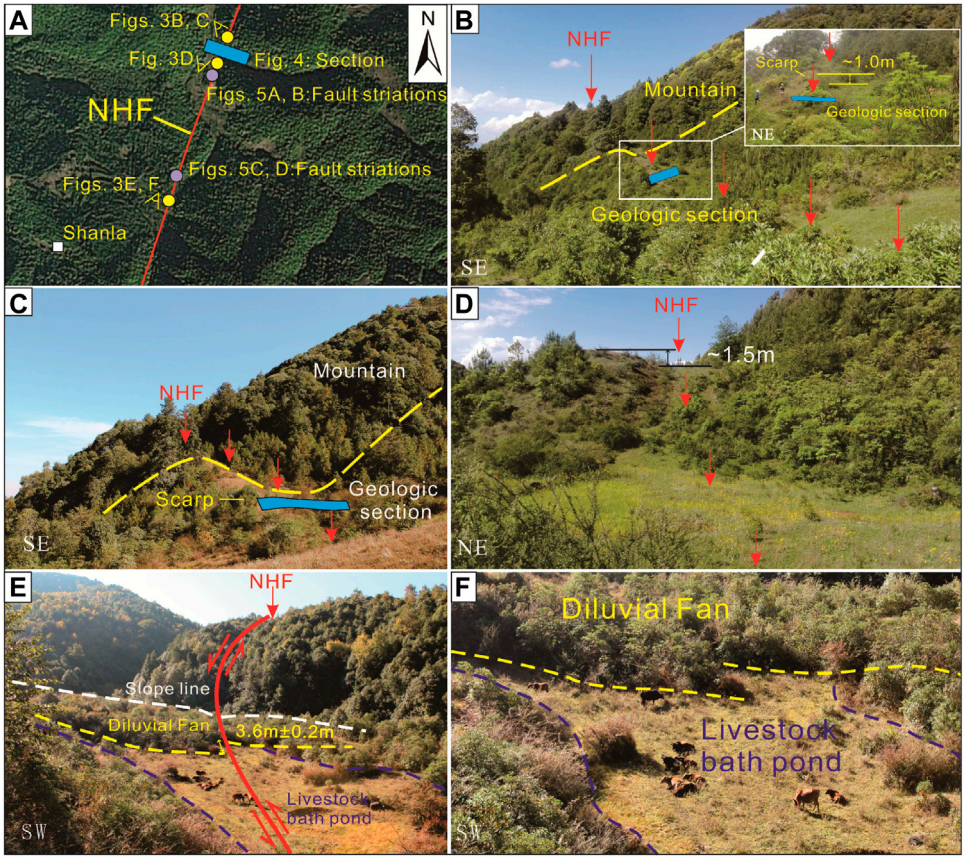

FIGURE 3
Landform displacement to the north of Shanla. **(A)** Satellite image from Google Earth that shows the location of the NHF survey points near Shanla, south of Yuangendi (see Figure 2 for location). **(B)** Field setting around the geological section (the geological section is shown in Figure 4). **(C)** Fault scarp of 1.0 m high near a geological section. **(D)** Fault scarp with a height of ~1.5 m. **(E)** Diluvial fan left-laterally displaced by 3.6 ± 0.2 m east of Shanla. **(F)** Nearby the diluvial fan, a depression occurs that is used as a livestock bath pond (according to local residents).

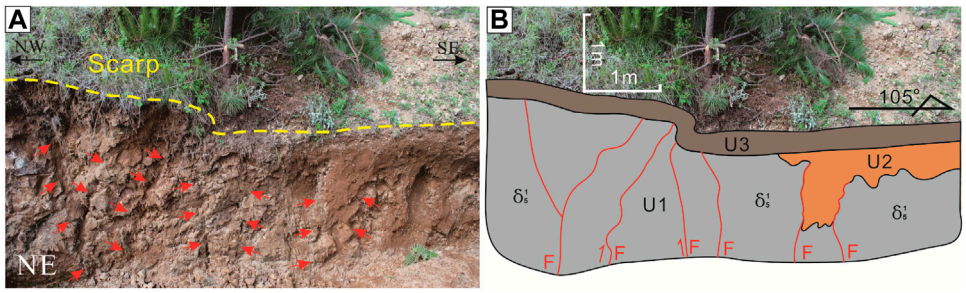

FIGURE 4
Geological section of the NHF south of Yuangendi (location is shown in Figures 2, 3). **(A)** Photograph of the location of the geological section. Red arrows and red lines indicate the fault trace/plane. **(B)** Annotations on **(A)**: U3, humus soil layer; U2: colluvium; U1, Triassic mixed diorite δ_5^1.

3 Methods

3.1 Fault mapping and surveying

Based on satellite imageries, such as the 2 m resolution GF-2 imagery and high-resolution Google Earth image, faults were identified and traced on a surface map. By interpreting the high-resolution imageries, fault-related geomorphic features, such as the displacement of terraces, gullies, vegetation boundaries, fault scarps, and troughs, were identified. In addition, geological maps, and digital elevation maps (DEMs) were used to refine the identification of geomorphic expressions and the tracing of faults.

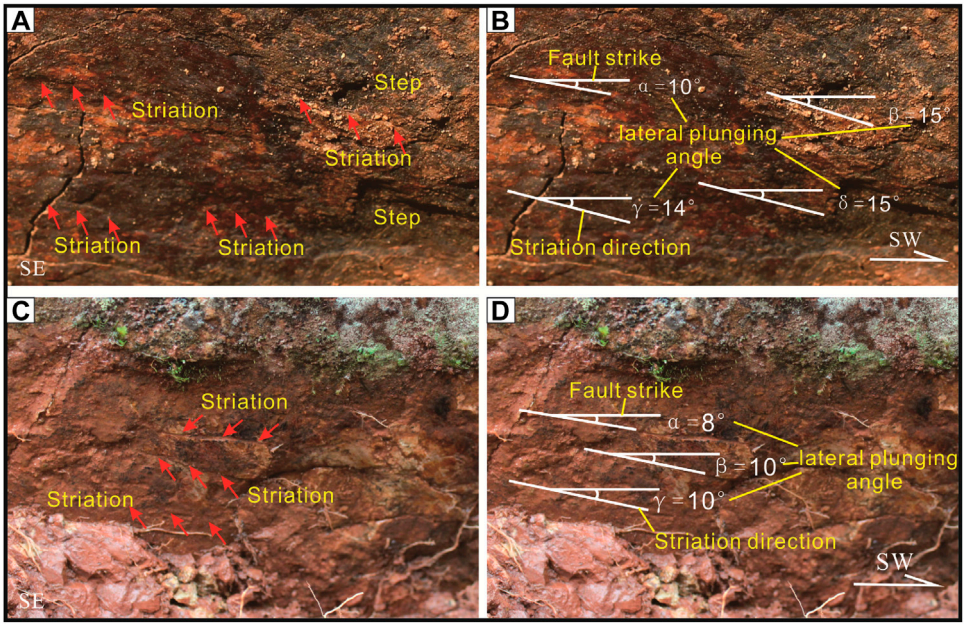

FIGURE 5
Fault striations. The location of these striations is marked in Figures 2A, 3A. **(A, C)** Red arrows mark the striations and steps. **(B, D)** Horizontal white lines trace the strike of the fault. Tilted white lines indicate the trend of the striations. Greek letters (α, β, γ, and δ) represent lateral plunging angles of the fault striations.

We validated and modified our indoor interpretations through field investigations. We conducted fault UAV field mapping and high-resolution migration geomorphological survey to understand the characteristics of the NHF in the late Quaternary. Based on the structure-from-motion technique, we used unmanned aerial vehicles (UAVs, DJI Phanton 3 Pro) at selected key locations to construct high-resolution digital orthographic and digital surface models (DSMs) using Agisoft PhotoScan software. Additionally, to improve the visual contrast of the geomorphic features, we established shaded relief maps, using resultant DSMs and Golden Surfer software. For base maps, we used printed orthographic and shaded relief maps to elaborate detailed tectonic landforms. The use of these maps enhances the visual contrast for visualizing geomorphic features, thus improving the identification of features on the maps. By utilizing high-resolution DSMs, we subsequently measured displacements of geomorphic features based on piercing points on both sides of the fault trace.

3.2 Trench investigation

To accurately reveal the paleoseismic history of the NHF, we excavated two trenches in a Holocene sedimentary environment which has been continuously filled with debris transported from hillslopes. Thus, the sedimentary successions record and preserve evidence of fault displacement. By excavating trenches that cut across the fault strike, evidence for displacement was recognized on the trench wall. To acquire clear strata and faulting information from the sedimentary layers, trench walls were cleaned and gridded into 0.5 × 1 m squares with white yarn. Subsequently, pictures were taken for the trench walls and edited using Adobe Photoshop and CorelDRAW. Finally, strata on the trench walls were interpreted to construct a schematic cross section that elucidates the determination of surface-rupturing events.

3.3 Sample dating

To constrain the age of surface-rupturing events that were identified from the trench walls, we collected samples for chronological analysis from the bottom of the diluvial fans and displaced sedimentary strata. The samples were collected from the trench wall and were sealed, preserved in plastic bags, and sent to Beta Analytic Inc. in Miami (United States) for further data processing and radiocarbon dating analysis.

As the slip rate of a fault is defined as the ratio of displacement to the time interval over which that slip accumulated (Keller and Pinter, 2002), we calculated the slip rates of the NHF by dividing the displacements of the gullies by the sediment ages around them. The displacements were measured in the field and the sediment ages were revealed from carbon dating. The timing of the paleoseismic events, which were revealed from the trench wall, was constrained by the age of the sedimentary layers above and below the faulting event. The radiocarbon ages were acquired through stratigraphic sequence calibration using the OxCal 4.3.2 program with the IntCal20 atmospheric curve (Bronk Ramsey, 2009; Reimer et al., 2020; https://c14.arch.ox.ac.uk/oxcal/OxCal.html). Conventional radiocarbon ages of the determined paleoseismic events were eventually converted into calendar years.

TABLE 3 Summary of stratigraphic units in Tc1 and Tc2.

Trench	Unit	Color	Dominant sediment	Avg. grain size (mm)	Sorting and roundness	Plant debris	Pebble	Carbon dating result
Tc1	U6	Brown (10 YR, 3/2)	Coarse silt	0.04	Well sorted	Sporadic Upper part	None	HB-01 AD 1669–1945
					Well rounded			HB-08 AD 1650–1953
Tc1	U5	Dark brown (10 YR, 4/2)	Medium silt	0.02	Well sorted	None	None	HB-05 AD 1646–1950
					Well rounded			
Tc1	U4	Reddish-brown (10 YR, 4/6)	Medium silty clay	0.008	Well sorted	Sporadic Upper part	None	None
					Well rounded			
Tc1	U3	Reddish-brown (10 YR, 4/8)	Medium sand	0.25	Well sorted	None	None	HB-03 AD 1491–1652
					Well rounded			
Tc1	U2	Reddish-brown (10 YR, 5/6)	Medium clay	0.002	Well sorted	None	None	HB-04 4604–4456 BC
					Well rounded			
Tc1	U1	Light yellow (10 YR, 7/4)	Fine clay	0.001	Well sorted	None	None	HB-07 5467–5329 BC
					Well rounded			
Tc2	U9	Gray (5 Y, 6/1)	Fine clay w/minor medium sand	0.001	Well sorted	Upper part	None	DF-03 AD 1631–1953
				0.3	Well rounded			DF-01 105.89 pMC.
Tc2	U8	Light gray (5 Y, 7/1)	Coarse sand	1.0	Well sorted	None	Moderately rounded and poorly sorted	DF-08 AD 1660–1953
					Well rounded		10–70 mm	DF-07 101.51 pMC
Tc2	U7	Gray (5 Y, 6/1)	Coarse sand	0.004	Well sorted	None	8 mm	DF-06 AD 1474–1644
					Well rounded		Moderately and poorly sorted	
Tc2	U6	Yellow gray (5 Y, 5/3)	Coarse sand	1.0	Well sorted	Few	Upper part	DF-09 AD 1492–1663
					Well rounded	Upper part	1–10 mm	
Tc2	U5	Dark gray (5 Y, 4/1)	Medium silt	0.025	Well sorted	None	None	None
			Coarse sand	1.0	Well rounded			
Tc2	U4	Light yellow (5 Y, 6/3)	Medium clay		Poorly sorted	Sporadic Upper part	1–20 mm	DF-13 AD 1157–1264
					Well rounded			
Tc2	U3	Light yellow (5 Y, 8/4)	Fine clay	0.0008	Well sorted	None	Lower part	DF-02 AD 1469–1640
					Well rounded		30 mm	DF-12 AD 1050–1255
Tc2	U2	Grayish yellow (5 Y, 6/2)	Coarse sand	0.5	Well sorted	None	Middle 0.5–40 mm	None
					Well rounded			
Tc2	U1	Light gray (5 Y, 8/1)	Medium silt	0.025	Well sorted	None	Sporadic 40 mm	None
					Well rounded			

3.4 Seismic hazard analysis

To predict the scale of possible future, seismic hazards on the NHF, we calculated the maximum magnitude of the earthquakes that may be induced by the NHF using five published equations (Bonilla et al., 1984; Deng et al., 1992; Wells and Coppersmith, 1994; Wen, 1995) (Table 1). Additionally, the maximum fault displacement that the NHF can generate was calculated using

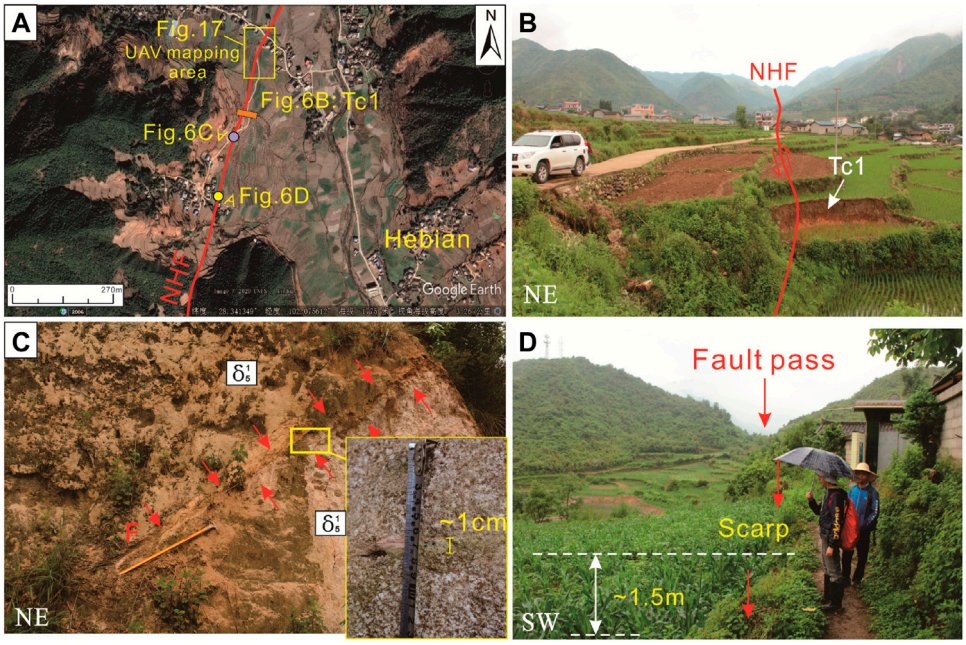

FIGURE 6
Tectonic landforms around Hebian Township where Tc1 was excavated. The location of this area is marked in Figure 2. **(A)** Satellite image (taken from Google Earth) showing geological and geomorphological survey sites, trench locations, and a UAV mapping area near Hebian. **(B)** Close-up of the geomorphology near Tc1 in Hebian. **(C)** Bedrock section of the NHF near Tc1. The fault occurs within the Triassic mixed diorite (δ_5^1), which strikes 305° and dips 39°. A 1-cm-wide fault gouge is recognized near this fault. The diorite is heavily weathered. **(D)** Series of fault scarps to the south of Tc1. The average height of these fault scarps is approximately 1.5 m. To the south, a fault pass is observed.

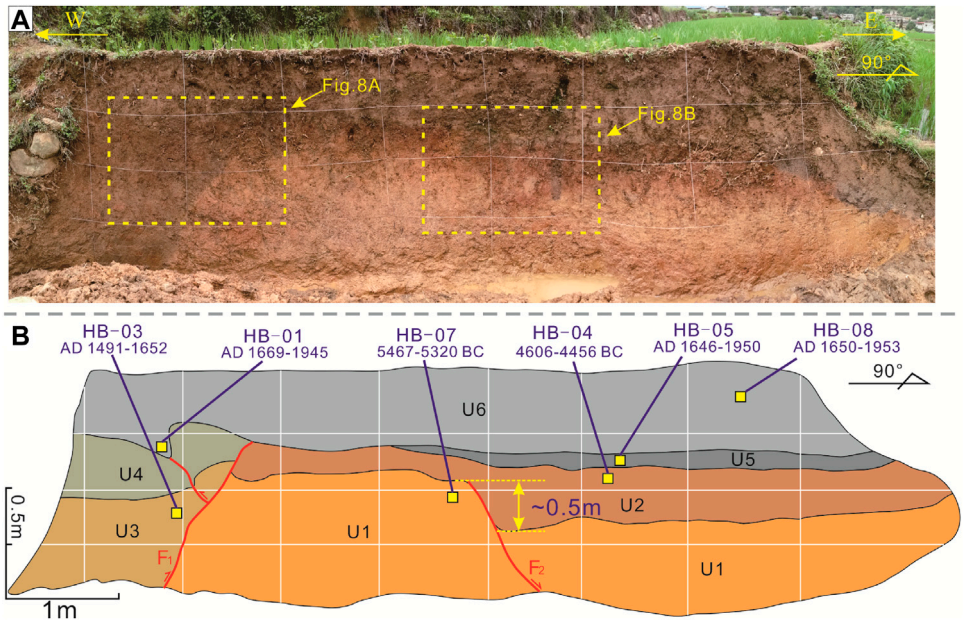

FIGURE 7
Northern wall of Tc1. **(A)** Photograph of Tc1. The dashed yellow rectangular marks of the region are shown in Figures 8A,B. **(B)** Interpretation of **(A)**. The yellow rectangles represent radiocarbon dating sample locations. The sample locations are labeled with their sample number and the corresponding radiocarbon age. The black lines show the contact relationship of the strata. The red lines represent faults. A vertical displacement of approximately 0.5 m is observed in U1.

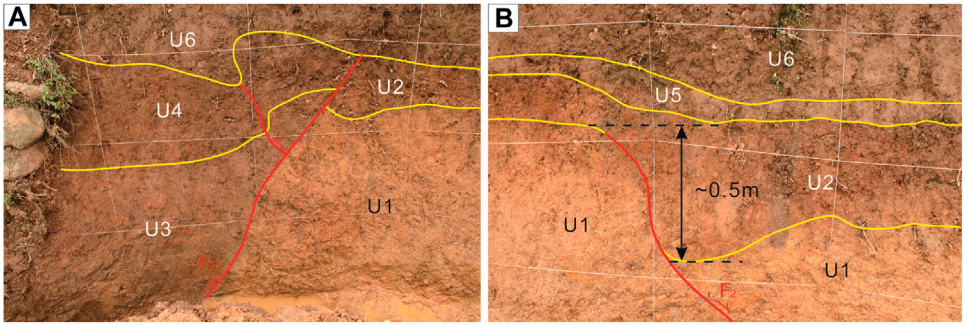

FIGURE 8
(A) Photograph on the western side of the TC1. **(B)** Photograph on the middle part of the TC1. Annotated photographs of close-up details of the faults in Tc1. The yellow lines show the contact relationships of the strata. The red lines represent faults. See Figure 7 for locations.

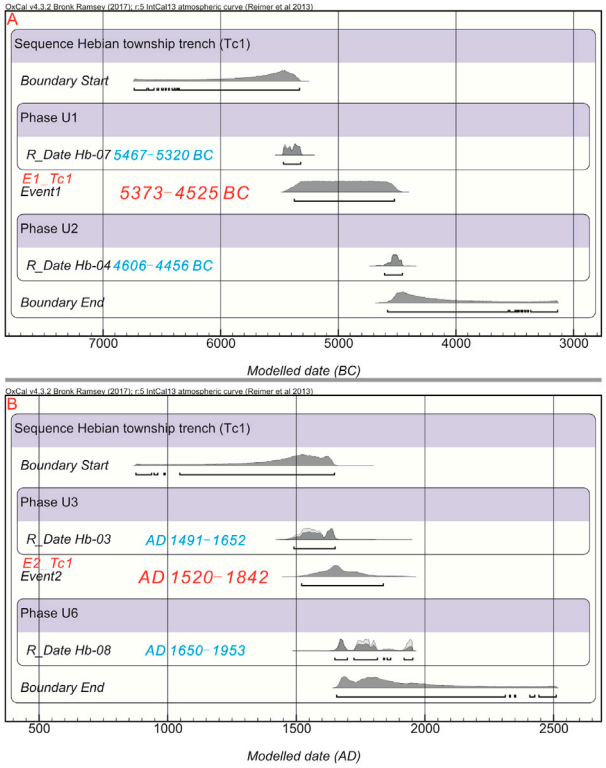

FIGURE 9
(A) The timing of paleoseismic event 1 (E1_Tc1) in Tc1 is constrained to 5373–4525 BC. **(B)** The timing of paleoseismic event 2 (E2_Tc1) in Tc1 is constrained to AD 1520–1842. Probability density functions (PDFs) for the timing of events observed at Tc1 were calculated using OxCal 4.3.2 (https://c14.arch.ox.ac.uk/oxcal/OxCal.html).

published equations, and the calculated result of the NHF was compared with other faults (Bonilla et al., 1984; Deng et al., 1992; Wells and Coppersmith, 1994; Wen, 1995; Li et al., 1997) (Table 2).

4 Results

4.1 Field investigation

Based on the interpretation of satellite images, we detected that the northern end of the NHF starts in the Anninghe valley and that the NHF intersects with the ANHF at an angle of around 30°. While the trend of the NHF is to the N25°E, the ANHF is roughly north–south-oriented (Figure 2). As the NHF extends to the southwest, it passes through Mianning County and Anjia Village, Yuangendi, Hebian Township, and Dongfang Village. After the NHF passes the village of Ermaga, its further continuation remains uncertain. Further south, the NHF is poorly visible on the satellite images. The total length of the NHF is about 70 km. Negative landforms, such as fault trough, fault scarp, and fault sag pond, are formed by fault displacements, which display obvious linear characteristics in the satellite images.

Based on the interpretation of satellite images, remote sensing, and field investigation, we detected one displacement of the diluvial fans, four displacements of gullies, four fault scarps, two geological sections, and two fault striations (Figure 2). Three locations with geomorphic features were mapped in more detail by UAV, and two trenches were excavated (Figure 2).

Around Anjia Village, we recognized the formations of fault troughs, gullies, left-lateral synchronous displacement, fault sag pond, fault scarp, and other landforms that are related to the faulting of the NHF. To the south of Anjia Village, about 1.5 km south of the Yuangendi, the NHF truncates the mountains, forming a 1.0-m-high fault scarp (Figures 3B,C). From the regional stress field of the SYB and field investigations, it is evident that the fault scarp is formed by the compressional tectonic regime. A geological section was excavated across the NHF in this area (Figures 3A–C, Figure 4), which revealed evidence of two seismic events. The geological section demonstrates the characteristics of compression and shows that the NHF is developed in Triassic mixed diorite at this locality. The first event caused the displacement of the bedrock (U1, the Triassic mixed diorite) before the deposition of U2 (U2 is the colluvial wedge formed by the seismic event). The second event is the deformation of U3 (surface soil) and the formation of fault

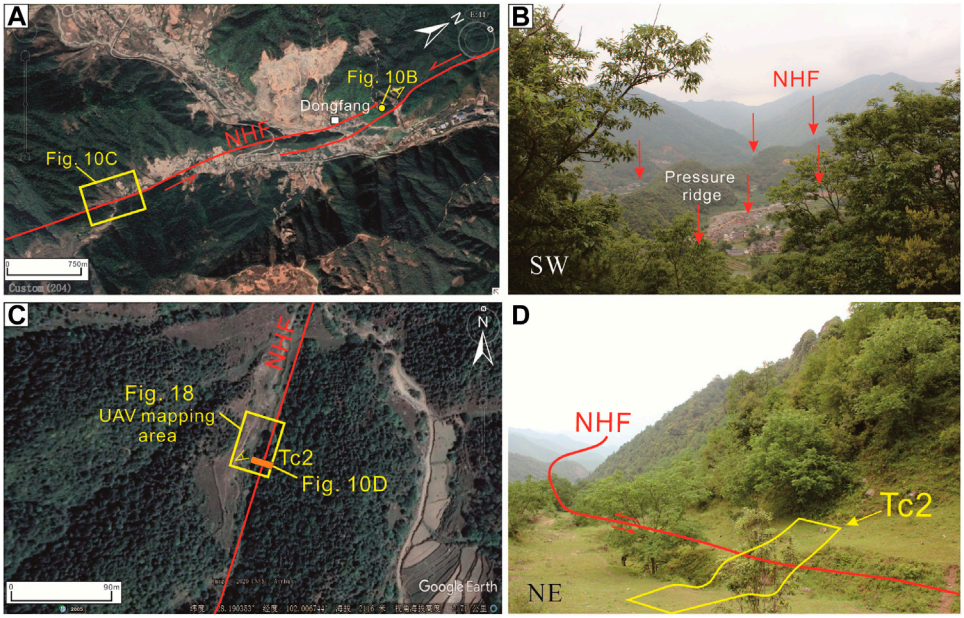

FIGURE 10
Tectonic landforms in Dongfang Village where Tc2 was excavated. The location of this area is marked in Figure 2. **(A)** Satellite image (taken from Google Earth) showing the location of the observed geomorphological features. **(B)** Location of the ridge near Dongfang. **(C)** Satellite image (from Google Earth) showing the trench locations and UAV mapping area near Dongfang. **(D)** Close-up geomorphology near Tc2 in Dongfang.

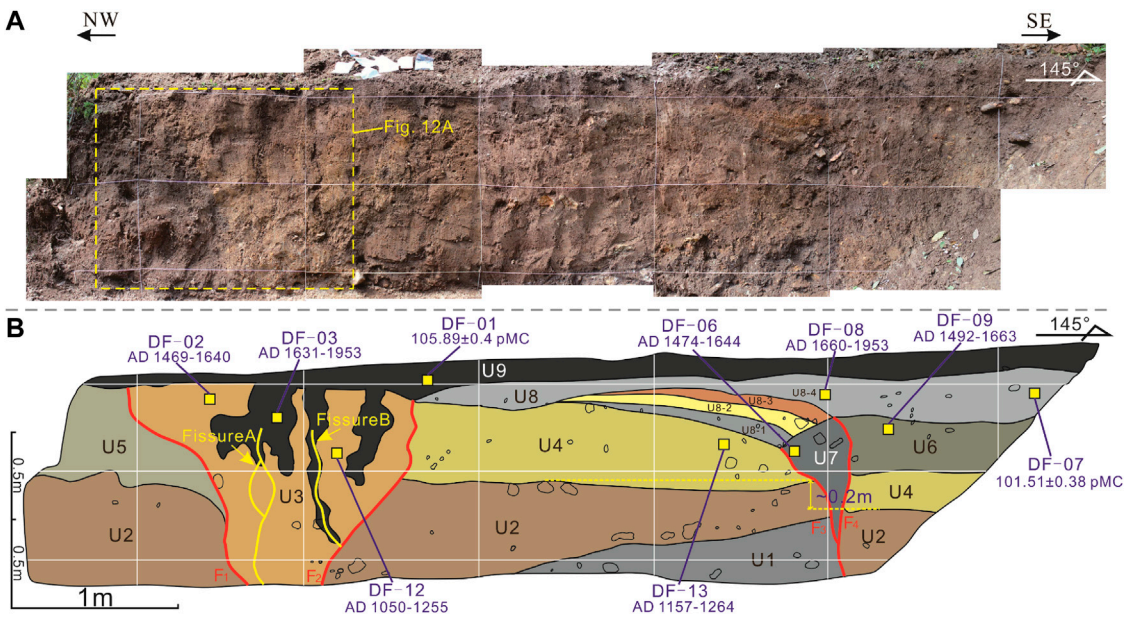

FIGURE 11
Eastern wall of Tc2. **(A)** Photograph of Tc2. The dashed yellow rectangle is the region shown in Figure 12A. **(B)** Interpretation of **(A)**. The yellow rectangles represent radiocarbon dating sample locations. The sample locations are labeled with their sample number and the corresponding radiocarbon age. The black lines show the contact relationships of the strata. The red lines represent faults, and the yellow lines represent fissures. A vertical displacement of approximately 0.2 m is observed in U2.

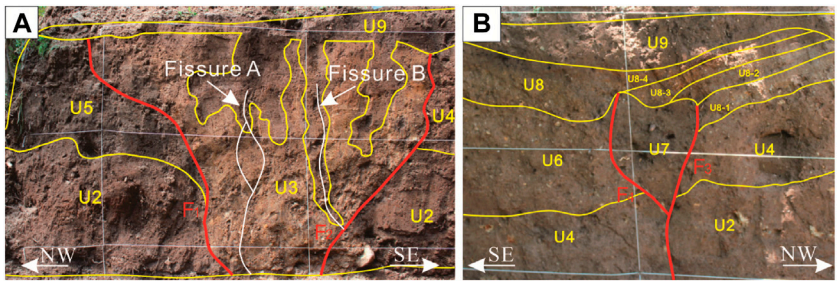

FIGURE 12
Annotated photograph of close-ups of the faults in Tc2. The yellow lines show the contact relationships of the strata. The red lines represent faults, and the white lines represent fissures. **(A)** (Partial) Eastern wall of the trench. **(B)** (Partial) Western wall of the trench.

scarps that are around 1 m high. This was the latest event revealed by the geologic investigation.

To the northeast of Shanla, the NHF traverses mountains and forms a 1.5-m-high fault scarp (Figure 3D). To the south of this fault scarp, we observed fault striations on the northeastern fault face near Shanla (GPS: 28.438,813°N; 102.105,692°E). The fault striations show a southwest–northeast orientation, and we observed developments of steps, indicating that the fault has a left-lateral strike-slip motion (Figure 5A). The plunge of the fault striations is 10°–15° (Figure 5B). Thus, we estimated ratios between 4:1 and 3:1 for the horizontal to vertical displacement of the fault. To the southwest of this striation, we recognized another fault striation on the fault surface of the NHF (GPS:28.436,158°N; 102.104,460°E). These fault striations strike NE (Figure 5C), and the dips are approximately 8°–10° (Figure 5D). Thus, a ratio of 5:1 is calculated for the horizontal to vertical displacement of the fault. Based on the plunge of the fault striations at the two locations, a left-lateral strike-slip with a minor thrust component is determined for the movement at the fault. The ratio of horizontal to vertical displacement is about 5:1–3:1.

To the east of Shanla, on the extension line of the fault–sill, the fault passes through a diluvial fan and subsequently displaces the diluvial fan margin (Figure 3E). The edge of the vegetation marks the boundary of the diluvial fan (Figure 3F). The left-lateral displacement of the boundary for the diluvial fan is about 3.6 ± 0.2 m, probably representing the surface displacement caused by the latest seismic event (Figure 3E).

According to the field investigation, the movement of the NHF is dominated by a left-lateral component, which is indicated by the left-laterally displaced rivers, vegetation boundary, and fault striations. A minor thrust component is constrained by the presence of 1.0–1.5-m-high fault scarps. Our field investigations demonstrate that the NHF and ANHF share the same type of tectonic movements which are dominated by left-lateral strike-slip with minor thrusting.

4.2 Paleoseismic analysis

4.2.1 Stratigraphic units from Tc1 and Tc2

We excavated two trenches for our study. The trench near Hebian Township was named Tc1, and the trench near Dongfang Village was named Tc2 (Figure 2). To constrain the age of the paleoseismic events, Tc1 was excavated across the diluvial fan near Hebian, and Tc2 was excavated across the first terrace (T1) of the gully near Dongfang. The two locations were chosen because they are characterized by the accumulation of recent sediments. In such an environment, successive layers of fine-grained sediments are deposited, and therefore organic-rich material, suitable for radiocarbon dating, may occur in such sequences.

By analyzing soil characteristics from the trench wall, the sediments were grouped into six stratigraphic units in Tc1 (Figures 7, 14) and nine stratigraphic units in Tc2 (Figures 11, 14). We analyzed the cross-cutting relationships and thus constrained the timing of paleoseismic events. Based on the cross-cutting relationships, the timing of two events was constrained in Tc1, and that of three events in Tc2. Details of each stratigraphic unit are summarized in Table 3.

4.2.2 Paleoseismic events revealed from Tc1 in Hebian Township

Based on the results of the field investigation in Hebian Township, we studied the displacements of two gullies to the north of Hebian (Figures 6A, 17). A left-lateral synchronous displacement of approximately 15 ± 0.2 m and 14 ± 0.2 m, respectively, of these two gullies, is obtained by UAV mapping (Figure 17) (see Section 4.4.2 for details). The bedrock section of the NHF is exposed in the south of the two gullies (Figure 6C). In this area, a series of fault scarps with an average height of 1.5 m occurs. An unequivocal fault pass is observed to the south of the fault scarp (Figure 6D). Tc1 was excavated on a diluvial fan, representing a fine sediment environment in the northern part of the central segment of the NHF (Figures 2, 6A,B). The trench has a length of 8 m and a depth of 2 m.

The radiocarbon ages of the six lithostratigraphic units detected for the samples of Tc1 are summarized in Table 3. Based on the age of each unit and their position, the units are labeled from U1 to U6 with U1 as the oldest unit and U6 as the youngest one. Two faults are identified which are marked as F1 and F2 (Figure 7) by analyzing the trench wall.

The first event (E1_Tc1): The fault F2 is considered to be formed by the first event that is revealed in Tc1. Because

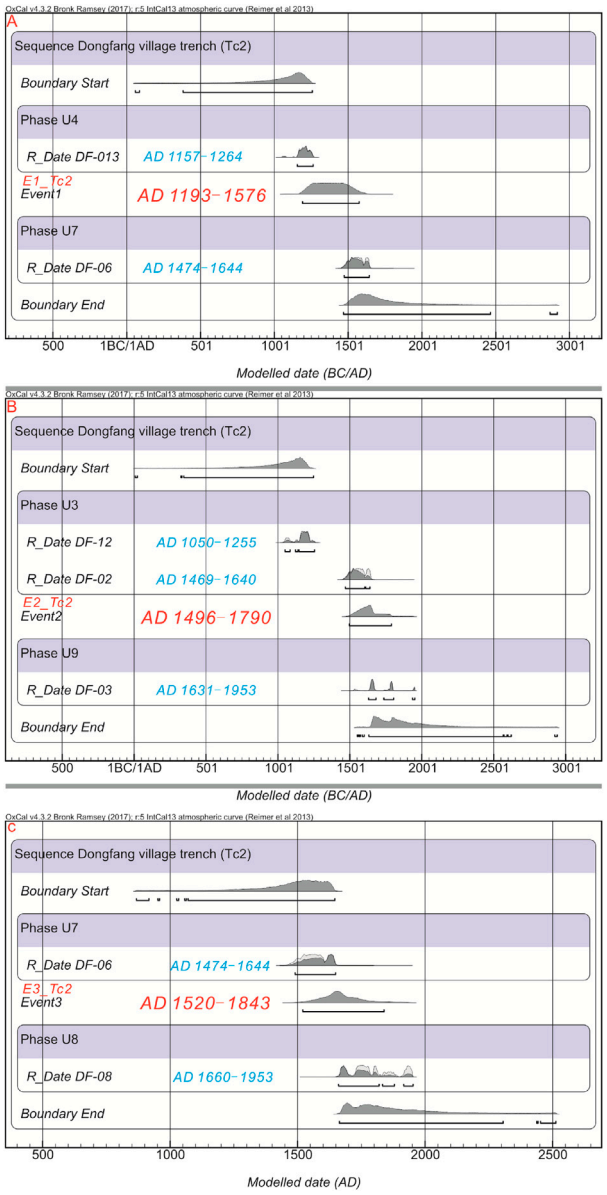

FIGURE 13
(A) The timing of paleoseismic event 1 (E1_Tc2) in Tc2 is constrained to AD 1193–1576. **(B)** The timing of paleoseismic event 2 (E2_Tc2) in Tc2 is constrained to AD 1496–1790. **(C)** The timing of paleoseismic event 3 (E3_Tc2) in Tc2 is constrained to AD 1520–1843. Probability density functions (PDFs) for the timing of events observed at Tc2 were calculated using OxCal 4.3.2 (https://c14.arch.ox.ac.uk/oxcal/OxCal.html).

F2 displaced the entire U1 and barely displaced U2, the timing of E1_Tc1 after the deposition of U1 but before or during the deposition of U2 is constrained. Since the F2 barely extends to the upper part of U2, it is most likely that E1_Tc1 occurred after the deposition of lower U2 but before the deposition of upper U2 (Figures 7, 8B). Thus, according to the ages of the carbon samples retrieved from U1 (HB-07) and U2 (HB-04), the timing of E1_Tc1 is constrained.

The second event (E2_Tc1): This event in Tc1 is considered the event that formed the fault F1, which marks the unit boundary between U3–U4 and U1–U2 on the trench wall. Because F1 transects U4 but does not truncate U6, E2_Tc1 must postdate the deposition of U4 but predate the deposition of U6. Because U5 is a thin layer that hardly provides a cross-cutting relationship for E2_Tc1, it remains uncertain whether the timing of E2_Tc1 predates or postdates the deposition of U5. At least, the formation of F1 is bracketed between the deposition of U4 and U6 (Figures 7, 8A). Therefore, the timing of E2_Tc1 should lie between the ages of U4 and U6 which were constrained by the samples HB-03 and HB-08.

After conversion into a common format, the timing of the events is constrained as 5373–4525 BC for E1_Tc1 (Figure 9A) and AD 1520–1842 for E2_Tc1 (Figure 9B).

4.2.3 Paleoseismic events revealed from Tc2 in Dongfang Village

According to the results of our field investigation close to Dongfang Village, the NHF constitutes a left-lateral and right-order pressure ridge (Figures 10A,B), forming a strip-shaped pressure uplift. Based on UAV mapping of landforms near Dongfang Village, another topographic profile is observed which is approximately 0.5–1.5 m high (Figures 18, 19) (see Section 4.4.3 for details). Tc2 is located on the southern segment of the NHF (Figures 2, Figures 10A, C, D). Along the NHF, the first terrace (T1) of the gully is well preserved. The height of the T1 above the gully is approximately 1–2 m, and the sediment is fine-grained, indicating that the location here is in a sedimentary environment, thus providing a high likelihood to obtain carbon samples suited for dating purposes. We excavated a trench perpendicular to the fault trace. The trench had a length of 12 m, a width of 2 m, and a depth of 1.8 m (Figures 10D, 11). Because of the wet soil at the trench site, and the rainy weather during the excavation, the northeastern wall of the Tc2 was partially destructed and the southwestern wall of the Tc2 collapsed. Therefore, we only present data for the well-preserved wall of the trench.

The radiocarbon ages of the nine lithostratigraphic units recognized in Tc2 are summarized in Table 3. Based on the age of each unit and their position, the units are labeled from U1 to U9 with U1 as the oldest and U9 as the youngest unit. By analyzing the trench wall, four faults are identified, which are marked as F1, F2, F3, and F4 (Figure 11), that are related to three events (E1_Tc2, E2_Tc2, E3_Tc2).

The first event (E1_Tc2): This event is considered the event that formed F3 and F4 in Tc2 (Figure 11). Because U4 is the youngest unit that is truncated by both F3 and F4, and U8 is on the top of U4, the timing of E1 in Tc2 is constrained after the deposition of U4 but before the deposition of U8. F3 displaces U2 and U4 and forms a vertical displacement of up to 0.2 m. Since no samples were collected at the bottom of U8 (U8-1), we have constrained the timing of this event with the samples DF-06 in U7 and DF-13 in U4.

The second event (E2_Tc2): F1 and F2 are formed by E2_Tc2 which displaces U2, U4, U5, and possibly U8 in Tc2. U9 overlies U8, U5, and U3 at the top of the trench. U2 is the oldest stratum that was displaced by F1 and F2, indicating that E2_Tc2 occurred after the deposition of U2. U4 and U8 are only found to the east of F2, which may have been displaced by the horizontal movement of the NHF. However, E2_Tc2 must have occurred after the deposition of U3. Moreover, sedimentary sequences of the other stratum are

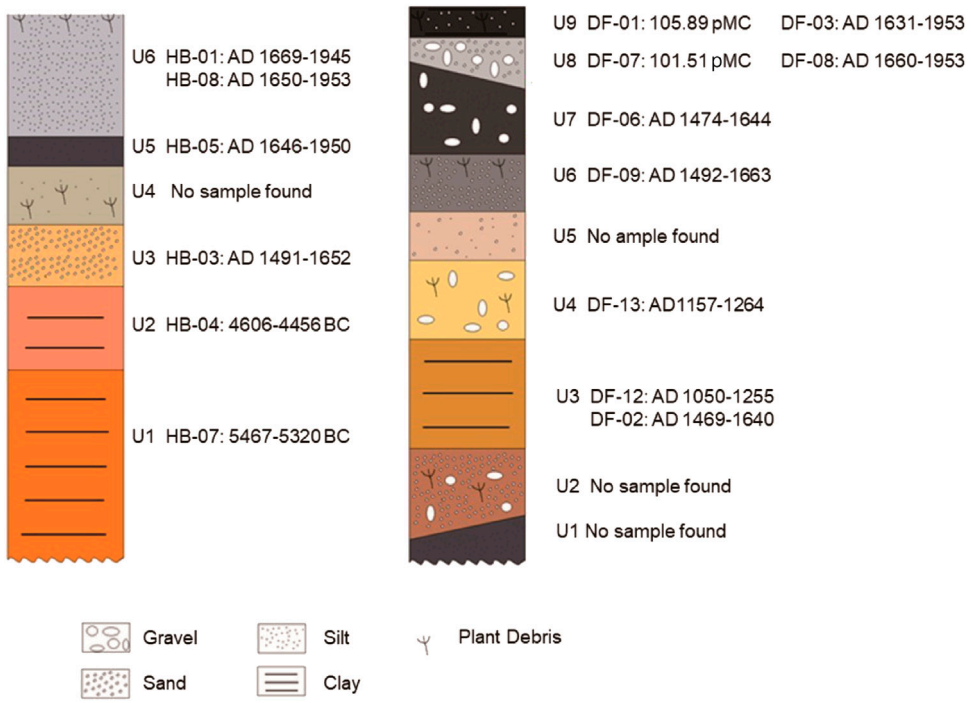

FIGURE 14
Schematic column of the units in Tc1 and Tc2. The age of the units is determined by radiocarbon samples detected within the units.

lacking in the middle and lower U3, indicating that U3 was displaced by the left-lateral fault movement. This seismic event may have been of major magnitude and probably comprises a major horizontal strike-slip component.

F1 and F2 exhibited compressive structures, as obtained from field investigation, and the fault plane was tightly closed. Seismic fissures A and B developed in U3 and the lower part of U9. During the E2_Tc2 earthquake, F1 and F2 formed a left-lateral and left-order structure and produced tensile stress that prompted the formation of the seismic fissures A and B (Figures 11, 12A). This event occurred after the deposition of U3 and before the deposition of upper U9. Thus, the timing of E2_Tc2 can be constrained by samples DF-12 and DF-02 in U3 and DF-03 in U9.

Third event (E3_Tc2): After deposition of U8-1 to U8-3, movement on F3 and F4 caused the flexing of U8-1 and U8-3. Because the top of U8-4 is flat, its deposition must postdate the flexing of the underlying units. Thus, the earthquake occurred after the deposition of U8-3 and before the deposition of U8-4. U8-1 is very thin and sampling was impossible. Therefore, sample DF-06 in U7 was used to constrain the lower limit of these seismic events, while sample DF-08 in U8 was used to establish the upper limit. Since sample DF-07 in U8 was modern carbon which provided no paleotiming information, it was discarded for further consideration. The E3_Tc2 was recorded by consistent stratigraphic deformation on the west wall of the trench (Figure 12B).

After converting the timing of events into common age data, the timing of the three events detected in Tc2 is AD 1193–1576 for E1_Tc2 (Figure 13A), AD 1496–1790 for E2_Tc2 (Figure 13B), and AD 1520–1843 for E3_Tc2 (Figure 13C).

4.3 Paleoseismic event analysis of the NHF

To understand the timing relationships of the paleoseismic events revealed from Tc1 and Tc2, we have projected the timing of the events on a timeline (Figure 20). Two events were identified in Tc1, which occurred between 5373–4525 BC and AD 1520–1842. Three paleoseismic events were identified in Tc2, which took place around AD 1193–1576, AD 1496–1790, and AD 1520–1843. For events with overlapping timing, we propose that these events are related to the same seismic event or they share a triggering relationship. Figure 20 documents that E2_Tc1, E2_Tc2, and E3_Tc2 occurred almost contemporaneously, and it is thus likely that the three seismic events are related to a common tectonic event. The event E2_Tc2, revealed from Tc2, widely overlaps with the age of E3_Tc2 in the same trench. Therefore, we propose that E2_Tc2 and E3_Tc2 in Tc2 record a common seismic event. However, considering the uncertainty of sample dating, the timing of this event that was identified as E2_Tc1 in Tc1 as well as E2_Tc2 and E3_Tc2 in Tc2 is roughly AD 1496–1843. Accordingly, the paleoseismic events detected in the NHF can be summarized as E1_NHF: 5373–4525 BC, E2_NHF: AD 1193–1576, and E3_NHF: AD 1496–1843 (Figure 21).

Additionally, a geological section in Yuangendi (Figure 4) shows that the most recent event on the NHF has caused surface deformation of soil and has formed a 1-m-high fault scarp. Therefore, the latest seismic event on the northern segment of the NHF may have occurred coevally with the latest event that was identified in Tc1 and Tc2. Following this model, the NHF may break through the entire fault in recent paleoseismic events.

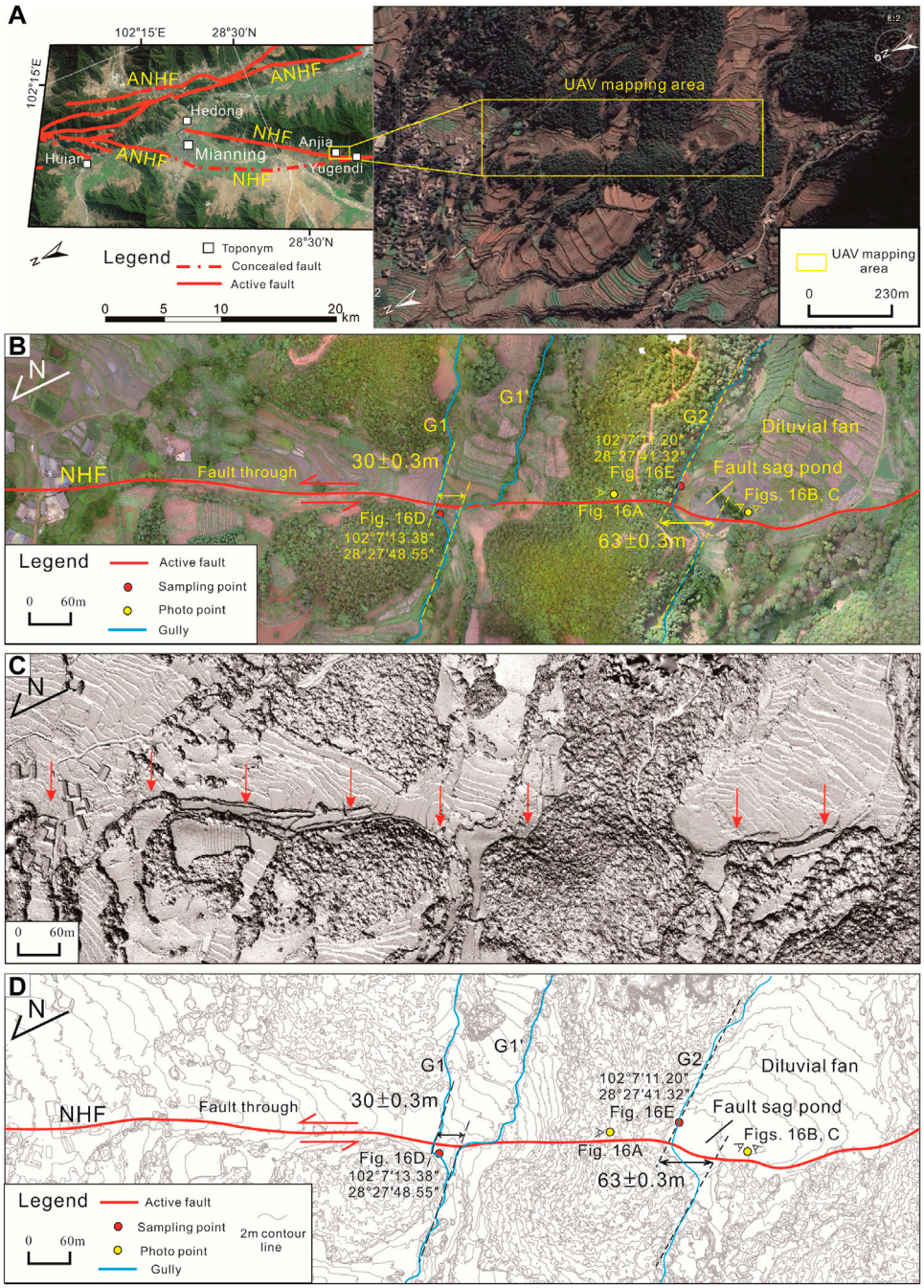

FIGURE 15
Tectonic landforms revealed by UAV mapping in the Anjia area. The position of this area is marked in Figure 2. **(A)** Satellite image (from Google Earth) of the UAV mapping area. **(B)** Landforms mapped by UAV. **(C)** Shaded relief map from UAV-derived DSM. **(D)** Interpreted map from UAV-derived contour, showing the displacement of the gullies (G1 and G2) displaced by the left-lateral displacement of NHF.

4.4 Slip rates

4.4.1 Anjia Village site

The NHF exhibits striking linear characteristics in satellite images and aerial photographs near Anjia Village. During our on-site investigations, we detected that these faulted structures are negative landforms, such as fault trough, fault scarp, and fault sag pond (Figures 15, 16). A major fault trough formed by the NHF is 10–25 m wide and about 1.4 km long (Figures 15B, 16A). In addition, left-lateral synchronous displacement of the gullies G1 and G2 is observed. The upstream width of the G1 gully is 3–4 m, which is equivalent to the downstream width. Thus, we propose that the formation age of the upstream and downstream are equivalent. Under the headward-migrating erosion, G1 forms G1'. The gully G1 was displaced left-laterally by the fault for about 30 ± 0.3 m (Figures 15B,D). The debris sample was taken near the bottom

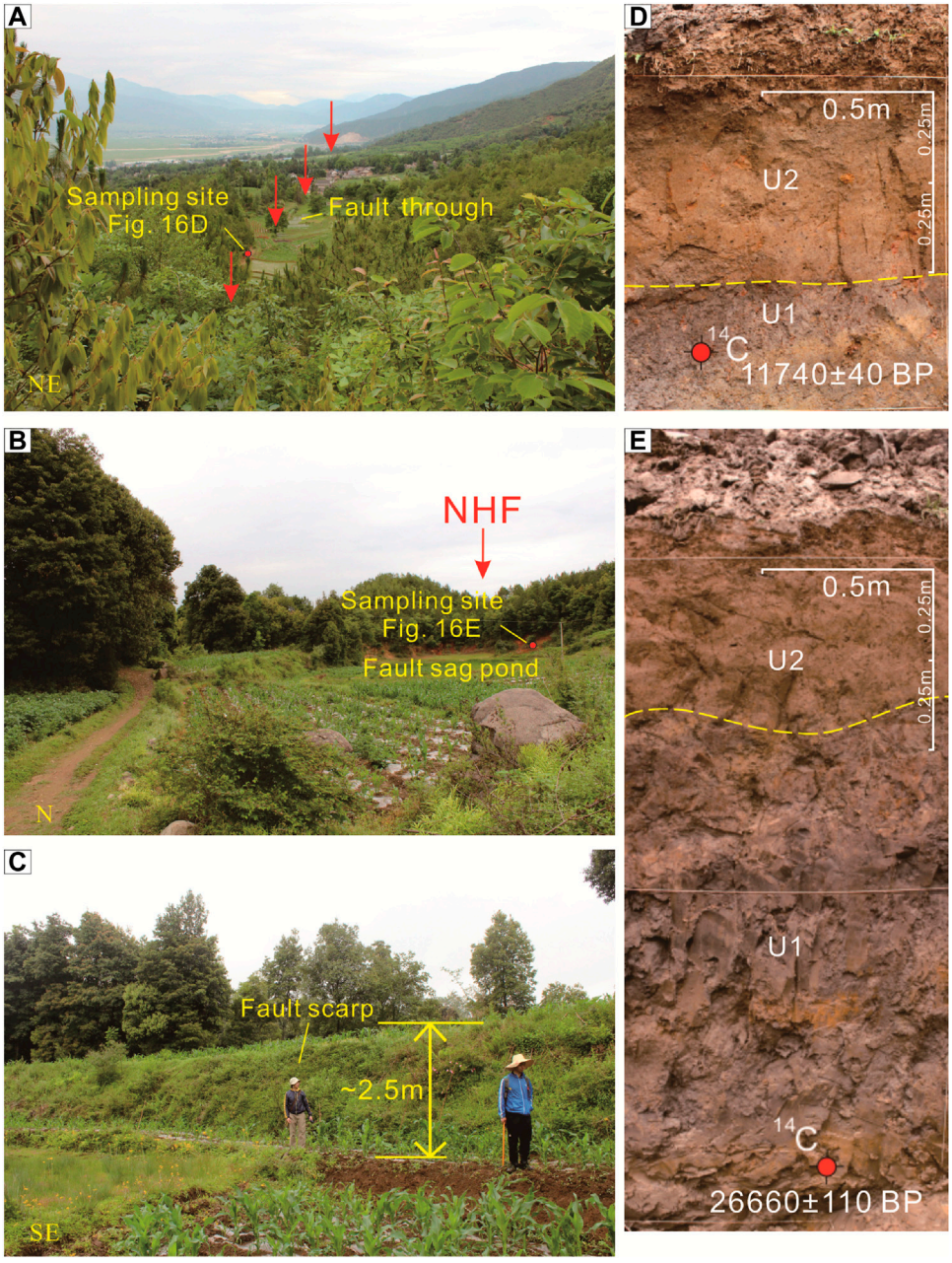

FIGURE 16
(A) Field photograph of the fault trough with red dots showing the sampling locations. **(B)** Field photograph of the fault sag pond; red dots show the sampling locations. **(C)** Field photograph of the fault scarp. **(D)**, **(E)** Field photographs of the locations and ages of the radiocarbon samples, respectively, (see Figures 15B,D) for the specific sampling locations. U2 represents the humus layer, U1 represents mucky soil, and the yellow dotted line indicates the stratigraphic boundary.

of the trough of the G1 gully fault for ^{14}C isotope analysis and was dated at 11,740 ± 40 BP (Figures 16A,D). The calculated left-lateral horizontal slip rate of the NHF at this position is 2.56 ± 0.03 mm/yr. Along the fault to the southwest, the NHF has displaced the diluvial fan and formed a 2.5 m high and 120 m long fault scarp (Figure 16C). A fault sag pond was developed on the south and east side of this scarp (Figure 16B). The gully G2 was displaced left-laterally for about 63 m ± 0.3 m (Figures 15B,D). A debris sample was collected for ^{14}C isotope analysis near the bottom of the fault sag pond and yielded an age of 26,660 ± 110 BP (Figures 16B, E). Thus, based on the calculations, the slip rate of the NHF is 2.40 ± 0.01 mm/yr. Consequently, the horizontal slip rate of the NHF since the late Late Pleistocene obtained near Anjia Village is 2.40–2.56 mm/yr.

4.4.2 Hebian Township site

On the diluvial fan to the north of Hebian Township, the fault synchronously displaced the two gullies G1 and G2. The left-lateral displacements of G1 and G2 are 15 ± 0.2 m and 14 ± 0.2 m,

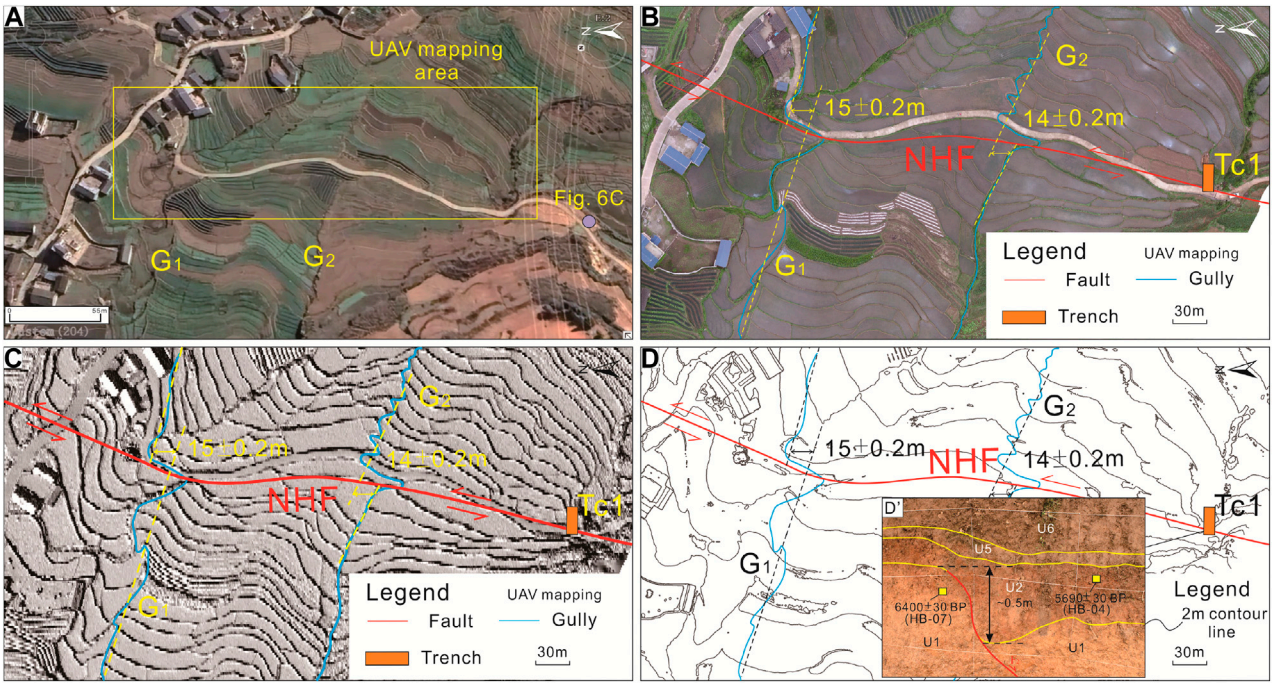

FIGURE 17
Tectonic landforms revealed by UAV mapping around Hebian Township. The location of this area is marked in Figure 2. **(A)** Satellite image of the UAV mapping area from Google Earth. The purple dot shows the location of the geological section in Figure 6C. **(B)** Landforms mapped by UAV, showing the location of displacement and Tc1. **(C)** Shaded relief map from UAV-derived DSM. **(D)** Interpreted map, illustrating the displacement of the gullies G1 and G2 caused by NHF left-lateral movement, and trench location. **(D′)** Simplified map showing the displacement revealed from Tc1.

respectively (Figure 17). Because no chronological samples were collected around the river, we used the timing of sample HB-4 after excluding the interference of the surface humus layer in Tc1 as the upper limit of the timing for the diluvial fan. The sample in Tc1 was collected on the south side of gully G1 and stemmed from the same geomorphic surface as the diluvial fan.

F2 in Tc1 displaces U1 vertically by about 50 cm (Figures 7B, 8B, 17D′). The timing of F2 was constrained by the carbon sample in U1 (HB-07: 6400 ± 30 BP) and U2 (HB-04: 5690 ± 30 BP). Thus, the left-lateral horizontal slip rates of the NHF near Hebian Township are calculated as 2.60 ± 0.09 mm/yr and 2.50 ± 0.09 mm/yr. The vertical slip rate of the NHF in Hebian can be approximated by the time that forms the vertical slip and the magnitude of the slip. By dividing the amount of slip by the time required for the formation of this slip, a vertical slip rate of 0.09–0.08 mm/yr, approximately about 0.10 mm/yr. Therefore, the late Holocene horizontal slip rate of the NHF near Hebian Township is 2.50–2.60 mm/yr, and the vertical slip rate is about 0.10 mm/yr.

4.4.3 Dongfang Village site

Near Dongfang Village, the NHF passes through the first-level terrace (T1) of gullies that spreads out SW-NE. The height of the terraces from the gully surface is about 1–2 m. We conducted UAV mapping (Figure 18) and took eight topographic profiles perpendicular to the fault to estimate the height differences between the two sides of the terraces. The height difference represents the vertical displacement of the fault and is in the range of 0.5–1.5 m (Figure 19), with an average value of 0.9 m. The data document a significant vertical component of the fault displacement.

By using the original 870 ± 30 BP age of the sample DF-12 in Tc2, after excluding the interference of the surface humus layer, as the age of the top of the terrace (T1), and the average vertical height, the late Holocene vertical component of the slip rate in Dongfang Village for NHF is calculated as 1.00 ± 0.04 mm/yr.

Combined with the vertical slip rate obtained in Hebian Township, which is 0.1 mm/yr, the vertical slip rate of the NHF is between 0.1 and 1.0 mm/yr, with an average of 0.60 mm/yr. Based on our calculations, the horizontal slip rate of the NHF since the late Holocene is 2.50–2.60 mm/yr. Consequently, the ratio of the horizontal slip rate to the vertical slip rate is about 4:1, which is generally consistent with the ratio of fault motion components revealed by fault striations.

Based on the integrated analysis of the aforementioned data, the horizontal slip rate of the NHF since the late Late Pleistocene is 2.40–2.56 mm/yr, the horizontal slip rate of the NHF since the late Holocene is 2.50–2.60 mm/yr, and the late Holocene vertical slip rate is about 0.60 mm/yr.

4.5 The calculation for further hazards

According to satellite imagery interpretations and field investigation, the length of the NHF is approximately 70 km. Based

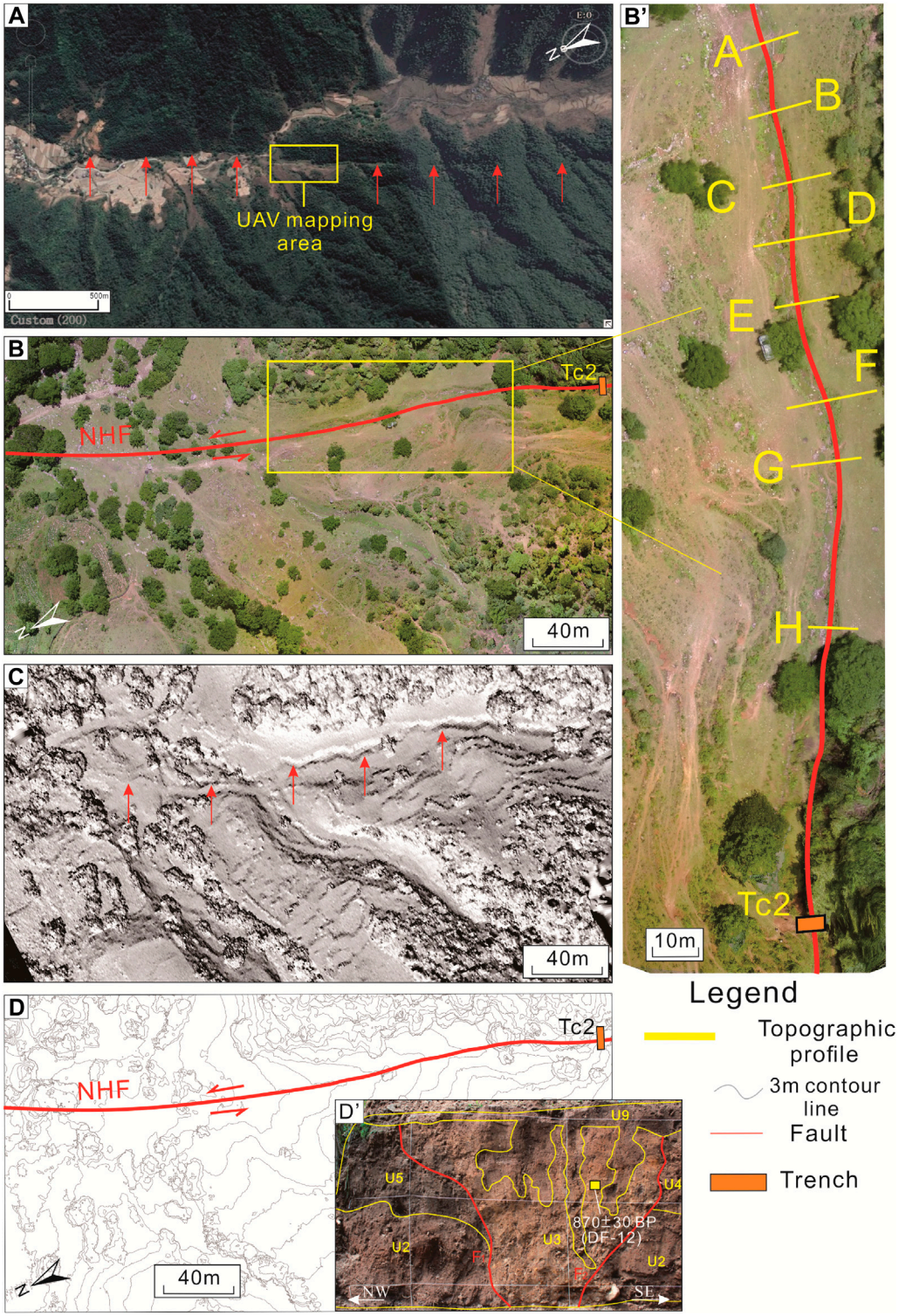

FIGURE 18
Tectonic landforms mapped by UAV around Dongfang Village. The location of this area is marked in Figure 2. **(A)** Satellite image of the UAV mapping area from Google Earth. **(B)** Landforms mapped by UAV. **(B')** Locally enlarged landforms mapped by UAV of **(B)**. Yellow lines in **(B')** show the location of terrain sections from Figure 19. **(C)** Shaded relief map (from UAV-derived DSM). **(D)** Interpreted map (from UAV-derived contour), representing terrain sections. **(D')** Sample in the Tc2.

on published equations (Bonilla et al., 1984; Deng et al., 1992; Wells and Coppersmith, 1994; Wen, 1995), the maximum earthquake magnitudes potentially induced by the NHF are 7.33 ± 0.19, 7.23 ± 0.29, 7.58 ± 0.21, and 7.54 ± 0.37, in M scale, with an average of M 7.4 ± 0.1. Based on the equation from Wells and Coppersmith (1994), the maximum magnitude of a triggered earthquake on the NHF is M 7.5 ± 0.2.

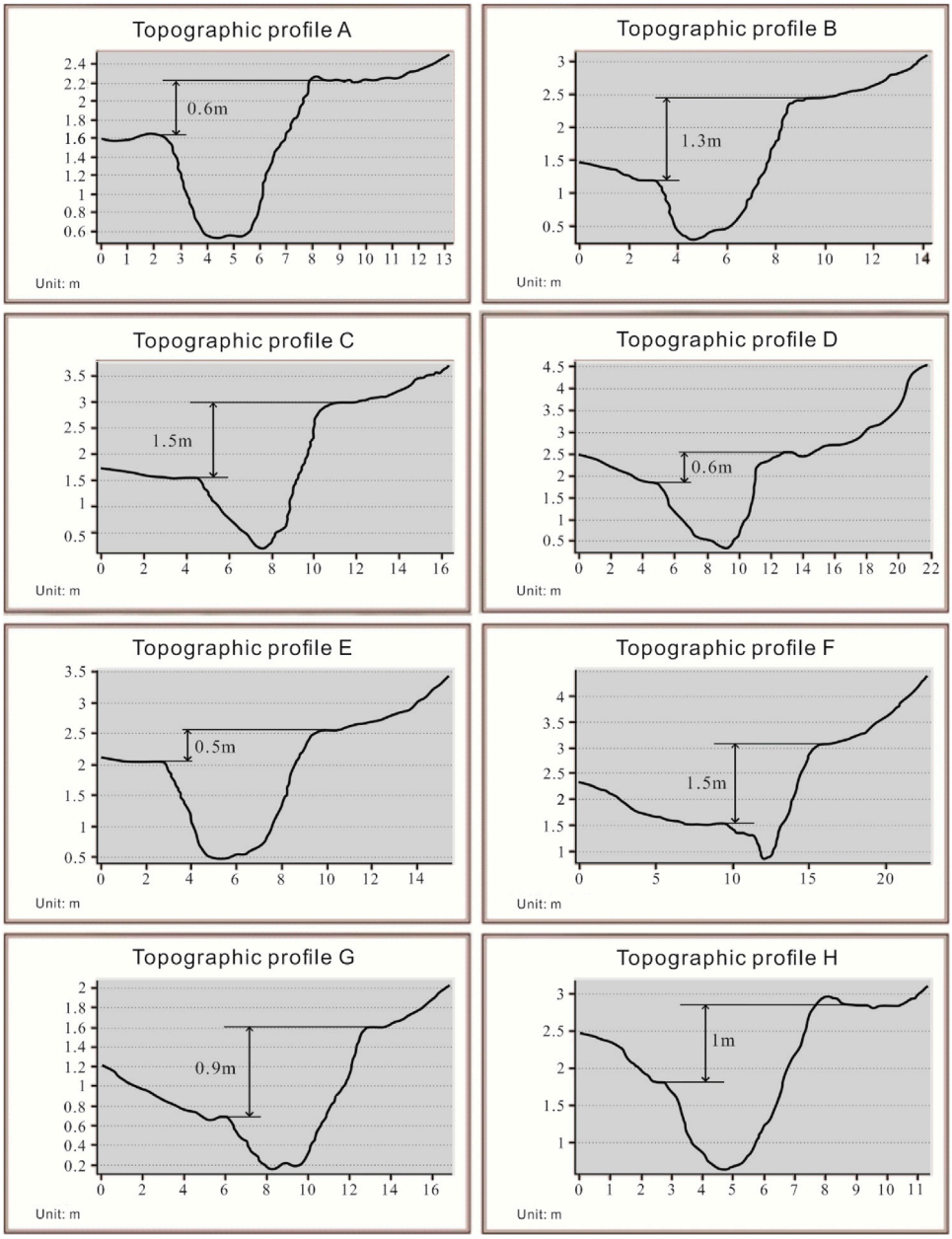

FIGURE 19
Profiles from Figures 18B, B′. Eight topographic profiles represent height differences in the range of 0.5–1.5 m between two sides of the terraces near the north of Tc2.

Based on the published equations (Deng et al., 1992; Wells and Coppersmith, 1994; Wen, 1995), the average maximum horizontal fault displacements of NHF are calculated by three empirical formulae. The calculated value of 3.55 ± 1.38 m resembles the value of left-lateral displacement of the diluvial fan (3.6 ± 0.2 m) that was obtained on the NHF (Figure 3E). Therefore, combined with the co-seismic displacements obtained on other faults in Table 2, we believe that the displacement of 3.6 ± 0.2 m revealed in the NHF represents the surface displacement caused by the latest seismic event.

5 Discussion

5.1 Relationship between the ANHF and NHF

Three paleoseismic events affected the Zimakua–Yejidong area on the northern segment of the ANHF (Wen et al., 2000a; Ran et al., 2008a). The three events occurred at approximately 280–550 BP, 1030–1050 BP, and 1634–1811 BP. On the northern segment of the ANHF, trench analysis at Dahaizi–Ganhaizi revealed four paleoseismic events (Ran et al., 2008a), which occurred at 50–1310 BP, 1768–1826 BP, 2755–4018 BP, and 4108–6593 BP.

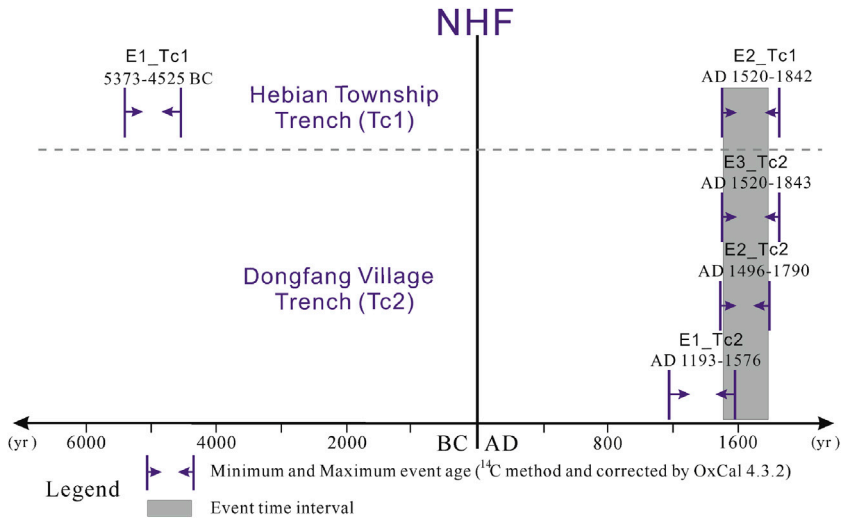

FIGURE 20
Timeline of the events constrained at Tc1 and Tc2 on the NHF.

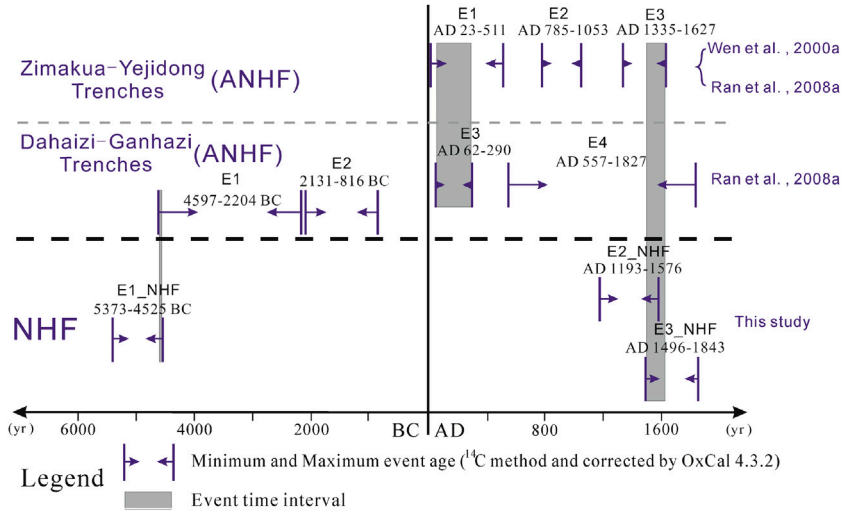

FIGURE 21
Timeline of events detected in the trenches along the NHF and ANHF. The data used in each of the studies were calibrated using OxCal 4.3.2.

After conversion into BC and AD, the paleoseismic events revealed by Wen *et al.* (2000a) and Ran *et al.* (2008a) on the Zimakua–Yejidong are AD 23–511 for E1, AD 785–1053 for E2, and AD 1335–1627 for E3. The paleoseismic events in the Dahaizi–Ganhaizi area are 4597–2204 BC for E1, 2131–816 BC for E2, AD 62–290 for E3, and AD 557–1827 for E4 (Figure 21). Trench analysis of the Dahaizi–Ganhaizi on the ANHF reveals that the time of the seismic event E4 is closer to AD 1800 (Ran et al., 2008a). In Figure 21, the events on the NHF are compared with events on the different segments of the ANHF in a common plot. A well-defined overlap of the timing of two events suggests a common event or a triggering relationship.

Figure 21 illustrates that E3_NHF on the NHF partially overlaps with E3 (revealed in the Zimakua–Yejidong area) and E4 (revealed in the Dahaizi–Ganhaizi area) of the ANHF. Thus, at least two possible correlations between the three earthquakes of the NHF and ANHF exist. 1) In the first model the earthquake on the ANHF triggered the earthquake on the NHF, or the earthquake on the NHF triggered the earthquake on the ANHF. However, because the NHF is a secondary fault, it is more likely that earthquakes on the ANHF triggered that on the NHF. 2) In the second model E3 (AD

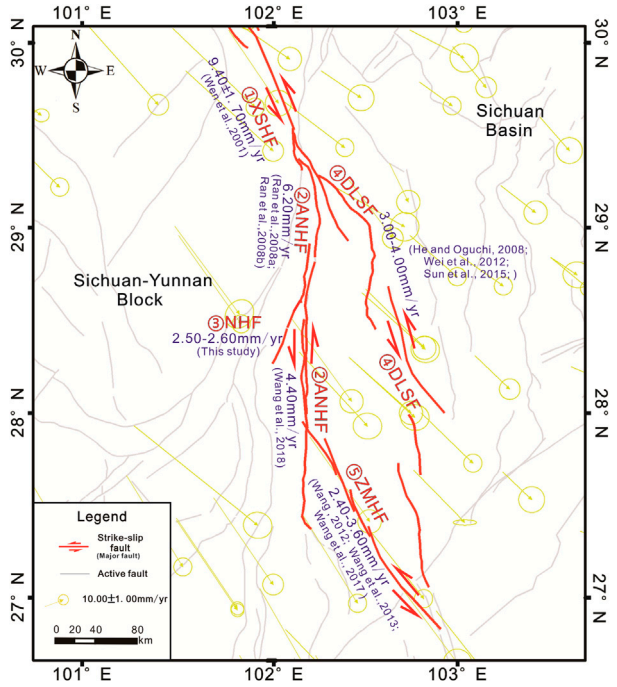

FIGURE 22
Slip rates of the major faults and at the eastern boundary of the Sichuan–Yunnan Block. Yellow arrows show GPS velocities (partial) of crustal motion of the southeastern Tibetan Plateau relative to Eurasia (Gan et al., 2007; Liang et al., 2013). ①XSHF, Xianshuihe Fault; ②ANHF, Anninghe Fault; ③NHF, Nanhe Fault; ④DLSF, Daliangshan Fault; ⑤ZMHF, Zemuhe Fault.

1335–1627) on the ANHF in the Zimakua–Yejidong area and the E4 (AD 557–1827) in the Dahaizi–Ganhaizi area ruptured with E3_NHF (AD 1496–1843) of the NHF. This co-rupture would imply that these events have occurred during the same earthquake, and thus the ANHF and NHF could represent a cascade rupture.

Based on our field investigation and paleoseismic analysis, we propose that during the E3_NHF of the NHF, surface rupture may have broken through the entire NHF which may make the ANHF and NHF both in the same seismic events. Therefore, the timing of the triggering or cascade rupture between the ANHF and the NHF may have happened between AD 1496–1627.

The NHF connects with the ANHF in the north of Mianning (Figures 1, 2). The connecting geometry between ANHF and NHF shows a "y" shape. Therefore, the NHF and ANHF also provide geological preconditions for the occurrence of triggered or cascade earthquakes.

The 2002 Denali Mw7.9 in the United States (Eberhart-Phillips et al., 2003) is a comparable example of the triggering effect. The earthquake started with a thrusting event on the Susitna Glacier Fault (SGF) and subsequently proceeded with a right-slip movement on the Denali Fault (DF), but the surface ruptures to the south do not extend along the DF. Then, the surface ruptures took a right step and continued with the right-slip movement on the Totschunda Fault (TF) (Eberhart-Phillips et al., 2003). During the earthquake, the SGF generated 48 km, the DF induced 218 km, and the TF formed 76 km of surface rupture (Eberhart-Phillips et al., 2003; Crone et al., 2004). The TF which is situated to the south of the DF also forms a "y"-shaped connection with the DF. On the medium-sized or secondary fault that forms a "y"-shaped connection with the main fault, cascade rupture or trigger earthquakes on the secondary faults are likely by the surface rupture of the main fault.

Thus, according to our paleoseismic analysis, the NHF can generate self-contained earthquakes and can also induce cascade rupture or trigger earthquakes with the ANHF. The timing of their triggering or cascade rupture events is dated AD 1496–1627.

5.2 Tectonic implication between the NHF and ANHF

5.2.1 Kinematic relationship between NHF and ANHF

Our remote sensing studies and field investigations indicate that the NHF is dominated by left-lateral strike-slip movement, which is consistent with the movement of the ANHF. In a previous study, a value of 3.0 ± 0.3 m has been reported for the fault displacements discovered in the north of the Yejidong (Wen et al., 2000a). A value of 2.7 m has been published for the horizontal displacement of the latest seismic event that is detected around Zimakua (Wen et al., 2000a; Ran et al., 2008a; Ran et al., 2008b). The horizontal displacement of the latest seismic event on the NHF, which we have recognized to the south of Yuangendi, is estimated as 3.6 ± 0.2 m. This value is roughly equivalent to the displacement in the ANHF. The ratio of horizontal to vertical displacement that is recorded by the striations on the NHF fault surface is about 3:1–5:1, which is equivalent to the displacement ratio of the ANHF reported in previous studies (Wen et al., 2000a; Ran et al., 2008a; Ran et al., 2008b).

5.2.2 Kinematic relationship in the eastern boundary of SYB

To understand the kinematic characteristics of the faults along the eastern margin of the SYB, we used the slip rate of faults during the same period (the late Holocene) and combined the GPS data to analyze the potential kinematic relationship between these faults.

The late Holocene left-lateral slip rate of the XSHF is about 9.40 ± 1.70 mm/yr (Wen et al., 2001). In the Shimian area, one part of the fault slip rate is transferred to the ANHF, and another part is decomposed by the DLSF. Since the late Holocene, the horizontal slip rate of the decomposition of the DLSF is 3.00–4.00 mm/yr and 3.10 mm/yr in the southern segment (He and Oguchi, 2008; Wei et al., 2012; Sun et al., 2015). Based on GPS data, the left-lateral strike-slip of both the ANHF and DLSF is about 4.00 ± 2.00 mm/yr (Shen et al., 2005). Based on calculations from the block model, the overall left-lateral strike-slip of the ANHF is about 5.10 ± 2.50 mm/yr (Wang et al., 2008). Ran et al. (2008a) and Ran et al. (2008b) obtained a left-lateral strike-slip of 6.20 mm/yr since the late Holocene on the northern segment of the ANHF from the displacement of the water system. Thus, the slip rates from the GPS data and that obtained on the northern of the ANHF in the late Holocene are broadly the same. The sum of the slip rates of the northern ANHF (6.20 mm/yr) and DLSF (3.00–4.00 mm/yr) is

almost the same as the slip rate of the XSHF (9.40 ± 1.70 mm/yr). This indicates that the decomposition of the slip rates is concentrated along the block boundary, whereas the amount of plastic deformation within the block is relatively small.

Shear slip continues to extend southward along the ZMHF with a rate of 2.40–3.60 mm/yr (Wang, 2012; Wang et al., 2013; Wang et al., 2017), with an average value of 3.00 mm/yr. The left-lateral strike-slip of the ANHF is about 2.8 ± 2.5 mm/yr, which is roughly equivalent to that obtained by the block model calculation (Wang et al., 2008). The question remains, how the loss of the slip rate of about 3.00–4.00 mm/yr since the late Holocene in the ANHF and ZMHF can be explained? The slip rate of the NHF is about 2.50–2.60 mm/yr, and the average left-lateral strike-slip rate on the southern segment of the ANHF in Dashuigou in the past 3,300 years is about 4.40 mm/yr (Wang et al., 2018). The data confirm that the NHF decomposed the slip rate of the northern segment of the ANHF. By comparing the kinematic relationship in the eastern boundary faults of the SYB, we propose that the NHF participates in strain partitioning along the boundary. This conclusion reasonably explains the loss of the sliding rate between the ANHF and ZMHF, which also supports the GPS inversion results and the discontinuous deformation model of the eastern edge of the Tibetan Plateau (Figure 22).

By comparing the structural characteristics, paleoseismic relationship, movement property, slip rate, and other seismic and geological elements of the NHF and ANHF, we re-interpret the NHF to be a part of the ANHF. The NHF represents a branch fault of ANHF that is connected to the northern segment of the ANHF near Mianning. Thus, to determine the seismic hazard in the Mianning area and to understand the crustal deformation mechanism of the southeastern Tibetan Plateau, the fault behavior of the ANHF and NHF should be analyzed as an entity.

6 Conclusion

Based on detailed satellite imagery interpretation, we conducted a field survey, high-resolution measurements of offset geomorphic features, and trench excavations on the Nanhe Fault to understand its tectonic activity. We demonstrated that the Nanhe Fault is active in the Holocene. The left-lateral strike-slip rate of the Nanhe Fault since the late Late Pleistocene is 2.40–2.56 mm/yr, the left-lateral strike-slip rate since the late Holocene is 2.50–2.60 mm/yr, and the late Holocene vertical slip rate is about 0.60 mm/yr. Based on our paleoseismic investigations and analysis in the Nanhe Fault and Anninghe Fault, we identified three paleoseismic events (5373–4525 BC, AD 1193–1576, AD 1496–1843) on the Nanhe Fault. Our analysis suggested that the Anninghe and Nanhe faults may have produced cascade rupture or triggered earthquakes, and such related events probably occurred between 1496–1627. We calculated that the maximum magnitude of a triggered earthquake in the Nanhe Fault is about M 7.5. By comparing the kinematic relationship in the eastern boundary faults of the Sichuan–Yunnan Block, we proposed that the Nanhe Fault participates in strain partitioning along the boundary. This conclusion reasonably explains the loss of the sliding rate between the Anninghe Fault and Zemuhe Fault, which also supports the GPS inversion results and the discontinuous deformation model of the eastern edge of the Tibetan Plateau.

Overall, by comparing the geometric structure, paleoseismic relationship, movement property, slip rate, and other seismic geological elements of the Nanhe Fault and Anninghe Fault, we re-interpret the Nanhe Fault as a part of the ANHF and as a branch fault of the Anninghe Fault in the Mianning area.

Data availability statement

The original contributions presented in the study are included in the article/supplementary material; further inquiries can be directed to the corresponding author.

Author contributions

CM contributed to all sections. YL contributed to field work, thesis conception and manuscript writing instruction. LA contributed to data compiling and processing. WZ and SL contributed to trench investigation and data sampling. XY contributed to seismic risk analysis and calculation.

Funding

This study was supported by the Spark Program of Earthquake Sciences (Grant Nos XH18039Y and XH20050Y) and the Earthquake Science and Technology Special Project of the Sichuan Earthquake Agency (Grant Nos LY2205 and LY2206). This work was also supported by the Sichuan Province Key R&D Program Project Research on the Structural Basis and Risk Assessment of Earthquake Pregnancy in Southern Sichuan (Grant No. 2020YFS0451) and the Research on Seismogenic Structure, Earthquake Disaster Risk Prevention and Earthquake Monitoring Network Layout Plan in Southern Sichuan.

Acknowledgments

The authors are very grateful to Wang Hu from Southwest Jiaotong University of China for detailed and constructive suggestions on the manuscript. The authors are grateful to the editor and three reviewers for their detailed suggestions and comments, which have significantly improved the quality of the manuscript.

Conflict of interest

The authors declare that the research was conducted in the absence of any commercial or financial relationships that could be construed as a potential conflict of interest.

Publisher's note

References

Aitchison, J. C., Ali, J. R., and Davis, A. M. (2007). When and where did India and Asia collide? *J. Geophys. Res.* 112 (B5), B05423. doi:10.1029/2006jb004706

Allen, C. R., Luo, Z. L., Qian, H., Wen, X. Z., Zhou, H. W., and H, W. S. (1991). Field study of a highly active fault zone: The Xianshuihe fault of southwestern China. *Geol. Soc. Am. Bull.* 103 (9), 1178–1199. doi:10.1130/0016-606(1991)103<1178:FSOAHA>2.3.CO;2

Bonilla, M. G., Mark, R. K., and Lienkaemper, J. J. (1984). Statistical relations among earthquake magnitude, surface rupture length, and surface fault displacement. *Bull. Seis. Soc. Am.* 74, 2379–2411.

Bronk Ramsey, C. (2009). Bayesian analysis of radiocarbon dates. *Radiocarbon* 51 (01), 337–360. doi:10.1017/s0033822200033865

Chen, G., Min, W., Song, F., Jiao, D., and Xu, H. (2011). Preservation of Co-seismic surface rupture in different geomorphological settings from the study of the 1786 Moxi earthquake. *Seismol. Geol.* 33 (4), 804–817. doi:10.3969/j.issn.0253-4967.2011.04.006·

Clark, M. K., Bush, J. W. M., and Royden, L. H. (2005). Dynamic topography produced by lower crustal flow against rheological strength heterogeneities bordering the Tibetan Plateau. *Geophys. J. Int.* 162 (2), 575–590. doi:10.1111/j.1365-246X.2005.02580.x

Crone, A. J., Personius, S. F., Craw, P. A., Haeussler, P. J., and Staft, L. A. (2004). The Susitna Glacier thrust fault: Characteristics of surface ruptures on the fault that initiated the 2002 Denali fault earthquake. *Bull. Seismol. Soc. Am.* 94 (6B), S5–S22. doi:10.1785/0120040619

Deng, Q. D., Yu, G. H., and Ye, W. H. (1992). *Relationship between earthquake magnitude and parameters of surface ruptures associated with historical earthquakes Research on Active Fault (2)*. Beijing: Seismological Press, 247–264. (in Chinese).

Deng, Q. D. (1980). *The main characteristics of Cenozoic fault block structures in China*. Beijing: Geological Press, 101–108. (in Chinese).

Deng, Q. (2007). *Map of active tectonics in China*. Beijing: Seismological Press. (in Chinese).

Ding, G. Y. (1991). *Introduction to lithospheric dynamics in China*. Beijing: Seismological Press, 1–49. (in Chinese).

Du, P. S. (2000). Slip displacement and its rate along Zemuhe fault. *Earthq. Res. Sichuan* 1, 49–64. doi:10.3969/j.issn.1001-8115.2000.02.004

Eberhart-Phillips, D., Haeussler, P. J., Freymueller, J. T., Frankel, A. D., Rubin, C. M., Craw, P., et al. (2003). The 2002 Denali Fault earthquake, Alaska: A large magnitude, slip-partitioned event. *Science* 300 (5622), 1113–1118. doi:10.1126/science.1082703

Feng, Y., and Du, P. (2000). Geologic tectonic and earthquake preparation conditions about the 1850 Xichang earthquake. *Earthq. Res. Sichuan* 2000 (1), 97–101. doi:10.3969/j.issn.1001-8115.2000.02.007

Gan, W., Zhang, P., Shen, Z., Niu, Z., Wang, M., Wang, Y., et al. (2007). Present-day crustal motion within the Tibetan Plateau inferred from GPS measurements. *J. Geophys. Research-Solid Earth* 112 (B8), B08416–B08596. doi:10.1029/2005jb004120

Gao, S. P. (2021). "Late Quaternary paleoseismology and faulting behavior of the internal and Western boundary faults of Northwest Sichuan Subblock," (China: Institute of Geology). Ph.D. thesis.

Gao, W., He, H., Sun, H., and Wei, Z. (2016). Paleoearthquakes along Puxiong fault of daliangshan Fault Zone during late quaternary. *Seismol. Geol.* 38 (4), 797–816. doi:10.3969/j.issn.0253-4967.2016.04.001

He, H., and Oguchi, T. (2008). Late Quaternary activity of the Zemuhe and Xiaojiang faults in southwest China from geomorphological mapping. *Geomorphology* 96 (1-2), 62–85. doi:10.1016/j.geomorph.2007.07.009

He, H., and Ren, J. W. (2003). Holocene earthquakes on the Zemuhe Fault in southwestern China. *Ann. Geophys.* 46 (5), 1035–1051. doi:10.4401/ag-3444

Huang, Z., and Tang, R. (1983). The Zemuhe fault and earthquake. *J. Seismol. Res.* 1983 (02), 167–177.

Keller, E. A., and Pinter, N. (2002). *Active tectonics: Earthquakes, uplift, and landscape*. New Jersey, U.S: Prentice Hall.

Kirby, E., Reiners, P. W., Krol, M. A., Whipple, K. X., Hodges, K. V., Farley, K. A., et al. (2002). Late Cenozoic evolution of the eastern margin of the Tibetan Plateau: Inferences from 40 Ar/39 Ar and (U-Th)/He thermochronology. *Tectonics* 21 (1), 1-1–1-20. doi:10.1029/2000tc001246

Li, T. S., Du, Q. F., and Yang, Z. L. (1997). *The active Xianshuihe Fault and seismic risk assessment*. Chengdu: Chengdu Cartographic Publishing House. (in Chinese).

Liang, S. M., Gan, W. J., Shen, C. Z., Xiao, G. R., Liu, J., Chen, W. T., et al. (2013). Three-dimensional velocity field of present-day crustal motion of the Tibetan Plateau derived from GPS measurements. *J. Geophys. Res. Solid Earth* 118 (10), 5722–5732. doi:10.1002/2013jb010503

Molnar, P., and Qidong, D. (1984). Faulting associated with large earthquakes and the average rate of deformation in central and eastern Asia. *Geophys. Res.* 89, 6203–6227. doi:10.1029/jb089ib07p06203

Peltzer, G., Tapponnier, P., Gaudemer, Y., Meyer, B., Guo, S., Yin, K., et al. (1988). Offsets of late Quaternary morphology, rate of slip, and recurrence of large earthquakes on the Chang Ma fault (Gansu, China). *J. Geophys. Res.* 93 (B7), 7793–7812. doi:10.1029/jb093ib07p07793

Qian, H. C., Allen, R., Luo, Z. L., Wen, X. Z., Zhou, H. Y., and Huang, W. X. (1988). The active characteristics of the Xianshuihe fault in the Holocene. *Earthq. Res. China* 02, 11–20.

Ran, Y., Chen, L., Cheng, J., and Gong, H. (2008a). Late Quaternary surface deformation and rupture behavior of strong earthquake on the segment north of Mianning of the Anninghe fault. *Sci. China Ser. D Earth Sci.* 51 (9), 1224–1237. doi:10.1007/s11430-008-0104-6

Ran, Y., Chen, L., Cheng, J., and Gong, H. (2008b). New evidence of paleoearthquakes and date of the latest event on the Xiaoxiangling Mountain segment of the Anninghe fault zone. *Seismol. Geol.* 22 (1), 1–8. doi:10.3969/j.issn.0253-4967.2008.01.006

Reimer, P., Austin, W., Bard, E., Bayliss, A., Blackwell, P., Bronk Ramsey, C., et al. (2020). The IntCal20 Northern Hemisphere radiocarbon age calibration curve (0-55 cal kBP). *Radiocarbon* 62 (4), 725–757. doi:10.1017/RDC.2020.41

Ren, J. (1994). Late quaternary displacement and slip rate of Zemuhe Fault In sichuan, China. *Seismol. Geol.* 16 (2), 146.

Ren, J., and Li, P. (1993). The characters of surface faulting of the 1850 earthquake in Xichang, Sichuan. *Seismol. Geol.* 15 (2), 97–106.

Ren, Z. K., Lin, A. M., and Rao, G. (2010). Late pleistocene-holocene activity of the Zemuhe Fault on the southeastern margin of the Tibetan plateau. *Tectonophysics* 495, 324–336. doi:10.1016/j.tecto.2010.09.039

Shen, Z. K., Lü, J. N., Wang, M., and Bürgmann, R. (2005). Contemporary crustal deformation around the southeast borderland of the Tibetan Plateau. *J. Geophys. Res.* 110 (B11409). doi:10.1029/2004JB003421

Song, F., Li, R., and Xu, X. (2002). Preliminary results of the investigation of paleo-earthquakes along the daliangshan Fault Zone, sichuan Province, China. *Seismol. Geol.* 24 (1), 27–34. doi:10.3969/j.issn.0253-4967.2002.01.003

Sun, H. Y., He, H. L., Ikeda, Y., Wei, Z. Y., Chen, C. Y., Xu, Y. R., et al. (2019). Paleoearthquake history along the southern segment of the Daliangshan fault zone in the southeastern Tibetan Plateau. *Tectonics* 38, 2208–2231. doi:10.1029/2018tc005009

Sun, H. Y., He, H. L., Wei, Z. Y., Shi, F., and Gao, W. (2015). The late Quaternary activity of Zhuma fault on the north segment of the Daliangshan fault zone. *Seismol. Geol.* 37 (02), 440–454. doi:10.3969/j.issn.0253-4967.2015.02.008

Tapponnier, P., Peltzer, G., Le Dain, A. Y., Armijo, R., and Cobbold, P. (1982). Propagating extrusion tectonics in Asia: New insights from simple experiments with plasticine. *Geology* 10 (12), 611–616. doi:10.1130/0091-7613(1982)10<611:petian>2.0.co;2

Tapponnier, P., Zhiqin, X., Roger, F., Meyer, B., Arnaud, N., Wittlinger, G., et al. (2001). Oblique stepwise rise and growth of the tibet plateau. *Science* 294 (5547), 1671–1677. doi:10.1126/science.105978

Tapponnier, P., Peltzer, G., and Armijo, R.(1986) On the mechanics of the collision between India and Asia. In M. P. Coward and A. C. Ries (Eds.) *Collision tectonics*. London: Special Publication Geological Society, 115–157.

Tian, Q., Ren, Z. K., and Zhang, J. L. (2008). Study of paleoearthquakes by combined trench on Zemuhe fault around Daqingliangzi Xichang, Sichuan. *Seismol. Geol.* 30 (2), 400–411. doi:10.3969/j.issn.0253-4967.2008.02.006

Wan, X. Q., Jansa, L. F., and Sarti, M. (2002). Cretaceous and Paleogene boundary strata in southern Tibet and their implication for the India-Eur-Asia collision. *Lethaia* 35 (2), 131–146. doi:10.1111/j.1502-3931.2002.tb00074.x

Wang, H., Ran, Y., Chen, L., and Li, Y. (2017). Paleoearthquakes on the Anninghe and Zemuhe fault along the southeastern margin of the Tibetan Plateau and implications for fault rupture behavior at fault bends on strike-slip faults. *Tectonophysics* 721, 167–178. doi:10.1016/j.tecto.2017.08.030

Wang, H., Ran, Y., Chen, L., Liang, M., Gao, S., Li, Y., et al. (2018). Determination of slip rate on the southern segment of the Anninghe fault. *Seismol. Geol.* 40 (5), 967–979. doi:10.3969/j.issn.0253-4967.2018.05.002

Wang, H., Ran, Y. K., and Li, Y. B. (2011). Growth of a small pull-apart basin and slip rate of strike-slip fault: With the example of the Zemuhe fault on the southeastern margin of the Tibetan Plateau. *Seismol. Geol.* 33 (4), 818–827. doi:10.3969/j.issn.0253-4967.2011.04.007

Wang, H., Ran, Y., Li, Y., and Chen, L. (2014). Paleoseismic behavior of the Anninghe fault and its comparison with the Zemuhe fault in Western Sichuan. *Seismol. Geol.* 36 (3), 706–717. doi:10.3969/j.issn.0253-4967.2014.03.013

Wang, H., Ran, Y., Li, Y., Gomez, F., and Chen, L. (2013). Holocene palaeoseismologic record of earthquakes on the Zemuhe fault on the southeastern margin of the Tibetan Plateau. *Geophys. J. Int.* 193 (1), 11–28. doi:10.1093/gji/ggs095

Wang, H. (2012). "Recurrence behavior and interactions of large earthquakes on the Anninghe Fault and Zemuhe Fault along the eastern margin of the sichuan-yunnan faulted block," (China: Institute of Geology). Ph.D. thesis.

Wang, M., and Shen, Z. K. (2020). Present day crustal deformation of continental China derived from GPS and its tectonic implications. *J. Geophys. Res. Solid Earth* 125, e2019JB018774. doi:10.1029/2019JB018774

Wang, Q., Zhang, P. Z., Freymueller, J. T., Bilham, R., Larson, K. M., Lai, X., et al. (2001). Present-day crustal deformation in China constrained by global positioning system measurements. *Science* 294 (5542), 574–577. doi:10.1126/science.1063647

Wang, Y. Z., Wang, E. N., Shen, Z. K., Wang, M., Gan, W. J., Qiao, X. J., et al. (2008). GPS-constrained inversion of present-day slip rates along major faults of the Sichuan-Yunnan region, *China.Scientia Sin. (Terrae)* 38(5), 582–597. doi:10.3321/j.issn:1006-9267.2008.05.006

Wei, Z. Y., He, H. L., Shi, F., Xu, Y. R., Bi, L. S., and Sun, H. Y. (2012). Slip rate on the south segment of Daliangshang fault zone. *Seismol. Geol.* 34 (02), 282–293. doi:10.3969/j.issn.0253-4967.2012.02.007

Wells, D. L., and Coppersmith, K. J. (1994). New empirical relationships among magnitude, rupture length, rupture width, rupture area, and surface displacement. *Bull. Seismol. Soc. Am.* 84 (4), 974–1002.

Wen, X. (2000b). The character of rupture segmentation of the Xianshuihe-Anninghe-Zemuhe fault zone, Western China. *Seismol. Geol.* 22 (3), 239–249. doi:10.3969/j.issn.0253-4967.2000.03.005

Wen, X. Z. (1989). An overview of the research on the future first risk of strong earthquakes in the xianshuihe fracture zone. *Recent Dev. World Seismol.* 7, 1–5.

Wen, X. Z. (1995). *Quantitative estimates of seismic potential on active faults*. Maharashtra: Seismological Press.

Wen, X. Z., Xu, X., Zheng, R., Long, D., Du, P., Xie, Y., et al. (2001). "The Late Quaternary activity of the Moxi fault and the recurrence interval of the large earthquake," in *Neostructure and environment* (Peking: Seismological Press), 255–265.

Wen, X., Du, P., and Long, D. (2000a). New evidence of paleoearthquakes and date of the latest event on the Xiaoxiangling Mountain segment of the Anninghe fault zone. *Seismol. Geol.* 22 (1), 1–8. doi:10.3969/j.issn.0253-4967.2000.01.001

Wen, X. Z., Ma, S. L., Lei, X. L., Nishizawa (Kuwahara), Y., Tsutomu, K., and Chen, Q. (2007). Newly found surface rupture remains of large historical earthquakes on and near the transition segment of the Anninghe and Zemuhe fault zones, Western Sichuan, China. *Seismol. Geol.* 29 (4), 826–833. doi:10.3969/j.issn.0253-4967.2007.04.013

Xu, X., Tan, X., Yu, G., Wu, G., Fang, W., Chen, J., et al. (2013). Normal-and oblique-slip of the 2008 yutian earthquake: Evidence for eastward block motion, northern Tibetan plateau. *Tectonophysics* 584, 152–165. doi:10.1016/j.tecto.2012.08.007

Xu, X., Wen, X., Zheng, R., Ma, W., Song, F., and Yu, G. (2003). Pattern of latest tectonic motion and its dynamics for active blocks in Sichuan-Yunnan region, China. *Sci. China Ser. D Earth Sci.* 46 (2), 210–226. doi:10.1360/03dz0017

Xu, X., Zhang, P., Wen, X., Qin, Z., Chen, G., and Zhu, A. (2005). Features of active tectonics and recurrence behaviour of strong earthquakes in the Western Sichuan Province and its adjacent regions. *Seismol. Geol.* 27 (3), 446–461. doi:10.1103/PhysRevB.73.104437

Yu, W. X., Song, F. M., Wen, X. Z., and Li, X. Z. (2001). Study of the surface rupture zone of the Xichang earthquake in 1850. *J. Seismol. Res.* 2001 (04), 346–350. doi:10.3969/j.issn.1000-0666.2001.04.011

Zhang, P. Z. (1999). Late Quaternary tectonic deformation and earthquake hazard in continental China. *Quat. Res.* 1999 (05), 404–413.

Zhang, P. Z., Deng, Q. D., Zhang, G. M., Ma, J., Gan, W., Min, W., et al. (2003). Active tectonic blocks and strong earthquakes in the continent of China. *Sci. China Ser. D Earth Sci.* 2003 (2), 13–24. doi:10.1360/03dz0002

Zhang, P. Z. (2008). Present tectonic deformation, strain distribution, and deep dynamic process in the Western Sichuan area on the eastern margin of the Qinghai-Tibet Plateau (in Chinese). *Sci. China Ser. D Earth Sci.* 38 (9), 1041. doi:10.1360/zd2008-38-9-1041

Zhang, P. Z., Shen, Z., Wang, M., Gan, W., Bürgmann, R., Molnar, P., et al. (2004). Continuous deformation of the Tibetan Plateau from global positioning system data. *Geology* 32 (9), 809–812. doi:10.1130/g20554.1

Zhang, P. Z., Wang, Q., and Ma, Z. (2002). GPS velocity field and active crustal blocks of contemporary tectonic deformation in continental China. *Earth Sci. Front.* 9 (2), 430–441. doi:10.3321/j.issn:1005-2321.2002.02.022

Zhou, R. J., He, Y., Huang, Z., Li, X., and Yan, T. (2001). The slip rate and strong earthquake recurrence interval on the Qianning-Kangding segment of the Xianshuihe fault zone. *ACTA Seismol. SIN.* 2001 (03), 250–261+336. doi:10.3321/j.issn:0253-3782.2001.03.004

Zhou, R. J., Li, X., and Huang, Z. (2003). Average slip rate of daliang mountain Fault Zone in sichuan in late quaternary period. *J. Seismol. Res.* 26 (2), 191–196. doi:10.3969/j.issn.1000-0666.2003.02.013

Frontiers in Earth Science

Investigates the processes operating within the major spheres of our planet

Advances our understanding across the earth sciences, providing a theoretical background for better use of our planet's resources and equipping us to face major environmental challenges.

Discover the latest Research Topics

See more →

Frontiers

Avenue du Tribunal-Fédéral 34
1005 Lausanne, Switzerland
frontiersin.org

Contact us

+41 (0)21 510 17 00
frontiersin.org/about/contact